Point Contact Andreev Reflection and Tunneling Spectroscopy using High-Field Superconductors, Topological Insulators and Compensated Ferrimagnets

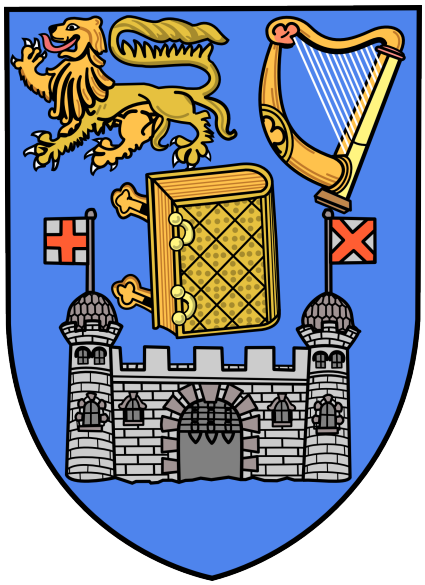

Kiril Borisov

Department of Physics

University of Dublin

A thesis submitted in part-fulfillment of the requirements for the degree of

Doctor of Philosophy

March 2017

Declaration

This thesis is submitted by the undersigned for examination for the degree of *Doctor of Philosophy* at the University of Dublin. I declare that this thesis has not been submitted as an exercise for a degree at this or any other university. It is entirely my own work, apart from the joint effort mentioned in the acknowledgments and in the text.

I agree to deposit this thesis in the University's open access institutional repository or allow the library to do so on my behalf, subject to Irish Copyright Legislation and Trinity College Dublin conditions of use and acknowledgments.

_____

Kiril Borisov

Dedicated to: Elena, Biser, Dimitar and Dilyana.

Acknowledgements

I would like to thank my thesis advisor Dr. Plamen Stamenov. He has been helpful in every aspect of my work and we have been holding discussions on experimental setup, data acquisition/analysis software and physical theories. He has given me all the freedom to progress at my own pace and to work on interesting topics. My often sluggish advancement has been always met with too much patience by him. Outside of the lab, Plamen has offered a lot of life important pieces of advice: which areas of Dublin have good price/quality ratios, which is the best rent-a-car company and others. It suffices to say that when I arrived in Dublin four years ago, he met me at the airport. He has been definitely more than just a thesis advisor.

I would like to thank Professor J.M.D. Coey for the opportunity to be part of the big Group D and benefit from the skills and expertise of the other members (and possibly contribute something). I had the chance to benefit from his vast knowledge in magnetism and spin electronics through participation in joint meetings and discussions.

I would like to acknowledge support from Dr. Karsten Rode, Dr. Gwenael Atcheson, and Dr. Naganivetha Thiyagarajah. Karsten has been the chief motivator behind the results in Chapter 6 and the progress on the Mn_2Ru_xGa would not have been so great if it was not for his passion on the subject. He had been trying to teach me to write clearly (and scientifically) and he quit on that. I am not sure whether I improved (slightly) or he gave up on a bad student but I think it is the latter. Gwenael and Naganivetha have provided me with many samples for measurements and many results in this thesis are exactly on their sputtered thin films. I would like to acknowledge as well Dr. Munuswamy Vanketasan for help with magnetometry measurements, Dr. Lorena Monzon for chemistry advices, Dr. Stephen Connaughton for everything I know about dilution refrigeration and wire bonding, and Dr. Zsolt Gercsi for help with the Janis cryostat.

From my fellow PhD students, my deepest thanks go to Dr. Davide Betto, Dr. Yong-Chang Lau, and (not-yet-Dr.) Stephen-Barry Porter. Davide has been a great inspiration with his knowledge and skills. I do not know how many coffees we have shared on many topics: from magnetism through football. I still can not understand where he was getting his energy to work so much. Yong-Chang has provided me many samples as well and I know everything about magnetic tunnel junctions patterning from him. He has been a quiet guy but whenever he has something to say it has been

always correct and relevant. Yong-Chang and Davide have significant contribution towards the tunneling magnetoresistance results with Mn_2Ru_xGa and it has been great privilege to work with them overall. We have had great late evening and weekend measurement sessions with Stephen but everything has failed spectacularly so far: multiferroic tunnel junctions, YBCO superconducting thin films, oh wait ... not everything ... the electric force microscopy on $BaTiO_3$ worked. We gave our best but it is obvious that our best is not enough. I would like to thank as well Dr. Pelin Tozman for rapid thermal annealing and magnetometry help. Dr. Huseyin Tokuc and Dr. Hongjun Xu are thanked for their guidance on the UHV organic deposition chamber. Akshara Verma is thanked for keeping me involved in her experimental measurements on Si nanowires and Jane O'Reilly* for not complaining too much to Stephen when he stayed late evenings with me and not with her.

A lot of my work has been achieved with overseas collaborators. I acknowledge the help of Dr. Ciarán Fowley, Ms. Alexandra Titova, and Dr. Alina Deac from Helmholtz-Zentrum Dresden-Rossendorf, Institute of Ion Beam Physics and Materials Research, Dresden, Germany on the Mn_2Ru_xGa magnetic tunnel junctions research. The work on the Ne^+-irradiated $Fe_{60}Al_{40}$ thin films has been done in collaboration with Dr. Rantej Bali from the same institution. The spin polarization measurements on the topological insulator family $(Bi_{1-x}Sb_x)_2Te_3$ have been performed in collaboration with Dr. Cui-Zu Chang and Prof. Jagadeesh Moodera from the Francis Bitter Magnet Laboratory, MIT, USA. Finally, superconducting MgB_2 thin films for some of my high-field PCAR measurements have been provided by Dr. Maros Gregor and Prof. Andrej Plecenik from the Comenius University in Bratislava.

I have shared office with many people and I thank them for keeping a good atmosphere: Dr. Huseiyn Tokuc, Dr. Jose Caridad, Dr. Kyle Ballantine, Dr. David McCloskey, Dr. Ronan Darcy, Dr. Joao Coelho†, Dr. Eleanor Holmes, Chuan Zhong, Sonia Metel, and Katarzyna Siewierska‡. The main co-user of the PPMS system, Cormac Ó Coileáin, is thanked for bearing with my demand on the system.

Finally, I would like to thank the bad financial management system in BOC Ireland. The company kept providing us with liquid helium while Trinity College Dublin had an outstanding balance of $\approx$ 50,000 EUR. The company should have blocked the supply and this thesis would have never become a reality.

*Or Porter?!

†Hereby, I officially apologize for that slap two years ago.

‡The last two Polish ladies are thanked for lovely cakes as well.

Abstract

Spin electronics is a young and thriving research and technology field which relies more on the spin of the electron rather than its charge. The tunneling magnetoresistance and giant magnetoresistance effects have been already utilized in novel non-volatile magnetic memories and highly sensitive magnetic sensors. The improvement of the current magnetic storage and detection devices depends critically on integration of new compositions with enhanced magnetic and magneto-transport properties. The data retention and further scalability depend on materials with higher anisotropy and lower magnetization. A critical parameter is the spin polarization, because the tunneling magnetoresistance and the giant magnetoresistance effects depend on it, so does the switching efficiency through the spin-transfer torque. Therefore, novel materials with higher anisotropy, lower magnetization and higher spin polarization are sought-after. Among the spin polarization measurement techniques, point contact Andreev reflection has established itself as a reliable, straight-forward and swift method. This thesis focuses on the technique of point contact Andreev reflection (PCAR) for spin polarization measurements in new materials like topological insulators and disorder ferromagnetic compositions. Systematic effort is made to extend the technique of Andreev reflection to high magnetic field in order to determine the sign of the spin polarization. The integration of novel compensated half-metallic ferromagnetic composition in magnetic tunnel junctions is presented as well.

The thesis starts with a brief theoretical overview of the spin electronic field in Chapter 1. The main devices and physical effects are described. The Blonder-Tinkham-Klapwijk (BTK) theory, which is the most widely used one for data analysis of PCAR experiments is outlined as well.

All measurement techniques and equipment used during this work are described in the experimental Chapter 2.

Topological insulators have become an intense scientific area during the last decade after the realization of Quantum Spin Hall effect by Molenkamp's group in 2007. Later, topological insulating state has been achieved in single materials with high spin-orbit interaction, where arguably the biggest success is the topological insulating family $(Bi_xSb_{1-x})_2Te_3$, in which case a total compensation of the bulk conductivity can be achieved. Chapter 3 focuses on the spin polarization measurements in this topological insulator family. The in-plane spin polarization of all pristine

compositions is extracted to be above 57 %, and it reaches 83 % for the composition which exhibits the most reduced bulk conductance. More importantly, carrier depletion has been demonstrated in the two end compositions, Bi_2Te_3 and Sb_2Te_3, by the observation of structure in the differential conductance when the superconducting tip is quenched in high-field. Furthermore, the influence of paramagnetic ion doping on the spin polarization values has been investigated. Both chromium and vanadium doping decrease the spin polarization values. The spin momentum locking in topological insulators provides spin polarization sign reversal by a mere switch in the polarity of a ballistic current, a functionality which can be very beneficial in future spin electronics devices.

The magnetotransport and magnetic properties of the $Fe_{60}Al_{40}$ disordered composition have been investigated in Chapter 4. The disorder is induced by irradiation with Ne^+-ions with variable fluences. The pristine $Fe_{60}Al_{40}$ is weakly paramagnetic, however, Fe-Al antisite defects lead to higher number of Fe-Fe nearest neighbours and ferromagnetic order with Curie temperature up to 620 K. The spin polarization is determined to increase from 10 % in the non-irradiated to 46 % in the sample with the highest irradiation dose. The spontaneous Hall angle is analyzed as well and extracted to reach 3 %, a value close to the highest reported so far for ordinary magnetic compositions *. Furthermore, the saturation magnetization and the Curie temperature are investigated to increase systematically as a function of the irradiation dose.

Chapter 5 focuses on Andreev reflection in high magnetic field. The main goal is extraction of the spin polarization sign through the observation of Zeeman-splitting in the superconductor quasiparticle density of states at temperature of 2 K. The experiments involve Nb-Ti superconducting wires and MgB_2 superconducting films. Clear PCAR signal has been observed up to 9 T with Nb-Ti wires, unfortunately, with no Zeeman splitting. This provides opportunity for spin polarization investigation of novel ferromagnetic compositions where the spin polarization depends strongly on the applied magnetic field. High-field PCAR with MgB_2 superconducting films have demonstrated clear Zeeman splitting of the density of states and the spin polarization sign has been correctly extracted as positive for Fe.

High tunneling magnetoresistance (TMR) effect of 40 % (at 10 K) has been achieved with compensated half-metallic ferrimagnet Mn_2Ru_xGa in Chapter 6. The TMR has been investigated as a function of the applied bias and it exhibits positive-negative sign reversal which is typically not observed in standard magnetic tunnel junctions. Extensive analysis is given of the magnetotransport properties of the devices and the latter demonstrates that the TMR effect is currently limited by the imperfection in the MgO barrier (mainly caused by Mn diffusion). Crucially, appreciable TMR effect has been observed at the very compensation point of the Mn_2Ru_xGa electrode where the magnetization is strictly zero. The latter is taken as a clear indication that the Fermi level spin

*Magnetic topological insulators have reached 99 % in the quantum anomalous Hall regime but they are not considered as "ordinary" magnetic compositions.

polarization in this composition is determined by one of the Mn sublattices rather than by the overall magnetization. Importantly, the devices have demonstrated high magnetic field immunity (at least 0.5 T) in broad temperature range (10 K-300 K), a property which will be critical in future high areal density magnetic random access memories.

Each result chapter finishes with a short conclusion and a more in-depth overview is given at the end of the thesis.

Contents

1 Spin electronics **1**

1.1 Definition of spin . . . 1

1.1.1 Orbital moment . . . 1

1.1.2 Spin of the electron . . . 3

1.1.3 Moment of an atom . . . 4

1.1.4 Exchange interaction and band splitting . . . 6

1.1.5 Spin polarization . . . 9

1.2 Spin electronic devices . . . 11

1.2.1 Spin valves . . . 11

1.2.2 Magnetic tunnel junctions . . . 13

1.2.3 Spin electronic devices as memory and oscillator elements . . . 20

1.3 Superconductivity . . . 24

1.3.1 Quasi-particle density of states . . . 26

1.3.2 Critical field-type I superconductors . . . 29

1.3.3 SQUID device . . . 31

1.4 Spin polarization measurements . . . 33

1.4.1 Spin-resolved photoemission spectroscopy . . . 33

1.4.2 Spin-polarized positron annihilation spectroscopy . . . 34

1.4.3 Spin-polarized scanning tunneling microscopy . . . 35

1.4.4 Anisotropic magnetoresistance sign method . . . 39

1.4.5 Spin polarized tunneling . . . 39

1.4.6 Point Contact Andreev Reflection . . . 44

1.5 Point Contact Andreev Reflection . . . 46

1.5.1 BTK theory . . . 47

1.5.1.1 Spin polarization in the BTK model . . . 51

1.5.2 Modified BTK theory . . . 54

1.5.3 Barrier strength . . . 56

1.5.4 Important remarks . . . 58

1.5.5 Transport regimes . . . 59
1.5.6 Importance of PCAR . . . 61

2 Experimental section **65**
2.1 Physical Properties Measurements System . . . 65
2.2 Point-contact Andreev reflection setup . . . 66
2.3 Differential spectroscopy . . . 72
2.4 SQUID-based PCAR . . . 73
2.5 Change of the spin polarization by induced strain in ferromagnetic layers . . . 75
2.6 Organic deposition chamber and argon ion milling . . . 76
2.7 Wire bonder . . . 77
2.8 Magnetometry . . . 78

3 Spin polarization of topological insulators **81**
3.1 Introduction to topological insulators . . . 81
3.2 Three-dimensional topological insulators . . . 84
3.3 PCAR of $(Bi_{1-x}Sb_x)_2Te_3$ . . . 91
3.4 High-field spectroscopy . . . 98
3.5 Magnetic topological insulators . . . 103
3.6 A peculiar case . . . 107
3.7 Conclusion and outlook . . . 109

4 Spin polarization and magnetotransport properties of irradiated $Fe_{60}Al_{40}$ thin films **111**
4.1 Modification of thin film magnetic properties by irradiation with Ne ions . . . 112
4.2 Spin polarization, magnetotransport and magnetometry properties of $Fe_{60}Al_{40}$ . . . 116
4.3 Conclusion and outlook . . . 124

5 High-field Andreev reflection **127**
5.1 Introduction and importance . . . 127
5.2 Theoretical analysis . . . 128
5.3 High-field experiments with Nb-Ti . . . 137
5.4 High-field PCAR experiments with MgB_2 . . . 149
5.5 Data on MgB_2-CoFe junctions . . . 157
5.6 Conclusions and outlook . . . 165

6 Magnetic tunnel junctions with the compensated half-metallic ferrimagnet Mn_2Ru_xGa **167**
6.1 Introduction . . . 167
6.2 Important characteristics of classical AlO_x and MgO-based magnetic tunnel junctions 170

6.3 Mn_2Ru_xGa: a half-metallic compensated ferrimagnet . . . 175
6.4 Tunneling magnetoresistance realized with Mn_2Ru_xGa . . . 181
6.5 Reasons for a switch in the TMR sign a function of the applied bias . . . 198
6.6 Tunneling magnetoresistance in MTJs with a zero magnetization Mn_2Ru_xGa electrode . . . 204
6.7 Analysis of the barrier properties . . . 210
6.8 Conclusion and outlook . . . 228

7 Conclusion and outlook **231**

A List of publications **235**

B PPMS cool down from warm dewar **237**

C Wire bonding MTJs **243**

D SQUID oven measurements **245**

E SQUID devices: a brief introduction **249**
E.1 Introduction . . . 249
E.2 Flux in a superconducting loop . . . 250
E.2.1 Flux in a homogeneous superconducting ring . . . 250
E.2.2 General theory of Josephson effect . . . 251
E.3 Principle of operation of an a.c. SQUID . . . 254
E.3.1 Josephson junction diffraction equation . . . 255
E.3.2 McCumber parameter and hysteresis . . . 257
E.3.3 Principle of operation . . . 259
E.4 Principle of operation of a DC SQUID . . . 262
E.4.1 Structure and Interference equation . . . 262
E.4.2 Working point and screening parameter . . . 264
E.5 Measuring principles, gradiometers, flux-locked loops . . . 268
E.5.1 Different structure of weak links . . . 268
E.5.2 Measurement principles . . . 268
E.5.2.1 AC SQUID basic readout . . . 268
E.5.2.2 DC SQUID basic readout . . . 270
E.5.3 Flux-locked loops . . . 270
E.5.3.1 RF SQUID flux-locked circuit . . . 271
E.5.3.2 DC SQUID flux-locked circuit . . . 271

E.6 Sensitivity of SQUIDs 272
E.6.1 Sensitivity, noise and gain of an a.c. SQUID 272
E.6.2 Sensitivity, noise and gain of a d.c. SQUID 274

List of Figures

1.1 Schematic representation of the spin (a) and orbital angular moment (b) magnitudes. The magnitudes and the projections along the z-axis are presented. The applied magnetic field $\mu_0 H$ defines the z-axis direction. 4

1.2 Bethe-Slater curve for the exchange interaction sign and magnitude of the $3d$ transition metal elements. 8

1.3 Schematic example of spin-split density of states. Panel (a) - zero spin polarization ($P = 0\,\%$), panel (b) - non-zero spin polarization $0\,\% < P < 100\,\%$, panel (c) - half-metal with $P = 100\,\%$. 10

1.4 Panel (a) - first demonstration of GMR effect by Baibich[14] in Fe(3 nm)/Cr(0.9 nm)) multilayers with 40 periods. The maximum observed GMR is 74 % at $T = 4\,\mathrm{K}$. Curve ⓐ - field is applied in the plane and along the current direction, curve ⓑ - field is in plane and perpendicular to the current direction, and curve ⓒ - field is perpendicular to the plane of the stack. Panel (b) - saturation magnetoresistance in Co/Ru(x)/Co multilayers which demonstrates RKKY coupling. The graph is after Parkin[267]. 11

1.5 Mott two current model for the spin dependent scattering in CIP-GMR spin valves. The top part represents the spin scattering at the two interfaces and the bottom part the corresponding circuits theory. Panel (a)-parallel configuration, Panel (b)-antiparallel configuration. 12

1.6 Panel (a)-the first demonstration of TMR effect. Graph is after Julliere [154]. Panel (b)-high room temperature TMR effect demonstrated by Moodera[235]. 14

1.7 Optimized stack structure for in-plane magnetization MgO-based MTJs. The thickness of each layer is displayed in brackets in nm. This structure has been optimized in our lab and achieves TMR of 295 %. The structure is after Lau[193]. 15

1.8 Schematic representation of the tunneling magnetoresistance between the spin-split density of states of the two ferromagnetic layers, 1 and 2. Positive spin polarization is assumed for both electrodes. Panel (a)-parallel resistance, panel (b)-antiparallel resistance. Red arrows indicate tunneling between spin-up states and blue arrows-between spin-down states. The magnetization directions, M_1 and M_2, are presented as green arrows. 15

1.9 Schematic representation of adiabatic tunneling through a rectangular barrier with thickness d and height U_0. Panel (a): positive bias, panel (b): close to zero bias, and panel (c): negative bias. The transport direction of the tunneling electrons is indicated with a red arrow. It is assumed that the barrier height is not reduced: $eV \ll U_0$. 17

1.10 Schematic representation of the quantum mechanical model of TMR by Slonczewski[310]. Spin-up electron plane wave is assumed to travel from $-\infty$ towards $x = 0$. The exchange axes in the two ferromagnets are generally non-colinear and their magnitude is different. In the barrier region $0 < x < d$, the electron wavefunction, $\psi_{\sigma 2}$, is evanescent. The important parameters are the spin-dependent transmission coefficients in the second ferromagnetic layer: $C_\uparrow$ and $C_\downarrow$. 18

1.11 Panel (a)-Dependence between the effective spin polarization P_{fb} and the barrier height $\kappa^2/k_\uparrow^2$ for different ratios between the Fermi wavevectors for spin-up and spin-down. Panel (b)-Dependence between the normalized TMR and the angle between the magnetizations of the two ferromagnetic electrode. The black curve corresponds to $P_1 = P_2 = 0.5$, and the red curve to $P_1 = P_2 = 0.8$. 20

1.12 Panel (a)-magnetization oscillation regimes under spin-transfer torque for magnetization along z with no anisotropy. Panel (b)-low current results in damped motion. Panel (c)-high current results in stable precession along the axis of the effective field. Panel (d)-higher current leads to magnetization switching. The picture is after Ralph and Stiles[274]. 22

1.13 Schematic representation of FMR resonance mode (a) and AFMR mode (b) in ferrimagnetic systems. The picture is after Geschwind[108]. 23

1.14 Panel (a)-Schematic representation of the concentration of the field lines in Abrikosov vortex cores. The picture is after Kleiner[173]. Panel (b)-Scanning tunneling microscopy of the Abrikosov vortex lattice in $NbSe_2$ at 1.8 K and applied field of 1 T. The figure is after Hess[136]. 26

1.15 Panel (a)-BCS ideal density of states in a superconductor. Panel (b)-the effect of the Dynes' quasiparticle lifetime broadening parameter on the density of states. . . 28

1.16 The total flux Φ_t in an a.c. SQUID as a function of the externally applied flux Φ_e. The black curve corresponds to $\beta_L = 1$, the red one to $\beta_L = 2$, and the blue dotted line is $\Phi_t = \Phi_e$. A hysteretic behaviour is present for $\beta_L > 1$. It is discernible, that the red curve is in effect a succession of quasilinear regions with jumps between them. These jumps are associated with energy dissipation in the SQUID ring, and are crucial for the operation of the detector. 32

1.17 Transfer function of an a.c. SQUID. 32

1.18 Simple schematic of a.c. SQUID read-out circuit. The input coil and tank circuit are represented. 33

1.19 Spin-polarized inverse photoelectron spectroscopy. Panel (a)-relative intensity for majority and minority spins and spin polarization (asymmetry) for Ni. Left side-angle of incidence $\alpha = 0°$, right side-$\alpha = 20°$. Panel (b)-schematic representation of the experimental setup-the photon detector was a Geiger-Müller counter. The sample is a single crystal Ni(110) crystal magnetized along the $(1\bar{1}1)$ direction by the C-shaped electromagnet. The data is after Unguris *et al.*[349]. 34

1.20 Panel (a)-schematic representation of SRPES measuring setup. Panel (b)-example of spin polarization measurement on Fe(110) by SRPES. The data is after Dedkov textitet al.[71]. 34

1.21 SP-STM imaging of magnetic vortex structure. Panel (A)-spin structure with in-plane sensitive tip, Panel (B)-spin structure with out-of-plane sensitive tip, Panel (C)-signal corresponding to the circular path on Panel (A). Panel (D)-the in- plane scan corresponds to the line scan on Panel (A), the out-of-plane scan corresponds to the line scan on Panel (B). The picture is after Wachowiak [362]. 36

1.22 Schematic representation of domain structure at the apex of a ferromagnetic (a) and antiferromagnetic tip (b). Panel (c)-schematic representation of a modulation coil wound around the tip. The picture is after Bode [32]. 37

1.23 Spin polarization bias dependence of Gd(0001) sample. Two different experimental techniques are compared: SP-STM[33] and spin-polarized inverse photoemission spectroscopy[76]. The picture is after Wiesendanger [373]. 38

1.24 Representation of the Zeeman-split quasiparticle density of states in a superconductor on panel (a). Simulated spin tunneling spectroscopy for the case of non-polarized metal with the parameters applied field $\mu_0 H = 2\,\mathrm{T}$, temperature $T = 0.3\,\mathrm{K}$, and superconducting gap $\Delta = 400\,\mu\mathrm{eV}$ on panel (b). 41

1.25 Spin-polarized tunneling simulated for three different spin polarizations $P = 0.0$ (black), $P = 0.4$ (red), and $P = 0.6$ (green curve). Constants for the simulation are temperature $T = 0.3\,\mathrm{K}$, and the ratio of the Zeeman splitting energy to superconducting gap is $\mu_B\mu_0 H/\Delta = 0.43$. 42

1.26 Simulated spin-polarized tunneling curve with polarization $P = 0.4$, temperature $T = 0.3\,\mathrm{K}$, superconducting gap $\Delta = 400\,\mu\mathrm{eV}$, and magnetic field $\mu_0 H = 2\,\mathrm{T}$. Panel (a) - the orbital depairing, ζ, is varied while the spin-orbit coupling, b, set to zero. Panel (b) - the spin-orbit coupling, b, is varied while the orbital depairing, ζ, is set to zero. 44

1.27 Schematic representation of the Andreev reflection process and the corresponding differential conductance. Panel (A)-spin sub-bands of a non- polarized metal (Cu). Panel (B)-the corresponding differential conductance of a Nb/Cu point contact with an increasing zero bias conductance. Panel (C)-spin sub-bands of a half-metallic ferromagnet (CrO_2). Note the Andreev reflection is forbidden. Panel (D)-the corresponding differential conductance of a Nb/CrO_2 point contact with a suppressed zero bias conductance. The picture is after Soulen *et al.*[314]. 45

1.28 Alternative view on the electron conversion between a normal metal (N) and a superconductor (S) at sub-gap bias. Panel (a): non-polarized material, there are equal density of spin-up and spin-down electrons and the conductance is high. Panel (b): fully spin polarized material, there are no electrons with opposite spin and the conductance is suppressed. 47

1.29 Simulated PCAR spectra following the BTK theory for different barrier strength Z and spin polarization P. The temperature for the simulations is set at $T = 4\,\mathrm{K}$. Each panel has curves for five different values of the spin polarization $P = 0.0, 0.25, 0.5, 0.75,$ and 1.0. Panel (a)-$Z = 0.0$, panel (b)-$Z = 0.25$, panel (c)-$Z = 0.5$, and panel (d)-$Z = 0.75$. 53

1.30 Simulated PCAR spectra for $P = 0.0$ (panel (a)) and $P = 1.0$ (panel (b)). Different barrier strengths ($Z = 0.0, 1.0, 2.0,$ and 5.0) are presented. The temperature is set at $T = 4\,\mathrm{K}$. 54

1.31 Simulated spectra following the modified BTK theory. The spin polarization is fixed to $P = 0.5$ on all panels. Panel (a)-$Z = 0.0$, Panel (b)-$Z = 0.25$, Panel (c)-$Z = 0.5$, and Panel (d)-$Z = 0.75$. Features known as finite bias dips are indicated with brown arrows on panel (a). The temperature is set at $T = 4\,\mathrm{K}$. 55

1.32 Superconducting order parameter at the interface between a superconductor and a normal metal (a), and between a superconductor and a ferromagnet (b). The picture is after Buzdin[47]. 56

1.33 Panel (a)-spin polarization of Co and Fe depending on Z^2 following the extrapolation $P = P_0 \exp(-2\alpha\psi Z^2)$. The inset demonstrates fit on the Co data with a parabola, the high Z region is not covered well. The graph is after Kant[158]. Panel (b)-spin polarization of Ni, Co, and Fe with the quadratic extrapolation. The graph is after Strijkers[321]. 57

2.1 PCAR sample space for standard needle(Nb)-anvil(sample) measurement configuration. Some of the important components of the setup are indicated: Nb tip, vertical piezo-stepper, horizontal piezo-stepper, and the Cernox temperature sensor. 67

2.2 Picture of the wired electro-optical probe for PCAR measurements. The 7 pin connectors are visible on the bottom-most brass baffle just above the samples space. 68

2.3 Schematic representation of the PCAR experimental setup and the electronic measurements circuit. Micrometer positioning rod is available in the old PCAR setup constructed by Dr. P. Stamenov for an Oxford cryostat. 68

2.4 Schematic representation of the electronic circuit for the two LIA PCAR data acquistion. 69

2.5 Experimental setup for in-plane PCAR spectroscopy measurements. The MgB_2 superconducting film is mounted on an L-shaped holder. The Fe tip is insulated from the sample holder with a slotted Teflon cylinder. An auxiliary two wire connector is present just to the left of the L-shaped holder. This connector is used for providing the polling voltage for the investigation of the spin polarization strain dependence in ferroelectric/ferromagnetic bilayers. 70

2.6 Pictures of the PCAR electronics rack (a) and the Physical Properties Measurements System (b). 71

2.7 Pictures of the SQUID pre-amplifier setup: old (a) and new (b). 74

2.8 Example of PCAR measurements with SQUID pre-amplifier: single PCAR (a) and PCAR magnetic field scan(b). 74

2.9 Example of spin polarization dependence on the applied electric field in AlN/CoFe bilayer. 75

2.10 Pictures of the organic deposition chamber. (a) - inside view of the sample stage rotational mechanism. The argon gun is switched on for illumination. (b) - overview picture of the chamber. 76

2.11 Picture of the wire bonder used for bonding of the Mn_2Ru_xGa-based magnetic tunnel junctions. 78

2.12 (1) - schematic representation of the second-order superconducting gradiometer pick-up coils configuration in a SQUID magnetometer. (2) - representation of the measured signal as a function of distance. The graph is after Black and Wellstood [29]. 80

2.13 SQUID oven measurement of a $Mn_2Fe_{0.75}Ga$ thin film with perpendicular magnetic anisotropy. The extracted Curie temperature is 695 K and the scan is done in the remanent magnetic state. 80

3.1 Panel (a): Example of the first demonstration of quantum Hall effect in Si-MOSFET. The graph is after von Klitzing[175]. Panel (b): Schematic representation of the locked electrons orbits and the edge transport in a quantum Hall effect. The magnetic field is applied outside of the plane. 82

3.2 Comparison between the edge states in Quantum Hall effect for fill factor $\nu = 2$ (a) and Quantum Spin Hall effect (b). 82

3.3 Panel (a)-demonstration of the Hall effect quantization once the Fermi level is tuned in the bulk bandgap (gate voltage = threshold voltage). Sample I-normal QW band structure $\rightarrow$ no quantization ($d = 5.5\,\text{nm}$), samples II, III, and IV are samples with inverted band structure ($d = 7.3\,\text{nm}$). The size of the devices is (20×13.2) μm^2 for I and II, (1.0×1.0) μm^2 for III, and (1.0×0.5) μm^2 for IV. The graph is after König[179]. Panel (b)-demonstration of the edge channel conductance additivity depending on the number of edges. The graph is after Roth[280]. 83

3.4 Panel (a)-ARPES study of $Bi_{0.91}Sb_{0.09}$ along the $\overline{\Gamma}$-$\overline{M}$ direction. Five bands cross E_F. The graph is after Hsieh[144]. Panel (b) and (c)-ARPES study of $Bi_2Se_3(111)$ along $\overline{\Gamma}$-$\overline{M}$ and $\overline{\Gamma}$-$\overline{K}$, respectively. Single Dirac cone is present. These graphs are after Xia[388]. 84

3.5 Panel (a)-tetradymite crystal structure of $(Bi_{1-x}Sb_x)_2Te_3$. Panel (b)-schematic representation of the band structure of Bi_2Te_3. Panel (c)-schematic representation of the band structure of Sb_2Te_3. The graph is after Zhang *et al.* [408]. 85

3.6 Temperature dependence of the sheet resistance of the $(Bi_{1-x}Sb_x)_2Te_3$. The figure is after Zhang *et al.*[408]. 86

3.7 Angular resolved photoemission spectroscopy of $(Bi_{1-x}Sb_x)_2Te_3$. Panel (a)-$x = 0$, panel (b)-$x = 0.88$, panel (c)-$x = 0.94$, and panel (d)-$x = 0.96$. The figure is after Zhang *et al.*[408]. The abbreviations are as follow: BCB-bulk conduction band, BVB-bulk valence band, SS-surface states, DP-Dirac point, and E_F-Fermi level. 87

3.8 Spin-momentum locking data on Bi_2Se_3/TiO_2/Co devices. Panel (a)-electrons flow from III to I in Bi_2Se_3, panel (b)-electrons flow in reversed direction. The TMR-like response is represented below the transport schematics. The graph is after Dankert[68]. 87

3.9 Panel (a)-example of a quantized AHE in magnetic TI with optimal composition $(Bi_{0.29}Sb_{0.71})_{1.89}V_{0.11}Te_3$ at the charge neutral point V_g^0. Note the high coercive field $\mu_0 H_c = 1.1\,T$ and that the longitudinal resistivity has spikes at H_c. Panel (b)-temperature dependence of ρ_{xx} and ρ_{xy} of the same sample in zero magnetic field. The graph is after Chang[55]. 89

3.10 Panel (a)-Schematic representation of the gapped Dirac cone and the hedge-hog like spin structure. Panel (b)-measured out of plane spin polarization. The in-plane momentum for each spin-resolved spectrum is indicated on top. The polar angle (θ) of the spin vectors is indicated as well. The graph is after Xu *et al.*[390]. 90

3.11 Schematic representation of the Andreev process between a superconducting Nb tip a TI sample. The spin direction of the surface carriers in the TI are locked in plane at right angles with respect to the momentum direction whereas the Cooper pairs have in general arbitrary spin orientation. 91

3.12 PCAR spectra along with the mBTK fit and the extracted parameters for Bi_2Te_3 (a) and Sb_2Te_3 (b). The obtained spin polarizations are $70(4)$ % in Bi_2Te_3 and $57(3)$ % in Sb_2Te_3. The extracted parameters from the fits are denoted with asterisks. Each PCAR curve is normalized with a spectrum above the critical temperature of Nb. The inset in panel (a) demonstrates two PCAR conductance curves obtained at $T = 2\,K$ and $T = 10\,K$. The two curves are offset for clarity. 93

3.13 PCAR spectrum along with the mBTK fit and the extracted parameters for a TI composition $(Bi_{0.18}Sb_{0.82})_2Te_3$. The obtained spin polarization is $83(9)$ %. The extracted parameters from the fit are denoted with asterisks. 94

3.14 PCAR temperature scans of Bi_2Te_3 (a) and Sb_2Te_3 (b). The x-axis is in units of Δ_2/q, where $\Delta_2 = 1.5\,meV$ is the bulk superconducting gap of Nb and q is the elementary charge. 96

3.15 Comparison between properly (a) and not corrected (b) PCAR temperature scans of the Bi_2Te_3. The x-axis is in units of Δ_2/q, where $\Delta_2 = 1.5\,meV$ is the bulk superconducting gap of Nb and q is the elementary charge. 97

3.16 Temperature evolution of the zero-bias anomaly of the PCAR data on Bi_2Te_3 (a) and Sb_2Te_3 (b). The phase transition approach is fitted with $(T_c - T)^\gamma$ and the extracted critical exponents are 0.91(2) (Bi_2Te_3) and 0.71(2) (Sb_2Te_3). 98

3.17 PCS temperature scans of Bi_2Te_3 (a) and Sb_2Te_3 (b). Note he amplitude in comparison with amplitudes on Fig. 3.14. The x- axis is in units of Δ_2/q, where $\Delta_2 = 1.5\,\text{meV}$ is the bulk superconducting gap of Nb and q is the elementary charge. 99

3.18 Arrhenius law fit of the zero-bias anomaly (ZBA) of the high-field point- contact spectroscopy (PCS). Panel (a)-PCS ZBA on Bi_2Te_3 with extracted gap of $E_g = 0.40(4)\,\text{meV}$, panel (b)-PCS ZBA on Sb_2Te_3 with extracted gap of $E_g = 0.28(2)\,\text{meV}$. 100

3.19 Magnetic field scan of a Nb/Bi_2Te_3 point contact. Panel (a)-low field scan up to 1 T. The superconductivity disappears around 0.5 T. Panel (b)-high-field scan up to 14 T. The structure does not vanish. 102

3.20 Magnetic field scan of a Nb/Sb_2Te_3 point contact. Panel (a)-low field scan up to 2 T. The superconductivity disappears around 1.0 T. Panel (b)-high-field scan up to 14 T. The structure does not vanish. 102

3.21 Magnitude of the zero-bias amplitude during a field scan of Bi_2Te_3 and Sb_2Te_3. . . 103

3.22 PCAR spectra along with the mBTK fit and the extracted parameters for two samples with Cr-doping : $Bi_{1.97}Cr_{0.03}Te_3$ (a) and $Sb_{1.975}Cr_{0.025}Te_3$ (b). The obtained spin polarizations are $52(1)$ % in $Bi_{1.97}Cr_{0.03}Te_3$ and $52(1)$ % in $Sb_{1.975}Cr_{0.025}Te_3$. The extracted parameters from the fits are denoted with asterisks. 104

3.23 PCAR spectra along with the mBTK fit and the extracted parameters for two samples with V-doping: $Bi_{1.975}V_{0.025}Te_3$ (a) and $Sb_{1.97}V_{0.03}Te_3$ (b). The obtained spin polarizations are $58(5)$ % in $Bi_{1.975}V_{0.025}Te_3$ and 50 % in $Sb_{1.97}V_{0.03}Te_3$. The extracted parameters from the fits are denoted with asterisks. 105

3.24 Anomalous Hall effect measurements on the magnetic topological insulator $Sb_{1.97}V_{0.03}Te_3$. The curves are vertically offset for clarity. The curve at 15 K (above the T_C) demonstrates slight paramagnetic signal. The violet arrow indicates the peak observed at the coercive field due to longitudinal resistance pick-up (see Fig. 3.9). 106

3.25 Panel (a)-Temperature dependence of the absolute anomalous Hall effect signal of $Sb_{1.97}V_{0.03}Te_3$ in remanent state after the sample was saturated in positive and negative direction, respectively. Panel (b)-temperature dependence of the AHE magnitude along with the extracted Curie temperature of $11.6(6)$ K. 106

3.26 Panel (a)-example of s-wave superconducting gap in Cu-intercalated Bi_2Se_3 by scanning tunneling spectroscopy. Panel (b)-example of zero-bias conductance peak when the Ir tip was crashed in the surface. The data is after Levy *et al.*[199]. 107

3.27 Normalized differential conductance (G/G_n) temperature scan of a zero-bias conductance peak (ZBCP) on a contact Nb/Bi_2Te_3. The x-axis is in units Δ_2/q, where $\Delta_2 = 1.5\,\text{meV}$ is the bulk Nb superconducting gap and q is the electrons charge. The bias axis is intentionally zoomed-in to emphasize the ZBCP small structure. . . 108

3.28 Second example of zero-bias conductance peak observed on an Nb/Bi_2Te_3 contact. 109

3.29 Temperature dependence of the zero-bias peak amplitude from Fig. 3.27 and Fig. 3.28. 109

4.1 Hysteresis loop measurements of Pt-Co(0.5 nm)-Pt sandwich irradiated with different fluences. (1) - as-grown sample, (2) - sample irradiated with a dose of 3.10^{15} ions/cm^2, and (3) - sample irradiated with a dose of 10^{16} ions/cm^2. All curves are normalized with the saturation magnetization of the as-deposited sample. The data is after Chappert *et al.*[56]. 113

4.2 Lattice parameter (a) and Curie temperature (b) change of $Fe_{1-x}Al_x$ alloy as a function of the Al atomic concentration. The data is after Yelsukov *et al.*[399]. 113

4.3 Equilibrium Fe-Al phase diagram. The graph is after Taylor *et al.*[333]. 114

4.4 Panels (a)-(c): definition of a pristine $Fe_{60}Al_{40}$ microwire through UV lithography, resist patterning for the Ne^+ exposure, and the magnetic contrast determined by Kerr microscopy. Panel (d) - magnetic contrast determined by spin-polarized photoemission electron microscopy. Schematic representation of the B2 crystal structure of as-deposited $Fe_{60}Al_{40}$ (e) and the A2 (disordered) structure of irradiated sample (f). The substitution with Al atoms on otherwise pure Fe planes is indicated with green arrows. Graphs are after Bali *et al.*[17]. 115

4.5 PCAR spin polarization measurements of $Fe_{60}Al_{40}$ thin films irradiated with Ne^+ ions. Panel (a): PCAR of a non-irradiated sample, which demonstrates negligible spin polarization of $P \approx 10(10)\,\%$. Panel (b): PCAR of a sample irradiated with 2.10^{16} ions/cm^2, which demonstrated the highest spin polarization of $46(3)\,\%$. Panel (c): PCAR spin polarization values of five samples irradiated with different doses. The blue interpolation line is drawn by hand. 116

4.6 Resistance-temperature dependence of $Fe_{60}Al_{40}$ thin films irradiated with different fluences. Black curve - as-deposited sample, red curve - irradiation dose 6.10^{14} ions/cm^2, green curve - irradiation dose 9.10^{15} ions/cm^2, and blue curve - irradiation dose 2.10^{16} ions/cm^2. 117

4.7 Anomalous Hall effect loop at variable temperature for two sample irradiated at doses 6.10^{14} ions/cm^2 (a) and 2.10^{16} ions/cm^2 (b), respectively. 120

4.8 Panel (a): comparison between the spontaneous Hall angle and the magnetization temperature dependence of a sample irradiated wit a dose of 2.10^{16} ions/cm^2. The temperature evolution of the spontaneous Hall angle (red curve) is approximated with a quadratic function. Panel (b): comparison between the spontaneous Hall angle at various temperatures of three samples irradiated at different doses of 2.10^{16} ions/cm^2, 2.10^{15} ions/cm^2, and 6.10^{14} ions/cm^2, respectively. The temperature dependence of the magnetization of each sample is given with a solid line. The magnetization is normalized to the SHA value at 10 K for comparison purposes. . . 120

4.9 Magnetization measurements of four $Fe_{60}Al_{40}$ thin films irradiated with different doses. Panel (a) - hysteresis loops obtained at $T = 4\,\mathrm{K}$ in magnetic field range $\mu_0 H = \pm 5\,\mathrm{T}$. Panel (b) - $M(T)$ scans of the four sample in temperature range 4 K-300 K in applied magnetic field of $\mu_0 H = 1.2\,\mathrm{T}$. The magnetic field is applied perpendicular to the plane of the films for both measurements. 123

4.10 SQUID oven magnetometry measurements of the Curie temperature of three $Fe_{60}Al_{40}$ samples irradiated with different doses. The magnetization of each sample is normalized with its magnetization at $T = 300\,\mathrm{K}$. The applied magnetic field is $\mu_0 H = 1.2\,\mathrm{T}$. 124

5.1 Simulated Tedrow-Meservey spin polarized tunneling for an ideal superconductor with $\Delta = 1.5\,\mathrm{meV}$. The applied magnetic field is $\mu_0 H = 5\,\mathrm{T}$ and the spin polarization is $P = 50\,\%$. 129

5.2 Simulated Zeeman-split PCAR with $Z = 0.0$, $P = 0.0$, $\mu_0 H = 5\,\mathrm{T}$. Panel(a) - PCAR process towards the spin-up and spin- down density of states, respectively. Panel(b) - comparison between PCAR in magnetic field and without magnetic field. 130

5.3 Simulated Zeeman-split PCAR with $Z = 0.0$, $P = 0.5$, $\mu_0 H = 5\,\mathrm{T}$. Panel(a) - PCAR process towards the spin-up and spin- down density of states, respectively. Panel(b) - comparison between PCAR in magnetic field and without magnetic field. 131

5.4 Panel(a): Schematic representation of the hexagonal honey-comb Abrikosov vortex lattice. Each vortex has approximately core size $\approx \xi$ and is surrounded by six neighbours. The circulating supercurrent around the vortex cores is indicated. The approximated circular cell with radius ρ_s is depicted as well. The points 1, 2, and 3 denote different positions in the circular cell: $0, \rho_s/2$, and ρ_s. Panel (b): numerically calculated density of states averaged over a vortex lattice following the solution of the Usadel equations. The curves (d)-(a) correspond to reduced magnetic field values H/H_{c2} = 0.0, 0.05, 0.2, and 0.5, respectively. The data is after Golubov and Kupriyanov[115]. 134

5.5 Scanning tunneling spectroscopy data of Abrikosov vortex bound states. Panel (a) - $\mathrm{d}I/\mathrm{d}V(V)$ of vortex lattice at three different positions: in the core (top), at distance of 7.5 nm (middle) and at distance of 200 nm from the core (bottom). The data is obtained on $NbSe_2$ at 1.85 K and 0.02 T and is after Hess *et al.*[136]. Panel (b) - higher resolution spacial evolution of local $\mathrm{d}I/\mathrm{d}V$. The data is obtained on $NbSe_2$ at 0.3 K in 50 mT. The splitting of the zero-bias peak is manifested in the vicinity of the vortex core. 136

5.6 Critical superconducting temperature of Nb-Ti wires. Panel (a) - superconducting transition of Nb-Ti at various fields. Panel (b) - superconducting transitions at various fields in normalized resistance R/R_{n}. Panel (c) - critical temperatures at various fields along with the superconducting transition width. Panel (d) - Critical temperature of $9.30(6)$ K of Nb-Ti in zero applied external field. 137

5.7 PCAR measurements with Nb-Ti on CoFe (a) and Au (b). The extracted spin polarization are $P_{\mathrm{CoFe}} = 48(3)\,\%$(a) and $P_{\mathrm{Au}} = 4(7)\,\%$, respectively. 138

5.8 PCAR scan of a Nb-Ti/CoFe contact in the temperature range from $T = 2\,\mathrm{K}$ to $T = 10\,\mathrm{K}$. All spectra are normalized with a background curve at 10 K. 139

5.9 Simulated PCAR data for barrier strength $Z = 0.4$ and spin polarization $P = 0.5$ in the temperature scan $T = 2\,\mathrm{K}$ to $T = 9.2\,\mathrm{K}$. 140

5.10 Demonstration of flux jumps (or contact reorientation) on the structure of Andreev reflection in a magnetic field scan of a Nb-Ti/CoFe point contact. The applied bias is in units Δ_2/q, where $\Delta_2 = 1.5\,\mathrm{meV}$, and q is the elementary charge. The temperature is 2 K. 141

5.11 PCAR field scan of a Nb-Ti/CoFe point contact: (a) - field scan from 0 T to 9 T and (b) - PCAR bias asymmetry of the data from panel (a). The temperature is 2 K. The most pronounced vortex jumps are indicated with black arrows on panel (a). 143

5.12 PCAR data and extracted parameters on point-contact between NbTi and CoFe at different applied magnetic field. Panel (a): $\mu_0 H = 0\,\mathrm{T}$, panel (b): $\mu_0 H = 1\,\mathrm{T}$, panel (c): $\mu_0 H = 2\,\mathrm{T}$, panel (d): $\mu_0 H = 3\,\mathrm{T}$, panel (e): $\mu_0 H = 4\,\mathrm{T}$, panel (f): $\mu_0 H = 5\,\mathrm{T}$, panel (g): $\mu_0 H = 6\,\mathrm{T}$, and panel (h): $\mu_0 H = 7\,\mathrm{T}$. Note the asymmetry at 7 T, which is most likely related to vortex dynamics. 145

5.13 Extracted parameters from the fits of the high-field NbTi/CoFe PCAR. Panel (a): spin polarization, P, as a function of the applied magnetic field $\mu_0 H$, panel (b): effective electronic temperature T_{e} as a function of the applied magnetic field $\mu_0 H$, and panel (c): barrier strength Z as a function of the applied magnetic field $\mu_0 H$. The bath temperature for all spectra is $T = 2\,\mathrm{K}$. The interpolation lines are drawn by hand on each graph. 146

5.14 PCAR measurements between Nb-Ti tip and CoFe sample in magnetic field from 10 T to 14 T on panel from (a) to (e). The temperature in all measurements is 2 K. . 147

5.15 PCAR magnetic field scan from $\mu_0 H = -9\,\mathrm{T}$ to $\mu_0 H = 0\,\mathrm{T}$ of a Nb-Ti/CoFe point contact. The applied bias is in units Δ_2/q, where $\Delta_2 = 1.5\,\mathrm{meV}$, and q is the elementary charge. The temperature is 2 K. 147

5.16 Demonstration of PCAR spectroscopy in a magnetic field scan from $\mu_0 H = -9\,\mathrm{T}$ to $\mu_0 H = 0\,\mathrm{T}$ of a Nb-Ti/CoFe point contact. The spectra are rescaled following the procedure described in Eq. (5.19) - Eq. (5.22). The applied bias is in units Δ_2/q, where $\Delta_2 = 1.5\,\mathrm{meV}$, and q is the elementary charge. The temperature is 2 K. Black arrows indicate the most pronounced flux jumps on panel (a). A square conductance asymmetry region is indicated with black dashed lines on panel (b). . 148

5.17 Critical superconducting temperature of MgB_2 films. Panel (a)-superconducting transition of MgB_2 at various fields. Panel (b)-superconducting transitions at various field in normalized resistance R/R_n. Panel (c)-critical temperatures at various fields along with the superconducting transition width. Panel (d)- critical temperature of $32.8(8)$ K of MgB_2 in zero applied external field. 150

5.18 PCAR measurements at zero-field with Fe tip on MgB_2. Panel (a)-example of spectrum which demonstrates single gap and the correct value of the spin polarization is extracted $P_\mathrm{Fe} = 44(4)\,\%$. Panel (b)-example of spectrum which exhibits dual gap. Such spectra are discarded in the high-field analysis. 151

5.19 PCAR measurements between MgB_2(thin film) and Fe(tip) in magnetic field $\mu_0 H = \pm 5\,\mathrm{T}$ perpendicular to the MgB_2 and temperature $T = 2\,\mathrm{K}$. Black arrows indicate pronounced asymmetric regions in the field scan. 152

5.20 Second demonstration of PCAR measurements between MgB_2 (thin film) and Fe (tip) in magnetic field $\mu_0 H = \pm 5\,\mathrm{T}$ perpendicular to the MgB_2 and temperature $T = 2\,\mathrm{K}$. 153

5.21 Example of the effect of vortex dynamics on the PCAR structure of MgB_2/Fe contact in constant field-two metastable asymmetric configurations are presented. The magnetic field is $\mu_0 H = 5\,\mathrm{T}$ and the temperature is $T = 2\,\mathrm{K}$. 154

5.22 Example of four-peak structure in PCAR experiments between MgB_2 thin film and Fe tip. The temperature is $T = 2\,\mathrm{K}$ and the field is applied in plane of the MgB_2 film. Panel (a)-experiment at field $\mu_0 H = 5\,\mathrm{T}$. Panel (b)-experiment at field $\mu_0 H = 7\,\mathrm{T}$. 155

5.23 Linear fit of the rescaled Zeeman split energies versus the applied magnetic field. The intercept corresponds to a zero field effective Zeeman splitting energy of $E_\mathrm{Z}^* = 1.25\,\mathrm{meV}$. 156

5.24 PCAR spectrum along with the BTK fit and the extracted parameters for an MgB_2/CoFe junctions at zero applied field of and $T = 2\,\mathrm{K}$. 158

5.25 In plane (a) and perpendicular to plane (b) high field PCAR scans of $MgB_2/Co_{50}Fe_{50}$ shadow-masked junction. The maximum applied field is $\pm 14\,\mathrm{T}$. The applied bias is in units Δ_2/q, where $\Delta_2 = 1.5\,\mathrm{meV}$, and q is the elementary charge. The temperature is 2 K. 159

5.26 Full angular scans of MgB_2/CoFe junction at applied field of 0 T (a) and 1 T (b). A feature, which is most likely related to noise, is observed on panel (a) for angle $\theta \approx 180^\circ$ (indicated with a black arrow). 160

5.27 Full angular scans of MgB_2/CoFe junction at applied field of 2 T (a) and 3 T (b). . . 161

5.28 Full angular scans of MgB_2/CoFe junction at applied field of 4 T (a) and 5 T (b). . . 161

5.29 Full angular scans of MgB_2/CoFe junction at applied field of 7 T (a) and 14 T (b). . 162

5.30 PCAR temperature evolution of MgB_2/CoFe shadow masked junctions. The temperature scan is performed in zero applied magnetic field. 162

5.31 Temperature decrease of the PCAR zero-bias anomaly for an MgB_2/CoFe shadow-masked junction. The red curve represents an exponential decay fit. 164

6.1 R_P, R_{AP}, TMR for an MgO-based MTJ annealed at 380 °C on the left hand side. Annealing dependence of the TMR and the RA product on the right hand side. The graphs are after Parkin *et al.*[268]. 172

6.2 Comparison between the tunneling spin polarizations (TSP) of Fe in Fe-MgO-$Al_{96}Si_4$ junctions. Panel (a)- TSP in the case of non-annealed junction-TSP = 57 %. Panel (b)-TSP in the case of a junction annealed at 380 °C-TSP = 74 %. The fitting is performed following the Maki-Fulde theory where the superconducting gap (Δ), the spin-orbit coupling (b), the orbital depairing (ζ), and the tunneling spin polarization (TSP) are considered free fitting parameters (see Sec.(1.4.5)). The graphs are after Parkin *et al.*[268]. 173

6.3 Left Hand Side: Resistance-area product as a function of thickness of the MgO barrier for the case of parallel and antiparallel resistance states. TMR effect of 247 % (20 K) and 180 % (293 K) for a junction with $t_{MgO} = 2.3\,\mathrm{nm}$. Right Hand Side: TMR dependence of the barrier thickness t_{MgO}. The picture is after Yuasa *et al.*[403]. 174

6.4 Left Hand Side: TMR(U) for different MgO thicknesses, t_{MgO}, at $T = 293\,\mathrm{K}$. The data is normalized to the value TMR(0 V) for each curve. The picture is after Yuasa *et al.*[403]. Right Hand Side: Differential spectroscopy, $\mathrm{d}I/\mathrm{d}V$, of MgO-based tunneling junctions at 10 K and 300 K for parallel and antiparallel state, respectively. The graph is after Wang *et al.*[365]. 175

6.5 Periodic table describing the possible combinations of elements in Heusler compounds. X is in red, Y is in blue, and Z is in green. The diagram is after Graf *et al.*[119]. 176

6.6 Panel (a)-$L2_1$ crystal structure of a full Heusler alloy X_2YZ (Mn_2RuGa) with X(green), Y(gray), and Z(red). Panel (b)-$C1_b$ half-Heusler XYZ (Mn_2Ga). 178

6.7 AHE data of an $Mn_2Ru_{0.9}Ga$ blanket film with approximate $T_{\mathrm{comp}} = 250\,\mathrm{K}$. Panel (a)-AHE loops at multiple temperatures from 10 K to 350 K and in applied field $\mu_0 H = \pm 14\,\mathrm{T}$. The AHE signal changes its sign above 250 K. Panel (b)-AHE signal dependence on the temperature from 300 K to 10 K in constant magnetic field of $\mu_0 H = 14\,\mathrm{T}$. The point of maximum slope corresponds to the compensation temperature. The inset demonstrates $\mathrm{d}R_{\mathrm{xy}}/\mathrm{d}T(T)$, the maximum value of the derivative demonstrates T_{comp}. 180

6.8 SQUID magnetometry measurements on an $Mn_2Ru_{0.9}Ga$ with compensation temperature of $T_{comp} \approx 250\,\mathrm{K}$, the AHE data on the same sample is presented in Fig. (6.7). The applied magnetic field is perpendicular to the plane of the sample. Panel (a)-$M(T)$ data acquired on warm up in small applied field of $\mu_0 H = 5\,\mathrm{mT}$. The sample was first saturated in 5 T at 10 K. Note that the magnetic moment switches from positive to negative at the compensation point. Panel (b)-$M(H)$ hysteresis curves on the same sample acquired at 300 K and 200 K, above and below compensation, respectively. Do note that the magnetization is always positive when the sample is saturated. The two curves are offset vertically for clarity. For this sample, the magnetic moment $\rightarrow$ magnetization is: $10\,\mathrm{nA\,m^2} \rightarrow 7.9\,\mathrm{kA\,m^{-1}}$. Hence, the saturation magnetization at 300 K is $M_{\mathrm{s}} \approx 26\,\mathrm{kA\,m^{-1}}$. 180

6.9 Schematic representation of the MTJs structure with MRG bottom electrode. The thickness of each layer is indicated in brackets in nm. 182

6.10 Tunneling magnetoresistance of an MTJ annealed at $T = 350\,^{\circ}\mathrm{C}$. Panel (a) shows the TMR effect at applied bias $U = 10\,\mathrm{mV}$ at different temperature. Panel (b) shows the TMR at the same MTJ but at applied bias of $U = -1\,\mathrm{V}$. 183

6.11 TMR(U)for an $Mn_2Ru_{1.0}Ga$ MTJ annealed at 350 °C. Panel (a) - The red curve shows the TMR(U) at 10 K, and the blue curve represents the TMR(U) at 300 K. The zero TMR points are indicated with orange arrows and the local TMR plateau at positive bias is indicated with magenta arrows. Panel (b) - TMR(U) at various different temperatures. 184

6.12 Parallel (R_P) and antiparallel (R_{AP}) resistance dependence on the applied bias U at $T = 10\,K$ and $T = 300\,K$. Panel (a) shows the $R_{P(U)}$ at $T = 10\,K$ and $T = 300\,K$. Panel (b) shows the $R_{AP(U)}$ at $T = 10\,K$ and $T = 300\,K$. 185

6.13 Parallel (R_P) and antiparallel (R_{AP}) resistance reduction as a function of the applied bias U. Panel (a) shows the $R_P(U)$ reduction for different temperature ratios $50\,K/10\,K$, $100\,K/10\,K$, $150\,K/10\,K$, $200\,K/10\,K$, $250\,K/10\,K$, and $300\,K/10\,K$. Panel (b) shows the $R_{AP}(U)$ reduction as a function of the applied bias U for the same temperature ratios. The orange, vertical dotted lines ($U \approx -0.2\,V$) indicate roughly the position where TMR switches sign. 186

6.14 Differential conductance (G) of an MTJ at 2 K. Panel (a)-G in parallel (red curve) and antiparallel state (black curve). Panel(b)-magnetoconductance calculated from the two curves in Panel (a). 187

6.15 Differential conductance G_{AP} on panel (a) and G_P on panel (b) at $T = 2\,K$, 10 K, 100 K, and 300 K. The curves at 2 K are kept as they are, and each of the others is offset vertically by 10 mS with respect to the lower temperature. 187

6.16 Differential conductance G_{AP} on panel (a) and G_P on panel (b) at $T = 2\,K$ in voltage range $|U| > 0.4\,V$ along with the Brinkman quadratic fit and the extracted average barrier height $\phi_{AP} = 4.879\,eV$ and $\phi_P = 4.940\,eV$ for the antiparallel and the parallel case, respectively. 191

6.17 Differential conductance G_{AP} on panel (a) and G_P on panel (b) at $T = 2\,K$ in voltage range $|U| < 0.2\,V$ along with the Brinkman quadratic fit and the extracted average barrier height $\phi_{AP} = 0.755\,eV$ and $\phi_P = 0.881\,eV$ for the antiparallel and the parallel case, respectively. 191

6.18 Differential conductance G_{AP} on panel (a) and G_P on panel (b) at $T = 2\,K$ in voltage range $|U| < 0.1\,V$ along with the Brinkman quadratic fit and the extracted average barrier height. $\phi_{AP} = 0.497\,eV$ and $\phi_P = 0.587\,eV$ for the antiparallel and the parallel case, respectively. 192

6.19 Panel(a)-TMR annealing dependence for applied biases of $U = 10\,\mathrm{mV}$ and $U = -1\,\mathrm{V}$ for as-deposited chips and chips annealed at $T_{\mathrm{anneal}} = 275\,^{\circ}\mathrm{C}, 300\,^{\circ}\mathrm{C}, 325\,^{\circ}\mathrm{C}$, and $350\,^{\circ}\mathrm{C}$. Panel(b)-dependence of the parallel and antiparallel resistance states on the annealing temperature. The measurements are done on a junction with area of $400\,\mu\mathrm{m}^2$ and $t_{\mathrm{MgO}} = 1.5\,\mathrm{nm}$. 194

6.20 Temperature dependence of the TMR effect and the low resistance state in the MTJs for three different annealing temperatures $275\,^{\circ}\mathrm{C}$, $300\,^{\circ}\mathrm{C}$, and $325\,^{\circ}\mathrm{C}$. Panel (a) and (b)-$R_{\mathrm{P}}(T)$ and TMR(T), respectively, for $U = 10\,\mathrm{mV}$. Panel (c) and (d)-$R_{\mathrm{AP}}(T)$ and TMR(T), respectively, for $U = -1\,\mathrm{V}$. 196

6.21 Three dimensional applied bias-temperature-TMR dependence of a sample annealed at $T_{\mathrm{anneal}} = 325\,^{\circ}\mathrm{C}$. Voltage step is $\Delta U = 1\,\mathrm{mV}$, temperature step is $\Delta T = 5\,\mathrm{K}$. 198

6.22 Quantum well states: TMR(U) curves on an Co/Au(t)/Al_2O_3/$Ni_{80}Fe_{20}$ MTJs. Panel (a)-$t \leq 0.3\,\mathrm{nm}$, panel (b)-$t \geq 0.4\,\mathrm{nm}$. The diagram is after Moodera *et al.*[238]. . . . 199

6.23 TMR effect between Co and LSMO with different insulation layers. Panel (a) TMR with $SrTiO_3$ barrier, panel (b) - TMR with CeLaO barrier, panel (c) - TMR(U) with $SrTiO_3$ barrier, panel (d) - TMR with Al_2O_3 barrier, panel (e) - TMR with Al_2O_3/$SrTiO_3$ barrier, and panel (e) - TMR(U) dependence with Al_2O_3/$SrTiO_3$ barrier. Please note that panel (a) demonstrates negative TMR, whereas panel (e) - positive one. The plots are after de Teresa *et al.*[70]. 200

6.24 TMR of Ni/NiO/Co tunnel junctions. Panel (a)-demonstrates classical TMR(U) behaviour with gradual symmetric decrease as the bias is raised. Panel (b)-TMR(U) for a junction with a resonant level located approximately 35 meV above the Fermi level. The TMR is positive close to zero bias, however, it changes sign when the Fermi level of the left electrode is raised to the point of the resonant level. The schematic with the Fermi levels of the two electrodes and the position of the localized state is presented on the right-hand side of the panel. Panel (c)-TMR(U) of a junction with a narrow localized state at the Fermi level. Panel (d)-statistical distribution of the TMR effect. The distribution peaks at small positive TMR values. The samples are measured at 4 K. The plots are after Tsymbal *et al.*[346]. 201

6.25 Panel (a)-TMR(U) dependence of a standard MgO-based MTJ. The stack has been exposed to atmosphere just after the MgO deposition (solid circles). The standard symmetric TMR(U) is recovered when the air-exposed MTJ is pre-etched with Ar-plasma before the deposition of the top ferromagnetic contact (empty circles). Similar result on intentionally C-contaminated MTJ interfaces has been reported before [343]. Panel (b)-TMR(U) dependence of an MTJ with a composite MgO/Alq3(t) tunnel barrier. Three different thicknesses of the organic barrier are presented. The graph is after H. Tokuc[344]. 203

6.26 TMR of an MTJ with $Mn_2Ru_{0.8}Ga$ at applied bias U 10 mV . Panel(a) - TMR measured at 10 K. Panel(b) - TMR measured at 300 K. Note that TMR switches sign as a function of temperature at close to zero bias. 204

6.27 TMR of an MTJ with $Mn_2Ru_{0.8}Ga$ close to compensation at an applied bias $U = 10$ mV. The black curve is recorded just below compensation (165 K), the red curve-at compensation (200 K), and the blue curve just above compensation (235 K). Note that the maximum applied field is $\mu_0 H = 14$ T. 206

6.28 TMR minor loops measured from 235 K to 190 K at interval $\Delta T = 5$ K. The MTJ is saturated at 235 K in 14 T. The field sweep direction is positive→negative→positive, and, hence, the TMR effect is negative. The minor loop at 190 K is kept as it is, while each of the others is offset downwards by -1 % with respect to the previous loop. The compensation temperature is indicated with a green asterisk. 207

6.29 Schematic representation of the MRG DOS behaviour when it is passed through the compensation T_{comp}. Panel(a)-when the applied field is much higher than the MRG coercive field. Panel(b)-when the applied field is lower than the MRG coercive field. It is assumed that MRG is saturated at the lowest possible temperature in both cases. The black curves represent the MRG magnetization in arbitrary units. The magenta arrows indicate the Fermi level spin polarization orientation with respect to the applied field. The spin-split DOS represent the Mn sublattice magnetization behaviour. Do note that on panel (a) the spin orientations of the Mn 4c and Mn 4a flip their signs through T_{comp}. The Fermi level (E_{F}) is indicated with a brown horizontal dashed line. The compensation temperature is indicated with a green vertical line. The x-axis is normalized with respect to the Curie temperature T_{C} and it is assumed that $T_{\text{comp}} \approx 0.5 T_{\text{C}}$. 209

6.30 TMR and resistance scans as a function of temperature through compensation. Panel (a)-TMR(T) scan for saturation below T_{comp}(black curve) and above T_{comp}(red curve). Panel (b)-$R_{\mathrm{AP}}(T)$ and $R_{\mathrm{P}}(T)$ for saturation above and below compensation. That data is used for the curves on Panel (a). The applied magnetic field during each measurement is $\mu_0 H = -0.5\,\mathrm{T}$. The applied bias for all measurements is $U = 10\,\mathrm{mV}$. 210

6.31 Spin independent conductance G_{SI} as a function of T for a chip annealed at 350 °C, the same as the one in Fig. (6.10) . Panel (a)-applied bias $U = 10\,\mathrm{mV}$ and extracted $\mathrm{N}(10\,\mathrm{mV}) = 2.2$, Panel (b)-applied bias $U = -1\,\mathrm{V}$ and extracted $\mathrm{N}(-1\,\mathrm{V}) = 2.8$. 212

6.32 Number of tunneling steps determined for the chip annealed at 325 °C(see Fig. (6.21)). Panel (a)-determined from $G_{\mathrm{SI}}^{\mathrm{dc}}$, panel (b)-determined from $G_{\mathrm{SI}}^{\mathrm{ac}}$. Note the broad peaks at $\approx \pm 75$ mV indicated with blue arrows. 213

6.33 Fitting of the normalized TMR dependence following the SNJM model[298] along with the extracted parameters. Panel (a)-$U = 10\,\mathrm{mV}$, Panel (b)-$U = -1\,\mathrm{V}$. 215

6.34 $\mathrm{G_{rel}}$ in the antiparallel (a) and parallel (b) configuration, respectively. Features, which are due to noise in the data are indicated with black arrows. 217

6.35 Absolute TMR decrease of the MTJ presented on Fig. (6.21). The bias range is $-0.1\,\mathrm{V} < U < 1\,\mathrm{V}$. 218

6.36 Relative TMR decrease for the MTJ presented on Fig. (6.21). Two features, which are caused by noise, are indicated with black arrows. 219

6.37 Resistance asymmetry $\tilde{R}$ for the cases of antiparallel (panel (a)) and parallel state (panel (b)). The data is obtained on a chip annealed at 325 °C (see Fig. (6.21)). . . 220

6.38 Inelastic electron tunneling spectroscopy measured in antiparallel (black) and parallel state (red). The data is measure at low temperature ($T = 2\,\mathrm{K}$) on a chip annealed at 350 °C. 220

6.39 TMR(U) behaviour comparison between an as-prepared and an annealed at 325 °C MTJ. The measurements are performed at 10 K and each curve is normalized to the maximum TMR at low bias. Blue arrow indicates the voltage range where the contribution from resonant states is most pronounced. The MTJs are physically from the same chip but treated differently. 221

6.40 TMR measurements on MTJs with $\mathrm{Mn_2Ru_{0.6}Ga}$ and no Al insertion layer. The compensation temperature is approximately 100 K. Panel (a)-TMR($\mu_0 H$) scans at temperatures: 10 K, 100 K, and 200 K and applied bias $U = 10\,\mathrm{mV}$. Panel(b)-TMR(U) dependences measured at 10 K for an MTJ set at 10 K-red curve and 200 K-black curve (above compensation). 223

6.41 Panel (a) - TMR loop for an MTJ without Al insertion layer at $T = 10\,\mathrm{K}$. The mutual MRG and CoFe magnetization orientations are indicated with arrows: blue arrows for CoFe, red arrows for MRG. The TMR scan is performed in the following direction: $14\,\mathrm{T} \rightarrow 0\,\mathrm{T} \rightarrow -14\,\mathrm{T} \rightarrow 0\,\mathrm{T} \rightarrow 14\,\mathrm{T}$. When the magnetization arrows are above the graph, this corresponds to the initial field scan: $14\,\mathrm{T} \rightarrow -14\,\mathrm{T}$. When the magnetization arrows are below the graph, this corresponds to the field scan in the opposite direction: $-14\,\mathrm{T} \rightarrow 14\,\mathrm{T}$. Panel (b) - the same TMR loop from panel (a) after background correction. 224

6.42 Example of the detrimental effects of resonant tunneling in MTJs with Mn_2Ru_1Ga bottom electrode. The MTJ is annealed in the magnetic annealing furnace at 325 °C. Panel (a)-TMR(H) curves measured at applied bias $U = -1\,\mathrm{V}$ and at different different temperatures. Panel (b)-TMR(U) of the same junction obtained at 10 K and 300 K. Note that the TMR is negative for positive bias this time in contrast with Fig. (6.11). The points where the TMR(U) curve at 10 K switches sign are indicated with blue circles. 225

6.43 Comparison of the resonant tunneling contribution between three samples prepared under similar conditions. All three MTJ chips are annealed at 325 °C. The temperature is 10 K for each measurement. Panel (a)-the sample with the highest TMR and best control of the Mn diffusion, this is sample presented completely in Fig. (6.21). Panel (b)-sample with intermediate quality and more pronounced resonant scattering contribution. Note that the TMR crosses twice the zero line for positive bias. Panel (c)-sample with the most apparent resonant scattering contribution. The TMR crosses zero for positive bias and does not changes sign back up to $U = 1\,\mathrm{V}$. Magenta arrows indicate on each graph the most obvious feature from the resonant spin-flip scattering contribution. The points, where the TMR changes sign, are indicated with brown circles. The resonant scattering contribution gradually increases from panel (a) through panel (c). 226

B.1 Setting low temperature and high cooling rate before flushing the system with He (panel (a)), the hissing valve and the pumping line are indicated (panel (b)). 241

B.2 The He gas line (panel (a)) and the nitrogen pre-cooling procedure (panel (b)). 241

B.3 The He gas line (panel (a)) and the nitrogen pre-cooling procedure (panel (b)). 241

E.1 Superconducting loop with applied magnetic field and indicated contour of integration. 251

E.2 Picture of a Josephson junction. 254

E.3 Josephson junction. Field and vector potential behaviour. 254

E.4 Josephson junction. 256
E.5 Maximum zero-voltage current as a function of the magnetic flux. 257
E.6 The black curve is a nonhysteretic RSJ I-V characteristic ($\beta_c \ll 1$). The blue dotted one is simply the bisector, which is the asymptote of the I-V Josephson junction curve, it is the I-V curve of a resistor R as well. 258
E.7 Numerical simulations of hysteretic properties of Josephson junction. The solid curves are obtained at zero temperature. The parameter $\Gamma = 2\pi kT/I_c\Phi_0$ is known as the normalized thermal energy. The dotted curves are numerically obtained when the Nyquist noise current contribution is added in the RCSJ model. The picture is taken from [10]. 259
E.8 The total flux Φ_t in an a.c. SQUID as a function of the externally applied flux Φ_e. The black curve corresponds to $\beta_L = 1$, the red one to $\beta_L = 2$, and the blue dotted line is $\Phi_t = \Phi_e$. A hysteresis behaviour is present for $\beta_L > 1$. It is discernible, that the red curve is in effect a succession of quasilinear regions with jumps between them. These jumps are associated with energy dissipation in the SQUID ring, and are crucial for the operation of the detector. 260
E.9 I-V characteristic of an AC SQUID. The flux-voltage transfer function $V - \Phi$ as a dependence on the I_{RF} current is presented on the right-hand side. 261
E.10 Schematic structure of a d.c. SQUID loop. 262
E.11 Maximum current dependence I_{max} of a balanced two Josephson junctions loop ($I_{c\alpha} = I_{c\beta}$) on the normalized applied flux Φ/Φ_0. 263
E.12 Circulating supercurrent in a current biased DC SQUID. 265
E.13 (a) - The d.c. SQUID with the RCSJ circuit model; (b) - I-V characteristics of a d.c. SQUID in the cases of integer and half-integer applied flux. 267
E.14 Numerical simulation for the flux-voltage transfer function of a d.c. SQUID. For two set of parameter β_L and β_C, the dependence on the reduced current $i = I/2I_0$ is studied. (a) $\beta_L = 1$, $\beta_C = 0$; (b) - $\beta_L = 1$, $\beta_C = 1$. Obviously, the quality of the transfer degrades as the McCumbert parameter β_C is increased. The picture is taken from [62]. 267
E.15 Different type of weak links. (a) - insulating barrier between two superconductors; (b) - microbridge; (c) - grain boundary junction. Methods (b) and (c) are specially used in high-T_c superconductors. The picture is taken from [10]. 269
E.16 Different type of weak links. (a) - insulating barrier between two superconductors; (b) - microbridge; (c) - grain boundary junction. Methods (b) and (c) are specially used in high-T_c superconductors. The picture is taken from [10]. 269
E.17 Basic readout circuit of an a.c. SQUID. 270

E.18 Basic readout circuit of an d.c. SQUID. 270
E.19 Flux-locked circuit of an a.c. SQUID. 271
E.20 Flux-locked circuit of a d.c. SQUID. 272

List of Tables

1.1 BTK theory reflection probabilities 50

1.2 Modified BTK theory reflection probabilities. The notations are represented as follow: $u_{01}^2 = 1 - v_{01}^2 = 0.5(1 + [(E^2 - \Delta_1^2)/E^2]^{1/2}), u_{02}^2 = 1 - v_{02}^2 = 0.5(1 + [(E^2 - \Delta_2^2)/E^2]^{1/2}), \gamma_1^2 = (u_{01}^2 + Z^2[u_{01}^2 - v_{01}^2])^2, \gamma_2^2 = u_{01}^2 v_{01}^2 + (u_{02}^2 - v_{02}^2)[u_{02}^2 + Z^2 + (u_{02}^2 - v_{02}^2)Z^2(1+Z^2)]$, and $\gamma_3^2 = (u_{02}^2 - v_{02}^2)[u_{02}^2 + Z^2 + (u_{02}^2 - v_{02}^2)Z^2(1+Z^2)]$. 55

1.3 Diffusive BTK theory after Mazin *et al.*[215]. β is defined as follows: $\beta = \frac{E}{\sqrt{|\Delta^2 - E^2|}}$. Z is the barrier strength. 59

1.4 Diffusive BTK theory after Mazin *et al.*[215]. $F(s)$ and β are defined as follows: $F(s) = \frac{\cosh^{-1}(2Z^2+s)}{\sqrt{(2Z^2+s)^2-1}}$ and $\beta = \frac{E}{\sqrt{|\Delta^2 - E^2|}}$. 59

1.5 Literature values of spin polarization of various materials measured by PCAR. . . . 63

1.6 Literature values of spin polarization of various materials measured by PCAR. . . . 64

6.1 TMR and R_P comparison for different annealing condition at applied bias $U = 10\,\mathrm{mV}$. 194

6.2 TMR and R_{AP} comparison for different annealing condition at applied bias $U = -1\,\mathrm{V}$. 195

C.1 Wire bonding parameters which have worked for bonding between bond pads of a PPMS resistivity puck. 244

C.2 Wire bonding parameters which have worked for bonding between an MTJ chip and a PPMS resistivity puck. 244

Chapter 1

Spin electronics

1.1 Definition of spin

The existence of an intrinsic angular momentum of an electron has been first postulated by Goudsmit and Uhlenbeck. In classical physics terms, the rotation of a charged ball produces current loops and, therefore, has magnetic moment. In reality, the electron is a fundamental particle, has no compound structure and, therefore, it has no volume charge density. Instead, the internal magnetic moment of the electron is a quantum mechanical property which cannot be interpreted in classical physics terms. The crucial Stern-Gerlach experiment (SGE) has led to the postulation of the electron spin. The imminent fundamental problem before this experiment is the fine structure of the hydrogen spectral lines. The SGE represents splitting of a beam of silver atoms in gradient magnetic field. The observation is that a well-collimated beam splits into two separate paths. The gradient magnetic force acts on a magnetic dipole and, therefore, the experiment is an indication of an intrinsic magnetic moment of the silver atoms. The orbital moment in the case of silver is zero, hence, the effect is ascribed to the intrinsic magnetic moment of the electron*. Historically, the spin of the electron has been introduced as a mathematical entity in the quantum mechanics by Wolfgang Pauli.

1.1.1 Orbital moment

Bohr's idea of the orbital motions of electrons is historically the first successful incorporation of the wave-particle duality. The basic postulate is that the circulating electron must form a standing wave along its orbit in order not to emit electromagnetic radiation. The theory is a remarkable

*In fact, the physical community has been unaware at that stage that the total orbital momentum of the silver is zero. Stern and Gerlach initial idea is that the orbital magnetic moment of the outermost valent electron of silver is measured. A few years later, it is realized that the orbital moment of an *s* electron is zero. An interesting review on how the experiment is performed and largely disbelieved for a few years is given by Friedrich and Herschbach[99]

success because it calculates accurately the observed spectral lines in the hydrogen spectrum. A significant leap is attributed to Schrödinger who has introduced the idea of the wavefunction and a quantum mechanical Hamiltonian. The time-independent form of the Schrödinger equation is

$$\left(-\frac{\hbar}{2m}\nabla^2 + V\right)\Psi = E\Psi, \tag{1.1}$$

where V is the potential acting on the electron wavefunction, E is the energy eigenvalue, and $\nabla^2(=\Delta) = (\partial^2/\partial x^2, \partial^2/\partial y^2, \partial^2/\partial z^2)$ is the Laplacian operator. The modulus of the wavefunction, $\Psi(\vec{r})^2$, gives the probability for locating the particle in infinitesimal volume dV at position $\vec{r}$. The Coulomb repulsion potential between the atom and the electron in the hydrogen atom has spherical symmetry and, therefore, the respective ∇^2 operator has the form:

$$\nabla^2 = \frac{\partial^2}{\partial r^2} + \frac{2}{r}\frac{\partial}{\partial r} + \frac{1}{r^2}\left(\frac{\partial^2}{\partial\theta^2} + \cot\theta\frac{\partial}{\partial\theta} + \frac{1}{\sin^2\theta}\frac{\partial^2}{\partial\phi^2}\right). \tag{1.2}$$

The fact that there are no mixed derivatives means that the wavefunction can be split into three components: radial(r), polar(θ), and azimuthal(ϕ):

$$\left[-\frac{\hbar}{2m}\nabla^2 - \frac{e^2}{4\pi\varepsilon_0 r}\right]R(r)\Theta(\theta)\Phi(\phi) = ER(r)\Theta(\theta)\Phi(\phi). \tag{1.3}$$

The separation leads to three independent differential equations:

$$\frac{1}{\Phi}\frac{\mathrm{d}^2\Phi}{\mathrm{d}\phi^2} = -m_l^2, \tag{1.4}$$

$$\frac{1}{\Theta}\left[\sin\theta\frac{\mathrm{d}}{\mathrm{d}\theta}\left(\sin\theta\frac{\mathrm{d}\Theta}{\mathrm{d}\theta}\right)\right] + l(l+1)\sin^2\theta = m_l^2, \tag{1.5}$$

$$\frac{\mathrm{d}}{\mathrm{d}r}\left(r\frac{\mathrm{d}R}{\mathrm{d}r}\right) - \frac{2mr^2}{\hbar^2}\left[-\frac{e^2}{4\pi\varepsilon_0 r} - E\right]R = l(l+1)R, \tag{1.6}$$

in which case the eigenfunctions and (some) eigenvalues of each part are

$$\Phi(\phi) = \exp(im_l\phi) \qquad m_l = 0, \pm1, \pm2, \ldots, \pm l \tag{1.7}$$

$$\Theta(\theta) = AP_l^{m_l}(\cos\theta) \qquad l = 0, 1, 2, \ldots, n-1 \tag{1.8}$$

$$R(r) = Aj_l(kr) + Bn_l(kr) \qquad k = \frac{\sqrt{2mE}}{\hbar}, \tag{1.9}$$

where $P_l^{m_l}$ is the associated Legendre function, $j_l(kr)$ and $n_l(kr)$ are the spherical Bessel and Neumann functions of order l. After imposing boundary conditions on the radial component, the principal quantum number n appears and $n = 0, 1, \ldots$. The three quantum numbers n, l, m_l appear from

the solution of the Schrödinger equation in a purely mathematical way. It can be demonstrated that if the quantum angular momentum operators are considered:

$$\hat{\boldsymbol{l}}_x = \mathrm{i}\hbar\left(\sin\phi\frac{\partial}{\partial\theta} + \cot\theta\cos\phi\frac{\partial}{\partial\phi}\right), \tag{1.10}$$

$$\hat{\boldsymbol{l}}_y = \mathrm{i}\hbar\left(-\cos\theta\frac{\partial}{\partial\theta} + \cot\theta\sin\phi\frac{\partial}{\partial\phi}\right), \tag{1.11}$$

$$\hat{\boldsymbol{l}}_z = -\mathrm{i}\hbar\frac{\partial}{\partial\phi}, \tag{1.12}$$

then the operator $\hat{\boldsymbol{l}}^2$ coincides with the differential operator acting on the polar component,Θ, above. Therefore, the magnitude of the angular momentum is $\hbar\sqrt{l(l+1)}$. The differential operator acting on the azimuthal component, Φ, coincides with $\hat{\boldsymbol{l}}_z$. Therefore, the z- axis projection of the angular momentum is $\hbar m_l$ (see Fig. (1.1) (b)). The commutator relations between the angular momentum operators are:

$$\left[\hat{\boldsymbol{l}}_x, \hat{\boldsymbol{l}}_y\right] = \mathrm{i}\hbar\hat{\boldsymbol{l}}_z, \quad \left[\hat{\boldsymbol{l}}_z, \hat{\boldsymbol{l}}_x\right] = \mathrm{i}\hbar\hat{\boldsymbol{l}}_y, \quad \left[\hat{\boldsymbol{l}}_z, \hat{\boldsymbol{l}}_y\right] = \mathrm{i}\hbar\hat{\boldsymbol{l}}_x. \tag{1.13}$$

It is important that the operators $\hat{\boldsymbol{l}}_z$ and $\hat{\boldsymbol{l}}^2$ commute which means in quantum mechanical terms that their eigenvalues can be simultaneously measured.

1.1.2 Spin of the electron

In a purely mathematical fashion, Pauli has proposed that the internal angular momentum operators of the electron must obey the same commutation rules. Furthermore, it is that required the eigenvalues to be $\pm\frac{1}{2}\hbar$ and the eigenvectors to be 'spin-up' $\binom{1}{0}$ and 'spin-down' $\binom{0}{1}$. The Pauli matrices are

$$\hat{\boldsymbol{s}}_x = \frac{\hbar}{2}\begin{pmatrix}0 & 1\\ 1 & 0\end{pmatrix} \qquad \hat{\boldsymbol{s}}_y = \frac{\hbar}{2}\begin{pmatrix}0 & -\mathrm{i}\\ \mathrm{i} & 0\end{pmatrix} \qquad \hat{\boldsymbol{s}}_z = \frac{\hbar}{2}\begin{pmatrix}1 & 0\\ 0 & -1\end{pmatrix} \tag{1.14}$$

It can be checked that the square of the total spin angular momentum is

$$\hat{\boldsymbol{s}}^2 = \hat{\boldsymbol{s}}_x{}^2 + \hat{\boldsymbol{s}}_y{}^2 + \hat{\boldsymbol{s}}_z{}^2 = \frac{3\hbar^2}{4}\begin{pmatrix}1 & 0\\ 0 & 1\end{pmatrix}. \tag{1.15}$$

Therefore, the magnitude of the spin is $\sqrt{3}\hbar/2 = \sqrt{s(s+1)}\hbar$ and it has projection along the z-axis: $\pm(1/2)\hbar$. The forth quantum number, m_s, is introduced, so that the spin moment is $m_s\hbar$ and $m_s = \pm(1/2)$ (see Fig. (1.1) (a)).In applied external magnetic field, the Zeeman effect results in two energy levels splitting

$$H_{\mathrm{Z}} = -\hat{m}.\mu_0\vec{H}, \tag{1.16}$$

where each has eigenvalues $g_e m_s \mu_B \mu_0 H$. The electron spin gyromagnetic ratio is $g_e \approx 2$.*. The Pauli exclusion principle states the two electrons cannot have the same combination of the four atomic numbers: n, l, m_l, and m_s. This law along with the empirical Hund's rules determine how electrons populate the energy levels in an atom.

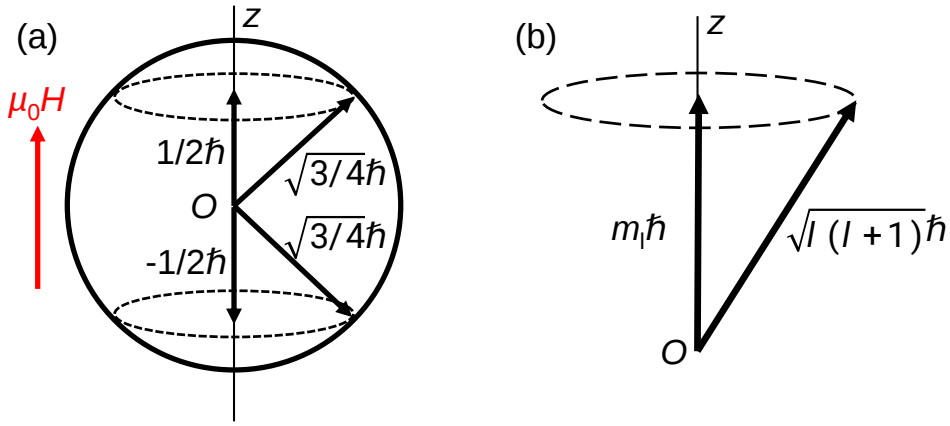

Figure 1.1: Schematic representation of the spin (a) and orbital angular moment (b) magnitudes. The magnitudes and the projections along the z-axis are presented. The applied magnetic field $\mu_0 H$ defines the z-axis direction.

1.1.3 Moment of an atom

The total magnetic moment of an isolated atom is a sum of its orbital and spin magnetic moments

$$\hat{m} = -\frac{\mu_B}{\hbar}(g_l \hat{\boldsymbol{l}} + g_s \hat{\boldsymbol{s}}), \tag{1.17}$$

$$\hat{m} = -\frac{\mu_B}{\hbar}(\hat{\boldsymbol{l}} + 2\hat{\boldsymbol{s}}), \tag{1.18}$$

where $g_l = 1$ and $g_e = 2$ are the orbital and spin g-factors, respectively.

There is an additional Coulomb repulsion term in a multi-electron atom

$$V_{e-e} = \frac{1}{2}\sum_{i,j}\frac{e^2}{4\pi\varepsilon_0 r_{ij}}, \tag{1.19}$$

and the Schrödinger equation is not analytically solvable for more than two electrons. A possible way to treat the system is by considering that each additional electron experiences a central potential of the rest of the electrons occupying lower levels. The potentials are then determined self-consistently following the Hartree-Fock approximation. An important consequence of the electron

*With quantum electrodynamics corrections, $g_e \approx 2.002319$

cloud shielding of the central potential is that the electron energy levels does not depend only on the principle quantum number n but on the orbital number l as well. This becomes important at level $n = 4, l = 0$ ($4s$) which has lower energy than $n = 3, l = 2$ ($3d$), and therefore, the $4s$ state is populated first. The latter is important for the electronic configuration of the transition metal elements. For instance, Fe ($Z = 26$) has configuration [Ar]$3d^6\ 4s^2$ and Co ($Z = 27$) is [Ar]$3d^7\ 4s^{2*}$. This rule leads to modified occupation of the higher energy levels as well. The electron fill up sequence looks like that: $1s \to 2s \to 2p \to 3s \to 3p \to 4s \to 3d \to 4p \to 5s \to 4d \to 5p \to 6s \to 4f \to 5d \to 6p$ Once the electronic configuration of an atom is known the spin and the orbital moments obey three empirical rules, Hund's rules:

1. The maximum total atomic spin $S = \sum m_{si}$ is obtained while obeying the Pauli exclusion principle.

2. The total orbital momentum $L = \sum m_{li}$ is maximized.

3. Total angular momentum, J, is equal to $|L-S|$ when the shell is less than half full, and is equal to $|L+S|$ when the shell if more than half full. If a shell is half full $L = 0$, and therefore $J = S$.

This means that electrons occupy the free states with all spin parallel within a shell as long as the Pauli principle is not violated.

The transition metal magnetic ions follow the $L-S$ coupling scheme[†]. In this case, the individual orbital m_{li} and spin quantum numbers m_{si} of each electron are "good" quantum numbers and they are added separately. Therefore, the total orbital number and the total spin number are

$$S = \sum m_{si} \quad , \quad L = \sum m_{li}. \tag{1.20}$$

in this case the total angular momentum $\vec{J}$ is a vector sum of the two: $\vec{J} = \vec{L} + \vec{S}$. Therefore, the magnitude is $|L-S| \leq J \leq L+S$. In elements with high-atomic number, the spin-orbit interaction is strong and tends to couple the orbital and spin moment of each electron individually. In this case, the coupling between the orbital and spin moments is stronger $\vec{J}_i = \vec{L}_i + \vec{S}_i$. Then the total moments of the electrons are added together $\vec{J} = \sum \vec{J}_i$. This case pertains to heavy elements in the lanthanide family.

An example is given here for the Cr^{3+} ion which is [Ar]$3d^{3\ddagger}$. The spin configuration in this case is:

*It is instructive to mention that after the $3p$ shell is filled up in Ar ($Z = 18$), K ($Z = 19$) is [Ar]4s1, then Ca ($Z = 20$) is [Ar]4s2, at this point $4s$ is filled up and the next element is Sc ($Z = 21$) with electronic configuration [Ar]$3d^1 4s^2$.

†Also known as Russell-Saunders

‡Starting from [Ar]$3d54s2$ for Cr atom, and removing first the two s electrons and then one d

m_l	2	1	0	-1	-2	2	1	0	-1	-2
m_s	1/2	1/2	1/2	1/2	1/2	1/2	1/2	1/2	1/2	1/2
polarity s	$\uparrow$	$\uparrow$	$\uparrow$							

Then, the total spin moment is $S = 3/2$. The orbital angular moment of the $3d$ elements is quenched ($L = 0$) and, therefore, $J = S$. Therefore, the moment of the Cr^{3+} is $m = 2\mu_B\sqrt{S(S+1)}$ $\approx 3.87\mu_B$. This type of calculations applies relatively well to the cases when the paramagnetic ions are isolated from each other. Such is the case in paramagnetic salts[134]. When paramagnetic ions interact between each other, bands are formed by the hybridization of the outermost valence electrons and the magnetic behaviour depends on the orbitals overlap and the distance between the neighbouring atoms.

1.1.4 Exchange interaction and band splitting

There are two general theories on the magnetic behaviour of the elements: the localized magnetism and the itinerant magnetism. The former describes well the heavy rare-earth elements while the latter fits the behaviour of the $3d$ transition elements. Whenever electrons are brought together, the wavefunction of the electron cloud is represented by the wavefunctions of all separate electrons. Consider the simple system of two electrons with single electron wavefunction $\psi(r_1)$ and $\psi(r_2)$, then the compound two-electron wavefunction $\Psi(r_1, r_2)$ could be:

$$\Psi(r_1, r_2) = \psi_a(r_1)\psi_b(r_2) + \psi_a(r_2)\psi_b(r_1) \tag{1.21}$$

$$\Psi(r_1, r_2) = \psi_a(r_1)\psi_b(r_2) - \psi_a(r_2)\psi_b(r_1), \tag{1.22}$$

where the $\psi_a(r_1)$ is the wavefunction of electron 1 on atom a, and $\psi_a(r_2)$ is the wavefunction of electron 2 on atom b. It is important that the modulus of the combined wavefunction $\Psi^*\Psi$ is unchanged when the electrons are swapped, *i.e.* $\Psi(r_1, r_2)$ must be antisymmetric. If $\Psi^*\Psi$ is symmetric upon electrons interchange, this is violation of the Pauli exclusion principle. The first combination above is symmetric and it should be excluded, while the second in antisymmetric. In this simple two-electron model, the energy is calculated in a Heilter-London approximation[133]

$$E = \int\int \Psi^*(r_1, r_2)\langle H\rangle\Psi(r_1, r_2)\mathrm{d}r_1\mathrm{d}r_2, \tag{1.23}$$

with the total Hamiltonian $\langle H\rangle = \langle H_1\rangle + \langle H_2\rangle + \langle H_{12}\rangle$, where $\langle H_1\rangle$ and $\langle H_2\rangle$ are the single particle Hamiltonians, and $\langle H_{12}\rangle$ is the electron-electron interaction Hamiltonian. In this case the single particle Hamiltonians obey the relations: $\langle H_1\rangle\psi_a(r_1) = E_a\psi_a(r_1)$ and $\langle H_2\rangle\psi_b(r_2) = E_b\psi_b(r_2)$.

Therefore, the total energy integral is reduced to

$$\begin{aligned} E =& E_a \int \psi_a^*(r_1)\psi_a(r_1)\mathrm{d}r_1 + E_b \int \psi_a^*(r_2)\psi_a(r_2)\mathrm{d}r_2 \\ &+ \frac{1}{\beta}\int\int \psi_a^*(r_1)\psi_b^*(r_2)\langle H_{12}\rangle \psi_a(r_1)\psi_b(r_2)\mathrm{d}r_1\mathrm{d}r_2 \\ &+ \frac{1}{\beta}\int\int \psi_a^*(r_1)\psi_b^*(r_2)\langle H_{12}\rangle \psi_b(r_1)\psi_a(r_2)\mathrm{d}r_1\mathrm{d}r_2, \end{aligned}$$

where two double integrals result from the Coulomb electrostatic interaction (Q) and the exchange energy (J) of the electrons between the two atoms. The latter exchange energy is the quantum mechanical reason for the formation of bulk magnetism.

In fact, the total wavefunction is a sum of the orbital (Ψ) and the spin component (ϕ): $\tilde{\Psi} = \Psi(r_1, r_2)\phi(s_1, s_2)$. Where the spin component is constructed in the same fashion as the orbital one:

$$\phi(s_1, s_2) = \phi_a(s_1)\phi_b(s_2) + \phi_a(s_2)\phi_b(s_1), \tag{1.24}$$

$$\phi(s_1, s_2) = \phi_a(s_1)\phi_b(s_2) - \phi_a(s_2)\phi_b(s_1). \tag{1.25}$$

Where symmetric spin wavefunction $\phi(s_1, s_2)$ means parallel spin alignment, and antisymmetric function - antiparallel spin alignment. Therefore, the Pauli exclusion principle requires the total wavefunction $\tilde{\Psi}$ to be antisymmetric. Hence, the allowed combinations are: 1. symmetric orbital and antisymmetric spin component; 2. antisymmetric orbital and symmetric spin component*. The exchange energy is equal to $-J\frac{1}{\beta}$ for parallel spin. Therefore, positive J means parallel spin order and, therefore ferromagnetic behaviour, whereas negative J corresponds to antiparallel orientation, and therefore, antiferromagnetic behaviour.

In the Heisenberg model, the Hamiltonian of the interaction between the spins of neighbouring atoms is calculated as a summation

$$\langle H\rangle = -2\sum\sum J_{ij}s_i s_j, \tag{1.26}$$

where the summation is usually assumed between the nearest neighbours. A simple observation within the Heisenberg model is that the atoms with filled shells have no exchange energy and, therefore, are not magnetic: $E_{\mathrm{ex}} = -2J\sum s_i \sum s_j = 0$, because $\sum s_i = 0$. Therefore, only unfilled shells contribute to the magnetic interaction.

An important contribution towards the physical understanding of the exchange interaction is the Bethe-Slater curve (see Fig. (1.2)). The latter pertains to the $3d$ transition metal chromium, manganese, iron, cobalt and nickel. Slater has compared the values of the interatomic distance r_{ab} and the r_d radii of the incomplete d shells for these elements. A clear correlation is found and in this

*That is why the symmetric combination in the orbital wavefunction has not been discarded.

case small ratios r_{ab}/r_d result in antiferromagnetic interaction with a cross-over to ferromagnetic interaction for higher r_{ab}/r_d. The exchange constant has maximum between the values of Fe and Co, and then decreases. Theory for calculation of the exchange integral J as a function of the atomic spacing and the orbital radius for the case of two one electron atoms is given by Bethe

$$J = \int\int \psi_a^*(r_1)\psi_b^*(r_2)\left(\frac{1}{r_{ab}} - \frac{1}{r_{a2}} - \frac{1}{r_{b1}} + \frac{1}{r_{21}}\right)\psi_a(r_1)\psi_b(r_2)\mathrm{d}r_1\mathrm{d}r_2, \tag{1.27}$$

where r_{ab} is the distance between the atomic cores, r_{a2} and r_{b1} are the distances between the electrons and the corresponding nuclei, and r_{21} is the distance between the two electrons. Good agreements is achieved with the experimental data of Slater. Although this model is proven to be

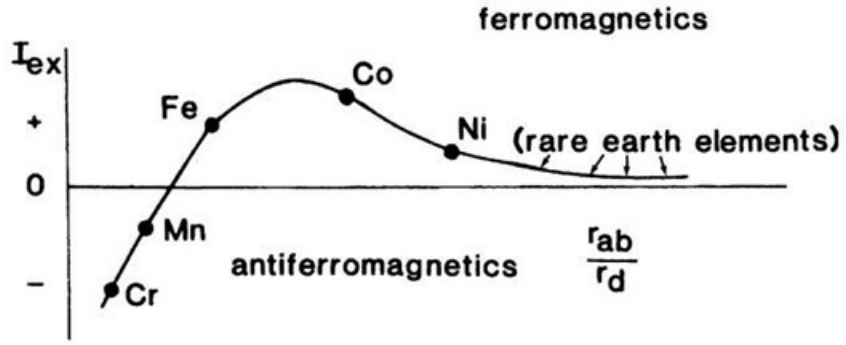

Figure 1.2: Bethe-Slater curve for the exchange interaction sign and magnitude of the 3*d* transition metal elements.

incorrect by Herring[135], it demonstrates good agreement for the 3*d* elements. One important point is the case of Mn. It is weakly antiferromagnetic with $T_N \approx 96\,\mathrm{K}$ and is positioned close to the cross-over of the exchange integral sign and on the maximum slope. Therefore, small changes in the interatomic separation of a Mn-containing composition might result in significant change in the magnetic behaviour. Such tunability is demonstrated in the ferrimagnetic composition Mn_2Ru_xGa in Chapter 6.

The magnetization of 3*d* elements and their alloys obey an empirical law known as the Slater-Pauling curve. The magnetization depends directly on the number of valence electrons. This is known as itinerant magnetism as the magnetic moments do not reside on localized electrons. The fact that the magnetic moment is carried by nearly-free conduction electrons implies that the electrical current has overall non-zero spin polarization. The spin electronics domain is built upon this feature. In a simple free electron picture, the electron spins aligned parallel with the applied field have lower energy, while antiparallel electron spins have higher energy. This is due to the fact that a magnetic moment experiences Zeeman energy $E = -\mu_0\vec{m}.\vec{H}$. In ferromagnetic materials, the band energy offset is determined by the exchange energy $J = 2\mu_0\mu_s H_{\mathrm{ex}}$. Where for 3*d* Fe and Co, the exchange energy is $\sim 1\,\mathrm{eV}$ and the exchange field is $\sim 1000\,\mathrm{T}$. In reality, the density

of states of the $3d$ ferromagnets consists of exchange-split d-pockets and parabolic s-bands. The Stoner criterion requires diverging susceptibility. The latter results in spontaneous band splitting and magnetization. The limit for this is set by

$$IN_{\uparrow,\downarrow}(E_{\mathrm{F}}) > 1, \tag{1.28}$$

where the density of states per atoms for each spin state is $N_{\uparrow,\downarrow}(E_{\mathrm{F}}) = \rho_{\uparrow,\downarrow}(E_{\mathrm{F}})/(2n)$. The latter means that the band population at the Fermi level must be sufficiently high. The Stoner exchange parameter I is similar to the exchange constant J defined above.

1.1.5 Spin polarization

The three distinct spin-split density of states structures are represented in Fig. (1.3). There is no exchange splitting in non-magnetic elements and alloys (like Cu, Al, Au), and the spin-up and spin- down bands have the same population for all energies. The case of $3d$ transition metal ferromagnetic elements and their alloys (Fe, Co, Ni, $\mathrm{Fe}_x\mathrm{Co}_{1-x}$, $\mathrm{Ni}_x\mathrm{Co}_{1-x}$), $4f$ rare-earth elements and the $3d$-$4f$ intermetallic alloys ($\mathrm{Co}_x\mathrm{Gd}_{1-x}$) results in finite exchange-splitting, magnetization and finite spin polarization. Generally, the transport value of the spin polarization for these materials has been determined to be in the range 40-50 %. The spin polarization can be defined at different binding energies with respect to the Fermi level*. However, the Fermi level spin polarization is the most important as the spin electronic devices are operated at low bias for two main reasons - smaller power dissipation and higher magnetoresistance effect. A clear distinction must be made between the spin polarization and the magnetization. The spin polarization is a differential property of the density of states in a very narrow energy window, ΔE, : $P(E) = (\mu^{\uparrow}(E) - \mu^{\downarrow}(E))\Delta E$, where the energy window ΔE is determined by the thermal energy. The net magnetization is an integral property of the spin-split density of states: $M = \int(\mu^{\uparrow}(E) - \mu^{\downarrow}(E))\mathrm{d}E$. Therefore, the Fermi level spin polarization might depend on narrow spin pockets which have small contribution towards the overall magnetization. It is generally assumed that the spin polarization decreases with temperature and this is attributed to spin-wave excitation and thermal smearing of the density of states. Unfortunately, there is no reliable technique for the extraction of the $P(T)$ dependence. The latter is sometimes estimated from the temperature dependence of the tunneling magnetoresistance effect in magnetic tunnel junctions, however, it is well-known that the tunneling spin polarization depends significantly on the quality and properties of the ferromagnetic/insulator interface rather than on the bulk properties of the ferromagnet.

Finally, the case of half-metallic compositions is considered. There is no density of states at

*For instance, spin polarization at different binding energies is studied by spin-resolved photoemission spectroscopy, however, the latter has limited energy resolution.

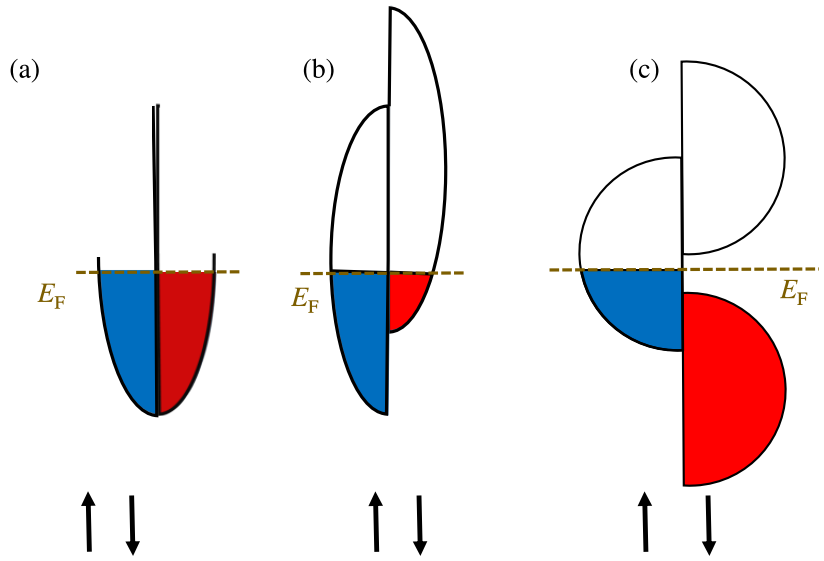

Figure 1.3: Schematic example of spin-split density of states. Panel (a) - zero spin polarization ($P = 0\,\%$), panel (b) - non-zero spin polarization $0\,\% < P < 100\,\%$, panel (c) - half-metal with $P = 100\,\%$.

the Fermi level for one of the spin sub-bands. The spin polarization is 100 %. Materials considered to be half-metals are CrO_2, $La_{0.67}Sr_{0.33}MnO_3$(LSMO), and some Heusler compounds like NiMnSb and $Mn_2Ru_{0.5}Ga$. The highest measured transport spin polarization has been reported for CrO_2($\approx$ 90 %) and LSMO($\approx$ 73 %). Unfortunately, they have little technogical significance due to low Curie temperature $\approx$ 360 K and poor carrier mobility. Half-metallicity is a property which is usually predicted by density functional theory calculations. In real materials, crystallographic disorder, interface imperfections and spin-orbit interaction may destroy this beneficial property.

Strictly speaking, the spin polarization has to be defined in multiple ways. For instance, the transport spin polarization does not depend only of the density of states but also on how mobile the electrons are. Therefore, the spin polarization definition is:

$$P^i = \frac{\rho_\uparrow v_\uparrow^i - \rho_\downarrow v_\downarrow^i}{\rho_\uparrow v_\uparrow^i + \rho_\downarrow v_\downarrow^i}, \tag{1.29}$$

where $\rho_{\uparrow(\downarrow)}$, $v^i_{\uparrow(\downarrow)}$ are the density of states and velocity for spin-up (spin-down), and $i = 0, 1$, and 2. Summation over all bands is assumed in the expression above. The bare density of states spin polarization is defined by $n = 0$ and is usually measured by spin-resolved photoemission spectroscopy. The ballistic definition of the spin polarization is given by $n = 1$ and can be measured by both spin-polarized tunneling and point contact Andreev reflection (PCAR). Finally, the diffusive definition ($n = 2$) is measurable by diffusive PCAR. The different velocities for the spin-subbands might lead to spin polarization in material which has otherwise close-to-zero bare density of states spin polarization. Such is the case for the $4d$ itinerant ferromagnet $SrRuO_3$[275].

1.2 Spin electronic devices

A brief overview will be presented on the effect of giant magnetoresistance (GMR) and tunneling magnetoresistance (TMR). The devices built upon the GMR effect are known as GMR spin valves (SVs), whereas these constructed around the TMR are known as magnetic tunneling junctions (MTJs). The basic structure of the devices and a concise review will be given.

1.2.1 Spin valves

The GMR effect has been discovered independently by Baibich *et al.*[14] and Binasch *et al.*[28] (see Fig. (1.4)). The multilayers are ferromagnet/non-magnetic(x) spacer with multiple periods. The thickness x is chosen so that there is antiferromagnetic coupling between the ferromagnetic layers and the stable configuration in the structure is alternating polarities in zero external applied field. The coupling between two ferromagnetic layers through a metallic spacer is known as the Ruderman-Kittel-Kasuya-Yoshida (RKKY) interaction[283, 165, 400]. The RKKY theory explains the coupling between the localized magnetic moments in a material via the indirect exchange interaction with the conduction electrons.

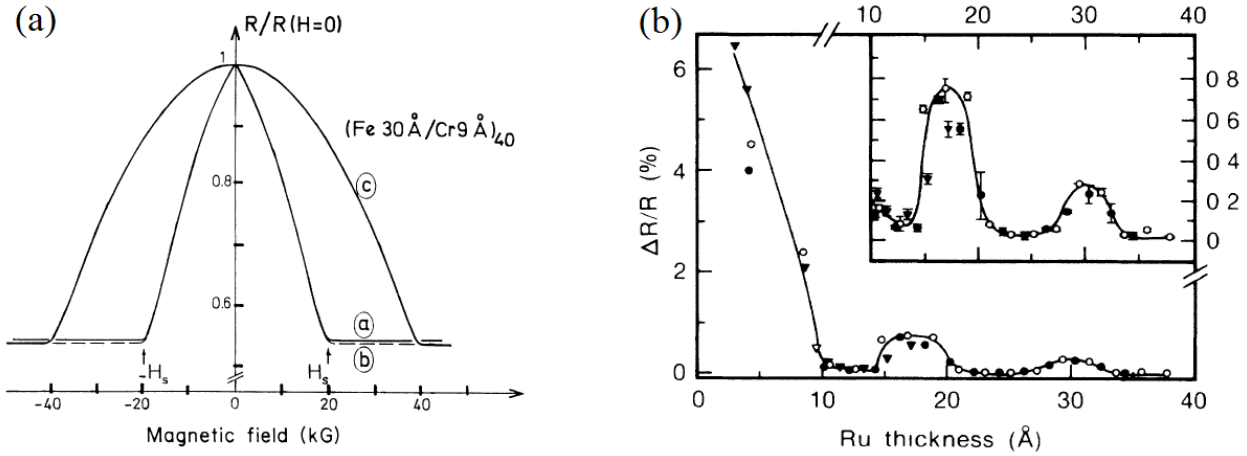

Figure 1.4: Panel (a) - first demonstration of GMR effect by Baibich[14] in Fe(3 nm)/Cr(0.9 nm)) multilayers with 40 periods. The maximum observed GMR is 74 % at $T = 4$ K. Curve ⓐ - field is applied in the plane and along the current direction, curve ⓑ - field is in plane and perpendicular to the current direction, and curve ⓒ - field is perpendicular to the plane of the stack. Panel (b) - saturation magnetoresistance in Co/Ru(x)/Co multilayers which demonstrates RKKY coupling. The graph is after Parkin[267].

The fact that the coupling is oscillatory and varies between ferromagnetic and antiferromagnetic is established shortly afterwards by Parkin[267, 266]. The current flows in the plane of the structure and it is demonstrated that the resistance in the antiparallel magnetization alignment is higher than in the parallel resistance alignment. This configuration is known as current-in-plane GMR (CIP-

GMR) and the GMR effect is defined as

$$\mathrm{GMR} = \frac{R_{\mathrm{AP}} - R_{\mathrm{P}}}{R_{\mathrm{P}}}, \tag{1.30}$$

where R_{AP} and R_{P} are the antiparallel and the parallel state resistances, respectively.

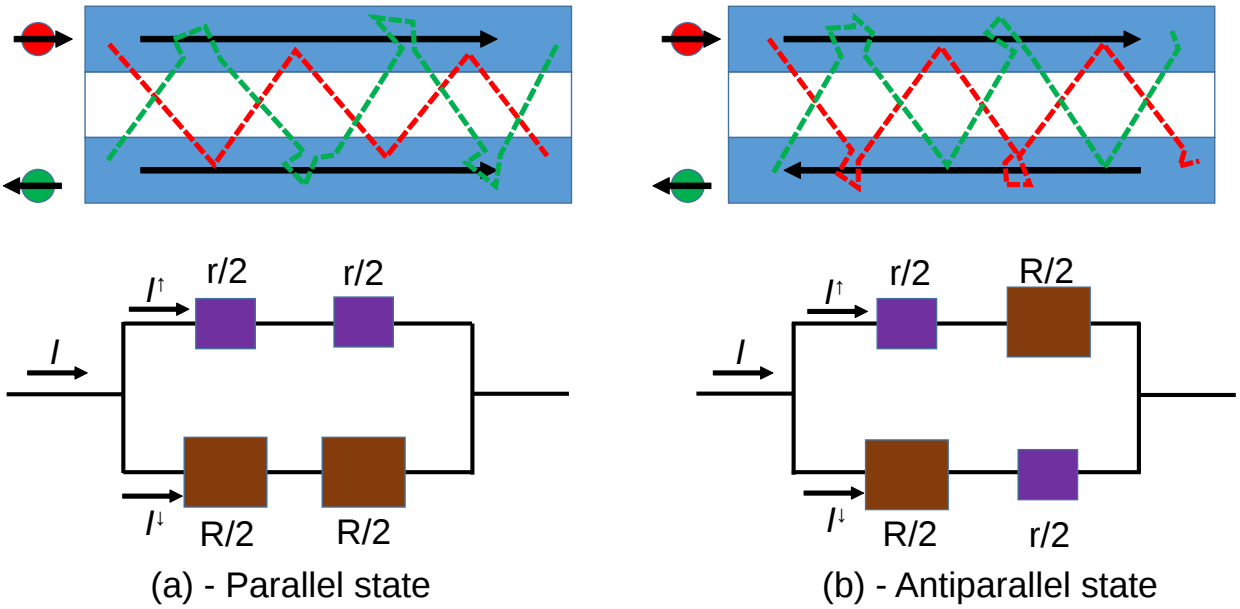

Figure 1.5: Mott two current model for the spin dependent scattering in CIP-GMR spin valves. The top part represents the spin scattering at the two interfaces and the bottom part the corresponding circuits theory. Panel (a)-parallel configuration, Panel (b)-antiparallel configuration.

The behaviour is ascribed to spin dependent scattering between the magnetic layers. Furthermore, the antiparallel resistance increases when the period of the multilayered structure is higher which is a further demonstration of spin related scattering. The effect can be phenomenologically described by the Mott two current model which is outlined in Fig. (1.5). In this case, the overall current, I, is split into spin-up, $I^{\uparrow}$, and spin-down, $I^{\downarrow}$, current components. Then the spin scattering of each component on the two ferromangetic/spacer interfaces is considered. For the parallel resistance case, the majority, spin-up, component has low scattering rate on both interfaces and, therefore, lower resistance $r/2$, whereas the minority, spin-down, component has high scattering rate on both interfaces and, therefore, higher resistance. For the antiparallel orientation, the spin-up electrons have high scattering rate on one of the interfaces $R/2$ and low scattering rate on the other interface $r/2$; the spin-down electrons have similar behaviour but the scattering rates are inversed.

Therefore, the resistance in the parallel and antiparallel case is

$$R_{\mathrm{AP}} = \frac{Rr}{R+r}, \quad R_{\mathrm{P}} = \frac{R+r}{4}, \tag{1.31}$$

it could be easily shown that the relation $R_{\mathrm{AP}} \geq R_{\mathrm{P}}$ is always true.

There is alternative measurements configuration in which the current flow perpendicular to the stack - CPP-GMR effect. Such measurements have been first done by Pratt *et al.*[272]. Due to the fact that the resistance in these devices is very low, they are measured with high sensitive current SQUID pre-amplifier for low impedances[272] or they have to be patterned into nano-pillars. The CPP-GMR devices attract significant attention because the CPP-GMR effect is higher[272, 410] and CPP-GMR nano-pillar magnetic sensor are projected to be integrated in higher areal density hard-disk drives[82]. While CIP-GMR effect is mainly due to spin scattering at the interfaces, the CPP-GMR is due to spin accumulation as the current is injected across the spacer. Recently, CPP-GMR effect up to 72 % has been realized with the structure $Co_2Fe(Ga_{0.5}Ge_{0.5})$-AgZn-$Co_2Fe(Ga_{0.5}Ge_{0.5})$ [82]. The extensive theory of the CPP-GMR is given by Valet and Fert[352].

1.2.2 Magnetic tunnel junctions

Another building block in the field of spin electronics is the magnetic tunnel junction (MTJ). It has close similarity with the GMR SV, however, in this case the role of metallic spacer is played by an insulating barrier (AlO_x, MgO, $SrTiO_3$, AlN are some of the exploited choices). The tunneling magnetoresistance (TMR) ratio in the MTJ devices is significantly higher than the GMR achieved with SVs. The room temperature records are 70 %[363] in AlO_x-based MTJs and 600 %[148] in MgO-based MTJs. The discussion on the difference between the incoherent (through AlO_x barriers) and coherent tunneling (through MgO barriers) is left for later (see Chapter 6). Because of the higher MR effects and the better electrical control of the magnetization through spin-transfer torque, MgO-based MTJs are more suitable for storage elements at present*.

The first observation of TMR has been made by Jilliere [154] in MTJs with the structure Fe/Ge/Co (see Fig. (1.6) (a)). The observed effect is approximately 11 % at 4.2 K at zero bias and decreased quickly both in bias and in temperature. The result has not attracted significant attention apart from a report of TMR with the antiferromagnetic barrier NiO by Maekawa and Gäfvert[208]. The breakthrough is made in 1995, when Moodera[235] and Miyazaki[229] demonstrate room-temperature TMR in excess of 10 % in MTJs with amorphous AlO_x barrier (see Fig. (1.6) (b)). Significantly higher TMR ratios are obtained in 2004 by Parkin[268] and Yuasa[403] when MTJs with a crystalline MgO barrier are grown and investigated. For technological reasons, the structure of an MTJ is significantly more complicated than the simple ferromagnet-insulator-ferromagnet trilayer. An optimized in-plane MgO-based MTJ grown on Si/SiO_2 standard wafer is presented on Fig. (1.7). The reason for most of the layers is explained on the graph. The synthetic antiferromagnetic (SAF) structure is utilized for the bottom electrode in order to reduce the stray field effect

*The resistance-area product in MTJs is constant. Therefore, the area reduction in the MTJs leads to higher resistance. Possible solution is reduction of the barrier thickness, however, this degrades the TMR ratios and generally results in lower device yield due to defects in the ultrathin barrier.

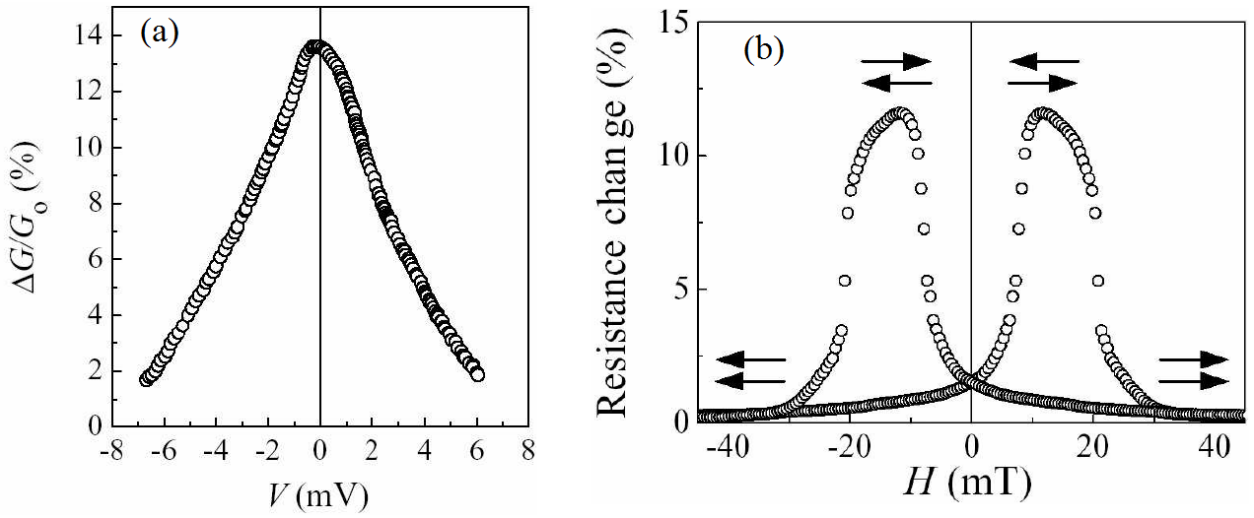

Figure 1.6: Panel (a)-the first demonstration of TMR effect. Graph is after Julliere [154]. Panel (b)-high room temperature TMR effect demonstrated by Moodera[235].

on the top electrode[212]. The Ru thickness is chosen so that the RKKY exchange interaction is antiferromagnetic and the two CoFe(B) layers in the SAF have opposite magnetizations. Therefore, the overall SAF stray field on the free ferromagnetic layer is reduced. The Ru layer acts as an efficient boron getter. The boron is pushed away upon annealing from the amorphous CoFeB and the CoFe crystallizes. If no boron getter layer is present, boron-oxide is formed at the MgO interfaces and this has detrimental effect on the TMR values[401]. Finally, the Ru layer acts as Mn diffusion barrier as well[212].

Julliere's model which describes the relation between the spin polarizations of the ferromagnetic electrodes and the TMR effect is considered in detail. The tunneling current between two electrodes is given by:

$$I(V) \propto \int_{-\infty}^{+\infty} \rho_1(E)T(E-eV)\rho_2(E-eV)(f(E)-f(E-eV))\mathrm{d}E, \tag{1.32}$$

where $\rho_1(E)$ and $\rho_2(E)$ is the density of states energy dependence of the two electrodes*, and $T(E-eV)$ is the tunneling probability for the particular energy and applied bias. When the tunneling is between ferromagnetic electrodes then it is spin dependent and depends on the particular spin-split density of states. Therefore, there are antiparallel (I_{AP}) and parallel (I_{P}) state currents. The representation of the tunneling between the spin sub-bands of the two ferromagnetic electrodes is shown on Fig. (1.8). In the parallel case, the current depends on the products of the majority-majority and minority-minority carriers density of states of the 1-2 electrodes. In the antiparallel case, the magnetization M_2 of the second electrode is assumed to be opposite with respect to the magnetization M_1 of the first electrode. The negative magnetization inverses the structure of the

*It is assumed that the electrodes have the same Fermi energy E_{F}, and that $E = 0$ is the Fermi level.

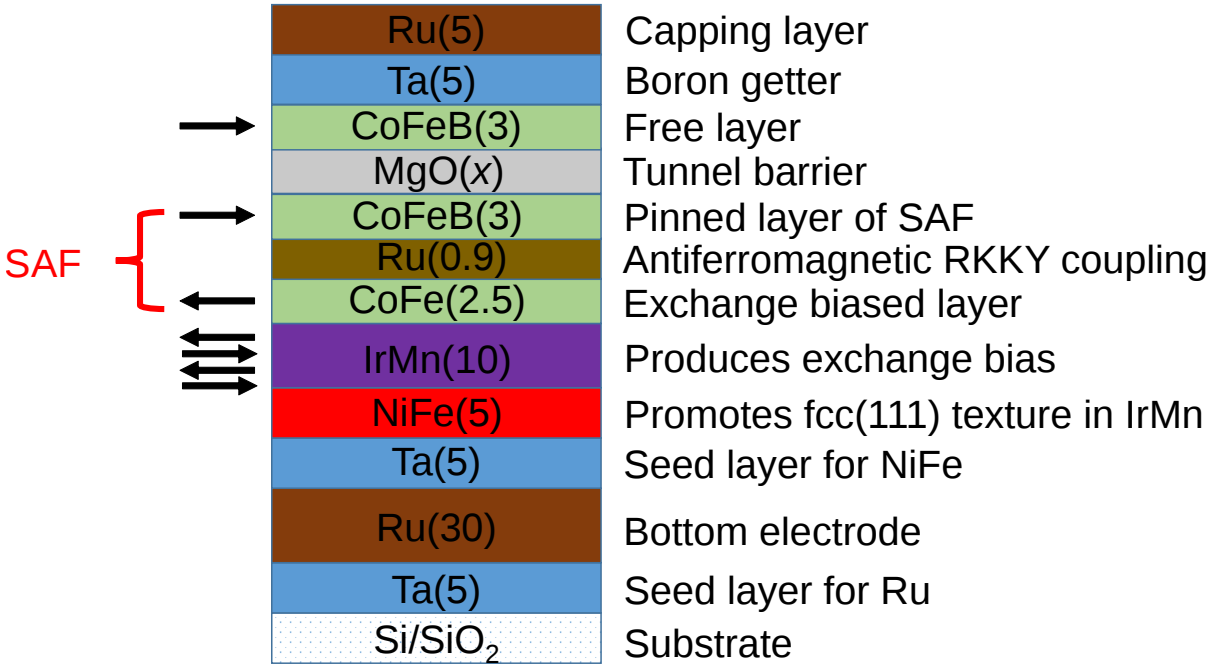

Figure 1.7: Optimized stack structure for in-plane magnetization MgO-based MTJs. The thickness of each layer is displayed in brackets in nm. This structure has been optimized in our lab and achieves TMR of 295 %. The structure is after Lau[193].

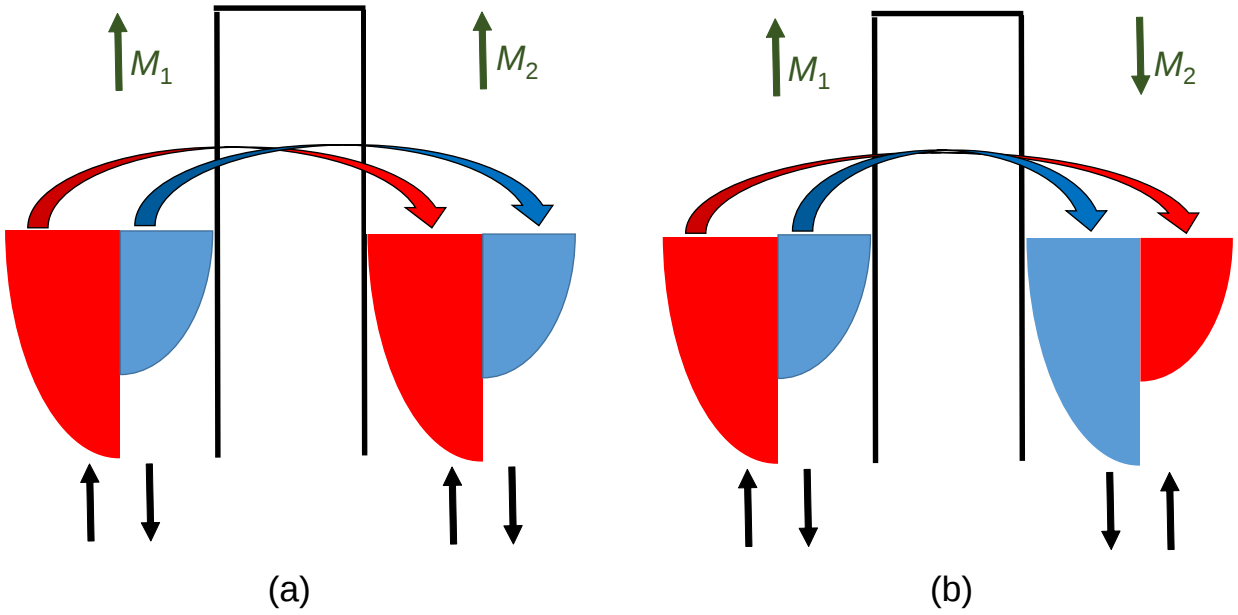

Figure 1.8: Schematic representation of the tunneling magnetoresistance between the spin-split density of states of the two ferromagnetic layers, 1 and 2. Positive spin polarization is assumed for both electrodes. Panel (a)-parallel resistance, panel (b)-antiparallel resistance. Red arrows indicate tunneling between spin-up states and blue arrows-between spin-down states. The magnetization directions, M_1 and M_2, are presented as green arrows.

spin-split bands. Therefore, the spin-up electrons are in this case minority, and the spin-down electrons are majority. The current in the antiparallel case depends on the products of the majority-

minority and minority-majority carriers DOS of the 1-2 electrodes.

Generally, the respective tunneling probabilities, T, are spin-dependent as well, then the tunneling current can be represented as

$$\begin{aligned} I_{\mathrm{AP}}(V) &\propto \int_{-\infty}^{+\infty} \left[\rho_1^{\uparrow}(E)T_{\uparrow\downarrow}(E-eV)\rho_2^{\downarrow}(E-eV) + \rho_1^{\downarrow}(E)T_{\downarrow\uparrow}(E-eV)\rho_2^{\uparrow}(E-eV)\right] \times \\ &\times (f(E)-f(E-eV))\,\mathrm{d}E, \\ I_{\mathrm{P}}(V) &\propto \int_{-\infty}^{+\infty} \left[\rho_1^{\uparrow}(E)T_{\uparrow\uparrow}(E-eV)\rho_2^{\uparrow}(E-eV) + \rho_1^{\downarrow}(E)T_{\downarrow\downarrow}(E-eV)\rho_2^{\downarrow}(E-eV)\right] \times \\ &\times (f(E)-f(E-eV))\,\mathrm{d}E. \end{aligned}$$

Then the differential conductances $G_{\mathrm{AP}} = \mathrm{d}I_{\mathrm{AP}}/\mathrm{d}V$, and $G_{\mathrm{P}} = \mathrm{d}I_{\mathrm{P}}/\mathrm{d}V$ are

$$\begin{aligned} G_{\mathrm{AP}}(V) &\propto \frac{\mathrm{d}}{\mathrm{d}V}\int_{-\infty}^{+\infty} \left[\rho_1^{\uparrow}(E)T_{\uparrow\downarrow}(E-eV)\rho_2^{\downarrow}(E-eV) + \rho_1^{\downarrow}(E)T_{\downarrow\uparrow}(E-eV)\rho_2^{\uparrow}(E-eV)\right] \times \\ &\times (f(E)-f(E-eV))\,\mathrm{d}E \\ G_{\mathrm{P}}(V) &\propto \frac{\mathrm{d}}{\mathrm{d}V}\int_{-\infty}^{+\infty} \left[\rho_1^{\uparrow}(E)T_{\uparrow\uparrow}(E-eV)\rho_2^{\uparrow}(E-eV) + \rho_1^{\downarrow}(E)T_{\downarrow\downarrow}(E-eV)\rho_2^{\downarrow}(E-eV)\right] \times \\ &\times (f(E)-f(E-eV))\,\mathrm{d}E. \end{aligned}$$

The integration is from $-\infty$ to $+\infty$, however, the sensible numerical limits are set by the spread of the difference of the Fermi distributions. In principle, the differentiation $\mathrm{d}/\mathrm{d}V$ must act on $\rho_2^{\downarrow}(E-eV)$ and $\rho_2^{\uparrow}(E-eV)$, however, for low bias or for large exchange splitting approximation the spin-split density of states might be assumed to be constant or their derivatives to be small. The transmission probabilities should also be differentiated but in amorphous barrier approximation it can be assumed that there is no particular spin dependent transmission and, therefore, the transmission probability is not bias or spin dependent ($T_{\uparrow\downarrow} = T_{\downarrow\uparrow} = T_{\uparrow\uparrow} = T_{\downarrow\downarrow} = T$). That means that essentially only the difference of the Fermi distributions is differentiated. The Fermi level derivative can be approximated by a Gaussian distribution with full-width-half- maximum (FWHM) of $\approx 3.8k_{\mathrm{B}}T$[318]. At low temperatures, the derivative might be assumed to be a delta function $\delta(E-eV)$:

$$G_{\mathrm{AP}}(V) \propto \int_{-\infty}^{+\infty} \left[\rho_1^{\uparrow}(E)T(E-eV)\rho_2^{\downarrow}(E-eV) + \rho_1^{\downarrow}(E)T(E-eV)\rho_2^{\uparrow}(E-eV)\right] \delta(E-eV)\mathrm{d}E \tag{1.33}$$

$$G_{\mathrm{P}}(V) \propto \int_{-\infty}^{+\infty} \left[\rho_1^{\uparrow}(E)T(E-eV)\rho_2^{\uparrow}(E-eV) + \rho_1^{\downarrow}(E)T(E-eV)\rho_2^{\downarrow}(E-eV)\right] \delta(E-eV)\mathrm{d}E, \tag{1.34}$$

Therefore, $G_{AP}(V) \propto \rho_1^{\uparrow}(eV)\rho_2^{\downarrow}(0)+\rho_1^{\downarrow}(eV)\rho_2^{\uparrow}(0)$ and $G_P(V) \propto \rho_1^{\uparrow}(eV)\rho_2^{\uparrow}(0)+\rho_1^{\downarrow}(eV)\rho_2^{\downarrow}(0)$. These expressions demonstrate an important concept: the tunneling process happens between the Fermi level of electrode 2 and the conduction band of electrode 1 at level $E = eV$ above E_F. When the bias is opposite, the tunneling happens between the Fermi level of electrode 1 and the conduction band of electrode 2 at level $E = eV$. Therefore, the bias dependence of the conduction gives information about the energy dependence of the spin polarization (see Fig. (1.9)). At zero bias approximation the tunneling transport is between the Fermi levels of the two electrodes: $G_{AP}(0) \propto \rho_1^{\uparrow}(0)\rho_2^{\downarrow}(0)+\rho_1^{\downarrow}(0)\rho_2^{\uparrow}(0)$ and $G_P(0) \propto \rho_1^{\uparrow}(0)\rho_2^{\uparrow}(0)+\rho_1^{\downarrow}(0)\rho_2^{\downarrow}(0)$. Starting from the DOS definitions of the spin polarizations

$$P_1(0)P_2(0) = \frac{\rho_1^{\uparrow}(0)-\rho_1^{\downarrow}(0)}{\rho_1^{\uparrow}(0)+\rho_1^{\downarrow}(0)}\frac{\rho_2^{\uparrow}(0)-\rho_2^{\downarrow}(0)}{\rho_2^{\uparrow}(0)+\rho_2^{\downarrow}(0)}, \tag{1.35}$$

it can be easily checked that

$$\frac{G_P(0)}{G_{AP}(0)} = \frac{1+P_1(0)P_2(0)}{1-P_1(0)P_2(0)}, \tag{1.36}$$

and the TMR is then

$$\mathrm{TMR}(0) = \frac{G_P(0)}{G_{AP}(0)} - 1 = \frac{1+P_1(0)P_2(0)}{1-P_1(0)P_2(0)} - 1, \tag{1.37}$$

$$\mathrm{TMR}(0) = \frac{2P_1(0)P_2(0)}{1-P_1(0)P_2(0)} \tag{1.38}$$

The last expression is known as the Julliere's formula as is often used to estimate spin polarization of ferromagnetic compositions. The expression can be generalized for finite bias*.

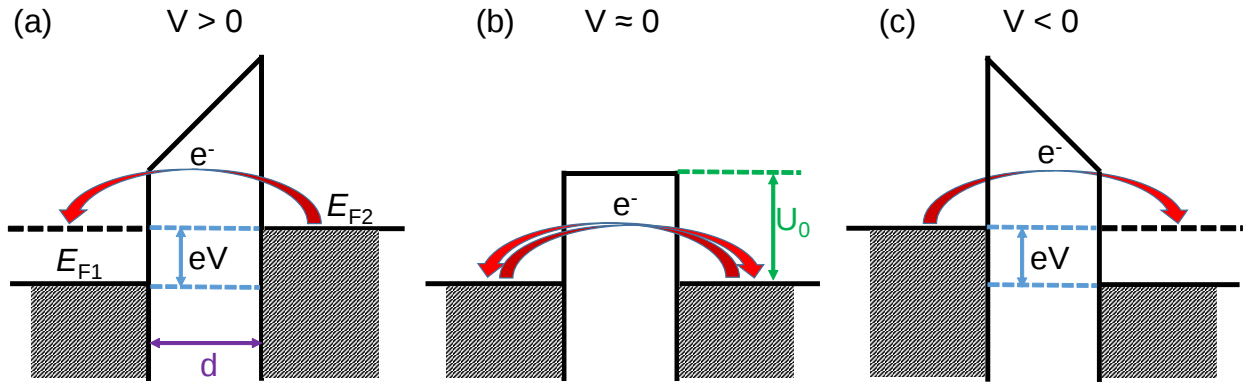

Figure 1.9: Schematic representation of adiabatic tunneling through a rectangular barrier with thickness d and height U_0. Panel (a): positive bias, panel (b): close to zero bias, and panel (c): negative bias. The transport direction of the tunneling electrons is indicated with a red arrow. It is assumed that the barrier height is not reduced: $eV \ll U_0$.

*Again, there is the assumption that there are no high-bias related inelastic excitations like magnons and phonons. In real devices, this conditions is not true.

$$\mathrm{TMR}(V) = \begin{cases} \frac{2P_1(eV)P_2(0)}{1-P_1(eV)P_2(0)}, & \text{if } V > 0, \\ \frac{2P_1(0)P_2(|eV|)}{1-P_1(0)P_2(|eV|)}, & \text{if } V < 0. \end{cases} \tag{1.39}$$

There has been a significant problem in the understanding of the spin transport because the spin-polarized tunneling (see Sec.(1.4.5)) measures positive spin polarization whereas the density of states spin polarization is negative. The tunneling spin polarization is demonstrated to depend not only on the density of states weight but as well on the Fermi velocities from the different bands. The lighter *s* electrons are delocalized and, hence, their contribution towards the tunneling current is higher than the localized *d* electrons.

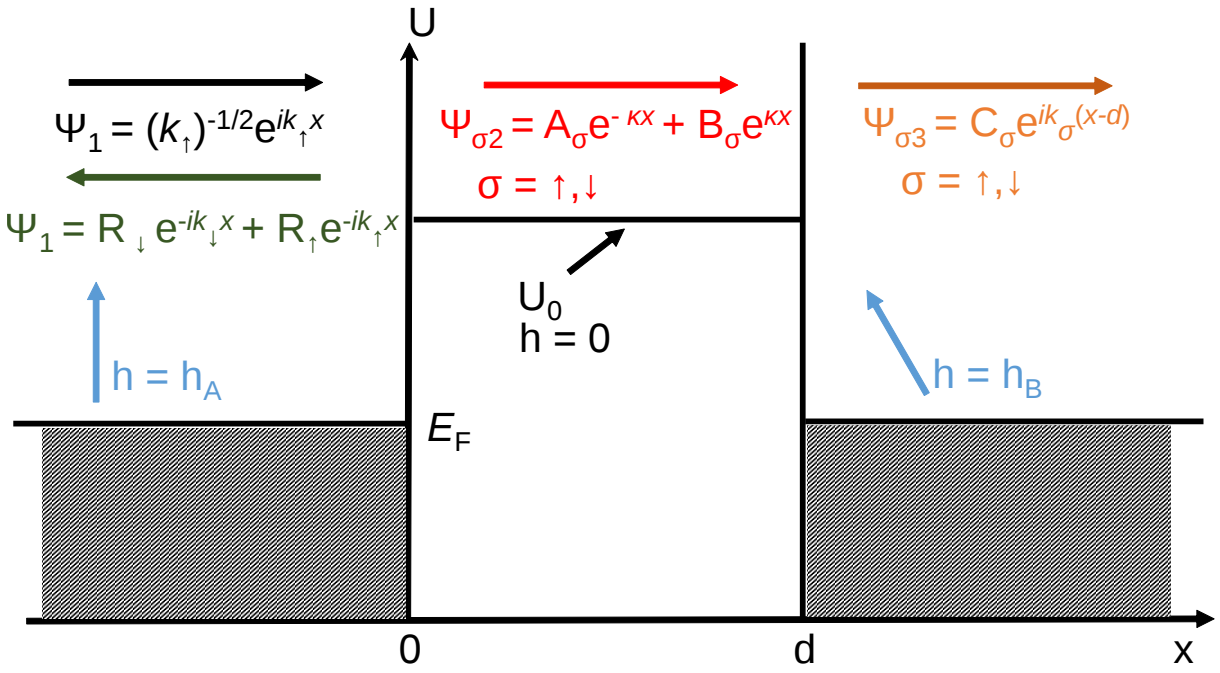

Figure 1.10: Schematic representation of the quantum mechanical model of TMR by Slonczewski[310]. Spin-up electron plane wave is assumed to travel from $-\infty$ towards $x = 0$. The exchange axes in the two ferromagnets are generally non-colinear and their magnitude is different. In the barrier region $0 < x < d$, the electron wavefunction, $\psi_{\sigma 2}$, is evanescent. The important parameters are the spin-dependent transmission coefficients in the second ferromagnetic layer: $C_\uparrow$ and $C_\downarrow$.

The models of Stearns[319] and Slonczewski[310] give theoretical overview of how the Fermi level and the barrier properties change the effective spin polarization. Stearns has suggested that the tunneling spin polarization depends on effective mass of the carriers located around the Fermi level. The simple model proposes that the electrical transport polarization is dominated by the more dispersive *s*- electrons* which are hybridized with the more localized *d*-bands. The carriers from the dispersive bands behave like free-electrons, therefore, Stearns has stated that the spin

*Stearns calls them "itinerant *d* electrons"

polarization depends on the Fermi wavevectors of the dispersive bands:

$$P_{\text{Stearns}} = \frac{k^{\uparrow} - k^{\downarrow}}{k^{\uparrow} + k^{\downarrow}}. \tag{1.40}$$

The term "tunneling density of states" is often used to designate the difference between the cumulative DOS and the part of the DOS which is relevant in the spin transport[208].

The model of Slonczewski considers one-dimensional tunneling transport between two semi-infinite ferromagnetic layers (layer 1: $x < 0$ and layer 3: $x > d$) through an insulating barrier (layer 2: $0 < x < d$) (see Fig. (1.10)). Low bias, close to Fermi level, transport is assumed. By stitching the spinor wavefunctions and their derivatives at the interfaces, the required spin-dependent transmission probabilities are calculated. The important conclusion from Slonczewski's model is that the effective spin polarization in the MTJ structure is not necessarily an intrinsic properties of the ferromagnetic layer instead it is considered as a general property of the ferromagnet-barrier bilayer

$$P_{\text{fb}} = \frac{k_{\uparrow} - k_{\downarrow}}{k_{\uparrow} + k_{\downarrow}} \frac{\kappa^2 - k_{\uparrow}k_{\downarrow}}{\kappa^2 + k_{\uparrow}k_{\downarrow}}, \tag{1.41}$$

where $k_{\uparrow}$ and $k_{\downarrow}$ are the spin-up and spin-down wavevectors at the Fermi level of the left ferromagnetic layer, and κ is the decay constant in the insulating barrier. The most important implication of this result is that both the magnitude and the sign of P_{fb} depend on the relative magnitude of the wavefunction decay κ and the geometric mean of the spin-up and spin-down Fermi wavevectors $\sqrt{k_{\uparrow}k_{\downarrow}}$. Therefore,

$$P_{\text{fb}} = \begin{cases} P_{\text{f}}, & \text{if } \kappa \gg \sqrt{k_{\uparrow}k_{\downarrow}}, \\ -P_{\text{f}}, & \text{if } \kappa \ll \sqrt{k_{\uparrow}k_{\downarrow}}, \end{cases} \tag{1.42}$$

where $P_{\text{f}} = (k_{\uparrow} - k_{\downarrow})/(k_{\uparrow} + k_{\downarrow})$ is the intrinsic Fermi level spin polarization of the ferromagnetic layer. The dependence of the effective spin polarization P_{fb} on the barrier height $\kappa^2/k_{\downarrow}^2$ is presented on Fig. (1.11 (a)). In fact, the TMR ratio is higher in MTJs with thicker barriers.The other crucial suggestion by the Slonczewski's model is that the conductance through the barrier depends on the angle Θ between the spin polarization axis of the two ferromagnetic layers

$$G = G_0 \left(1 + P_{\text{fb}} P_{\text{f'b}} \cos(\Theta)\right), \tag{1.43}$$

Apart from the trivial cases of antiparallel ($\Theta = 0$) and parallel alignment ($\Theta = \pi$), the above expressions suggests that the measured TMR is reduced when the magnetization axes of the two

ferromagnetic layers are non-colinear. The TMR is represented in this case as:

$$\mathrm{TMR}(\Theta_\mathrm{m}) = \frac{G_\mathrm{P} - G_\mathrm{AP}}{G_\mathrm{AP}} = \frac{G_0(1 - P_1P_2\cos(\Theta_\mathrm{m})) - G_0(1 + P_1P_2\cos(\pi - \Theta_\mathrm{m}))}{G_0(1 + P_1P_2\cos(\pi - \Theta_\mathrm{m}))}, \tag{1.44}$$

$$\mathrm{TMR}(\Theta_\mathrm{m}) = \frac{2P_1P_2\cos(\Theta_\mathrm{m})}{1 - P_1P_2\cos(\Theta_\mathrm{m)}} = \mathrm{TMR}(0)\frac{1 - P_1P_2}{1 - P_1P_2\cos(\Theta_\mathrm{m})}\cos(\Theta_\mathrm{m}), \tag{1.45}$$

where Θ_m is the angle between the two spin polarization axes and the dependence $\mathrm{TMR}(\Theta_m)$ is presented on Fig. (1.11) (b).

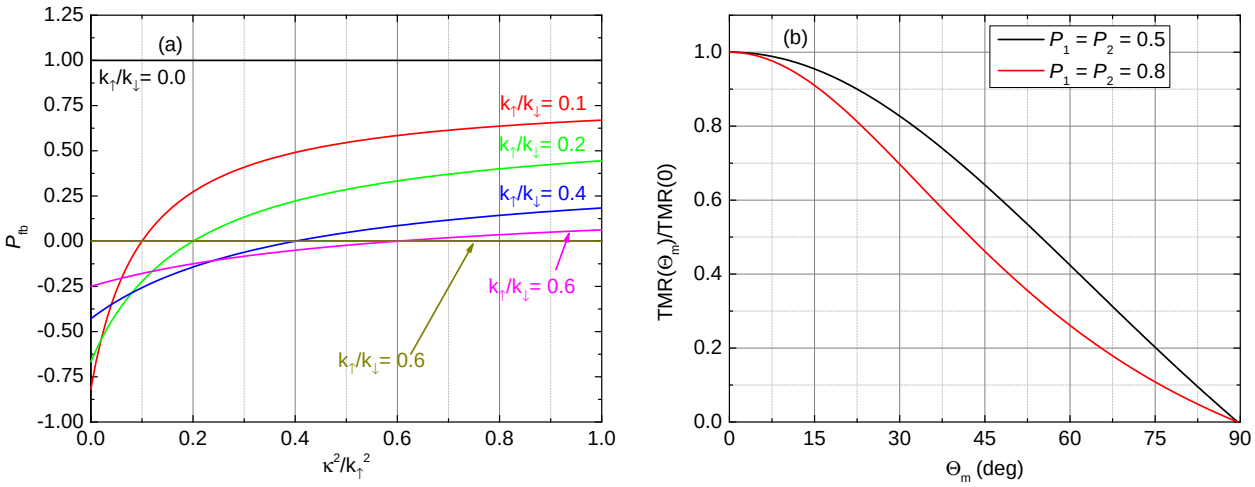

Figure 1.11: Panel (a)-Dependence between the effective spin polarization P_fb and the barrier height $\kappa^2/k_\uparrow^2$ for different ratios between the Fermi wavevectors for spin-up and spin-down. Panel (b)-Dependence between the normalized TMR and the angle between the magnetizations of the two ferromagnetic electrode. The black curve corresponds to $P_1 = P_2 = 0.5$, and the red curve to $P_1 = P_2 = 0.8$.

1.2.3 Spin electronic devices as memory and oscillator elements

Magnetic tunnel junctions can be used as memory cells. In that case, the magnetic alignment of the electrodes determines whether the bit is '1'(antiparallel state) or '0'(parallel state). The application of MTJs as non-volatile magnetic memory is particularly intriguing. This concept is known as magnetic random access memory (MRAM). The two main competitors in the RAM domain are the DRAM and the SRAM but they both rely on the charge accumulated either on capacitors or transistors, and hence are volatile memory elements. Furthermore, there is a necessity for data refreshment due to charge leakage and this adds up to the energy consumption in the DRAM case, while a single bit memory cells contains 4-6 transistors in the SRAM case and has large footprint. In that sense, the non-volatility of the MRAM is very beneficial. The state of the MTJs must be electrically, and not magnetically, controlled. There are three main approached for the electrical control of MTJs: toggle switching (TS)[91], spin Hall effect (SHE)[228], and spin-transfer torque (STT) switching[311]. The most prospective and investigated approach nowadays is

the the STT-based MRAM → STT-MRAM. Such memory chips are already commercially available and their density scalability is of particular scientific and technological interest. The essence of the STT is that the spin polarized electrons from the bottom electrode carry not only charge but angular momentum as well. If the spin polarization axis from the polarizing electrode, $\hat{\boldsymbol{\sigma}}$, is not co-linear with the magnetization unit vector of the analyzer, $\hat{\boldsymbol{m}}$, then the total angular momentum must relax. The lost angular momentum is absorbed by the magnetization of the analyzer. Due to this absorbed angular momentum, the magnetization gets offset from its equilibrium position and starts precessing around the direction of the effective magnetic field. The precession is naturally damped for low current densities, however, if the spin-transfer torque is sufficiently strong, the damping is overcome and the magnetization switches from up to down state. The effect of STT is theoretically predicted by Slonczewski[311] and Berger[21]. Other extensive treatment on the topic is given by Stiles[320]. The equation which describes the magnetization dynamics under spin-polarized current is the Landau-Lifshitz-Gilbert equation*:

$$\frac{\partial \hat{\boldsymbol{m}}}{\partial t} = -\gamma \hat{\boldsymbol{m}} \times \mu_0 \boldsymbol{H}_{\text{eff}} + \alpha \hat{\boldsymbol{m}} \times \frac{\partial \hat{\boldsymbol{m}}}{\partial t} - a_{\text{SL}} \hat{\boldsymbol{m}} \times (\hat{\boldsymbol{\sigma}} \times \hat{\boldsymbol{m}}) - b_{\text{FL}} \hat{\boldsymbol{m}} \times \hat{\boldsymbol{\sigma}}. \tag{1.46}$$

The first term above is the usual Larmor precession of the magnetization around the local effective field $\boldsymbol{H}_{\text{eff}}$ with a gyromagnetic ratio γ. The second term, Gilbert torque, describes magnetization dynamics damping with a material constant α, Gilbert damping parameter. The third term, Slonczewski torque a_{SL}, describes the transfer of angular momentum between the spin polarized incoming electrons and the magnetization of the free layer. The forth term, b_{FL}, is known as field-like torque. The latter is due to the Oersted field created by the electron flow. The important figure of merit for the STT-based switching is the critical switching current density (j_{c}). For the case of in-plane easy axis ferromagnetic layer with thickness, t, and coercive field H_{c} in the macrospin approximation[326]:

$$j_{\text{c}} = \frac{2e}{\hbar} \frac{2\alpha \mu_0 M_{\text{s}} t}{\eta} \left(H_{\text{c}} + \frac{H_{\text{eff}}}{2} \right), \tag{1.47}$$

where η is the STT efficiency and H_{eff} is the effective out-of-plane demagnetizing field. Whereas, the critical current density for the case of a layer with perpendicular magnetic anisotropy (PMA) is

$$j_{\text{c}} = \frac{2e}{\hbar} \frac{\alpha \mu_0 M_{\text{s}} t}{\eta} \frac{H_{\text{an}}}{2}, \tag{1.48}$$

where H_{an} is the anisotropy field. In the case of MTJs with PMA, lower switching currents can be achieved for the same value of thermal stability[211]. It is projected that next generation of MRAM cells will be with PMA layers in order to achieve areal density of 1 Gbit/in^2 while maintaining the data stability figures. For an asymmetric structure with different spin polarizations of the two

*It is true within the macrospin approximation or neglecting the demagnetizing field.

ferromagnetic layers, the complete dependence is rather complicated[389], while for symmetric structure the expression is:

$$\eta \approx \frac{P\Lambda^2 \sin\theta}{(\Lambda^2+1)+(\Lambda^2-1)\cos\theta}, \tag{1.49}$$

where θ is the angle between the magnetizations of the two ferromagnetic layers, P is the spin polarization and Λ^2 is a device- and material- related constant, which is independent of the magnetic properties (see Eq. (2) in [389]). The important information out of Eq. (1.49) is that for a fixed angle, θ, the STT efficiency increases linearly with the spin polarization.

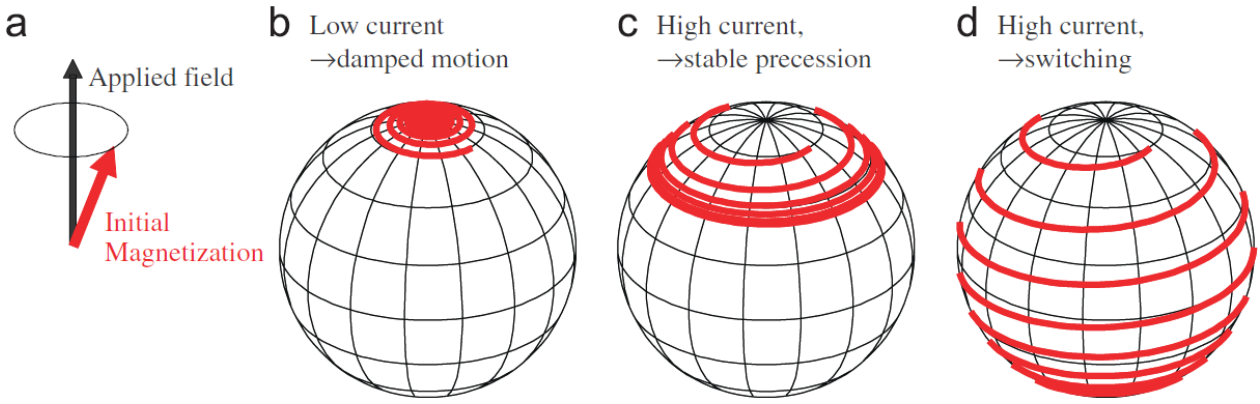

Figure 1.12: Panel (a)-magnetization oscillation regimes under spin-transfer torque for magnetization along z with no anisotropy. Panel (b)-low current results in damped motion. Panel (c)-high current results in stable precession along the axis of the effective field. Panel (d)-higher current leads to magnetization switching. The picture is after Ralph and Stiles[274].

Apart from the magnetization switching by STT, another mode of operation is stable oscillations. The MTJs must be patterned into nano-pillars in order to utilize the STT effect, and, therefore, these devices are called spin-transfer nano-oscillators (STNO). In this case, the current density is sufficiently high so that the magnetization precession is not damped but on the other hand the STT is not too strong, so that the magnetization is not switched (see Fig. (1.12)). Application of different current through the device leads to tunability of the output frequency[277].

The maximum output frequency in STNO devices to date is 65 GHz[35]. Such high frequencies are achieved by application of strong magnetic field of more than 1 T which is not very practical. High operational frequencies can be achieved with materials with higher anisotropy constants. For instance, very high sub-THz magnetization precession frequencies of 280 GHz and 500 GHz are measured in $Mn_{3-\delta}Ga$[233] and Mn_3Ge[232], respectively. There has been no integration of these compositions in STNO so far. Particularly intriguing is the excitation of the antiferromagnetic resonance frequency (AFMR) in compensated ferrimagnets or in antiferromagnets. This mode provides theoretically oscillations at much higher frequencies. Following the original work by

Kittel[171], the AFMR frequency is:

$$f_{\mathrm{AFMR}} = \frac{\gamma}{2\pi}\left[H_{\mathrm{eff}} + \sqrt{H_{\mathrm{an}}(H_{\mathrm{an}} + 2H_{\mathrm{ex}})}\right], \tag{1.50}$$

where H_{an}, H_{ex} are the anisotropy and exchange fields, respectively. In approximation $H_{\mathrm{an}} \ll H_{\mathrm{ex}}$ and for $H_{\mathrm{eff}} = 0$, the frequency is

$$f_{\mathrm{AFMR}} = \frac{\gamma}{2\pi}\sqrt{2H_{\mathrm{an}}H_{\mathrm{ex}}}. \tag{1.51}$$

The situation is far more complicated in the AFMR with ferrimagnets as the two (or more) sublattices have different gyromagnetic ratios and anisotropies*. The reader is referred to the works of Kaplan[160], Geschwind[108] and Wangness[366]. In fact, both the usual FMR and the AFMR modes can be observed in ferrimagnetic compositions. Schematically, the FMR mode corresponds to the two sublattice magnetizations, M_1 and M_2 , being colinear and oscillating synchronously around the effective field H_{eff}. The sublattice magnetizations are not colinear in the case AFMR (see Fig. (1.13)).

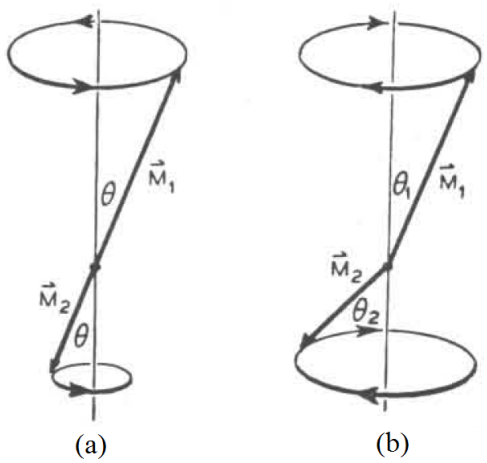

Figure 1.13: Schematic representation of FMR resonance mode (a) and AFMR mode (b) in ferrimagnetic systems. The picture is after Geschwind[108].

The limitation of the present STNOs is the small output power. The output power in GMR SVs is in the order of 1 pW whereas the output power in MTJs is in order of 100 nW[405].† Significant progress has been made recently towards in-phase synchronous oscillations of multiple GMR SV-based STNOs[142].

*This resonance is often referred to as exchange mode.

†MTJs have the apparent disadvantage that current pulsing might cause dielectric breakdown.

1.3 Superconductivity

The most technogically important quality of superconductors is their capacity to carry very large electric current which is used to produce high magnetic field for MRI scanners*. In this thesis, the focus falls on two other properties: the excitation density of states in superconductors and the macroscopic coherence of their wavefunctions which leads to very high magnetic flux sensitivity of the superconducting quantum interference devices (SQUIDs) based on the Josephson effect. The structure of the quasiparticle density of states plays crucial role in the superconducting based techniques for spin polarization extraction. The microscopic theory of superconductivity is developed by Bardeen, Cooper and Schrieffer (BCS) theory. The theory is based on the Cooper's prediction that even weak attractive potential can cause instability of the Fermi sea of electrons and lead to formation of at least one bound pair[65]-Cooper pair. The electron-phonon interaction is the reason for this attractive potential. The assumption is that the potential is constant below a cut-off energy, $\hbar\omega_c$, and is zero above. The threshold energy of the Cooper attractive potential is of the order of the Debye energy $\hbar\omega_{\mathrm{D}} = k_{\mathrm{B}}\Theta_{\mathrm{D}}$ which is characteristic of the phonon spectrum cut-off energy. The Cooper pair consists of two electrons with opposite spins and momentum vectors-$(\boldsymbol{k}_{\uparrow}, -\boldsymbol{k}_{\downarrow})$. A finite energy Δ is required to break apart a pair. Δ is known as the superconducting excitation gap: below that energy all electrons are paired, there are unpaired electrons above it. Some of the successes of the BCS theory are the explanation of the Meissner effect, the relation between the superconducting gap Δ and the critical temperature T_{c}, and the derivation of the energy dependence of the quasiparticle density of states†. The relation between the low temperature gap, $\Delta(0)$, and the critical temperature, T_{c}, which holds for all classical superconductors is:

$$\Delta(0) = 1.76 k_{\mathrm{B}} T_{\mathrm{c}}. \tag{1.52}$$

The BCS theory is based on the assumption that the superconducting gap Δ and the superconducting electrons density, n_{s}, are constant in space. On the other hand, the Ginzburg-Landau theory treats the spatial variation of the superconducting pseudowavefunction $\phi(r)$ at the vicinity of the critical temperature[112]. The modulus $|\phi(r)|^2$ represents the local density of the superconducting electrons $n_{\mathrm{s}}(r)$‡.

There are two important length scales which describe the properties of the superconducting condensate and appear naturally in the Ginzburg-Landau (GL) theory: coherence length ξ and

*It is expected that liquid nitrogen superconducting winding will be installed on the next generation wind turbines. The Meissner effect has been used to demonstrate the viability of frictionless train transport, however, presently the construction of such "Maglev" train track is financially unjustifiable-almost two orders of magnitude more expensive than the conventional one.

†An unpaired electron is called a quasi-particle in a superconductor.

‡It is demonstrated by Gor'kov that the GL theory is a limiting case of the microscopic BCS theory[117].

penetration depth λ. The coherence length sets a scale over which the Cooper pairs recover exponentially to equilibrium after an external perturbation. The penetration depth sets the scale over which external applied field decays exponentially in the superconductor. The postulate of the GL theory is how the free-energy density F can be represented as

$$F = F_{\mathrm{n0}} + \alpha|\psi|^2 + \frac{\beta}{2} + \frac{1}{2m^*}\left|\left(\frac{\hbar}{i}\nabla - \frac{e^*}{c}\boldsymbol{A}\right)\psi\right|^2 + \frac{h^2}{8\pi}, \tag{1.53}$$

where h is the constant external field, $\boldsymbol{A}$ is the vector potential, $m^* \approx 2m_{\mathrm{e}}{}^*$ is the mass of the Cooper pair, α and β are parameters. Relation about the α and β parameters could be extracted from physical arguments. For instance, the superconducting state is more energetically favourable only for $\alpha < 0$. The coherence length ξ is related to α: $\xi = \hbar/\sqrt{2m^*\alpha}$. The important GL parameter κ is

$$\kappa = \frac{\lambda}{\xi}. \tag{1.54}$$

The paramameter $\kappa \ll 1$ for classical superconductors. The value $\kappa = 1/\sqrt{2}$ separates the classes of type I and type II superconductors. Abrikosov[2] predicted theoretically that above certain external field H_{c1} for $\kappa > 1/\sqrt{2}$, it is energetically more favourable the field to be concentrated in normal cylindrical regions-type II superconductivity. These regions are known as Abrikosov vortices and each one carries a flux quantum $\Phi_0 = h/(2e)$. There are two critical fields in type II superconductors: lower critical field H_{c1} is the field at which vortex penetration starts but there are still superconducting regions, and upper critical field H_{c2} at which the sample has no superconducting regions. A vortex consists of a central core of radius $\approx \xi$ with a maximum field H_{c2} and circulating supercurrent region where the internal magnetic field decays exponentially at large distance from the core[†]

$$h(r) \approx \frac{\Phi_0}{2\pi\lambda^2}\left(\frac{\pi\lambda}{2r}\right)^{1/2}\exp\left(-\frac{r}{\lambda}\right). \tag{1.55}$$

The applied field is concentrated in the core of the vortex and maintained by the circular supercurrents (see Fig. (1.14 (a)).

The superconducting order parameter is totally suppressed in the vortex and increases to its equilibrium value following the dependence

$$f(r) \approx \tanh\left(\frac{r}{\xi}\right), \tag{1.56}$$

where $f(r) = |\psi(r)|/|\psi_\infty|$. In a thin superconducting film, the vortices form a regular hexagonal

[*]This is strictly speaking effective mass and it is higher than the mass of a free electron in heavy fermion superconductors.

[†]This is a single vortex, or very large inter-vortex, separation, the exact solution is $h(r) = \Phi_0/(2\pi\lambda^2)K_0(r/\lambda)$, where K_0 is a zeroth-order Hankel function (see Tinkham[342] p.152).

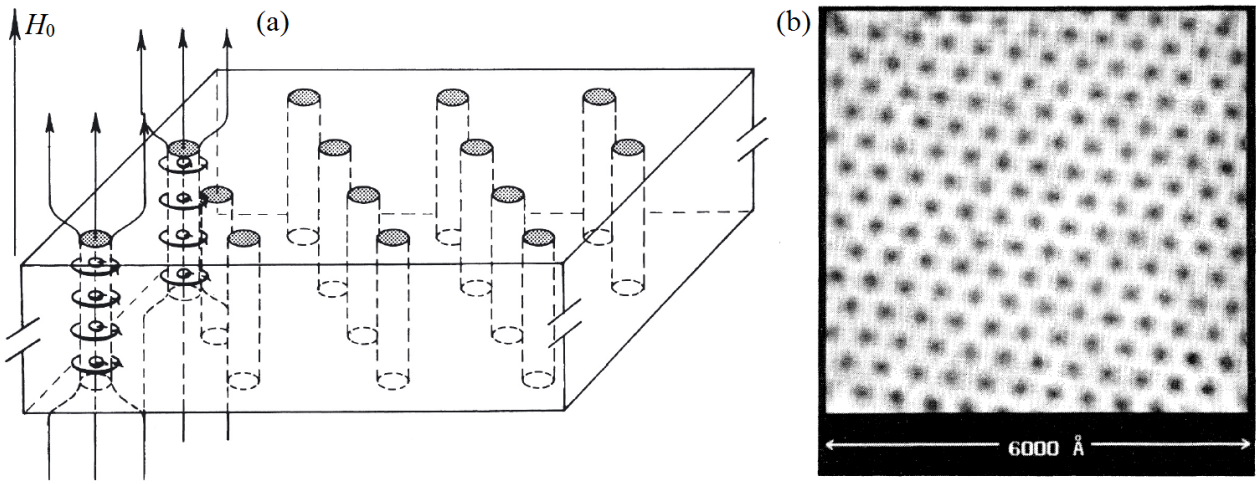

Figure 1.14: Panel (a)-Schematic representation of the concentration of the field lines in Abrikosov vortex cores. The picture is after Kleiner[173]. Panel (b)-Scanning tunneling microscopy of the Abrikosov vortex lattice in $NbSe_2$ at 1.8 K and applied field of 1 T. The figure is after Hess[136].

honeycomb structure*. A problem is that the vortex pattern might move (vortex flow) which leads to non-zero resistance in the superconductor. In practical materials, defects are used to pin the vortices.

1.3.1 Quasi-particle density of states

There are two ways to obtain the energy dependence of the free states in the DOS above the Δ gap. The first, canonical approach is following the BCS theory and introducing the elementary excitation operator γ_k - often called Bogoliubon (see Tinkham[342] pp. 59-62 and pp. 67-70). The other one is a less demanding approach following the Bogoliubov-de Gennes equation (see Kant[159] pp. 22-24). In superconductors, the unpaired electrons are referred to as quasiparticles. The quasiparticles are known as electron-like ($|e\rangle$) and hole-like ($|h\rangle$) depending on whether they are in the conduction or valence band. In this case, the wavefunction describing the unpaired condensate is

$$\Psi(x,t) = \psi_1(x,t)|e\rangle + \psi_2(x,t)|h\rangle, \tag{1.57}$$

where $|\psi_1(x,t)|^2$ and $|\psi_2(x,t)|^2$ are the probabilities for finding the quasi-particle in the electron-like or hole-like state, respectively. The spinor wavefunction Ψ must obey the Bogoliubov-de Gennes (BdG) equation

$$\begin{bmatrix} H_0 & \Delta \\ \Delta & -H_0 \end{bmatrix} \Psi = \mathrm{i}\hbar \frac{\partial \Psi}{\partial t}, \tag{1.58}$$

*The original prediction is that the vortices should form square pattern. However, it was demonstrated that the hexagonal structure is slightly more energetically favourable.

where the one-dimensional single particle Hamiltonian is

$$H_0 = -\frac{\hbar^2}{2m}\frac{\mathrm{d}^2}{\mathrm{d}x^2} - E_\mathrm{F} + V(x), \tag{1.59}$$

where m is the effective mass, E_F is the Fermi level and $V(x)$ is the potential. For heavy-fermion superconductors, the effective electron mass is significantly higher than the rest electron mass $m \gg m_\mathrm{e}$. However, the focus falls on (almost) classical s-wave superconductors with $m \approx m_\mathrm{e}$ in our experiments. The gap parameter Δ has the role of coupling strength. Apart from that, the electron-like particle obeys the Schrödinger equation and the hole-like particle obeys the time-reversed Schrödinger equation. The time-dependent BdG equation can be reduced to time-independent by the substitution $\Psi(x,t) = \psi(x)e^{-\mathrm{i}\omega t}$, where $E = \hbar\omega$, when there are no time-dependent interactions*. Then, the BdG equation becomes

$$\begin{bmatrix} H_0 & \Delta \\ \Delta & -H_0 \end{bmatrix} \psi = E\psi. \tag{1.60}$$

For the case of $V(x) = 0$ and a trial wavefunction $\psi = \binom{1}{0} e^{\mathrm{i}kx}$, the eigenvalues are

$$E^2 = \left(\frac{\hbar^2 k^2}{2m} - E_\mathrm{F}\right)^2 + \Delta^2. \tag{1.61}$$

The density of states in momentum space is $\rho(k)\mathrm{d}k$:

$$\rho(k)\mathrm{d}k = \frac{V}{(2\pi)^3} 4\pi k^2 \mathrm{d}k, \tag{1.62}$$

where $V/(2\pi)^3$ is the density of states in k-space. Therefore, the density of states can be calculated straightforward if the energy dispersion $E(k)$ is known. The important quantities in order to convert $k \to E$ are k and $\mathrm{d}k$. Starting from Eq. (1.61), it can be easily checked that:

$$k = \sqrt{\frac{2m}{\hbar}}\sqrt{\tilde{E} + E_\mathrm{F}}, \tag{1.63}$$

$$\mathrm{d}k = \sqrt{\frac{m}{2\hbar^2}}\frac{E}{\tilde{E}}\frac{\mathrm{d}E}{\sqrt{\tilde{E} + E_\mathrm{F}}}, \tag{1.64}$$

where $\tilde{E}^2 = E^2 - \Delta^2$. Therefore, it can be derived that the superconducting density of states is

$$\rho_s(E)\mathrm{d}E = \frac{V}{2\pi^3}\frac{\sqrt{2m^3}}{\hbar^3}\frac{\sqrt{\tilde{E} + E_\mathrm{F}}E}{\tilde{E}}\mathrm{d}E, \tag{1.65}$$

*like strong a.c. magnetic and electric fields

for material in normal state: $\tilde{E} = E$, and therefore the normal metal density of states is

$$\rho_0(E)\mathrm{d}E = \frac{V}{2\pi^3}\frac{\sqrt{2m^3}}{\hbar^3}\sqrt{E+E_\mathrm{F}}\mathrm{d}E, \tag{1.66}$$

The normalized superconducting density of states is hence written as

$$\frac{\rho_\mathrm{s}(E)}{\rho_0(E)} = \frac{\sqrt{\tilde{E}+E_\mathrm{F}}}{\sqrt{E+E_\mathrm{F}}}\frac{E}{\tilde{E}}. \tag{1.67}$$

In classical BCS superconductors the gap parameter $\Delta \sim 1\,\mathrm{meV}$, whereas the Fermi energy $E_\mathrm{F} \sim 1\,\mathrm{eV}$, and therefore $E_\mathrm{F} \gg \tilde{E}, E$. Therefore, the quasi-particle density of states for a BCS superconductor is obtained as

$$\rho_\mathrm{s}(E) = \rho_0 \begin{cases} \frac{E}{\sqrt{E^2-\Delta^2}}, & \text{if } E > \Delta, \\ 0, & \text{if } E \leq \Delta, \end{cases} \tag{1.68}$$

where ρ_0 is the superconductor DOS at very high bias, and the energy E is measured with respect to E_F (see Fig. (**??**) (a)).

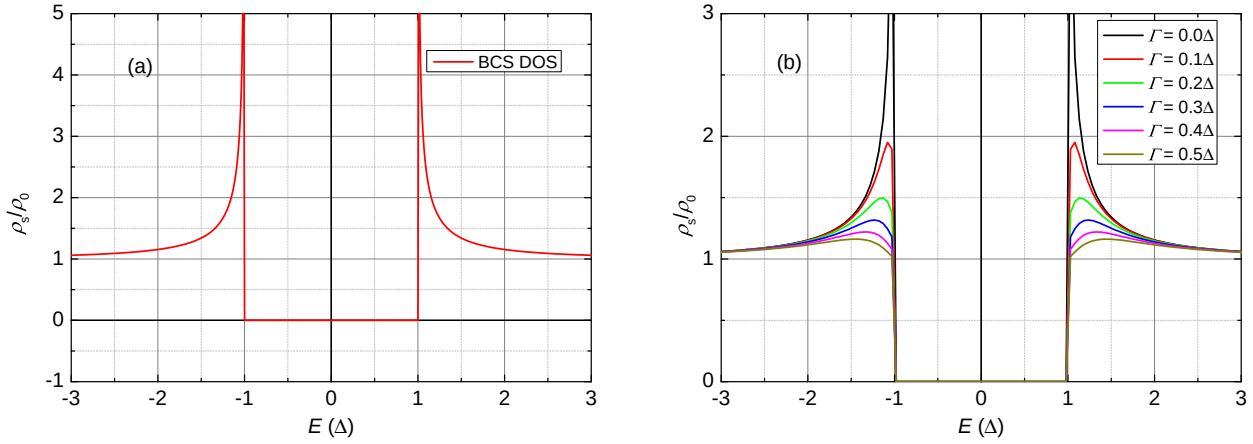

Figure 1.15: Panel (a)-BCS ideal density of states in a superconductor. Panel (b)-the effect of the Dynes' quasiparticle lifetime broadening parameter on the density of states.

In strongly-coupled superconductors, the quasiparticles recombination time into the superconducting fluid is longer than in weakly-coupled superconductors. The effect of this extended lifetime is that the density of states is not that sharp. The change can be incorporated in the BCS form in Eq. (1.68) by the introduction of imaginary component to the energy $E \rightarrow E + i\Gamma$. The parameter Γ is known the Dynes parameter [85]. The DOS becomes

$$\rho_s(E) = \rho_0 \mathrm{Re}\left(\frac{E - \mathrm{i}\Gamma}{(E-\mathrm{i}\Gamma)^2 - \Delta^2}\right). \tag{1.69}$$

The modification of the DOS by Γ is shown in Fig. (1.15) (b). The Dynes parameter has been used

in Point Contact Andreev Reflection measurements to account for experimental spectral broadening of unknown origin. * Another important functional dependence $\Delta(T)$ is the temperature dependence of the superconducting gap. It can be computed numerically from the BCS theory:

$$\frac{1}{N_0 V} = \int_0^{\hbar\omega_c} \frac{\tanh\left[0.5\beta(\varepsilon^2+\delta^2)^{1/2}\right]}{(\varepsilon^2+\delta^2)^{1/2}} \mathrm{d}\varepsilon, \tag{1.70}$$

where $\hbar\omega_c$ is the cutoff energy of the electron-phonon interaction, V is the electron-phonon attractive constant, $N(0)$ is the density of states at the Fermi level for one spin orientation at the Fermi level, and $\beta = 1/(k_B T)$. An approximate formula which is true to within 2 % in classical superconductors is:

$$\Delta(T) = \Delta(0)\tanh\left(1.74\sqrt{(T_c/T)-1}\right). \tag{1.71}$$

Another important relation is the temperature evolution of the gap on the applied field[124] in classical type I superconductors

$$\frac{\Delta(T,H)}{\Delta(T,0)} = \left(1 - \frac{H^2}{H_c^2(T)}\right)^{1/2} \tag{1.72}$$

These dependences were studied by Giaver[110], Douglass[78], and Meservey[223]. Various pair-breaking mechanisms like current, field, spin-orbit interaction or presence of magnetic impurities have been demonstrated to be equivalent and change the structure of the DOS beyond simple gap suppression. If sufficiently strong, they might cause non-zero density of states below the superconducting gap-a regime known as gapless superconductivity.

1.3.2 Critical field-type I superconductors

Very important property of type I superconductors is that their critical field increases when they are grown ultrathin†. This relation is particularly important in the field of spin polarized tunneling spectroscopy where Al is typically employed[49]. The bulk critical field of Al is just 10 mT at 300 mK, however, the ultrathin-grown films have critical fields > 3 T and this makes the Zeeman-split density of states observation possible. A superconducting film of thickness d is under applied magnetic field of H_a. Then, the boundary conditions at the surface of the film are $h(\pm d/2) = H_a$.

*Possibly related to partially oxidized interfaces or non-equilibrium effects in the superconductor due to injection of spin polarized current.

†This is fundamental property which is true whenever the superconductors can be grown ultrathin and continuous. The island-like growth leads to not-well maintained electron-phonon interaction and this fundamental relation does not hold.

Then, the penetrated magnetic field is

$$h = H_{\mathrm{a}} \frac{\cosh(x/\lambda)}{\cosh(d/2\lambda)}, \tag{1.73}$$

where λ is the penetration depth and, then, the magnetic field is reduced to a minimum value $H_{\mathrm{a}}/\cosh(d/2\lambda)$ at the midplane of the slab. Averaged over the sample thickness d, the median magnetic field is

$$\overline{h} = H_{\mathrm{a}} + 4\pi M = H_{\mathrm{a}} \frac{2\lambda}{d} \tanh \frac{d}{2\lambda}. \tag{1.74}$$

Two special cases are clearly distinguished. When $d \gg \lambda$, $\overline{h} \rightarrow 0$ and $M \rightarrow -H_{\mathrm{a}}/4\pi$. This is the classical Meissner effect of perfect diamagnetism. In the other extreme $d \ll \lambda$, the expansion of $\tanh(x) \approx x - x^3/3 + \ldots$ leads to $\overline{h} \rightarrow H_{\mathrm{a}}(1 - d^2/12\lambda^2)$, so that

$$M \rightarrow -\frac{H_{\mathrm{a}}}{4\pi} \frac{d^2}{12\lambda^2}. \tag{1.75}$$

This relations was used in the early investigations of superconductors as an approach to determine the penetration depth, λ, in superconductors. More importantly, the magnetization determines the experimental critical field. The superconducting state becomes energetically unfavourable above certain magnetic field, H_{c}, because the magnetic energy associated with the diamagnetic behaviour of the superconductor becomes bigger than its contribution in zero field. Then, free energy difference between the superconducting and the normal states is

$$(F_{\mathrm{n}} - F_{\mathrm{s}})|_{H=0} = \int_0^{H_{\mathrm{c}}} M(H)\mathrm{d}H. \tag{1.76}$$

In the Meissner state ($M = -H/4\pi$), the maximum field is known as thermodynamic critical field and in this case

$$(F_{\mathrm{n}} - F_{\mathrm{s}})|_{H=0} = \frac{H_{\mathrm{c}}^2}{8\pi}. \tag{1.77}$$

For the case $d \ll \lambda$ considered above the expression $M \approx (H_{\mathrm{a}}/4\pi)(d^2/12\lambda^2)$ is used. Then the critical field for applied in plane field is

$$H_{\mathrm{c}\|} = \sqrt{12} H_{\mathrm{c}} \lambda / d. \tag{1.78}$$

This results is correct to a good approximation, but the Ginzburg-Landau theory replaces $\sqrt{12}$ with $\sqrt{24}$.

1.3.3 SQUID device

The **S**uperconducting **QU**antum **I**nterference **D**evice (**SQUID**) is the most sensitive field detector to date*. The SQUID is based on the Josephson effect. The Josephson effect is the existence of a non-zero superconductor in an unbiased superconductor-insulator-superconductor (SIS) loop structure. There are two types of SQUIDs: a superconducting loop with a single weak link is known as a.c. SQUID, and a superconducting loop with two weak links is known as d.c. SQUID. Some general properties of an a.c. SQUID are described here but a more in-depth treatment is given in Appendix. When a magnetic flux is applied to a SQUID loop, the total flux Φ_t has two terms-the externally applied flux Φ_e and the flux due to the induced circulating current along the loop

$$\Phi_t = \Phi_e - LI = \Phi_e - LI_c \sin\left(2\pi\frac{\Phi_t}{\Phi_0}\right), \tag{1.79}$$

where the first Josephson relation $I = I_c \sin(\phi)$ has been used and, the phase difference must comply with the flux quantization condition

$$\phi + \frac{2\pi\Phi_t}{\Phi_0} = 2\pi n. \tag{1.80}$$

After introducing the important parameter $\beta_L = 2L_c/\Phi_0$, the relation between the externally applied flux and the total flux is

$$\frac{\Phi_t}{\Phi_0} = \frac{\Phi_e}{\Phi_0} - \frac{\beta_L}{2}\sin\left(2\pi\frac{\Phi_t}{\Phi_0}\right). \tag{1.81}$$

The relation on the parameter β_L. For $\beta_L = 2$, the curve is actually a succession of quasilinear regions with jumps between them (see Fig. (E.8)). Regions with positive slope are stable. The effect is that an increase (or decrease) of the external flux Φ_e leads to jumps in the total flux Φ_t. Therefore, a hysteretic behaviour exists as the flux is ramped up or down. These jumps are associated with dissipated energy $I_c\Phi_0$. The a.c. SQUID is inductively coupled, with a mutual inductance M, to a resonant L_TC_T tank circuit (see Fig. (1.18)). An r.f. current source supplies a current to the tank circuit, in this way inducing flux in the SQUID loop. The current frequency is typically in the radio-frequency range†. The voltage across the coil of the resonant circuit depends on the magnitude of the RF current and the value of the externally applied flux. *I-V* curves for an a.c. SQUID for flux values $n\Phi_0$ and $(n+1/2)\Phi_0$ are presented of Fig. (1.17). When the rf current is fixed at particular values, the voltage turns out to be a triangular- shaped dependence with amplitude $\omega L_T/(2M)$. The

*In fact, it is a flux-to-voltage converter, but the area is usually constant.

†The a.c. SQUID is often known as RF SQUID.

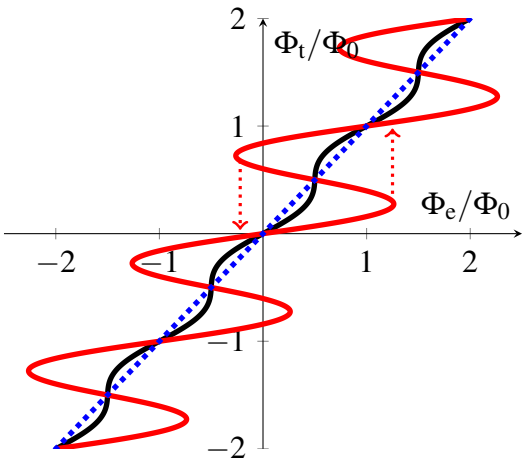

Figure 1.16: The total flux Φ_t in an a.c. SQUID as a function of the externally applied flux Φ_e. The black curve corresponds to $\beta_L = 1$, the red one to $\beta_L = 2$, and the blue dotted line is $\Phi_t = \Phi_e$. A hysteretic behaviour is present for $\beta_L > 1$. It is discernible, that the red curve is in effect a succession of quasilinear regions with jumps between them. These jumps are associated with energy dissipation in the SQUID ring, and are crucial for the operation of the detector.

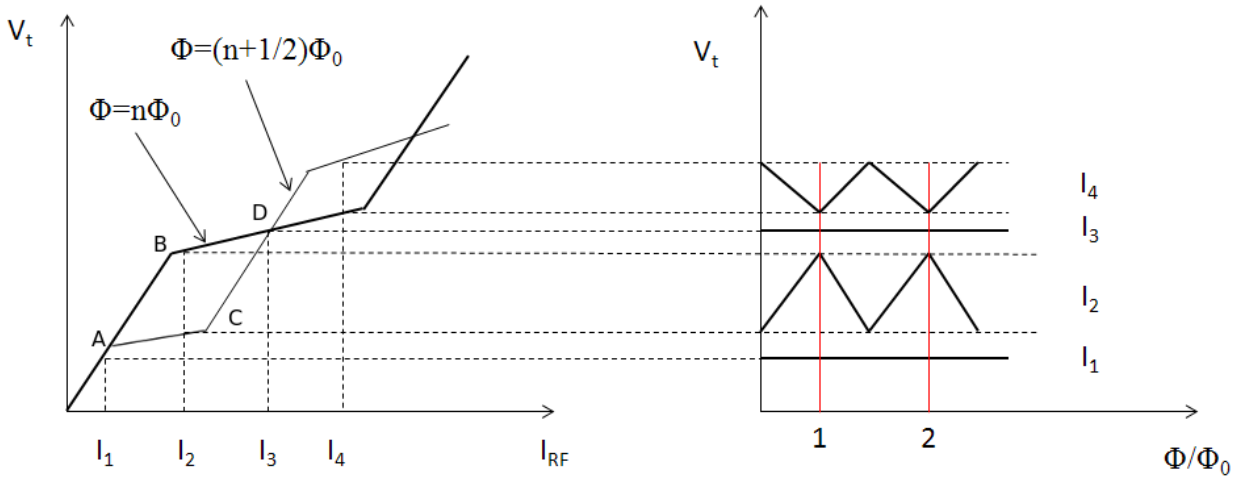

Figure 1.17: Transfer function of an a.c. SQUID.

optimum flux-to-voltage transfer is

$$\frac{\partial V}{\partial \Phi} = \frac{\omega L_T}{M}. \tag{1.82}$$

SQUIDs usually operate in flux-locked loops in which case the external flux is adjusted, so that the SQUID operates at a point of maximum sensitivity. A counting circuit can be used to track the number of quantum flux jumps. The SQUIDs are used from their very invention as precise current pre-amplifiers. In that case, the SQUID detects the oersted field from the current carrying input coil. All superconducting circuitry has to be housed within a superconducting shielding capsule in order to reduce the detrimental effect of stray parasitic magnetic field. The SQUID is a very sensitive detector for low impedance devices*.

*This is mainly limited by the Johnson noise in the input circuit.

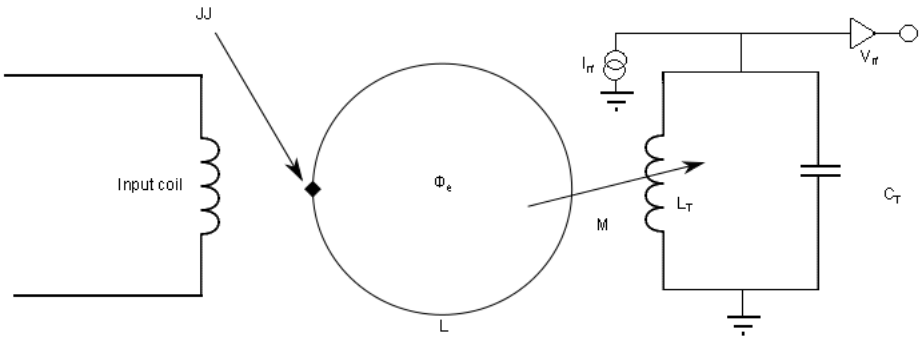

Figure 1.18: Simple schematic of a.c. SQUID read-out circuit. The input coil and tank circuit are represented.

1.4 Spin polarization measurements

1.4.1 Spin-resolved photoemission spectroscopy

Spin-resolved photoemission spectroscopy (SRPES) and spin-polarized inverse photoemission spesctroscopy (SPIPES) are the two main radiative techniques for spin polarization measurements. The electrons are ejected by soft X-rays or ultraviolet radiation in the SRPES technique (see Fig. (1.20)). The spin-resolution is provided by relatively high energy spin-dependent scattering mechanisms. The deflection of different spins is often achieved by the spin-orbit scattering in heavy element metals. A gold foil is utilized and is known as Mott detector. SRPES investigates successfully the spin polarization of core levels. It has poor Fermi level resolution due to detector limitations.

On the other hand, SPIPES[349] relies on bombarding the sample with variable energy spin-polarized electrons[270] and detecting the emitted photon flux due to radiative transitions. The impinging electrons populate the empty levels between the Fermi level and the vacuum level. Therefore, SPIPES is a complementary technique to the SRPES (see Fig. (1.19)).

Both methods are surface sensitive as the escape depth of the photoemitted electrons is approximately 1 nm in the electron energy range 10 eV to 1000 eV*. Therefore, careful capping of the samples is required before transfer to the measurement, often synchrotron facility, or *in-situ* transfer between the growth and the measurement chambers. The extracted spin polarization (both magnitude and sign) of the Fe, Ni, Co have been demonstrated to depend on the excitation energy. The latter is in line with the simple band structure theory by Wohlfarth[375]. More importantly, Fermi level spin polarization[189, 71] has been demonstrated to be negative. This is as well expected from Wohlfarth's model where the majority (spin-up) band is fully populated and, hence, below the Fermi level, while the minority spin band is not full. Therefore, the density of states contribution from the minority spins at the Fermi level is higher than the majority spins. As will be explained below, these negative values have been a significant puzzle because the spin polarized

*The reader is referred to [313] for a graph of the escape depth dependence on the electron energy.

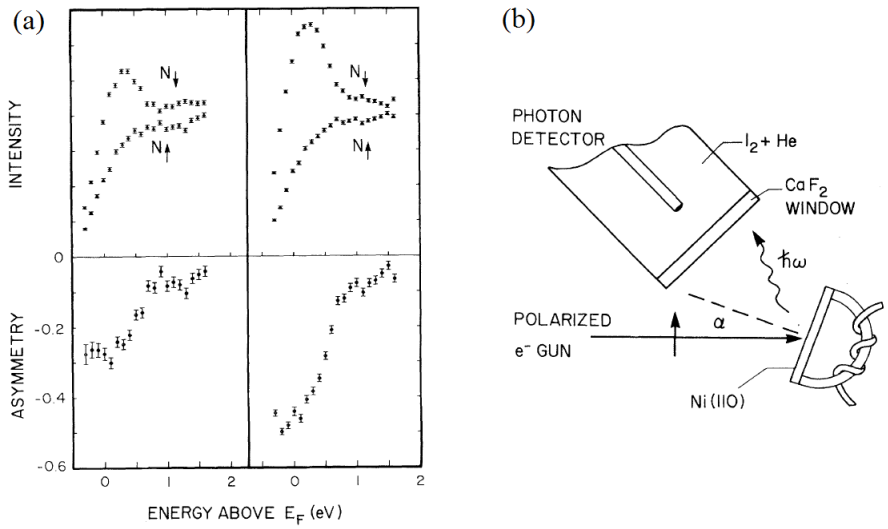

Figure 1.19: Spin-polarized inverse photoelectron spectroscopy. Panel (a)-relative intensity for majority and minority spins and spin polarization (asymmetry) for Ni. Left side-angle of incidence $\alpha = 0°$, right side-$\alpha = 20°$. Panel (b)-schematic representation of the experimental setup-the photon detector was a Geiger-Müller counter. The sample is a single crystal Ni(110) crystal magnetized along the $(1\bar{1}1)$ direction by the C-shaped electromagnet. The data is after Unguris *et al.*[349].

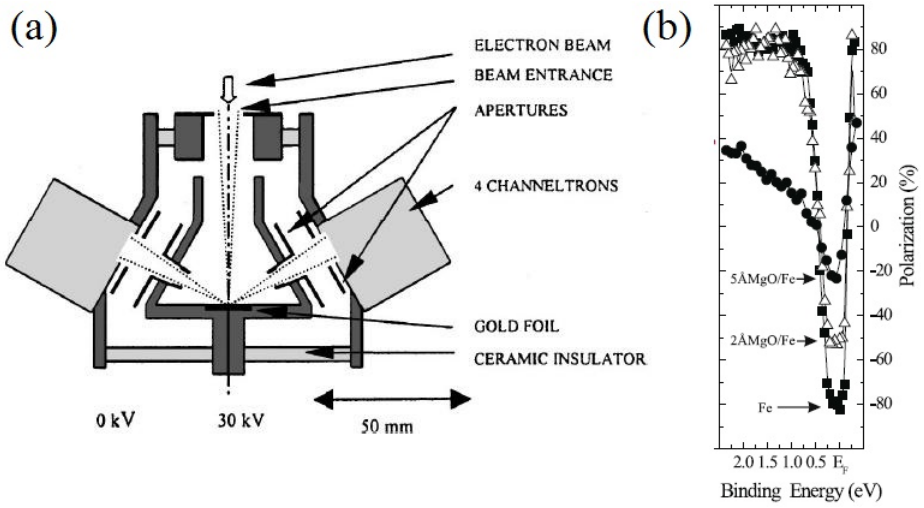

Figure 1.20: Panel (a)-schematic representation of SRPES measuring setup. Panel (b)-example of spin polarization measurement on Fe(110) by SRPES. The data is after Dedkov textitet al.[71].

tunneling extracts positive sign for the transport spin polarization.

1.4.2 Spin-polarized positron annihilation spectroscopy

The spin-polarized positron annihilation spectroscopy (SP-PAS) is a technique which bears some similarity with SPIPES technique described above. The SP-PAS has been pioneered by Hanna and Preston [127, 128] and later developed by Berko and Zuckerman [22, 23]. The sample is bombarded with a beam of positrons from a radioactive source. One particular advantage of the SP-PAS is that it is less surface sensitive and more bulk sensitive due to the larger implantation depth of

the positrons ($> 10\,\mu$m)[40]. The positron beam by a radioactive source has finite spin polarization along the axis of the beam because parity is not conserved in β decay. The source often used is ^{22}Na with approximate $P \approx 30\,\%$. The longitudinal spin polarization is determined by the helicity, v/c, with v-positron velocity and c-speed of light, respectively. Therefore, higher spin polarization can be achieved in beams emitted by radioisotopes with high Q values, like ^{68}Ge-^{68}Ga[168]. The impinging positrons annihilate with the electrons in the sample and 2 γ rays are produced so that energy and momentum of the system are conserved. Spin-up positron will annihilate with spin-down electrons and this determines a two-dimensional angular correlation of the annihilation radiation. The band structure of the ferromagnetic sample can be inverted by saturating it in different directions. The analysis of the annihilation radiation can give reconstruction of the spin polarization and the Fermi surfaces of the investigated ferromagnetic compositions following the analysis of Hanssen *et al.*[129, 130]. The SP-PAS has been successfully applied to bulk samples, however, it is more complicated and less applicable to thin films. SP-PAS has been used recently to investigate the current-induced spin polarization on metal surfaces [407].

1.4.3 Spin-polarized scanning tunneling microscopy

Scanning tunneling microscopy (STM) has been providing deeper insight into the structure of conducting surfaces since its invention. The technique relies on the recording of the small tunneling current between the apex of a sharp tip and the surface of the investigated sample. The topography of the surface can be investigated either in the constant current or in the constant height mode. The piezo-scanners adjust the distance between the tip and the sample in order to maintain constant separation in the constant current mode. The displacements of the piezo-steppers are used as a topography indicator when the surface of the sample is scanned in the latter mode. In the constant height mode, there is no vertical motion of the piezo-scanner. In this configuration, terraces or dips on the surface of the sample result in increase or decrease in the tunneling current, respectively. More relevant to our discussion is the scanning tunneling spectroscopy (STS). In this case, the current-voltage characteristic of the tip-surface configuration is investigated. The tunneling $I-V$ characteristic is directly dependent on the convolution between the density of states of the tip and the sample.

$$I(V) \propto \int_{-\infty}^{+\infty} \rho_{\mathrm{s}}(E-eV)\rho_{\mathrm{t}}(E)T(E,eV)\left[f(E-eV)-f(E)\right]\mathrm{d}E, \tag{1.83}$$

where ρ_{s}, ρ_{t} are the density of states of the sample and the tip, respectively. The transmission probability $T = |M_{\mu\nu}|^2$ is represented by the modified wavefunctions of the tip and the sample surface. The tunneling matrix element is

$$M_{\mu\nu} = -\frac{\hbar^2}{2m}\int_{\Sigma}\left(\chi_{\nu}^{*}\Delta\Psi_{\mu} - \Psi_{\mu}\Delta\chi_{\nu}^{*}\right).\mathrm{d}\mathbf{S}, \tag{1.84}$$

where the integration is over the Fermi surfaces. The tunneling matrix element represents the energy lowering due to the interaction between the two electrodes. ψ is the sample wavefunction modified by the tip potential, and χ is the tip wavefunction modified by the sample potential. Therefore, information about the local density of states (LDOS) structure of the investigated sample can be obtained since the tip is metallic and its DOS is essentially flat close to E_F. STS has been successfully used to extract quantitative information about the LDOS structure of molecules, semiconducting compositions and the gap of superconducting materials. Of course, the techniques of STM and STS can be unified in order to gain insight about the spatial variation in the LDOS. An example of such experiment is the imaging of the Abrikosov vortex lattice in type II superconductors[136]. The analysis of the data in a quantitative manner is not straight-forward though since the tunneling current depends on both the LDOS, the topography structure and the tunneling matrix coefficients[94]. If the tip (or at least its apex) and the sample are magnetic, then the tip-sample configuration can be imagined as an MTJ with an "ideal" vacuum tunnel barrier. The first demonstration of such experiment is made by Wiesendanger *et al.*[372]. As in an MTJ, the conductance depends on the angle (Θ) between the two spin polarization

$$G = G_0 \times (1 + P_1 P_2 \cos(\Theta)). \tag{1.85}$$

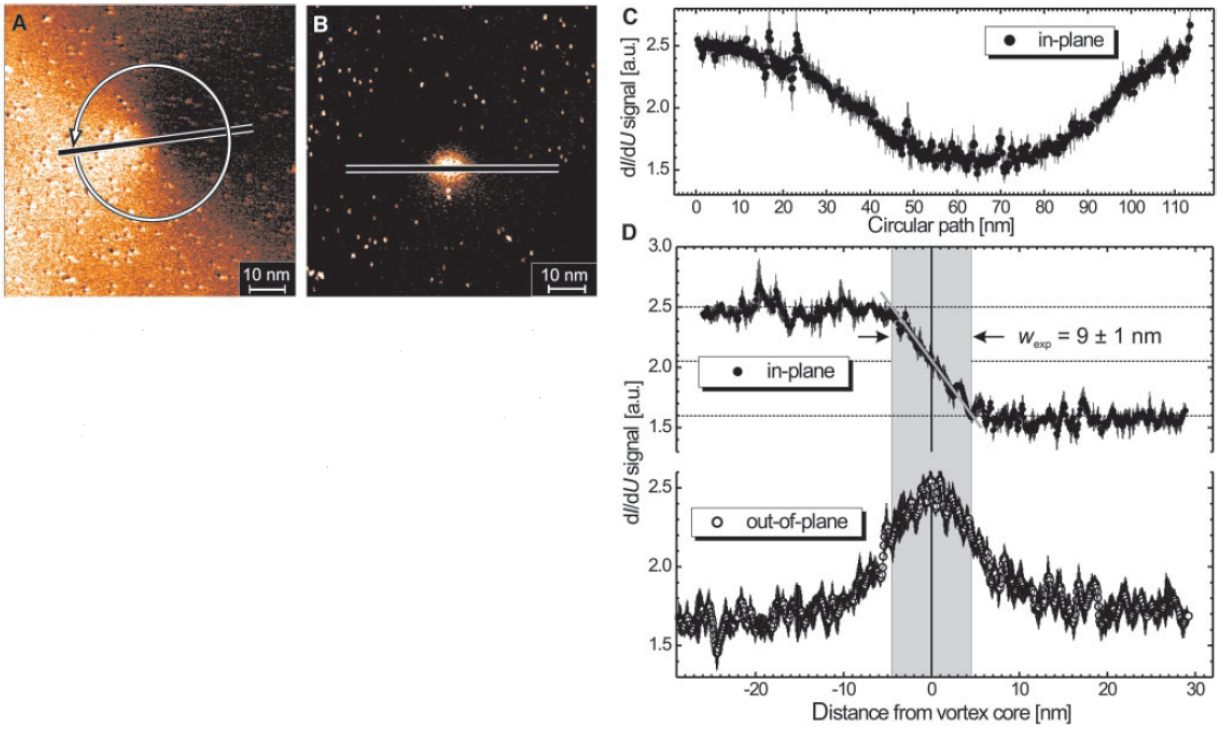

Figure 1.21: SP-STM imaging of magnetic vortex structure. Panel (A)-spin structure with in-plane sensitive tip, Panel (B)-spin structure with out-of-plane sensitive tip, Panel (C)-signal corresponding to the circular path on Panel (A). Panel (D)-the in- plane scan corresponds to the line scan on Panel (A), the out-of-plane scan corresponds to the line scan on Panel (B). The picture is after Wachowiak [362].

The are two choices for tip in SP-STM: ferromagnetic or antiferromagnetic. The disadvantage of the ferromagnetic tip is that its stray field might influence the state of the sample below. In order to reduce the moment and the stray field, the ferromagnetic tip is often prepared by *in-situ* evaporation of very thin Fe on the tip. Another possibility is the tip to be "functionalized" by pick-up of magnetic atoms. It is possible to achieve easy-axis both in-plane and perpendicular to plane for the tip by different preparation procedures. The natural pointed structure of the apex favours out-of-plane (or along tip axis) anisotropy, and this is indeed the case for thin coatings [362]. A brilliant demonstration of the high spatial resolution of SP-STM is given by Wachowiak *et al.*[362] in imaging of a magnetic vortex structure. With a thick film Cr-coated tip, the in-plane component of the spin structure is imaged (see Fig. (1.21)). The fact that the spins have predominantly in-plane spin alignment is demonstrated both in the circular scan around the core and the line scan through the core of the vortex (Fig. (1.21) (A) and (C)). With a thin film Cr-coated tip, the out-of-plain component of the spin structure is investigated. The out-of-plain direction of the spin orientation in the core of the vortex is demonstrated by the line scan through the core in this case (Fig. (1.21) (B) and (D)).

Magnetic film-coated tip could be used for several days at room temperature before residual gas absorption becomes excessive and contaminates too much the surface of the tip[34]. In order to completely suppress detrimental mechanical or stray field effects from ferromagnetic tips, anti-ferromagnetic tips are often used. The sharp apex has uncompensated moment whereas the overall magnetization is zero. Both antiferromagnetically coated[182], or bulk antiferromagnetic tips (Cr or MnNi[245]) have been used.

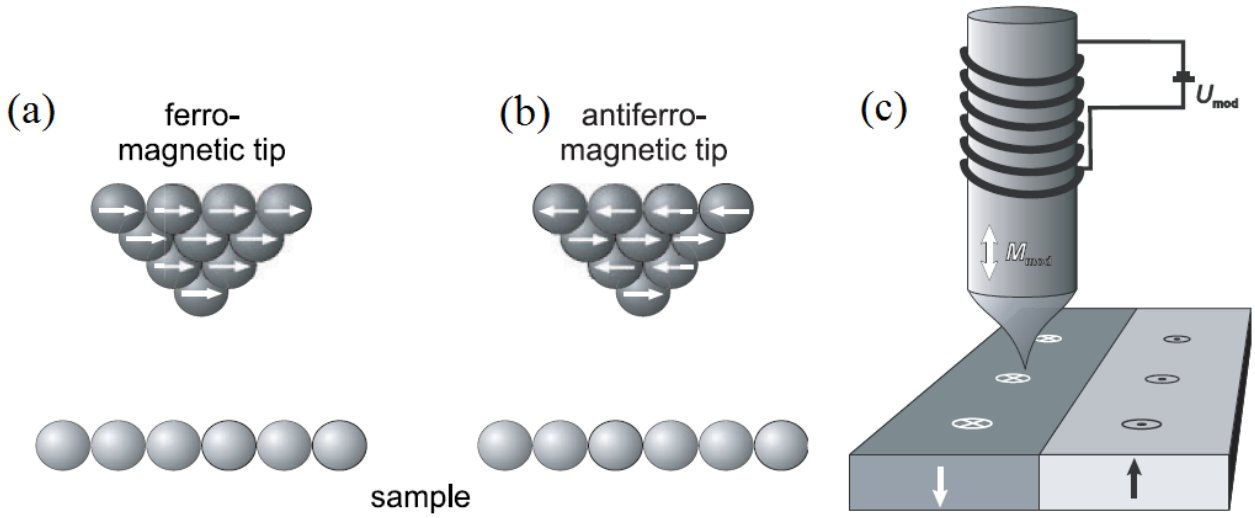

Figure 1.22: Schematic representation of domain structure at the apex of a ferromagnetic (a) and antiferromagnetic tip (b). Panel (c)-schematic representation of a modulation coil wound around the tip. The picture is after Bode [32].

An important mode of operation of the SP-STM is known as local magnetoresistance (see 1.22 (c)). In this case, the magnetic state of the apex is changed periodically. The polarization of the

tip is modulated with a coil wound around the tip. The applied a.c. current has frequency much higher than the cut-off of the feedback loop for the piezo-steppers. In this way, the feedback loop compensates the spin averaged conductance. It is important that the tip has low coercivity, so that the switching field is low and the stray field from the coil is minimized*. Furthermore, the magnetostriction must be low in order to minimize off-axis movement of the tip in which case the tip will become partially sensitive to the perpendicular component of the magnetization†. An example is the utilization of amorphous CoFeNiSiB tip[385]. The conductance asymmetry, δ, is

$$\delta = \frac{G_{\mathrm{P}} - G_{\mathrm{AP}}}{G_{\mathrm{P}} + G_{\mathrm{AP}}}. \tag{1.86}$$

Since $\delta = P_{\mathrm{t}} P_{\mathrm{s}}$, and the spin polarization of the tip P_{t} is assumed to be constant, the spin polarization of the sample is essentially proportional to δ: $P_{\mathrm{s}} \propto \delta$. Furthermore, the dependence of the asymmetry on the bias is a direct indication of the sample-bias spin polarization $P_{\mathrm{s}}(V) \propto \delta(V)$ (see Fig. (1.23)).

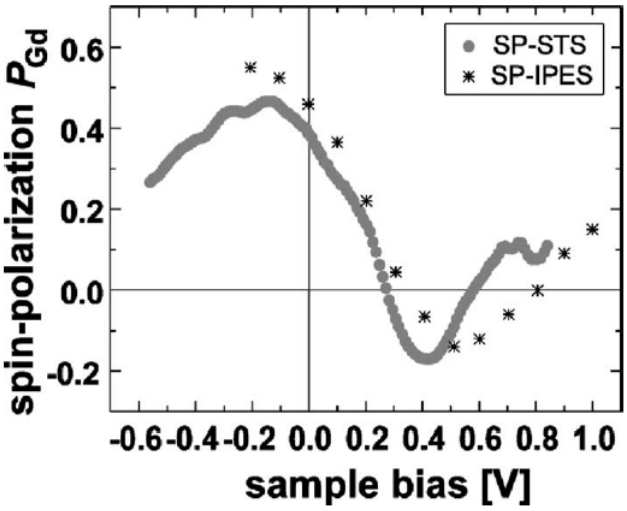

Figure 1.23: Spin polarization bias dependence of Gd(0001) sample. Two different experimental techniques are compared: SP-STM[33] and spin-polarized inverse photoemission spectroscopy[76]. The picture is after Wiesendanger [373].

A demonstration of superconducting spin polarized tunneling with V-tip has been recently demonstrated by Eltschka *et al.*[89] at mK temperatures.The reader is referred to Wiesendanger for extensive review on the SP-STM [373].

*The stray field from the tip is often far bigger problem.

†It is assumed here that the tip has in-plane easy-axis.

1.4.4 Anisotropic magnetoresistance sign method

The anisotropic magnetoresistance (AMR) is the resistance change in ferromagnetic materials depending on the angle between the applied current and the magnetization. Predominantly positive AMR is observed* and in this case the electrical resistance is smaller when when the magnetization is orthogonal to the current direction and is larger when their orientation is co-linear. The AMR is due to the spin-orbit interaction which mixes the spin-up and spin-down carriers. A theoretical proposal by Kokado *et al.*[177, 176] suggests that half-metallicity can be quickly tested by a measurement of the AMR sign method. Their prediction is based on the fact that the *s*-*d* electron scattering, responsible for the AMR, happens preferentially from $s^{\uparrow}$ to $d^{\uparrow}$ or $s^{\downarrow}$ to $d^{\downarrow}$ states in fully spin polarized compositions and this leads to negative AMR effect†. Investigation of the AMR sign dependence in $Co_2Fe_xMn_{1-x}Si$ has been performed by Yang[392]. In this material, the AMR changes sign from negative to positive for $x > 0.8$ which implies loss of the high spin polarization. This AMR study is corroborated by TMR[183] and CPP- GMR[286] measurements on devices with the same electrode. The AMR sign has been systematically investigated in the Heusler compounds Co_2MnZ and Co_2MnZ (where Z = Al, Si, Ge, and Ga) by Sakuraba[285]. The Heusler compounds are briefly discussed in Sec. (6.3). In this case, the varying number of valence electrons modify the spin polarizaion. The AMR effect on $Co_2Fe_xMn_{1-x}Si$ switch sign from positive to negative when $x > 0.2$, and furthermore, it is demonstrated that the Gilbert damping parameter α decreases significantly for $x > 0.2$. The latter is indication of high spin polarization as well[358]. The AMR sign of the compositions $Co_2MnGa_{0.25}Ge_{0.75}$ and $Co_2FeGa_{0.5}Ge_{0.5}$ is shown to be negative. Finally, the annealing dependence of the AMR amplitude in these materials follows the same trend as the ΔRA values obtained in CPP-GMR devices with the same compositions[330, 201].

1.4.5 Spin polarized tunneling

Historically, spin polarized tunneling (SPT) has given the impetus on the research of spin electronic devices. The technique is initiated and developed over the years by Tedrow, Meservey and Moodera. The basic building block in the SPT is the tunnel junction with the general structure: superconductor-insulator-ferromagnet‡. The measurement procedure relies on the sharp structure of the quasiparticle density of states of a superconductor. The application of high magnetic field leads to Zeeman-splitting of the density of states. When the Zeeman-energy becomes appreciably higher than the thermal smearing, a distinguishable four-peak structure appears in the differential conductance spectrum. In this case, the quasiparticle DOS in the superconductor is sum of the

*for instance in $Ni1-xFe_x$

†The low resistance is when the magnetization and the current are parallel to each other, and the high resistance is when they are perpendicular to each other.

‡or any metal

spin-up and spin-down components $\rho_s = \rho_s^{\uparrow} + \rho_s^{\downarrow}$ and the spin-split DOS is offset from the Fermi level with the Zeeman energy $\mu_B \mu_0 H$:

$$\rho_s^{\uparrow} = \frac{1}{2}\rho_0 \left(\frac{u}{\sqrt{u^2 - 1}} \right), \tag{1.87}$$

$$\rho_s^{\downarrow} = \frac{1}{2}\rho_0 \left(\frac{d}{\sqrt{d^2 - 1}} \right), \tag{1.88}$$

where the normalized energies for spin-up (u) and spin-down (d) sub-bands are

$$u = \frac{E - \mu_B \mu_0 H}{\Delta}, \tag{1.89}$$

$$d = \frac{E + \mu_B \mu_0 H}{\Delta}. \tag{1.90}$$

The spin dependent conductances are then

$$G^{\uparrow,(\downarrow)}(V) \propto \int \rho_s^{\uparrow,(\downarrow)}(E) f'(E - eV) \mathrm{d}E, \tag{1.91}$$

which in approximation of very low temperature is $G^{\uparrow}(V) \propto \rho_s^{\uparrow}(V)$ and $G^{\downarrow}(V) \propto \rho_s^{\downarrow}(V)$. It has been assumed that the normal metal electrode has flat density of states for the small applied bias in the SPT experiments. Furthermore, no explicit tunneling probability as in Eq. () is taken into account in this case*. The spin polarization is defined as the imbalance in the spin-dependent conductance

$$P = \frac{G^{\uparrow} - G^{\downarrow}}{G^{\uparrow} + G^{\downarrow}}, \tag{1.92}$$

in which case the total conductance is represented as

$$G(V) = (1 + P) G^{\uparrow}(V) + (1 - P) G^{\downarrow}(V), \tag{1.93}$$

$$G(V) = (1 + P) \rho_s^{\uparrow}(V) + (1 - P) \rho_s^{\downarrow}(V). \tag{1.94}$$

Example of the spin-up and spin-down quasiparticle DOS splitting in applied magnetic field is presented in Fig. (1.24) (a). The full normalized conductance spectrum for the case of zero spin polarization with thermal smearing is presented in Fig. (1.24 (b)). The spectrum is symmetric since the conductance contributions of the spin-up and spin-down DOS are equal. The indicated four peaks due to the Zeeman splitting should be noted.

For a spin-polarized metal there will be unequal conductances from the spin-up ($G^{\uparrow}$) and spin-down ($G^{\downarrow}$) subbands. For most known ferromagnetic compositions the transport spin polarization is positive: $G^{\uparrow} > G^{\downarrow}$. The latter leads to higher contribution of the quasiparticle spin-up DOS in

*The reason is again related to the fact that the bias range is very narrow.

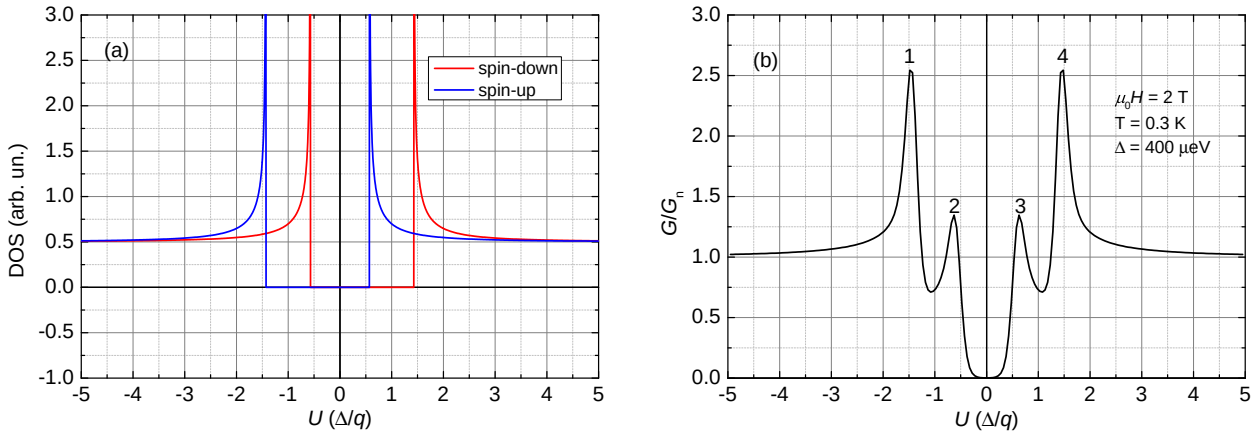

Figure 1.24: Representation of the Zeeman-split quasiparticle density of states in a superconductor on panel (a). Simulated spin tunneling spectroscopy for the case of non-polarized metal with the parameters applied field $\mu_0 H = 2\,\mathrm{T}$, temperature $T = 0.3\,\mathrm{K}$, and superconducting gap $\Delta = 400\,\mu\mathrm{eV}$ on panel (b).

the superconductor and the four-peak structure becomes asymmetric. Three different SPT curves are simulated and presented on Fig. (1.25). In the case $P \neq 0.0$, the spin polarization can be estimated by the height of the conductance peaks using one of the following two formulas

$$P = \frac{G_3 - G_2}{G_3 + G_2}, \tag{1.95}$$

$$P = \frac{G_3 - G_2 + G_4 - G_1}{G_3 + G_2 + G_4 + G_1}, \tag{1.96}$$

From Fig. (1.24), it is obvious that the peaks G_3 and G_2 are the clearer indicators of the spin-up and spin-down DOS, respectively. They are better estimators because they are inside the main superconducting gap and their height is dependent only on the quasiparticle sub-bands. The other two peaks G_1 and G_4 originate from the spin-up and spin-down DOS, respectively, however, each has a small contribution from the opposite DOS*. However, the simplified expressions lead to underestimation of the spin polarization. That is because the approximate equations do not account for the effects of magnetic field depairing, spin-orbit interaction in the superconductor and tunneling matrix elements.

The most widely used superconductors for SPT is aluminum. There are a few experimental reasons for that:

- Low atomic number
- Well-established growth as ultra-thin films
- Beneficial increase in the critical field when grown ultra-thin

*For instance, consider the leftmost peak on Fig. (1.24). It is mainly determined by the spin-up DOS but there is structure from the spin-down DOS at the same bias as well.

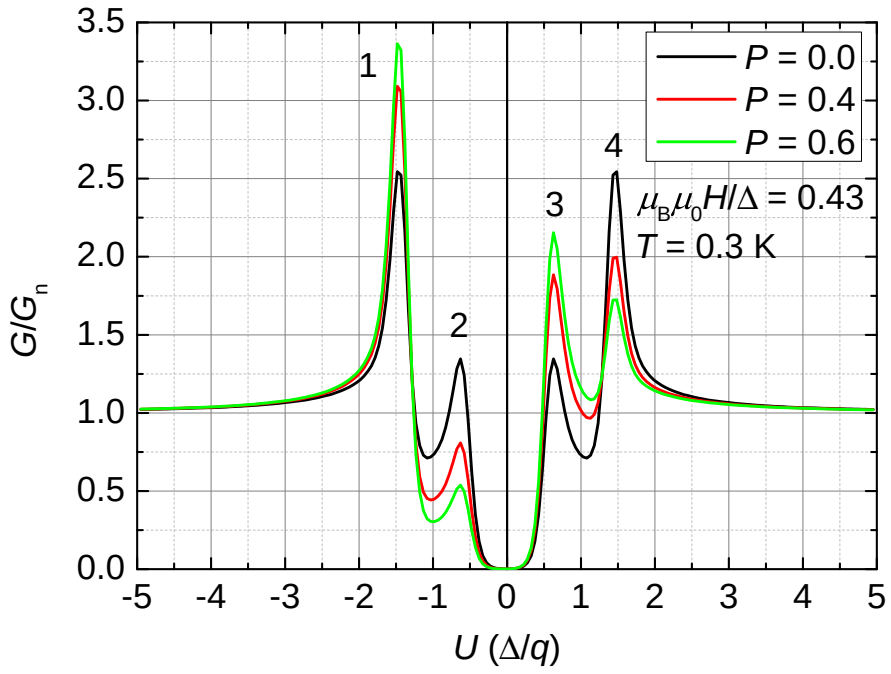

Figure 1.25: Spin-polarized tunneling simulated for three different spin polarizations $P = 0.0$ (black), $P = 0.4$ (red), and $P = 0.6$ (green curve). Constants for the simulation are temperature $T = 0.3\,\mathrm{K}$, and the ratio of the Zeeman splitting energy to superconducting gap is $\mu_B\mu_0 H/\Delta = 0.43$.

- Formation of high-quality pinhole-free oxide barrier

The low atomic number is important because higher atomic number leads to higher spin-orbit coupling. Higher spin-orbit coupling causes mixture of the spin-up and spin-down quasiparticle density of states and this results in poorer resolution of the four-peak structure of the differential conductance.

The correction for the spin-split quasiparticle DOS due to spin-orbit coupling and orbital depairing is then given by Bruno and Schwarz[44] following the Maki-Fulde theory

$$u = \frac{E - \mu_B\mu_0 H}{\Delta} + \zeta\frac{u}{\sqrt{1-u^2}} + b\frac{d-u}{\sqrt{1-d^2}}, \tag{1.97}$$

$$d = \frac{E + \mu_B\mu_0 H}{\Delta} + \zeta\frac{d}{\sqrt{1-d^2}} + b\frac{u-d}{\sqrt{1-u^2}}, \tag{1.98}$$

where ζ and b are the orbital depairing and the spin-orbit scattering constants, respectively. This system of equations must be self-consistently solved. Pathological cases in the numerical solution of this system are clarified by Worledge and Geballe[381].

The orbital depairing parameter depends significantly on the thickness of the superconducting film t and the angle between the field direction and the plane of the film

$$\zeta = \zeta_0 + \frac{\tau_m v_F (e v_F \mu_0 H_\perp)}{3\Delta} + \frac{\tau_m t^2 (e v_F \mu_0 H_\parallel)^2}{18\hbar\Delta}, \tag{1.99}$$

where ζ_0 is a natural depairing parameter, v_F is the Fermi velocity, τ_m is the momentum scattering time, $H_\perp$ and $H_\parallel$ are the perpendicular and the in-plane projections of the applied field. It could be noticed that for equal magnitude of the two field projections ($H_\perp = H_\parallel$), the ratio between the two contributions towards the depairing parameter is $6\hbar/(t^2 e\mu_0 H)$. For typical applied field of $\mu_0 H \approx 3\,\mathrm{T}$ and usual thickness ($t \approx 3\,\mathrm{nm}$), the ratio is $\sim 10^3$. This estimation demonstrates that the perpendicular field is much more efficient pair breaker. The orbital motion of the electrons induced by the in-plane field is naturally quenched by the film thickness whereas the perpendicular field creates cyclotron motion in the plane of the field, *i.e.* non-restricted. The importance of the alignment of the magnetic field with the plane of the film is demonstrated by Kant[159], where only few degrees off-plane tilt results in loss of the four peak structure and smearing of the Zeeman-split density of states.

The spin-orbit coupling parameter b is mainly determined by the average atomic number of the composition. From the perspective of the moving electrons the charged nuclei represent electric current. The latter creates magnetic field which interacts with the magnetic moment of an electron. The spin-orbit interaction is proportional to the fourth order of the average atomic number. The spin-flip scattering rate is

$$\frac{1}{\tau_{so}} \propto Z^4 \frac{1}{\tau_m}. \tag{1.100}$$

Then, the spin-orbit scattering rate is defined as a dimensionless spin-orbit scattering rate by the relation

$$b = \frac{\hbar}{3\Delta}\frac{1}{\tau_{so}}. \tag{1.101}$$

The orbital depairing ζ and spin-orbit scattering b are usually set as free fitting parameters. They can be determined independently for each superconductor if a junction with the structure superconductor-insulator-unpolarized metal is used. Then, since $P = 0$, only ζ and b are unknown. Such analysis was performed on Al-Al_2O_3-Ag junctions by Meservey *et al.* [225]. When Al is used as superconducting electrode, the spin-orbit scattering is usually very small-$b \approx 0.02$.

When type I superconductors are grown ultra-thin, their critical field scales up, as the thickness decreases. This is discussed above in Eq. (1.78) and it is a fundamental relation which should always hold for type I superconductors. However, experimentally this is not the case for superconductors like V and Ta. They cannot be grown ultrathin with very low surface roughness and this is the reason why their critical field does not scale up as the thickness is decreased. Aluminum is the closest example to an ideal BCS superconductor and its critical field reaches the Pauli paramagnetic limit*.

The detrimental effect of the magnetic field (orbital depairing) and the high atomic number superconductors (spin-orbit scattering) are crucial for the discussion of the point contact Andreev

*It is also known as Clogston- Chandrasekhar limit[63, 52].

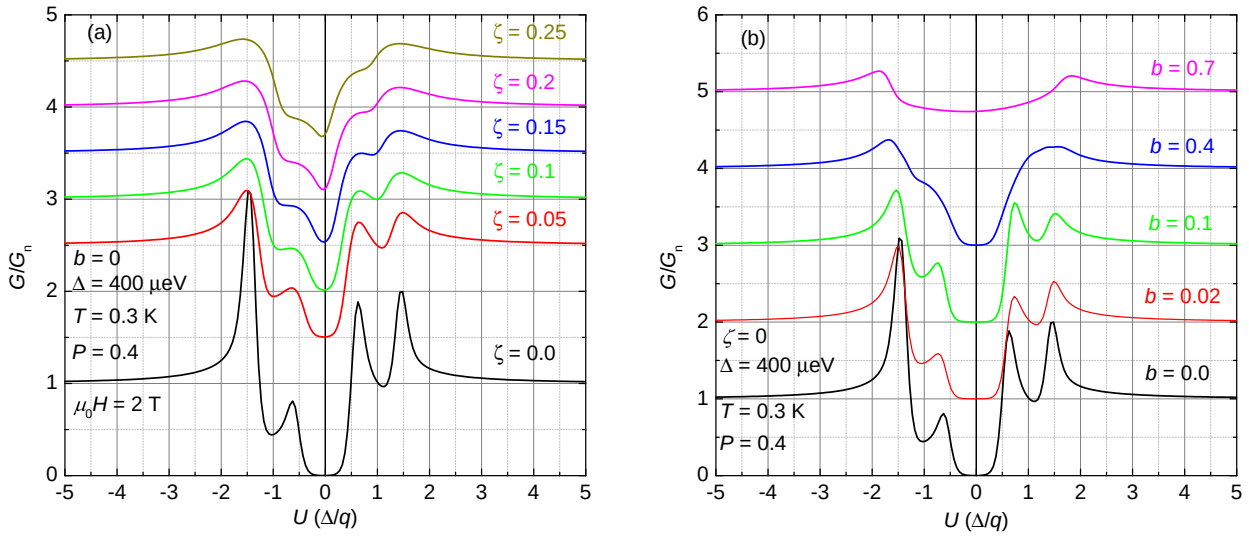

Figure 1.26: Simulated spin-polarized tunneling curve with polarization $P = 0.4$, temperature $T = 0.3\,\mathrm{K}$, superconducting gap $\Delta = 400\,\mu\mathrm{eV}$, and magnetic field $\mu_0 H = 2\,\mathrm{T}$. Panel (a) - the orbital depairing, ζ, is varied while the spin-orbit coupling, b, set to zero. Panel (b) - the spin-orbit coupling, b, is varied while the orbital depairing, ζ, is set to zero.

Reflection in high-magnetic field. In order to gain better insight into how the SPT spectra change, multiple curves are generated for different values of ζ and b on Fig (1.26). It is important to stress the effect of the spin-orbit scattering on the spectra (Fig (1.26) (b)). For the value of $b = 0.7$ (which corresponds roughly to Nb), the spin-split quasiparticle DOS are completely smeared and the four peaks can not be distinguished.

Superconducting Zeeman-splitting has been demonstrated with V[89], V-Ti[336], $Al_{98}Cu_2$[234], and NbN[393] superconductors. One of the big advantages of the spin polarized tunneling is that it measures the tunneling spin polarization, *i.e.* the cumulative spin polarization of the ferromagnetic-insulator interface. Exactly the tunneling spin polarization definition is the most relevant for TMR devices. For instance, SPT confirms that the CoFe-MgO spin polarization is higher than the CoFe-AlO_x spin polarization due to the spin filtering in the MgO barrier [268]. Unfortunately, this is a disadvantage of the technique as well. It has been demonstrated that the extracted spin polarization depends significantly on the deposition conditions and the quality of barrier[226]. A technique which investigates the direct, unweighted by tunneling probabilities, Fermi level spin polarization of materials is very much needed. Such method is the point contact Andreev reflection.

1.4.6 Point Contact Andreev Reflection

The technique of Point Contact Andreev Reflection (PCAR) uses as well a superconductor for spin polarization detection, however, in this case there is a highly transparent, metallic, contact between the superconductor and the investigated material[31]. PCAR relies on the effect of Andreev reflection which is the only allowed process for injection of electrons into the superconductor at

applied bias lower than the superconducting gap ($|U| < \Delta$)[9]. It is assumed for definiteness that a spin-up electron impinges from the superconductor into the normal metal. For $|U| < \Delta$, there are no available states in the single particle density of states of the superconductor, and, hence, an impinging spin-up electron must pair with a spin-down electron in order to be injected as a Cooper pair in the superconductor. When a spin-up is injected through Andreev reflection, the spin and charge conservation laws require that a hole with spin-down is back propagated into the normal metal. Exactly the back-scattering of a hole is the process of Andreev reflection (see Fig. (1.27)). The process of Andreev reflection is forbidden, if there are no spin-down density of states in the normal metal. That is the case in half-metallic ferromagnets where only one of the spin bands has states at the Fermi level. It is instructive to consider how the process of Andreev reflection changes quantitatively the differential conductance of the point contact at sub-gap applied bias.

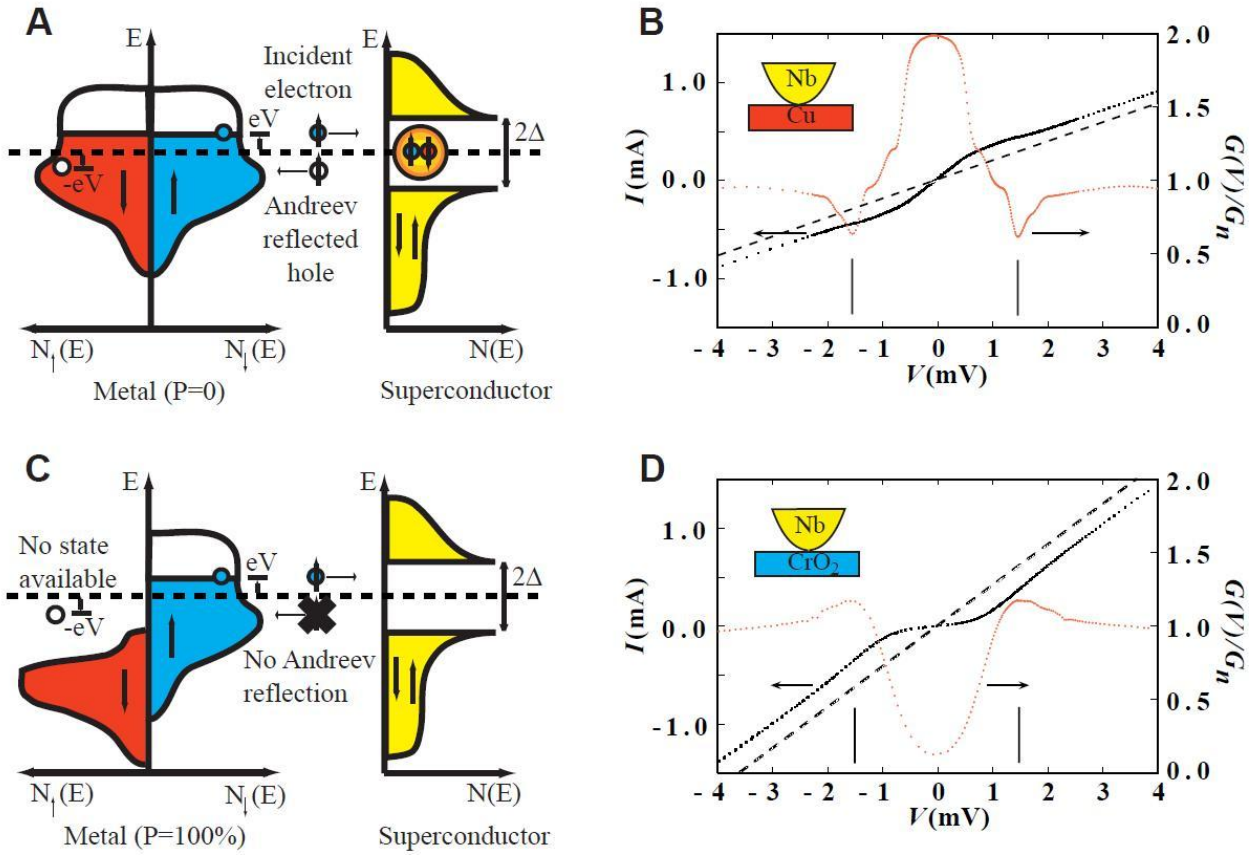

Figure 1.27: Schematic representation of the Andreev reflection process and the corresponding differential conductance. Panel (A)-spin sub-bands of a non- polarized metal (Cu). Panel (B)-the corresponding differential conductance of a Nb/Cu point contact with an increasing zero bias conductance. Panel (C)-spin sub-bands of a half-metallic ferromagnet (CrO_2). Note the Andreev reflection is forbidden. Panel (D)-the corresponding differential conductance of a Nb/CrO_2 point contact with a suppressed zero bias conductance. The picture is after Soulen *et al.*[314].

In the case of non-polarized metal, the Andreev reflection is fully allowed in which case the differential conductance at zero-bias increases with respect to the high-bias background due to the conversion from a single electron to two electrons Cooper pair. In the opposite case of fully-spin

polarized metal, the Andreev reflection is fully forbidden and, hence, the zero bias conductance is suppressed with respect to the high bias conductance. The magnitude of the zero bias anomaly was initially used as a crude estimate for the spin polarization P:

$$\frac{G_{\mathrm{NS}}}{G_{\mathrm{NN}}} = 2 \times (1 - |P|), \tag{1.102}$$

where G_{NS} is the differential conductance of the contact and G_{NN} is the high-bias different conductance. In the intermediate case for the spin polarization $0.0 < P < 1.0$, the current in the ferromagnetic material must be decomposed into fully spin polarized (I_{pol}) and fully spin unpolarized components (I_{unpol}). Then, the Andreev reflection is allowed for the I_{unpol}, and forbidden for the I_{pol}. The two current components, the total current and the spin polarization P are then related accordingly:

$$I = (1 - P)I_{\mathrm{unpol}} + PI_{\mathrm{pol}} \tag{1.103}$$

The Andreev reflection is a fundamentally different process from the SPT. The Andreev reflection represents conversion of single electron to two electron injection at the superconductor-normal metal interface whereas the SPT represents single electron tunneling transport between the superconductor and the normal metal.

Similar argument can be put through for the transfer between a normal metal and a superconductor without referring to the Andreev reflected holes (see Fig. (1.28)). For a non-polarized material, there would be equal amount of spin-up and spin-down electrons impinging on the N/S interface. Therefore, they will all pair together and be injected as Cooper pairs. Hence, the subgap differential conductance is high. On the opposite side is the case of fully polarized material, all electrons are with the same spin orientation and therefore can not find partners in order to be injected as Cooper pairs. This leads to suppressed conduction through the contact. Although some readers might prefer this view, the transmission coefficients are calculated quantum mechanically using a single electron plane wave conventionally, as it will be outlined below.

1.5 Point Contact Andreev Reflection

This section will discuss in depth the processes of Andreev reflection starting from the original Blonder-Tinkham-Klapwijk (BTK) theory[31], progressing through the modified BTK by Strijkers *et al.* [321] and finishing with a discussion on the effect of barrier strength Z on the extracted spin polarization P.

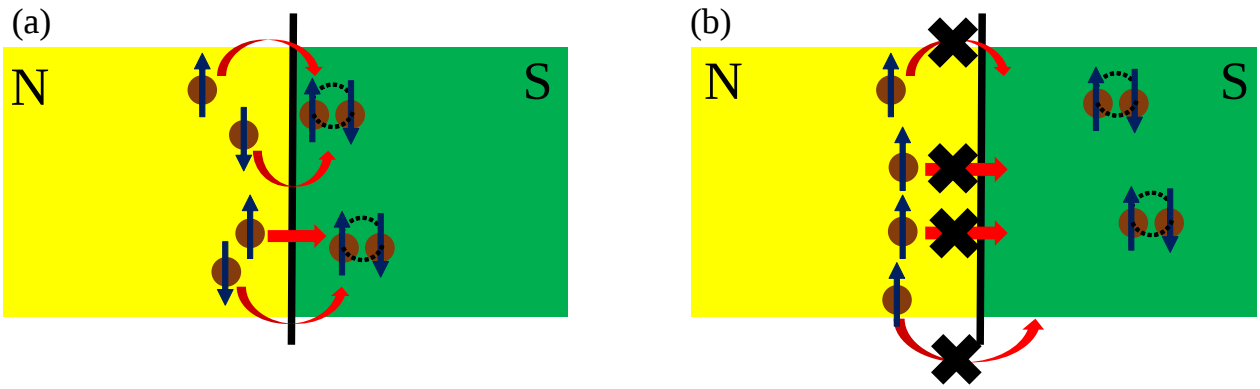

Figure 1.28: Alternative view on the electron conversion between a normal metal (N) and a superconductor (S) at sub-gap bias. Panel (a): non-polarized material, there are equal density of spin-up and spin-down electrons and the conductance is high. Panel (b): fully spin polarized material, there are no electrons with opposite spin and the conductance is suppressed.

1.5.1 BTK theory

Starting from Eq. (1.103) and differentiating with respect to the voltage, the differential conductance through the point contact is

$$G = (1-P)G_{\text{unpol}} + PG_{\text{pol}}, \tag{1.104}$$

where G_{unpol} and G_{pol} are the unpolarized and polarized differential conductances, respectively. The BTK theory treats the two differential conductances independently using the spinor representation for the wave-functions of the electrons and using the Bogolubov-de Gennes (BdG) equation.

At the interface, an electron can undergo either specular (normal) reflection, or Andreev reflection in which a Copper pair propagates in the superconductor. Because of the charge and spin conservation laws, in the Andreev reflection, a hole with an opposite spin must propagate backward into the normal metal*. Based on the last considerations, the wavefunction of the electron in the normal metal is:

$$\Psi_{\text{n}} = \begin{pmatrix}1\\0\end{pmatrix} \mathrm{e}^{\mathrm{i}k_{\text{e}}x} + b\begin{pmatrix}1\\0\end{pmatrix} \mathrm{e}^{-\mathrm{i}k_{\text{e}}x} + a\begin{pmatrix}0\\1\end{pmatrix} \mathrm{e}^{\mathrm{i}k_{\text{h}}x}. \tag{1.105}$$

In a similar fashion, the possible quasiparticle states in the superconductor are quasielectron and quasihole. Then, the wavefunction of the electron in the superconductor is:

$$\Psi_{\text{s}} = c\begin{pmatrix}u_0\\v_0\end{pmatrix} \mathrm{e}^{\mathrm{i}q_{\text{e}}x} + d\begin{pmatrix}v_0\\u_0\end{pmatrix} \mathrm{e}^{-\mathrm{i}q_{\text{h}}x}. \tag{1.106}$$

The coherence factors u_0 and v_0 are directly related to the BCS DOS of the superconductor. The

*Strictly speaking, electrons enter evanescent states in the gap which decay into the condensate within a distance $\sim \xi$, the superconducting coherence length.

probabilities for creation and annihilation of quasi-particles are described by the coherence factors. Extensive treatment can be found in Tinkham [342]. In the above expression k_e, k_h, q_e and q_h are the momenta of the electron and hole in the normal metal, quasielectron and quasihole in the superconductor, respectively. The so-constructed wavefunctions must be solutions to the Bogoliubov-de Gennes (BdG) equation

$$\begin{bmatrix} H_0 & \Delta \\ \Delta^* & -H_0 \end{bmatrix} \Psi_{s,n} = E\Psi_{s,n}. \tag{1.107}$$

Where H_0 is the single particle Hamiltonian and Δ is the gap parameter. The gap parameter is zero in the normal metal. Then, the wavefunction in the normal metal must satisfy

$$\begin{bmatrix} \frac{-\hbar^2}{2m}\frac{\partial^2}{\partial x^2} - E_F & 0 \\ 0 & \frac{\hbar^2}{2m}\frac{\partial^2}{\partial x^2} + E_F \end{bmatrix} \Psi_n = E\Psi_n. \tag{1.108}$$

The energy of the electron and the hole eigenstates are respectively

$$\begin{pmatrix} 1 \\ 0 \end{pmatrix} \rightarrow E = \frac{\hbar^2 k^2}{2m} - E_F, \tag{1.109}$$

$$\begin{pmatrix} 0 \\ 1 \end{pmatrix} \rightarrow E = -\frac{\hbar^2 k^2}{2m} + E_F. \tag{1.110}$$

Hence, the wavevectors the electron and hole states are

$$k_e = k_F\sqrt{1 + \frac{E}{E_F}} \approx k_F\left(1 + \frac{E}{2E_F}\right), \tag{1.111}$$

$$k_h = k_F\sqrt{1 - \frac{E}{E_F}} \approx k_F\left(1 - \frac{E}{2E_F}\right). \tag{1.112}$$

The above approximations are correct when $E_F = \frac{\hbar^2 k_F^2}{2m} \gg E$. The last assumption is essentially always true in PCAR and it will be clarified later in this section. In a similar fashion, the wavefunction in the superconductor must satisfy the BdG equation with a non-zero gap

$$\begin{bmatrix} \frac{-\hbar^2}{2m}\frac{\partial^2}{\partial x^2} - E_F & \Delta \\ \Delta & \frac{\hbar^2}{2m}\frac{\partial^2}{\partial x^2} + E_F \end{bmatrix} \Psi_s = E\Psi_s. \tag{1.113}$$

The energy of the quasielectron and quasihole eigenstates are

$$\begin{pmatrix} u_0 \\ v_0 \end{pmatrix} \rightarrow E = \sqrt{\left(\frac{\hbar^2 q^2}{2m} - E_F\right) + \Delta^2}, \tag{1.114}$$

$$\begin{pmatrix} v_0 \\ u_0 \end{pmatrix} \rightarrow E = -\sqrt{\left(\frac{\hbar^2 q^2}{2m} - E_{\mathrm{F}}\right) + \Delta^2}. \tag{1.115}$$

In the above equations, it has been tacitly assumed that the effective electron mass in the superconductor is the same as in the normal metal. Furthermore, zero mismatch in the Fermi level of the two materials is considered. The wavevectors of the states in the superconductor are then:

$$q_{\mathrm{e,h}} = k_{\mathrm{F}} \sqrt{1 \pm \sqrt{\frac{E^2 - \Delta^2}{E_{\mathrm{F}}^2}}}. \tag{1.116}$$

Again the assumption $E_F \gg E, \Delta$ is valid, hence:

$$q_{\mathrm{e,h}} = \begin{cases} k_{\mathrm{F}} \left(1 \pm \frac{\nu}{2}\right), & \text{if } E > \Delta, \\ k_{\mathrm{F}} \left(1 \pm \frac{i\nu}{2}\right), & \text{if } E < \Delta, \end{cases} \tag{1.117}$$

where $\nu = \sqrt{\frac{E^2 - \Delta^2}{E_{\mathrm{F}}^2}}$. Once the expressions for the electron and hole wavevectors in the normal metal and the quasiparticles in the superconductor have been derived, the stitching of the wavefunctions has to be made at the N/S interface. A Dirac delta function potential with an arbitrary strength W models the interface in the BTK theory $U(x) = W\delta(x)$. Then the boundary conditions for the wavefunctions are:

$$\begin{aligned} \Psi_{\mathrm{n}}(0) &= \Psi_{\mathrm{s}}(0), \\ \Psi_{\mathrm{s}}'(0) - \Psi_{\mathrm{n}}'(0) &= \tfrac{2m}{\hbar^2}\Psi(0). \end{aligned} \tag{1.118}$$

Where $\Psi_{\mathrm{n,s}}'(0)$ must be interpreted as the value of the derivative at $x = 0$. The wavefunctions are spinors. Therefore, the boundary conditions provide effectively four equations which determine uniquely the transmission coefficients a, b, c and d:

$$\begin{bmatrix} -1 \\ 0 \\ 2Z + i \\ 0 \end{bmatrix} = \begin{bmatrix} 1 & u_0 & 0 & -v_0 \\ 0 & -v_0 & 1 & -u_0 \\ i - 2Z & iu_0 & 0 & -iv_0 \\ 0 & iv_0 & -i - 2Z & -iu_0 \end{bmatrix} \begin{bmatrix} b \\ c \\ a \\ d \end{bmatrix}, \tag{1.119}$$

where $Z = \frac{W}{\hbar v_F}$. After solving the above system, we get the reflection and transmission coefficients:

$$\begin{aligned} a &= \tfrac{u_0 v_0}{\gamma}, \\ b &= -\tfrac{Z(u_0^2 - v_0^2)(Z+i)}{\gamma}, \\ c &= -\tfrac{u_0(1 - Zi)}{\gamma}, \\ d &= \tfrac{iv_0 Z}{\gamma}, \end{aligned} \tag{1.120}$$

where $\gamma = u_0^2 + Z^2(u_0^2 - v_0^2)$. The important information out of this calculation is the probability for Andreev reflection $A(E,Z) = a^*a$ and normal reflection $B(E,Z) = b^*b$. Therefore, the probabilities for two processes are:

$E < \Delta$	$E > \Delta$
$A = \frac{\Delta^2}{E^2+(\Delta^2-E^2)(1+2Z^2)^2}$	$A = \frac{u_0^2 v_0^2}{\gamma^2}$
$B = 1 - A$	$B = \frac{(u_0^2-v_0^2)Z^2(1+Z^2)}{\gamma^2}$

Table 1.1: BTK theory reflection probabilities

The expressions for the BCS coherence factors u_0 and v_0 are

$$\begin{bmatrix} u_0^2 \\ v_0^2 \end{bmatrix} = \begin{cases} \frac{1}{2}\left(1 \pm \frac{\sqrt{E^2-\Delta^2}}{E}\right), & \text{if } E > \Delta, \\ \frac{1}{2}e^{\pm i \arccos(\frac{E}{\Delta})}, & \text{if } E < \Delta. \end{cases} \tag{1.121}$$

The reflection probabilities derived above will be used to calculate the current through the contact. Two reservoirs (named **n** and **s** in this case) biased at voltage V are considered. The convention that the bias lifts the Fermi function is assumed, hence the electrons coming from **n**-reservoir have Fermi distribution $f(E-eV)$, while those coming from **s**-reservoir have $f(E)$. There exist transport currents in both directions: from the normal metal to the superconductor ($I_{\mathrm{n}\to\mathrm{n}}$), and from the superconductor to the normal metal ($I_{\mathrm{s}\to\mathrm{n}}$). The currents in an energy window dE at energy E are expressed respectively as:

$$I_{\mathrm{n}\to\mathrm{s}} = eSv(E)\rho(E)f(E-eV)T(E)dE, \tag{1.122}$$

$$I_{\mathrm{s}\to\mathrm{n}} = eSv(E)\rho(E)f(E)T(E)dE, \tag{1.123}$$

where S is the area of the junction, $v(E)$ is the velocity of the electron, $\rho(E)$ is the density of states in the normal metal, and $T(E)$ is the transmission probability. The total transport current is the difference between the currents in the two directions and the difference integrated over the energy

$$I = eSv\rho \int (f(E-eV) - f(E))T(E)dE. \tag{1.124}$$

The energy scale is set by the size of the thermal energy $k_{\mathrm{B}}T$, whereas the applied bias is normally in the range $[-10\Delta, 10\Delta]$, where Δ is the superconducting gap. The superconducting gap of niobium is around 1.5 meV, hence $E \gg eV$. This is the reason why the velocity and the density of

states could be taken in front of the integral as these characteristics do not change. Furthermore, the normal density of states of the superconductor is taken to be constant. The transmission probability is $T(E) = 1 - R(E)$, where $R(E)$ is the reflection probability. The reflection probability is $R(E) = B(E) - A(E)$. It is reminded again that the Andreev reflection is in effect a backpropagated hole which carries opposite charge and that is why the Andreev reflection probability comes with negative sign in the reflection probability $R(E)$. The current is then

$$I = eSv\rho \int (f(E-eV) - f(E))(1 + A(E) - B(E))dE. \tag{1.125}$$

The Fermi distributions mismatch could be approximated using the Taylor series expansion as $f^{'}(E-eV)(-e)$. The applied bias V is taken in front of the integral. It is natural to get rid of the voltage variable by taking the differential conductance $G_{\mathrm{ns}} = dI/dV$. In the experimental section it will become clear that actually it is experimentally easier to measure directly the differential conductance. The result for the last is

$$G_{\mathrm{ns}} = -e^2 Sv\rho \int (f^{'}(E-eV))(1 + A(E) - B(E))dE. \tag{1.126}$$

From Table(1.1), it is obvious that in the case of contact between two normal metals, there is no probability for Andreev reflection and the only possible process is normal reflection $B = Z^2/(1 + Z^2)$. Then the normal-to- normal metal differential conductance is:

$$G_{\mathrm{nn}} = -e^2 Sv\rho \frac{1}{1+Z^2} \int f^{'}(E-eV)dE \tag{1.127}$$

$$= -e^2 Sv\rho \frac{1}{1+Z^2} \tag{1.128}$$

At cryogenic helium temperatures (1.9 - 4.2 K), the derivative of the Fermi function behaves almost as a Dirac delta-function ($f^{'}(E-eV) \approx \delta(E-eV)$) *, and the integral over the energy is one. The normalized differential conductance is expressed as:

$$\frac{G_{\mathrm{ns}}}{G_{\mathrm{nn}}} = -(1+Z^2) \int (f^{'}(E-eV))(1 + A(E) - B(E))dE. \tag{1.129}$$

1.5.1.1 Spin polarization in the BTK model

The expression for the differential conductivity obtained above still does not provide the opportunity to utilize Andreev reflection for measuring the spin polarization. The total current I is split into a fully-polarized I_{p} and fully-unpolarized I_{u} components. The current could be then written

*This approximation is taken only for the derivation of a clear mathematical form. The actual form of the Fermi function derivative is considered and calculated in our analysis software. The proper normalization of the spectrum is critical, otherwise the spin polarisation is underestimated.

with the spin polarization P

$$I = PI_{\mathrm{p}} + (1-P)I_{\mathrm{u}}. \tag{1.130}$$

Each of the two current components have their own probabilities for normal and Andreev reflection:

$$\begin{aligned} I &= -P(1+Z^2)\int f^{'}(E)(1+A_{\mathrm{p}}(E)-B_{\mathrm{p}}(E))dE - (1-P)(1+Z^2)\int f^{'}(E)(1+A_{\mathrm{u}}(E)-B_{\mathrm{u}}(E))dE, \\ &= -P(1+Z^2)\int f^{'}(E)(1-B_{\mathrm{p}}(E))dE - (1-P)(1+Z^2)\int f^{'}(E)(1+A_{\mathrm{u}}(E)-B_{\mathrm{u}}(E))dE. \end{aligned} \tag{1.131}$$

The Andreev reflection for the fully-spin polarized current I_{p} is forbidden, hence $A_{\mathrm{p}}(E) = 0$. On the other hand, the reflection probabilities $A_{\mathrm{u}}(E), B_{\mathrm{u}}(E)$ are the same as the ones derived in Table(1.1). What is left to be clarified is the normal reflection probability for the fully-spin polarized. It is obvious, that at energies below the superconducting gap Δ, the only possible process is normal reflection, as the transmission is not allowed, hence $B_{\mathrm{p}}(E) = 1$ for $|E| \leq \Delta$. The reflection probability is derived on the assumption that the ration between the reflected and transmitted electron should not depend on the type of the spin. In other words

$$\frac{B_{\mathrm{p}}}{C_{\mathrm{p}}+D_{\mathrm{p}}} = \frac{B_{\mathrm{u}}}{C_{\mathrm{u}}+D_{\mathrm{u}}}, \tag{1.132}$$

furthermore, in the fully-spin polarized case

$$B_{\mathrm{p}} + C_{\mathrm{p}} + D_{\mathrm{p}} = 1, \tag{1.133}$$

$$\Rightarrow C_{\mathrm{p}} + D_{\mathrm{p}} = 1 - B_{\mathrm{p}} \tag{1.134}$$

Then the expression for the normal reflection of the spin polarized component at energies $E \geq \Delta$ is

$$\begin{aligned} \frac{B_{\mathrm{p}}}{1-B_{\mathrm{p}}} &= \frac{B_{\mathrm{u}}}{C_{\mathrm{u}}+D_{\mathrm{u}}}, \\ \Rightarrow B_{\mathrm{p}} &= \frac{B_{\mathrm{u}}}{1-A_{\mathrm{u}}}. \end{aligned} \tag{1.135}$$

In order to demonstrate clearly the effect of the barrier strength Z on the PCAR spectra with different spin polarization, multiple curves are generated on Fig. (1.29). All spectra are simulated with assumed temperature of $T = 4\,\mathrm{K}$. The case of a perfectly transparent barrier $Z = 0.0$ (panel (a)), demonstrates that the zero bias anomaly roughly follows the simplified expression $G_{\mathrm{ns}} = 2G_{\mathrm{nn}}(1-P|)$. Another general trend, which is apparent, is that the spectra with high spin polarization, $0.75 < P < 1.0$, exhibit the same overall shape for $Z < 1.0$. In other words, modest barrier strength does not affect the spectral features as long as the spin polarization is high.

However, the situation is very different for low values of the spin polarization. The spectral features for unpolarized metal $P = 0.0$ change dramatically from $Z = 0.0$ to $Z = 0.75$. The reason is that the Andreev reflection probability is inversely proportional to the square of the barrier strength $A \propto Z^{-2}$. Therefore, less transparent interfaces suppress the sub-gap conductance and result in spectral features which are dominated by the structure of the quasiparticle density of states of the superconductor. For $Z = 0.5, 0.75$, moderate values of the spin polarization ($0.3 < P < 0.6$) become more difficult to be distinguished and to be fitted to the correct value of P. The spectra are closer to each other. Experimentally, it is important the tip to land multiple times on the sample in order to have good statistics on spectra of contacts with different barrier heights. Alternative approach to distinguish between low and high barrier heights is a temperature scan of the contact.

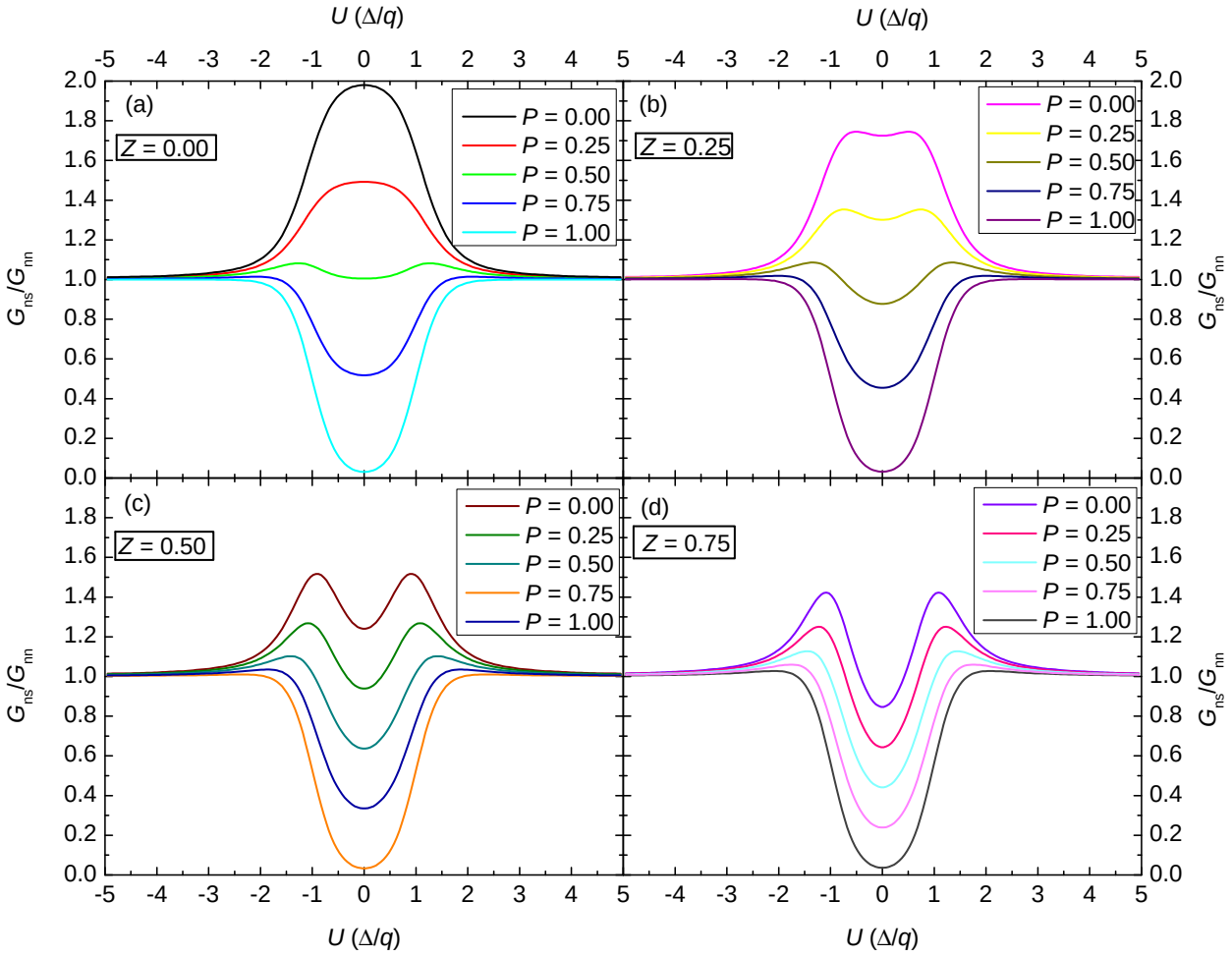

Figure 1.29: Simulated PCAR spectra following the BTK theory for different barrier strength Z and spin polarization P. The temperature for the simulations is set at $T = 4$ K. Each panel has curves for five different values of the spin polarization $P = 0.0, 0.25, 0.5, 0.75$, and 1.0. Panel (a)-$Z = 0.0$, panel (b)-$Z = 0.25$, panel (c)-$Z = 0.5$, and panel (d)-$Z = 0.75$.

Two set of curves for 0 % and 100 % spin polarizations and $Z = 0.0, 1.0, 2.0$, and 5.0 are presented in Fig. (1.30). It is obvious that in the case of $Z = 5.0$, the spectra for non and full spin

polarization are essentially identical. A clear indication of high Z is the appearance of the sharp singularities in the quasiparticle DOS of the superconductor around $U = \pm\Delta/q$. The offset and the smearing of the DOS in the present simulated curves is due to thermal broadening. For large barrier heights, the Andreev reflection is fully suppressed and the spectra are analyzed as tunneling. The case of $Z \gg 1.0$ corresponds to spin polarized tunneling which is discussed before in Sec. (1.4.5). The increased height of the δ barrier can be considered as oxide barrier at the interface. In SPT, the spin resolution is achieved due to the Zeeman splitting of the quasiparticle DOS and not due to the Andreev reflection process.

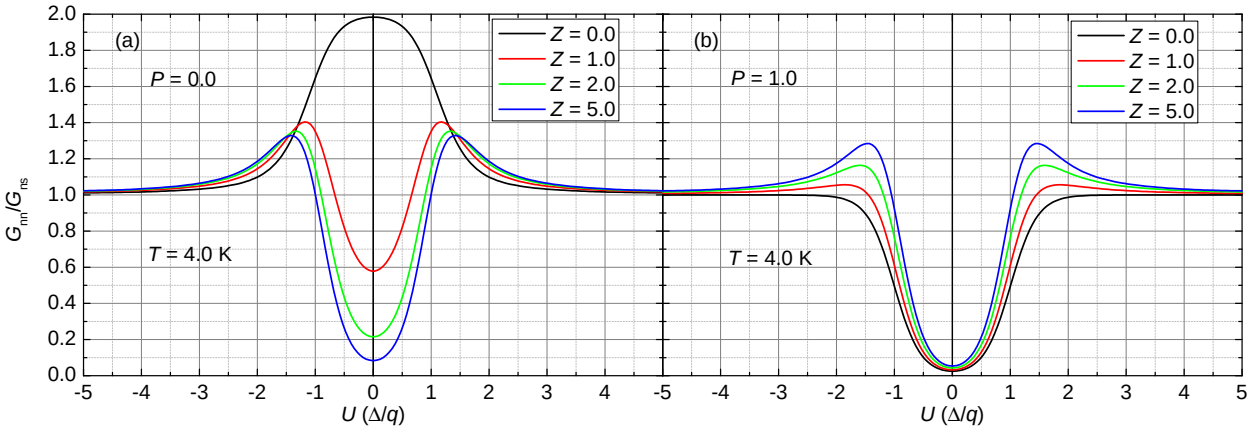

Figure 1.30: Simulated PCAR spectra for $P = 0.0$ (panel (a)) and $P = 1.0$ (panel (b)). Different barrier strengths ($Z = 0.0, 1.0, 2.0$, and 5.0) are presented. The temperature is set at $T = 4\,\mathrm{K}$.

1.5.2 Modified BTK theory

In the original BTK theory, presented above, the superconducting properties are supposed to change with a jump at the N/S interface. It has been observed in the contact between a superconducting electrode and a normal metal electrode, that the superconductor induces small superconductivity in the normal metal. The effect is known as **superconducting proximity effect**[47]. Furthermore, there exists the opposite effect in which the presence of the normal metal destroys slightly the superconducting properties of the superconductor. The last is known as **inverse proximity effect**[342]. The proximity effect is incorporated by introducing two gap values, one for the Andreev reflection (Δ_1, the proximity gap), and one for the quasiparticle transport(Δ_2). The model is developed by Strijkers *et al.*[321] and is known as modified BTK (mBTK) theory.

An important contribution of the mBTK is the explanation of the finite bias conductance dips (FBD), which have been previously observed but unexplained. The proximity effect broadens the spectrum as well. Though, there is still controversy among the community about the validity of the approach, whether the proximity effect is the only contributing effect, and whether the proximity effect could be so easily incorporated. An extension of the BTK model for spatial variation of

$\lvert E\rvert \leq \Delta_1$	$\Delta_1 < \lvert E\rvert < \Delta_2$	$\lvert E\rvert \geq \Delta_2$
$A_u = \frac{\Delta_1^2}{E^2+(\Delta_1^2-E^2)(1+2Z^2)^2}$	$A_u = \frac{u_{01}^2 v_{01}^2}{\gamma^2}$	$A_u = \frac{u_{01}^2 v_{01}^2}{\gamma_2^2}$
$B_u = 1 - A_u$	$B_u = 1 - A_u$	$B_u = \frac{(u_{02}^2-v_{02}^2)^2 Z^2(1+Z^2)}{\gamma_2^2}$
$B_p = 1$	$B_p = 1$	$B_p = \frac{(u_{02}^2-v_{02}^2)^2 Z^2(1+Z^2)}{\gamma_3^2}$

Table 1.2: Modified BTK theory reflection probabilities. The notations are represented as follow: $u_{01}^2 = 1 - v_{01}^2 = 0.5(1 + [(E^2 - \Delta_1^2)/E^2]^{1/2}), u_{02}^2 = 1 - v_{02}^2 = 0.5(1 + [(E^2 - \Delta_2^2)/E^2]^{1/2}), \gamma_1^2 = (u_{01}^2 + Z^2[u_{01}^2 - v_{01}^2])^2, \gamma_2^2 = u_{01}^2 v_{01}^2 + (u_{02}^2 - v_{02}^2)[u_{02}^2 + Z^2 + (u_{02}^2 - v_{02}^2)Z^2(1+Z^2)]$, and $\gamma_3^2 = (u_{02}^2 - v_{02}^2)[u_{02}^2 + Z^2 + (u_{02}^2 - v_{02}^2)Z^2(1+Z^2)]$.

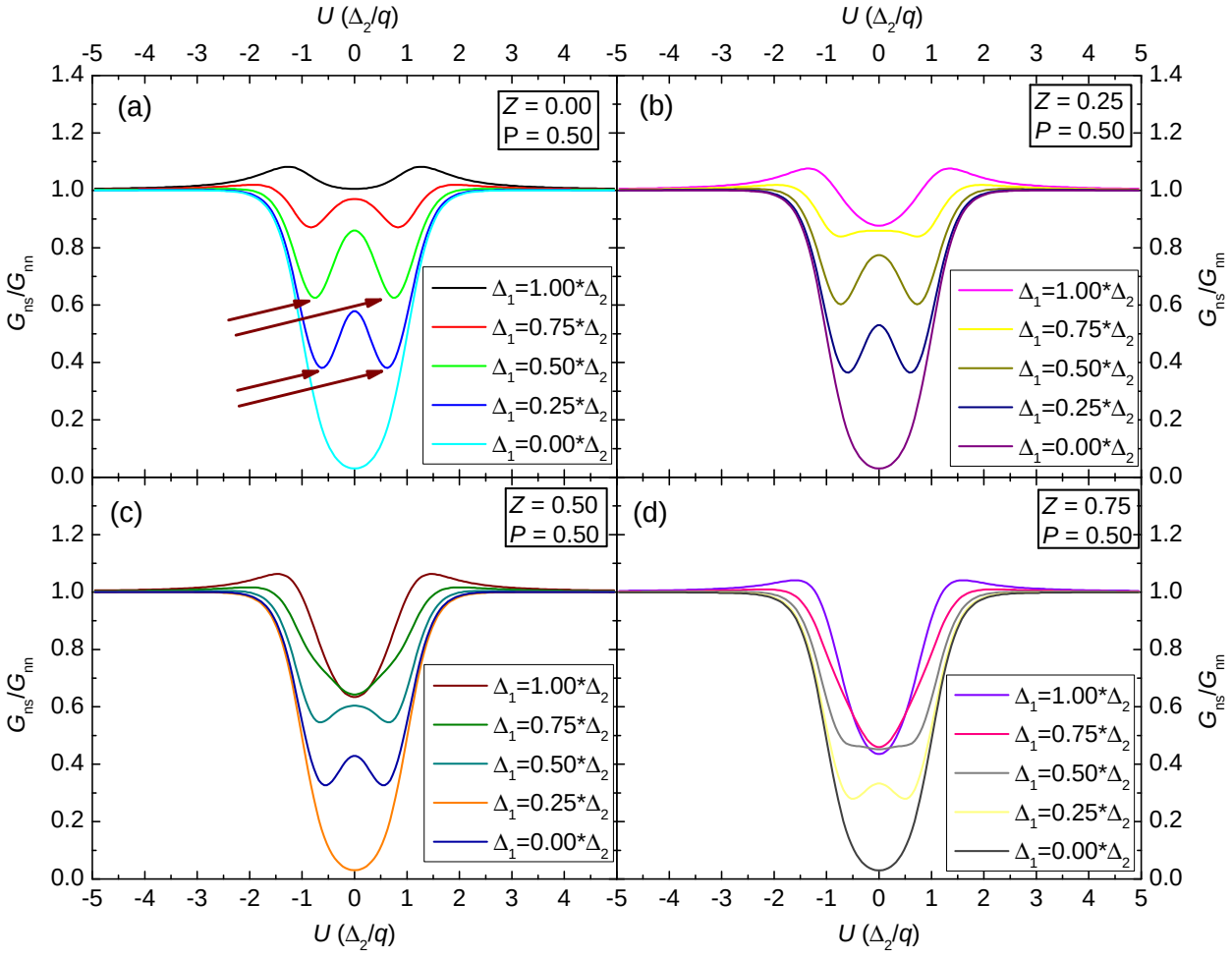

Figure 1.31: Simulated spectra following the modified BTK theory. The spin polarization is fixed to $P = 0.5$ on all panels. Panel (a)-$Z = 0.0$, Panel (b)-$Z = 0.25$, Panel (c)-$Z = 0.5$, and Panel (d)-$Z = 0.75$. Features known as finite bias dips are indicated with brown arrows on panel (a). The temperature is set at $T = 4$K.

the order parameter both in the superconductor and in the normal metal is given by van Son *et al.* [355]. The proposed model has been applied to thin-film sandwiches of normal metal-ferromagnet but it is unclear what is a realistic distribution of the proximity effect in the point contact geometry. Extensive review of the superconductor-ferromagnet proximity effect is given by Buzdin[47]. Westbrook and Javan [370] argue that the finite bias conductance dips can be due to quenching of part of the contact, however, the conductance features are much sharper in this case. Evolution of the proximity gap effect in the depth of the superconductor is studied extensively by the superconductivity community. The function exhibits simple exponential decay for the case of contact with non-magnetic materials. On the other hand, the superconducting gap is a damped sine function in the case of contact with a ferromagnetic material. The latter is known as FFLO state* [104, 192].

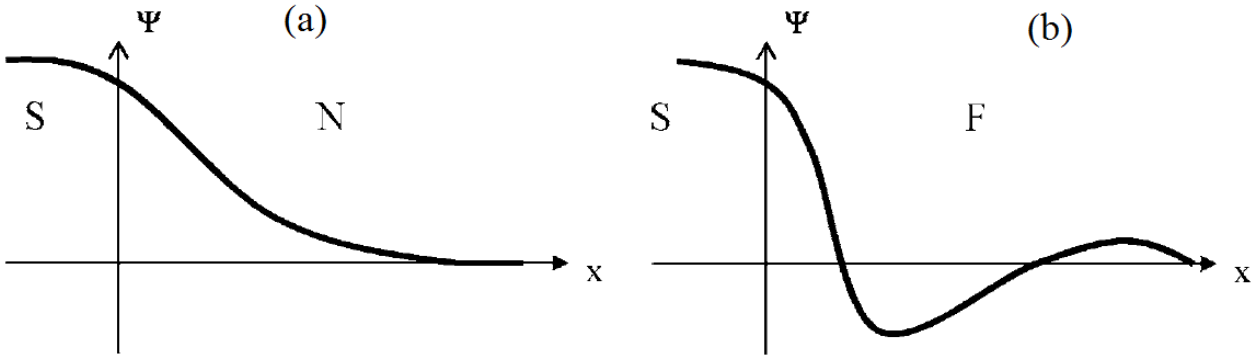

Figure 1.32: Superconducting order parameter at the interface between a superconductor and a normal metal (a), and between a superconductor and a ferromagnet (b). The picture is after Buzdin[47].

1.5.3 Barrier strength

It is demonstrated in Fig. (1.30) that the barrier strength can completely suppress the Andreev reflection. The Z parameter is a parameter which absorbs a few physical effects: Fermi level mismatch between the two metals, oxide at the interface and scattering by impurities or interfacial defects[158]. The band mismatch is an inevitable contribution present even in a nominally "clean" contact. Fermi level mismatch between the two electrodes is considered in the follow-up work by Blonder[30]. In this case, the effective barrier strength is

$$Z_{\text{eff}} = \sqrt{Z^2 + \frac{1-r^2}{4r}}, \tag{1.136}$$

where $r = v_{\text{F1}}/v_{\text{F2}}$ is the ratio between the Fermi velocities in the two metals. For instance, $r \approx 1.15$ for Nb/Cu contact and $r \approx 1.45$ for Nb/Fe contact. Therefore, the effect of the Fermi

*Fulde-Farrell-Larkin-Ovchinnikov

mismatch towards the Z^2_{eff} is up to 0.03 in the free-electron approximation*. If an *ab initio* calculation accounting for the band structure of transition metals is considered, the contribution towards Z^2 is 0.1[387].

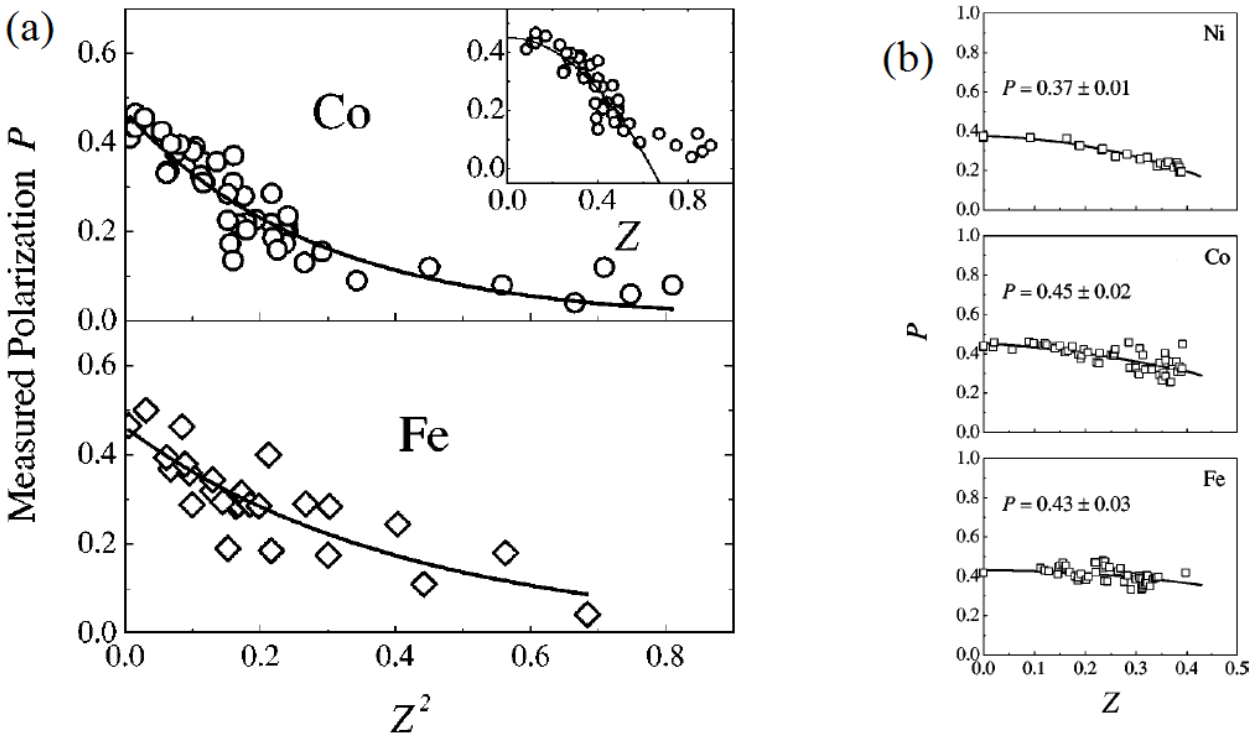

Figure 1.33: Panel (a)-spin polarization of Co and Fe depending on Z^2 following the extrapolation $P = P_0 \exp(-2\alpha\psi Z^2)$. The inset demonstrates fit on the Co data with a parabola, the high Z region is not covered well. The graph is after Kant[158]. Panel (b)-spin polarization of Ni, Co, and Fe with the quadratic extrapolation. The graph is after Strijkers[321].

The effect of the interfacial oxides is often manifested as a dependence between the barrier strength of the contact and the spin polarization (see Fig. (1.33)). High resistance, low cross-section area contact might have unbroken oxide interface and, therefore, the impinging electrons undergo multiple scattering events and/or the Cooper pairs cannot maintain coherence. The effect has been reported by Strijkers[321], Bugoslavsky[45], Kant[158]. Varying the pressure on the contact results in significant change in the spectral features when the sample/tip is oxidized. It is reported that the fitted spin polarization decreases with higher barrier strength. Two models are utilized to extract the inherent spin polarization out of the $P(Z)$ dependence for $Z \to 0$. The model by Kant *et al.*[158] considers the interface as an extended scattering region with width l. The transmission process is calculated as a random walk problem of an electron with mean free path λ and scattering anisotropy

*If the initial $Z = 0$, $Z_{\text{eff}} \approx 0.2$ only due to Fermi velocities mismatch. It is a significant contribution!

ψ^*. In this approximation, the barrier strength is

$$Z^2 = \frac{1}{1+\psi}\frac{l}{\lambda}. \tag{1.137}$$

Each scattering event has a spin-flip probability α. Electrons with initial spin polarization P_0 are impinging on the disordered region and then the transmitted polarization P is calculated to be

$$P = P_0 \frac{(1+Z^2\eta)}{(1+2\alpha\phi)\sinh(\eta Z^2)+\eta\cosh(\eta Z^2)}, \tag{1.138}$$

where $\eta^2 = 4\alpha(1+\psi)+4\alpha^2(\psi^2-1)$. For large forward scattering, *i.e.* large ψ, the cumbersome expression above is approximated by

$$P \approx P_0 \exp(-2\alpha\psi Z^2). \tag{1.139}$$

The other fitting procedure is suggested by Strijkers[321] and it is based on parabolic extrapolation towards $Z = 0$. There is, however, no theoretical justification of such a model. In our work, extrapolation the value of P towards $Z = 0$ is avoided. Large number of different spectra are obtained and the one with the highest spin polarization is considered to be the intrinsic value for the material. First of all, extrapolation towards $Z = 0$ is not always physically reasonable because such transparent contacts are unattainable even in high quality *in-situ* grown point contacts. Second, the dependence $P(Z)$ is not always true and it might be a spurious correlation due to the fit converging in a local minimum.

1.5.4 Important remarks

As it is outlined in the work of Blonder and Tinkham [30], the barrier strength, Z, depends on the Fermi velocity mismatch between the superconducting and the ferromagnetic electrodes. The Fermi velocities for the two spin channels are often different, therefore, there should be two different barrier strengths in principle. The theoretical work of Zutic and Valls discusses the band mismatch and its effect on the conduction spectrum[146]. It might be difficult to distinguish between the effect of spin polarization and band mismatch (for example see Fig. 6 in Chalsani *et al.*[51]). Furthermore, the effect of interfacial scattering and spin-flip scattering may have significant effect on the observed PCAR features[51]. Additionally, spurious $P(Z)$ dependence might appear when the superconducting gap is left as a free fitting parameter [379] (the gap is fixed in our analysis routine). Therefore, it could be generally more appropriate to trace the $P(Z)$ dependence although it is not well established what is the correct theoretical dependence [321, 158]. Extrapolation of the

*The scattering anisotropy represents the probability for forward and backward scattering

$P(Z)$ towards $Z = 0$ is performed in one of our published results [36].

Another point which should be mentioned is that the used theory of Strijkers *et al.*[321] has the shortfall of incorrect normalization. The correct treatment is given in the work of Mazin *et al.* [215]. Expressions are outlined in their work both for ballistic and diffusive transport regimes (see Table 1.3 and Table 1.4). It is important to mention that usually the difference in the extracted spin polarization between the theories of Mazin and Strijkers is within a few percents. Nevertheless, in order to be consistent fitting approaches following the two models must be compared for particular experimental data set.

	$\lvert E\rvert < \Delta$	$\lvert E\rvert \geq \Delta$
I_{u}	$\frac{1+\beta}{2\beta}\mathrm{Im}[F(-i\beta) - F(i\beta)]$	$\frac{2\beta}{1+\beta+2Z^2}$
I_{p}	0	$\frac{4\beta}{(1+\beta)^2+4Z^2}$

Table 1.3: Diffusive BTK theory after Mazin *et al.*[215]. β is defined as follows: $\beta = \frac{E}{\sqrt{\lvert\Delta^2 - E^2\rvert}}$. Z is the barrier strength.

	$\lvert E\rvert < \Delta$	$\lvert E\rvert \geq \Delta$
I_{u}	$\frac{1+\beta}{2\beta}\mathrm{Im}[F(-i\beta) - F(i\beta)]$	$2\beta F(\beta)$
I_{p}	0	$\beta F[(1+\beta^2)/2 - 1]$

Table 1.4: Diffusive BTK theory after Mazin *et al.*[215]. $F(s)$ and β are defined as follows: $F(s) = \frac{\cosh^{-1}(2Z^2+s)}{\sqrt{(2Z^2+s)^2-1}}$ and $\beta = \frac{E}{\sqrt{\lvert\Delta^2 - E^2\rvert}}$.

1.5.5 Transport regimes

There are three different transport regimes through a point contact: ballistic, diffusive, and inelastic (or thermal). The type of the transport regime is determined by the relation between three characteristic lengths: the size of the nanoconstriction d, the elastic mean free path l_{el}, and the inelastic mean free path l_{in}.

The most sough-after regime in PCAR experiments is ballistic transport in which case $d < l_{\mathrm{el}}$. In this situation, the carriers move through contact region without experiencing even elastic scattering, the transport is considered one dimensional and is described by the BTK theory outlined in Sec. (1.5.1). The ballistic spin polarization is what matters the most for MTJs because the transmission probability through the oxide barrier is exponentially decreased for electrons with in-plane momentum vector component. The ballistic nature of the contact can be checked by the Sharvin's formula[300, 13]:

$$R_{\mathrm{S}} = \frac{4\rho l}{3\pi d^2}, \tag{1.140}$$

where ρ is the characteristic resistivity of the contact area and l is the mean free path, which is calculated following Matthiesen's rule. The product $\rho l = mV_{\mathrm{F}}/(ne^2)$ is a material specific ratio, where m, V_{F}, and n are the effective mass, Fermi velocity and carrier concentration, respectively[120]. The contact resistivity is usually assumed to be an average of the resistivities of the left and right electrodes: $\rho = (\rho_1 + \rho_2)/2$ and $\rho l = (\rho_1 l_1 + \rho_2 l_2)/2$. Gramich *et al.*[120] have used second derivative , $\mathrm{d}^2I/\mathrm{d}V^2$, as an indicator whether a contact is in a ballistic or diffusive regime. If it is ballistic, the characteristic phonon excitation modes of the metallic electrodes should be observed.

The diffusive transport regime happens when $l_{\mathrm{el}} < d < l_{\mathrm{in}}$. In this case, the electrons experience elastic scattering in the area of the contact. This configuration is very probable to occur in a PCAR experiment, although it has the disadvantage that the spectral information is averaged over the momentum direction. The resistance of the contact area in this case is given by Wexler's formula[371, 13]:

$$R_{\mathrm{W}} = \frac{4\rho l}{3\pi d^2} + \gamma\frac{\rho}{2d}, \tag{1.141}$$

where the second, Maxwell's term, is multiplied by a slowly varying function, γ, which can be approximated using Padé fit[255, 120].

The final transport regime is the inelastic or thermal regime, where the relation $d > l_{\mathrm{in}}, l_{\mathrm{el}}$ holds and the electrons lose both their initial momentum orientation and some of their energy. This is a transport regime which must be avoided as the energy resolution is no longer well-defined. The thermal regime results in local Joule heating in the contact area which may have two manifestations: the superconducting tip is quenched at temperature significantly below the bulk critical temperature of the composition, and/or the PCAR spectrum exhibits significant quadratic background[13]. The resistance of a thermal contact is given at low bias by Maxwell's formula:

$$R_{\mathrm{M}} = \frac{\rho}{2d}. \tag{1.142}$$

It is not well-established how justifiable is the contact size estimation following the Sharvin's Eq. (1.140), Wexler's Eq. (1.141) and Maxwell's Eq. (1.142) formulas because the Fermi surface

mismatch of the two metals have significant contribution towards the resistance of the point contact. An extreme case in that respect is the work of Turel *et al.*[348], where a radius in the range 0.7 nm-6.0 nm is determined from the resistance of $YBa_2Cu_3O_7/CrO_2$(Au) point contacts.

As outlined above, the second derivative can be used as an indicator of whether the contact is in the diffusive or ballistic regime[120]. The latter technique is known as point-contact spectroscopy (PCS) and it has been pioneered by Yanson[397, 396]. PCS is a handy tool to investigate electron-phonon interactions in normal metals and in superconductors [216]. In a ballistic contact, electrons release their energy eV upon reaching the counter-electrode by generating phonons. Such scattering process produces non-linear I-V curve. It has been demonstrated by Kulik *et al.*[184] that the characteristic is representative for the electron-phonon interaction. Why a ballistic current through a nanoconstriction would excite phonons? It is intuitively expected that ballistic electrons do not scatter. They do not within the contact region but they do scatter outside of it (into the electrodes). Ballistic electrons preserve their total energy, eV, and their wavevector direction as they pass through the point contact. Therefore, they realize high energy upon scattering beyond the nanoconstriction. On the other hand, diffusive electrons would scatter elastically multiple times within the contact region and lose their wavevector directionality. Upon scattering in the counterelectrode, their momentum vector loss will be averaged off and this is the reason why phonon modes are not excite by diffusive electrons. More quantitative description is given by Yanson and Naidyuk [396]. In the thermal regime, there will be multiple inelastic scattering events within the contact region, therefore big portion of the eV energy will be lost before the electrons reach the counterelectrode. Hence, phonon modes are again not excited.

1.5.6 Importance of PCAR

Critical parameters of spin electronic devices depend on the spin polarization of the ferromagnetic electrodes. The TMR increases for higher spin polarization following Julliere's model and the critical current switching density of STT-based MTJs depends hyperbolically on the spin polarization of the analyzer. Therefore, it is important to extract the Fermi level spin polarization of potential spin electronic materials in a swift and reliable manner. PCAR offers exactly that. There is no need for device fabrication as is the case for spin-polarized tunneling, and there is no necessity for *in-situ* transfer of the sample between the deposition chamber and the analyzing one in ultra-high vacuum conditions as is the case for the spin-resolved photoemission spectroscopy. Furthermore, PCAR probes the direct transport spin polarization unaffected by the quality of tunneling barriers. The PCAR can be performed on both thin films and tiny single crystals*. Extensive

*During the course of this work, attempt has been made to measure PCAR on the $NdFeAsO_{1-x}Fe_x$ superconductor in order to investigate its order parameter. The investigated sample is in pressed sintered powder. Unfortunately, the measurement has been unsuccessfully, but that might be related to the fact that the surface of the sample oxidizes

review of the compositions studied by PCAR goes beyond the limit of this work but some overview is given in the two tables below.

Outside of the spin electronics area, PCAR has been used for extraction of the size and the symmetry of the gap of superconductors. The measurement idea is similar to original tunneling configuration of superconductor-insulator-superconductor by Giaever *et al.*[109], however, a direct electrical contact between the two electrodes in this case. For instance, a few important achievements have been made folliwing this approach: the dual gap superconductivity nature of MgB_2[116], gap symmetry in Fe-based superconductors [287, 66, 66, 345], gap parameters in $Bi_2Sr_2CaCu_2O_y$ [271] and *d*-wave superconductivity in $PuCoGa_5$[67],

quickly after its polishing.

1 - PCAR literature values of spin polarization, P		
Composition	P	Reference
p-$In_{0.96}Mn_{0.04}As$	72.5 %	Akazaki[3]
CoFeMnGa	70(1) %	Bainsla[16]
CoFeCrAl	67(2) %	Bainsla[15]
Mn_2Fe_xGa	51(2) %	Betto[a]
$SrRuO_3$	51(2) %	Raychaudhuri[275]
NiMnSb	45 %	Branford[41]
$(Fe/Co)_n$	60 %	Chu[61]
$La_{0.65}Ca_{0.35}MnO_3$	80 %	D'yachenko[83]
Co_2FeSi	49(2) %	Gercsi[107]
$SrLaVMoO_6$	50 %	Goteh[118]
Fe-N	52 %	Ji[152]
$Co_2Cr_xFe_{1-x}Si$	64 %	Karthik[164]
$Co_{75}Fe_{25}$	58(3) %	Karthik[163]
Co_3FeN	62 %	Kawai[167]
MnBi	63(1) %	Kharel[169]
Mn_2Ga	40 %	Kurt[188]
Mn_3Ga	58(6) %	Kurt[188]
Mn_3Ge	46(2) %	Kurt[185]
$Mn_2Ru_{0.48}Ga$	54(3) %	Kurt[186]
$Ni_{76}Al_{24}$	51 %	Mukhopadhyay[243]
Co_2MnSi	55 %	Miyoshi[231]
Ni_xFe_{1-x}	45 %	Nadgorny[247]
$La_{0.7}Sr_{0.3}MnO_3$	75 %	Nadgorny[246]
Mn_5Ge_3	42(5) %	Panguluri[260]
$Co_2FeAl_xSi_{1-x}$	60(1) %	Nakatani[250]

Table 1.5: Literature values of spin polarization of various materials measured by PCAR.

[a] To be submitted in PRB with title "Structure, element-specific magnetism and magneto-transport properties of epitaxial DO_{22} Mn_2Fe_xGa thin films".

2 - PCAR literature values of spin polarization, P		
Composition	P	Reference
Fe_4N	59 %	Narahara[251]
$Co_{1-x}Gd_x$	55 %	Naylor[253]
$Fe_{1-x}V_x$	52(3) %	Osofsky[256]
MnAs	49 %	Panguluri[259]
$In_{1-x}Mn_xSb$	52(3) %	Panguluri[258]
(Ga, Mn)As	83 %	Panguluri[257]
(Ga, Mn)Sb	57(5) %	Panguluri[262]
$Cr:In_2O_3$	50(5) %	Panguluri[261]
$Eu_{1-y}La_yO_{1-x}$	91 %	Schmehl[292]
FePt	42 %	Seemann[295]
$Ru_{1-x}Fe_xCrSi$	53 %	Shigeta2011[302]
$CeMnNi_4$	60 %	Singh[307]
CrO_2	90 %	Soulen[314]
$Co_2MnSi_xSn_{1-x}$	67(1) %	Srinivasan[315]
Th	41(8) %	Stamenov[317]
Er	58(2) %	Stamenov[316]
$In_{0.95}Cr_{0.05}N$	50(2) %	Thapa[338]
Ho	42 %	Usman[350]
Gd	52 %	Valentine[351]
Dy	50 %	Valentine[351]
$Co_2MnGa_{0.5}Sn_{0.5}$	72 %	Varaprasad[356]
$Co_2Mn(Ga_{0.5}Sn_{0.5})$	66 %	Varaprasad[357]
CoS_2	56 %	Wang[364]
$(In_{0.95}Sn_{0.05})_2O_3$	58 %	Xia[386]

Table 1.6: Literature values of spin polarization of various materials measured by PCAR.

Chapter 2

Experimental section

"You have to make again this electrical break-box. It is disgusting!"

Dr. Plamen Stamenov

2.1 Physical Properties Measurements System

Most Point Contact Andreev Reflection (PCAR) measurements in this thesis have been performed in our Physical Properties Measurements System (PPMS) with a superconducting solenoid with maximum applied magnetic field of $\mu_0 H = 14\,\mathrm{T}$. The PPMS is a highly versatile cryostat with measurement capabilities like Vibrating Sample Magnetometry (VSM), Heat Capacity, Thermal Transport, DC and AC (magneto-)transport with a possible rotation option. This is not a conventional helium vapour through sample space cryostat, instead the helium is injected into a cooling annulus through an impedance valve. The sample chamber is inserted into the cooling annulus but the sample chamber is completely gas insulated from the sample space. This means that the sample is never in direct contact with helium gas or liquid from the cooling space. More importantly, the impedance valve is not exposed to atmosphere when the sample space is vented, therefore, the icing probability of the impedance valve (from the back end) is significantly reduced and the lifetime of the system between cool-down and a necessary warm-up is greatly extended. The sample chamber itself is made of stainless steel in order to reduce thermal loss between the cold bottom and the warm top of the system. Only the bottom-most $\approx 10\,\mathrm{cm}$ of the sample chamber is made of copper, so that the sample is in good thermal equilibrium with the cooling annulus. The continuous low- temperature control (CLTC) option provides smooth transition through the helium boiling point (4.2 K)[74]. The CLTC is a low helium flow procedure, and therefore, it fails when the impedance valve is partially blocked and the helium flow is reduced. In such cases, the

system can be switched to "on-the-pot" option*. In this regime, liquid helium is accumulated in the cooling annulus for 30 min-40 min, then the impedance valve is fully closed and then this helium bath is used. Once the bath is exhausted, the system loses temperature control for $\approx$ 30 min before the impedance valve cools down again.

2.2 Point-contact Andreev reflection setup

An electro-optical probe is wired with insulated copper twisted pairs. The twisted pairs are organized in three separate bundles in order to reduce cross talk between the different signals:

- Bundle for temperature sensors
- Bundle for PCAR signals
- Bundle for piezo-steppers

The bundles for the temperature sensors and the PCAR signals are wound around the rod in different directions - clockwise and counter-clockwise, respectively. The twisted pairs are tightened to the rod with fishing cord and nail varnish is applied between the fishing cord and the stainless steel rod†. The twisted pairs must be as immobilized as possible in order to reduce the vibration noise. The bundle of twisted pairs for the piezo-steppers is intentionally passed through the core of the hollow stainless steel probe rod in order to minimize the influence of the relatively high stepper voltages (30 V-50 V) on the PCAR signal and on the temperature sensor‡. The PCAR signal and the temperature sensor wires are soldered to 7-pin push-pull connectors close to the sample space assembly. In this way, the sample space can be disconnected without affecting the wiring from the top of the rod. These intermediate connectors are placed on a brass baffle. The four standard aluminum baffles are used as guidance for the twisted pair bundles. There are small segments of rubber insulation tube between the bundles and the baffles in order to prevent direct contact. The latter would lead to destruction of the insulation of the twisted pair due to contraction/expansion of the assembly after multiple cool-down cycles. The main purpose of the aluminum baffles is reduction of the infrared radiation from the top of the rod to the bottom, because of that each baffle is rotated at an angle of 120° with respect to the other.

There are 4 twisted pairs in total for two temperature sensors. One Cernox sensor is presently in use and it is placed just below the sample holder. The sensor is calibrated in the range 2 K-300 K

*This is mainly important for measurements below 5 K. The "on-the-pot" option can be used in cases where the CLTC fails to cool down in general. Beware that this option has higher helium consumption.

†Beware that nail varnish must not touch the wires because it dissolves the insulation!

‡During the automatic landing procedure, the PCAR signal does pick-up small contribution from the stepper voltages.

and the calibration table is uploaded on the PPMS Model 6000 internal memory. The resistance measurement bridge on the PPMS is used for the temperature measurements. The sample holder is designed by the author and machined out of brass in the mechanical workshop in the School of Physics, Trinity College Dublin. The PCAR measurement procedure is usually based on two

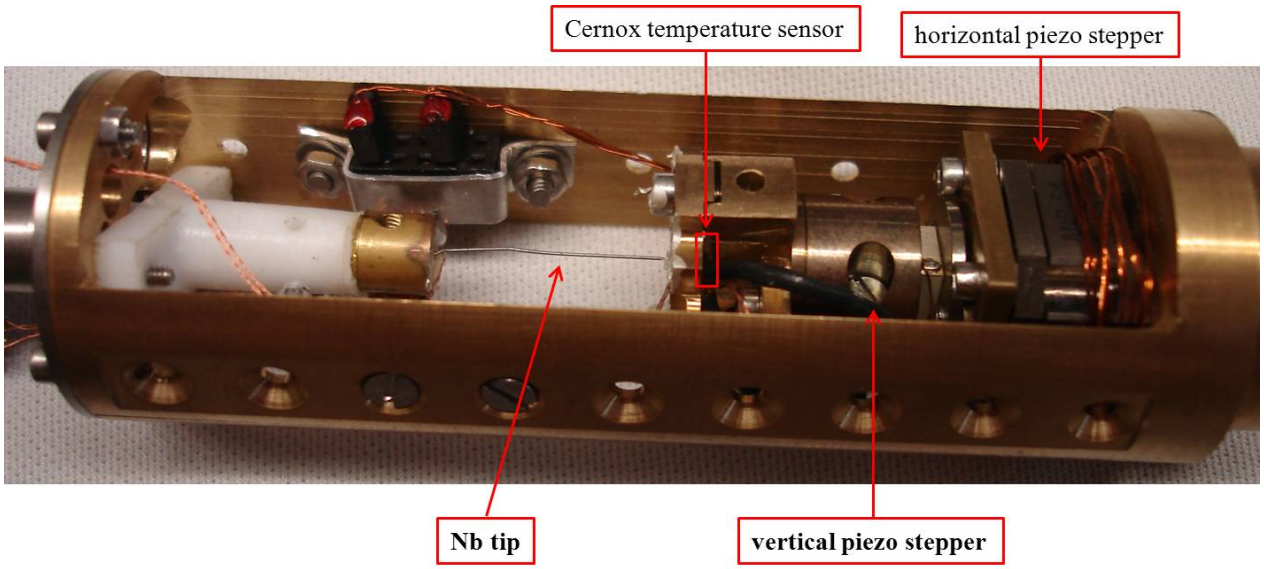

Figure 2.1: PCAR sample space for standard needle(Nb)-anvil(sample) measurement configuration. Some of the important components of the setup are indicated: Nb tip, vertical piezo-stepper, horizontal piezo-stepper, and the Cernox temperature sensor.

point differential conductance ($\mathrm{d}I/\mathrm{d}V$) measurement. The $\mathrm{d}I/\mathrm{d}V$ is obtained in an a.c. procedure instead of current-voltage measurement and its numerical differentiation. This preferred approach has better signal-to-noise ratio because of the narrow-band lock-in detection. An analog triangular voltage waveform is provided by a Thandar (TG102) function generator. The frequency of the triangular waveform is $\approx$ 0.5 Hz, therefore, the V_{min} to V_{max} trend takes $\approx$ 1 s and this is the duration of a single spectrum acquisition. The analog waveform is modulated with a sine wave from the internal oscillator of a Perkin Elmer 7265 lock-in amplifier (LIA). The a.c. signal frequency is conventionally 1.23 kHz. It is chosen high enough in order to avoid the $1/f$ noise from the amplifiers and low enough in order to have insignificant inductive pick-up in the sample leads. The triangular voltage waveform is divided with a simple two resistors divider with a ratio 1:100, while the a.c. sine wave is divided with a ratio 1:10000. The a.c. signal amplitude should always be kept at least an order of magnitude smaller than the quasi-d.c. bias in order not to distort the applied bias waveform. The output impedance of the divider is 10 Ω. Therefore, the current through the circuit is due to d.c. bias, v, and a small a.c. bias, $v = v_0 \sin(\omega t)$:

$$I(V+v) \approx I(V) + \frac{\mathrm{d}I}{\mathrm{d}V} v_0 \sin(\omega t). \tag{2.1}$$

The modulated waveform is fed into the contact and the current is passed to a current pre-amplifier SR570, where it is amplified with a bandpass filter (300 Hz - 3 kHz) with a filtering slope 6 dB/octave. The latter cuts off low frequency signals like thermal offsets and higher harmonics of the a.c. power supply. The amplified current is passed to the LIA, where it is recorded synchronously with a voltage reference form the TG102 generator *. The LIA is operated in a curve buffer mode. The transistor-to-transistor logic (TTL) signal of the TG102 is used as a trigger. Schematic of the electric circuit is shown on Fig. 2.3. Once a TTL signal is obtained from the TG102, data is collected in a predetermined array by the LIA: 200 points, with time separation of 5 ms and saving the signals - X, Y components on the input and the auxiliary voltage. Once the buffer is filled up, the data is transferred to the program where it is concatenated with the PPMS temperature, Cernox temperature and field values obtained from the PPMS controller program. The curve buffering acquisition is preferred because the LIA is not queried during data collection and this reduces the noise.

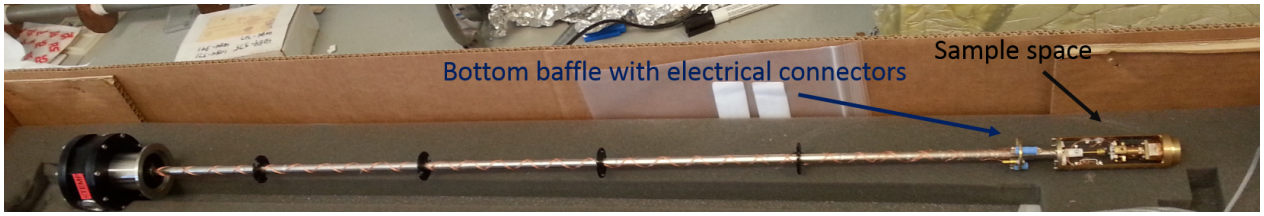

Figure 2.2: Picture of the wired electro-optical probe for PCAR measurements. The 7 pin connectors are visible on the bottom-most brass baffle just above the samples space.

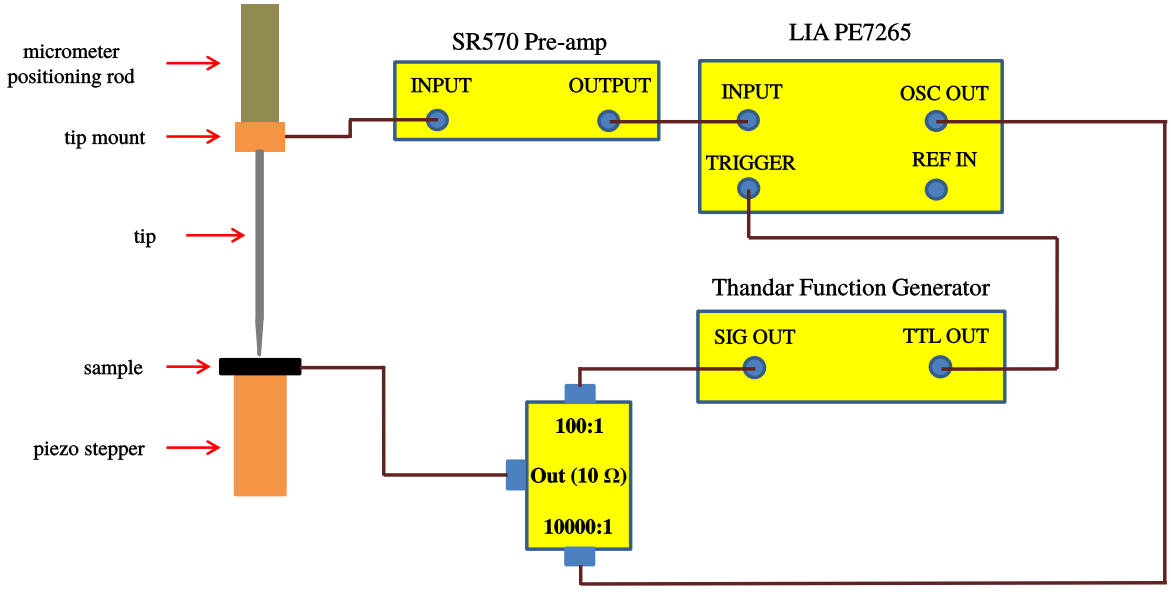

Figure 2.3: Schematic representation of the PCAR experimental setup and the electronic measurements circuit. Micrometer positioning rod is available in the old PCAR setup constructed by Dr. P. Stamenov for an Oxford cryostat.

*The TG102 reference signal is passed to one of the auxiliary channels at the back panel of the LIA

The outlined procedure above describes a single LIA acquisition only on the upward trend of the triangular waveform. This means that essentially 50 % of the measurement time is lost. A second, slave, LIA is introduced in order to reduce the dead time practically to zero. An HP 4284A waveform generator delays the TTL signal from the TG102, so that the slave LIA is triggered on the downward trend of the triangular waveform. In this way, the two LIAs measure concurrently on the upward and downward trend of the triangular waveform, respectively. The same acquisition routine is used for the slave LIA. The circuit is presented on Fig. (2.4).

The real time, raw, acquired data is consequently preprocessed. This allows contact drifts and reorientations to be avoided in the averaging. The signals from the two LIAs are averaged separately and then manually overlapped. There is a small impedance mismatch between the LIAs and this results in offset of the master and slave spectra along both the bias and the conduction axes. No matter how well the delay of the second LIA is adjusted, the applied bias range of the two LIAs never overlap perfectly. Therefore, a common bias window is determined for two LIAs and then the raw data is interpolated using this window before averaging.

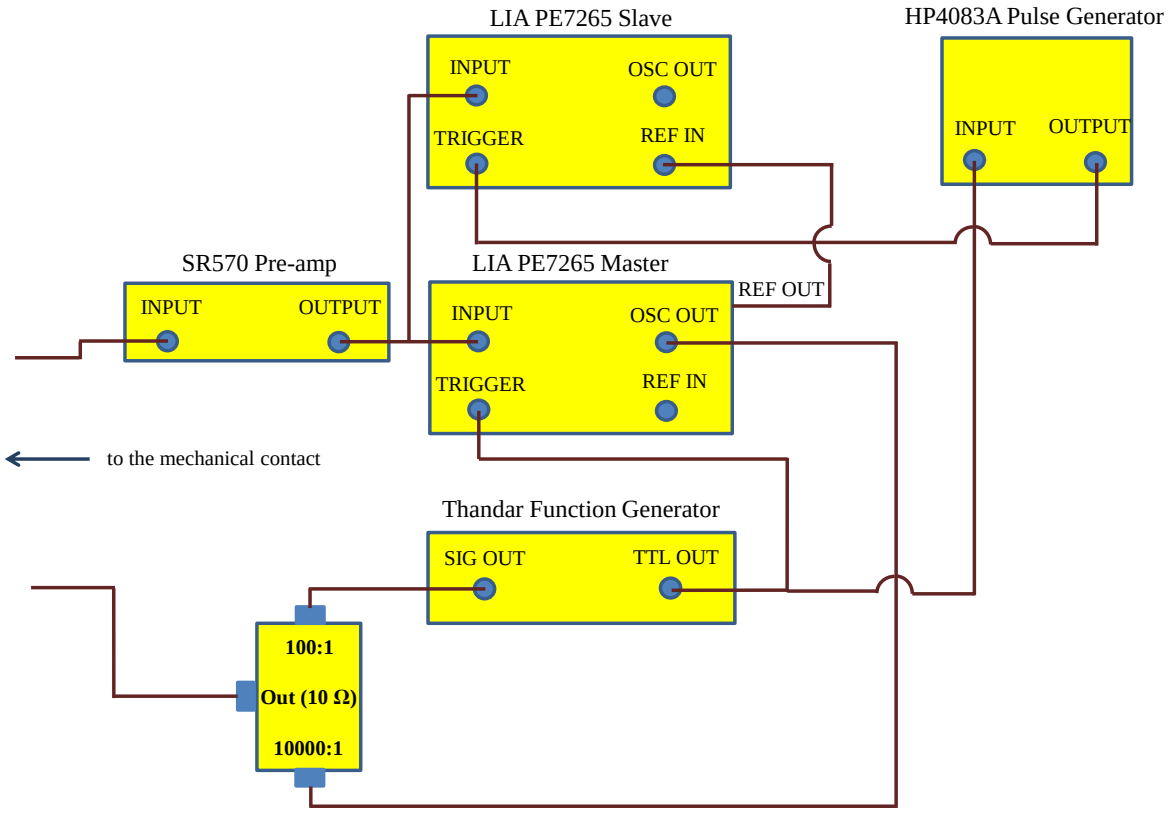

Figure 2.4: Schematic representation of the electronic circuit for the two LIA PCAR data acquistion.

The point contact between the tip and the investigated sample is achieved with a vertical piezo-stepper ANPz30. The landing procedure is fully automatic and it is terminated when a particular contact conductance threshold is achieved*. Two horizontal piezo-steppers ANPx51 are used as well in order to land on a pristine area of the sample. They can be used as well in order to make a two-dimensional investigation of the spin polarization or to scan through a feature†.

Some of the measurements with the MgB_2 superconductor are performed in setup configuration which is rotated to 90° with respect to the original one. In this case, the applied magnetic field is in plane of the superconducting thin film and an Fe tip lands on the MgB_2 (see Sec.(5.4)). Only the two horizontal piezo-steppers are used in this case: the top one is used to adjust the point contact between the MgB_2/CoFe while the bottom one is used in order to change the landing position on the MgB_2. The ferromagnetic (Fe) tip is soldered on a small brass platform which is insulated from the sample holder with a slotted teflon cylinder with 6 mm outer diameter and 3 mm inner diameter. The brass platform is glued with nail varnish to the teflon cylinder. The measurements on

Figure 2.5: Experimental setup for in-plane PCAR spectroscopy measurements. The MgB_2 superconducting film is mounted on an L-shaped holder. The Fe tip is insulated from the sample holder with a slotted Teflon cylinder. An auxiliary two wire connector is present just to the left of the L-shaped holder. This connector is used for providing the polling voltage for the investigation of the spin polarization strain dependence in ferroelectric/ferromagnetic bilayers.

the MgB_2-CoFe shadow-masked junctions are performed with the standard rotator option for the PPMS (see Sec.(5.5)). The sample with the junction is mounted on top of the rotational platform and, therefore, as the sample is rotated, the field direction changes from in-plane of the MgB_2 thin film to perpendicular to plane. The junctions are measured in two point configuration and the same measurement electronic configuration is used as for the conventional needle-anvil approach. The PPMS Labview controller for the junction measurements is modified and the angle‡ can be changed and is constantly recorded in the PCAR data files. The angle, θ, can be varied in the range $-5°$ to

*Usually set at 20 G_0.

†Such approach is used for the investigation of Sb $_2$Te$_3$ and $Bi_{0.36}Sb_{1.64}Te_3$ in Sec. (3.3). A very narrow strip of TI is left and the Nb tip is scanned through it.

‡And the rotation speed

365°. There is always small angular offset between the real orientation and the measured one due to backlash in the rotational mechanism* and imperfection in the mounting of the sample on the platform. From the measurements in Sec. (5.5), it is extracted that the maximum angular offset is always below 10°. The speed of rotation varies between $0.1\,^{\circ}\,s^{-1}$ and $1.0\,^{\circ}\,s^{-1}$. An intermediate speed of $\approx 0.4\,^{\circ}\,s^{-1}$ is chosen for the full angular dependencies. The smallest rotational speed is chosen for the fine angular scans around the field in-plane direction ($80° < \theta < 100°$ and $260° < \theta < 280°$). PCAR spectra are recorded on-the-fly, therefore, there is error in the angle of each PCAR scan of approximately $\Delta\theta \approx 0.4°$ in the full range angular scans†. No appreciable difference is observed between the scans obtained on-the-fly and scans performed at constant field. The outlined procedure can be easily extended, so that there is a wait of a few seconds at each angle value‡.

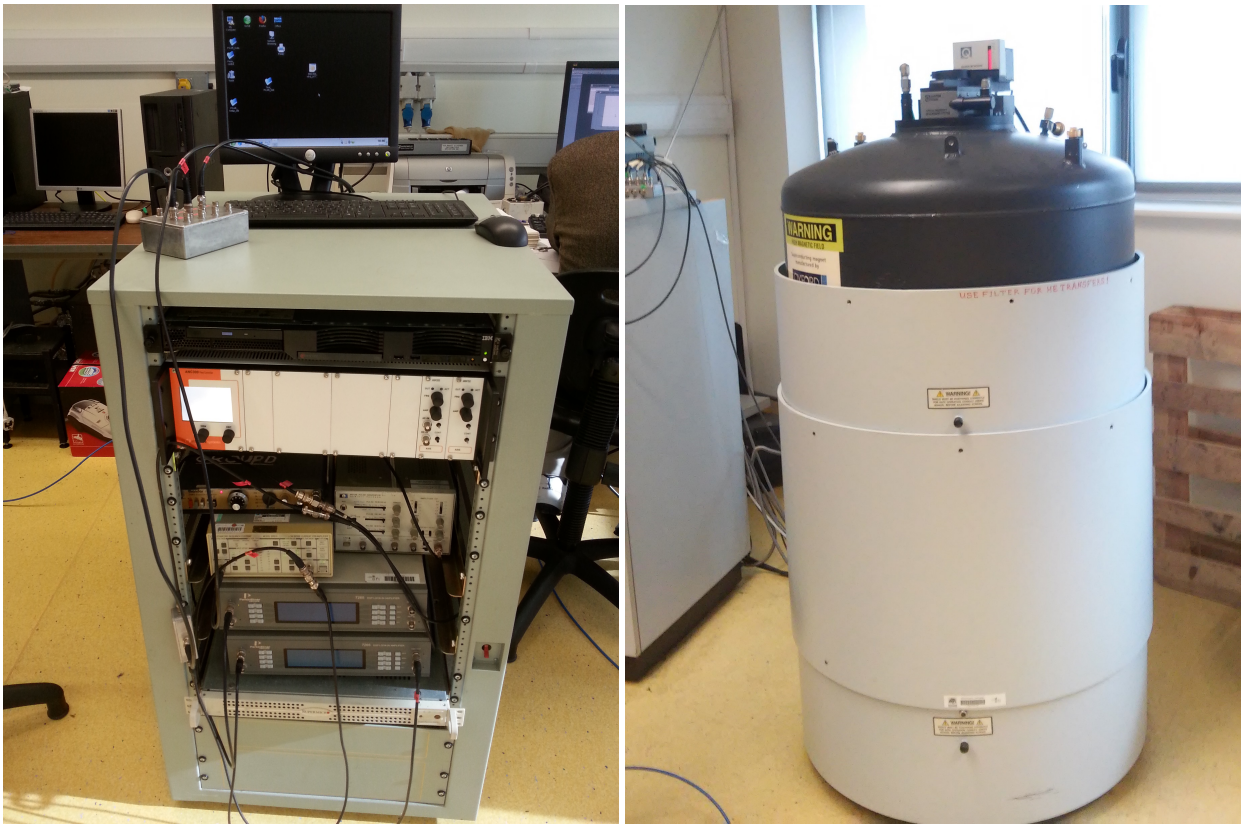

(a) Picture of the PCAR setup electronics rack.

(b) Picture of our group Physical Properties Measurement System.

Figure 2.6: Pictures of the PCAR electronics rack (a) and the Physical Properties Measurements System (b).

*The backlash is more pronounced for rotation with high speed because the mechanism is spring-loaded.

†Because the spectra are acquired at frequency of 1 Hz, the error in the angle is assumed to be equal to the rotational speed. Therefore, swift rotation should be avoided.

‡The latter will result in significantly bigger size of the data files and reduced data acquisition speed but it will improve the noise as multiple spectra will be averaged at each θ.

2.3 Differential spectroscopy

Differential spectroscopy (DS) is recorded on magnetic tunnel junctions with a layer of the highly spin polarized ferrimagnet Mn_2Ru_xGa in Sec. (6.4). DS provides valuable information about the density of states of the electrodes of the tunnel junctions as well information about the inelastic processes involved in the tunneling [*]. The measurement setup is similar to the PCAR setup outlined above. This time the bias range is ± 1 V and the voltage is supplied by a Keithley 2400. The d.c. bias step is $\Delta V = 1\,\mathrm{mV}$. The voltage modulation between the Keithley and the LIA is achieved in this case with differential amplifiers. As before, the current is preamplified by an SR570 and then recorded by the LIA. The modulation frequency is again 1.23 kHz and the modulation amplitude is $V_{\mathrm{rms}} = 3\,\mathrm{mV}$. The pre-amplifier is calibrated beforehand with a resistor similar to the resistance of the magnetic tunnel junctions[†].

Two other possible approaches for DS measurement are mentioned here. A small resistor can be connected in series with the investigated junctions [‡], then the voltage drop across this resistor is measured and the current through the circuit is determined in this way. The voltage should be amplified with voltage amplifiers. This measurement approach can be used when the current pre-amplifier is not available. It has a disadvantage due to Johnson noise on the additional resistor. Another approach is DS in current sourcing setup. In this case, the a.c. sine wave and the d.c. voltage are passed through resistors much bigger that the resistance of the investigated device[§]. The a.c. and d.c. current components are added together and are fed into the investigated device. This measurement scheme is particularly suitable for investigation of relatively low resistance devices ($R < 10\,\mathrm{k}\Omega$) because this is a natural configuration for four-wire measurement.

Monsma and Parkin have suggested a four-point voltage sourced $\mathrm{d}I/\mathrm{d}V(V)$ as the most accurate experimental approach in their spin polarized tunneling experiments[234]. A dc bias in range from -1.5 mV to 1.5 mV is modulated with a 10 µV sine waveform at frequency of 42.8 Hz and fed into the two input electrodes. The ac current through the circuit is measured with the sourcing lock-in. The ac/dc voltage drop on the junction is measured at two separate output electrode using a second lock-in, which is synchronized with the first one and a separate dc voltmeter. This methodology has the following advantages: the voltage over the junction is measured explicitly, so are the ac components $\mathrm{d}I$ and $\mathrm{d}V$. As mentioned by the authors, current sourcing leads to poor gap resolution because the sub-gap resistance is very high.

More sophisticated measurement approaches in resistance bridge configuration are used as well. They have significantly higher sensitivity with the disadvantage that measurements in bridge con-

[*] For instance, phonon or magnon scattering.

[†] The same amplification range is used both for the calibration and for the differential spectroscopy.

[‡] Small with respect to the resistance of the junctions

[§] Or better, the Keithley is directed set in current sourcing mode.

figuration are usually very time consuming and, furthermore, they are more prone to mechanical drifts. An extensive review of the differential spectroscopy methodology is given by Magno and Adler[209].

2.4 SQUID-based PCAR

Superconducting quantum interference devices (SQUID) are known as the most sensitive flux-to-voltage converters. SQUIDs have been used since their invention as very sensitive current pre-amplifiers. The SQUID pre-amplfier is especially useful when the impedance of the device is very low. For instance, the initial studies on CPP-GMR structures are carried out on high-area stacks with a SQUID pre-amplifier[272]. SQUID pre-amplifier is utilized here for measurements of low-resistance, high-area, Andreev contacts. The first configuration for which data is recorded is as follows: the PCAR is performed in one cryostat while the SQUID pre-amplifier is in a separate cryostat. The current is brought from low temperature to high temperature and then again to low temperature for the amplification at the SQUID washer. The measurements are performed between Nb and bulk polished Fe piece.

The obvious disadvantage of the above experimental configuration is that there is Johnson noise on the current leads which go from 4 K to 300 K. In order to circumvent this problem, an old Oxford instruments cryostat is repurposed. A different top plate is designed by the author and machined out of stainless steel in the School of Physics mechanical workshop. In this configuration, the SQUID washer is brought close to the probe and the connections between the sample and the SQUID are made with mono-filament superconducting Nb-Ti wire. The SQUID is positioned approximately 10 cm above the superconducting magnet in order to reduce the effect of the stray field on the Nb shield. This experiment is constructed as a dipper probe, *i.e.* there is no variable temperature insert and the temperature of the whole helium bath, which include the PCAR probe, the SQUID chip, and the magnet, can be changed only by the pressure. The maximum attainable field with this magnet is 7 T.

An example of PCAR measurements of bulk Fe with superconducting Nb tip are given in Fig. (2.7). The contact is large area and the conductance is high: $G_{\mathrm{n}} = 332.0(5)G_0$. The extracted spin polarization of $45(2)$ % is in accordance with literature data on Fe. The field scan in the range ± 1 T demonstrates the shrinking of the superconducting gap.

(a) Old SQUID setup with the pre-amplifier in a separate dewar.

(b) New SQUID setup with the PCAR probe and the SQUID chip in the same dewar.

Figure 2.7: Pictures of the SQUID pre-amplifier setup: old (a) and new (b).

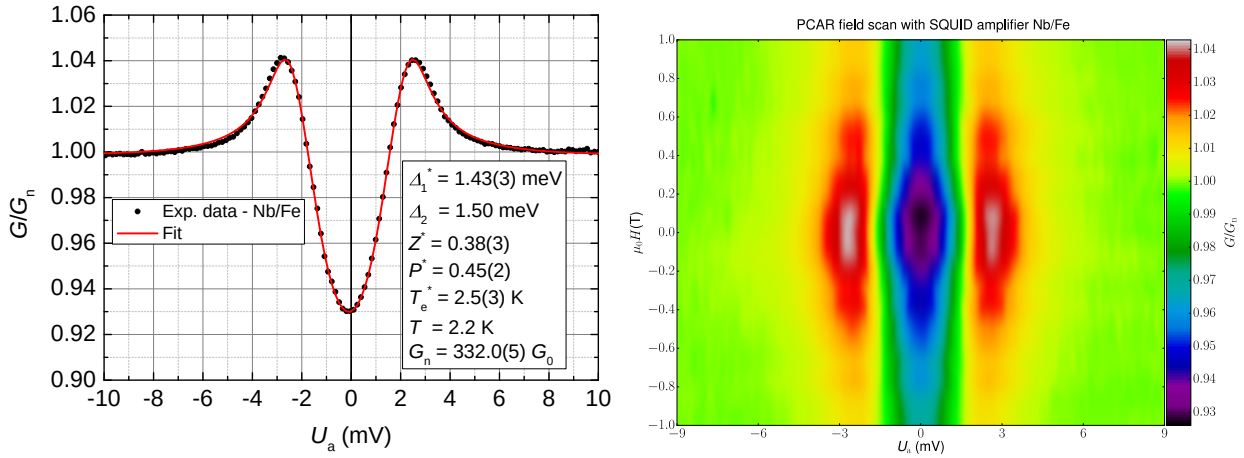

(a) PCAR measurements of Nb/Fe with a SQUID pre-amplifier.

(b) Field scan of an Nb/Fe PCAR with a SQUID pre-amplifier. Temperature is 2.2 K.

Figure 2.8: Example of PCAR measurements with SQUID pre-amplifier: single PCAR (a) and PCAR magnetic field scan(b).

2.5 Change of the spin polarization by induced strain in ferromagnetic layers

Another experimental extension of the PCAR methodology which has been attempted over the course of this work is the investigation of the spin polarization dependence on the strain of ferromagnetic layers. The effect is sought after in bilayers of ferroelectric-ferromagnetic materials (AlN/CoFe) and piezoelectric- ferromagnetic materials ($BaTiO_3$/$La_{0.7}Sr_{0.3}MnO_3$). In this experimental configuration, there is a pair of leads which provide the polling voltage for the ferro-(piezo-)electric layers. The negative polarity is given to the ferromagnetic layer and the positive polarity is set to the back gate. High biases of up to 220 V are used for polling thick piezo-(ferro-)electric layers and the negative polarity is at the same potential with the lead for the current pre-amplifier. Otherwise, the current pre-amplifier overflows in d.c. biases $\geqslant$ 1 V. An additional precaution is taken by placing two arresting diodes in front of the pre-amplifier input and this prevents the blow up of the the JFET amplifiers by a possible discharge of the piezo-(ferro-)electric layers. The result of these experiments are inconclusive and only a single PCAR example of the effect of strain on the spin polarization of CoFe is given here (see Fig. (2.9) (b)). There is little decrease in the zero-bias conductance when the applied bias is 200 V which correspond to electric field of $E = 0.4\,\mathrm{V\,\mu m^{-1}}$. The latter is an indication that the spin polarization increases slightly. The extracted change within the mBTK model in the spin polarization is rather low $\approx 0.8\,\%$. Future research effort are needed toward measuring PCAR on lithographically patterned structures in order to reduce the detrimental effect of the multidomain states in both the ferromagnetic and the piezo-(ferro-)electric layers.

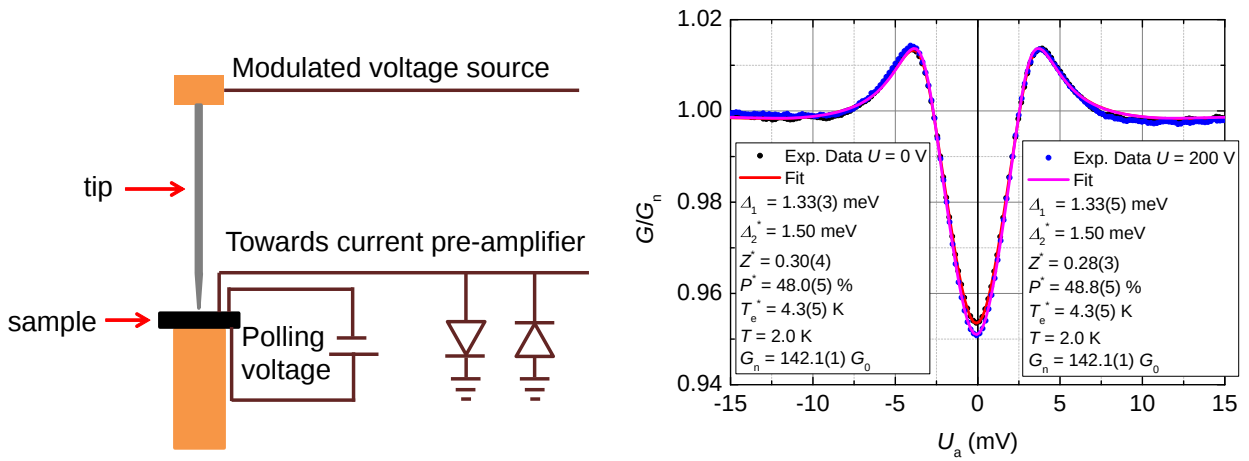

(a) Wiring configuration for PCAR biasing setup.

(b) Example of two PCAR measurements on AlN/CoFe bilayers in applied bias of 0 V and 200 V.

Figure 2.9: Example of spin polarization dependence on the applied electric field in AlN/CoFe bilayer.

2.6 Organic deposition chamber and argon ion milling

A home-built thermal evaporation ultrahigh vacuum chamber is used for the deposition of the MgB_2-CoFe shadow-masked junctions investigated in Sec (5). The base pressure is $< 5 \times 10^{-9}$ mbar and the maximum current is 300 A*. The chamber is constructed with the main aim for preparation of magnetic tunnel junctions with organic barrier. The system chamber consists of main deposition chamber and a load lock which are separated with a gate vale. The main chamber has a low angle argon plasma gun and the sample can be pre-cleaned before additional layers are deposited. The main chamber is pumped with a Pffeifer™turbomolecular pump, which is backed by an Agilent™scroll pump, and there is a Perkin Elmer™ion pump for achieving the low base pressure. Quartz crystal monitor is used for determination of the thickness of the layers. SiO is thermally evaporated when insulation is needed between the devices on the chip. The sample stage can be heated up to 200 °C or cooled down to −196 °C (with liquid nitrogen) when it is required.

(a) Inside view of the organic deposition chamber. (b) Outside view of the organic deposition chamber.

Figure 2.10: Pictures of the organic deposition chamber. (a) - inside view of the sample stage rotational mechanism. The argon gun is switched on for illumination. (b) - overview picture of the chamber.

The Millatron is an Ar ion milling machine with base pressure $\leqslant 10^{-6}$ mbar which can be used for variable purposes: cleaning of thick oxide layers, patterning of Hall bars and magnetic tunnel junctions. It has plasma gun which is usually operated at a power of 300 W-400 W and there are four adjustable knobs for tuning of the impedance of the gun. The sample stage holder is water-cooled and rotatable in both angular directions. The ϕ direction rotation assures that the features are uniformly milled while the θ direction adjustment provides opportunity for low-angle milling which cleans the redeposited material on the side walls of multi-layer stacks. The side-wall cleaning is of critical importance in patterning of magnetic tunnel junctions because redeposited material electrically shorts the device otherwise. There is a secondary ion mass spectrometer (SIMS) detector which is located on top of the chamber. The latter is used for real time detection of the layer

*This is limited presently by the melting temperature of the insulation of the high current leads and not by the capabilities of the power supply.

which is milled*. The deflecting voltages on the plates in the SIMS have to be adjusted depending on the angle of milling. The SIMS relies on quadrupole mass spectrometer (QMS) for detection. Different ac and dc electric fields are set in order to adjust for particular charge/mass ratio. The selected ions impinge on a multiplier tube and secondary ion cascade is created which is then detected†. If more than one element is scanned overall by the SIMS, the QMS is tuned to a single ion at a time and multiple ions scans suffer from worse time resolution. It is advisable to limit the number of traced elements to 4-6 otherwise the procedure is too slow.

2.7 Wire bonder

The wire bonder used is Kulicke and Soffa Ltd. model 4700. The wire bonder is an industrial widely used machine for interconnects between integrated circuits and chip carriers. The wire bonding is in essence a process in which a thin wire is locally attached by ultrasound frequency vibration on top of the bond pads of the device. Wire bonding is done in either wedge bonding or ball bonding method‡. All magnetic tunnel junctions (MTJs) are wedge bonded due to concern over the electrical current which flows during the ball formation in the ball bonding method. All MTJs are bonded with gold wire on gold bond-pads. Before bonding the MTJs, the surface of the chip is bonded to ground; also the chip carrier contacts are shorted between each other and one is connected to ground. These precautions are taken in order to reduce the chance for an dielectric breakdown of the insulating barrier during the bonding procedure. The force, time and power are the main parameters which determine the bonding process. The tail and loop determine how much wire is left after a bond is made and how high the wedge is retracted after the first bond. Heating of the sample stage facilitates the adhesion process, however, no heating is applied in the wire bonding of the MTJs due to a ground loop concern. A short manual on the wire bonding is provided in Appendix. The bonding parameters depend on the geometry of the wedge as well as the adhesion of the bond pads, therefore, there are no magical parameters which work on any machine and any device. An important note is that the bonding is heavily affected by contamination of the wedge, the wire and the chip§.

*The SIMS and the main chamber are pumped separately and, hence, the SIMS may not be pumped and used for simpler processes like patterning of Hall bars.

†The absolute amplitude of the signal can be adjusted accordingly in order to extend the life-time of the detector.

‡Ball bonding is the preferred method in the industry.

§The wire must never be touched with hands due to carbon contamination reasons, the chip should be sonicated in isopropanol for 2 minutes before bonding, and the wedge should be cleaned often as well.

Figure 2.11: Picture of the wire bonder used for bonding of the Mn_2Ru_xGa-based magnetic tunnel junctions.

2.8 Magnetometry

Only DC magnetometry measurements are performed during this work. The used experimental tools are the Vibrating Sample Magnetometer (VSM) in the PPMS or SQUID magnetometer in a Magnetic Properties Measurements System (MPMS). Both setups are conceptually similar although the detection scheme and, ultimately, the sensitivity are greatly different. An investigated sample is vibrated and thus following the Lenz' law an electromotive voltage is induced in the pick-up coils due to the variable magnetic flux. The induced voltage is detected synchronously at the frequency of the oscillator drive of the sample. The induced voltage is amplified by JFET transistors in the VSM, whereas it is fed to a SQUID detector in the SQUID magnetometry. The SQUID detection is much more sensitive mainly due to the superior flux-to-voltage characteristics of a SQUID (see Appendix E). Another difference is that the pick-up coils of the VSM are made of normal metal whereas the SQUID pick-up coils are superconducting. The latter contributes to the superior SQUID sensitivity*. Another difference between the measurement tools is the gradiometer configuration of the pick-up coils. There are inevitable magnetic field gradients within the sample area and a single pick-up coil would detect not only the magnetic moment of the sample. In order to prevent that, the pick-up coils are constructed in a gradiometer configuration. A first-order gradiometer is essentially two coils which has induced voltage with opposite polarities. In this way, it can be shown that the configuration detects only odd derivatives $\mathrm{d}B^n/\mathrm{d}z^n$. The contribution from the external field is canceled is canceled and the lowest derivative which contributes to the signal is $\mathrm{d}B^1/\mathrm{d}z^2$. First order gradiometer is used in the VSM setup. Second-order gradiometer is in essence

*The superconducting coils might trap magnetic flux and there are separate heaters for quenching of the coils.

a configuration of three coils. This configuration detects only even derivatives, the first derivative is canceled and the lowest derivative detected is d^2B/dz^2. Second-order gradiometer is used in the SQUID magnetometry. The sensitivity of the VSM is 10^{-9} A m^2, whereas the sensitivity of the SQUID magnetometry is two orders of magnitude better-10^{-11} A m^2*.

The oven options of the VSM and the SQUID have been used as well for Curie temperature determination of novel materials - Mn_2Fe_xGa and Ne^+ ions irradiated $Fe_{60}Al_{40}$. The two setups have different approach towards the high temperature measurement. The VSM relies on a ceramic platform with an integrated meander heater and a temperature sensor. The sample is placed on top of the heater either with a high-temperature cement paste or wrapped around with copper foil. The VSM oven option is under high vacuum conditions provided by the PPMS cryopump so that the power from the heater does not overheat the whole chamber. On the other hand, the SQUID magnetometry oven is essentially "dewar in dewar". The oven itself has a thin insulating annulus ($\approx$ 1 mm) and the oven is inserted into the standard SQUID sample space. The central tube of the SQUID oven is with diameter 4 mm. In this case, the whole oven sample space is heated unlike the VSM local heat-up by the meander heater. The SQUID oven sample rod ends far above the pick-up coil, therefore, a sample mounting approach is needed. Sealing a sample in a thin wall quartz tube is perhaps the best approach for bulk samples. The thin film mounting procedure used in this work is to wrap the sample in long and narrow stripe of aluminum foil ($l \approx$ 22 cm and $w \approx$ 1.2 cm) and attach the sample to the bottom of the rod with a bare copper wire. The aluminum is a very good choice because it has low paramagnetic susceptibility which is essentially temperature independent. A disadvantage of the Al is that it has low melting point, and, therefore, the temperature measurement range should be limited to $T < 800$ K. The sensitivity of the VSM and SQUID magnetometry is an order of magnitude lower in the oven setup than in the standard configuration due to the added background from other elements in the sample area. A short summary of the SQUID oven mounting procedure is given in Appendix D. It is possible to mount thin films in direction perpendicular to the plane but significant effort must be taken in mounting the sample in this direction and the sample has to be very small†. An example is given here of a Curie temperature measurement of Mn_2Fe_xGa, a composition with perpendicular magnetic anisotropy.

*It can reach 3×10^{-12} A m^2 in AC magnetometry.

†Since the oven has a bore of 4 mm, the sample size has to be at most 2 mm $\times$ 2 mm when it has to measured in the field perpendicular to plane direction.

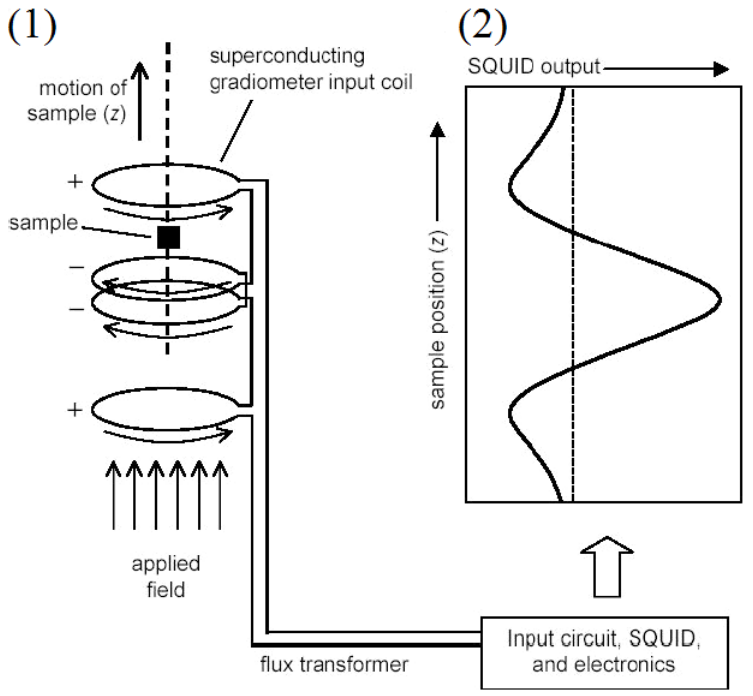

Figure 2.12: (1) - schematic representation of the second-order superconducting gradiometer pick-up coils configuration in a SQUID magnetometer. (2) - representation of the measured signal as a function of distance. The graph is after Black and Wellstood [29].

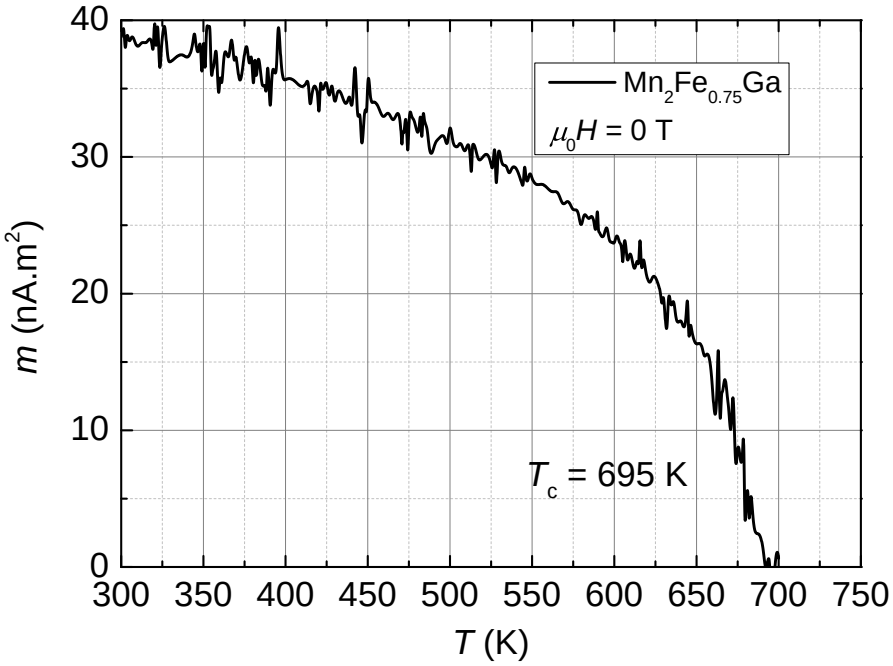

Figure 2.13: SQUID oven measurement of a $Mn_2Fe_{0.75}Ga$ thin film with perpendicular magnetic anisotropy. The extracted Curie temperature is 695 K and the scan is done in the remanent magnetic state.

Chapter 3

Spin polarization of topological insulators

"No experiment is so dumb, that it should not be tried."

Walther Gerlach

3.1 Introduction to topological insulators

Topological insulators (TIs) are a novel kind of quantum materials and artificial structures. They are characterized by bulk bandgap and gapless conductive surface states with correlation between the direction of the momentum and the spin directions. There are two types of TIs: two-dimensional (2D) and three-dimensional (3D). The observation of topological insulation in 2D is known as Quantum Spin Hall (QSH) effect. The quantum Hall effect (QHE) is the first fundamental physical observation which demonstrates the importance of topology on the transport properties. The integer quantum Hall (IQH) effect was theoretically predicted by Ando[7] and realized by von Klitzing[175] in a silicon-based metal-oxide-semiconductor field-effect-transistor (MOSFET). A two dimension electron gas (2DEG) is created in the invertion layer of a MOSFET and when the Hall effect is investigated in high magnetic field, the Hall conductivity, σ_{xy}, is quantized:

$$\sigma_{xy} = \nu \frac{e^2}{h}, \quad \nu = 1, 2, \ldots, \tag{3.1}$$

where e^2/h is the quantum of conductance. There are plateaus in the $\sigma_{xy}(B)$ scan which occur at fields $B = (n/\nu)\Phi_0$, where n is the electron density and $\Phi_0 = h/(2e)$ is the magnetic flux quantum. The longitudinal conductance σ_{xx} is zero everywhere apart from the fields at which a step in σ_{xy} occurs where a sharp spike is observed. The quantization happens due to fill up of the Landau levels (LLs). When electrons are subjected to magnetic field and restricted in 2D, their energy is quantized: $E_\nu = (\nu + \frac{1}{2})\hbar\omega_c$, where $\omega_c = eB/m$ is the cyclotron angular frequency.

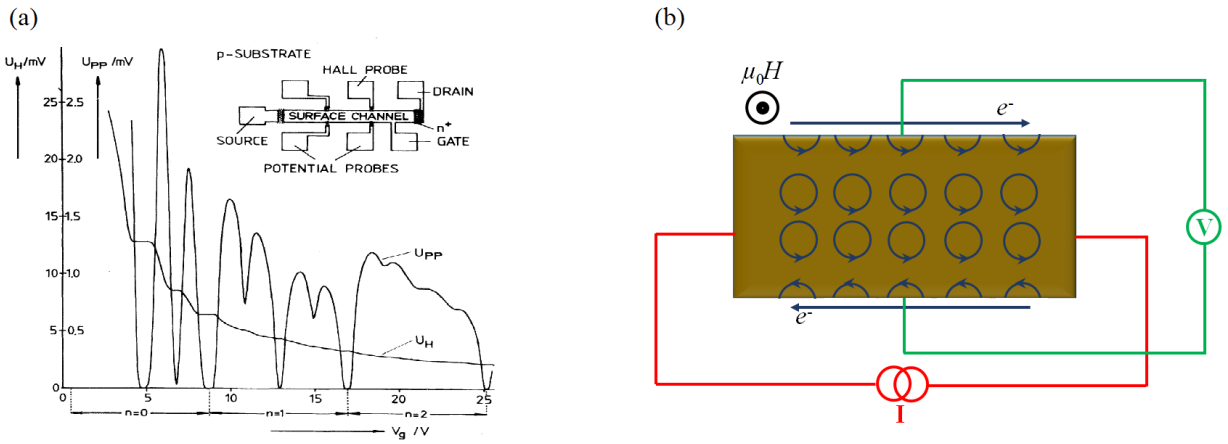

Figure 3.1: Panel (a): Example of the first demonstration of quantum Hall effect in Si-MOSFET. The graph is after von Klitzing[175]. Panel (b): Schematic representation of the locked electrons orbits and the edge transport in a quantum Hall effect. The magnetic field is applied outside of the plane.

When exactly ν LLs are filled, there is an energy gap and this explains the zero σ_{xx}. The electrons are locked in circular orbits in the middle of the Hall bar. However, there are skipping orbits at the edge of the Hall bar because the circular motion is terminated at end of the sample. The electrons bounce back and, therefore, there is linear motion of the electrons along the edges of the Hall bar. The chirality of the electron flow depends on the direction of the magnetic field. For the field direction on Fig. 3.1 (b), electrons move along $\vec{x}$ of the top edge and along $-\vec{x}$ on the bottom edge. The σ_{xy} can be determined if the expectation value of the current is computed in a quantum mechanical sense[194].

On the other hand, the QSH in 2D TIs can be considered as dual versions of the QHE. Two edge states propagate in opposite direction and the spin and momentum directions are correlated. The latter is known as helical edge states. The spin-momentum locking means that backscattering is forbidden because an electron must flip its spin in order to reverse its proparagation direction*.

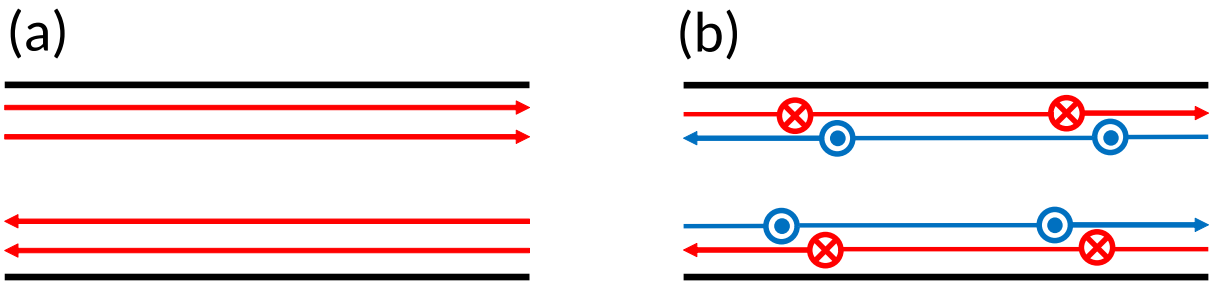

Figure 3.2: Comparison between the edge states in Quantum Hall effect for fill factor $\nu = 2$ (a) and Quantum Spin Hall effect (b).

Historically, 2D TIs have been realized first in semiconducting quantum wells (QWs) with

*This requirement can be lifted by perturbations which break the time-reversal symmetry: inelastic scattering and magnetic impurities, for instance.

inverted band structure. Kane and Mele[157] and Bernevig and Zhang[26] have theoretically proposed realization of QSH in graphene and in semiconductors with strain gradients. However, it is the later prediction by Bernevig *et al.*[25] about inverted type-III HgTe/CdTe QWs that is realized experimentally. The band ordering of HgTe is inverted with respect to the (Hg,Cd)Te compound. When a QW is formed in a $Hg_{0.32}Cd_{0.68}Te/HgTe/Hg_{0.32}Cd_{0.68}Te$ sandwich structure, the quantum confinement depends critically on the QW thickness. For narrow QW with $d < 6.3\,\text{nm}$, the band ordering is normal and the structure has positive energy gap. For wider QWs with $d > 6.3\,\text{nm}$, the hole band becomes the conduction band and this band structure is referred to as inverted. A conductance of $2e^2/h$ has been achieved by electrical gating and tuning of the Fermi level, E_F, in the bulk bandgap (see König[179]). The latter corresponds to one pair of edge states. This is presented on Fig. 3.3 (a). For regular band structure (sample I), quantum regime is not reached and the sample becomes just insulating when the Fermi level is in the bandgap. For inverted band structure, QSH state is achieved; however, the exact quantization is maintained only when the size of the Hall bars is comparable with the inelastic scattering mean-free path $l_{in} \approx 1\,\mu\text{m}$. Different possible reasons for the instability of the QSH are discussed by Schmidt[293], Maciejko[207], and Ström[322] and among them are thermal fluctuations, charge pockets and crystallographic disorder.

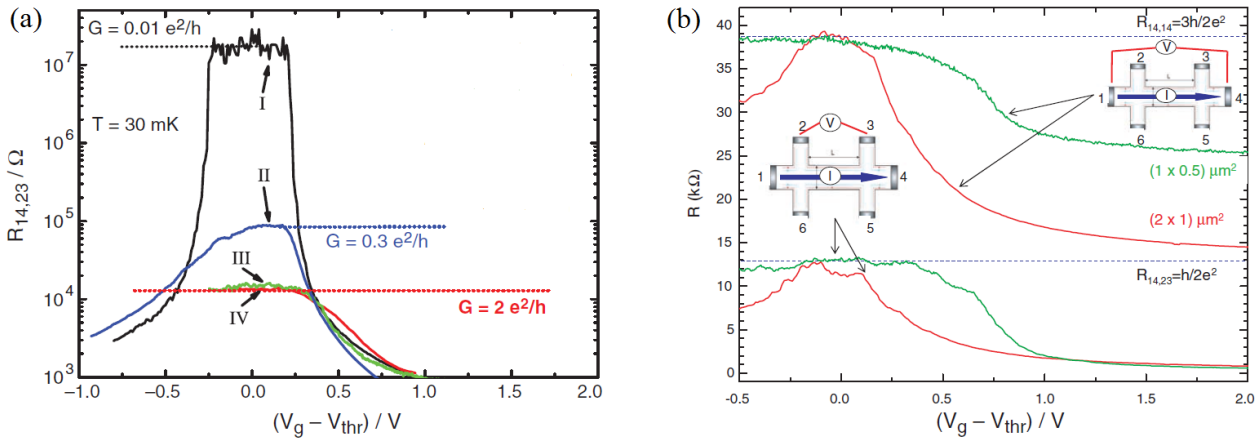

Figure 3.3: Panel (a)-demonstration of the Hall effect quantization once the Fermi level is tuned in the bulk bandgap (gate voltage = threshold voltage). Sample I-normal QW band structure → no quantization ($d = 5.5\,\text{nm}$), samples II, III, and IV are samples with inverted band structure ($d = 7.3\,\text{nm}$). The size of the devices is $(20 \times 13.2)\,\mu\text{m}^2$ for I and II, $(1.0 \times 1.0)\,\mu\text{m}^2$ for III, and $(1.0 \times 0.5)\,\mu\text{m}^2$ for IV. The graph is after König[179]. Panel (b)-demonstration of the edge channel conductance additivity depending on the number of edges. The graph is after Roth[280].

The helical nature of the edge states has been proven by nonlocal transport[280] and the demonstration of the edge nature of the transport is presented on Fig. 3.3 (b). If the voltage probe is connected between contacts 2-3, the voltage is detected along a single edge and the resistance reaches a single half quantum of resistance. On the other hand, if the voltage probe is connected between contact 1-4, then there are three edges involved and, hence, the measured resistance is $3h/(2e^2)$.

Therefore, in a general case, the resistance is:

$$R_n = n\frac{h}{2e^2}, \tag{3.2}$$

where n is the number of independent edges along the path between the two voltage probes. The spin polarization of the edge states is demonstrated by inverse spin Hall effect on H-bar geometry[43]. Similar demonstration of 2D topological insulating nature is made on inverted InAs/GaSb QWs[327, 81].

3.2 Three-dimensional topological insulators

Shortly after the discovery of the 2D topological insulators, theoretical predictions are made for realization of 3D TIs by Fu[102], Moore[241], and Roy[282]. In the case of 3D TIs, the cross-over from topologically trivial (bulk insulator) to topologically non-trivial surface states depends on the surface band-bending and the spin-orbit interaction in these materials. A topological phase transition study has been performed on $BiTl(S_{1-\delta}Se_{\delta})_2$[391] and a 3D topological insulator is predicted in $Bi_{1-x}Sb_x$[100] and demonstrated by ARPES[144]. Five distinct surface state bands cross the Fermi level in this composition and the existence of multiple bands at E_F complicates the investigation of the DOS structure and the analysis of electrical transport. Next generation 3D TIs were experimentally realized shortly afterwards in Bi_2Te_3[143], Sb_2Te_3, and Bi_2Se_3[388] where the advantage of the second generation TIs is the existence of larger bulk bandgap of up to 300 meV (for Bi_2Se_3) and simpler DOS structure of the surface states.

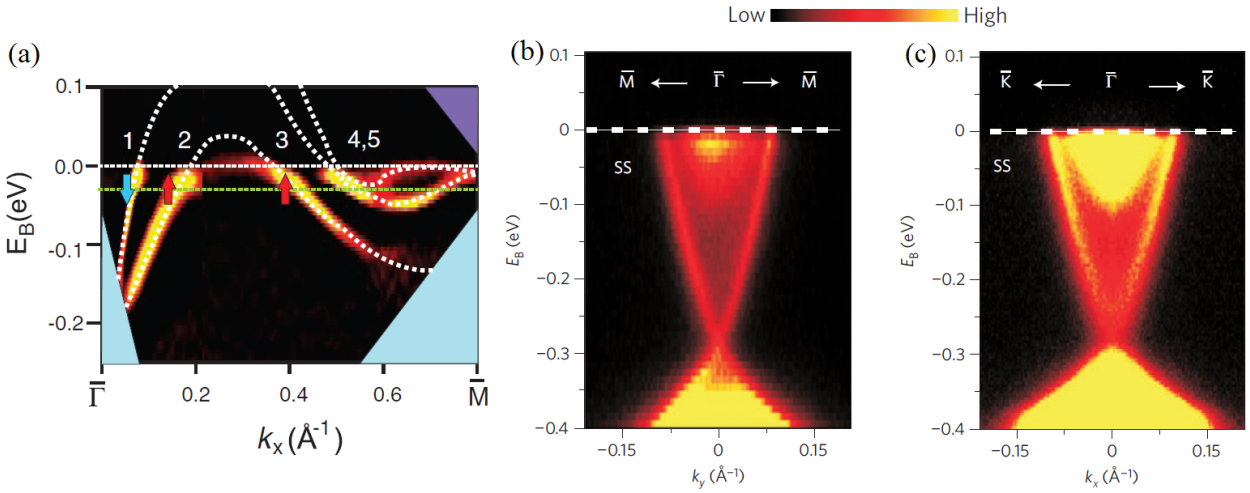

Figure 3.4: Panel (a)-ARPES study of $Bi_{0.91}Sb_{0.09}$ along the $\overline{\Gamma}$-$\overline{M}$ direction. Five bands cross E_F. The graph is after Hsieh[144]. Panel (b) and (c)-ARPES study of Bi_2Se_3(111) along $\overline{\Gamma}$-$\overline{M}$ and $\overline{\Gamma}$-$\overline{K}$, respectively. Single Dirac cone is present. These graphs are after Xia[388].

In this second generation 3D TIs, there is a well-defined single Dirac cone of the surface states and the Dirac point is buried in the bulk-valence band in the cases of Bi_2Se_3 and Bi_2Te_3, while the Fermi level is in the bulk conduction band. Therefore, these compositions demonstrate degenerate semiconducting behaviour. The placement of the Dirac cone within the bulk bandgap with the Fermi level above is very beneficial for ARPES studies of the surface states, however, not for electrical transport. The Bi_2Se_3 Fermi level can be tuned by Ca addition where the substitution of Bi^{3+} with Ca^{2+} is essentially hole doping. For instance, $Bi_{1.9975}Ca_{0.0025}Se_3$ has Fermi level tuned at the Dirac point, alias in very close proximity to the bulk valence band as well (see Fig. (2) (d) and (j) from Hsieh *et al.*[143]). In most experimental situations, the bulk insulation state is achieved with electrical gating.

These 3D TI compositions (Bi_2Se_3, Bi_2Te_3, Sb_2Te_3) have a tetradymite structure with covalently bonded quintuple layers (QLs) where the QLs are separated by weak van der Walls gaps. Because of that, many of the ARPES and STM/STS studies on the TIs have been performed on cleaved flakes from bulk crystals. The procedure results in atomically sharp surfaces terminated by chalcogen atoms because the nature of the bonding makes the (111) orientation the natural cleavage plane. High-quality TI films are prepared as well by molecular beam epitaxy on heat-treated substrates in order to reduce crystallographic defects which have detrimental effects on the band structure.

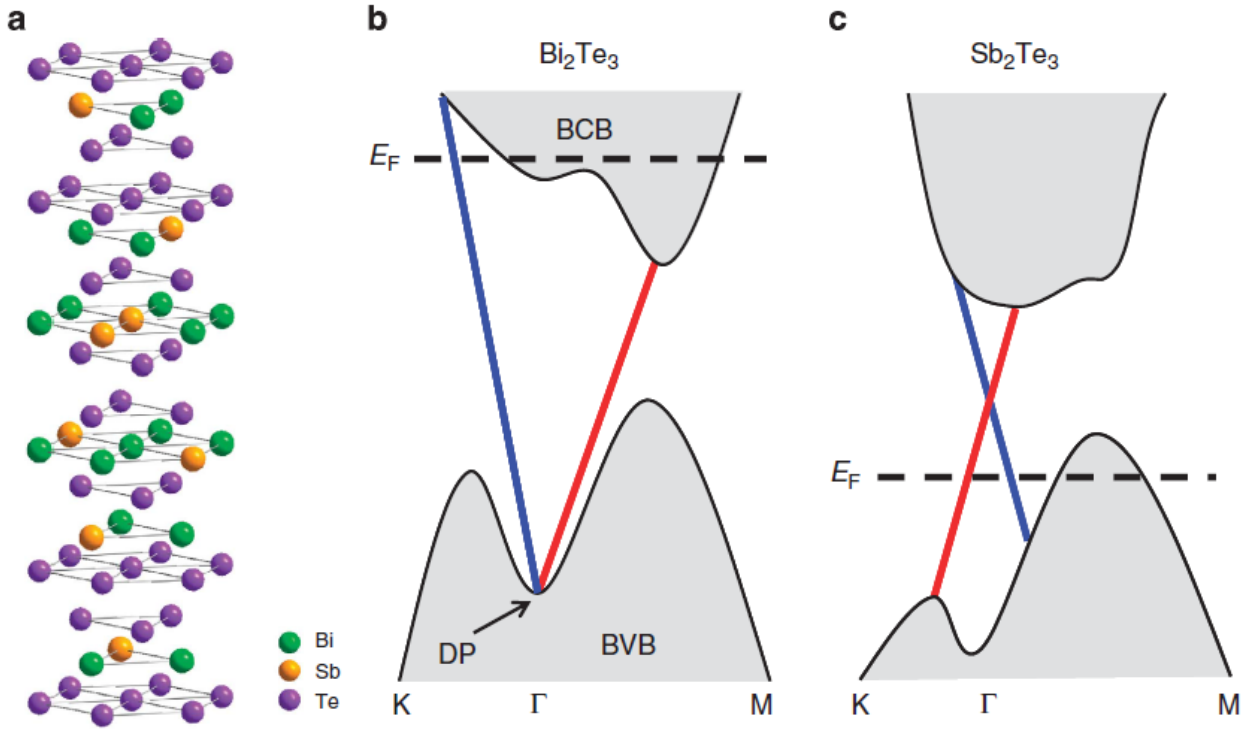

Figure 3.5: Panel (a)-tetradymite crystal structure of $(Bi_{1-x}Sb_x)_2Te_3$. Panel (b)-schematic representation of the band structure of Bi_2Te_3. Panel (c)-schematic representation of the band structure of Sb_2Te_3. The graph is after Zhang *et al.* [408].

One of the biggest issues in the field of TIs is the uncompensated bulk conductivity and the topologically protected spin-polarized surface states coexist with the bulk states, therefore, the contribution from the surface states is lower than it would be in ideal topological insulators. A significant progress in this respect has been achieved in the work of Zhang *et al.*[408] on the family $(Bi_{1-x}Sb_x)_2Te_3$*. The two end compositions, Bi_2Te_3 and Sb_2Te_3, are electron and hole conductors, respectively, and the Fermi level is positioned near the bulk conduction and valence band edges, accordingly. There is bulk band gap, however, the Fermi level is not positioned in it, therefore, these compositions are degenerate semiconductors, but total compensation of the bulk states can be achieved with a suitable tuning of the Bi:Sb ratio. For $x \approx 0.9$, the Fermi level is positioned in the center of the band gap and the resistance increases on cool down, as expected for a semiconductor. The low temperature resistance reaches half the value of the resistance quantum, $R_0 = 25.8\,\mathrm{k\Omega}$, indicating that the transport is two-dimensional and is, therefore, dominated by the surface states. This isovalent, isostructural TI composition family resembles the famous semiconducting composition $Al_xGa_{1-x}As$ which has been utilized in epitaxial, low strain, multilayer quantum well structures. Two important characteristics, $R_{xx}(T)$ and the density of states around the Fermi level for the $(Bi_{1-x}Sb_x)_2Te_3$ family, are presented in Fig. 3.6 and Fig. 3.7, respectively. As $x \to 1$, the composition becomes progressively more insulating but for $x > 0.94$ the carriers are holes. The ARPES measurements demonstrate that the Dirac point is shifted from the bulk valence band towards the bulk conduction band.

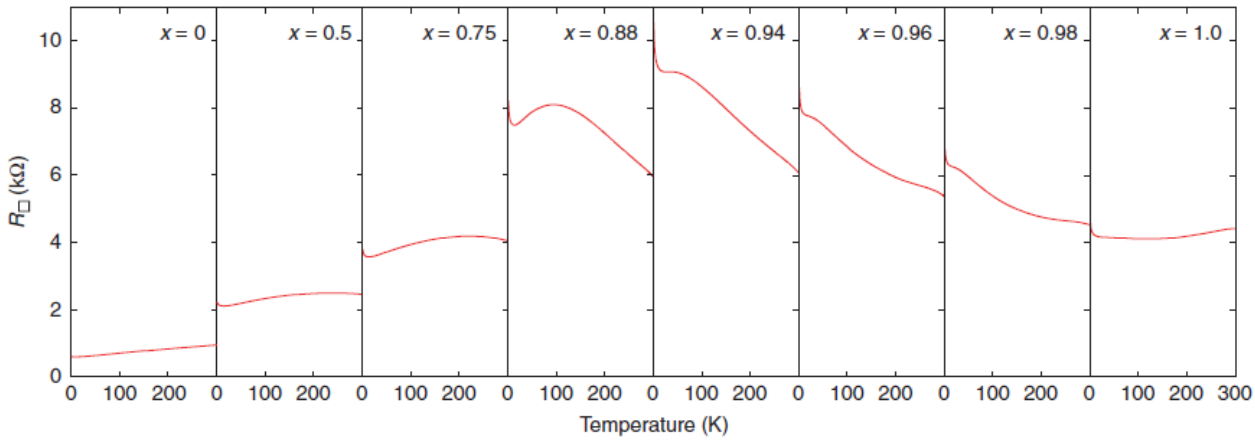

Figure 3.6: Temperature dependence of the sheet resistance of the $(Bi_{1-x}Sb_x)_2Te_3$. The figure is after Zhang *et al.*[408].

*Similar tunability of the Fermi level and the Dirac cone has been achieved in quarternary composition $Bi_{2-x}Sb_xTe_{3-y}Se_y$ by Arakane[11].

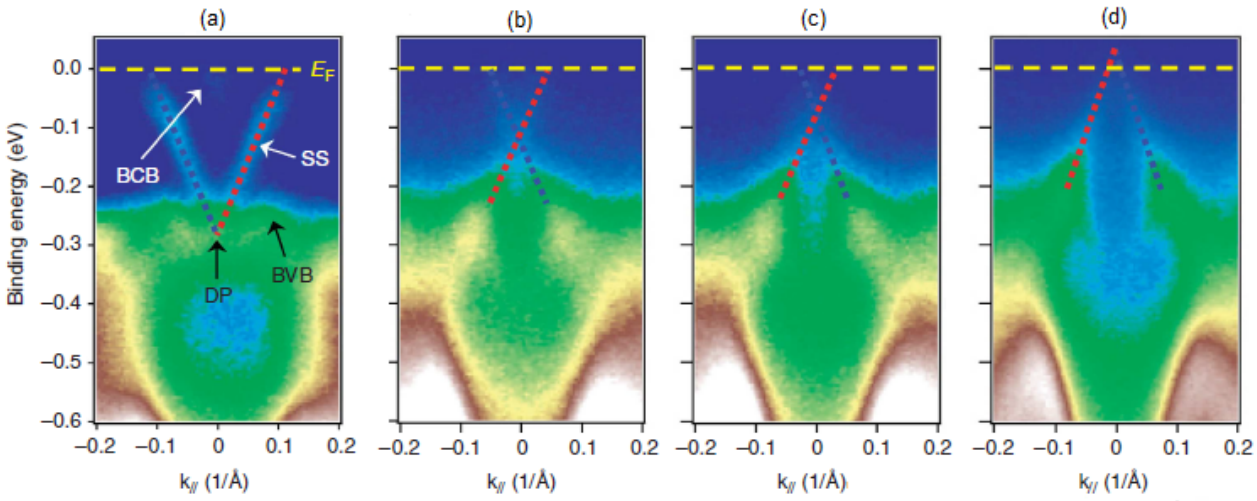

Figure 3.7: Angular resolved photoemission spectroscopy of $(Bi_{1-x}Sb_x)_2Te_3$. Panel (a)-$x = 0$, panel (b)-$x = 0.88$, panel (c)-$x = 0.94$, and panel (d)-$x = 0.96$. The figure is after Zhang *et al.*[408]. The abbreviations are as follow: BCB-bulk conduction band, BVB-bulk valence band, SS-surface states, DP-Dirac point, and E_F-Fermi level.

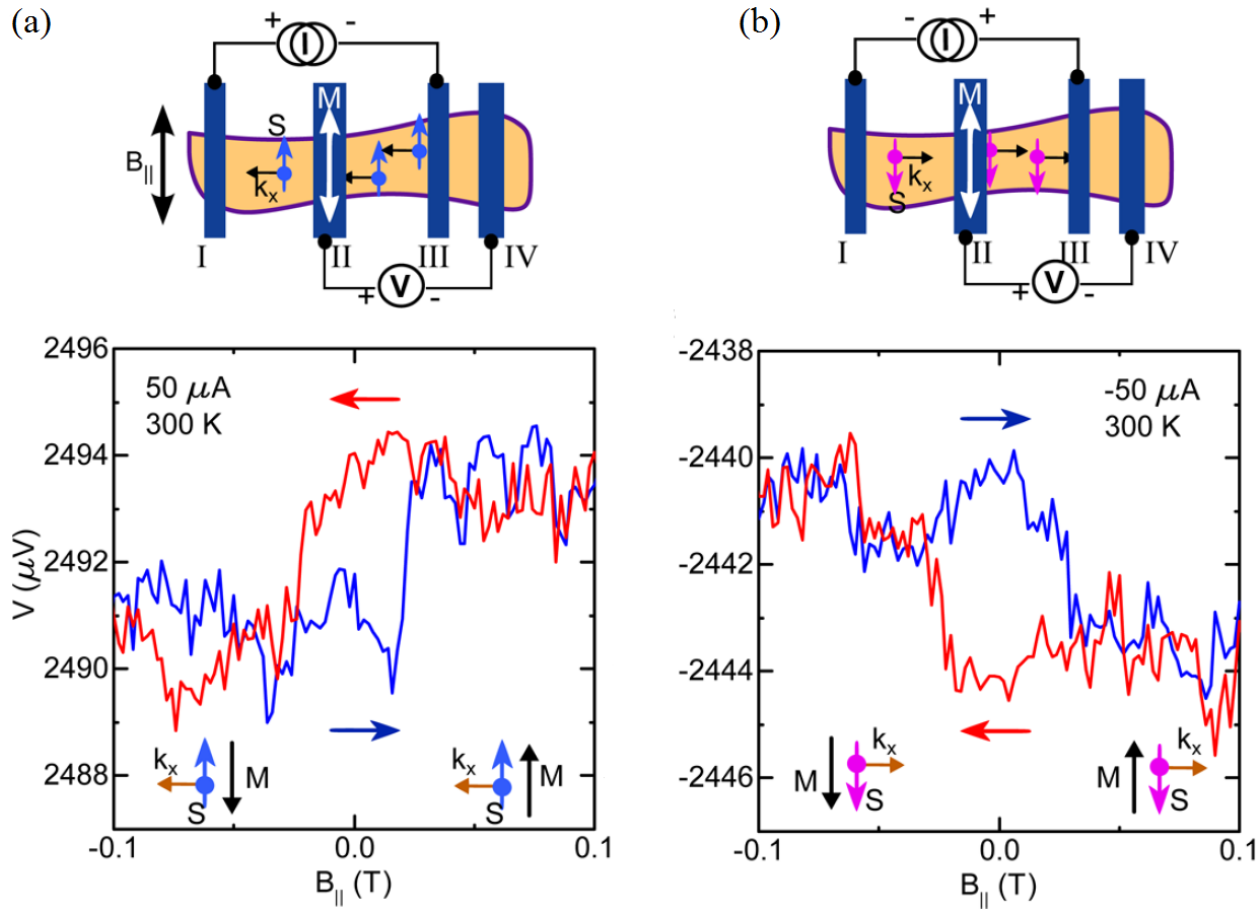

Figure 3.8: Spin-momentum locking data on Bi_2Se_3/TiO_2/Co devices. Panel (a)-electrons flow from III to I in Bi_2Se_3, panel (b)-electrons flow in reversed direction. The TMR-like response is represented below the transport schematics. The graph is after Dankert[68].

Importantly, 3D TIs provide the opportunity for direct integration is MTJ-like structures where

a mere flip in the current polarity should result in change of the spin polarization sign. Demonstration of the helical spin structure has been achieved in tunnel junction geometries and in non-local spin injection: such experiments are performed with $(Bi_{0.53}Sb_{0.47})_2Te_3$[332], $Bi_{1.5}Sb_{0.5}Te_{1.7}Se_{1.3}$[8], Bi_2Se_3[125] and Sb_2Te_3[200]. Recently, room-temperature spin momentum locking has been shown in Bi_2Se_3/TiO_2/Co tunnel MTJ type devices in four contact configuration by Dankert *et al.*[68] (see Fig. (3.8)). In their case, a current is passed between contacts I and III, and the spin accumulation is detected as a voltage signal between contacts II and IV (see Fig. (3.8)), where IV is a reference electrode outside of the current path. For a constant current polarity through Bi_2Se_3, the magnetization direction of the Co electrode is changed by an in-plane field and this results in TMR-like response due to parallel-antiparallel alignment of the spin polarization of the TI surface carriers and the majority carriers in the ferromagnetic electrode. When the current polarity is reversed, similar a TMR-like curve is observed, however, mirrored with respect to 0 T and this is a direct demonstration that the spin orientation in the surfaces states depends on the current propagation direction.

Despite these demonstrations, the magnitude of the effect is disappointingly small*. The reasons are possibly related to defects induced in the TI structure by the deposition of other layers on top, Schottky barrier formation or destruction of the spin-momentum locking due to close proximity with a ferromagnetic layer.

Very large spin Hall effect has been observed in TI/Magnetic TI and TI/Ferromagnet bilayers[93, 221] where demonstration is made up to room temperature in the latter case. The results do not depend on whether the TI is insulating in the bulk and the spin Hall effect is attributed to the spin-orbit interaction in the TI compositions rather than to the electronic properties of the surfaces states. Spin Hall angles larger than 1 are reported while the authors themselves question these values because the deposition of an overlayer influences the crystal structure, and hence, the bulk conductivity of the TI underlayer†. The latter might lead to wrong estimation of the current flowing densities in the topological insulator and ferromagnetic layers. If real, this "spin amplification" might have significant impact in the development of future devices.

Ferromagnetic TI have been grown by Cr[53], V[84], and Mn[140] doping and, interestingly, some of these compositions have been investigated years ago as diluted magnetic semiconductors. These compositions exhibit perpendicular magnetic anisotropy (PMA). Quantum Anomalous Hall effect (QAHE) has been a long sought phenomenon which has bee realized recently in Cr-[53, 181] and V-doped[55] TIs. The origin of QAHE lies in the intrinsic spin-orbit coupling and ferromag-

*For instance, Tang[332] estimated that the effective spin polarization of the surface states is 1.02 % in $(Bi_{0.53}Sb_{0.47})_2Te_3$.

†The spin Hall effect is the generation of transverse spin current, $\vec{j}_{\text{spin}}$, when a longitudinal charge current, $\vec{j}_{\text{charge}}$, flows in a material with high spin-orbit interaction: $\vec{j}_{\text{spin}} = (\hbar/2e)\theta_{\text{SHE}}\vec{j}_{\text{charge}} \times \vec{\sigma}$, where $\vec{\sigma}$ is the unit vector of the spin angular momentum and θ_{SHE} is the spin Hall angle. If $\theta_{\text{SHE}} > 1$, this means that an electron generates transverse spin higher than its own; an unrealistic physical situation.

netism. The QHE is the quantization of ρ_{xy} in a 2DEG in the presence of strong magnetic field, whereas QAHE represents quantization without external field while the longitudinal conductance decreases almost to zero. Therefore, QAHE represents a possibility for realization of dissipationless Hall transport. Very high spontaneous Hall angle in zero field of $89.993(4)^\circ$ is achieved by Chang *et al.*[55] in V-doped Sb_2Te_3 and the Curie temperature of this compositions reaches 115 K for $Sb_{1.73}V_{0.27}Te_3$. While Cr-doped TIs have exhibited QAHE as well, the Curie temperature in this case is lower and the sample requires magnetic training in order to enter the QAHE regime. The magnetic training is required due to the fact that the ferromagnetism in the Cr-doped magnetic TI is weaker. The coercive field, $\mu_0 H_c$, in Cr-doped TIs is roughly an order of magnitude smaller than in V-doped ones. For optimal doping, Cr-TIs have $\mu_0 H_c \approx 0.1\,\mathrm{T}$, while V-TIs have $\mu_0 H_c \approx 1.1\,\mathrm{T}$. Furthermore, the Curie temperature in Cr-doped TIs is three times smaller than in V-doped TIs for the same concentration of doping ions. Because of these reasons, the cool down in zero external field of Cr-doped TIs results in spontaneous magnetic state with more domain walls than in V-doped compositions and the multidomain state impedes the observation of QAHE.

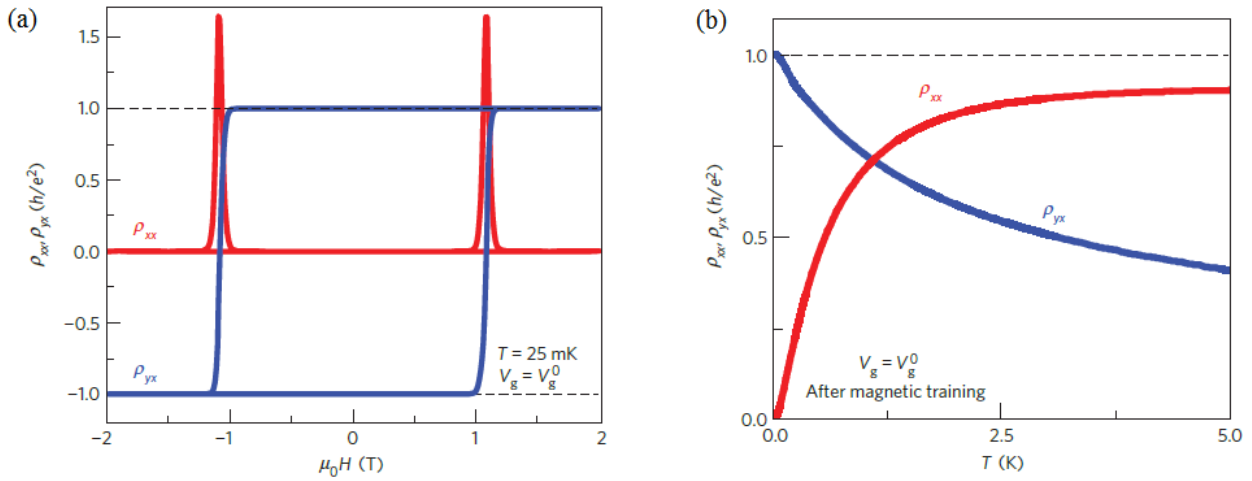

Figure 3.9: Panel (a)-example of a quantized AHE in magnetic TI with optimal composition $(Bi_{0.29}Sb_{0.71})_{1.89}V_{0.11}Te_3$ at the charge neutral point V_g^0. Note the high coercive field $\mu_0 H_c = 1.1\,\mathrm{T}$ and that the longitudinal resistivity has spikes at H_c. Panel (b)-temperature dependence of ρ_{xx} and ρ_{xy} of the same sample in zero magnetic field. The graph is after Chang[55].

Apart from the realization of QAHE in magnetic TIs, these compositions are interesting for two other reasons. The first is that magnetic doping is predicted to open a small gap in the surface states Dirac cone due to the breaking of the time-reversal symmetry, however, the literature data is contradictory on this topic. For instance, Wray *et al.*[382] and Chen *et al.*[57] have demonstrated gap opening of up to $\approx 100\,\mathrm{meV}$ in the Dirac cone of Fe-doped Bi_2Se_3. At the same time, robust behaviour of the surface states upon deposition of both magnetic and non-magnetic impurities has been shown by Valla *et al.*[353]. Sanchez-Barriga *et al.*[288] have demonstrated that the gap opening persists in $(Bi_{1-x}Mn_x)_2Se_3$ at temperatures far above the Curie temperature, and they

question the idea that the Dirac cone opening is due to the magnetic nature of the impurities.

The second interesting research direction stems from the competition between the topological order and the PMA. The latter promotes out-of-plane spin polarization while the former locks the spins in a helical in-plane texture and this competition might result in a peculiar hedge-hog type spin structure. The investigation of the latter effect is more of fundamental interest rather than technological. A brief example is given by the spin-resolved ARPES results on Mn-doped Bi_2Se_3 by Xu *et al.*[390]*.

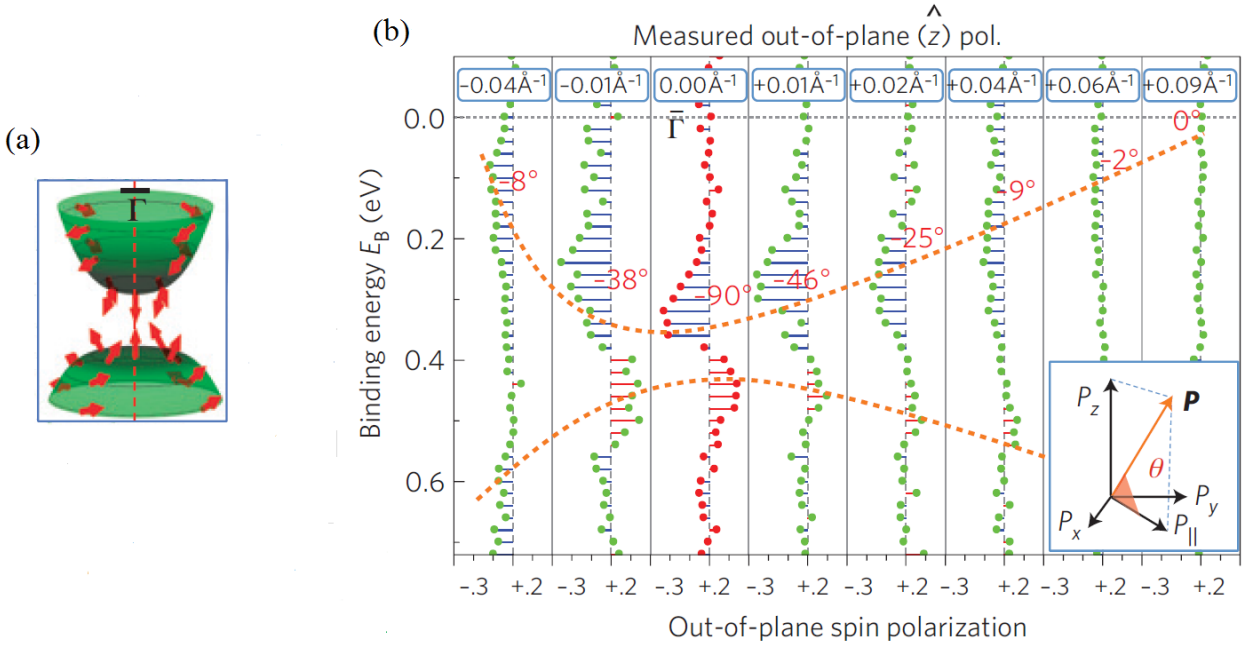

Figure 3.10: Panel (a)-Schematic representation of the gapped Dirac cone and the hedge-hog like spin structure. Panel (b)-measured out of plane spin polarization. The in-plane momentum for each spin-resolved spectrum is indicated on top. The polar angle (θ) of the spin vectors is indicated as well. The graph is after Xu *et al.*[390].

In this case, there is a small gap in the Dirac cone and, hence, there are top and bottom Dirac bands. The out-of-plane spin polarization component, P_z, has been demonstrated to be close to zero far away from the gapped Dirac point. Closer to the Dirac point, however, there is an apparent difference in the spin polarization along $+\vec{z}$ and $-\vec{z}$. The imbalance becomes more pronounced as the gapped Dirac point is approached. Furthermore, at momentum $k_{\|} = 0$ ($\overline{\Gamma}$ point), the spin polarization is completely out-of-plane at the vertices of the gapped Dirac cone and the spin polarization is along $-\vec{z}$ in the top Dirac band and along $\vec{z}$ in the bottom Dirac band.

*Another interesting result of their work is the fact that the Dirac cone structure is more stable when the composition is doped with the same concentration of non-magnetic Zn.

3.3 PCAR of $(Bi_{1-x}Sb_x)_2Te_3$

All samples in this investigation are provided by Dr. C.-Z. Chang from Prof. Moodera's group in the Francis Bitter Magnet Laboratory, Massachusetts Institute of Technology, Cambridge, MA, United States. The thin films are deposited by evaporation from Knudsen cells with high-purity Bi(99.999 %), Sb(99.9999 %), and Te(99.9999 %), while Cr(99.999 %) and V(99.995 %) are evaporated using electron guns. All films have been grown on heat-treated α-Al_2O_3 substrates in a custom-built molecular beam epitaxy system with a base pressure better than 5×10^{-10} torr and the compositions are confirmed by element ratios obtained *in-situ* on separate quartz crystal monitors. Cross-calibration is performed *ex-situ* with inductively-coupled plasma secondary ion mass spectroscopy (ICP-SIMS). Further details concerning the growth optimization can be found in the manuscripts from Zhang[408] and Chang[55]. The TI thickness of each sample is 20 quintuple layers (QLs) and they are capped all with insulating Te (2 nm). Some of the samples have been partially shadow-masked with Al(40 nm)/Au(30 nm) due to the high-sheet resistance. A narrow strip of 125 µm is left from the TI sample, while the rest is covered with the Al-Au layers, and horizontal stepping with the *x*-axis piezo-stepper has been performed in order to land on it. The main results from this chapter can be found in a recent article[38].

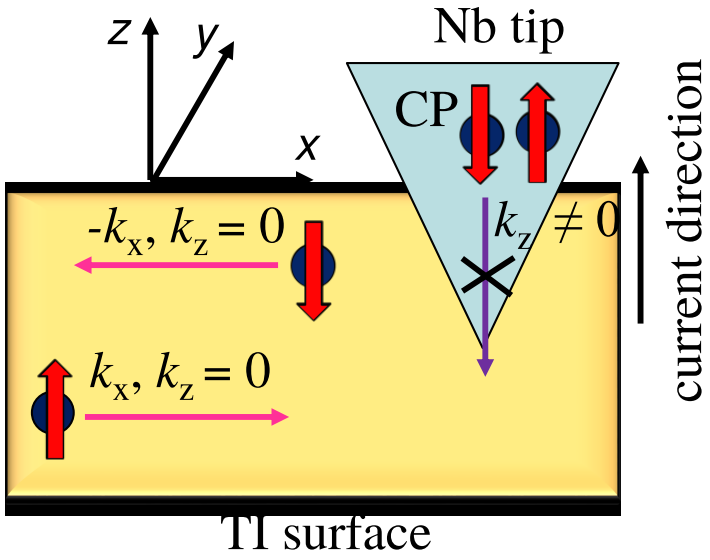

Figure 3.11: Schematic representation of the Andreev process between a superconducting Nb tip a TI sample. The spin direction of the surface carriers in the TI are locked in plane at right angles with respect to the momentum direction whereas the Cooper pairs have in general arbitrary spin orientation.

PCAR is a well-established technique for spin polarization measurements of bulk exchange-split ferro- and ferri-magnets, however, it is not intuitively clear why PCAR would be helpful in the investigation of topological insulators. In this case, PCAR probes the alignment of the spins with respect to the in-plane direction. The argument is related to symmetry: the Cooper pairs have

arbitrary wavevector direction in the Nb tip, and more importantly, they have a non-zero z-axis projection $\vec{k}_z \neq 0$ (see Fig. (3.11)). Furthermore, the Cooper pairs have preferential spin orientation along the z-axis when the transport is ballistic and when there is finite spin-orbit interaction in the tip*. On the other hand, the spin-polarized surface electrons in the TI have spin restricted in the plane of the sample ($\vec{k}_z = 0$) and, therefore, the injection of Cooper pairs in the TI sample is partially suppressed because the momentum at the interface must be conserved. Spin-flip scattering or highly diffusive transport in the contact area will lead to reduced value of the spin polarization. The maximum possible spin polarization which can be measured in such geometry is unrestricted, *i. e.* 100 %, provided that there are three requirements: no out-of-plane spin component of the topological surface carriers, no bulk conduction and no spin-flip scattering in the contact region. The average spin polarization for a given wavevector direction in the plane might be significantly different from the theoretical value of 100 % due to strong spin-orbit entanglement [398]. Such prediction is shown to depend on the photoexcitation energy[296]. What is important for our experimental configuration is the out-of-plane spin polarization, P_z, which is demonstrated experimentally to be very small, though finite [296]. The extracted spin polarization values presented in this section are always the highest obtained during the measurements of each sample. This procedure is followed because pronounced interface spin scattering may decrease the spin polarization in some of the measurements.

The focus falls first on the two end composition samples, which exhibit metallic behaviour (see Fig. 3.12). The extracted spin polarization of Bi_2Te_3 and Sb_2Te_3 is 70(4) % and 57(3) %, respectively, where both values are high and demonstrate the significant in-plane spin polarization in these compositions. The literature data suggests that the bulk carrier concentration in Sb_2Te_3 should be lower than in Bi_2Te_3[408]. The latter should lead in principle to higher spin polarization in Sb_2Te_3. However, it is well known that the bulk conduction is very sensitive to crystallographic defects. This is the probable explanation for the relation between the spin polarization values. An interesting correlation which will be elaborated later is that the spectrum with the higher spin polarization, P, exhibits the higher effective electronic temperature, T_e. The latter is $\approx$ 6.0(3) K for Bi_2Te_3, and 3.9(9) K for Sb_2Te_3.

The compositions Bi_2Te_3 and Sb_2Te_3 exhibit quasi-metallic behaviour, and their resistance decreases on cool down (see Fig. 3.6). The tuned composition $(Bi_{0.18}Sb_{0.82})_2Te_3$ is studied as well and its spin polarization reaches 83(9) % (see Fig. (3.13)). This is attributed to the fact that the bulk conduction is suppressed and, therefore, the contribution from the spin polarized surface states towards the total current is higher. The maximum conduction through the PCAR attained is $\approx 6.0G_0$ which is an indication of the high sheet resistance of this sample.

These analyzed spectra exhibit insignificant proximity effect and the extracted proximity gaps

*Indeed, Nb has appreciable spin- orbit interaction.

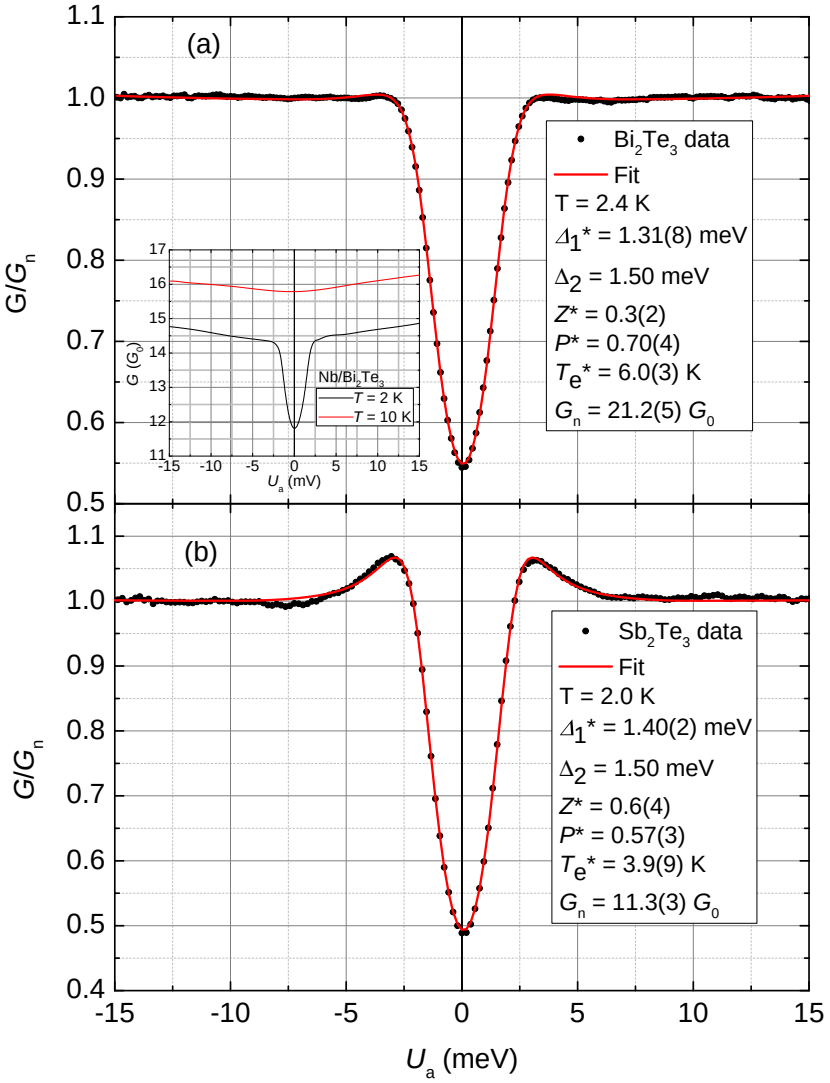

Figure 3.12: PCAR spectra along with the mBTK fit and the extracted parameters for Bi_2Te_3 (a) and Sb_2Te_3 (b). The obtained spin polarizations are 70(4) % in Bi_2Te_3 and 57(3) % in Sb_2Te_3. The extracted parameters from the fits are denoted with asterisks. Each PCAR curve is normalized with a spectrum above the critical temperature of Nb. The inset in panel (a) demonstrates two PCAR conductance curves obtained at $T = 2\,\mathrm{K}$ and $T = 10\,\mathrm{K}$. The two curves are offset for clarity.

are in the range $\Delta_1 = 1.3$ to 1.4 meV which is close to the value of the bulk Nb gap, $\Delta_2 = 1.5\,\mathrm{meV}$*. This is expected because there is energy mismatch between the two spin sub-bands in materials with strong magnetic or spin-orbit interaction, hence, a Cooper pair is easily destroyed and the superconducting order parameter decays very quickly with distance[47]. Another important point is that the effective temperature of the electrons is in the range 3.9 to 6.0 K, significantly above the bath temperature of $T \approx 2.0\,\mathrm{K}$. Such observations are often encountered in PCAR measurements and there are few possible reasons: tunneling process of some sort, local Joule heating in the contact area and the sheet resistance of the sample. There might be an unbroken thin insulating layer between

*Reminder: appreciable proximity effect exists when there is a serious difference between Δ_1 and Δ_2, see Sec. (1.5.2).

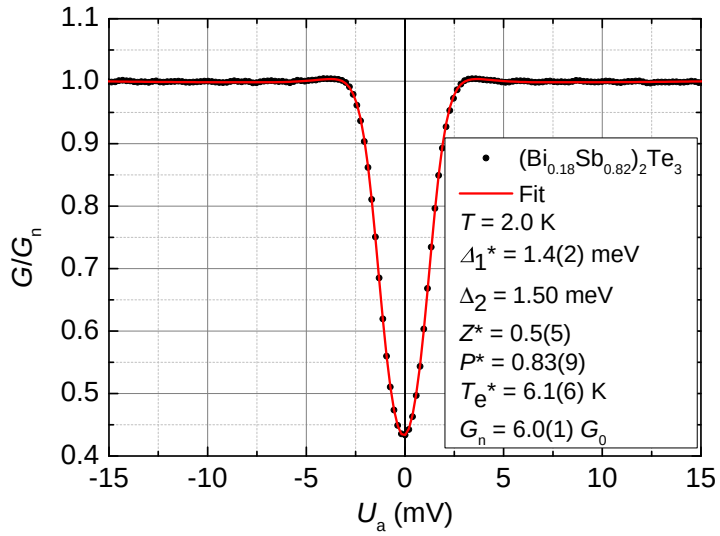

Figure 3.13: PCAR spectrum along with the mBTK fit and the extracted parameters for a TI composition $(Bi_{0.18}Sb_{0.82})_2Te_3$. The obtained spin polarization is $83(9)\,\%$. The extracted parameters from the fit are denoted with asterisks.

the tip and the sample which creates tunnel barrier and causes the usual quasi-quadratic form of the differential spectroscopy curve[306, 42]. Therefore, "hot" electrons with higher energy are the predominant tunneling carriers and this leads to higher electronic temperature. However, a serious tunneling contribution should manifest itself in the appearance of sharp spikes at applied bias equal to superconducting gap due to the superconducting quasi-particle density of states. Furthermore, significant tunneling results in very high barrier strength parameter, Z, which is not the case in the presented spectra.

The measured differential spectroscopy is a sum of two components in series: the point contact resistance and the sheet resistance of the sample. Therefore, the sheet resistance changes the relative voltage drop on the contact area and the PCAR features are broader in voltage and smaller in conductance. The latter experimental effect might be corrected by additional thermal smearing. The additional thermal smearing broadens the voltage scale and reduces the conductance profile. Such correction of an additive effect (series resistance) with a completely different physical parameter (effective temperature) is not physically correct. The inset of Fig.3.12 (a) demonstrates the "raw" PCAR curves for the Nb/Bi_2Te_3 contact. It is apparent that the uncorrected PCAR signal at $T = 2\,\mathrm{K}$ has significant non-linear background. This background might be caused by various reasons. A possibility is tunneling component through the contact, another explanation is non-flat density of states of the investigated composition. All PCAR spectra presented in this chapter have been normalized with a background spectrum at $T = 10\,\mathrm{K}$, above the critical temperature of Nb ($T_C = 9.2\,\mathrm{K}$).

It is important to comment on the different resistance values obtained in the PCAR spectra. The presented spectra in Fig. (3.12) and Fig. (3.13) have normalized conductance of 21 G_0 (Bi_2Te_3), 11

G_0 (Sb_2Te_3), and 6 G_0 ($(Bi_{0.18}Sb_{0.82})_2Te_3$). The sheet resistance of these samples is approximately 500 Ω (Bi_2Te_3), 1 kΩ (Sb_2Te_3), and 10 kΩ ($(Bi_{0.18}Sb_{0.82})_2Te_3$) (see Fig. (3.6)). It is clear that the sheet resistance and the contact resistance are comparable in magnitude. A further complication is that the sheet resistance of topological insulators depends on defects in the crystal structure and the Nb tip has detrimental effect on the crystallinity. An estimate for the point contact resistance itself is between 100 Ω (Bi_2Te_3) and 4 kΩ ($(Bi_{0.18}Sb_{0.82})_2Te_3$). The determined resistivities are $\rho(Bi_2Te_3) = 3 \times 10^{-6}$ Ω m and $\rho((Bi_{0.18}Sb_{0.82})_2Te_3) = 5.25 \times 10^{-5}$ Ω m [408]. The mean free path is approximately $l \approx 20$ nm (for Bi_2Te_3 [75]) based on the Hikami-Larkin-Nagaoka [138] fit of the topological insulators magnetoresistance. Following Wexler's formula 1.141, the contact dimensions are calculated to be 16 nm (for Bi_2Te_3) and 80 nm (for $(Bi_{0.18}Sb_{0.82})_2Te_3$). The first value is below the mean free path and, therefore, the transport regime is assumed to be ballistic. The point contact radius for the $(Bi_{0.18}Sb_{0.82})_2Te_3$ case is above the mean free path for Bi_2Te_3, however, the mean free path in $(Bi_{0.18}Sb_{0.82})_2Te_3$ is expected to be higher because the bulk conductivity is suppressed and the latter leads to reduced scattering processes. Both contact radii are smaller than the coherence length, l_ϕ, which is indicative of inelastic processes in TIs. Therefore, the PCAR on Bi_2Te_3 can be assumed to be in ballistic regime, while the PCAR on $(Bi_{0.18}Sb_{0.82})_2Te_3$ in quasi-ballistic regime.

The temperature evolution of the PCAR spectra of Bi_2Te_3 and Sb_2Te_3 are presented in Fig. (3.14). The temperature scans are measured during slow warm-up (0.4 K min^{-1}) in order to acquire enough statistics and avoid contact drifts. Subsequently the raw data is averaged in narrow temperature intervals ($\Delta T = 0.2$ K) and thus multiple, smooth and low noise PCAR curves are produced for $T[i] = 2\,\text{K}, 2.2\,\text{K}, \ldots, 9.8\,\text{K}$. Each PCAR curve between 2 K and 9.8 K is normalized to a background spectrum obtained at 10 K (above the critical temperature of Nb). The background curve corrects possible high bias density of states contribution from the sample and tunneling contribution of the contact.

First of all, the PCAR signal follows the expected temperature change and this proves definitely that the observed features are due to Andreev reflection. The superconducting gap progressively shrinks and the magnitude of the PCAR decreases, while Andreev-related signal persists all the way to the critical temperature of Nb ($T_c = 9.2$ K) and the latter is a demonstration that there is no Joule heating effect. In principle, the high level contours $G/G_n = [0.96, 0.99]$ can be used as a direct measure of the temperature change of the superconducting gap, however, these contours first surprisingly expand and then close up around the T_c. This deviation suggests that there is some small contribution towards the PCAR signal which is not of superconducting nature. This effect could be due to tunneling contribution, which has quadratic shape and becomes more obvious as $T \geq 0.5 \times T_c$, where the PCAR features lose magnitude. Another possibility is that the DOS of the investigated sample is not flat within the experimental bias range $U \approx \pm 10$ meV and evolves

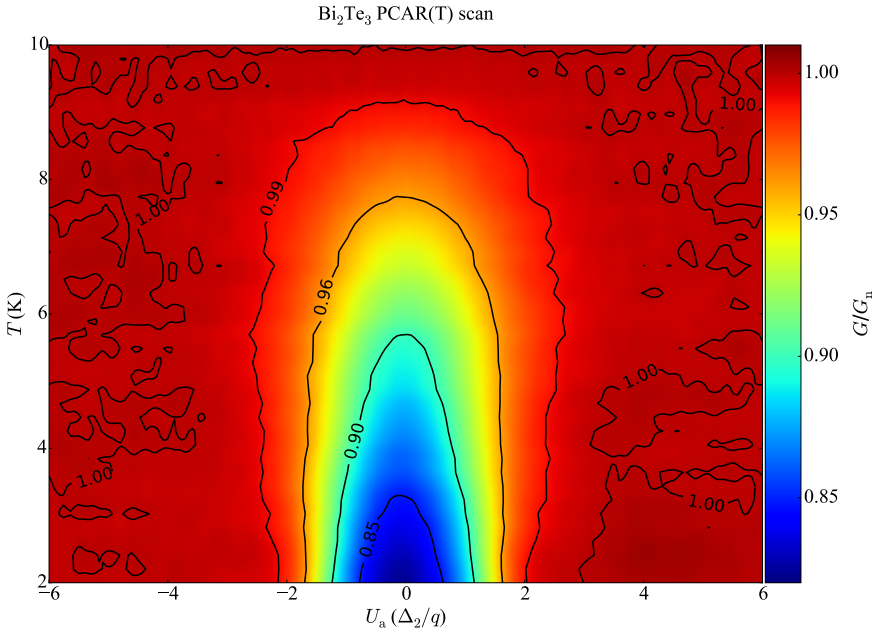

(a) PCAR temperature scan of Bi_2Te_3

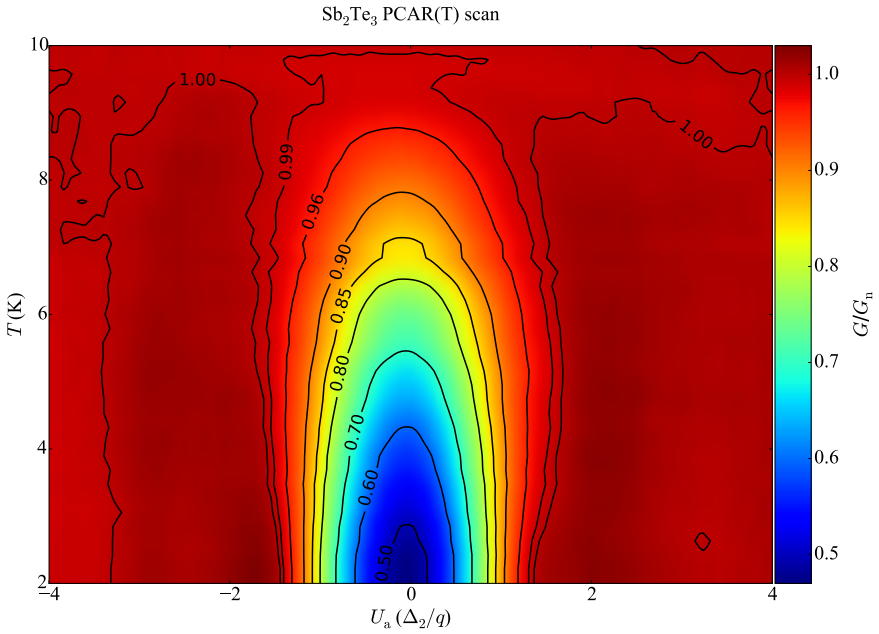

(b) PCAR temperature scan of Sb_2Te_3.

Figure 3.14: PCAR temperature scans of Bi_2Te_3 (a) and Sb_2Te_3 (b). The x-axis is in units of Δ_2/q, where $\Delta_2 = 1.5\,\text{meV}$ is the bulk superconducting gap of Nb and q is the elementary charge.

significantly with temperature, so that the normalization with the background curve at $T = 10\,\text{K}$ is not a sufficient correction. This is the case for semi-metals or very small gap semiconductors which is exactly our experimental situation and it is be proven later.

There is a potential pitfall in the temperature scans analysis which must be clarified. The high-bias conductance of each spectrum might change with temperature. This evolution could be either

due to contact drift* or due to the change in the sheet resistance of the sample. Therefore, after each PCAR($T[i]$) curve is normalized to the background curve at 10 K, it must be normalized further with respect to the high bias conductance profile: $G(U \to \infty, T[i])/G(U \to \infty, T = 10\,\mathrm{K})$†. This is a sufficient procedure in almost all experimental situations. However, the last normalization does not account for the fact that, as the high-bias conductance increases, the applied bias axis expands and the PCAR amplitude shrinks‡. The last effect is due to the resistance contribution in series with the contact itself (sample sheet resistance and lead resistance) and, hence, the applied bias and the conductance axes must be rescaled. A comparison between corrected and non-corrected temperature scans is presented in Fig. 3.15. In this particular case, the additional scaling procedure does not alter significantly the shape but the difference is still apparent, for instance, in the contour at level $(G/G_\mathrm{n}) = 0.99$. In fact, this simple rescaling procedure is only partially correct because the impedance of the voltage divider in our experimental setup must be taken into account as well. A calibration with standard resistors must be done, therefore, in order to properly correct the contact drift. This drift is small in our scans but it is worth noting that such correction is indeed needed in some cases.

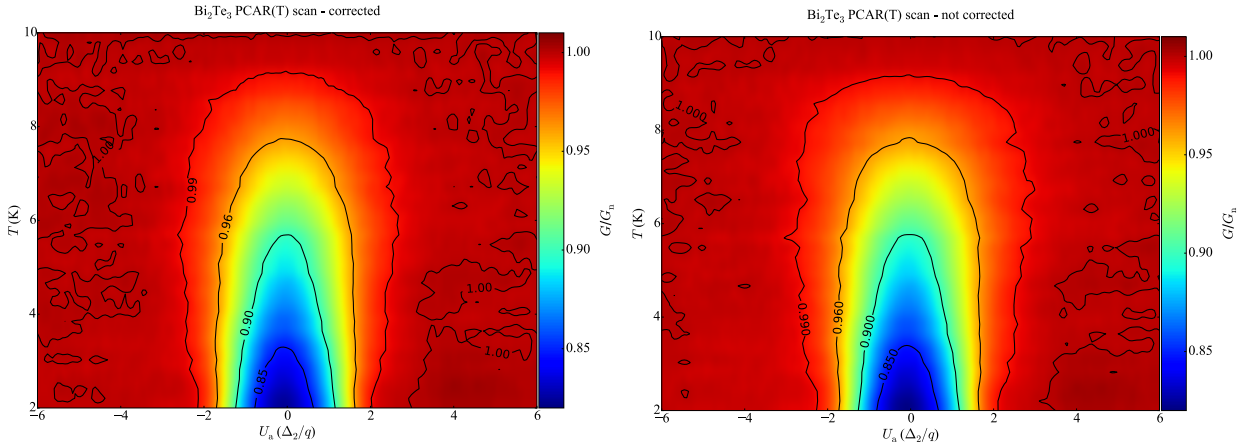

(a) Corrected scan

(b) Not corrected scan

Figure 3.15: Comparison between properly (a) and not corrected (b) PCAR temperature scans of the Bi_2Te_3. The x-axis is in units of Δ_2/q, where $\Delta_2 = 1.5\,\mathrm{meV}$ is the bulk superconducting gap of Nb and q is the elementary charge.

It is interesting to discuss the temperature change of the PCAR zero-bias anomaly (ZBA). The PCAR ZBA anomaly should directly follow the superconducting gap evolution. However, both samples demonstrate almost linear behaviour of the ZBA with the temperature. The extracted critical exponents are $\gamma = 0.91(2)$, and $0.71(2)$, respectively for Bi_2Te_3 and Sb_2Te_3 (see Fig. (3.16)).

*For instance, the metallic pieces of the tip and sample holders might expand slightly and push the tip further down into the sample. In the worst case, there might be a complete contact reorientation. The latter is manifested by a very sharp change in the spectral features.

†$U \to \infty$ indicates high-bias.

‡Respectively, if the high-bias conductance decreases, the applied bias axis shrinks and the PCAR amplitude expands.

The values are significantly higher than what is expected from the BCS theory ($\gamma = 0.5$, see Eq. (**??**)). Furthermore, there is correlation between the critical exponent and the extracted spin polarization: the higher the spin polarization is, the higher the critical exponent is, because a higher spin polarization results in more significant deviation from the classical superconducting properties. The latter is attributed to the formation of narrow Schottky barrier at the interface between the tip and the sample (see Fig. (3.18)). It is proven in the next section that this narrow barrier reduces the coherence of the Cooper pairs and leads to this stronger than usual decrease of the superconducting gap.

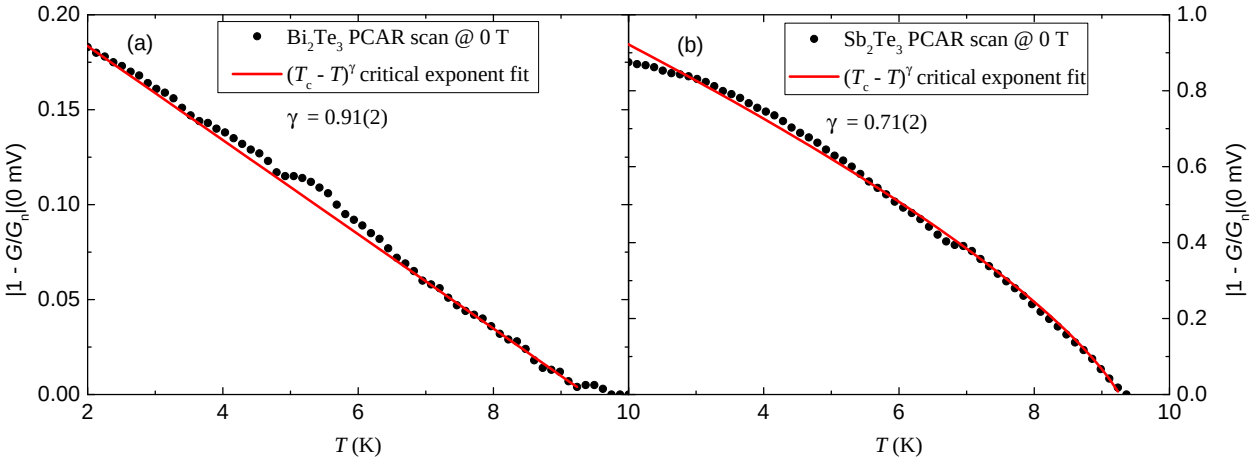

Figure 3.16: Temperature evolution of the zero-bias anomaly of the PCAR data on Bi_2Te_3 (a) and Sb_2Te_3 (b). The phase transition approach is fitted with $(T_c - T)^\gamma$ and the extracted critical exponents are 0.91(2) (Bi_2Te_3) and 0.71(2) (Sb_2Te_3).

3.4 High-field spectroscopy

Point contact spectroscopy (PCS) is measured on the same Bi_2Te_3 and Sb_2Te_3 samples. The magnetic field is increased to $\mu_0 H = 14\,\mathrm{T}$ and the Nb tip quenches in modest field magnitude $\mu_0 H_{c2} \approx 0.5\,\mathrm{T} - 1.0\,\mathrm{T}$. The latter is close to the reported Nb upper critical field, $\mu_0 H_{c2}$, reported in literature, however, the PCS demonstrates features when the tip is normal. The spectral line-shape changes from a PCAR structure to a Lorentzian curve. The latter is attributed to the semiconducting behaviour of these TI compositions. The magnitude of the PCS at 14 T is less than 10 % of the magnitude of the PCAR magnitude at 2 K, hence, the contribution of the PCS towards the PCAR on Fig. (3.12) and Fig. (3.13) is negligible.

The ZBA of the PCS scans is an indication of the size of the semiconducting gap in these close-to-degenerate semiconducting compositions. The PCS temperature scans of Bi_2Te_3 and Sb_2Te_3 between 2 K and 10 K are shown on Fig. (3.17) and the ZBA-temperature dependence of the two compositions is plotted separately on Fig. (3.18). The anomaly follows the exponential decay shape

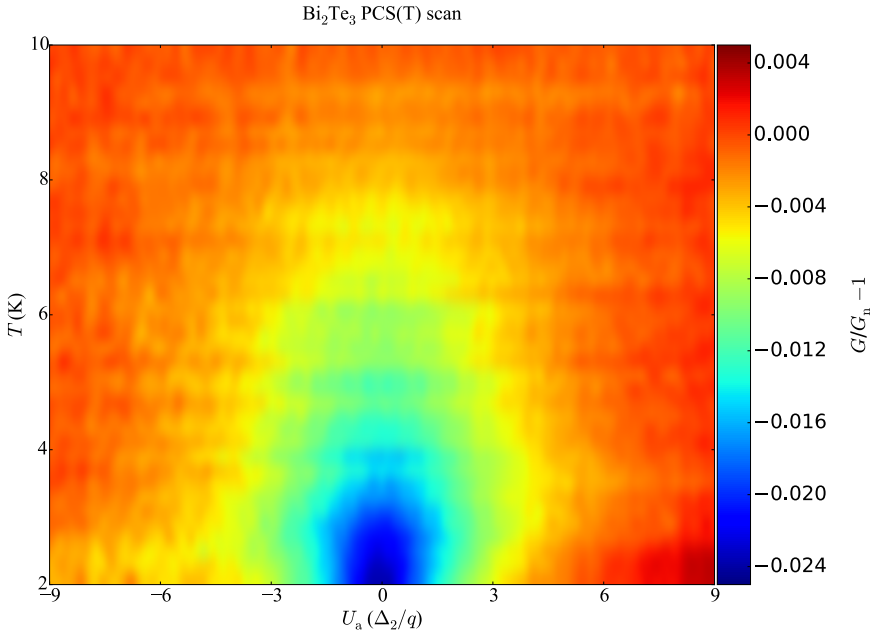

(a) PCS temperature scan of Bi_2Te_3

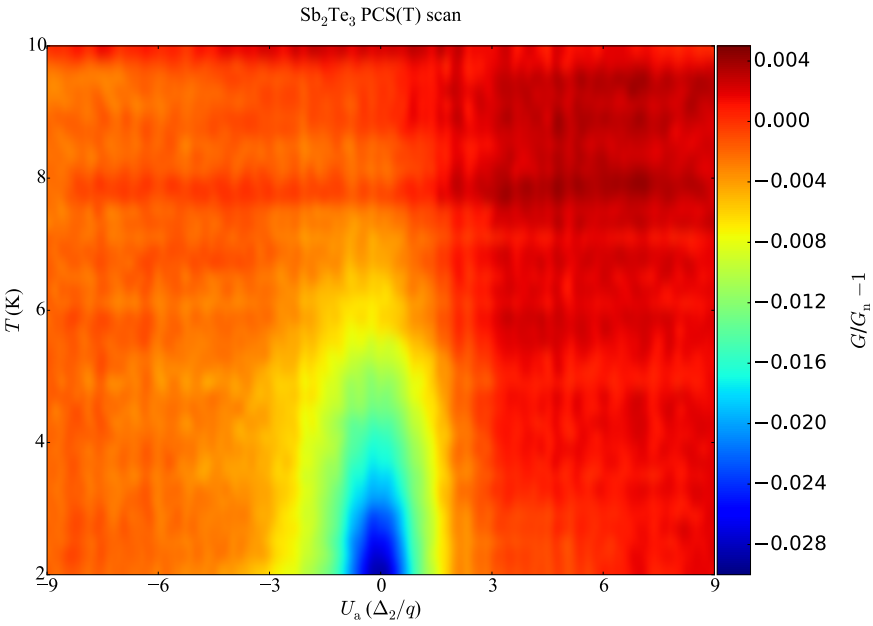

(b) PCS temperature scan of Sb_2Te_3.

Figure 3.17: PCS temperature scans of Bi_2Te_3 (a) and Sb_2Te_3 (b). Note he amplitude in comparison with amplitudes on Fig. 3.14. The x- axis is in units of Δ_2/q, where $\Delta_2 = 1.5\,\text{meV}$ is the bulk superconducting gap of Nb and q is the elementary charge.

typical for the resistance of semiconductors and the data is fitted with the Arrhenius law:

$$\delta = \exp\left(-\frac{E_\text{g}}{k_\text{B}T}\right), \tag{3.3}$$

where E_g is the semiconducting gap. The extracted gaps for the Bi_2Te_3 and Sb_2Te_3 compositions

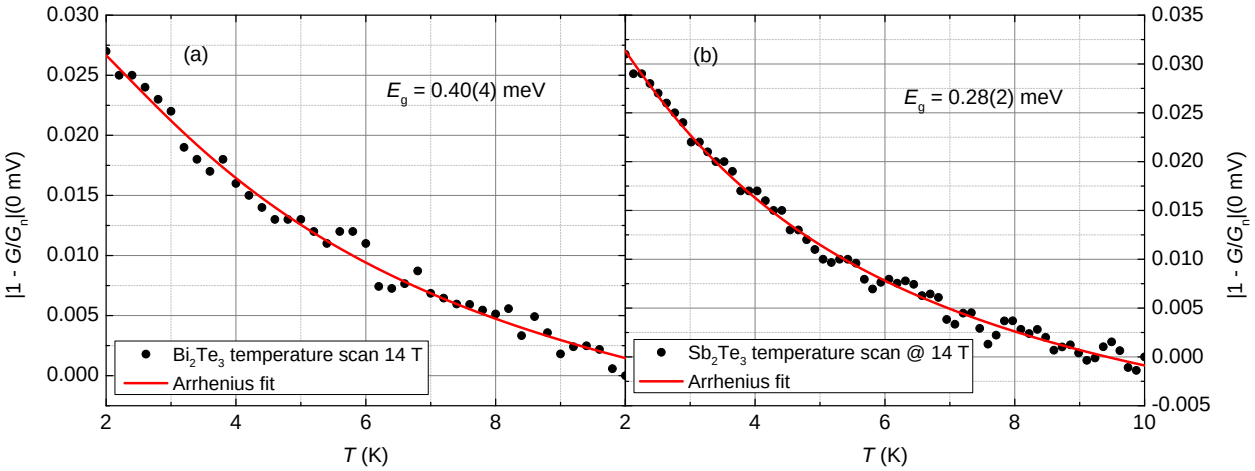

Figure 3.18: Arrhenius law fit of the zero-bias anomaly (ZBA) of the high-field point- contact spectroscopy (PCS). Panel (a)-PCS ZBA on Bi_2Te_3 with extracted gap of $E_g = 0.40(4)$ meV, panel (b)-PCS ZBA on Sb_2Te_3 with extracted gap of $E_g = 0.28(2)$ meV.

are $E_g = 0.40(4)$ meV and $0.28(2)$ meV, respectively. There is a positive correlation between the gap, the critical exponent and the spin polarization. The relation between the gap and the spin polarization is expected because the more insulating the bulk of the sample is, the higher the contribution from the surface states is with respect to the overall electrical transport. It has to be noted that the values of the extracted gaps are much lower than the ones reported in literature (100 meV-200 meV). As noted before, the Bi_2Te_3 and the Sb_2Te_3 are close to degenerate semiconductors and the Fermi level does not lie in the gap (see Fig. (3.6) and Fig. (3.7)), therefore, the extracted gaps by PCS are not the full band gaps of these compositions but the difference between the Fermi level and the respective band edge. Furthermore, the tip might induce defects in the crystal structure and, therefore, in the band structure.

There is another correlation which needs clarification: between the electronic temperature, T_e, and the extracted gap, E_g. For Bi_2Te_3: $T_e = 6.0(3)$ K and $E_g = 0.40(4)$ meV while for Sb_2Te_3: $T_e = 3.9(9)$ K and $E_g = 0.28(2)$ meV. Therefore, the higher electronic temperature correlates with the higher extracted gap (and the higher spin polarization) which can be interpreted as the formation of a very narrow Schottky barrier at the tip/topological insulator interface.

These barriers explain the elevated electronic temperature because bulk electrons will have to tunnel through the formed Schottky barrier. The differential conductance of a Schottky barrier has been investigated experimentally and the problem is solved analytically by Conley *et al.*[64]. If a parabolic depletion layer barrier is assumed, it results in:

$$\phi(x) = \frac{e^2 N_D (d-x)^2}{2\varepsilon} + eV - \mu, \quad 0 < x < d, \tag{3.4}$$

$$d = \sqrt{\frac{2\varepsilon(U_B + \mu - V)}{eN_D}}, \tag{3.5}$$

where ϕ is measured with respect to the Fermi energy of the semiconductor, the coordinate x goes from the metal-semiconductor interface into the semiconductor, N_D is the donor concentration and ε is the dielectric constant and positive bias is assumed to raise the energy of the semiconductor conduction band. The width of the depletion layer d depends on the bias voltage, and U_B is the barrier height at the metal-semiconductor interface. N-type germanium with doping concentrations $\sim 10^{18}\text{cm}^{-3}$ is considered in this case. In principle, the minimum in the differential conductance provides the opportunity to determine the band edge (the Fermi degeneracy μ). The effect of random fluctuations of donor impurities in the depletion layer at very high dopant concentrations have been discussed by Wolf[376] in a study of silicon Schottky barrier junctions. Similar zero-bias, strongly-temperature-dependent features have been observed in the differential conductance of In-Ge:As (irradiation compensated) Schottky barrier tunnel junction by Christopher *et al.* [60]. In this case, the effect is attributed to a variable range phonon-assisted tunneling model by Wolf[377, 378].

Unfortunately, in our experimental data the minimum in the differential conductance spectra is comparable to the instability of the voltage source and, hence, no reliable extraction of μ is possible. Cross-over from Andreev reflection dominated to Schottky barrier dominated transport process has been discussed before by Kleinsasser *et al.*[174] in Nb/InGaAs with various doping concentrations.

It is important to comment on the full field scan of Bi_2Te_3 and Sb_2Te_3 and the extracted field dependence of the zero-bias magnitude which are presented in Fig. (3.19) and Fig. (3.20), respectively. The three-dimensional plots demonstrate that the Nb tip is fully quenched in a magnetic field of $\approx 1\,\text{T}$. This value is slightly above the typical bulk quench field of Nb ($\mu_0 H_{c2} \approx 0.5\,\text{T}$)[161]. There are two possible explanations for this effect: small proximity maintained superconductivity* or increase of the critical field in thin superconductors. The latter option is considered first. The critical field in ultrathin superconductors is increased beyond the bulk value (see Sec. 1.4.5). For instance, PCAR has been measured in magnetic field up to 3 T with bulk Nb by Shan[297]† and this can be the case if the superconducting tip is very sharp. The option of proximity maintained superconductivity at the contact area is very probable. An evidence is given by the shape of the PCAR spectrum on Fig. 3.20 (a). The features around $U_a \approx 2$ are indicative of the superconducting density of states. These features disappear close to 0.4 T which means that the superconductivity order nature perhaps changes slightly.

The focus shifts now towards the high field scans in Fig. 3.19 (b) and Fig. 3.20 (b). The scan of Bi_2Te_3 demonstrates that the gap feature shrinks in bias as the field increases. The same is true for the zero-bias amplitude of Bi_2Te_3 as well. The behaviour of the gap feature and the zero-bias amplitude is completely opposite for Sb_2Te_3 in the high-field scan and they demonstrate small

*Josephson effect has been demonstrated in Nb/Bi_2Te_3/Nb structure over very large distance-see [360].

†Such high field PCAR has not been achieved by our group with Nb tips.

magnitude increase as the magnetic field goes towards 14 T.

The zero-bias amplitude in Fig. 3.21 is normalized to the value at 0 T for both scans. The high-field gap amplitude in the case of Sb_2Te_3 is much smaller than the PCAR signal at 0 T. However, this appears not to be the case for Bi_2Te_3. The temperature scan used for the Bi_2Te_3 exhibits overall lower spin polarization than the spectrum in Fig. 3.12 (a) and it explains why the ZBA due to the semiconducting behaviour looks significant in this temperature scan. The contribution from the semiconducting ZBA is never higher than 10 % in the PCAR spectra analyzed for spin polarization.

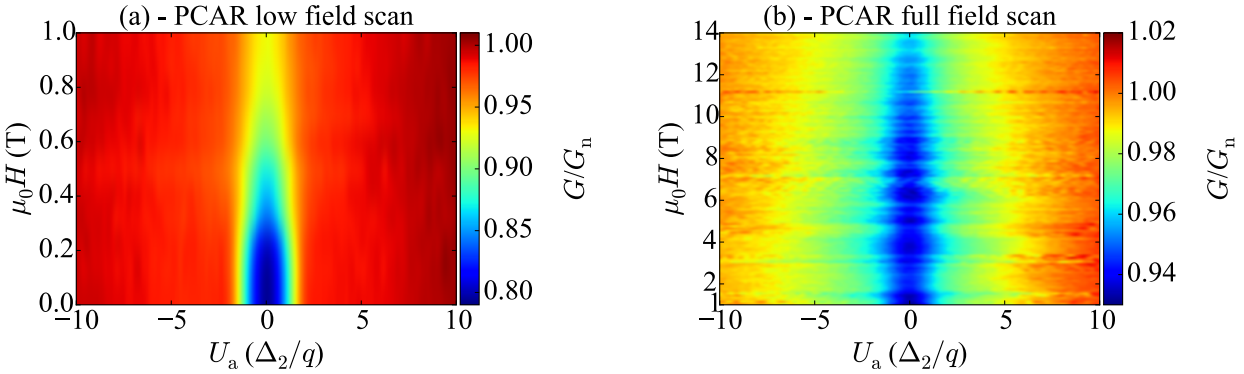

Figure 3.19: Magnetic field scan of a Nb/Bi_2Te_3 point contact. Panel (a)-low field scan up to 1 T. The superconductivity disappears around 0.5 T. Panel (b)-high-field scan up to 14 T. The structure does not vanish.

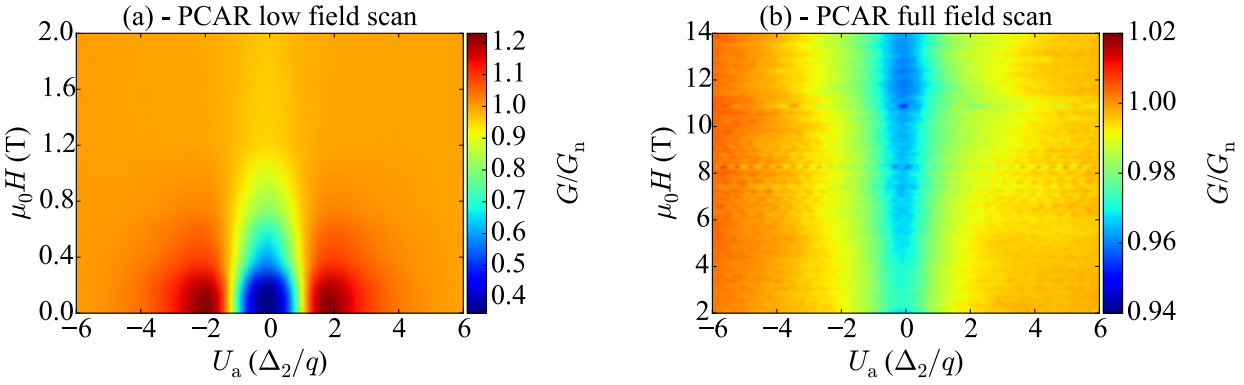

Figure 3.20: Magnetic field scan of a Nb/Sb_2Te_3 point contact. Panel (a)-low field scan up to 2 T. The superconductivity disappears around 1.0 T. Panel (b)-high-field scan up to 14 T. The structure does not vanish.

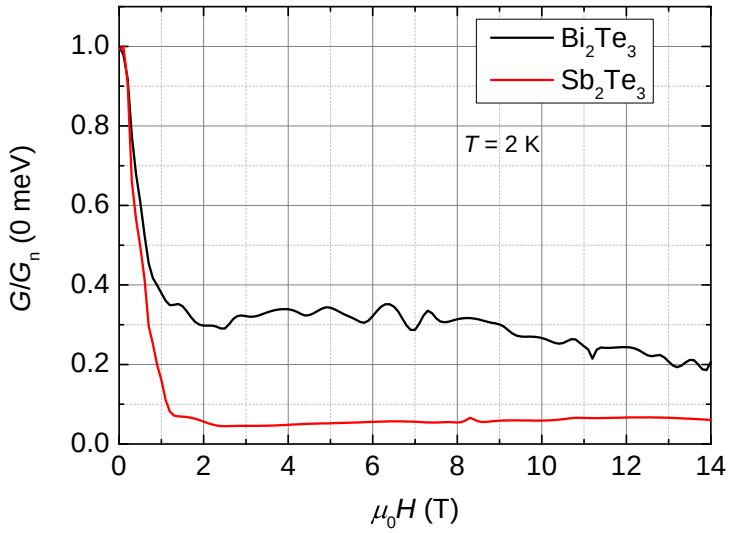

Figure 3.21: Magnitude of the zero-bias amplitude during a field scan of Bi_2Te_3 and Sb_2Te_3.

3.5 Magnetic topological insulators

Magnetic topological insulators with Cr and V doping have attracted significant attention recently due to the realization of the quantum anomalous Hall effect and the achieved Curie temperature of $T_C \approx 115\,K$. Both Cr and V are substitutional on the Bi(Sb) atomic positions and apart from having magnetic moment, the dopants affect the carrier concentration in the TI compositions as well. Vanadium is an electron donor in Sb_2Te_3, whereas the contribution of chromium is generally lower but of the hole type in the same initial composition. Four topological insulators with small concentration of Cr and V doping are investigated: $Bi_{1.97}Cr_{0.03}Te_3$, $Sb_{1.975}Cr_{0.025}Te_3$, $Bi_{1.975}V_{0.025}Te_3$ and $Sb_{1.97}V_{0.03}Te_3$. The idea behind these experiments is to study the spin polarization of a magnetic topological insulator below and above T_C*.

*It proved to be elusive so far because the Curie temperature must be tuned around 5 K, so that the PCAR can be measured reliably both above and below T_c.

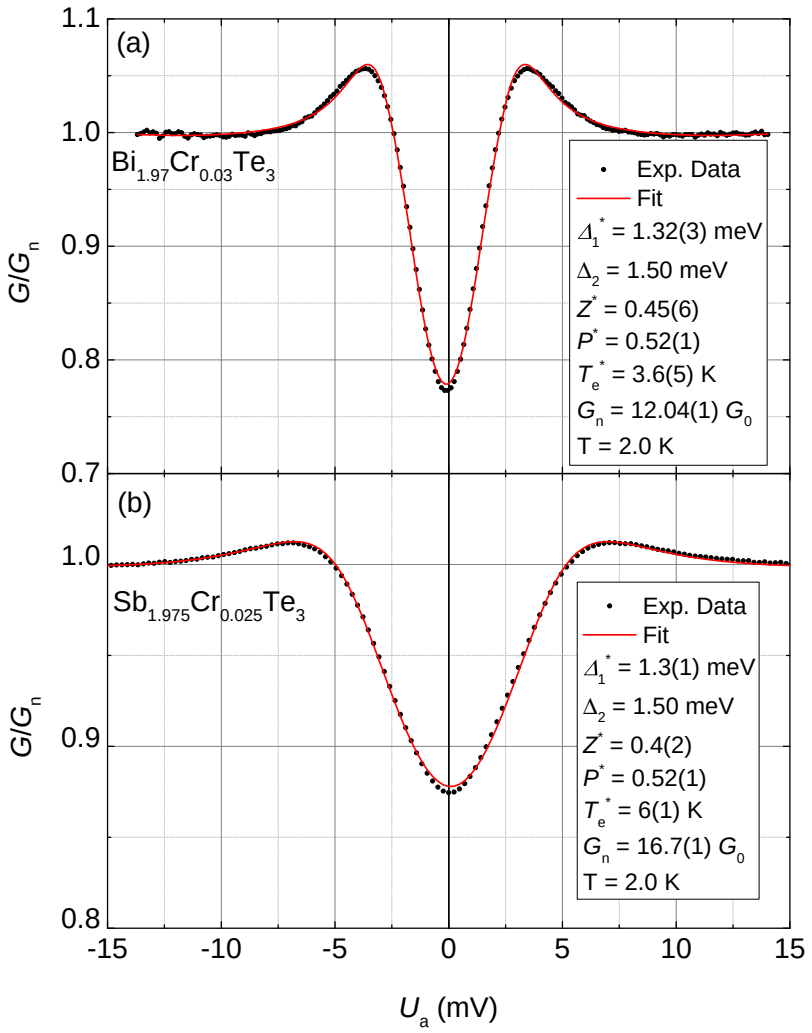

Figure 3.22: PCAR spectra along with the mBTK fit and the extracted parameters for two samples with Cr-doping : $Bi_{1.97}Cr_{0.03}Te_3$ (a) and $Sb_{1.975}Cr_{0.025}Te_3$ (b). The obtained spin polarizations are $52(1)$ % in $Bi_{1.97}Cr_{0.03}Te_3$ and $52(1)$ % in $Sb_{1.975}Cr_{0.025}Te_3$. The extracted parameters from the fits are denoted with asterisks.

The spin polarizations of the Cr-doped $Bi_{1.97}Cr_{0.03}Te_3$ and $Sb_{1.975}Cr_{0.025}Te_3$ are $52(1)$ % and $52(1)$ %, respectively (see Fig. (3.22)). As it is the case on the pristine samples, the proximity effects are negligible ($\Delta_1 \approx \Delta_2$) and the electronic temperature is significantly above the bath one ($T_e > T$). The carrier concentration in Cr-Bi_2Te_3 is expected to be reduced and, therefore, the spin polarization should increase[58, 54] because the bulk conduction is decreased. On the contrarily, Cr-doped Bi_2Te_3 demonstrates spin polarization of $52(1)$ %, lower than in the pristine composition (see Fig. 3.12 (a)). This reduction is attributed to spin-flip scattering by the paramagnetic dopants. On the other hand, the Cr addition in Sb_2Te_3 should increase slightly the bulk hole carrier concentration. The latter should lead to a small decrease in the spin polarization with respect to the pure Sb_2Te_3, which is exactly what is observed. Spin-flip scattering from the paramagnetic ions is a possible contribution as well. Both compositions do not exhibit magnetic ordering above 2 K.

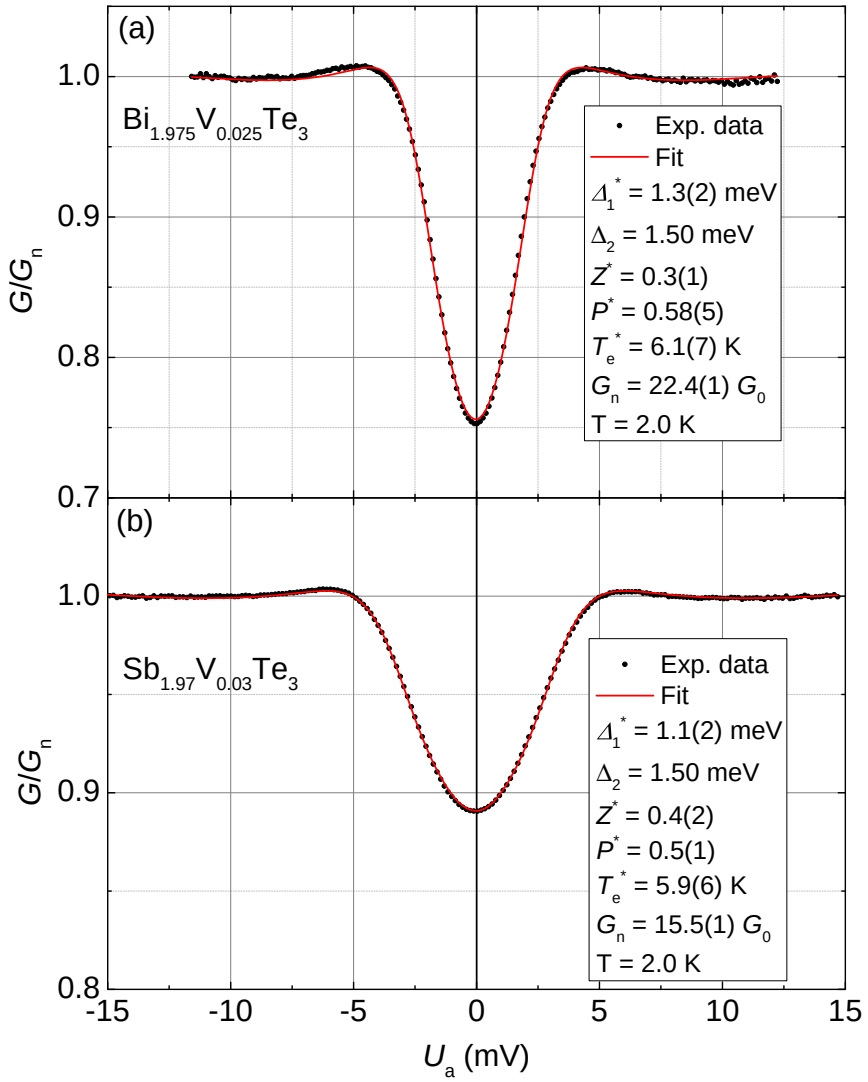

Figure 3.23: PCAR spectra along with the mBTK fit and the extracted parameters for two samples with V-doping: $Bi_{1.975}V_{0.025}Te_3$ (a) and $Sb_{1.97}V_{0.03}Te_3$ (b). The obtained spin polarizations are $58(5)$ % in $Bi_{1.975}V_{0.025}Te_3$ and 50 % in $Sb_{1.97}V_{0.03}Te_3$. The extracted parameters from the fits are denoted with asterisks.

Vanadium-doped magnetic TIs exhibit higher coercivity and T_c. PCAR on V-doped TI compositions is presented in Fig. 3.23. Vanadium has small electron donor contribution in Bi_2Te_3[84]. The extracted spin polarization of $Bi_{1.975}V_{0.025}Te_3$ is found to be $58(5)$ % which is lower than in the pristine composition and this composition does not exhibit magnetic order above 2 K. Overall, these three magnetically doped compositions demonstrate lower values of the spin polarization than the pristine samples which is attributed to the detrimental effect of the paramagnetic impurities on the spin-momentum locking. It has been predicted theoretically that scattering by magnetic impurities destroys the TI surface properties and the stability of the topological surface states with additional Mn and Fe doping has been investigated before experimentally by spin-resolved photoemission spectroscopy[382, 288].

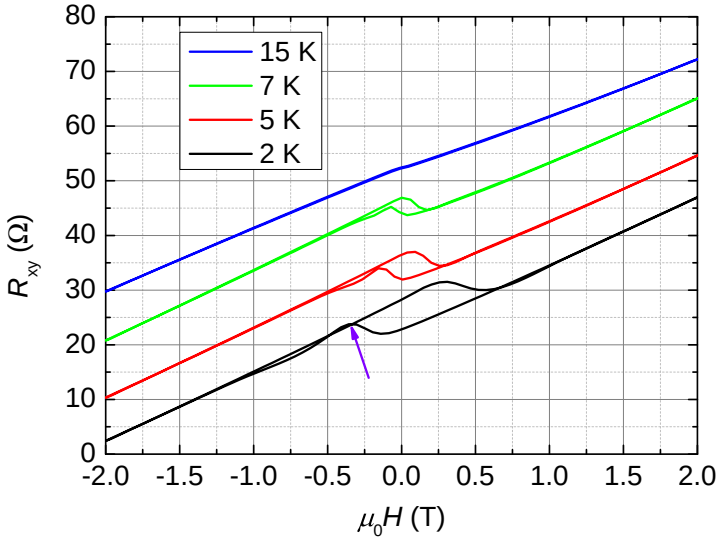

Figure 3.24: Anomalous Hall effect measurements on the magnetic topological insulator $Sb_{1.97}V_{0.03}Te_3$. The curves are vertically offset for clarity. The curve at 15 K (above the T_C) demonstrates slight paramagnetic signal. The violet arrow indicates the peak observed at the coercive field due to longitudinal resistance pick-up (see Fig. 3.9).

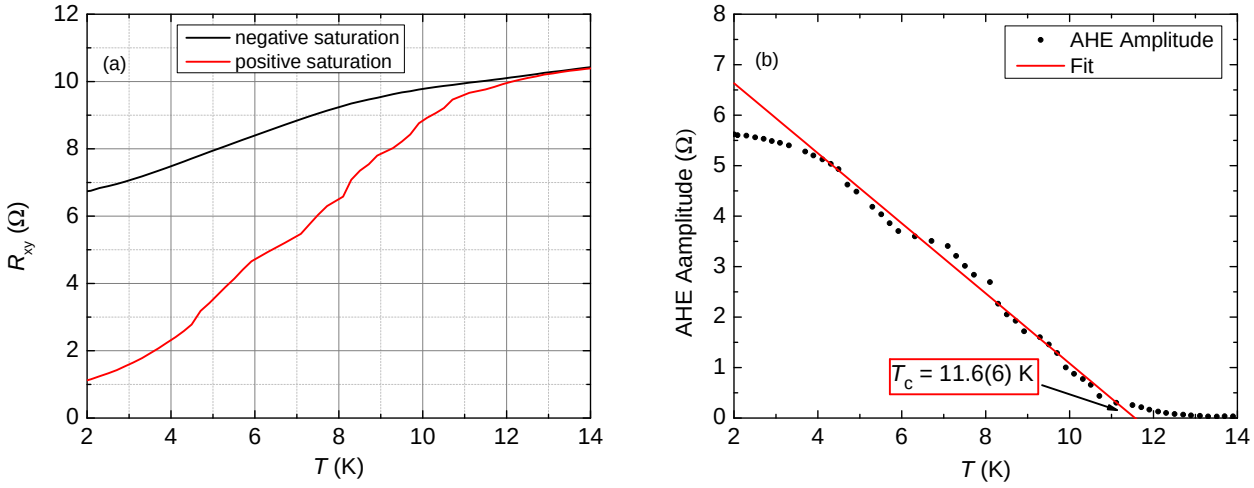

Figure 3.25: Panel (a)-Temperature dependence of the absolute anomalous Hall effect signal of $Sb_{1.97}V_{0.03}Te_3$ in remanent state after the sample was saturated in positive and negative direction, respectively. Panel (b)-temperature dependence of the AHE magnitude along with the extracted Curie temperature of 11.6(6) K.

Finally, the composition $Sb_{1.97}V_{0.03}Te_3$ has been investigated where vanadium acts as electron donor and should suppress the hole conductivity in Sb_2Te_3[84, 55]. Spin polarization of only 50 % has been demonstrated and this is the lowest measured value on all samples. This composition exhibits ferromagnetic order above 2 K. The significant decrease in the spin polarization is attributed to the competition between the in-plane spin structure of a pristine TI and the perpendicular magnetic anisotropy of the magnetic topological insulator.

The magnetic order in $Sb_{1.97}V_{0.03}Te_3$ is measured by anomalous Hall effect in van der Pauw configuration and an example of four AHE loops is presented in Fig. 3.24. There is inevitable

longitudinal resistance pick- up when AHE is measured on an unpatterned film, therefore, in order to correct for this contribution, two separate temperature scans are performed. The sample is first saturated in positive field, then left in remanence and the Hall resistance is measured while the temperature increases. Then the sample is saturated in negative direction, and another temperature scan has been performed. In this way the temperature dependence of the AHE magnitude is obtained by subtracting the two curves and the Curie temperature $T_C = 11.6(6)$ K is determined (see Fig. 3.25).

3.6 A peculiar case

An interface between a TI and a superconductor has been proposed to be a testing ground for the observation of new interesting effects like Majorana fermions[101]. There is no real creation-annihilation of fundamental particles, instead a very low energy pronounced peak in the differential conductance is interpreted as a quasiparticle excitation. Such excitations have potential to be exploited as fault-stable superconducting qubits. For instance, $Cu_xBi_2Se_3$ has been theoretically predicted to be a topological superconductor and it is indeed superconducting with critical temperature of 3.8 K[141]. A "soft" point-contact spectroscopy on the same composition has shown low bias conduction spike[289]. The latter is a possible indication for such Majorana fermion[203]. The scanning tunneling spectroscopy on this material, however, shows that it behaves as a classical Bardeen-Cooper-Shrieffer superconductor with a gap of ≈ 0.4 meV. The presence of states within the gap has been expected, however, the superconductivity has been demonstrated to be classical *s*-wave type without any nodal symmetry of the gap or sub-gap structure. Interestingly, when the tip is crashed in the sample, a zero-bias conductance peak is observed[199].

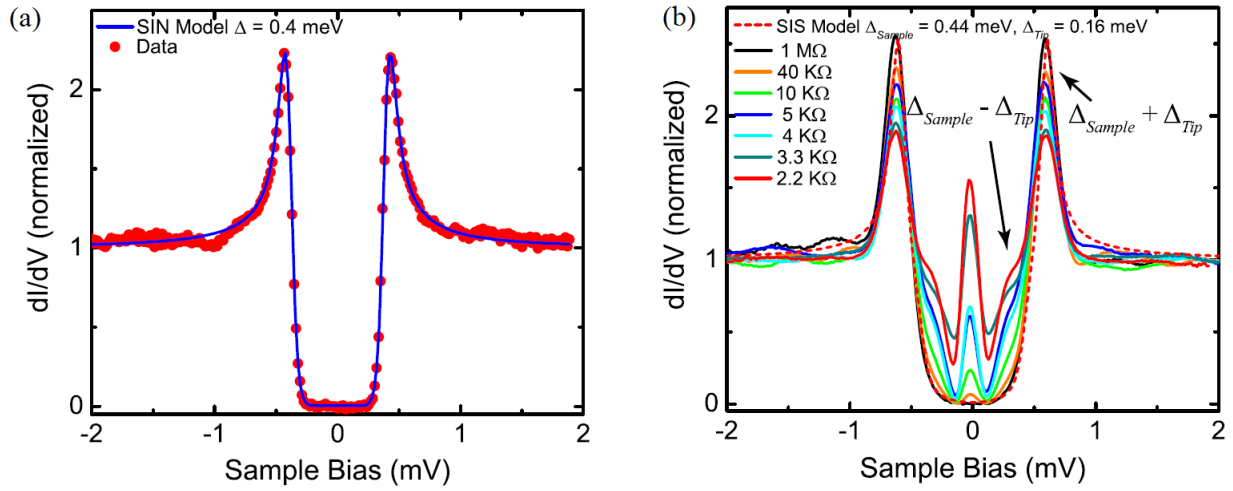

Figure 3.26: Panel (a)-example of *s*-wave superconducting gap in Cu-intercalated Bi_2Se_3 by scanning tunneling spectroscopy. Panel (b)-example of zero-bias conductance peak when the Ir tip was crashed in the surface. The data is after Levy *et al.*[199].

Here, two such examples are presented on some of the contacts which are investigated during the PCAR measurements of Nb/Bi_2Te_3 (see Fig. (3.27) and Fig. (3.28)). The zero-bias spike is observed multiple times with various intensities. In all cases, the spike disappears at temperature $T' = 3\,\mathrm{K} - 4\,\mathrm{K}$, significantly lower than the critical temperature of Nb. For $T > T'$, an usual PCAR spectrum is observed. The (non)existence of this spike definitely depends on the contact geometry because these irregular zero-bias features are not observed in approximately 90 % of the cases (see Fig. (3.12) for a "clean" Andreev reflection on Bi_2Te_3). No similar contact features have been measured on any of the other investigated compositions, and, therefore, this observation might be related to particular density of states structure of Bi_2Te_3. Allowance is made for two other very probable explanations of this peculiar result. First, such features are represented and fitted very well by the model of Strijkers[321], which considers Andreev reflection with significant proximity. In this case, the contact area can be seen as a Josephson junction of S-c-S$'$ type, where S is the superconducting tip, c is the constriction, *i. e.* the contact itself, and S$'$ is the proximity induced superconducting area is the sample. Once the S$'$ region is quenched, the Josephson supercurrent is lost. Another possibility is the formation of multiple (at least two) contacts in parallel at the end of the tip. In this case, one of the sections might be quenched and its conductance contribution is responsible for the existence of the zero-bias peak[370].

Large superconducting proximity effect and Josephson effect have been achieved in Nb/ Bi_2Te_3/-Nb[360] where Josephson effect is maintained over a length of 1 µm. The Bi_2Te_3 has significant bulk conduction and low bulk mean free path and , therefore, the supercurrent is carried by the surface states. Proximity induced superconductivity in TI has been reported by Zhang*et al.*[406] in W/Bi_2Se_3. Finally, supercurrent and Josephson effect have been reported in Al/Bi_2Se_3 and Ti/Bi_2Se_3 by Sacepe *et al.*[284] and by Williams *et al.*[374], respectively.

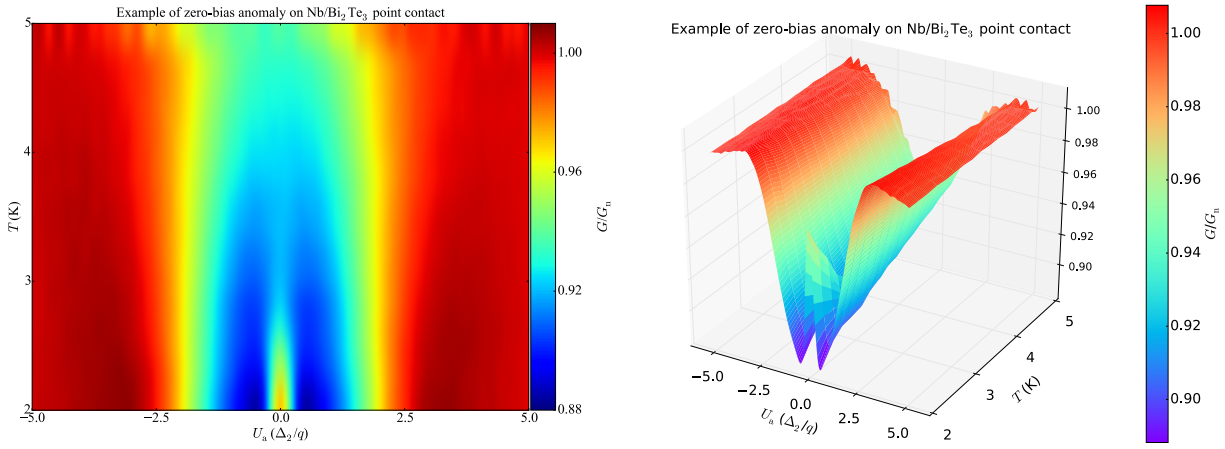

(a) Example of a zero-bias anomaly on Nb/Bi_2Te_3

(b) The same graph but from another point of view

Figure 3.27: Normalized differential conductance (G/G_n) temperature scan of a zero-bias conductance peak (ZBCP) on a contact Nb/Bi_2Te_3. The x-axis is in units Δ_2/q, where $\Delta_2 = 1.5\,\mathrm{meV}$ is the bulk Nb superconducting gap and q is the electrons charge. The bias axis is intentionally zoomed-in to emphasize the ZBCP small structure.

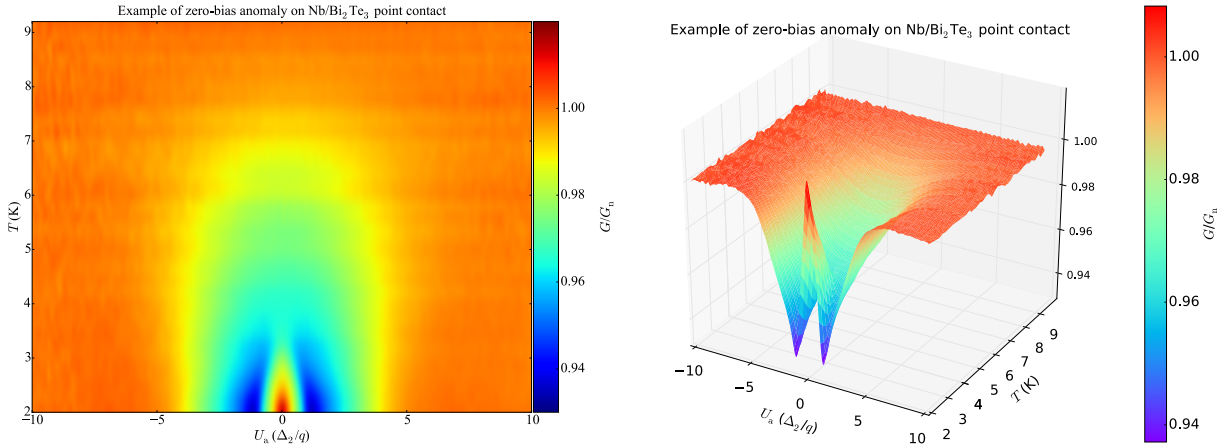

(a) Example of a zero-bias anomaly on Nb/Bi_2Te_3 (b) The same graph but from another point of view

Figure 3.28: Second example of zero-bias conductance peak observed on an Nb/Bi_2Te_3 contact.

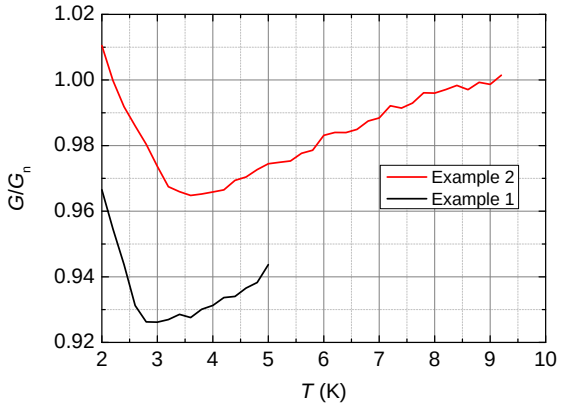

Figure 3.29: Temperature dependence of the zero-bias peak amplitude from Fig. 3.27 and Fig. 3.28.

3.7 Conclusion and outlook

Very high in-plane spin polarization of the $(Bi_{1-x}Sb_x)_2Te_3$ TI family has been determined by PCAR measurements. The extracted spin polarizations for the end compositions Bi_2Te_3 and Sb_2Te_3 are $70(4)$ % and $57(3)$ %, respectively. It has been confirmed that the PCAR effect persists up to the critical temperature of bulk Nb ($T_C \approx 9.2\,K$) and the zero-bias anomaly does not obey the BCS behaviour. The spectra are not featureless above the critical field of the Nb because of the existence of a bulk bandgap. The extracted gaps of $0.40(4)$ meV (Bi_2Te_3) and $0.28(2)$ meV (Sb_2Te_3) correlate with the determined spin polarization. When the Fermi level is finely tuned in the bulk bandgap, which is the case in the $(Bi_{0.18}Sb_{0.82})_2Te_3$ composition, the bulk carrier concentration is reduced and even higher spin polarization of $83(9)$ % is measured. The obtained values are the low limits of the intrinsic TIs spin polarization because the Nb tip induces inevitably small defects in

the sample and there is a finite probability of spin-flip scattering due to disorder at the contact area resulting in a non fully ballistic transport regime.

Additionally, the spin polarization of four TI compositions doped with magnetic Cr and V ions is investigated: $Bi_{1.97}Cr_{0.03}Te_3$, $Sb_{1.975}Cr_{0.025}Te_3$, $Bi_{1.975}V_{0.025}Te_3$ and $Sb_{1.97}V_{0.03}Te_3$. The compositions $Bi_{1.97}Cr_{0.03}Te_3$, $Sb_{1.975}Cr_{0.025}Te_3$, and $Bi_{1.975}V_{0.025}Te_3$ demonstrate no magnetic order above 2 K and have spin polarization of $52(1)$ %, $52(1)$ % and $58(5)$ %, respectively. The decrease of the spin polarization in the Cr- and V-doped TIs is attributed to the spin-flip scattering by the paramagnetic ions. Only the composition $Sb_{1.97}V_{0.03}Te_3$ is magnetic above 2 K and it has Curie temperature of $T_C = 11.6(6)$ K, extracted by AHE, and possesses the lowest spin polarization of 50 %. The further reduction in the magnetic $Sb_{1.97}V_{0.03}Te_3$ is related to the competition between the perpendicular anisotropy of the magnetic ordering and the in-plane spin polarization of pristine topological insulators.

Contact structures between superconductors and topological insulators have been gaining more and more popularity. From a fundamental perspective, it is interesting to investigate the interplay between two different spin correlations: Cooper pairing and the surface spin-locking. From application perspective, superconductors-TI junctions are investigated as hosts for quantum computing systems.

Spin polarization measurement of magnetic topological insulators in the QAHE regime at mK-temperature is a possible extension of the current methodology. The progress in the high-field PCAR with Nb-Ti (see Chapter (5)) makes PCAR measurements in variable magnetic field possible without the limitation of the relatively low upper critical field of Nb ($\mu_0 H_{c2} \approx 0.5$ T). This opens the opportunity for investigation of the magnetic TIs throughout their hysteresis loop. Finally, the gating of TIs is known to influence the bulk conductivity and, therefore, to increase the contribution of the surface states. PCAR measurements with variable gate bias could be investigated in order to confirm the correlation between the overall conductivity and the spin polarization.

Chapter 4

Spin polarization and magnetotransport properties of irradiated $Fe_{60}Al_{40}$ thin films

"Why think about this? Let's do it."

Dr. Yong Chang Lau

Crystallographic disorder in condensed matter systems is usually a state which experimental physicists avoid. However, this is not always the case. For instance, thin Si film is strained when deposited on SiGe and this results in higher carrier mobility, faster switching and reduced power consumption*. Another two examples of beneficial disorder in condensed matter systems are hard magnetic materials and high-current superconductors. Hard magnetic materials have always small concentration of secondary component. The secondary component inclusions act as magnetic domain pinning centers and this increases the coercive field and the remanent magnetization. Impurity inclusions have similar effect in high-critical-current superconductors. All high-current superconductors are type-II and the Abrikosov vortex lattice displacement results in non-zero resistance. Therefore, vortex pinning is extremely important for the technological application of type-II superconductors. For instance, α-Ti grain inclusions are known to act as vortex pinning centers in Nb-Ti superconductors[219, 218]. Similarly, natural twin boundaries in ceramic superconductors[190, 191] (like $YBa_2Cu_3O_{7-\delta}$) and metallic inclusions like Zn, Fe act as vortex pinning centers. Bombardment with heavy ions is demonstrated to improve significantly the critical current as well, because dislocations are created along the extended stopping path.

In this chapter, the focus falls on spin polarization, magnetotransport and magnetic property measurements of thin $Fe_{60}Al_{40}$ films which are irradiated with Ne^+ ions with energy $E = 30\,\mathrm{keV}$ and variable fluences. This work is done in collaboration with Dr. Rantej Bali and Dr. Ciaran Fowley from Helmholtz Centrum Dresden-Rossendorf (HZDR), Germany. All samples are deposited

*The straining is not exactly crystallographic disorder but it can be considered as non-equilibrium state.

by co-sputtering from stoichiometry Fe and Al targets on Si/SiO_2(100 nm) substrates. The thickness of the film is 40 nm and the surface of the films has thick, natural oxide ($\approx$ 5 nm). The ion irradiation is performed with the facilities of the Ion Beam Center at HZDR. All samples are annealed for one hour after the deposition (and irradiation) in a high vacuum annealing furnace (10^{-5} mbar) at 500 °C.

4.1 Modification of thin film magnetic properties by irradiation with Ne ions

The idea of magnetic properties modification by irradiation with heavy ions is historically first demonstrated on Pt-Co(0.5 nm)-Pt sandwich by Chappert *et al.*[56]. The multilayer has perpendicular magnetic anisotropy due to the induced surface anisotropy from the heavy element - Pt. The irradiation with Ne^+ ions with energy $E = 30$ keV and dose up to 2×10^{16} ions/cm^2 result in gradual modification of the magnetic properties. The magnetic anisotropy field decreases from 1.15 T in the as-deposited sample to 0.13 T in the irradiated sample with dose 10^{16} ions/cm^2 ions (see Fig. (4.1)). The latter is related to the fact that the interfaces are no longer smooth after the irradiation and this leads to reduced interface magnetic anisotropy. The perpendicular magnetic anisotropy is destroyed completely for higher fluences and the easy axis is in the plane. The coercivity decreases from 20 mT in the as-deposited sample to practically zero in the sample irradiated with dose of 10^{16} ions/cm^2. Upon irradiation with higher dose, the remnant magnetization decreases as well due to the loss of perpendicular anisotropy. Finally, it is shown that the Curie temperature decreases from above 120 °C in the as-grown to 60 °C after irradiation with 10^{16} ions/cm^2. Patterning of magnetic regions down to 1 μm is achieved. This method is proposed for patterning of perpendicular magnetic anisotropy bits which are embedded in the matrix of in-plane magnetization of the same material*.

The idea in the present chapter is similar, however, the mechanism is opposite. The $Fe_{60}Al_{40}$ thin films are paramagnetic (or weakly ferromagnetic) as-deposited. Upon irradiation, the crystallographic order is destroyed and the film is partially amorphosized. An experimental proof for the effect of irradiation on the crystal structure of $Fe_{60}Al_{40}$ is given by X-ray diffraction. The (100) superstructure peak is demonstrated to disappear upon ion irradiation (see Fig. 2 (b) in Bali *et al.*[17]). In this case, the nearest-neighbour coordination between Fe-Fe atoms increases on average and this leads to higher exchange energy and magnetic order is induced. The latter is known as local environment model[369, 329]. Before discussing in detail the so far achieved magnetic

*Presently, bit patterned recording media is not considered viable because of the large area density which is lost. Instead perpendicular anisotropy compositions are considered to be deposited on textured matrix underlayer, so that there is natural bit formation with practically no area lost between the bits.

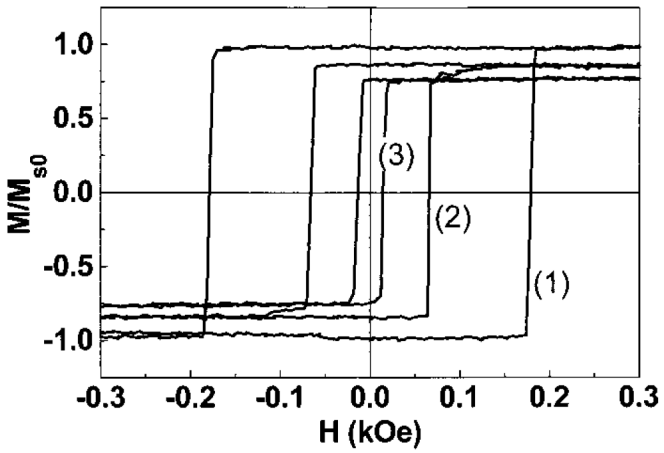

Figure 4.1: Hysteresis loop measurements of Pt-Co(0.5 nm)-Pt sandwich irradiated with different fluences. (1) - as-grown sample, (2) - sample irradiated with a dose of 3.10^{15} ions/cm^2, and (3) - sample irradiated with a dose of 10^{16} ions/cm^2. All curves are normalized with the saturation magnetization of the as-deposited sample. The data is after Chappert *et al.*[56].

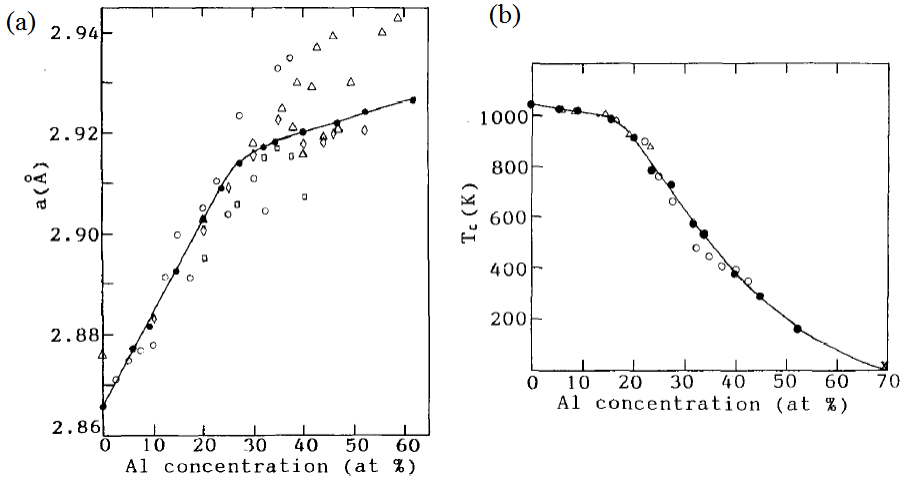

Figure 4.2: Lattice parameter (a) and Curie temperature (b) change of $Fe_{1-x}Al_x$ alloy as a function of the Al atomic concentration. The data is after Yelsukov *et al.*[399].

modification of thin films, the magnetic properties of bulk $Fe_{1-x}Al_x$ alloy are reviewed briefly. The magnetization of bulk iron-aluminum alloys decreases as x increases and the ordered composition is paramagnetic for $x > 0.32$ according to Taylor[333] and Menendez[222]. On the other hand, Yelsukov *et al.*[399] reported that the Curie temperature is higher than 4 K for compositions with $x < 0.7$. The properties of the alloy depend significantly on the preparation conditions. It is demonstrated that single phase composition samples for $x > 0.32$ is paramagnetic, however, if the composition is quenched from high temperature disorder exists and the composition exhibits ferromagnetism. The addition of Al leads to small lattice expansion. Therefore, apart from reducing Fe-Fe nearest-neighbours coordination, Al reduces the exchange interaction by increasing the Fe-Fe average interatomic distance. There is a general agreement in literature that two ranges of parameters evolution exist. For $x < 0.2$, there is smooth linear decrease of the magnetization

and the lattice parameter increases linearly at the same time (see Fig. (4.2)). The average magnetic moment of an Fe atom in the alloy follows a simple dilution model $\overline{\mu} = 2.2\mu_B\alpha(1-x)$, where α is constant. At $x \approx 0.2$, there is a kink in both characteristics. When the annealed samples are quenched from temperature up to 1000 °C, there is a plateau in the lattice constant for $0.2 < x < 0.35$, which is attributed to formation of Fe_3Al phase[333]. For higher annealing temperatures, there is no plateau but the slope of the lattice constant evolution changes with x. The magnetic configuration of the alloys in the range $0.2 < x < 0.4$ is debatable. Arrott and Sato[12] have proposed ferro-antiferromagnetic transition, however, this is not confirmed by neutron scattering experiments[269]. Vincze *et al.*[361] considers the existence of Fe_3Al super-paramagnetic clusters near the stoichiometric concentration and a reasonable agreement with the experimental data is observed. A ferro-mictomagnetic transition on cool down is proposed by Huffman *et al.* [145]. This is confirmed by Shull *et al.*[305] in Fe_3Al and FeAl and it is verified in $Fe_{0.7}Al_{0.3}$ by Cable *et al.*[48]. Shukla[304] and Grest[122] have proposed that alloys with $0.27 < x < 0.5$ are spin glasses at low temperature and this is substatiated with 4 K Mössbauer spectroscopy by Shiga *et al.*[301]. In this composition range, there is competition between the Fe-Fe ferromagnetic exchange and the Fe-Al-Fe antiferromagnetic superexchange. Bernal-Correa *et al.*[24] have investigated the magnetic and structural properties of $Fe_{60}Al_{40}$ ball milled alloys for various preparation time. The magnetization decreases from the state of separated pure Fe and Al powders towards the ordered Fe-Al alloy and then increases again when the alloys become disordered. The magnetic ordering and the hyperfine field have been investigated through Mössbauer spectroscopy in $Fe_{1-x}Al_x$ by Alcazar *et al.*[4], Huang *et al.*[73], and Schmool *et al.*[294].

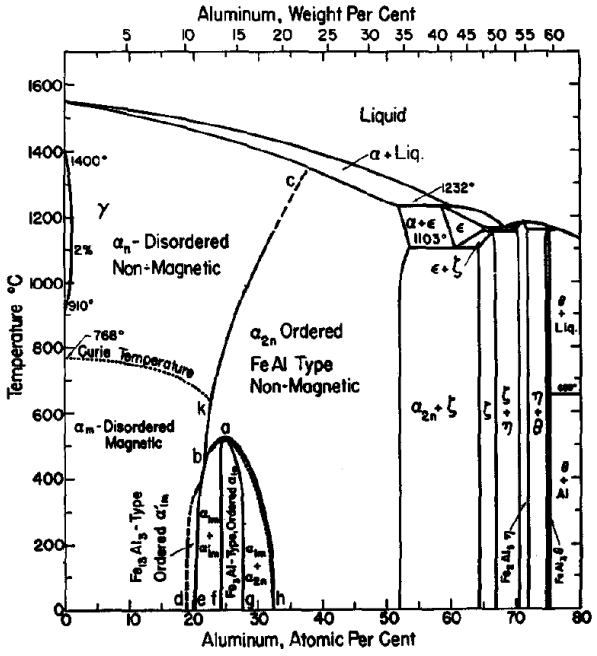

Figure 4.3: Equilibrium Fe-Al phase diagram. The graph is after Taylor *et al.*[333].

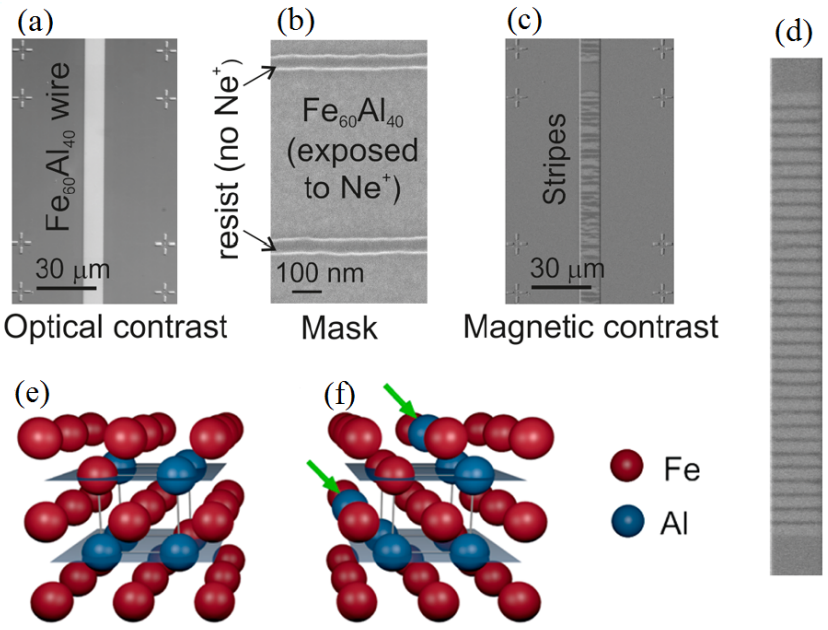

Figure 4.4: Panels (a)-(c): definition of a pristine $Fe_{60}Al_{40}$ microwire through UV lithography, resist patterning for the Ne^+ exposure, and the magnetic contrast determined by Kerr microscopy. Panel (d) - magnetic contrast determined by spin-polarized photoemission electron microscopy. Schematic representation of the B2 crystal structure of as-deposited $Fe_{60}Al_{40}$ (e) and the A2 (disordered) structure of irradiated sample (f). The substitution with Al atoms on otherwise pure Fe planes is indicated with green arrows. Graphs are after Bali *et al.*[17].

In the current investigation, the focus falls on the thin film of composition $Fe_{60}Al_{40}$ which is preferred because the equilibrium phase diagram demonstrates single phase up to the melting point for this value of Al concentration (see Fig. (4.3)). Heavy ion irradiation induced chemical disorder has similar effect to the mechanical preparation approach outlined above. The stopping power of the heavy ions results in knock-out of Fe and Al atoms from their crystallographic positions in the ordered B2 structure. This leads to destruction of the crystal structure (B2→A2) and an increase in the number of Fe-Fe nearest-neighbours number which leads to higher exchange interaction and ferromagnetic ordering. The amorphosizing effect of the irradiation is demonstrated through the disappearance of the (100) superstructure reflection[17]. The irradiation induced magnetism provides the opportunity for patterning of high resolution structure when a lithographic step is performed beforehand on the crystallographically ordered film. For instance, Bali *et al.*[17] have demonstrated sub-50 nm magnetic stripe patterning with spacers of 40 nm (see Fig.(4.4)). The irradiation is performed with Ne^{+*} at energy of 30 keV because it provides in depth homogeneous distribution of the stopping power and, therefore, the magnetic order is induced in the whole thickness of the film (see Röder *et al.*[279]). The magnetic contrast of the irradiated areas is demonstrated by Kerr microscopy and spin polarized photoemission electron microscopy (SPEEM). In principle, the proposed method provides the opportunity for patterning of planar GMR structures where the irradiated areas are the ferromagnetic electrodes and the non-exposed film region is utilized as a

*The irradiation can be performed with a He-Ne ion microscope.

non-magnetic spacer*. The main thrust behind this chapter is the analysis of the spin polarization values and the magnetic properties of the irradiated samples in order to understand whether such magnetic structures are feasible.

4.2 Spin polarization, magnetotransport and magnetometry properties of $Fe_{60}Al_{40}$

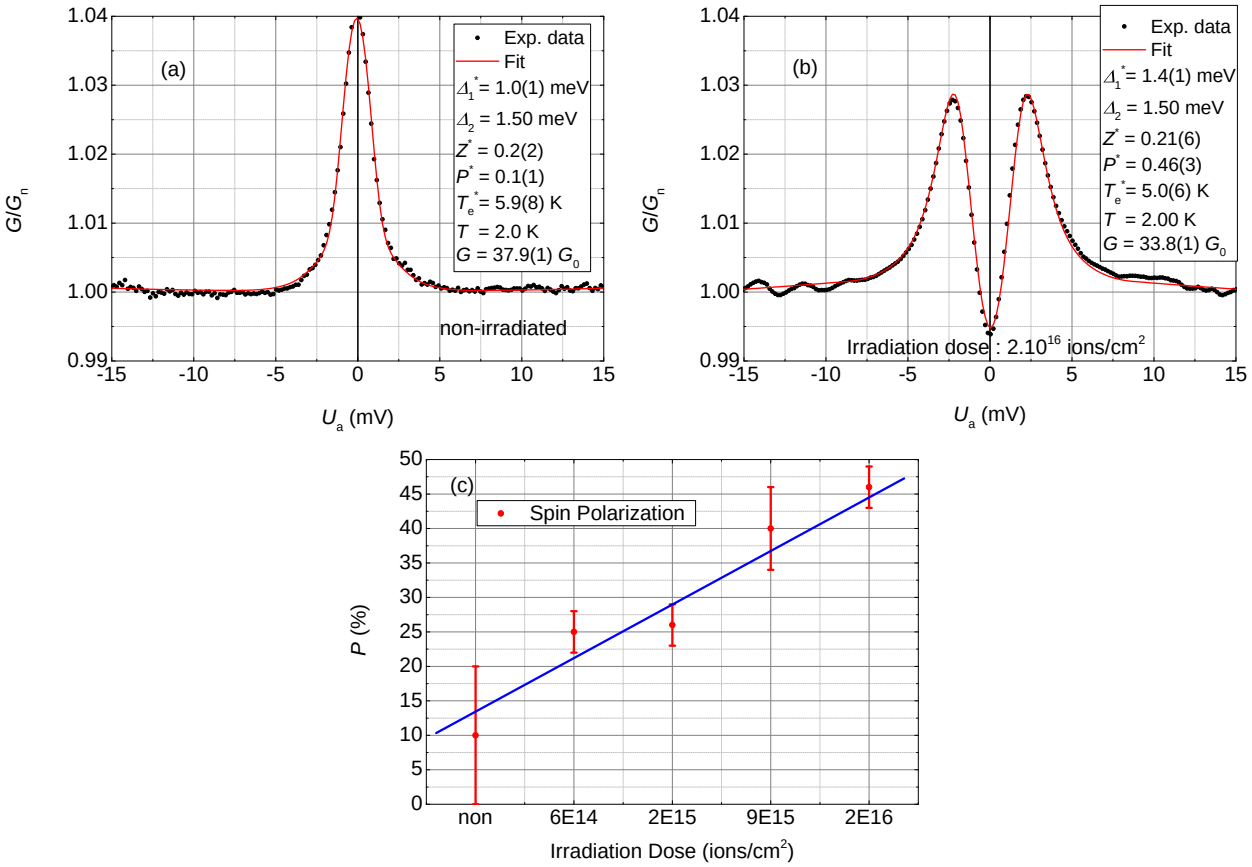

Figure 4.5: PCAR spin polarization measurements of $Fe_{60}Al_{40}$ thin films irradiated with Ne^+ ions. Panel (a): PCAR of a non-irradiated sample, which demonstrates negligible spin polarization of $P \approx 10(10)\,\%$. Panel (b): PCAR of a sample irradiated with 2.10^{16} ions/cm^2, which demonstrated the highest spin polarization of $46(3)\,\%$. Panel (c): PCAR spin polarization values of five samples irradiated with different doses. The blue interpolation line is drawn by hand.

Spin polarization measurements are performed on $Fe_{60}Al_{40}$ sample with different irradiation doses in the conventional needle(Nb)-anvil(sample) PCAR configuration. The surface oxidation layer of a sample is removed by low power Ar ion milling for 2 minutes and the pre-cleaned sample is quickly transferred to the PCAR probe stick. The spin polarization measurements are shown in Fig. (4.5). The as-deposited sample exhibits very low spin polarization of $10(10)\,\%$ which is essentially a vanishing value due to the high error. It is well established that the PCAR technique

*In this case, current perpendicular to plane GMR configuration is achieved without pillar patterning.

is not very sensitive to low spin polarization values of $P < 20\,\%$[45]. The spin polarization of the sample with the highest irradiation dose of 2.10^{16} ions/cm^2 is $P = 46(3)\,\%$. This might be considered as a surprising result because the value reaches the value of the spin polarization of bulk Fe, while the magnetization of the irradiated $Fe_{60}Al_{40}$ is demonstrated below to be approximately three times lower than the bulk Fe magnetization. This implies that the spin polarization at the Fermi level is determined by complicated (narrow) spin-split bands rather than by the overall magnetization picture. The evolution of the spin polarization with the irradiation dose is presented on Fig. (4.5 (c)). The spin polarization demonstrates steady increase as the irradiation dose increases. The spin polarization of a sample irradiated with 6.10^{14} ions/cm^2 is $P = 25(3)\,\%$, a sample irradiated with 2.10^{15} ions/cm^2 is $P = 26(3)\,\%$, a sample irradiated with 9.10^{15} ions/cm^2 is $P = 40(6)\,\%$.

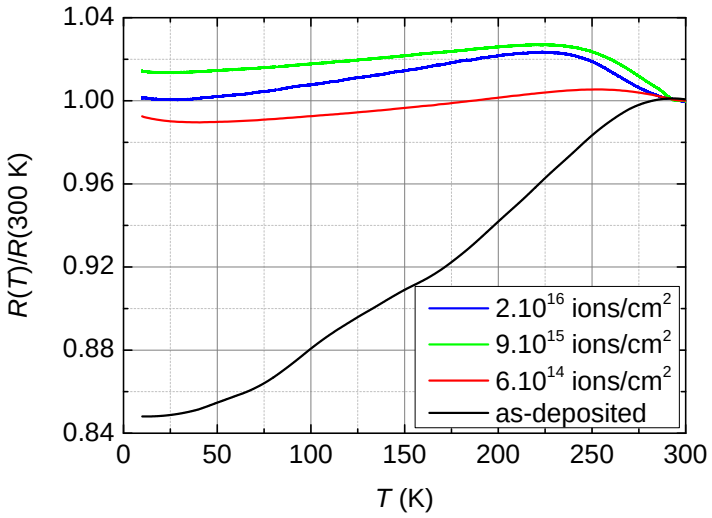

Figure 4.6: Resistance-temperature dependence of $Fe_{60}Al_{40}$ thin films irradiated with different fluences. Black curve - as-deposited sample, red curve - irradiation dose 6.10^{14} ions/cm^2, green curve - irradiation dose 9.10^{15} ions/cm^2, and blue curve - irradiation dose 2.10^{16} ions/cm^2.

The resistance temperature dependence of samples irradiated with different dose is investigated and presented in Fig. (4.6). The measurements are performed in van der Pauw configuration. First of all, the resistance of the as-deposited sample demonstrates decrease expected for a metallic sample on cool down. The residual resistance ratio at 10 K is 0.85, which is a typical value for thin films deposited by sputtering with expected significant concentration of dislocations. An important observation is that the curvature of the $R(T)$ has multiple slopes between 300 K-10 K which might implies two scenarios: either there are multiple narrow carrier pockets contributing to the transport, or there are multiple scattering mechanisms activated at different temperatures. The irradiation with even the lowest dose of 6.10^{14} ions/cm^2 changes drastically the $R(T)$ characteristics. The resistance changes within a very narrow range of $\pm 1\,\%$ with respect to its value at 300 K which shows that the irradiation induced disorder leads to destruction of the metallic density of states structure. Amorphous materials with essentially temperature independent resistance have been

used as standard resistance calibration. The resistance first increases slightly with a local maximum at approximately 250 K and then decreases. The latter indicates that multiple carrier pockets (or even phases) are involved in the electronic transport close to the Fermi level. There is a resistance minimum at approximately 40 K, which is usually attributed to Kondo effect in magnetic systems. This possibility is ruled out because the temperature position of the resistance minimum does not change its position with the application of magnetic field. The irradiation with higher fluence results in even more complicated density of states structure close to E_F. For irradiation dose of 9.10^{15} ions/cm^2, the resistance goes up on cool down with local maximum at $T \approx 225$ K and then it is decreases slightly. In this case, the resistance at the lowest measured temperature is higher than the room temperature value. Interestingly, the resistance dependence of the sample with the highest irradiation dose of 2.10^{16} ions/cm^2 exhibits behaviour which is expected for a more ordered sample than the irradiated at 9.10^{15} ions/cm^2. First of all, the increase in the resistance on cool down is less pronounced in the range $225\,\mathrm{K} < T < 300\,\mathrm{K}$, then the resistance decreases more on further cool down than is the case for irradiation dose of 9.10^{15} ions/cm^2, and finally the residual resistance ratio at the lowest temperature is approximately 1.0. This unexpected behaviour is attributed to annealing process during the irradiation process with the highest dose. The sample is heated up and this decreases to some extent the disorder and therefore the resistance behaviour looks closer to a more metallic composition. The disorder leads to partial localization of the electrons. In this case, the conduction is through variable range hopping and the resistance increases on cool down because the thermal activation energy decreases. A dated, but extensive, review of the electrical conductivity in disordered alloys is given by Mooij[240]. The behaviour of the $Ti_{1-x}Al_x$ is similar to our case and the residual resistance ratio increases as x increases and the latter becomes higher than 1 for $x > 0.33$. Localization dependent low temperature resistance upturn is observed in ultrathin Fe film[383] as well. The temperature dependence of the resistivity of a metal, $\rho(T)$, is given by:

$$\rho(T) = \rho_0 + \beta_1 T + \beta_2 T^3 + \beta_3 T^2 + \beta_4 T^{3/2} + \beta_5 \ln(T/T_0), \tag{4.1}$$

where ρ_0 is the residual low-temperature sample resistivity due to sample imperfections*, the terms $\propto T$ and $\propto T^3$ are due to electron-phonon scattering while the terms $\propto T^2$ and $\propto T^{3/2}$ are magnetic scattering related. The phonon terms contribution decreases when the crystal structure is destroyed. It is important to note that the $T^{3/2}$ represents two separate physical effects within the spin-disorder model[166, 249]: inelastic electron-magnon scattering and elastic scattering of conduction electrons from the randomly oriented temperature-dependent local moments. This term does not exist for crystalline ferromagnets whereas it is finite for amorphous ferromagnets. Finally, the term $\propto \ln(T/T_0)$ has negative factor in front and is due to localization of electrons[205]. Fischer

*In high quality single crystals, the ratio $\rho(4\,\mathrm{K})/\rho(295\,\mathrm{K})$ can reach $\sim 10^{-5}$[87].

has proposed an alternative formula for the electrical resistivity of spin glasses : $\rho(T) = AT^2 - BT^{5/2}$[97]. Kondo effect term is not considered here but it contains a term $\propto \ln(\mu/T)$ and it has resistivity minimum at low temperature[178].

The $R(T)$ dependence of the irradiated samples can be explained in a different way if coexistence of two disordered phases is considered. Apart from the general disordering effect of the Ne^+ irradiation, the stopping of the ions creates extended, columnar dislocations in the depth of the film. These cracks provide path which might facilitate oxidation of not only the interface but along the dislocations in the depth of the film. In this case, the film can be considered as disordered $Fe_{60}Al_{40}$ and disordered Fe-Al-O. The last oxide compositions are expected to be non-stoichiometric, however, FeO_x and AlO_x exhibit insulating or semiconducting behaviour[132]. Therefore, the $R(T)$ of the irradiated $Fe_{60}Al_{40}$ can be considered as a superposition of two contributions: a metallic one which drives the resistance down and a disordered oxide which drives the resistance up upon cool down. The proposed scenario can explain the $R(T)$ with resistance maximum at $T \approx 250\,\mathrm{K}$ and resistance minimum at $T \approx 50\,\mathrm{K}$.

Anomalous Hall effect (AHE) at various temperature of two samples irradiated with dose of 6.10^{14} ions/cm^2 and 2.10^{16} ions/cm^2, respectively, is presented in Fig. (4.7). The measurements are done in the van der Pauw geometry and there is always small longitudinal resistance contribution*. In order to determine only the AHE part of the signal, the raw data is antisymmetrized and the corrected version is obtained as follows:

$$\mathrm{AHE}(\mu_0 H) = \frac{1}{2}\left(R_{\mathrm{xy}}(\mu_0 H) - R_{\mathrm{xy}}(-\mu_0 H)\right). \tag{4.2}$$

The magnetic field is applied perpendicular to the plane of the film, and therefore perpendicular to the easy-axis. There is essentially no coercivity in the data, and therefore, the easy direction is completely in the plane. The AHE signal is normalized with the longitudinal resistance and the spontaneous Hall angle (SHA) is obtained in this way. The AHE contains both signal due to the magnetization and due to the usual Hall effect. Once the magnetization is fully driven out of the plane†, the AHE should demonstrate straight line which is due to the carrier concentration. The focus fall first on the sample with the lower irradiation dose - panel (a). The AHE signals at temperatures 10 K, 50 K, 100 K and 200 K are essentially indistinguishable. The initial slope up to $\approx 1.2\,\mathrm{T}$ is due mainly to the anisotropy field of the film. Beyond that, there are two contributing effect: small paramagnetic related rotation and linear slope due to the carrier concentration. The small paramagnetic signal is typical for a sample with low irradiation dose which has low magnetization and the change in carrier concentration with temperature is expected as well from the $R(T)$ characteristics[404, 202]. On the other hand, the sample with the highest irradiation dose

*It is magnetoresistance in this case

†For applied magnetic field higher than the anisotropy field

does not exhibit significant quadratic high field AHE signal. The latter is attributed to the higher magnetization and the higher exchange energy*. More interesting is the change in linear slope of the AHE. The fact that slope decreases at lower temperatures is a prove of carrier depletion due to localization of carriers or due to fuzzy density of states structure around the Fermi level. However, the observation that the slope changes to negative at 10 K is even more peculiar. One possibility is change of the carrier type from electrons to holes, however, this is unlikely the case. Since the effect is rather small, the change in the slope is attributed to change of the carrier localization by the magnetic field.

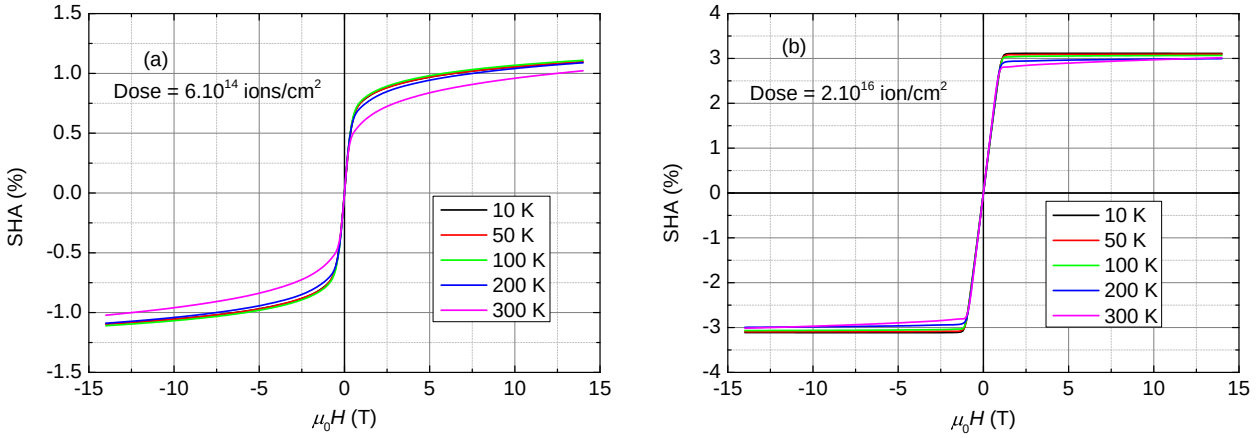

Figure 4.7: Anomalous Hall effect loop at variable temperature for two sample irradiated at doses 6.10^{14} ions/cm^2 (a) and 2.10^{16} ions/cm^2 (b), respectively.

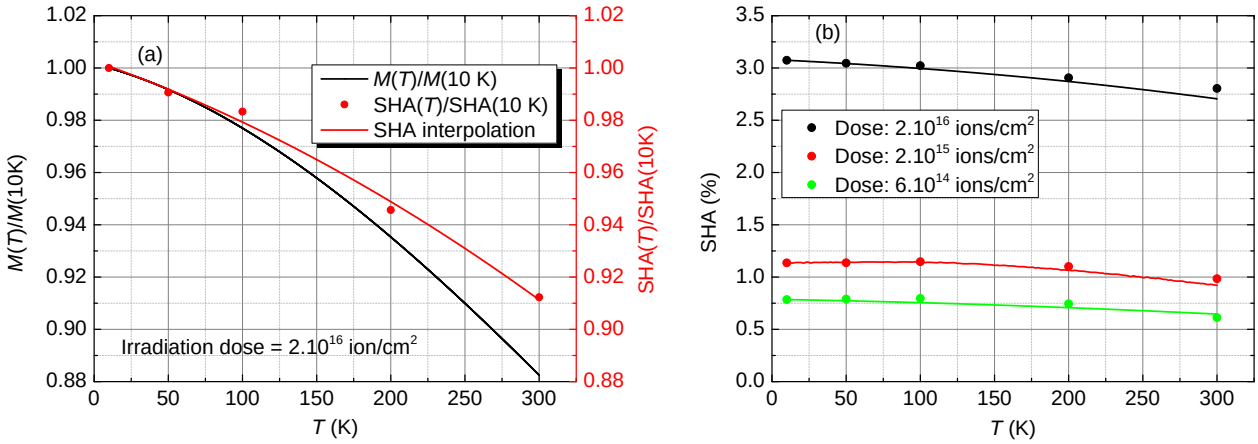

Figure 4.8: Panel (a): comparison between the spontaneous Hall angle and the magnetization temperature dependence of a sample irradiated wit a dose of 2.10^{16} ions/cm^2. The temperature evolution of the spontaneous Hall angle (red curve) is approximated with a quadratic function. Panel (b): comparison between the spontaneous Hall angle at various temperatures of three samples irradiated at different doses of 2.10^{16} ions/cm^2, 2.10^{15} ions/cm^2, and 6.10^{14} ions/cm^2, respectively. The temperature dependence of the magnetization of each sample is given with a solid line. The magnetization is normalized to the SHA value at 10 K for comparison purposes.

Comparison between the spontaneous Hall angle temperature evolution and the magnetiza-

*This is demonstrated below in terms of the Curie temperature in Fig. (4.10).

tion temperature dependence of a sample irradiated with a dose of 2.10^{16} ions/cm^2 is presented in Fig. (4.8) (a). It is observed that the spontaneous Hall angle has slightly different temperature dependence than the magnetization temperature decrease. The spontaneous Hall angle amplitude is determined at applied magnetic field of $\mu_0 H = 1.2\,\mathrm{T}$ in order to avoid the high-field non-linear background, the $M(T)$ is obtained at the same applied field. The dependence between the magnetization and the anomalous Hall effect in various ferromagnetic materials have attracted significant attention, however, there is no universal functional dependence. It has been demonstrated for the 3*d* ferromagnetic metals that the anomalous Hall effect is approximately proportional to the perpendicular component of the magnetization[273]. On the other hand, investigation by Thiygarajah *et al.*[340] on the very low moment ferrimagnet Mn_2Ru_x Ga has demonstrated that the spontaneous Hall angle is high and constant in a broad temperature range irrespective of the size of the magnetization. The latter is taken as an indication that the Fermi level transport properties are not determined by the overall magnetization. Similar should be the situation in the irradiated $Fe_{60}Al_{40}$ samples. The spin polarization is probably determined by complicated spin-split structure of the density of states. The SHA is defined as the ratio between the Hall conductance, σ_{xy}, and the longitudinal conductance, σ_{xx}:

$$\mathrm{SHA} = \arctan\left(\frac{\sigma_{xy}}{\sigma_{xx}}\right), \tag{4.3}$$

because $\sigma_{xy} \ll \sigma_{xx}$, $\mathrm{SHA} = (\sigma_{xy}/\sigma_{xx})$. Where the resistivity $\hat{\boldsymbol{\rho}}$ and the conductivity tensors $\hat{\boldsymbol{\sigma}}$ abide by Ohm's law between the current density, $\vec{j}$, and the applied electric field, $\vec{E}$: $\vec{j} = \hat{\boldsymbol{\sigma}}.\vec{E}$ and $\hat{\boldsymbol{\rho}}.\vec{j} = \vec{E}$. It can be demonstrated by matrix inversion that:

$$\rho_{xx} = \frac{\sigma_{xx}}{\sigma_{xx}^2 + \sigma_{xy}^2}, \quad \rho_{xy} = \frac{\sigma_{xy}}{\sigma_{xx}^2 + \sigma_{xy}^2}, \tag{4.4}$$

therefore $\sigma_{xy}/\sigma_{xx} = \rho_{xy}/\rho_{xx}$. In Fig. (4.8) (b), the temperature dependence of the spontaneous Hall angle (SHA) of three samples irradiated at different doses is presented. The sample irradiated at the highest dose of 2.10^{16} ions/cm^2 has spontaneous Hall angle of $\approx 3\,\%$ which is much higher compared with the SHA observed in high-quality Fe, Ni thin film [77] (0.2 %-0.3 %), but is comparable to the value of 2.3 % reported in amorphous $Co_{40}Fe_{40}B_{20}$[323]. The SHA is shown to scale with the irradiation dose and the sample irradiated with doses of 2.10^{15} ions/cm^2 and 6.10^{14} ions/cm^2 exhibit SHA of 1.2 % and 0.8 %, respectively. The last values are still higher than the SHA in pure 3*d* ferromagnetic films and signify the importance of disorder on the anomalous Hall effect magnitude. It is very important to point out that the temperature dependencies of the SHA and the magnetization are essentially the same for the lower irradiation doses (see the green and red curve in Fig. (4.8) (b)). The anomalous Hall effect is considered to depend on three mechanisms:

intrinsic, skew scattering and side jump*. Karplus and Luttinger theory predicts that spin-orbit interaction and interband mixing lead to carrier drift perpendicular to the applied electric field which gives a $\rho_{int} \propto \rho_{xx}^2$ contribution[162]. On the other hand, the skew scattering at impurities is predicted to scale as $\rho_{sk} \propto \rho_{xx}$[312]. Finally, the side jump mechanism, proposed by Berger, scales as $\rho_{sj} \propto \rho_{xx}^2$[20]. The distinction between the extrinsic and the intrinsic contributions is not straightforward due to the same functional dependence of ρ_{int} and ρ_{sj}. It has been generally accepted that the anomalous Hall effect dependence is $\rho_{xy} = a\rho_{xx} + b\rho_{xx}^2$, although different scaling has been reported for different samples: $b\rho_{xx}^2$ (for Fe)[150], $a\rho_{xx}$ (ultrapure Ni at low temperature)[95], $a\rho_{xx} + b\rho_{xx}^2$ (for Co)[404], and $b\rho_{xx}^{\alpha}$ (for Ni)[195], where $1 < \alpha < 2$. Another general scaling relation is proposed by Tian *et al.*[341]:

$$\rho_{xy} = (\alpha\rho_{xx0} + \beta\rho_{xx0}^2) + b\rho_{xx}^2, \tag{4.5}$$

where ρ_{xx0} is the residual low temperature resistivity.

The SQUID magnetometry of four samples with different irradiation doses is presented in Fig. (4.9). Panel (a) demonstrates the hysteresis loops obtained at $T = 4\,\mathrm{K}$ with magnetic field applied perpendicular to the plane of the film, *i.e.* along the hard direction. The saturation magnetization of the irradiated samples is demonstrated to increase gradually with the irradiation dose. For instance, the M_s is $630\,\mathrm{kA\,m^{-1}}$ for the sample irradiated with the lowest dose of 6.10^{14} ions/cm^2, and the M_s is $800\,\mathrm{kA\,m^{-1}}$ for the sample irradiated with the highest dose of 2.10^{16} ions/cm^2. The latter is significantly lower than the saturation magnetization of bcc Fe ($M_s \approx 1.7\,\mathrm{MA\,m^{-1}}$). From hysteresis loops along the hard direction, the anisotropy field of the sample can be determined as the field where the magnetization reaches its saturation value: $\mu_0 H_{an} \approx 1.0\,\mathrm{T}$ for the different irradiation doses. The effective anisotropy constant, K_{eff}, can be estimated following the Stoner-Wohlfarth model: $K_{eff} = (\mu_0 H_{an} M_s)/2$. For the highest dose, $K_{eff} = 800\,\mathrm{kJ\,m^{-3}}$. The anisotropy constant, K_{eff}, is the sum of the magnetocrystalline anisotropy, K_1, and the demagnetizing energy: $K_{eff} = K_1 + \frac{1}{4}\mu_0 M_s^2(1-3N)$, where N is the demagnetizing factor for the sample along the applied field direction†. Another approach to extract the magnetocrystalline anisotropy of the irradiated thin films is to determine the internal anisotropy field after correcting for the demagnetizing field. This approach is followed here. The value of the extracted applied anisotropy field is $\mu_0 H_{an} = 1.0\,\mathrm{T}$ or $H_{an} = 795.8\,\mathrm{kA\,m^{-1}}$. The internal anisotropy when corrected for the demagnetizing field is $(H_{an})_{int} = H_{an} - NM_s$. The internal anisotropy field for the highest irradiation dose is: $(H_{an})_{int} = 795.8\,\mathrm{kA\,m^{-1}} - 1 * 800\,\mathrm{kA\,m^{-1}} \approx -4\,\mathrm{kA\,m^{-1}}$. After this calculation, the internal anisotropy field is used in the Stoner-Wohlfarth model to extract the magnetocrystalline anisotropy

*The latter two effects are from extrinsic nature and are considered to happen at impurities or sample crystallographic defects.

†For thin film, $N = 0$ in the plane of the film and $N = 1$ perpendicular to the plane of the film.

($K_1 = (\mu_0(H_{an})_{int}M_s)/2$) and $K_1 \approx -2\,\mathrm{kJ\,m^{-3}}$. The magnetocrystalline anisotropy is very small and this is expected for an essentially amorphous composition with no crystal structure.

On panel (b), the normalized $M(T)$ dependence for the same four samples in applied magnetic field of $\mu_0 H = 1.2\,\mathrm{T}$, just above the anisotropy field, is presented. The magnetization decreases slower for the sample irradiated with the highest dose and this implies that the Curie temperature and the dose are directly related as well. While the sample with the highest irradiation dose is clearly distinguished, the temperature dependencies of the others have intersecting curves.

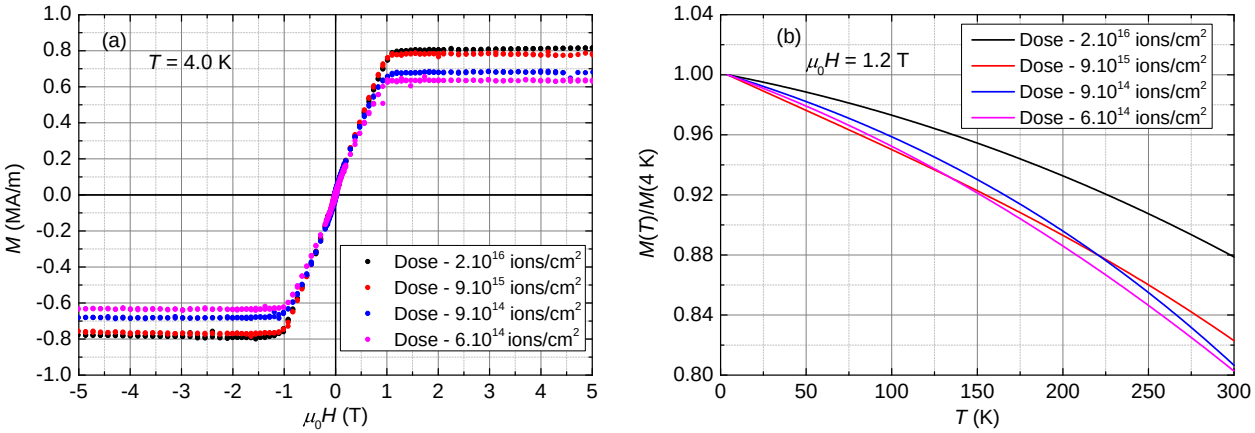

Figure 4.9: Magnetization measurements of four $Fe_{60}Al_{40}$ thin films irradiated with different doses. Panel (a) - hysteresis loops obtained at $T = 4\,\mathrm{K}$ in magnetic field range $\mu_0 H = \pm 5\,\mathrm{T}$. Panel (b) - $M(T)$ scans of the four sample in temperature range 4 K-300 K in applied magnetic field of $\mu_0 H = 1.2\,\mathrm{T}$. The magnetic field is applied perpendicular to the plane of the films for both measurements.

The Curie temperature measurements of a few samples irradiated with different doses is presented in Fig. (4.10). The experiments are performed with the SQUID oven option which is described in Sec. (2.8). All temperature scans are done under applied magnetic of field of $\mu_0 H = 1.2\,\mathrm{T}$ and this explains the rather broad phase transition. The point of maximum magnetization decrease is determined ($\mathrm{d}M/\mathrm{d}T$) and then a linear fit is taken in a narrow temperature interval $\Delta T = \pm 20\,\mathrm{K}$ around the point of maximum slope. In this way, the Curie temperatures are extracted. There is always some small residual moment after the magnetization flattens out above the Curie temperature due to the paramagnetic signal from the Al sample holder. The highest Curie temperature of 620 K is obtained on the sample irradiated with the highest dose of 2.10^{16} ions/cm^2. The Curie temperature decreases to 560 K for irradiation dose of 9.10^{15} ions/cm^2. Finally, the Curie temperature of 505 K is measured on a sample irradiated with fluence of 9.10^{14} ions/cm^2. The Curie temperature increases with the irradiation dose which is expected because the disorder increases the Fe-Fe nearest neighbours coordination and hence the exchange energy[369, 329]. Samples with lower irradiation dose are measured as well, however, due to the low moment of the samples and the background from the Al sample holder foil, reliable extraction of the Curie temperature is not possible.

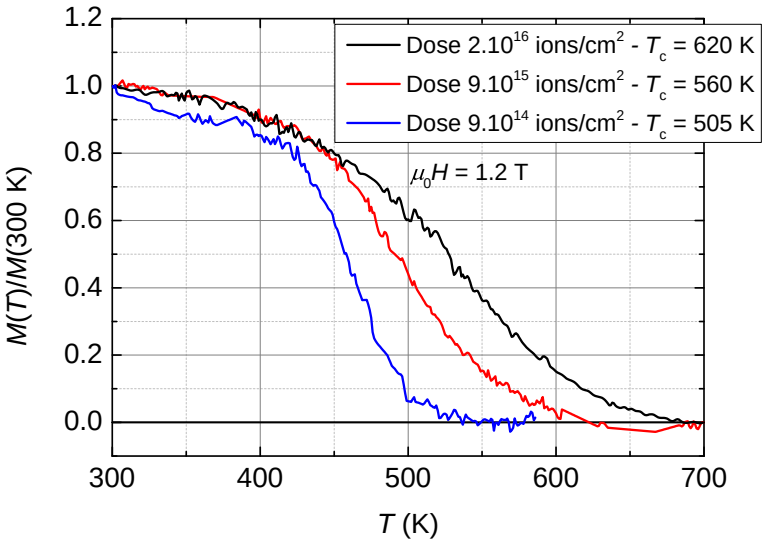

Figure 4.10: SQUID oven magnetometry measurements of the Curie temperature of three $Fe_{60}Al_{40}$ samples irradiated with different doses. The magnetization of each sample is normalized with its magnetization at $T = 300\,\mathrm{K}$. The applied magnetic field is $\mu_0 H = 1.2\,\mathrm{T}$.

4.3 Conclusion and outlook

High spin polarization of 46(3) % is measured in $Fe_{60}Al_{40}$ thin film which is irradiated with Ne^+ ions with fluence of 2.10^{16} ions/cm^2. This value is essentially equal to the spin polarization of bulk Fe and, therefore, it is expected that the spin polarization is saturated. As anticipated, there is positive correlation between the spin polarization and the irradiation dose. The electrical measurements demonstrate that the irradiation makes the sample amorphous and the latter leads to increased residual resistance ratios. The observed different curvatures in the $R_{xx}(T)$ on cool down give evidence that there are at least two different scattering mechanisms involved. The magnetotransport of the samples shows high spontaneous Hall angle of 3 %. The latter scales up with the irradiation dose. The very high Hall angle should be further investigated as well as its temperature dependence. The temperature evolution of the anomalous Hall effect is shown to be different from the magnetization temperature dependence and, therefore, the Fermi level spin polarization is governed by complicated band structure rather than by the overall magnetization. Finally, the Curie temperature is demonstrated to scale up with the irradiation dose and reaches 620 K for the highest irradiation dose of 2.10^{16} ions/cm^2.

Future investigation directions on these samples are scanning tunneling spectroscopy, spin-polarized scanning tunneling spectroscopy, magnetotransport measurements on Hall bars, Curie temperature of samples irradiated with even higher doses and reproducibility tests. Scanning tunneling spectroscopy has the capability to unravel the peculiar density of states structure close to the Fermi level. If the latter is performed is performed with spin polarized tip a further insight can be gained in the spin-split structure of the density of states and in the energy dependence of the spin

polarization. It is advisable to investigate the anomalous Hall effect amplitude on patterned Hall bars in order to study in greater detail the temperature dependence of the spontaneous Hall angle and its relation to the magnetization. The Curie temperature increase is expected to saturate and to stay constant above some threshold irradiation dose which must be determined by further investigations. The reproducibility of the irradiation procedure must be tested, *i.e.* if samples are subjected to the same irradiation procedure do they exhibit the same magnetic properties afterwards. Finally, the spin diffusion length, λ_s, in the pristine $Fe_{60}Al_{40}$ layer has to be estimated in order to understand whether it can be used as a metallic spacer in GMR structures*.

*The general expectation is that λ_s is short due to spin scattering from Fe or from secondary Fe-Al phase which is slightly ferromagnetic.

Chapter 5

High-field Andreev reflection

"Oh, my God! Your knowledge of Star Wars is very limited."

Dr. Davide Betto

5.1 Introduction and importance

Andreev reflection has established itself as one of the most straightforward techniques for swift spin polarization measurements of new potential magnetic materials for application in spin electronic devices. One shortfall of the technique is the lack of spin polarization sign resolution. The spin-polarized tunneling (the other superconductor-based spin polarization measurement technique) relies on the Zeeman-split quasiparticle density of states for spin-polarization measurements and sign extraction. The resolution of the Zeeman splitting depends significantly on the spin-orbit interaction in the superconductor and the orientation of the applied field with respect to the plane of the superconducting film. Therefore, the spin-polarized tunneling (SPT) spectroscopy has been mainly limited to measurements with ultrathin superconducting Al films at temperatures of $\approx$ 300 mK. Furthermore, tunnel junctions have to be patterned, which provides additional experimental complication. The spin-polarized tunneling is as well very dependent on the quality of the oxide barrier. For instance, the initial spin polarization of NiFe is estimated to be 32 %[226] and it has improved later to 48 %[238] with enhanced device quality. Attempts to extend the technique towards higher temperatures have been made by Yang *et al.*[394]. They have demonstrated successfully subtle features of Zeeman splitting in SPT experiments with NbN at temperature of 1.2 K*. NbN has spin-orbit interaction stronger than Al, but weaker than Nb, and that makes it a suitable superconductor for the purpose. The necessity for ^{3}He cryostat is eliminated with this

*Interestingly, they demonstrate spin resolution with Nb as well although at $T = 250$ mK.

material choice. Recently, very clear Zeeman splitting has been demonstrates in scanning tunneling spectroscopy with V at mK temperatures by Eltschka *et al.*[89]. The experimental configuration is complicated in that case due to the necessity for pristine surface quality and low temperature*.

PCAR provides, at least in principle, determination of the direct Fermi level spin polarization unmasked by tunneling probability or oxide quality†. It is our aim to perform high-field Andreev reflection in order to extract the spin polarization sign in a more accessible experimental configuration. In order to do that, high-field type-II superconductor are used in wire and thin film form. Since the spin-orbit interaction depends on the atomic number ($\propto Z^4$), superconductors with low Z are chosen: Nb-Ti and MgB_2. Since these are type II superconductors, the existence of vortex lattice and the accompanying (possible) flux flow means that the PCAR spectral structure might be significantly time-dependent due to trapping and release of vortices.

5.2 Theoretical analysis

Observation of Zeeman-splitting in Andreev reflection at $T = 2\,\mathrm{K}$ has two important difficulties related to the thermal smearing and the nature of the Andreev process. The Zeeman splitting results in $\approx 2\mu_\mathrm{B}\mu_0 H$ energy separation of the superconducting quasiparticle density of states in ideal free-electron approximation at very low temperature. The Fermi level thermal smearing can be approximated with a Gaussian with full width at half maximum of $\approx 3.8 k_\mathrm{B} T$[318]. Because the Boltzmann constant and Bohr magneton have very similar values‡, the thermal energy tends to smear out the Zeeman splitting and this leads to less distinguishable effect at elevated temperature. A simulation is presented of the detrimental effect of the thermal smearing in Fig. (5.1). A superconductor with a gap of $\Delta = 1.5\,\mathrm{meV}$ is assumed and the gap does not change with the temperature while the latter is varied in the range $T = 0.3\,\mathrm{K} - 4\,\mathrm{K}$, and the magnetic field is set at $\mu_0 H = 5\,\mathrm{T}$. The simulation is performed in pure tunneling regime§ with no correction related to spin-orbit interaction or magnetic field depairing effect and the spin polarization is $P = 50\,\%$. The detrimental effect of the temperature smearing on the Zeeman-splitting is apparent. The effective splitting energy decreases as the temperature increases because the peak structure of the DOS is rounded off. The sharp spikes are smeared to broad local extrema in the range $T = 0.3\,\mathrm{K} - 1.5\,\mathrm{K}$, then the four peak structure is further suppressed and is practically indistinguishable as four separate peaks at temperature of 2 K. The Zeeman splitting is still evident as asymmetry in the spectral lineshape at

*There are only a handful of systems in the world which possess deposition chamber connected *in-situ* to a mK STM with high magnetic field.

†Diffusive transport averaging in the contact area leads to decreased value of the spin polarization.

‡The Bohr magneton is $\mu_\mathrm{B} = 5.7883818066(38) \times 10^{-2}\ \mathrm{meV\,T^{-1}}$ and the Boltzmann constant is $\mu_\mathrm{B} = 8.6173324(78) \times 10^{-2}\ \mathrm{meV\,K^{-1}}$, therefore for same values of field in tesla and temperature in kelvin, the Zeeman splitting and thermal excitation energy are comparable

§Tedrow-Meservey type

$T = 4\,\mathrm{K}$ ($G(U_\mathrm{a}) \neq G(-U_\mathrm{a})$). This idealized example sets a rough limit for the temperature at which the Zeeman effect related asymmetry is still observable*.

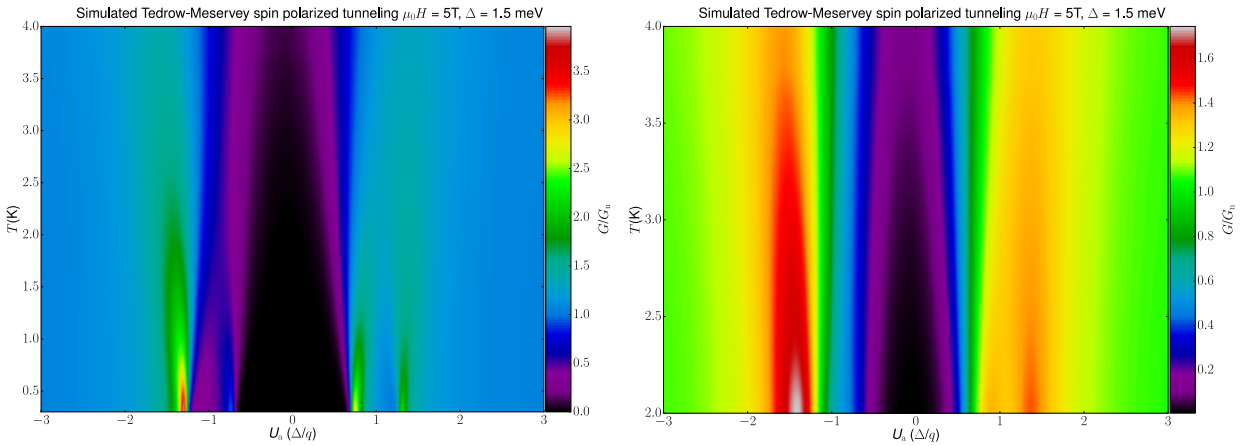

(a) Temperature range 0.3 K-4.0 K.

(b) Temperature range 2.0 K-4.0 K.

Figure 5.1: Simulated Tedrow-Meservey spin polarized tunneling for an ideal superconductor with $\Delta = 1.5\,\mathrm{meV}$. The applied magnetic field is $\mu_0 H = 5\,\mathrm{T}$ and the spin polarization is $P = 50\,\%$.

A further complication arises from the nature of the Andreev reflection process. As it is discussed in Chap. 1, the tunneling can be considered as an extreme case of Andreev reflection for $Z \to \infty$ and the Andreev reflection process is completely forbidden in this situation. For the usual experimental range of barrier strength ($0.1 < Z < 0.6$), the spectral signal at subgap voltages is non-negligible part of the normalized conductance, G_n. This means that the Andreev reflection itself decreases the apparent Zeeman splitting since the peak structure is observed as sub-gap contribution. The effect of magnetic field in the Andreev reflection is introduced as a correction towards the coherence factors u_0 and v_0, and, therefore, this time the Andreev reflection process is considered to happen between the ferromagnetic exchange-split DOS and Zeeman-split superconducting DOS. The theory modification is given by Melin[220] and Ren *et al.*[276]. In this case, the spin dependent coherence factors are

$$u^2_{\uparrow,(\downarrow)} = 1 - v^2_{\uparrow,(\downarrow)} = \frac{1}{2}\left(1 + \frac{\sqrt{(E \pm \mu_\mathrm{B}\mu_0 H)^2 - \Delta^2}}{|E \pm \mu_\mathrm{B}\mu_0 H|}\right). \tag{5.1}$$

The Andreev reflection is still a single electron-Cooper pair conversion at the interface, however, this time there are two separate processes towards the spin-up and spin-down quasiparticle density of states of the superconductor. Therefore, the PCAR signal is calculated in the usual fashion, however, the two transfer processes are now offset in energy due to Zeeman energy term. The

*Higher field leads to higher Zeeman splitting, however, the orbital depairing effect scales as $\propto H$(field applied perpendicular to plane, which is the preferred orientation in our setup) or $\propto H^2$ (field applied in-plane). This is given by Eq. (1.99).

Zeeman-split PCAR signal is then:

$$G_Z = \frac{1+P}{2} G_\uparrow + \frac{1-P}{2} G_\downarrow, \tag{5.2}$$

where the two conductances $G_{\uparrow(\downarrow)}$ are calculated with the respective coherence factors. A few graphs are generated in order to demonstrate that the Zeeman-split Andreev reflection process is less resolvable than the spin polarized tunneling. The case of PCAR of an unpolarized metal with a fully transparent contact in magnetic field of $\mu_0 H = 5\,\mathrm{T}$ and temperature $T = 2.0\,\mathrm{K}$ is presented in Fig. (5.2). The PCAR signal due to two spin sub-bands in the superconductor is plotted in panel (a). Since the assumed spin polarization is zero, the spin-up and the spin-down contributions are equal and no asymmetry in bias should be observed. The Zeeman-split PCAR signal has different lineshape compared with the PCAR simulated spectrum without magnetic field because the Zeeman energy term shifts the contribution of the spin sub-bands towards higher bias. Such slight variation in the curve is unresolvable in real experimental situation and can easily be accounted by free fitting parameters used in literature like effective temperature(T_{eff})[38], superconducting gap (Δ)[45] or Dynes parameter(Γ)[85, 244].

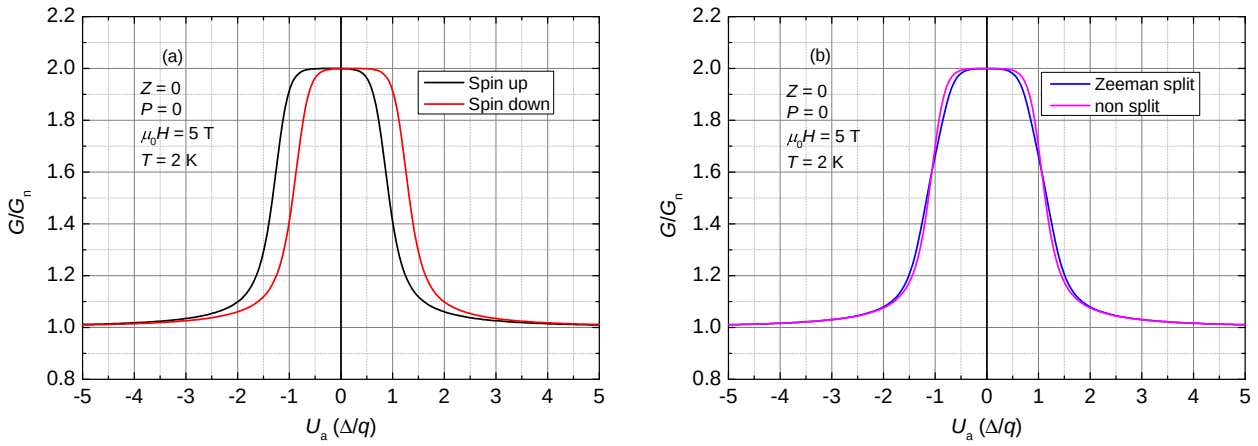

Figure 5.2: Simulated Zeeman-split PCAR with $Z = 0.0$, $P = 0.0$, $\mu_0 H = 5\,\mathrm{T}$. Panel(a) - PCAR process towards the spin-up and spin- down density of states, respectively. Panel(b) - comparison between PCAR in magnetic field and without magnetic field.

The more important and experimentally often observed situation of spin polarization of 50 % and modest barrier strength of $Z = 0.5$ in the same magnetic field and temperature is demonstrated in Fig. (5.3). In this case, the Zeeman splitting becomes apparent as asymmetry, however, clear four-peak structure can not be distinguished due to the thermal broadening. The conductance bias asymmetry is determined in order to gain insight into the maximum observable effect. The conductance asymmetry peaks at around 20 % under such conditions* but the applied bias position

*It is clarified below but the correction due to Abrikosov vortex shunting results in approximately 1/3 of this value in superconductors like Nb-Ti.

of this extremum is very important. The maximum asymmetry occurs at subgap bias, where usually peaks 2 and 3 are located in the classical spin polarized tunneling (see Fig. (1.24) in Chapter (1)). This peaks can not be distinguished here but the change in the lineshape is most dramatic at their positions. On the other hand, the pronounced peak structure* observed around the gap biases results in a smaller asymmetry with opposite sign. Therefore, the most important experimental range for high field PCAR study is $|U_a| < 2.0\Delta/q$, where Δ is the bulk superconducting gap. The comparison between the PCAR curve without applied field and with applied field demonstrates that the Zeeman-split signal is broader along the bias axes which, as is intuitively expected due to energy offset of the Zeeman-split spin sub-bands. It is only proper to establish an experimental fingerprint for Zeeman-split Andreev reflection: that is the observation of pronounced asymmetry at sub-gap bias, followed by a much smaller asymmetry† with opposite sign at bias slightly above the gap values. Since thermal smearing has non-negligible detrimental effect and clear four peak splitting is not evident, the above indication is very suitable for real measurements.

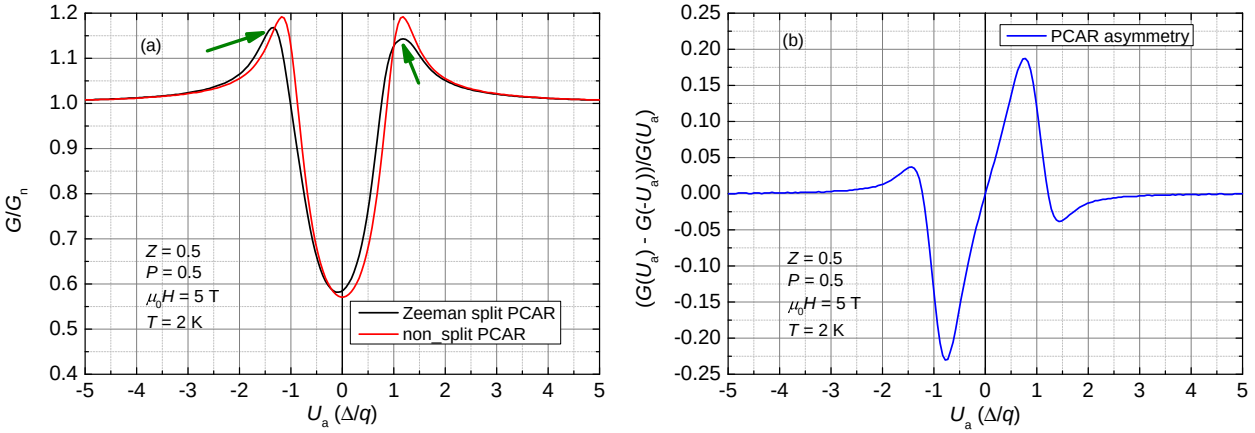

Figure 5.3: Simulated Zeeman-split PCAR with $Z = 0.0$, $P = 0.5$, $\mu_0 H = 5$T. Panel(a) - PCAR process towards the spin-up and spin- down density of states, respectively. Panel(b) - comparison between PCAR in magnetic field and without magnetic field.

The gap is assumed to be constant with the applied magnetic field and the shunting contribution from the Abrikosov vortices is not taken into account for the simulated Zeeman-split Andreev reflection considered above. It has been computationally verified that the above Zeeman-split PCAR model is reduced to the spin-polarized tunneling case[225, 336, 226] for $Z \gg 1$. The spin-orbit interaction and the orbital depairing can be introduced the same way as in the Maki-Fulde theory. Andreev reflection related conductance asymmetry is observed in Al/EuS by Ren *et al.*[276]. PCAR asymmetry and spin polarization sign extraction has been demonstrated as well on Er by Stamenov[316].

The focus falls now on the effect of the magnetic field on the overall PCAR spectral structure.

*Indicated with dark green arrows in Fig. (5.3) (a).

†The below-gap asymmetry is approximately -4 times bigger than the above-gap asymmetry in this particular case.

Experiments with high-field type-II superconductors are performed above the lower critical field, H_{c1}. Therefore, there are four important complications in the data analysis:

- Existence of normal transport through the cores of the Abrikosov vortices
- Modification of the superconducting quasiparticle density of states
- Temporal variation of the PCAR spectra due to dynamics of the flux lattice
- Vortex density of states

The simplest approach towards treatment of superconducting vortices is presented by Miyoshi *et al.*[230]. In their, approach the vortices are treated as rigid rectangular structures. Hence, the superconducting order parameter (Δ) has two values:

$$\Delta = \begin{cases} 0, & \text{within the vortex ,} \\ \Delta_0, & \text{outside of the vortex ,} \end{cases} \tag{5.3}$$

where Δ_0 is the bulk equilibrium superconducting gap. Therefore, the cores act as normal conductance channels which do not contribute towards the Andreev reflection. In this case, the overall conductance through the channel is

$$G = (1-h)G_{ns} + hG_{nn}, \tag{5.4}$$

where G_{ns} is a PCAR-related conductance and $G_{nn} = 1$ is flat bias-independent conductance through the vortex cores and $h = H/H_{c2}$ is assumed in this case. For instance, if magnetic field of $\mu_0 H \approx 5\,\mathrm{T}$ is applied to a superconductor with an upper critical field of $\mu_0 H_{c2} \approx 15\,\mathrm{T}$ (like Nb-Ti, see Fig. (5.6)), this means that the overall contribution of the Andreev reflection related signal towards the overall conductance is reduced to approximately $2/3$.

This model is applicable only to field values which are below the limit where the vortices start overlapping. It has been investigated by Shan *et al.*[297] that the simplified two-channel model breaks down above a cross-over field $\mu_0 H^*$. For $\mu_0 H > \mu_0 H^*$, the fitting of the PCAR data results in distorted extracted parameters, for instance, the barrier strength Z becomes significantly field dependent.

The density of states of a type II superconductor is position dependent in the mixed state: the superconductivity is completely suppressed in the core of a vortex and, therefore, the density of states is flat in this case, whereas the equilibrium BCS DOS is recovered at a position exactly between two vortex cores. The equilibrium Abrikosov lattice represent hexagonal honey-comb structure. Accurate treatment of the vortex lattice influence on the superconductor density of states

is given by Golubov and Hartmann[114]. In this case, the hexagonal vortex cell is treated as a circular one in a fashion similar to the Wigner-Seitz cell. The circular cell has radius

$$\rho_s = \sqrt{\frac{\Phi_0}{\pi\mu_0 H}}, \tag{5.5}$$

where Φ_0 is the flux quantum. This approximation is demonstrated to be accurate within 0.2 %[147, 367]. The critical cell radius at which the whole sample turns normal is $\rho_c = \sqrt{\Phi_0/(\pi\mu_0 H_{c2})}$. The normal, G, and anomalous, F, Green functions abide by the Usadel equations in the case of a "dirty" superconductor, *i.e.* the mean free l is smaller than the coherence length ξ. Usadel equations are an approximation of the more general Eilenberger[86] equations.The Usadel equations are the following two coupled equations:

$$\omega F - \frac{D}{2}\left[G\left(\nabla - \frac{2\pi i\vec{A}}{\Phi_0}\right)^2 - F\nabla^2 G\right] = \nabla G, \tag{5.6}$$

$$\ln\left(\frac{T}{T_c}\right) + 2\pi T\sum_{\omega}\left(\frac{\Delta}{\omega} - F\right) = 0, \tag{5.7}$$

where $D = v_F l/3$ is the diffusion constant, $\omega = \pi T(2n+1)$ are the Matsubara frequencies, and $\vec{A}$ is the vector potential. The two Green functions can be substituted with a new function θ: $F = \sin\theta$ and $G = \cos\theta$ and after transforming to cylindrical coordinates, the system above becomes:

$$\theta'' + \frac{1}{\rho}\theta' - \omega\sin\theta - Q^2(\rho)\sin\theta\cos\theta + \Delta\cos\theta = 0, \tag{5.8}$$

$$\ln\frac{T}{T_c} + 2\pi T\sum_{\omega}\left(\frac{\Delta}{\omega} - \sin\theta\right) = 0, \tag{5.9}$$

where the prime represents differentiation with respect to ρ, and the gradient-invariant vector potential, $Q(\rho)$, in the limit $\kappa \gg 1$ is

$$Q(\rho) = \frac{1}{\rho} - \frac{\rho}{\rho_s}, \tag{5.10}$$

where $\rho = 0$ signifies the center of the vortex. The latter approximation pertains to strong type-II superconductors where the coherence length is much shorter than the penetration depth. The system of equations above is complemented with the boundary conditions at the center and the edge of a circular cell:

$$\Delta(0) = \theta(\omega,0) = 0, \quad \Delta'(\rho_s) = \theta'(\omega,\rho_s) = 0. \tag{5.11}$$

The boundary conditions essentially denote that the superconductivity is completely suppressed

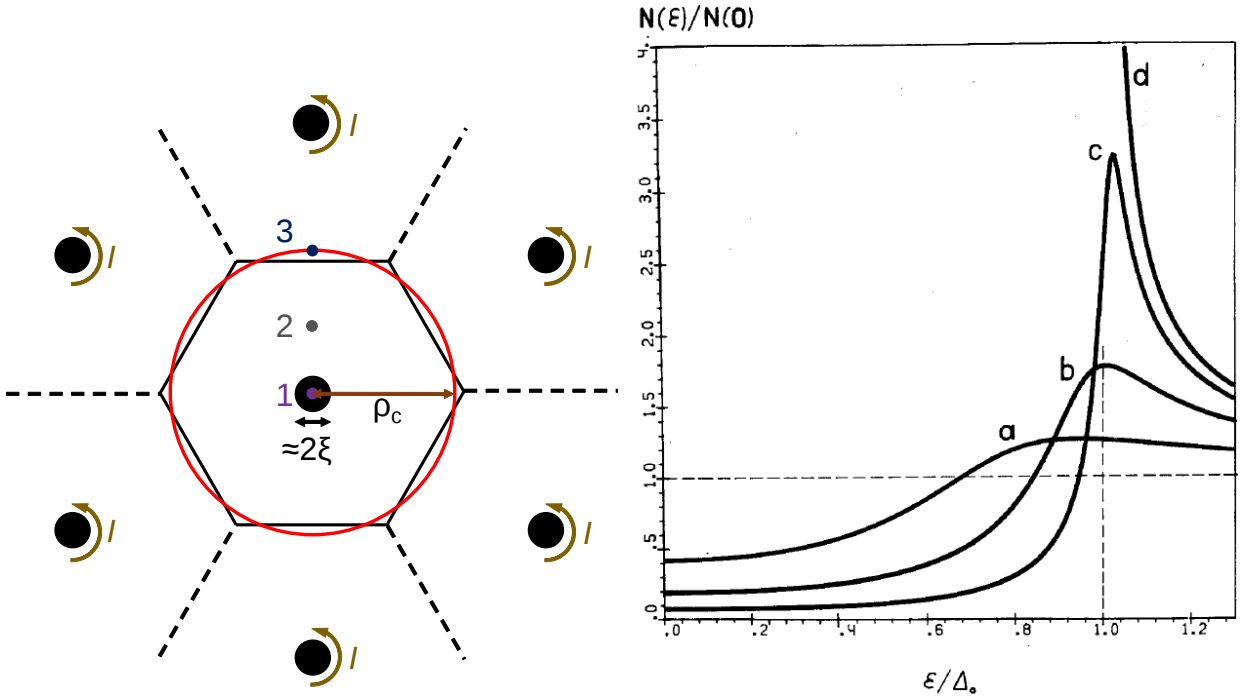

(a) Vortex cell.

(b) Vortex cell averaged superconducting density of states.

Figure 5.4: Panel(a): Schematic representation of the hexagonal honey-comb Abrikosov vortex lattice. Each vortex has approximately core size $\approx \xi$ and is surrounded by six neighbours. The circulating supercurrent around the vortex cores is indicated. The approximated circular cell with radius ρ_s is depicted as well. The points 1, 2, and 3 denote different positions in the circular cell: $0, \rho_s/2$, and ρ_s. Panel (b): numerically calculated density of states averaged over a vortex lattice following the solution of the Usadel equations. The curves (d)-(a) correspond to reduced magnetic field values $H/H_{c2} = 0.0$, 0.05, 0.2, and 0.5, respectively. The data is after Golubov and Kupriyanov[115].

in the core of a vortex and that the gap parameter* has reached its equilibrium value at the edge of the circular cell. The gap, $\Delta(\rho)$, and the DOS parameter, $\theta(\omega,\rho)$, are normalized to πT_c, the length to the coherence length $\xi_s = \sqrt{(D/(2\pi T_c))}$, and the vector potential to $\Phi_0/(2\pi\xi_s)$. The density of states is given by the real part of the normal Green function, G: $N(E,\rho) = \mathrm{Re}G(E,\rho) = \mathrm{Re}[\cos\theta(E,\rho)]$. The quasi-particle density of states has to be calculated numerically for different positions of the vortex circular cell and then averaged over the vortex:

$$\overline{N}(E) = \frac{1}{\pi\rho_s^2}\int_0^{\rho_s} N(E,\rho)2\pi\rho\,\mathrm{d}\rho. \tag{5.12}$$

In fields close to H_{c2}, the functions are small and this allows linearization of the self-consistent equations. A relation between the temperature dependence of the critical cell radius $\rho_c(T)$ and the upper critical field $H_{c2}(T)$, known as Maki-de Gennes equation, can be obtained in this approximation:

$$\ln\left(\frac{T_c}{T}\right) = \psi\left(\frac{1}{2}+\frac{T_c\xi_s^2}{T\rho_c^2}\right) - \psi\left(\frac{1}{2}\right), \tag{5.13}$$

*and the density of states

where $\psi(x) = \Gamma'(x)/\Gamma(x)$ is the digamma function*. The numerical self-consistent solution of the Usadel equations goes beyond the scope of this work, however, the detrimental effect is demonstrated in Fig. (5.4) (b). Even small field values of $h = 0.05$ cause significant rounding of the sharp quasiparticle density of states, and moderately high field values of $h = 0.5$ result in practically indistinguishable maximum in the DOS structure. Since the sharp features are important for Zeeman splitting observation in PCAR, this vortex induced DOS modification makes the experimental observation more complicated. The existence of density of states at sub-gap voltages is known as gapless superconductivity. Gapless superconductivity exists in type I superconductors as well, however, at field values very close to the critical field: $H = 0.95H_c$[198, 227]. The method of vortex cell averaging is extended to two-band superconductors (like MgB_2) by Koshelev[180].

It is especially important to suppress vortex dynamics in superconducting wires for high-field solenoid magnets but the concern falls here on the PCAR spectral temporal evolution due to flux flow. There is dissipative force between the current in the superconductor and the flux threading it, which is the Lorentz force density:

$$\vec{F} = \vec{J} \times \frac{\vec{B}}{c}, \tag{5.14}$$

where $\vec{J}$ is the current density. It can be shown (see Tinkham[342] p. 154-155) that the force on a single vortex is:

$$\vec{f} = \vec{J} \times \vec{n} \frac{\Phi_0}{c}, \tag{5.15}$$

where $\vec{n}$ is the unit vector normal to the surface of the superconducting film. The vector product determines that this force moves the vortices in direction which is transverse to the current direction. If the vortices move at velocity $\vec{v}$, this leads to induced electric field:

$$\vec{E} = \vec{B} \times \frac{\vec{v}}{c}, \tag{5.16}$$

which is parallel to the current density $\vec{J}$. This means that there is potential drop and therefore power is dissipated. It is more important from PCAR perspective that there is vortex movement rather than the dissipated power. The flux flow is reduced in practical superconductors with the introduction of inhomogeneities with average distance $\approx \lambda - \zeta$ between them. Nevertheless, there is still thermally activated flux creep for strong current in which case usually whole bundles of vortices jump from one equilibrium position to another. The Bardeen-Stephen model[19] describes the flux flow dissipation as limited only by viscous damping η, and therefore the viscous force per unit length of a vortex line is $-\eta\vec{v}$. In this case, the ratio between the resistance in the mixed state and the normal resistance, ρ_m/ρ_n, is proportional to the ratio between the applied magnetic field

*$\Gamma(z) = \int_0^\infty x^{z-1}e^{-x}\mathrm{d}x$ is the gamma function

and the upper critical field:

$$\frac{\rho_{\mathrm{m}}}{\rho_{\mathrm{n}}} = \frac{H}{H_{\mathrm{c2}}}. \tag{5.17}$$

More sophisticated treatment is given by Caroli and Maki[50]. The Anderson-Kim flux creep theory[6] treats the flux jumps due to thermal excitations. Since variable magnetic field induces winding electric field ($\nabla \times \vec{E} = -\partial \vec{B}/\partial t$), this will mean that variable magnetic field has detrimental effect on the vortex lattice stability as well. High-field PCAR experiments have to be performed in variable $\vec{B}$ in order to observe the evolution of the Zeeman spliting as a function of $\vec{B}$ and, therefore, the ramp rate has to be minimized. In our experiments, the magnetic field increase is limited to $5\,\mathrm{mT\,s^{-1}}$. Another problem, which is difficult to quantify is the vortex lattice behaviour in the contact between the tip and the sample. Concentration of Abrikosov vortices in the contact area leads to significant reduction in the Andreev-related signal. Mechanical vibration and the contact reorientation lead to different pinning structure and, therefore, it is advisable to analyze multiple high-field spectra in order to statistically average out vortex induced dynamical effects on the PCAR conductance.

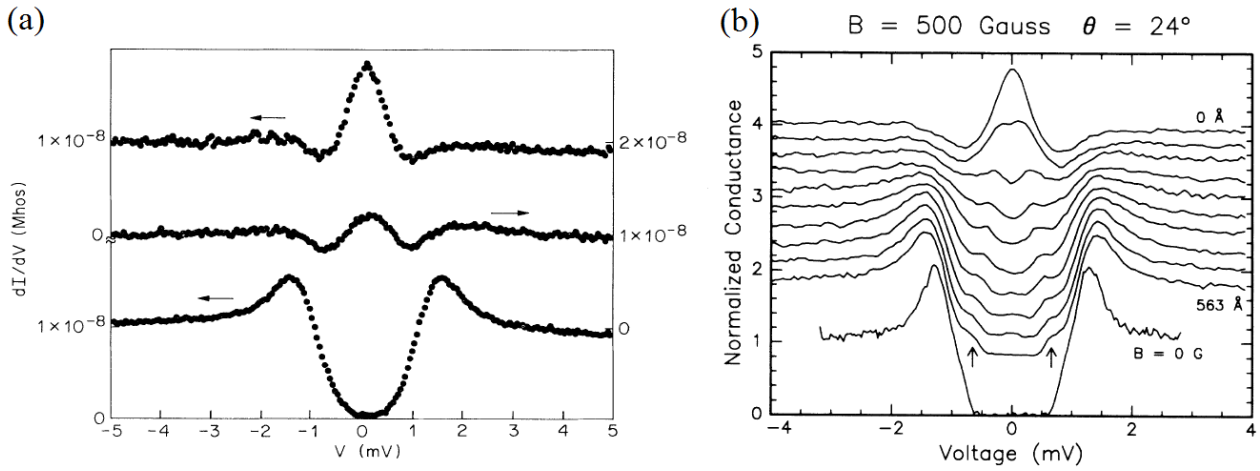

Figure 5.5: Scanning tunneling spectroscopy data of Abrikosov vortex bound states. Panel (a) - $\mathrm{d}I/\mathrm{d}V(V)$ of vortex lattice at three different positions: in the core (top), at distance of 7.5 nm (middle) and at distance of 200 nm from the core (bottom). The data is obtained on $NbSe_2$ at 1.85 K and 0.02 T and is after Hess *et al.*[136]. Panel (b) - higher resolution spacial evolution of local $\mathrm{d}I/\mathrm{d}V$. The data is obtained on $NbSe_2$ at 0.3 K in 50 mT. The splitting of the zero-bias peak is manifested in the vicinity of the vortex core.

Another complication is the existence of vortex bound states. The different nature of density of states within the core of a superconducting vortex is predicted by Kramer and Pesch and is confirmed by Hess *et al.*[136, 137] shortly after the advent of scanning tunneling microscopy (spectroscopy). The density of states evolves from a peaked structure in the core of a vortex towards a BCS fully-gapped structure very far away from the vortex. Perhaps more intriguing is the observation that the zero-bias peak splits up as a function of the distance from the vortex core. It has been successfully theoretically modeled by Shore *et al.*[303] that the in-core zero-bias peak is due

to quasiparticle bound states. The latter theory successfully predicts the splitting of the zero-bias anomaly at distance $r \approx \xi$ observed by Hess *et al.* [137]. The investigation of vortex bound states, quasiparticle interference, moving vortex lattice and lattice dependence on the crystallographic defects is a vast research field. Extensive review of the so far achieved imaging of superconducting vortex lattice in different superconductors is given by Suderow *et al.*[324]. It is worth noting that vortex bound states have not been observed in MgB_2, a superconductor used in this work.

5.3 High-field experiments with Nb-Ti

Contemporary superconducting magnets are mainly wound with Nb-Ti and Nb_3Sn multifilamentary wires. Nb_3Sn has superior superconducting properties: its critical temperature is 15.3 K and its upper critical field is 15 T at 4.2 K. It has two disadvantages for our PCAR aims: it has high average atomic number and it is rarely prepared in monofilament wire forms. Therefore, the focus falls on Nb-Ti. The latter is easily obtainable in monofilament superconducting wire form with Cu sheath and insulation.

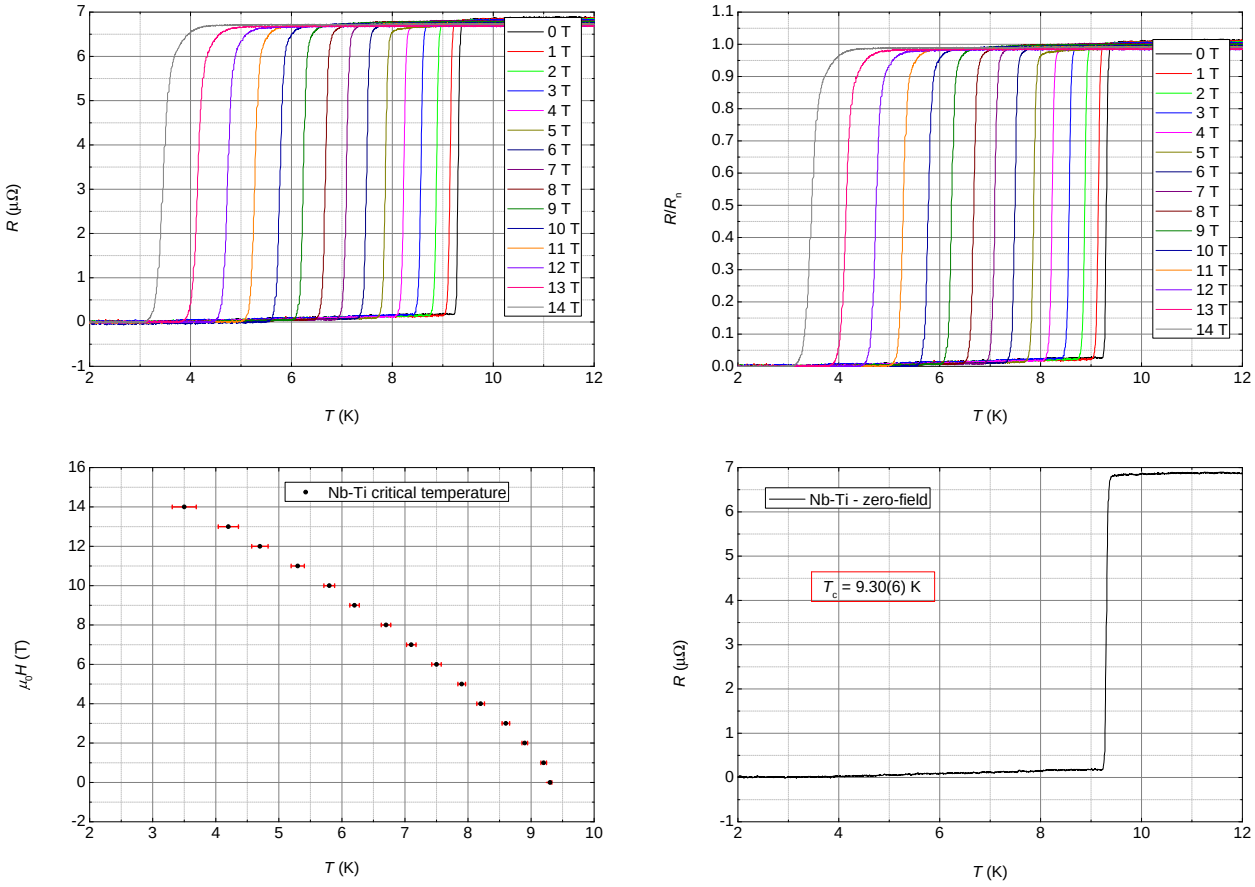

Figure 5.6: Critical superconducting temperature of Nb-Ti wires. Panel (a) - superconducting transition of Nb-Ti at various fields. Panel (b) - superconducting transitions at various fields in normalized resistance R/R_n. Panel (c) - critical temperatures at various fields along with the superconducting transition width. Panel (d) - Critical temperature of 9.30(6) K of Nb-Ti in zero applied external field.

The insulation layer is stripped mechanically. The Cu sheath is etched for 10 min in concentrated nitric acid (HNO_3). After the etching, the surface of the cylindrical Nb-Ti core is gently scrapped with scalpel in order to remove any left-over contaminants from the etching process. The Nb-Ti wire is brittle, hence, scissors shear cutting results in sharp, good quality tips for PCAR. First of all, the electrical properties of the Nb-Ti wires are presented in Fig. 5.6. Since the resistance of a short (10 mm) wire segment is below 1 mΩ, the electrical properties are measured in standard four-point a.c. configuration. Constant current is provided by a lock-in voltage source in series with a 1 kΩ resistor and the voltage is pre-amplified with bandpass filter before being fed back to the lock-in for detection. The zero-field critical temperature is approximately $T_c = 9.30(5)$ K, close to the one of bulk Nb $T_c \approx 9.25$ K. The critical temperature of Nb-Ti at our highest possible field of $\mu_0 H = 14$ T is 3.5(2) K*.

Since systematic PCAR experiments with Nb-Ti have not been performed before, it is important to demonstrate that this superconductor is reliable. PCAR measurements on classical 3*d* ferromagnetic alloy CoFe and the non-polarized Au are performed in this case, their spin polarization is very well studied in literature. The gold layer (30 nm) is deposited by thermal evaporation on Al_2O_3 substrate with Al(30 nm) adhesion layer. The CoFe(40 nm) is deposited by sputtering on Si/SiO_2 with Ta(10 nm) adhesion layer and capped with AlO_x(3 nm). The PCAR measurements on this well established compositions demonstrate the expected values. The spin polarization of CoFe is $P_{CoFe} \approx 48(3)\,\%$, while measurement on the Au film results in negligible spin polarization of $P_{Au} \approx 4(7)\,\%$ (see Fig. (5.7)). More than 30 landings have been performed on the films and the observed PCAR features have not demonstrated any peculiar structure. Therefore, the Nb-Ti wire behaves as an *s*-wave superconductor and has potential to be used in PCAR, routinely.

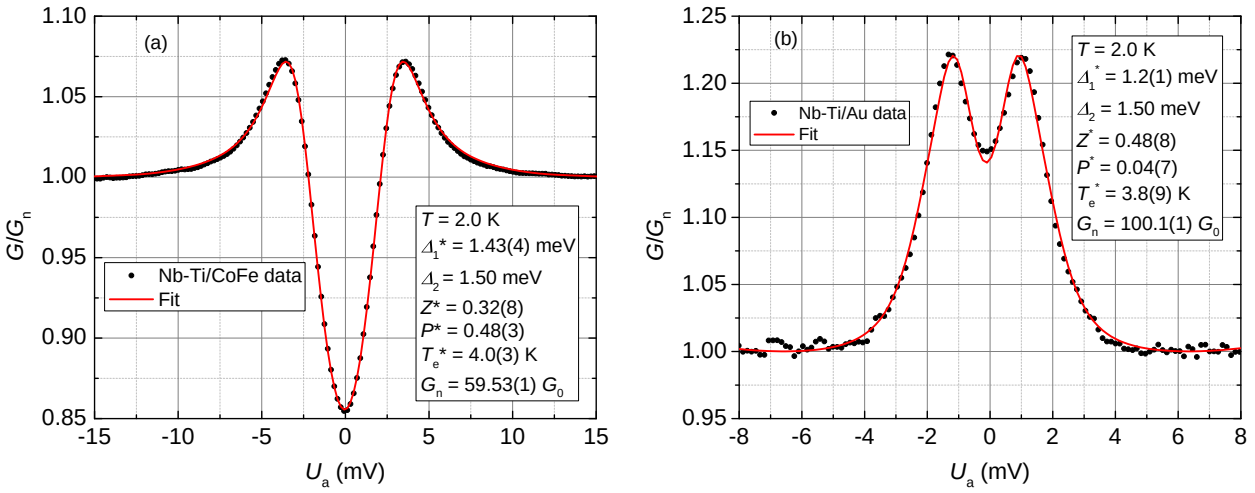

Figure 5.7: PCAR measurements with Nb-Ti on CoFe (a) and Au (b). The extracted spin polarization are $P_{CoFe} = 48(3)\,\%$(a) and $P_{Au} = 4(7)\,\%$, respectively.

*The careful reader will notice that there is a very small residual resistance below the superconducting transition. It is not clear whether this is due to vortex lattice motion or due to inductive pick-up in the measurement leads.

Furthermore, the temperature evolution of the PCAR signal on the CoFe sample has been investigated. The same measurement, data analysis and normalization procedure is applied as in Fig. 3.14. Separate PCAR temperature scans are obtained at T = 2 K, 2.2 K, ... 10 K. All individual spectra are normalized with a background curve recorded at 10 K*. The temperature evolution demonstrates the behaviour of a polarized ferromagnet, the conductance features shrink in amplitude and the spread along the applied bias axis decreases because of the reduction of the superconducting gap as the critical temperature is approached. A comparison is made between the experimental PCAR data in Fig. (5.8) and a simulated PCAR spectrum in Fig. (5.9). The simulated data is obtained with the following constants: barrier strength $Z = 0.4$, spin polarization $P = 0.5$, and bulk superconducting gap of $\Delta_2 = 1.55$ meV. No proximity effect is taken into account for the simulation, the electronic temperature is assumed to follow the temperature of the bath and the superconducting gap temperature evolution is considered to follow the approximate formula $\Delta(T) = \Delta_0 \tanh(1.74\sqrt{(T_c/T)-1})$. There is very high similarity between the experimental and the simulated temperature scans, apart from the broader structure along the bias axis and smaller conductance amplitude in the experimental set. The latter is attributed to the existence of resistance contributions in series with the contact. The qualitative agreement between the last temperature scans shows conclusively that the Nb-Ti is a reliable alternative to the widely used Nb for PCAR experiments. The focus falls now on high magnetic field PCAR measurements with Nb-Ti superconducting tips.

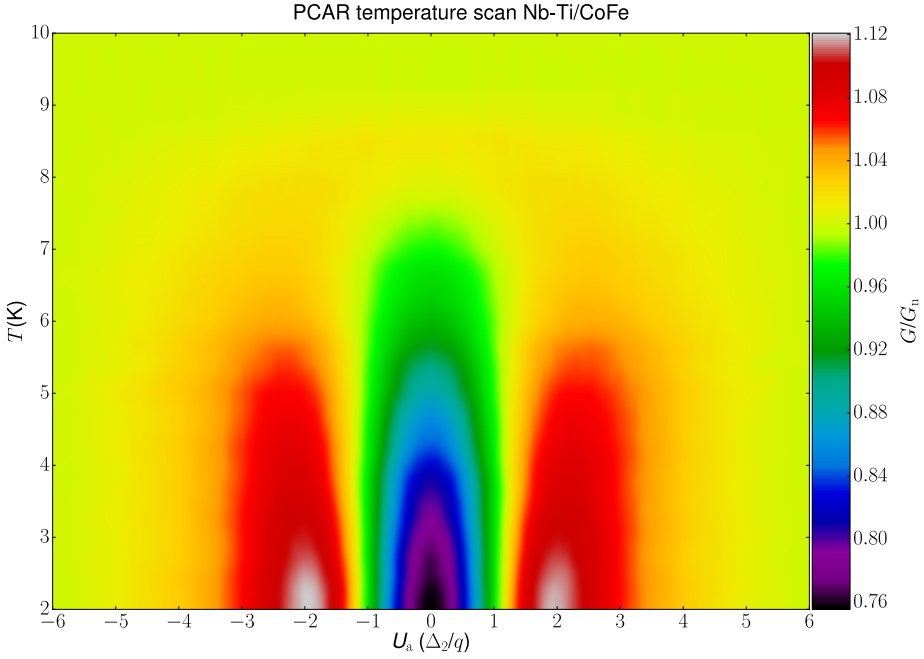

Figure 5.8: PCAR scan of a Nb-Ti/CoFe contact in the temperature range from $T = 2$ K to $T = 10$ K. All spectra are normalized with a background curve at 10 K.

*above the critical temperature of Nb-Ti

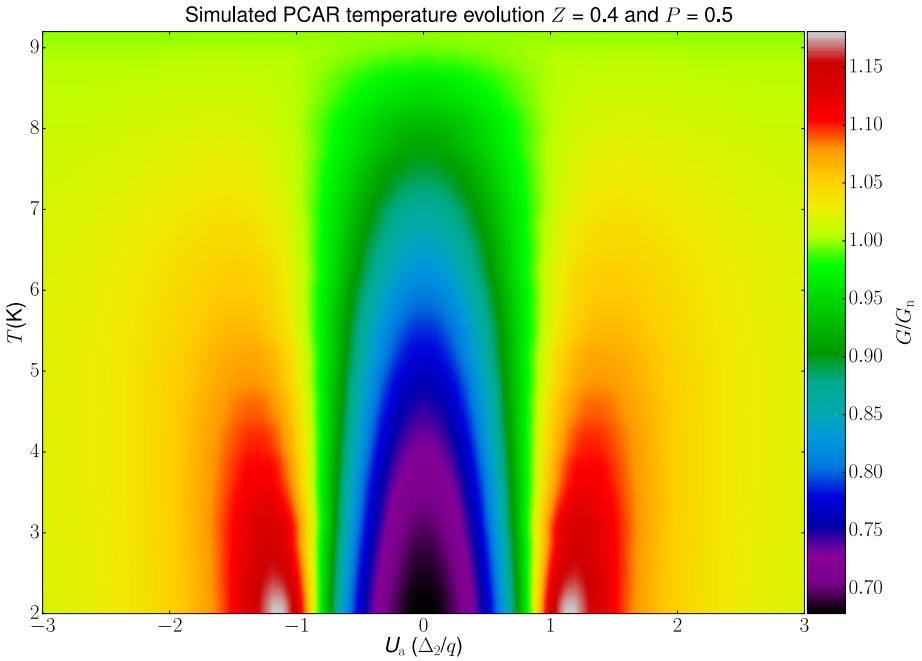

Figure 5.9: Simulated PCAR data for barrier strength $Z = 0.4$ and spin polarization $P = 0.5$ in the temperature scan $T = 2\,\mathrm{K}$ to $T = 9.2\,\mathrm{K}$.

An example of magnetic field scan at 2 K of an Nb-Ti/CoFe point contact up to 9 T is presented in Fig. 5.10. Low field ramp rate of 5 mT s^{-1} is used usually during the PCAR field scans in order to minimize induced flux flow and mechanical vibrations. Consequently, the data is averaged at field values $\mu_0 H[i] = 0.0, 0.1, 0.2 \ldots 9.0\,\mathrm{T}$ in this way producing 91 low noise spectra. Figure (5.10) represents the normalized PCAR conductance. The normalization of each field scan, $\mu_0 H[i]$, is achieved with the high-bias points

$$\overline{G}(U_\mathrm{a}, \mu_0 H[i]) = \frac{2G(U_\mathrm{a}, \mu_0 H[i])}{G(-\infty, \mu_0 H[i]) + G(+\infty, \mu_0 H[i])}, \tag{5.18}$$

where $G(-\infty)$ and $G(\infty)$ denote the conductance at the highest available negative and positive bias, and $G(U_\mathrm{a}, \mu_0 H[i])$ represents the full PCAR array at field $\mu_0 H[i]$. The Andreev reflection contribution towards the overall conductance decreases as the magnetic field increases. The latter is evidenced by the fact that the spectra become flatter as a function of applied bias for higher magnetic field. The detrimental effect of the flux lattice is apparent as jumps in the three-dimensional plot. Such flux jumps in the area of the contact are clearly discernable, for instance, at field values approximately: 2.5 T, 4.0 T, 5 T, and 6 T*. Spectra without drift can be obtained up to 2 T in most of the cases. The landing of the Nb-Ti tip inevitably creates crystallographic defects which act as pinning centers for the vortices. However, this disorder is expected to be irreproducible and, hence, the behaviour of the Abrikosov lattice is different in each separate point contact formation.

*In fact, the vortex dynamics is significant above 6 T but the colour scale distorts the perception.

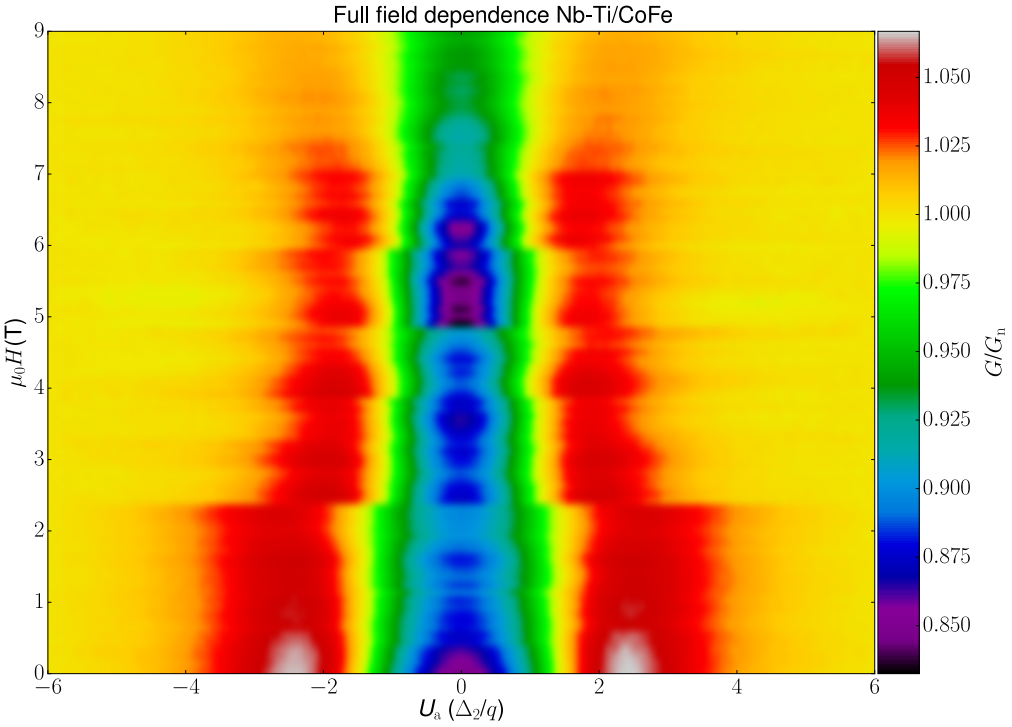

Figure 5.10: Demonstration of flux jumps (or contact reorientation) on the structure of Andreev reflection in a magnetic field scan of a Nb-Ti/CoFe point contact. The applied bias is in units Δ_2/q, where $\Delta_2 = 1.5\,\text{meV}$, and q is the elementary charge. The temperature is 2 K.

It has been observed occasionally that the PCAR in-field scans demonstrates no superconducting features at fields much smaller than the upper critical field. This happens because the concentration of multiple vortices in the contact area leads to a quench of the point contact. A simple rescaling procedure for PCAR temperature/field scans is described in Fig. (3.16). The same rescaling procedure is applied here on the data from Fig. (5.10). In this situation, the high bias profile, $G(\mu_0 H[i])^\dagger$, is first determined for each separate field scan. Then, the zero-field spectrum $G(\mu_0 H[0])^\dagger$ is used as reference and a multiplicative rescaling factor, $M[i]$, is defined with respect to it. After that, the conductance and voltage axis of each PCAR spectrum (at different field) are shrunk/expanded accordingly. The full procedure is summarized in the equations below:

$$G(\mu_0 H[i])^\dagger = \frac{G(-\infty, \mu_0 H[i]) + G(\infty, \mu_0 H[i])}{2}, \tag{5.19}$$

$$M[i] = \frac{G(\mu_0 H[i])^\dagger}{G(\mu_0 H[0])^\dagger}, \tag{5.20}$$

$$\tilde{U}(\mu_0 H[i]) = \frac{U(\mu_0 H[i])}{M[i]}, \tag{5.21}$$

$$\tilde{G}(\mu_0 H[i]) = G(\mu_0 H[i]).M[i], \tag{5.22}$$

where $\tilde{U}(\mu_0 H[i])$ and $U(\mu_0 H[i])$ are the rescaled and original voltage axis arrays of a PCAR scan

recorded at field $\mu_0 H[i]$, respectively. The rescaled and original PCAR conductances at field $\mu_0 H[i]$ are $\tilde{G}(\mu_0 H[i])$ and $G(\mu_0 H[i])$, respectively. This rescaling procedure is approximately correct for small variations of the contact resistance. The rescaled version of the same graph is plotted in Fig. (5.11) (a). This simple procedure smooths out well some of the features. However, there are contact reorientations with the changes in the barrier strength Z. The most apparent such feature is at $\mu_0 H \approx 4.9\,\mathrm{T}$. There is no established way to correct for such effects. The PCAR bias asymmetry as a function of magnetic field is presented in Fig. (5.11) (b). The outlined fingerprint for Zeeman-split Andreev reflection from Fig. (5.3) shows that the conductance asymmetry below the gap should be with higher magnitude than the above gap one and the two asymmetries should be with opposite signs. The PCAR scan in Fig. (5.11) (a) exhibits maximum conductance at $U_\mathrm{a} \approx \pm 2.5$, therefore, the focus should fall on the bias range $|U_\mathrm{a}| \leq 2.5$ for the asymmetry scan. The low bias asymmetry appears to be most pronounced at applied bias of $U_\mathrm{a} \approx 1.0$. It increases gradually in magnitude up to 5 T where it suddenly changes sign*. The latter is attributed to vortex dynamics. The vortex lattice contribution leads to another change of the sign at field of around 6.5 T. The highest sub-gap asymmetry is at approximately 7.8 T, however, it is unclear whether the observation is not caused by vortex dynamics. The high bias asymmetry at $U_\mathrm{a} \approx 2.5 - 3.0$ demonstrates overall negative asymmetry with a magnitude lower than the low bias asymmetry. An exclusion from this picture presents the field range from 5 T to 7 T where both the low and high bias asymmetry behave randomly. As a brief conclusion on the high field PCAR, the asymmetry field range 0 T-5 T demonstrates features similar to the expected fingerprint of positive-negative asymmetry. Similar tendency is present in the field range 7 T-9 T. Unfortunately, the asymmetry bias picture is very dynamic and complicated and an overall tendency cannot be certainly established†. In order to crosscheck some of the observation on the field scan from Fig. (5.11), a separate one this time in the field range from 0 T to -9 T is presented later in Fig. (5.15) and Fig. (5.16).

*If a look is taken at panel (a) of the same figure, there is a definite change in the contact configuration at approximately 4.9 T.

†It appears that vortex contribution distorts the picture the most in the field range from 5 T to 7 T in this particular contact.

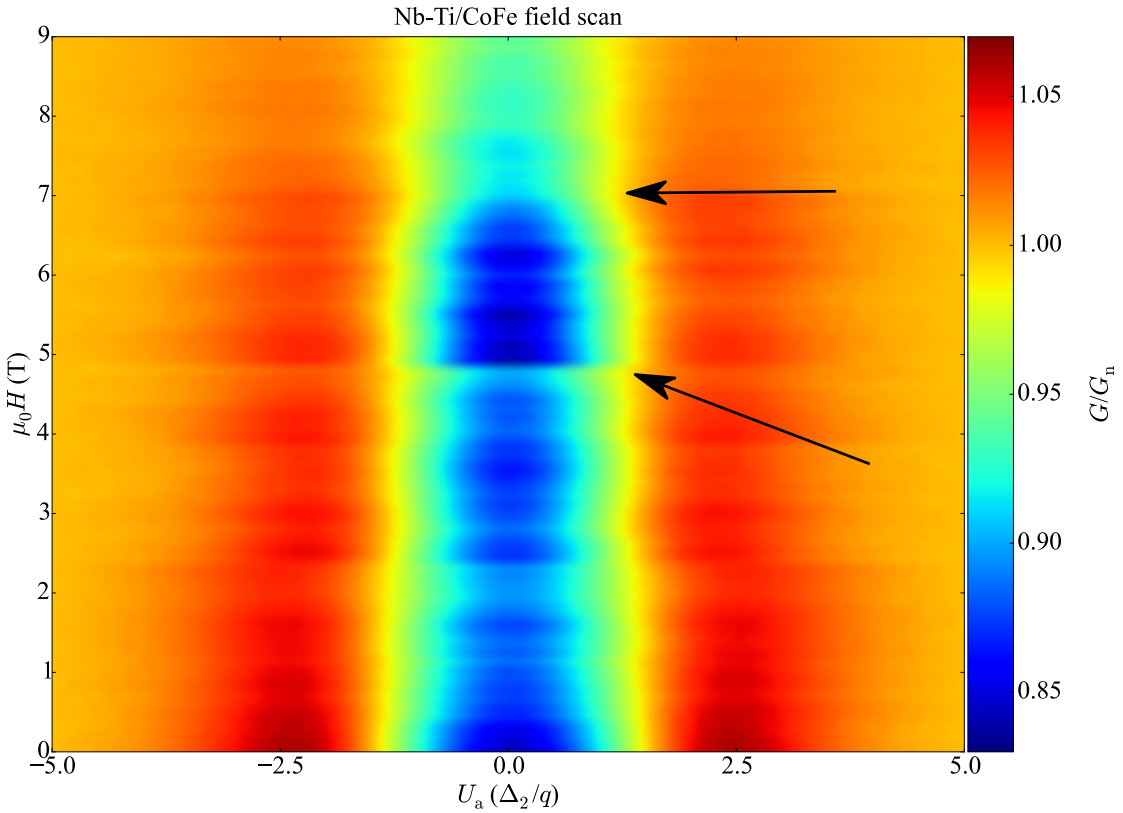

(a) PCAR field scan from $\mu_0 H = 0\,\mathrm{T}$ to $\mu_0 H = 9\,\mathrm{T}$.

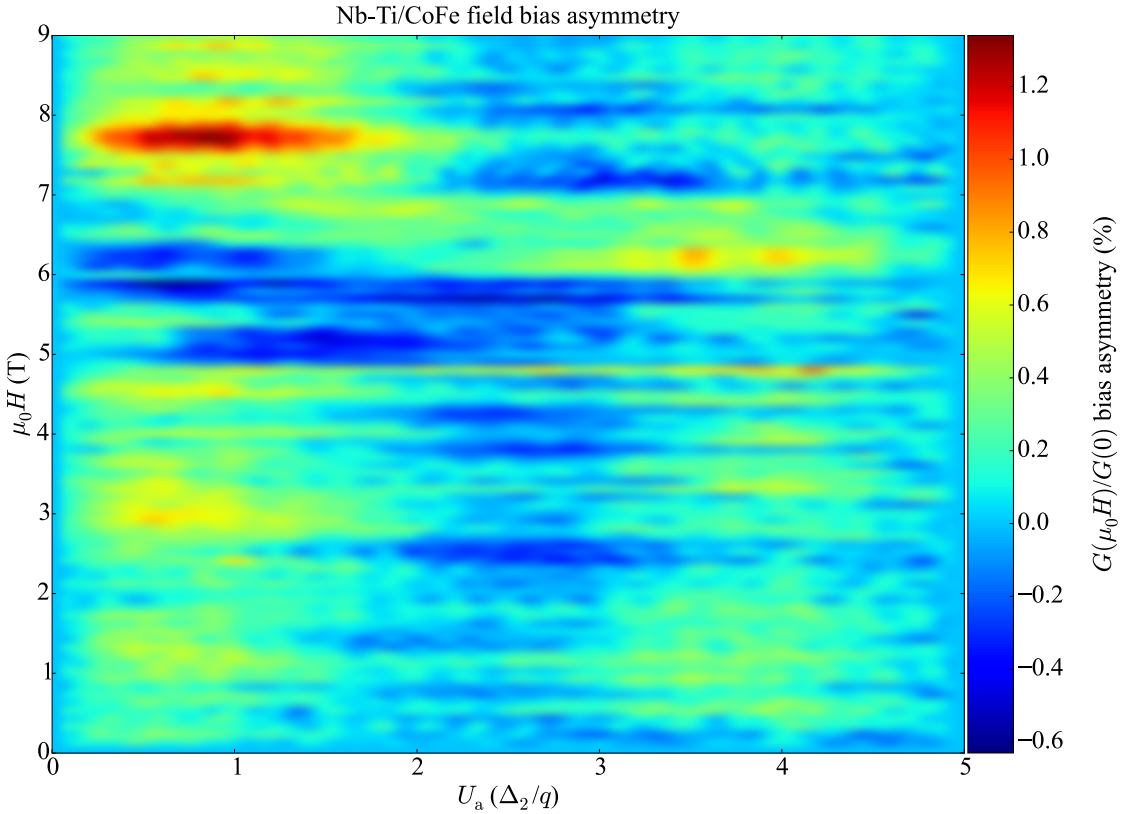

(b) PCAR bias asymmetry of field scan from (a).

Figure 5.11: PCAR field scan of a Nb-Ti/CoFe point contact: (a) - field scan from 0 T to 9 T and (b) - PCAR bias asymmetry of the data from panel (a). The temperature is 2 K. The most pronounced vortex jumps are indicated with black arrows on panel (a).

PCAR fits have been performed on the high-field NbTi/CoFe spectra. The data along with the fits and the extracted parameters for the applied fields $\mu_0 H = 0\,\mathrm{T}, 1\,\mathrm{T}, \ldots 7\,\mathrm{T}$ is presented in Fig. 5.12. It is apparent from the individual scans, that the PCAR conductance signal is shrunk due to the fact the Abrikosov vortices contribution increases its weight towards the overall conductance, and therefore, the PCAR-related signal is diminished. As is usually the case in our fitting routine, the rescaling factors of the voltage and conductance axes are left as free fitting parameters. These parameters vary slightly due to the shrinking of the gap and pinning/depinning of vortices within the contact area. The proximity gap Δ_1 is always close to the bulk gap Δ_2, therefore, no appreciable proximity effect is observed. Furthermore, the proximity gap is essentially magnetic field independent. The reader should pay attention to the lineshape of the fitted curve (always in red). As the magnetic field is increased, the BTK model can not account accurately for some fine details of the spectral features. The most pronounced disagreement is evident close to zero bias. The PCAR scan at around $\mu_0 H = 7\,\mathrm{T}$ demonstrates the effect of vortex dynamics, the scan is very asymmetric, for instance, the normalized conductance G/G_n at $U_\mathrm{a} \approx 3\,\mathrm{mV}$ is significantly higher than at $U_\mathrm{a} \approx -3\,\mathrm{mV}$. The focus shifts towards the three most important parameters-spin polarization P, the effective electronic temperature T_e, and the barrier strength Z. The field evolution of these parameters is presented in Fig. 5.13. First of all, the spin polarization is shown to be almost constant within the experimental error for all fields in the range from 0 T to 7 T. It has to be noted that this is in contrast with the result demonstrated by Gifford *et al.*[111] in their experimental investigation of spin polarization with Nb-Ti in magnetic field of up to 1.5 T. Their spin polarization increases slightly from 38.5 % ($\mu_0 H = 0\,\mathrm{T}$) to 41.5 % ($\mu_0 H = 1.5\,\mathrm{T}$), however, their values do not quote errors and it might be case that the spin polarization is constant within the error in their experiments, as well. The magnetic field evolution of the effective electronic temperature, T_e, is presented in Fig. 5.13 (b). The electronic temperature systematically increases from $\approx 3.9\,\mathrm{K}$ ($\mu_0 H = 0\,\mathrm{T}$) to $\approx 7.1\,\mathrm{K}$ ($\mu_0 H = 7\,\mathrm{T}$). This is actually the most apparent indicator of the increased vortex contribution towards the overall conductance. As the magnetic field is increased, more current is carried through the normal conducting channel of the vortex cores. The latter results in broadening of the PCAR spectral features and this leads to the increased effective electronic temperature. Finally, the magnetic field dependence of the barrier strength is presented on Fig. 5.13 (c). It is demonstrated that the barrier strength is constant within the experimental error.

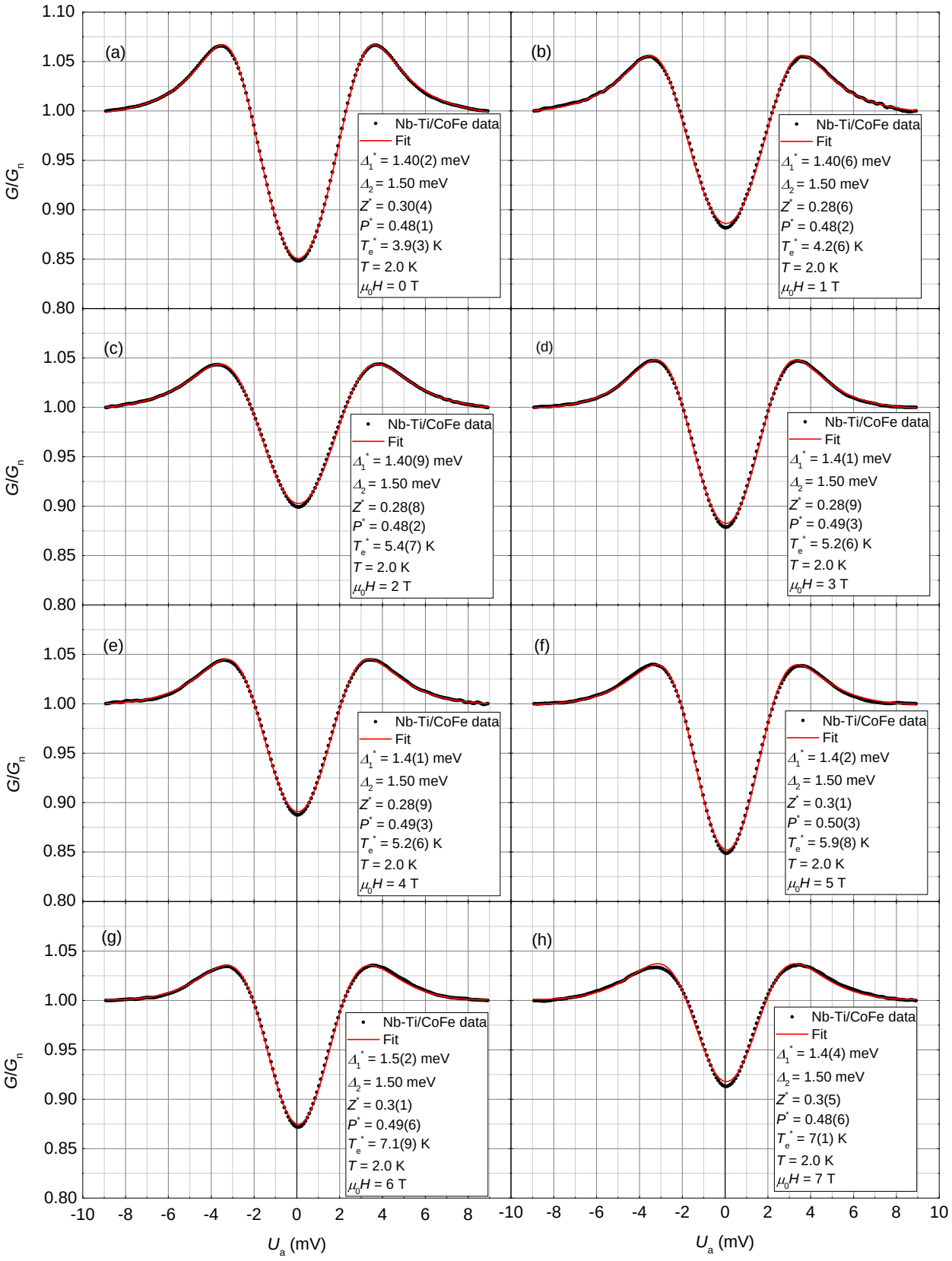

Figure 5.12: PCAR data and extracted parameters on point-contact between NbTi and CoFe at different applied magnetic field. Panel (a): $\mu_0 H = 0\,\mathrm{T}$, panel (b): $\mu_0 H = 1\,\mathrm{T}$, panel (c): $\mu_0 H = 2\,\mathrm{T}$, panel (d): $\mu_0 H = 3\,\mathrm{T}$, panel (e): $\mu_0 H = 4\,\mathrm{T}$, panel (f): $\mu_0 H = 5\,\mathrm{T}$, panel (g): $\mu_0 H = 6\,\mathrm{T}$, and panel (h): $\mu_0 H = 7\,\mathrm{T}$. Note the asymmetry at 7 T, which is most likely related to vortex dynamics.

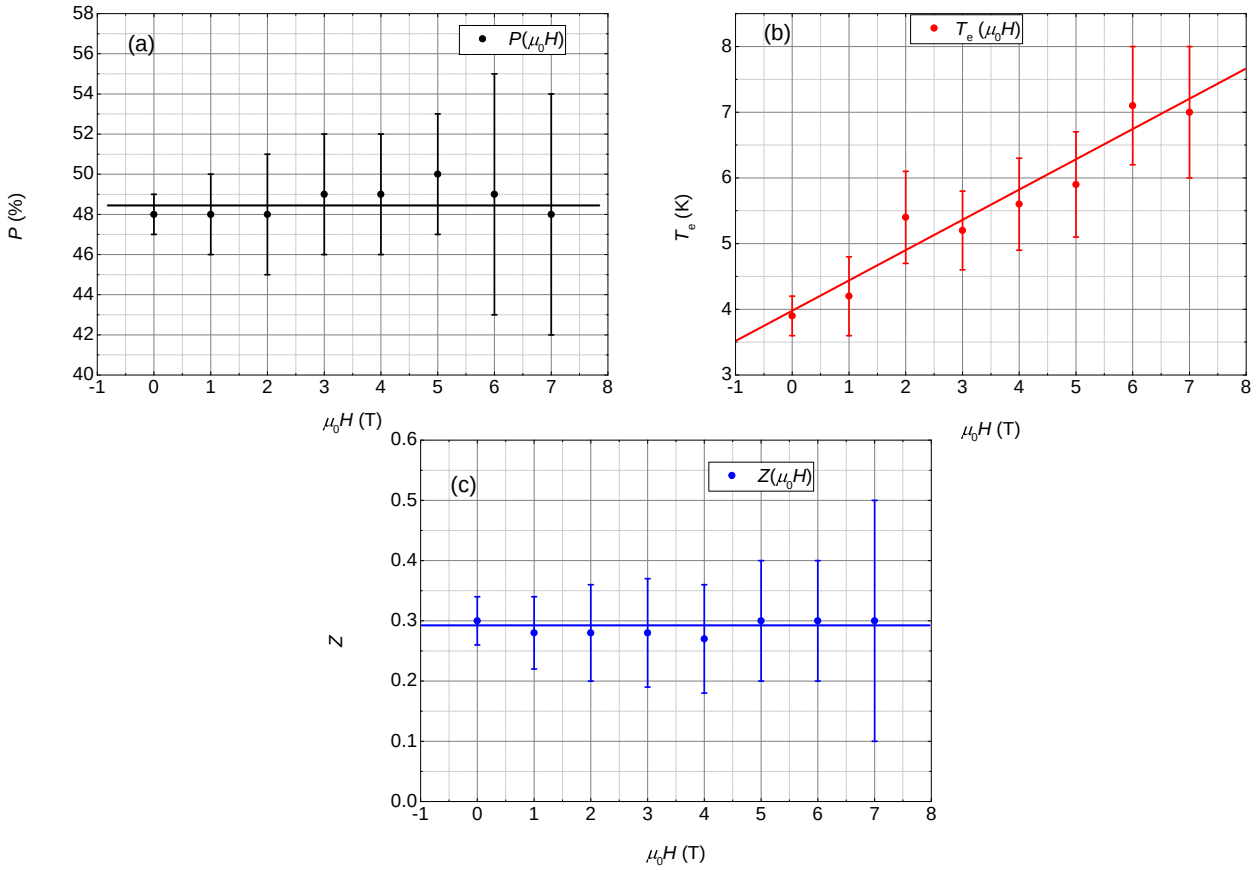

Figure 5.13: Extracted parameters from the fits of the high-field NbTi/CoFe PCAR. Panel (a): spin polarization, P, as a function of the applied magnetic field $\mu_0 H$, panel (b): effective electronic temperature T_e as a function of the applied magnetic field $\mu_0 H$, and panel (c): barrier strength Z as a function of the applied magnetic field $\mu_0 H$. The bath temperature for all spectra is $T = 2\,\mathrm{K}$. The interpolation lines are drawn by hand on each graph.

PCAR signal at fields of 9 T-14 T is observed as well, however, the density of states is heavily affected and the vortex induced motion has significant effect on the signal-to-noise level. The PCAR spectra obtained at 10 T, 11 T, and 12 T still demonstrate the expected shape for Andreev reflection with the accompanying dwindling of the magnitude. The effect of the vortex dynamics is again very clear in the scan at $\mu_0 H = 11\,\mathrm{T}$, where there is pronounced asymmetry in the conductance ($G(4\,\mathrm{mV}) \neq G(-4\,\mathrm{mV})$). However, this asymmetry is not reproduced in the PCAR scans at 10 T and 12 T, therefore, the latter is attributed certainly to vortex dynamics and not to Andreev Zeeman splitting. The broad PCAR conductance maxima observed before at $U_a \approx \pm 4\,\mathrm{mV}$ have disappeared completely in $\mu_0 H = 13\,\mathrm{T}$ and the latter absence can be wrongly attributed to higher spin polarization. The suppression happens most probably due to the rounding of the DOS structure (see Fig. (5.4)). Finally, the PCAR scan at $\mu_0 H = 14\,\mathrm{T}$ demonstrates almost completely destroyed superconducting order and the Andreev reflection magnitude is a very small feature on top of a quadratic background. The latter could be due to small tunneling component. Alternative explanation is gapless superconductivity in which case the BCS density of states is heavily distorted and, therefore, the PCAR signal as well. Reliable spin polarization extraction is not possible with Nb-Ti

in fields $\mu_0 H > 9\,\mathrm{T}$.

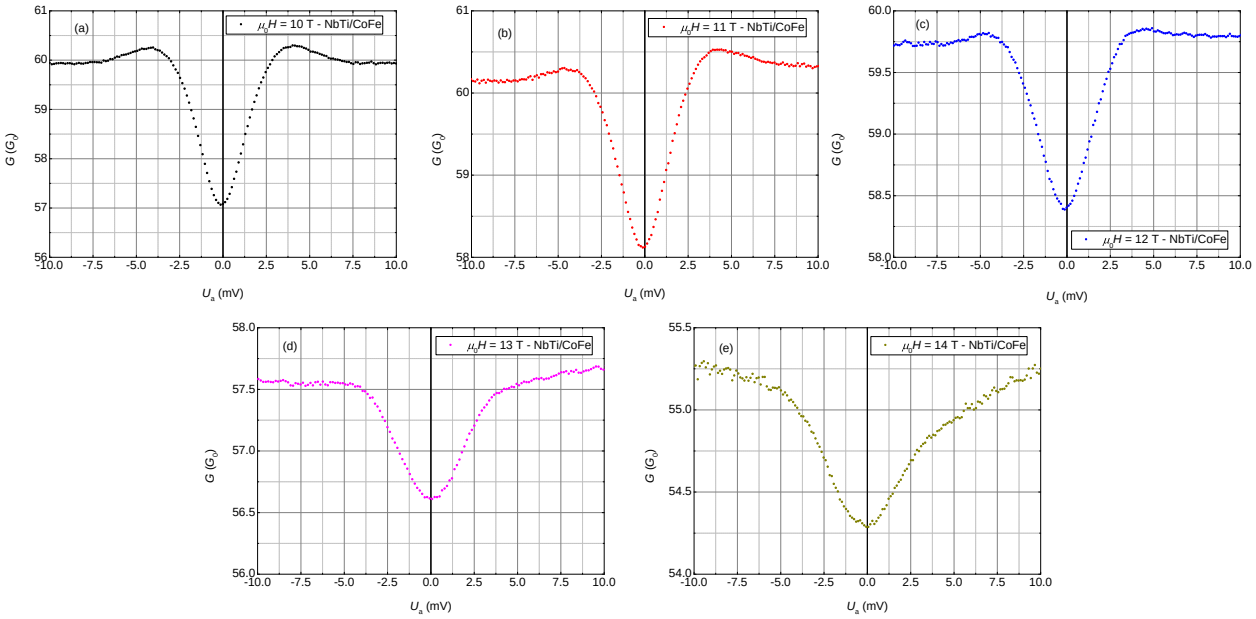

Figure 5.14: PCAR measurements between Nb-Ti tip and CoFe sample in magnetic field from 10 T to 14 T on panel from (a) to (e). The temperature in all measurements is 2 K.

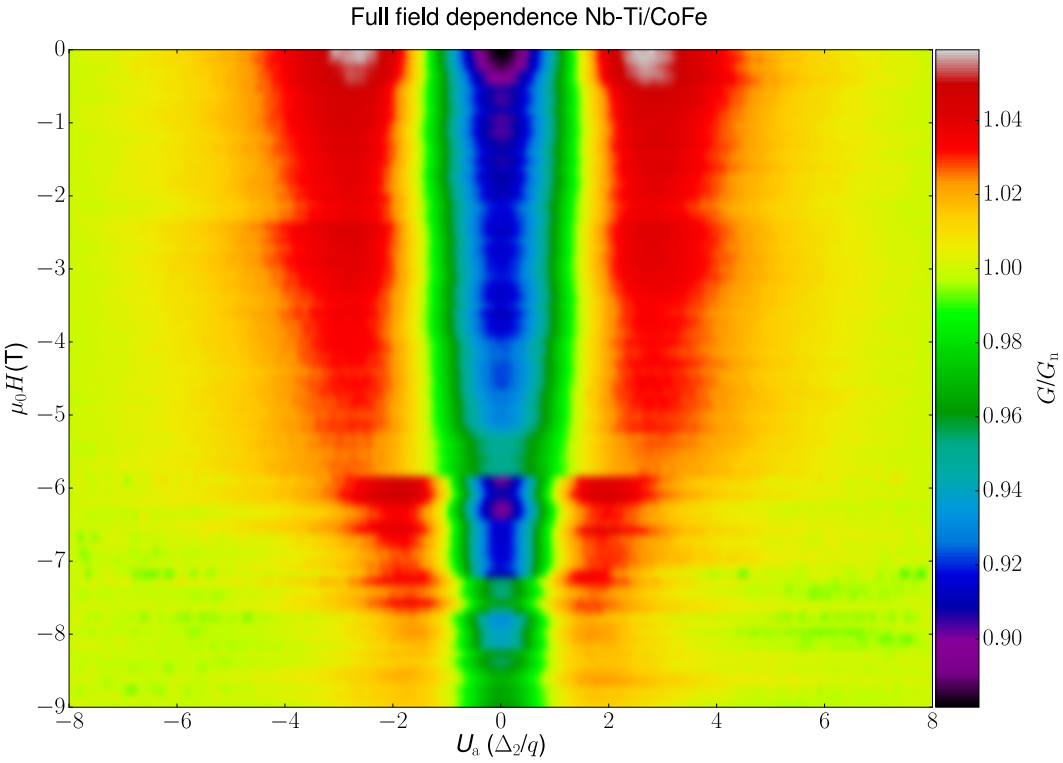

Figure 5.15: PCAR magnetic field scan from $\mu_0 H = -9\,\mathrm{T}$ to $\mu_0 H = 0\,\mathrm{T}$ of a Nb-Ti/CoFe point contact. The applied bias is in units Δ_2/q, where $\Delta_2 = 1.5\,\mathrm{meV}$, and q is the elementary charge. The temperature is 2 K.

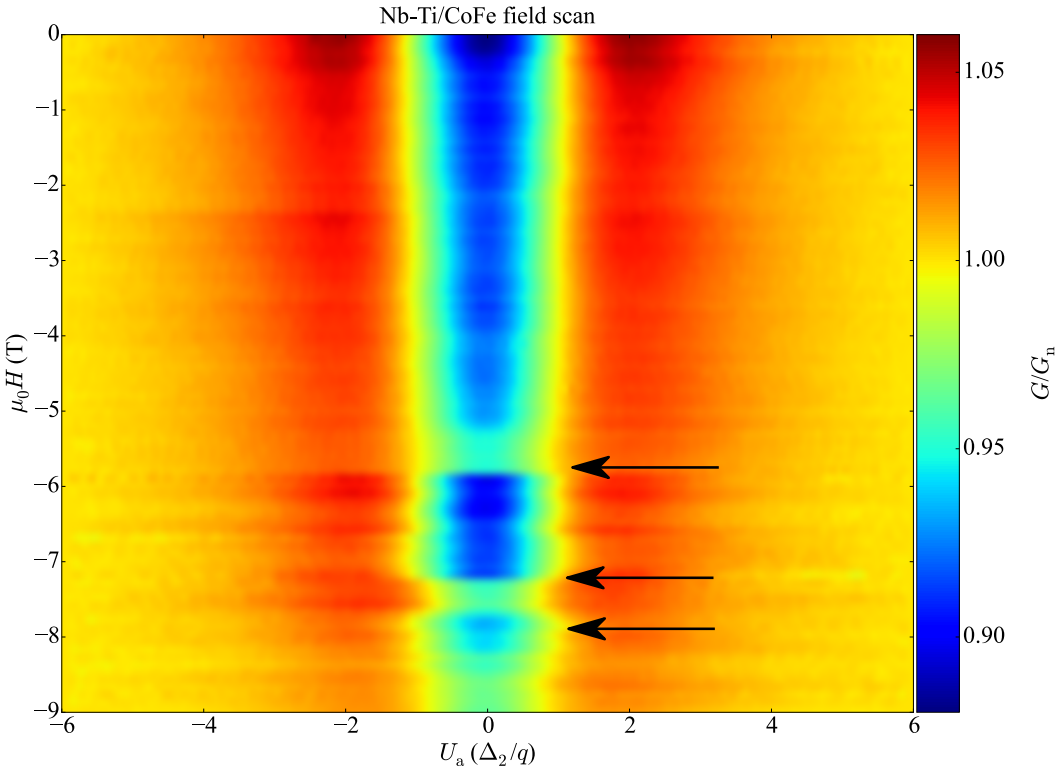

(a) Nb-Ti/CoFe high field PCAR.

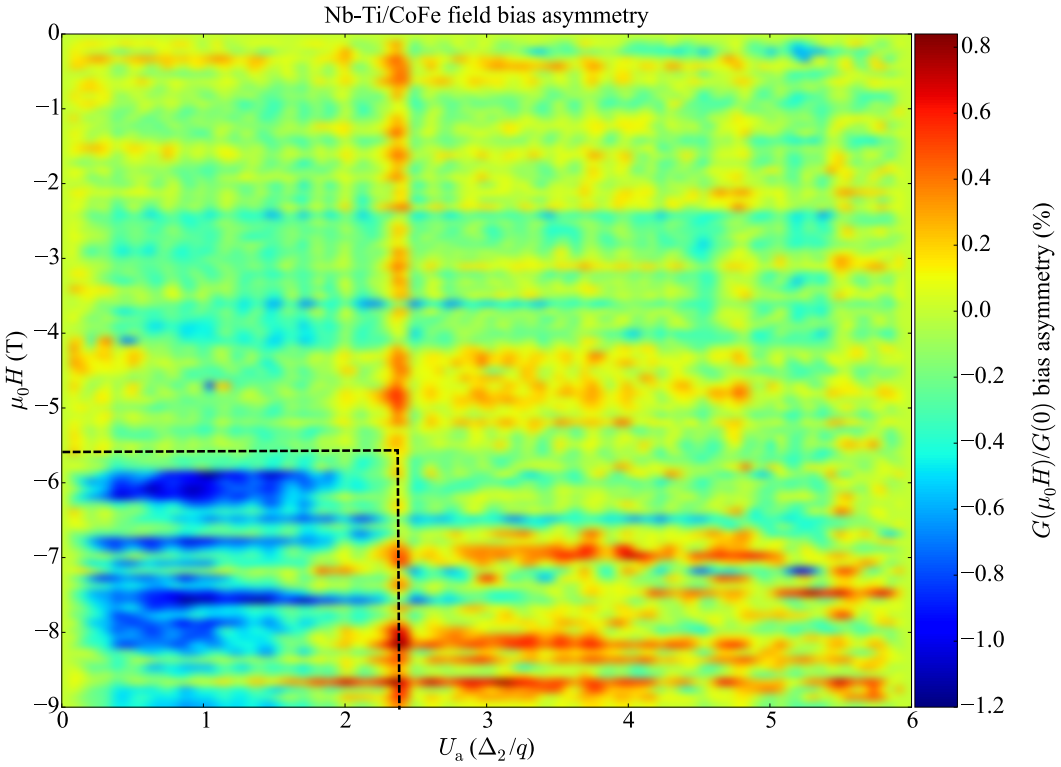

(b) Conductance asymmetry with respect to the applied bias U_a. The spectra are rescaled.

Figure 5.16: Demonstration of PCAR spectroscopy in a magnetic field scan from $\mu_0 H = -9\,\mathrm{T}$ to $\mu_0 H = 0\,\mathrm{T}$ of a Nb-Ti/CoFe point contact. The spectra are rescaled following the procedure described in Eq. (5.19) - Eq. (5.22). The applied bias is in units Δ_2/q, where $\Delta_2 = 1.5\,\mathrm{meV}$, and q is the elementary charge. The temperature is 2 K. Black arrows indicate the most pronounced flux jumps on panel (a). A square conductance asymmetry region is indicated with black dashed lines on panel (b).

Another set of high-field PCAR measurements on a Nb-Ti/CoFe contact in the field range from 0 T to −9 T is presented in Fig. (5.15) and Fig. (5.16). The colour plots contain individual PCAR field scans at fields $\mu_0 H$ = 0 T, −0.1 T, ..., −9.0 T. Figure (5.15) represents the raw spectral data which is only normalized with the high-bias conductance of each individual field scan. A few contact changes related to vortex dynamics or mechanical movement of the tip are clearly visible at fields of −5.8 T and −7.5 T. The drift corrected picture following the Eq. (5.19)-Eq. (5.22) is shown in Fig. (5.16) (a), however, it is evident that this routine does not help significantly in the considered field scan. From the same panel, it is extracted that the PCAR conductance maxima occur at $U_a \approx 2.5\,\Delta_2/q$ and, hence, the focus on the asymmetry scan should fall in the bias range $U_a \leq 2.5\,\Delta_2/q$. There is a pronounced positive PCAR asymmetry maximum running through the colour plot as a line at applied bias of $U_a = 2.5\,\Delta_2/q$ on Fig. (5.16) (b). The asymmetry is expected to reduce to zero for $U_a > 2.5\,\Delta_2/q$(see Fig. (5.3)), however, this is not the case and the high bias asymmetry is high in the field ranges −4.2 T:−5.2 T and −7 T:−9 T. The sub-gap asymmetry behaviour is essentially random. It is switching from positive to negative as a function of the bias in the field range −1 T: −4 T, then it is predominantly positive in the field range −4.2 T:−5.8 T, and finally it is mainly negative in the range −6 T:−9 T. A direct comparison between the asymmetry pictures of the two PCAR high field scans on Fig. (5.11) (b) and Fig. (5.16) (b) shows that the behaviour is not reproducible and most likely due to small experimental noise and/or vortex-related dynamics. The maximum asymmetry observed is ±1 % which is within the noise level for PCAR measurements in the needle-anvil configuration. Similar field scans have been measured multiple times and they have shown similar structure with no obvious Zeeman splitting of the PCAR signal. It is possible that the PCAR experimental configuration is directly responsible for the inability to resolved Zeeman splitting. Eltschka[88] have clarified that the density of states of superconducting tips depends critically on the cone opening. Zeeman splitting is observed with V tips at mK temperature in scanning tunneling spectroscopy in magnetic field of 3 T-5 T but the presence/absence of clear splitting depends on the geometry of the tip[90]. Zeeman splitting is not observable with blunt tips but it is clear in spectroscopy with sharper tips. The experimental data is confirmed by numerical solution of the Usadel equations in cone geometry. Since the superconducting tip is in direct electrical contact with the investigated sample in a PCAR experiment, it is perhaps squashed and with big cone angle at the apex. Therefore, this might be the reason for the inability to reliably observe conductance asymmetry due to Zeeman splitting in the Nb-Ti measurements.

5.4 High-field PCAR experiments with MgB_2

MgB_2 is discovered as a superconductor in 2001 by Nagamatsu *et al.* [248] and the maximum achieved critical temperature is 39 K, and the maximum achieved critical field in thin film form is

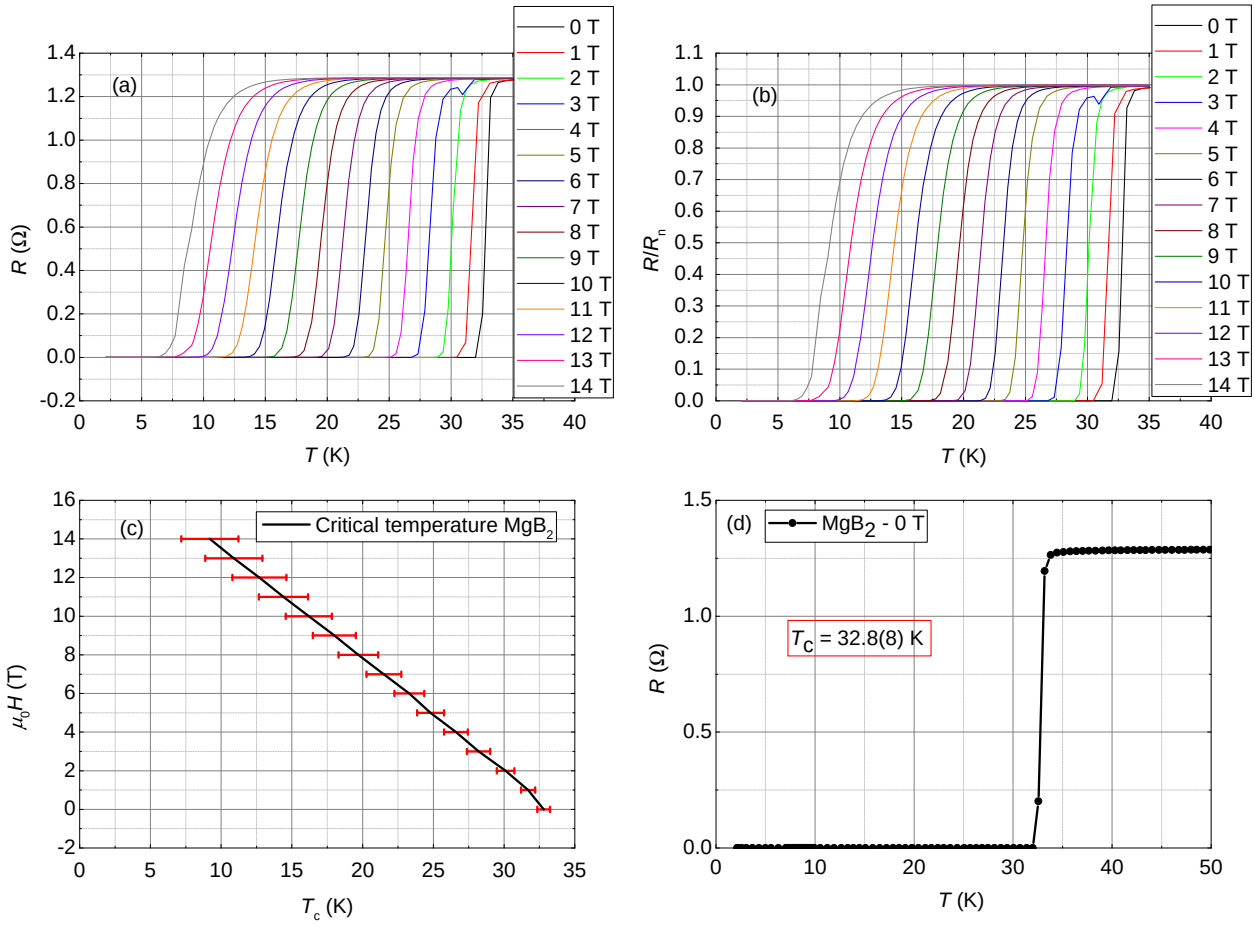

Figure 5.17: Critical superconducting temperature of MgB_2 films. Panel (a)-superconducting transition of MgB_2 at various fields. Panel (b)-superconducting transitions at various field in normalized resistance R/R_n. Panel (c)-critical temperatures at various fields along with the superconducting transition width. Panel (d)- critical temperature of $32.8(8)$ K of MgB_2 in zero applied external field.

70 T[39]. Recently, multi-filament MgB_2 superconducting wires have broken the record for critical current density at 20 K. MgB_2 is projected as replacement wires for future MRI scanners. The reason behind is that MgB_2 provides similar current density at 20 K to the one, which is maintained by Nb-Sn-Ti wires at 4.2 K*. From fundamental perspective, MgB_2 is the highest critical temperature superconductor which obeys roughly the BCS theory. It is an anisotropic superconductor with two distinct gaps. Two separate bands are responsible for the superconducting properties: π-band, which is associated to the boron p_z orbitals, and σ-band, which is associated to the boron p_{xy} orbitals. The π-band is essentially isotropic, whereas the σ-band is two-dimensional and lies in the $a-b$ plane[59]. The gap values have been extracted to be Δ_π = 2.2 - 2.4 meV and Δ_σ = 6.3 - 6.8 meV by tunneling spectroscopy in MgB_2/Al_2O_3/V junctions[170]. Only the Δ_π is observed if the transport is fully ballistic along the c-axis. However, if the MgB_2 crystallographic orientation is slightly tilted or the transport is diffusive, the Δ_σ band is manifested in tunneling and point contact

*which are presently the most widely used superconducting windings

spectroscopy as well. The MgB_2 thin films have been prepared by our collaborators Dr. M. Gregor and Prof. A. Plecenik from Comenius University, Bratislava, Slovakia. The Mg and B have been deposited on $Al_2O_3(001)$ substrate by thermal and electron-beam evaporation, respectively. The samples have been annealed *ex situ* in Ar atmosphere with pressure of 700 Pa and temperature of 800 °C[121].

From PCAR point of view, MgB_2 is interesting for high-field measurements because it has low atomic number and that means low spin-orbit interaction which is needed for clear resolution of the Zeeman-split density of states.

The superconducting critical temperatures of the MgB_2 films are measured in van der Pauw geometry at various magnetic fields and all scans are performed on cool down (see Fig. 5.17). The magnetic field is applied perpendicular to the plane. The critical temperature in zero field is 32.8(8) K. The critical temperature of a superconducting transition is conventionally defined as the temperature at which the resistance falls to half of its normal state value: $T = T_c$ when $R = 0.5R_n$. The superconducting transition width, ΔT, is defined as the difference between the temperatures at 90 % and 10 % of the normal resistance value: $\Delta T = T(0.9R_n) - T(0.1R_n)$. The superconducting critical temperatures along with the transition region widths are presented in Fig. 5.17 (c). The MgB_2 is fully superconducting for $T < 7$ K for our maximum magnetic field of 14 T*. All field-related PCAR experiments are performed at the base temperature of 2 K.

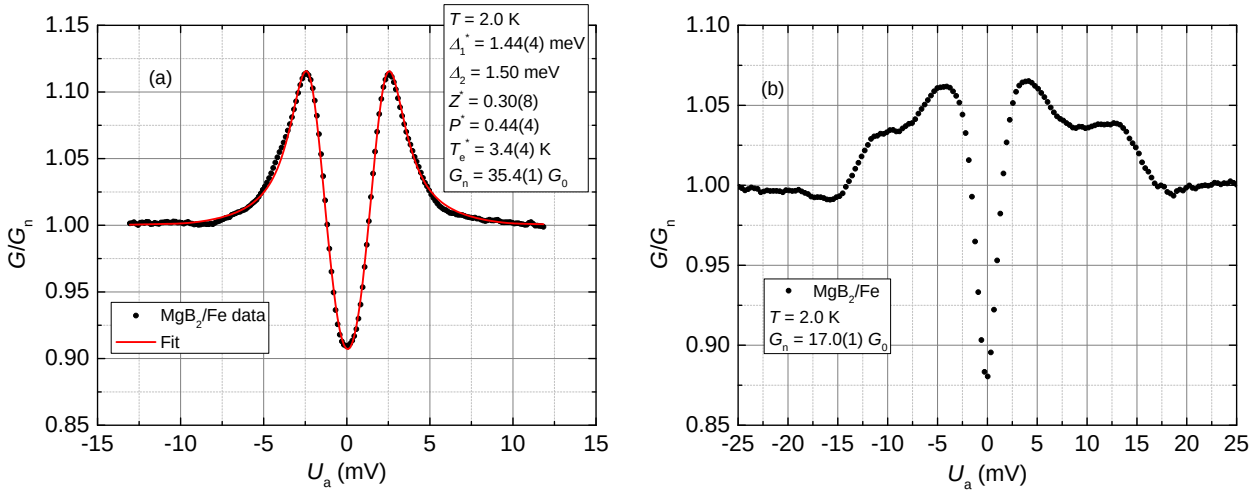

Figure 5.18: PCAR measurements at zero-field with Fe tip on MgB_2. Panel (a)-example of spectrum which demonstrates single gap and the correct value of the spin polarization is extracted $P_{Fe} = 44(4)\,\%$. Panel (b)-example of spectrum which exhibits dual gap. Such spectra are discarded in the high-field analysis.

The PCAR with the MgB_2 films is performed in reversed geometry: the anvil is the superconductor and the needle is a polycrystalline ferromagnetic tip (Fe). Initial PCAR measurements without external magnetic field are presented in Fig. (5.18). First of all, a PCAR spectrum exhibiting a single gap feature is analyzed. The extracted spin polarization is in accordance with the values

*There are Abrikosov vortices, of course.

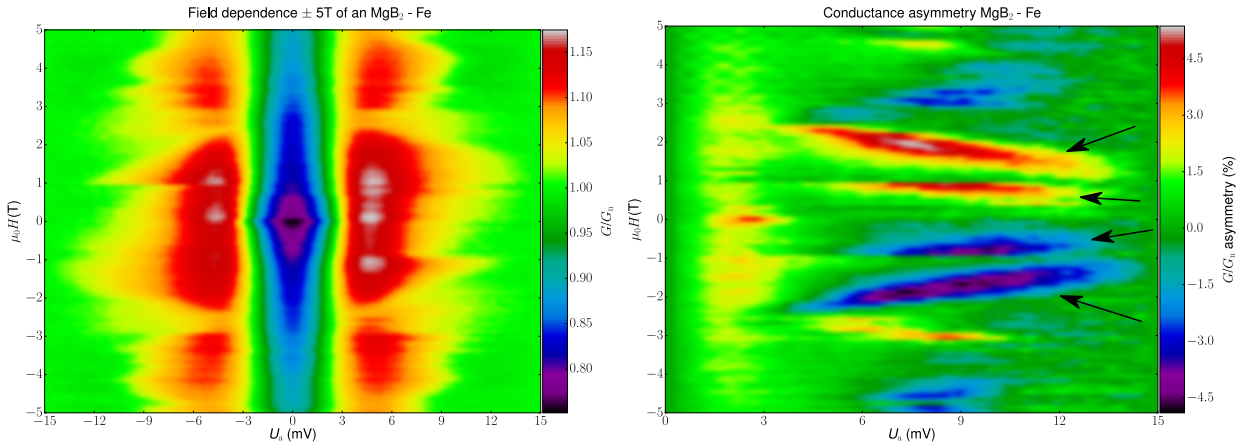

(a) PCAR normalized spectra

(b) PCAR bias asymmetry

Figure 5.19: PCAR measurements between MgB_2(thin film) and Fe(tip) in magnetic field $\mu_0 H = \pm 5\,\mathrm{T}$ perpendicular to the MgB_2 and temperature $T = 2\,\mathrm{K}$. Black arrows indicate pronounced asymmetric regions in the field scan.

reported before for Fe, $P \approx 44\,\%$. An example of a dual-gap PCAR spectrum is presented on the right-hand side of the same figure. The observation of dual gap features significantly complicates the analysis and the interpretation of the high-field data. Therefore, the focus falls on PCAR spectra which demonstrate a single gap feature*.

First of all, PCAR high-field measurements are performed with the field applied perpendicular to the surface of the MgB_2 superconducting film. This configuration is the less favourable one because the circular orbits of the Cooper pairs are not quenched by the thickness of the film and the orbital depairing effects are more significant in this case. Furthermore, the mixed states vortex lattice is more detrimental in the perpendicular configuration. The effect of vortex dynamics (pinning/depinning) in the contact are presented in Fig. (5.19) in magnetic fields $\mu_0 H = \pm 5\,\mathrm{T}$. As it has been case with Nb-Ti (see Fig. (5.11) and Fig. (5.16)), the decrease of the zero bias amplitude and the shrink of the PCAR signal with increasing field demonstrates the shunting effect of the vortex lattice and the fact that the superconducting gap becomes smaller. The PCAR line scans in the range from 2.5 T to 3.0 T and from -2.5 T to -3.0 T are indicative of vortex dynamics because the Andreev signal suddenly becomes flatter and then returns to its previous shape. There is pronounced bias asymmetry at the 0 T field scan which indicates that complicated vortex configuration is trapped in the contact area as the field is ramped down from 5 T towards 0 T. There are other smaller indications of vortex reorientation: for instance, the sudden increase in PCAR asymmetry at -1 T. The bias asymmetry of the field scan is calculated and presented in Fig (5.19) (b). The PCAR conductance maximum is observed at $U_\mathrm{a} \approx 5\,\mathrm{meV}$. Therefore, the Zeeman splitting induced asymmetry should be most pronounced at $U_\mathrm{a} \leq 5\,\mathrm{meV}$ following the fingerprint from Fig. (5.3). Such asymmetry profile is not observed. Interestingly, another asymmetry behaviour at

*Or more correctly, the contribution from the second gap is indistinguishable.

higher bias can be clearly distinguished. Four pronounced asymmetry regions are observed at high bias, $5\,\text{meV} < U_a < 13\,\text{meV}$, and modest magnetic field $-2\,\text{T} < \mu_0 H < 2\,\text{T}$ (see the black arrows in Fig.(5.19) (b)). These features are antisymmetric with respect to the applied field. This result is reminiscent of the PCAR observed asymmetry on Er by Stamenov[316]. MgB_2 is an anisotropic superconductor with different penetration depths and coherence lengths. The latter leads to elliptical vortices when the field is not perfectly along the c-axis[206]*. Therefore, the possibility for a peculiar vortex dynamics cannot be ruled out completely.

Another magnetic field scan of MgB_2/Fe in the range $\mu_0 H = \pm 5\,\text{T}$ is shown in Fig (5.20). The PCAR field scan shows essentially symmetric behaviour with respect to bias with no effect of the magnetic field on the asymmetry change. The PCAR conductance maximum happens at $|U_a| \approx 2.5\,\text{meV}$ and, hence, the conductance asymmetry should be most pronounced for $|U_a| \leqslant 2.5\,\text{meV}$. The latter is not observable and instead the asymmetry is almost featureless (see Fig. (5.20) (b)). The purpose of this measurement is to demonstrate that the field induced PCAR bias asymmetry is not reproducible and therefore is most probably due to vortex dynamics. The direct comparison between Fig. (5.19) and Fig. (5.20) shows that there is no reproducible magnetic field effect on the asymmetry of the PCAR signal in the field perpendicular to plane configuration.

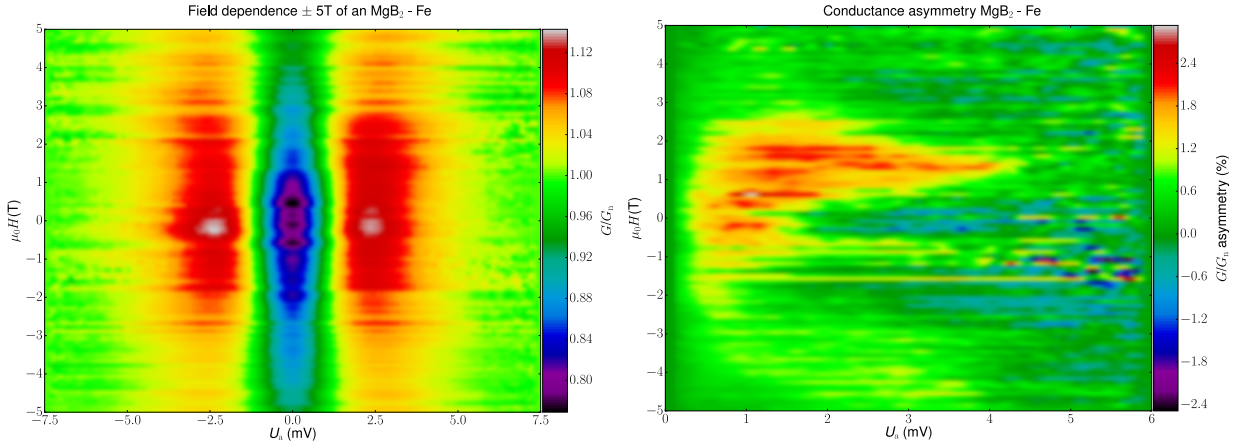

(a) PCAR normalized spectra

(b) PCAR bias asymmetry

Figure 5.20: Second demonstration of PCAR measurements between MgB_2 (thin film) and Fe (tip) in magnetic field $\mu_0 H = \pm 5\,\text{T}$ perpendicular to the MgB_2 and temperature $T = 2\,\text{K}$.

A demonstration of the detrimental effect of vortex pinning in the contact area is given in Fig. (5.21). In this case, the field is set constant at 5 T and the data is acquired real time with a single spectrum each second. Two metastable PCAR spectra have been observed at this relatively high field and it can be clearly noticed that the two PCAR spectra have different asymmetry sign. This implies that the temporal evolution of the Abrikosov vortex lattice is very important and might hinder the correct interpretation of the features.

*Because the MgB_2 films in this study are polycrystalline, this situation is very probable.

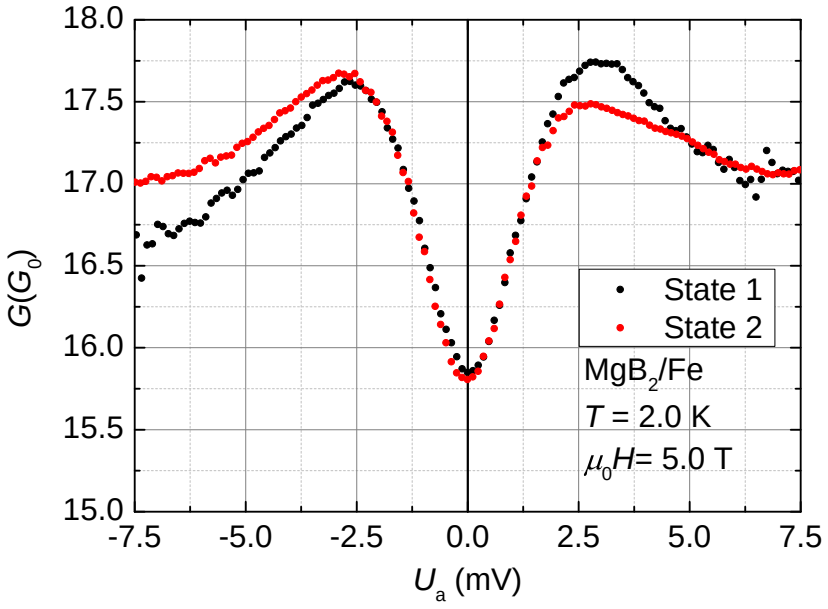

Figure 5.21: Example of the effect of vortex dynamics on the PCAR structure of MgB_2/Fe contact in constant field-two metastable asymmetric configurations are presented. The magnetic field is $\mu_0 H = 5\,\mathrm{T}$ and the temperature is $T = 2\,\mathrm{K}$.

Measurements are performed in the orthogonal direction as well. In this case, the magnetic field is applied in plane of the MgB_2 superconductor and the Fe tip is horizontal, this configuration is presented in Fig. (2.5). A problem arises from the fact that the axis between the magnetic field and the plane of the MgB_2 can not be adjusted. As it is well known from spin polarized tunneling experiments with Al, the angle is a critical parameter and even a degree offset has a detrimental consequence for the quasiparticle density of states. Another problem is the fact that the MgB_2 is a polycrystalline film and, therefore, the applied field direction does not necessarily coincide with the $a-b$ plane of the MgB_2. Some of the scans demonstrate four peak structure which is reminiscent of a Zeeman-split PCAR, see Fig. (5.22). The experiment at $\mu_0 H = 5\,\mathrm{T}$ demonstrates four-peak structure, while the one at $\mu_0 H = 7\,\mathrm{T}$ does not show the outer peak probably due to high-field modification of the quasiparticle density of states. It is critical to comment on the spin polarization sign in these Zeeman-split PCAR spectra. The bias in these experiments is defined as follows: positive on the Fe tip, negative on the MgB_2 thin film. The heights of the peaks 2 and 3 are used in order to determine the sign of the spin polarization (see Fig. (1.25)), because the heights of the peaks 1 and 4 are more affected by the orbital depairing and the spin-orbit coupling (see Fig. (1.26)). A positive spin polarization for the Fe is determined in this way, because peak 2 is higher than peak 3. The latter is in accordance with the SPT by Tedrow and Meservey (see Fig.7, Fig.8 and Fig.9 in [334]).

The energy splitting between the inner and outer peaks can be easily determined at 5 T and it is $\Delta E = 2.3\,\mathrm{meV}$ (see Fig. (2.5)). The Zeeman-split energy cannot be determined unambiguously at 7 T as the outer peaks are not present. If it is assumed that the position of the outer peaks

in unchanged*, then the Zeeman splitting energy is $\Delta E(7\,\mathrm{T}) = 2.7\,\mathrm{meV}$. However, there is an apparent discrepancy which needs clarification. The Zeeman splitting energy between the spin-up and spin-down electrons is determined by $\Delta E_\mathrm{Z} = 2 g_\mathrm{s} s \mu_\mathrm{B} \mu_0 H$, where g_s is the g-factor of the electron, $s = 1/2$ is the spin of the electron, and μ_B is Bohr magneton. The g-factor is $g_\mathrm{s} \approx 2$ for most superconductors†. Therefore, the Zeeman splitting has to be $\Delta E_\mathrm{Z}(5\,\mathrm{T}) \approx 0.58\,\mathrm{meV}$, and this value is approximately four times smaller than the experimentally observed splitting.

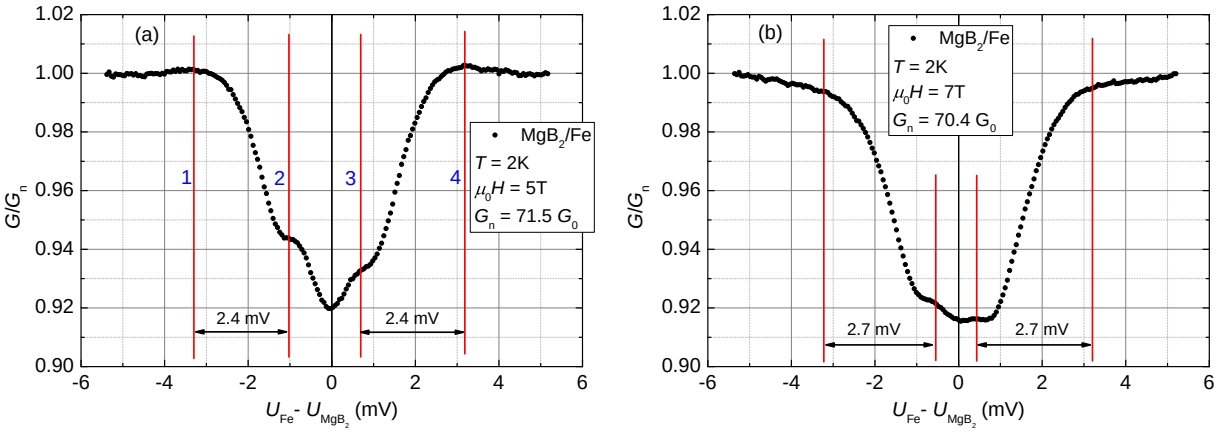

Figure 5.22: Example of four-peak structure in PCAR experiments between MgB_2 thin film and Fe tip. The temperature is $T = 2\,\mathrm{K}$ and the field is applied in plane of the MgB_2 film. Panel (a)-experiment at field $\mu_0 H = 5\,\mathrm{T}$. Panel (b)-experiment at field $\mu_0 H = 7\,\mathrm{T}$.

The following four possible explanations for the observed four peak structure and the energy splitting are discussed:

- Dual gap contribution
- High g-factor
- Abrikosov bound states
- High effective magnetic field

First of all, the possible simultaneous contribution from the MgB_2 two superconducting gaps is considered. The outer peaks are located at applied bias $U_\mathrm{a} = \pm 3.3\,\mathrm{meV}$ at $\mu_0 H = 5\,\mathrm{T}$, which is slightly higher than the smaller MgB_2 gap ($\Delta_\pi = 2.2\,\mathrm{meV}$) but it is significantly below the larger gap ($\Delta_\sigma = 6\,\mathrm{meV} - 7\,\mathrm{meV}$). Additionally, the two inner peaks are located at very low bias of $U_\mathrm{a} \leq 1\,\mathrm{mV}$. Therefore, the four peak structure can not be attributed to simultaneous contributions of Andreev reflection from the Δ_π and Δ_σ gaps.

Another possibility is that the experimentally observed energy splitting can be due to high g-factor, because the Zeeman splitting is $\Delta E_\mathrm{Z} = 2 g_\mathrm{s} s \mu_\mathrm{B} \mu_0 H$. However, it has been shown before by

*This means that the gap does not shrink from 5 T to 7 T.

†Exclusion from that are the heavy-fermion superconductors[328].

electron paramagnetic resonance measurements that $g \approx 2$ for MgB_2[254]. Hence, high g-factor cannot be a correct explanation for the observed structure.

Another pathological situation might happen if there are Abrikosov bound states contributing to the PCAR signal. Zero bias peaks have been observed in the density of states of vortex cores of some superconductors (see Fig. (5.5)). Peculiar dynamics of these low energy excitations might lead to Andreev reflection with similar structure, however, bound states have not been observed in the MgB_2 superconductor[92]. Therefore, the observation cannot be attributed to this, as well.

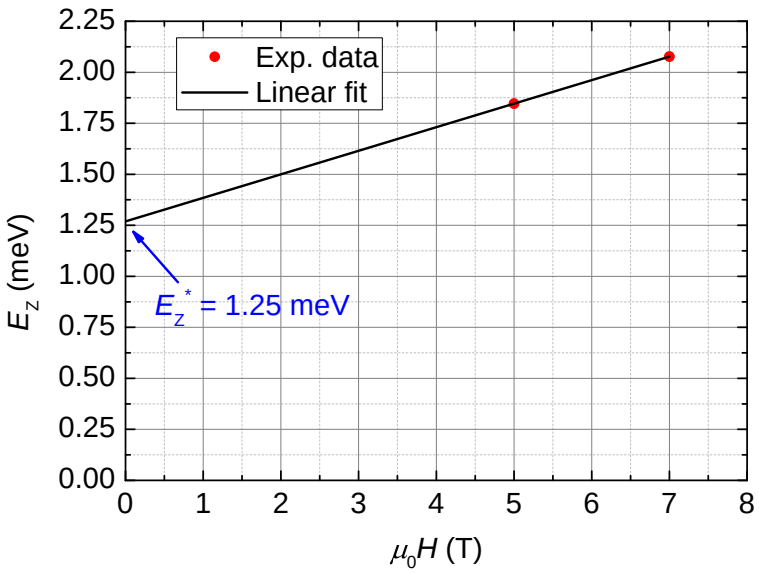

Figure 5.23: Linear fit of the rescaled Zeeman split energies versus the applied magnetic field. The intercept corresponds to a zero field effective Zeeman splitting energy of $E_Z^* = 1.25\,\text{meV}$.

Finally, the possibility of high effective field due to the proximity effect from the ferromagnet is considered. It has to be noted that the applied bias scale in the PCAR experiments is not well defined due to two main reasons: barrier strength and series resistance. The barrier strength "opens up" the bias axis as it is presented in Fig. (1.30), and the series resistance has the same effect because the potential drop is shared between the Andreev point contact and the leads. The outer peaks are located at $U_a \approx \pm 3.3\,\text{mV}$, and if the MgB_2 gap is assumed to be $\approx 2.2\,\text{meV}$*, the maximum rescaling factor is 1.5. It is interesting to comment on how much the Zeeman splitting opens up between 5 T and 7 T. The experimentally observed increase is 0.3 meV, while the theoretical prediction is for 0.23 meV. Hence, the correct rescaling ratio is $0.3\,\text{meV}/0.23\,\text{meV} \approx 1.3$, not far off from the previous estimate of 1.5. Ren *et al.*[276] have introduced an effective field in order to fit their Zeeman split PCAR. The latter is justified by the stray field of the EuS ferromagnetic layer and its exchange field. Nevertheless, their extracted field offset is not very high: 0.52 T. The Zeeman split points from our experiments are rescaled with a correction factor of 1.3 and a linear fit is passed

*Here it is again assumed that the MgB_2 gap is constant from 0 T to 5 T.

through them in Fig. (5.23). The intercept indicates that the effective zero field Zeeman splitting amounts to $E_Z^* \approx 1.25\,\text{meV}$ which corresponds to $\mu_0 H^* \approx 10.7\,\text{T}$. This value is significantly above the polarization of Fe ($\approx 2\,\text{T}$). The fact that the Fe tip is in direct electrical contact with the MgB_2 film means that there is an inevitable proximity effect in the contact area (see Fig. (1.32)). The ferromagnetic electrode proximity means that the superconducting layer experiences part of the exchange field. The latter is $\sim 1000\,\text{T}$ in classical $3d$ ferromagnetic materials and following Heisenberg model the Curie temperature is directly related to the exchange integral. This relation clarifies why there is so significant difference between the cases of EuS and Fe, the former has significantly lower Curie temperature of $\approx 17\,\text{K}$[242]. There is literature experimental data which confirms partially this explanation. For instance, exchange splitting of $\mu_0 H^* \approx 3\,\text{T}$ has been observed by Hao *et al.*[131] in Al/EuS/Al junctions and by Tedrow *et al.*[335] in EuO-Al/Al_2O_3/Fe junctions with $\mu_0 H^* \approx 1\,\text{T}$. However, the full justification of an effective field of 10.7 T in our measurements would require further analysis and more data collected with variable ferromagnetic (and non-magnetic) compositions on top of the MgB_2 film.

5.5 Data on MgB_2-CoFe junctions

High-field PCAR measurements in the usual needle-anvil configuration are more susceptible to mechanical vibration. Apart from contact reorientation (with change in the Z parameter), the vortex configuration at the tip apex might change significantly. Shadow-masked junctions have been prepared in the organic evaporator chamber (see Fig. (2.10)). The blanket MgB_2 thin film has been first Ar-ion milled in the Millatron and then transferred quickly to the organic thermal evaporation chamber. In the organic chamber, it is pre-cleaned again with Ar. Then insulating layer of SiO has been evaporated through shadow mask which leaves stripes of 200 µm from the MgB_2 film. After that, the top contact $Co_{50}Fe_{50}$ stripes have been evaporated perpendicular with respect to the MgB_2 stripes at thickness of 20 nm. In this way, rather large junctions are made of size $200\,\mu\text{m} \times 200\,\mu\text{m}$. These cannot be considered point-contact junctions but usual PCAR with spin polarization expected for CoFe has been observed nevertheless (see Fig. (5.24)). The advantage of this large geometry configuration is that the vortex lattice contribution is averaged spatially over very large area. First, the discussion starts with high-field PCAR in range $\mu_0 H = \pm 14\,\text{T}$ on Fig. 5.25. The experiments are performed with the horizontal rotator option of the PPMS and two configuration are presented: in-plane and perpendicular to plane.

The zero-bias amplitude demonstrates the expected behaviour from a superconductor in external magnetic field. The increase of the magnetic field results in denser vortex lattice, therefore, more pronounced normal conductance through the junction. The Andreev reflection is suppressed and the zero-bias value is closer in value to the high-bias conductance. However, the supercon-

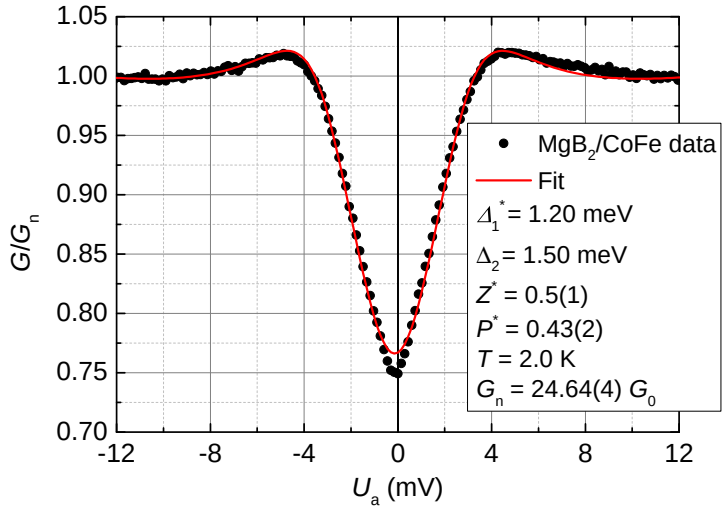

Figure 5.24: PCAR spectrum along with the BTK fit and the extracted parameters for an MgB_2/CoFe junctions at zero applied field of and $T = 2\,\mathrm{K}$.

ducting density of states is modified beyond the simple two-channel model (see Eq. 5.2). The latter is most clearly distinguished at bias $U_\mathrm{a} = \pm 3\,\Delta_2/q$ if the cut from $-14\,\mathrm{T}$ to $14\,\mathrm{T}$ is taken. The smearing of the superconducting density of state could be roughly described with the introduction of the Dynes' imaginary gap (see Eq. (1.69) and Fig. (1.15)). This can be understood as extended lifetime of the superconducting quasiparticles before they recombine into Cooper pairs. The accurate treatment is given in terms of the Usadel equation which gives the DOS averaged over the vortex cell (Fig. (5.4)). More interesting is to comment on the difference in the behaviour between the in-plane and perpendicular to plane scans. Two contours at levels 0.92 and 0.86 are presented in order to outline the (a)symmetry. The perpendicular to plane geometry demonstrates essentially symmetric spectra with respect to the zero bias line. This is expected because in this geometry the vortex dynamics is more pronounced. Furthermore, the Maki-Fulde theory explains that orbital depairing effect is much more pronounced in perpendicular geometry (Eq. (1.99)). This explains why no appreciable voltage asymmetry is observed in perpendicular geometry. If the same level contours are followed on the in-plane full field scan, there is an apparent voltage asymmetry. For instance, the negative bias contour at level 0.92 evolves slightly towards zero-bias while the positive bias contour 0.92 evolves differently. First, it moves inwards towards zero bias in field range from $0\,\mathrm{T}$ to $\pm 4\,\mathrm{T}$. This contour has a local minimum there. After that, it starts drifting towards higher bias. The behaviour of the contours is symmetric with respect to field. The slight bias asymmetry is an indication of the Zeeman-splitting of the density of states. The conductance bias asymmetry effect is very small. This is attributed to the large area of the Andreev junction. In this is case, the Zeeman-splitting contribution towards the Andreev reflection is crystallographically averaged because both the MgB_2 and the $Co_{50}Fe_{50}$ electrodes are polycrystalline. The Zeeman-asymmetry contribution comes from MgB_2 grains which are well-aligned with the field direction.

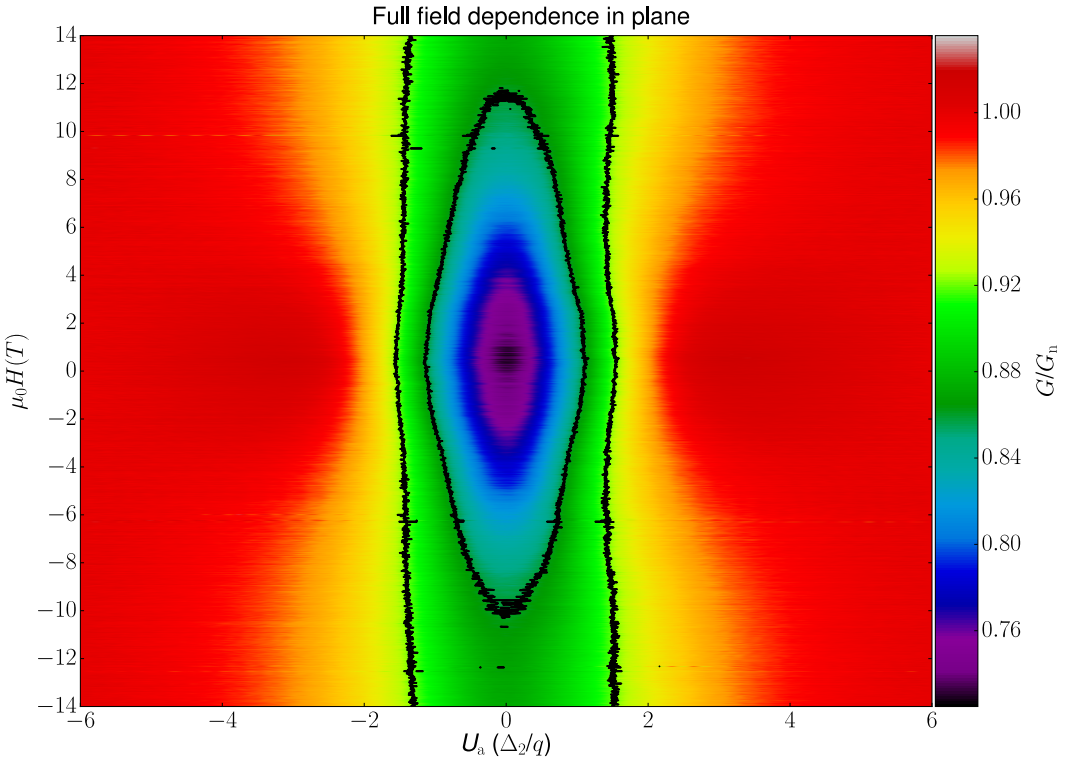

(a) In plane field scan.

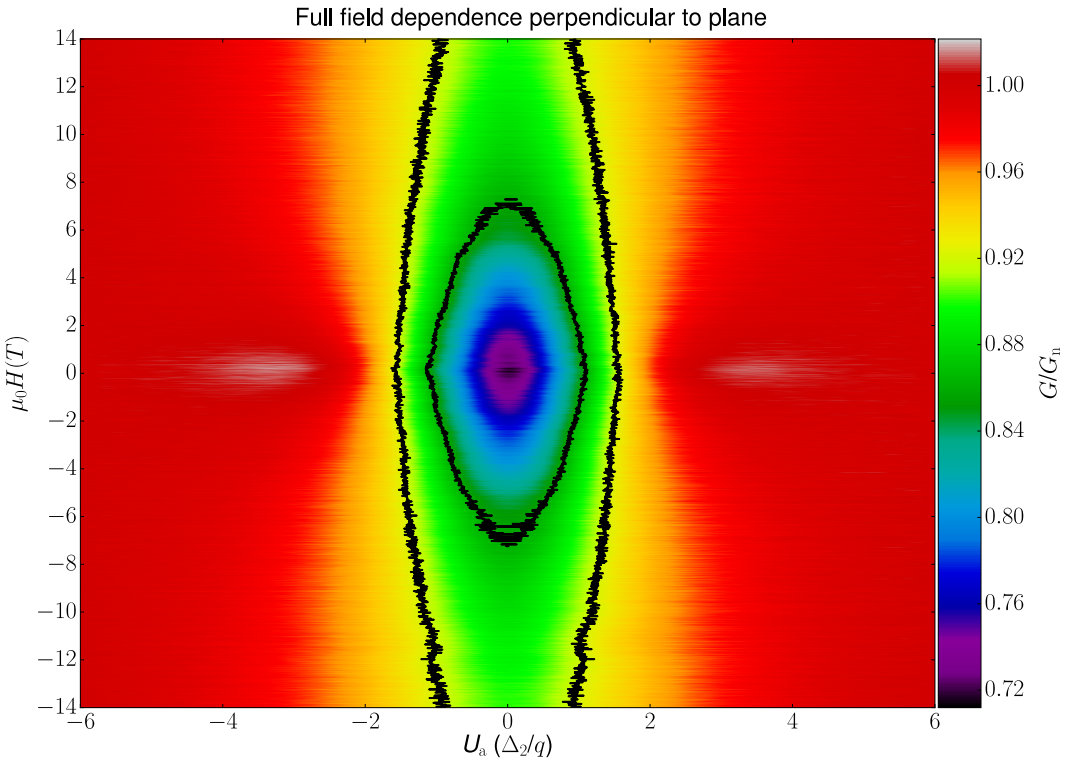

(b) Perpendicular to plane field scan.

Figure 5.25: In plane (a) and perpendicular to plane (b) high field PCAR scans of MgB_2/$Co_{50}Fe_{50}$ shadow-masked junction. The maximum applied field is ± 14 T. The applied bias is in units Δ_2/q, where $\Delta_2 = 1.5$ meV, and q is the elementary charge. The temperature is 2 K.

Full PCAR angular dependences are presented in Fig. (5.26), Fig. (5.27), Fig. (5.28), and Fig. (5.29) for applied magnetic field of $\mu_0 H = 0\,\mathrm{T}, 1\,\mathrm{T}, 2\,\mathrm{T}, 3\,\mathrm{T}, 4\,\mathrm{T}, 5\,\mathrm{T}, 7\,\mathrm{T}$, and $14\,\mathrm{T}$, respectively. The zero-field scan is, as expected, featureless and demonstrates independence of the PCAR signal on angle*. The maximum PCAR conductance is observed at $|U_\mathrm{a}| \approx 3.5\,\Delta_2/q$. The scan in $1\,\mathrm{T}$ starts showing the effect of the magnetic field orientation on the PCAR structure. In this case, the PCAR-related conductance maxima are clearly visible at $|U_\mathrm{a}| \approx 3.5\,\Delta_2/q$ around angles $\theta = 90°$ and $270°$ (when the field is in plane of the MgB_2 film) but the maxima disappear for field orientation $\theta = 180°$ and $360°$ (when the field is perpendicular to the plane of the MgB_2 film). The latter is due to the dependence of the orbital depairing parameter ζ on the field orientation (Eq. (1.99) and Fig. (1.26) (a)). The orbital depairing distorts more the PCAR density of states in the field perpendicular to plane configuration and that is why the the sharp DOS structure is not present for $\theta = 180°$ and $360°$. The dependence of the PCAR on the angle of the applied magnetic field is more apparent for higher magnetic field of $2\,\mathrm{T}$ where the conductance maxima are present as more compact areas in angular dependence very close to 90° and 270°. Furthermore, the zero-bias anomaly starts showing clearly the suppression of the PCAR signal at perpendicular fields. The applied field $3\,\mathrm{T}$ shows further suppression of the PCAR conductance maxima and this time they are barely observable for field in plane orientation. The angular dependence of the zero-bias anomaly is sharper as well.

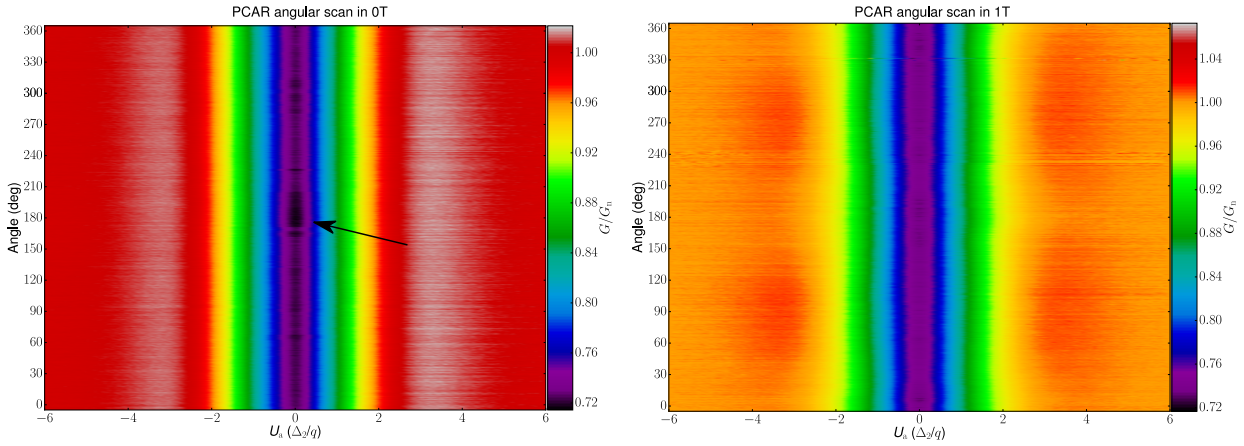

(a) Full angular scan of MgB_2/CoFe Andreev junctions in applied field of $0\,\mathrm{T}$.

(b) Full angular scan of MgB_2/CoFe Andreev junctions in applied field of $1\,\mathrm{T}$.

Figure 5.26: Full angular scans of MgB_2/CoFe junction at applied field of $0\,\mathrm{T}$ (a) and $1\,\mathrm{T}$ (b). A feature, which is most likely related to noise, is observed on panel (a) for angle $\theta \approx 180°$ (indicated with a black arrow).

*There is small zero-bias feature at $\theta \approx 180°$ in Fig. (5.26) (a) which should be related to noise. It is indicated with an arrow.

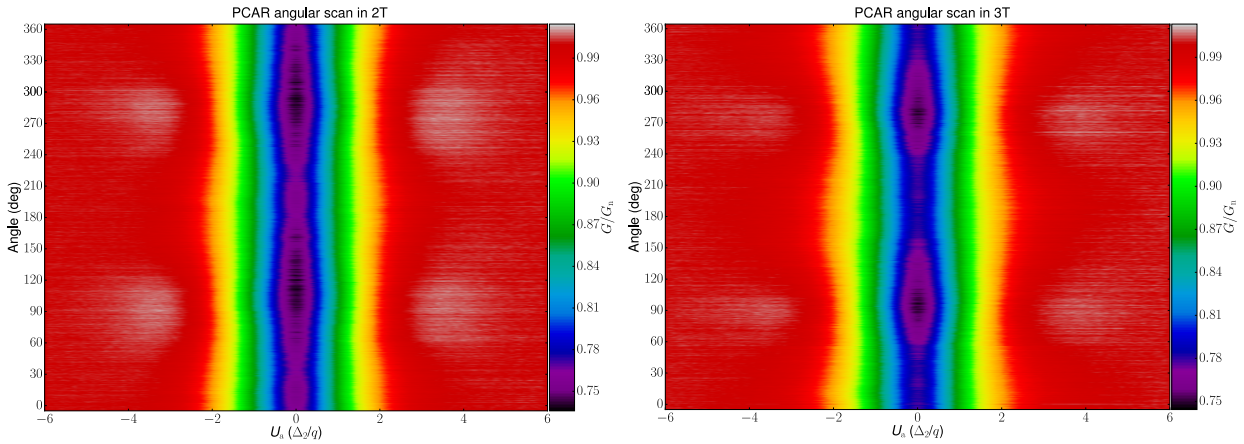

(a) Full angular scan of MgB_2/CoFe Andreev junctions in applied field of 2 T.

(b) Full angular scan of MgB_2/CoFe Andreev junctions in applied field of 3 T.

Figure 5.27: Full angular scans of MgB_2/CoFe junction at applied field of 2 T (a) and 3 T (b).

PCAR conductance maxima are no longer distinguishable at higher magnetic field of 4 T and the zero-bias conductance demonstrates that the low-bias anomaly is pronounced very close to in-plane orientations. The PCAR angular scan at 5 T has similar features to the one at 4 T with further shrinking of the zero-bias anomaly and indistinguishable maxima around $U_a \approx 3.5\Delta_2/q$. The highest fields of 7 T and 14 T show that the orbital depairing is very significant in the plane configuration as well. Furthermore, the spectral features are much broader which is due to the presence of higher concentration of Abrikosov vortices. The highest field scan of 14 T demonstrates that the Andreev reflection contribution towards the overall conductance is very small.

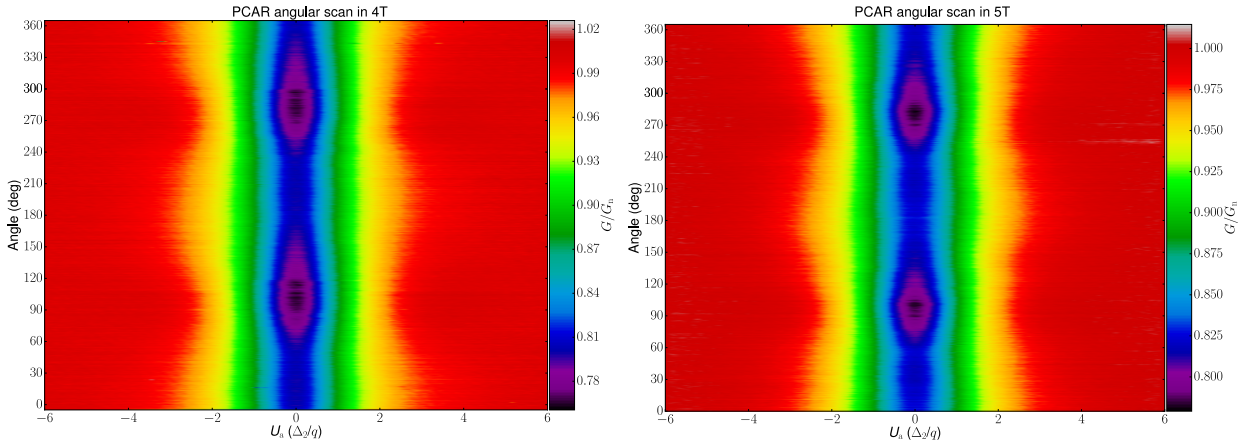

(a) Full angular scan of MgB_2/CoFe Andreev junctions in applied field of 4 T.

(b) Full angular scan of MgB_2/CoFe Andreev junctions in applied field of 5 T.

Figure 5.28: Full angular scans of MgB_2/CoFe junction at applied field of 4 T (a) and 5 T (b).

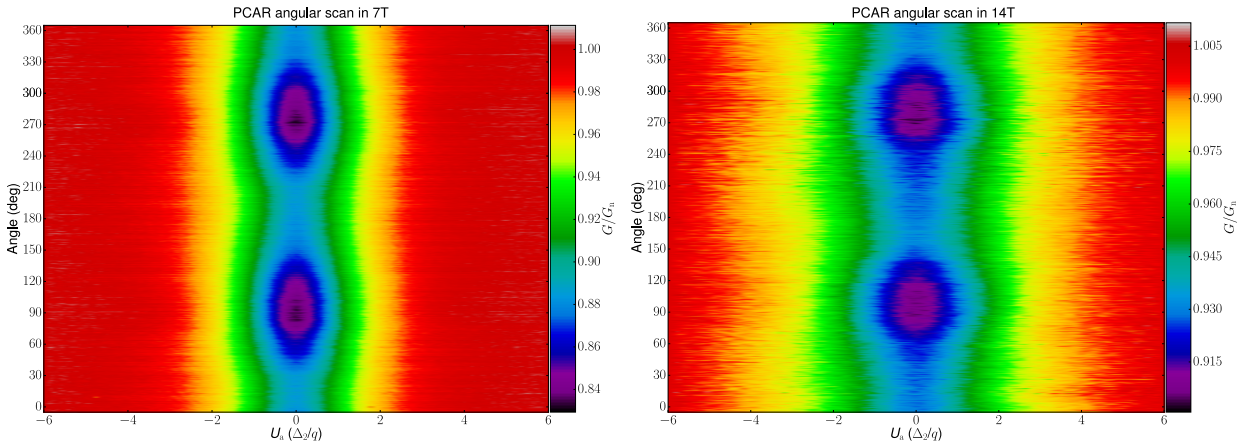

(a) Full angular scan of MgB_2/CoFe Andreev junctions in applied field of 7 T.

(b) Full angular scan of MgB_2/CoFe Andreev junctions in applied field of 14 T.

Figure 5.29: Full angular scans of MgB_2/CoFe junction at applied field of 7 T (a) and 14 T (b).

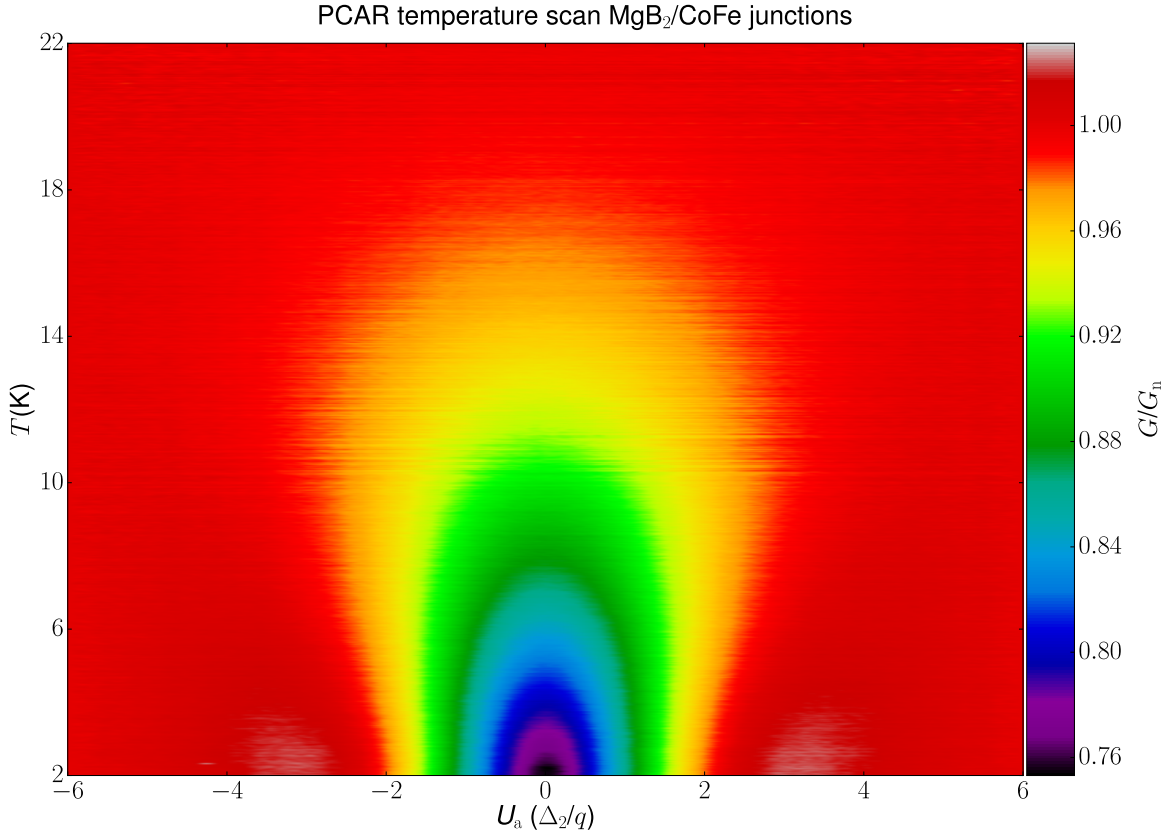

Figure 5.30: PCAR temperature evolution of MgB_2/CoFe shadow masked junctions. The temperature scan is performed in zero applied magnetic field.

The temperature dependence of the PCAR signal of the MgB_2/CoFe junctions is presented in Fig. 5.30. The data is acquired on slow warm-up ($0.5\,\mathrm{K\,min^{-1}}$) and individual spectra are saved in narrow temperature interval $\Delta T \approx 40\,\mathrm{mK}$. The background curve used for normalization is ac-

quired at 22 K. As before, each separate curve is normalized with the high bias conductance*. The most notable feature is that the PCAR signal is completely suppressed at temperature of $\approx$ 20 K. The latter is significantly below the T_c of our MgB_2 thin films ($\approx$ 32.8 K). This is due to suppression of the surface superconductivity of the MgB_2 films. Two are the possible reasons for that: magnetic impurities or amorphous interface. The MgB_2 surface quality is degraded by the Ar plasma cleaning procedure *in-situ* the chamber. This approach probably modifies the electron-phonon interaction at the interface and, therefore, the interface superconductivity. Another possible reason is critical temperature depression due to magnetic impurities. The effect of magnetic inclusions on the critical temperature of thin films is discussed theoretically by Abrikosov and Gor'kov (AG)[308] and the first systematic experimental investigation is performed by Woolf and Reif[380]. It is expected that the MgB_2 surface is corrugated after the Ar cleaning process, therefore, after the CoFe deposition the MgB_2/CoFe interface is an "orange-peel" of interpenetrating supeconductor-ferromagnet regions†. The original AG theory describes that the critical temperature is significantly suppressed and the density of states is modified in the presence of magnetic impurities. Later extensions by Maki[210] and de Gennes[69] demonstrate that the same effect is played by other time-reversal perturbation like magnetic fields, current, rotations, spin exchange and hyperfine fields[342]. The relation between the critical temperature and the pair-breaking energy, α, is given by:

$$\ln \frac{T_c}{T_{c0}} = \psi\left(\frac{1}{2}\right) - \psi\left(\frac{1}{2} + \frac{\alpha}{2\pi k_B T_c}\right), \tag{5.23}$$

where T_{c0} is the nominal superconductor transition temperature‡, T_c is the observed critical temperature, and $\psi(x)$ is the digamma function. The pair breaking energy α is related to a time constant τ_K: $2\alpha = \hbar/\tau_K$ (see Tinkham[342] p. 391). The latter constant is equal to the average time needed for randomization of the relative phase of the Cooper pair electrons by the time-reversal perturbation. The original AG theory considers the exchange interaction coupling effect between a magnetic impurity spin $\vec{S}$ and the electron spin $\vec{s}$ in the form $J(r)\vec{S}.\vec{s}$, where $J(r)$ is the local exchange interaction. The approximate relation between the pair-breaking energy α and the averaged exchange J is:

$$2\alpha \approx \frac{xJ^2}{E_F}, \tag{5.24}$$

where x is the fractional impurity concentration and E_F is the Fermi energy. The relevant parameters for the case of MgB_2 with and without CoFe deposited are $T_{c0} = 32.8$ K and $T_c = 20$ K and the pair breaking constant calculated is then $\alpha = 1.3$ meV. The latter corresponds to a reduced pair-

*No rescaling is required in this case, as the high-bias conductance is essentially temperature independent. To be more precise, the normalization conductance is $G_n = 24.6\, G_n$ at 2 K and $G_n = 24.3\, G_n$ at 22 K.

†As a possible future investigation direction, the quality of this interface might be investigated by electron microscopy techniques.

‡Which is assumed to be equal to $T_c \approx 32.8$ K from Fig. (5.17).

breaking energy of $\alpha/\Delta_\pi = 0.6$. The density of states modification as a function of the ratio α/Δ has been theoretically treated by Skalski *et al.*[308] and for $\alpha/\Delta > 0.5$ the sharp structure of the superconducting quasiparticle DOS is no longer present. A way to distinguish whether the magnetic scattering or the surface amorphization is more prevalent is to investigate PCAR junctions between MgB_2 and non-magnetic metal. If the observed PCAR T_c is similar to the ferromagnetic junctions, then the interface roughness is the main culprit. Otherwise, it is the magnetic nature of the electrode.

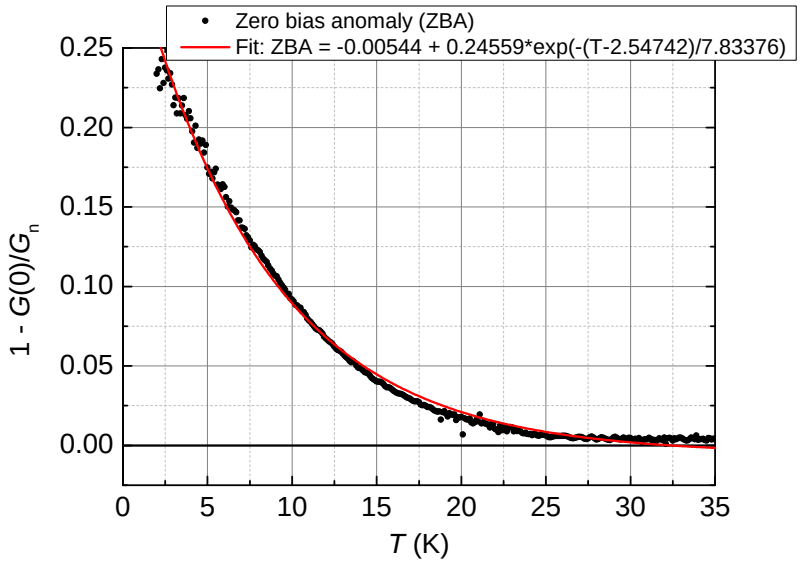

Figure 5.31: Temperature decrease of the PCAR zero-bias anomaly for an MgB_2/CoFe shadow-masked junction. The red curve represents an exponential decay fit.

Finally, it is important to comment on the zero-bias conductance temperature evolution from Fig. (5.30). The zero-bias conductance demonstrates essentially exponential decrease with the temperature on Fig. (5.31). The latter behaviour is rather surprising because the MgB_2 has almost classical BCS temperature dependence of the superconducting gap. The PCAR zero-bias conductance should follow the temperature dependence of the gap. However, there are two additional effects in this case: elevated temperature and the existence of a ferromagnetic layer on top. The higher critical temperature of the MgB_2 superconductor means that the thermal smearing will have a more significant effect on the zero bias conductance than is the case for more classical superconductors like Nb, Nb-Ti, with $T_c \leq 9.3\,\mathrm{K}$. Equally important is the presence of a ferromagnetic layer on top of the superconductor. The effect of magnetic impurities on the quasiparticle density of states of a superconductor has been investigated for the cases of lead and indium by Woolf and Reif[380]. The superconducting gap is not as sharp as in the classical case because there are sub-gap states. The existence of subgap states along with the more pronounced Fermi distribution thermal smearing are responsible for the exponential decrease of the PCAR zero-bias conductance as a function of temperature.

5.6 Conclusions and outlook

High-field PCAR measurements with MgB_2 have demonstrated small but reliable asymmetry which indicates the sign of the spin polarization. Angular dependence scans on $MgB_2/Co_{50}Fe_{50}$ junctions have been performed in order to investigate the depairing effect of the field on the MgB_2 superconductor. Presently, high-field PCAR with MgB_2 is possible only in reversed geometry where the superconducting film is the anvil.

In future, high-field experiments with MgB_2 very thin films ($d < \xi$) must be performed in order to quench the depairing effect when the field is applied in-plane of the film. Furthermore, the application of magnetic field in type-II superconducting films with thickness lower than the coherence length prevents entrance of vortex lattice*. The arrival of MgB_2 superconducting wires in mono-filament form provides the opportunity to perform high-field PCAR on thin films.

The demonstration of very high-field PCAR spectroscopy with Nb-Ti opens new fundamental research directions like investigation of the spin polarization as a function of the applied field, for instance, investigation on magnetic topological insulators as the applied field is swept through the coercivity. Over the course of our work, high-field PCAR with Nb-Ti has been investigated by Gifford *et al.*[111]. Their measurements demonstrate clear PCAR in field up to 1.5 T.

Another potential superconductor for high-field Andreev reflection in reversed geometry is NbN. Zeeman-splitting has been demonstrated with it in spin-polarized tunneling[394], and the nitrides are more stable in atmosphere.

*The determined coherence length for MgB_2 is $\approx 30\,\text{nm} - 50\,\text{nm}$ [92, 206].

Chapter 6

Magnetic tunnel junctions with the compensated half-metallic ferrimagnet Mn_2Ru_xGa

"Great, great, great! Brilliant, brilliant, brilliant! Now we need a plan!"

Dr. Karsten Rode

6.1 Introduction

Giant magnetoresistance (GMR) and tunneling magnetoresistance (TMR) are the effects which the field of spin electronics is biult upon. The basic unit in the area is the spin-valve (SV) for the GMR and magnetic tunnel junction (MTJ) for the TMR. The SV comprises roughly of a ferromagnetic electrode/non-magnetic spacer/ferromagnetic electrode trilayer, while for the MTJ the non-magnetic spacer is replaced with an insulating barrier. There are three main classes of functional devices biult around the concepts of SVs and MTJs presently:

- Magnetic Random Access Memory
- Magnetic Sensors
- Spin-transfer torque (STT) based nano-oscillators

The magnetic sensors area is highly relevant both for construction of more sensitive read-heads for hard disk drives and novel biomagnetic sensors[98]. This area is essentially not related to the present work.

The idea of STT-based magnetic random access memory (STT-MRAM) is the most perspective candidate for non-volatile memory and it is already commercially available (for a brief introduction see Sec. (1.2.3)). A crucial quality of each contemporary memory storage is scalability. In other words, can the device size be reduced while maintaining data retention and the same read-write characteristics of the memory element? The stability in MTJs depends critically on two effects:

- Cross-talk between adjacent bits
- Thermal stability of the ferromagnetic layers

The thermal stability depends on the magnetic anisotropy energy barrier of the magnetic storage layers which are patterned to form the MTJs. The magnetic anisotropy barrier K_{eff} is a sum of the magnetocrystalline (K_{mag}), shape (K_{shape}), and interface (or surface) anisotropy(K_{s}):

$$K_{\text{eff}} = K_{\text{mag}} + K_{\text{shape}} + K_{\text{s}}/t, \tag{6.1}$$

where t is the thickness of the ferromagnetic layer. The thermal stability criterion Δ is determined by the ratio between the total anisotropy energy and the thermal excitation energy

$$\Delta = \frac{K_{\text{eff}} V}{k_{\text{B}} T}, \tag{6.2}$$

where V is the volume of the ferromagnetic layer, k_{B} is Boltzmann's constant, and T is the temperature.* The parameter Δ determines the probability for reversal of the magnetic state due to thermal excitation. The figure of merit for 20 year data retention is $\Delta \geqslant 70$. If the size of the storage elements shrinks, the effective anisotropy must increase in order to keep the anisotropy energy (and, hence, Δ) constant. The main ferromagnetic compositions used in present MTJ-containing memories and sensors are based on $3d$ transition metal alloys with the elements Fe, Co, Ni: $Co_{100-x}Fe_x$, $Ni_{100-x}Fe_x$, and Co/Ni multi-layers. These alloys are cubic and have low values of the magnetocrystalline anisotropy. In order to enhance the overall anisotropy, the storage elements are patterned into elliptical pillars with aspect ratios between $1/3$ and $1/2$. The demagnetizing field of the elliptical form provides additional shape anisotropy. Furthermore, the vertices of the ellipse act as domain pinning centers, therefore, even if a domain is nucleated at the vertex, its propagation is seriously impeded. The problem with the shape-stabilized MTJs is that the scalability is limited because an elliptic junction occupies higher area than a circular one and the critical switching current is lower for pillar with PMA (see Eq. (1.47) and Eq. (1.48)). Materials with perpendicular magnetic anisotropy (PMA) must be used in order to reduce the critical current density and to avoid the area limitation. There are two main classes of materials with PMA. The first class are materials

*It is assumed to be 300 K.

which exhibit high perpendicular magneto-crystalline anisotropy, and the second class are materials with induced surface anisotropy. The surface anisotropy is presently more widely used and it is induced by sandwiching thin ferromagnetic layers between a layer of heavy element (like W, Ta, Pt) and an MgO-insulating layer. The spin-orbit coupling from the heavy elements and the CoFe-MgO interface provide the interfacial anisotropy. The most widely-used example is junctions with the structure Ta/CoFe/MgO/CoFe/Ta, where the Ta layer and the CoFe/MgO interface provide the PMA[149]. The ferromagnetic CoFe electrode has to be grown very thin in order to utilize the surface anisotropy. On the other hand, it cannot be grown ultra-thin as there is a magnetic dead layer in extremely thin ferromagnetic films and the spin polarization decreases. Therefore, there is a narrow thickness region where PMA is present and the magnetotransport properties are preserved: $0.8\,\mathrm{nm} < t_{\mathrm{CoFe}} < 1.2\,\mathrm{nm}$. The main reason for the Ta/CoFe/MgO utilization is that it is a natural extension of the in-plane CoFe/MgO/CoFe MTJs which exhibit high TMR ratios[268, 403]. This electrode structure has uniaxial anisotropy $K_{\mathrm{u}} = 0.2\,\mathrm{MA\,m^{-3}}$. The value could be enhanced 1.9 times when two CoFe/MgO interfaces are provided in a MgO/CoFeB/Ta/CoFeB/MgO structure[290]. The Ta thickness must be kept low enough so that there is ferromagnetic coupling between the two ferromagnetic layers otherwise they would switch independently. Another examples of PMA electrodes are the multi-layer structures: Co/Pt[265], Co/Pd[139], and Fe/Pt[1] where both the ferromagnetic and the heavy metal layers are grown at sub-nm thicknesses. The problem of these multi-layers is that the uniaxial anisotropy is low. If it were only for the anisotropy problem, it could be solved in principle by the use of highly anisotropic tetragonally-distorted hard magnetic layers. However, there is another face to the problem. The hard magnetic compositions have very high magnetization and, therefore, the stray field is very high. The latter leads to magnetic cross-talk between the two layers in an MTJ and between adjacent MTJ pillars. This problem exacerbates as the distance between the pillars decreases and, therefore, a magnetic material with very low magnetization and high spin polarization is the Holy Grail of spin electronic materials. The idea of such material has been initially proposed by van Leuken and de Groot and termed "half-metallic antiferromagnet"[354]. So far, there has been no successful growth of spin-polarized antiferromagnetic compositions. The two magnetic sublattices are chemically and crystallographically similar and it is unlikely that one of them would have higher contribution towards the Fermi level spin polarization. Furthermore, magnetic storage elements must be rewrittable and both the electrical and the magnetic control of the antiferromagnetic state is very difficult at present. The main topic of interest in this chapter is the incorporation of the ferrimagnetic composition Mn_2Ru_xGa (MRG) in magnetic tunnel junctions. The expositions will start with a brief literature review of the electrical properties of AlO_x- and MgO-based MTJs in Sec. (6.2) as this will serve as a comparison with the properties of our MRG-containing devices. Brief overview of the development of this novel material as well as the magnetic and electrical characterization of its properties so far is given in

Sec. (6.3). High TMR values of up to 40 % at 10 K and up to 6.6 % at 300 K are presented in Sec. (6.4) with the composition Mn_2Ru_1Ga. The unusual TMR-bias dependence is discussed as well as the effect of the annealing on the TMR values. The most important result is the observation of appreciable TMR values in MTJs with strictly zero moment $Mn_2Ru_{0.8}Ga$ electrodes in Sec. (6.6). The barrier properties are analyzed in Sec. (6.7). The main results from this chapter are summarized in a recent publication[37].

6.2 Important characteristics of classical AlO_x and MgO-based magnetic tunnel junctions

This short section has the main aim to remind the reader about some general characteristics observed in "standard" high-quality MTJs. This overview will serve as a comparison basis with the characteristics of our MRG containing MTJs. The important characteristics we would like to keep in mind are:

- Parallel resistance state change as a function of temperature: $R_P(T)$
- Behaviour of the resistance-area product upon annealing
- Tunneling spectroscopy of the MTJs
- Maximum achieved TMR

The first technologically relevant TMR values of $\geq$ 10 % were achieved almost simultaneously by Moodera[235] and Miyazaki[229] in the structures CoFe/Al_2O_3/Co and Fe/Al_2O_3/Fe, respectively. AlO_x had been used extensively at that stage for growth of TJs for spin-polarized tunneling in the standard trilayer Al-AlO_x-ferromagnet. The ease of growth of ultrathin alumina, its uniformity and lack of pinholes, makes it the perfect candidate for MTJs. On top of that, slight composition variation (possible Al clustering) does not affect the barrier quality significantly*. The electron transport through AlO_x is by incoherent tunneling. The latter means that the amorphous barrier has no significant effect on the evanescent wavefunction of the electrons. The amorphous (or polycrystalline barrier) forms hopping centers at grain boundaries and impurities. A very important characteristic of all MTJs is the temperature decrease of the parallel resistance ($R_P(T)$). In the case of AlO_x barrier, there is a slight decrease in the R_P of approximately 20 %-25 % from 10 K to 300 K. Tunneling through a high gap insulator should not be in principle affected by the relatively modest thermal excitation energy ($\approx$ 25 meV) at room temperature. Unfortunately, thin amorphous and polycrystalline barriers tend to have lower effective barrier due to interface charges and impurities in the

*MTJs with ferromagnetic oxides, NiO, have been grown as well but ferromagnetic ions clustering leads to formation of spin-flip scattering centers which are detrimental to the TMR values of the devices.

barrier*. However, the decrease of the parallel resistance temperature decrease $R_P(T)$ in magnetic tunnel junctions is significantly higher than the decrease of the resistance of non-magnetic AlO_x containing tunnel junctions. The resistance drop in the latter is 10 %-15 %. This implies that the magnetic nature of electrodes has detrimental effect. The important characteristic for the TMR(V) decrease is the voltage at which the TMR is reduced to half-magnitude compared with the zero bias one. For the case of AlO_x, the initial values were around 250 mV but increased with improved barrier quality to about 500 mV. The TMR(V) decrease is generally attributed to density of states effects, magnon excitations or spin-flip scattering in the barrier[347]. Electron tunneling at higher bias corresponds to injection towards a level above the Fermi level of one of the ferromagnetic electrodes. As such a ferromagnet has finite exchange energy ($\sim$ 1 eV), the energy dependence of the spin-split density of states changes significantly and, hence, the "effective" spin polarization does as well. However, counter arguments are provided by a spin polarized scanning tunneling microscopy on Co films through vacuum[384]. In this case, the spin polarization signal demonstrated no voltage dependence up to 1 V, in this way supporting the idea that the interfaces and the barrier quality are responsible for the TMR decrease and not the DOS of the ferromagnetic electrodes. The perceived spin polarization in tunneling (hence, the TMR) depends significantly on the quality of the barrier. A perfect example is the spin polarization of NiFe which is initially determined to be 32 %[226] and reaches later 48 %[237] with improved deposition conditions. Another important contributing effect is the "hot-electron" injection. As higher applied bias means injection above the E_F, electrons must relax upon reaching the counter electrode. This relaxation might lead to spin-flip event or spin-wave excitation. Finally, migration of ions from the ferromagnetic electrodes is possible. Paramagnetic impurities in the barrier act as spin-scattering centers and might flip the spin of a tunneling electron.

Another important characteristic of a tunnel barrier is the resistance-area product change upon annealing. Annealing improves the crystallinity of a barrier which leads to higher band gap and reduction of the grain boundaries which act as scattering centers. In agreement with that, the *RA* product of AlO_x barriers increases upon annealing. The maximum achieved TMR with AlO_x MTJs is approximately 70 %[363].

A major breakthrough is caused by the realization of giant TMR ratios with MgO-based MTJs. Initially the values are in the range from 120 % to 250 %[403, 268] but with improvement in the growth and the annealing conditions the TMR reaches 350 %. The maximum room-temperature TMR achieved in this configuration is 600 % with enhanced Ta diffusion suppression[148] in pseudo SVs. It has been predicted that transport through crystalline barriers should result in coherent tunneling and higher TMR[214]. In particular for MgO, evanescent states from the CoFe electrode with particular symmetry are filtered and, hence, the overall tunneling spin polarization

*Each hopping step has finite probability for energy loss or spin-flip.

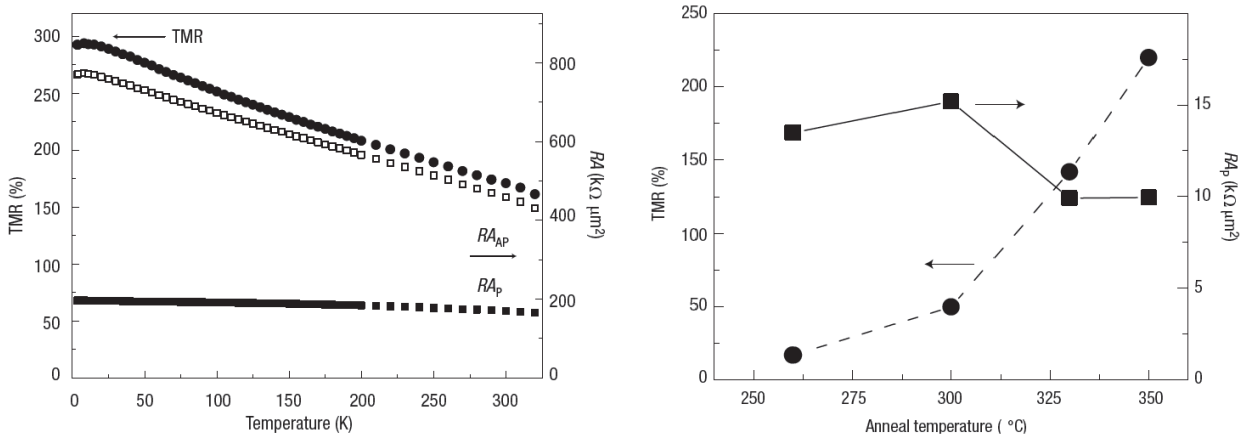

Figure 6.1: R_P, R_{AP}, TMR for an MgO-based MTJ annealed at 380 °C on the left hand side. Annealing dependence of the TMR and the RA product on the right hand side. The graphs are after Parkin *et al.*[268].

is higher that the bulk value of the same ferromagnetic composition[46, 213]. The original papers of Yuasa[403] and Parkin[268] are published for fully crystalline epitaxial Fe/MgO/Fe (grown by MBE), and polycrystalline ferromagnet/crystalline barrier/polycrystalline ferromagnet (grown by sputtering), respectively. Because of technological ease and yield, the sputtering approach is the preferred method at the moment. The polycrystalline (or fully amorphous for the case of CoFeB) ferromagnetic layers crystallize by utilizing the crystalline MgO as a template. Because of the very close lattice match, a high-quality, low-strain CoFe/MgO interface is achieved. There are significantly different TMR(V) and $R_P(T)$ characteristics in the MgO-based MTJs than in the AlO_x-based ones. First, the $R_P(T)$ remains essentially constantly from 10 K to 300 K as evidenced in Fig. (6.1). Thus, the TMR(T) is almost only dependent on the $R_{AP}(T)$. That means that the TMR is determined predominantly by the overlap between the spin-split density of states of the two ferromagnetic electrodes. The constancy of R_P is due to the crystallinity and the larger gap of the MgO barrier. The high crystallinity means that there are very few hopping centers in the MgO barrier then thermal activation does not play significant role in increasing the conductance of the MTJ when the temperature is changed. Furthermore, the wider gap in MgO leads to the fact that elevated tunneling probability due to higher thermal energy is insufficient to have a significant effect on the R_P resistance. On right hand panel of Fig. (6.1), the TMR and the parallel resistance-area product (RA_P) are presented as a function of the annealing temperature. First of all, TMR increases from $\approx 20\,\%$ in an as-deposited junction to $\approx 220\,\%$ in an annealed junction at 350 °C. The annealing crystallizes the CoFe electrode, so that the CoFe/MgO interface becomes epitaxial as is evidenced by the transmission electron microscopy data on the same junctions[268]. Second, the crystallized CoFe electrode has higher spin polarization because of the Δ-bands filtering by MgO. The higher spin polarization due to spin filtering is proven to increase from $P \approx 57\,\%$ (in the as-prepared state) to $P \approx 74\,\%$ (in the annealed state) by superconducting spin-polarized

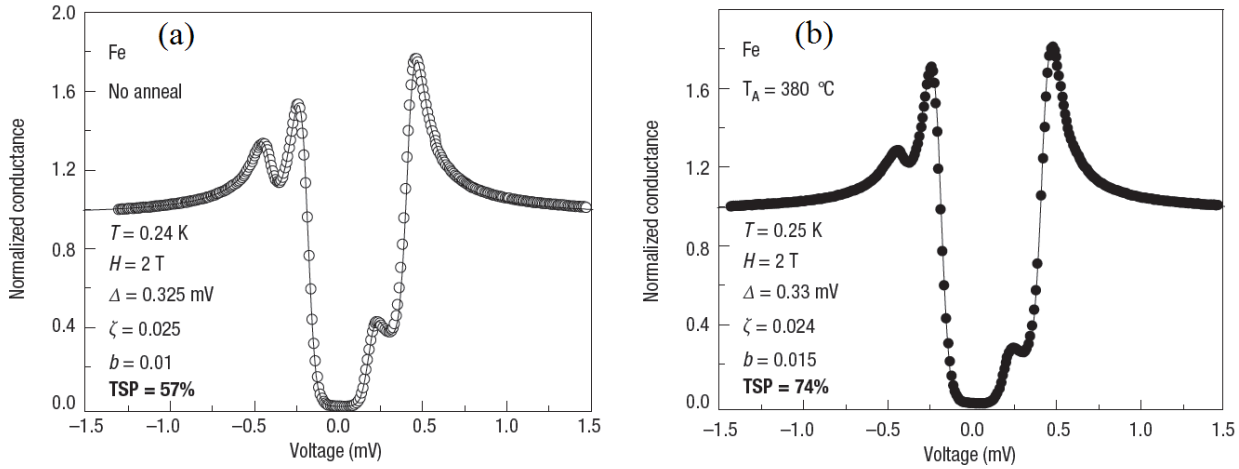

Figure 6.2: Comparison between the tunneling spin polarizations (TSP) of Fe in Fe-MgO-$Al_{96}Si_4$ junctions. Panel (a)-TSP in the case of non-annealed junction-TSP = 57 %. Panel (b)-TSP in the case of a junction annealed at 380 °C-TSP = 74 %. The fitting is performed following the Maki-Fulde theory where the superconducting gap (Δ), the spin-orbit coupling (b), the orbital depairing (ζ), and the tunneling spin polarization (TSP) are considered free fitting parameters (see Sec.(1.4.5)). The graphs are after Parkin *et al.*[268].

tunneling in $Co_{70}Fe_{30}$/MgO/$Al_{96}Si_4$ (see Fig. (6.2)). Another important observation is that the R_P decreases upon annealing. Due to the improved CoFe/MgO interface (and the crystalline barrier), the coherent tunneling electrons experience less scattering events in the tunnel barrier.

It is demonstrated in the work of Yuasa *et al.*[403] that the $RA_P \approx 1\,k\Omega\,\mu m^2$ (for $t_{MgO} = 2.0\,nm$) and that it roughly changes by an order of magnitude for every 0.4 nm. On the other hand, Parkin *et al.*[268] found $RA_P \approx 10\,k\Omega\,\mu m^2$ for the same barrier thickness*. The difference is that the latter stacks are deposited by sputtering whereas the former are grown by MBE. The resistance-per-nanometer of MgO is higher than the AlO_x because MgO has higher bandgap. RA_{AP} and RA_P exhibit exponential dependence on the barrier thickness which is expected from the Wenzel-Kramer-Brillouin (WKB) approximation and proves that MgO behaves as a very high quality tunnel barrier in the window 1.5 nm-3.0 nm. The slope of the $\ln(RA)(t_{MgO})$ must be a equal to $4\pi\sqrt{2m\phi}/h$, where m is the mass of the electron, h is Planck's constant, and ϕ is the height of the barrier. The slope on the LHS of Fig. (6.3) corresponds to barrier height $\phi \approx 0.39\,eV$.

Another approach to determine the barrier height is to fit the current-voltage characteristic following Simmon's [306] or Brinkman's model[42]. The procedure produces similar low values for the barrier height: 0.37 eV-0.40 eV. These values are significantly lower than the expected half-magnitude of the MgO bulk bandgap. The MgO bulk bandgap is $E_g = 7.8\,eV$. In fact, it is quite common even high-quality MTJs to demonstrate $\phi < 1\,eV$. The discrepancy is often ascribed to oxygen vacancies in the insulating barrier. Another possible contribution comes from interface charges and small concentration of diffused atoms. The interface and image charges lead to "rounding" of the rectangular walls of the potential barrier. This results in lower effective height of the

*The sputtering results are more relevant to our junctions

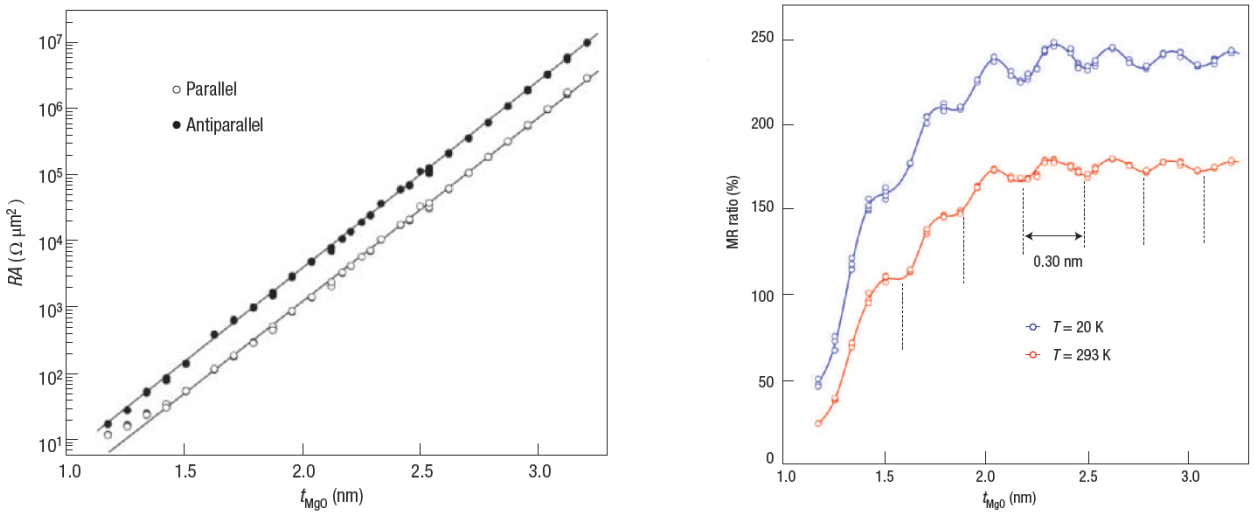

Figure 6.3: Left Hand Side: Resistance-area product as a function of thickness of the MgO barrier for the case of parallel and antiparallel resistance states. TMR effect of 247 % (20 K) and 180 % (293 K) for a junction with $t_{\mathrm{MgO}} = 2.3\,\mathrm{nm}$. Right Hand Side: TMR dependence of the barrier thickness t_{MgO}. The picture is after Yuasa *et al.*[403].

barrier. The latter is especially important in MTJs because the insulating layers are very thin and even small charging might significantly alter the barrier profile. Second, diffused metallic atoms from the electrodes into the barrier act as hopping centers for electron transport. If a sharp, δ-like, distribution of such metallic atoms is assumed to be in the middle of the insulating layer, the tunneling electrons will effectively "see" half of the barrier and the tunneling process is assisted by the impurities. In reality, the distribution of the hopping centers could be much more complicated, and, furthermore, the existence of metallic centers will change even further the barrier profile. In the latter case, there is additional rounding of the potential barrier wall around the impurity centers*. The right hand side of Fig. (6.3) demonstrates that the TMR ratio increases as the thickness of the barrier increases. Tunneling electrons with wave-vectors normal to the barrier are prevalent because the tunneling probability decreases significantly when momentum vectors are tilted with respect to the junction axis. Furthermore, the evanescent wavefunctions of the Fe minority spin band decay faster than the evanescent wavefunctions of the majority spin band in the MgO barrier. Therefore, the effective spin polarization of the Fe electrode is higher[46]. The oscillation pattern in TMR(t_{MgO}) dependence is not due to oscillations from addition of another monolayer of MgO, because the thickness of the latter along the (001) direction is 0.22 nm. Yuasa *et al.*[403] have attributed that to wave-vector "beating" from the two main evanescent state (Δ_1 and Δ_5). This oscillatory behaviour is a confirmation of the coherent tunneling through MgO.

Furthermore, the conductance voltage dependence, $G(V)$, of the CoFe-MgO-CoFe tunnel junctions is significantly different from the $G(V)$ for AlO_x-based ones. The parallel conductance curve does not show any zero-bias dip feature[365] contrary to the case for AlO_x-based MTJs[409]. The

*The oxygen vacancies and defects are a type of hopping center as well.

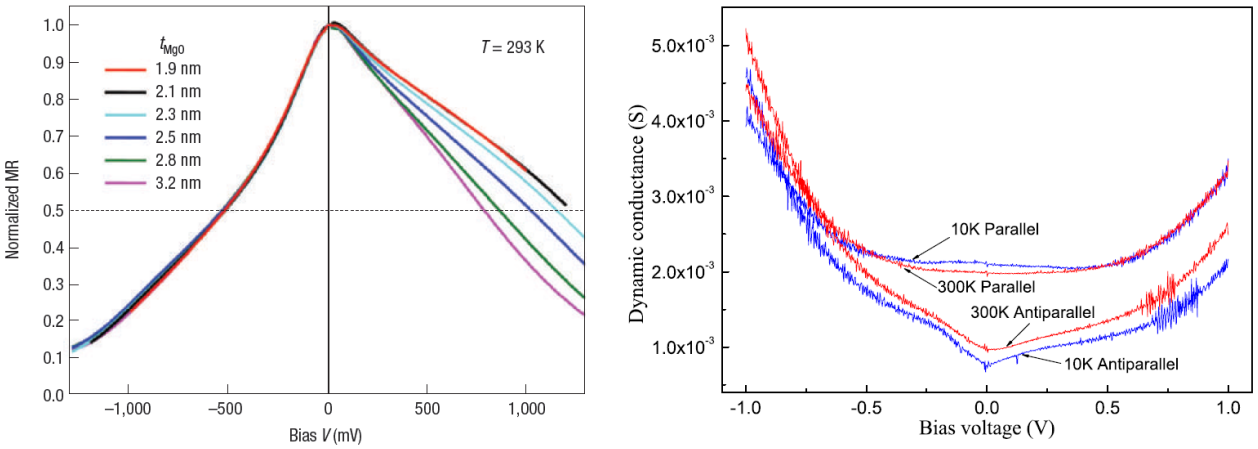

Figure 6.4: Left Hand Side: TMR(U) for different MgO thicknesses, t_{MgO}, at $T = 293\,K$. The data is normalized to the value TMR(0 V) for each curve. The picture is after Yuasa *et al.*[403]. Right Hand Side: Differential spectroscopy, dI/dV, of MgO-based tunneling junctions at 10 K and 300 K for parallel and antiparallel state, respectively. The graph is after Wang *et al.*[365].

low bias plateau demonstrates the transport is coherent and elastic up to $U \approx 0.5\,V$ (see RHS of Fig. (6.4)).

6.3 Mn_2Ru_xGa: a half-metallic compensated ferrimagnet

The vast family of Heusler alloys has attracted the attention of the spin electronic community due to tunable magnetic properties. As it will be discussed, Heusler compounds obey empirical rules for their magnetic moment per formula unit, the latter is always an integral number of Bohr magnetons. The periodic table along with the possible choice of elements for a Heusler compound is presented in Fig. (6.5). Different Heusler alloys exhibit semiconducting, ferro-(ferri-)magnetic, and superconducting behaviour. Interestingly, many properties of these alloys are found to depend on the number of their valence electrons rather than the chemical elements in the composition. For instance, non-magnetic Heusler compounds with 27 valence electrons are superconducting. Heusler alloys are a class of materials with one of the chemical formulas-XYZ (known as half-Heusler) or X_2YZ (full Heusler). X and Y are transition metals and Z is a main group element. Y could be replaced by a rare earth or an alkaline earth element. From magnetic point of view, the two classes obey an empirical relation between the number of valence electrons and the demonstrated magnetization per formula unit. Elements with integer Bohr magnetons magnetization per formula unit are particularly interesting for spintronic application because they should be half-metallic. The full Heusler alloys usually crystallize in cubic $L2_1$ structure and their moment per unit cell obeys the modified Slater-Pauling rule:

$$m = N_v - 24, \tag{6.3}$$

where N_v is the number of valence electrons per formula unit. The corresponding valences are $N_v = 1$ for Li; $N_v = 2$ for Be, Mg; $N_v = 3$ for B, Al, Ga, In, Sc, Y; $N_v = 4$ for Si, Ge, Sn, Pb, Ti, Zr, Hf; $N_v = 5$ for As, Sb, Bi, V, Nb; $N_v = 6$ for Cr, Mo, W; $N_v = 7$ for Mn, $N_v = 8$ for Fe, Ru; $N_v = 9$ for Co, Rh, Ir; $N_v = 10$ for Ni, Pd, Pt. On the other hand, the magnetization on the cubic half-Heusler compositions obey another modified Slater-Pauling rule:

$$m = N_v - 18 \tag{6.4}$$

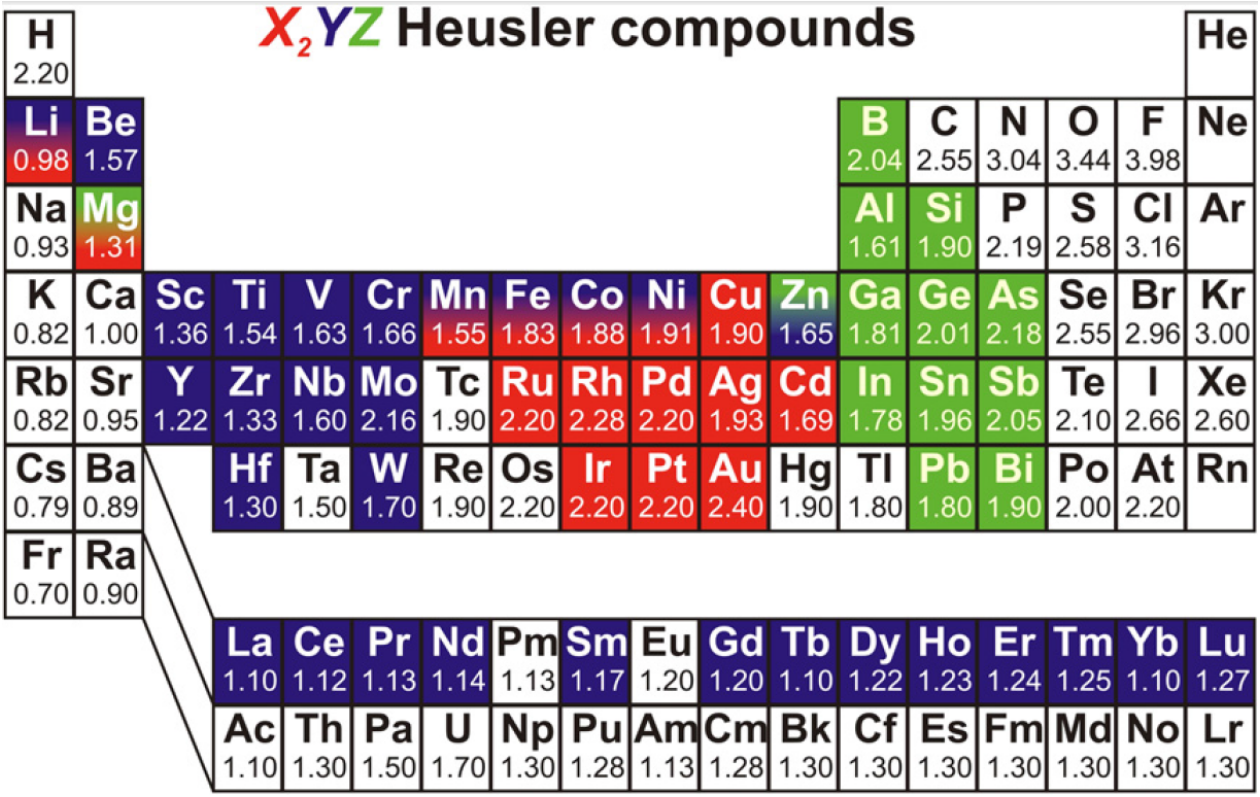

Figure 6.5: Periodic table describing the possible combinations of elements in Heusler compounds. X is in red, Y is in blue, and Z is in green. The diagram is after Graf *et al.*[119].

Significant investigations have been performed over the last two decades mainly on Co-based Heusler alloys. Some of the successful results are the realization of TMR $> 300\,\%$ and coherent tunneling with Co_2MnSi[204]. Recently, extremely high current-perpendicular-to-plane GMR effect of $\approx 60\,\%$ have been demonstrated with the quarternary Heusler composition $Co_2FeGa_{0.5}Ge_{0.5}$ and Ag-Zn spacer[82]. Many Co-based Heusler have been incorporated in MTJs and spin valves and have demonstrated high Fermi level spin polarization. The reader is referred to Takahashi[331] for an extensive review of the spin polarization in Heusler alloys. However, these compositions exhibit in-plane anisotropy whereas future generation of MRAM will require materials with perpendicular magnetic anisotropy in order to scale down the bit size without affecting negatively data retention. On the other hand, tetragonally-distorted Mn-based compounds exhibit both high

perpendicular uniaxial anisotropy and high spin polarization[187, 185, 186].

Bulk (α) manganese is a weak antiferromagnet with $T_N = 95\,K$ and the exchange interaction of Mn is close to the switch between antiferromagnetic to ferromagnetic. This provides the tunability of the Mn exchange interaction in different crystal structures due to variation in the Mn-Mn interatomic distance and bonding angles (see Fig. (1.2)). Ferrimagnetic Mn_3Ge and Mn_3Ga in the tetragonal DO_{22} have been investigated by Kurt *et al.*[185, 187]. Both compositions demonstrate small room temperature magnetization of approximately $73\,kA\,m^{-1}$(Mn_3Ge) and $110\,kA\,m^{-1}$ (Mn_3Ga), respectively. Very importantly, the uniaxial anisotropy constant is high and equal to $0.91\,MJ\,m^{-3}$ (Mn_3Ge) and $0.89\,MJ\,m^{-3}$ (Mn_3Ga). Both compositions demonstrate small soft in-plane component due to canting of the Mn 2*b* moment[278]. The spin polarization has been measured by PCAR to be 46 % (Mn_3Ge) and 58 % (Mn_3Ga). A distinction must be made between the tetragonal DO_{22} and the hexagonal DO_{19} structures. Mn_3Ga and Mn_3Ge can crystallize in both, however, the hexagonal structure results in antiferromagnetic order whereas the tetragonal is ferrimagnetic. Recently, there have been tremendous developments in the area of spin Hall effect magnetization switching using antiferromagnets [103]. There are observations of large anomalous Hall effect in Mn_3Ge[172, 252] and a theoretical prediction for a large spin Hall angle. The antiferromagnetic compositions, however, are not directly relevant to the present thesis.

The search for high spin polarized materials has naturally led to the idea of fully spin polarized materials with no net magnetization. The term "half-metallic antiferromagnet" itself is introduced by van Leuken and de Groot[354]. Materials with such predicted properties have been investigated. However, they either decompose[217] (Co_2CrGa), have no magnetic moment on the transition metal element[126], or do not crystallize in a cubic structure. A potential half-metallic ferrimagnet which will not be dicussed here is Cr_2CoGa[126].

Mn_2Ga is a member of the half-Heusler family while the Mn_3Ga, and Mn_2RuGa are members of the full Heusler family. In these films, Mn_2Ga crystallizes in the non-centrosymmetric $C1_b$ structure (see Fig. (6.6)). It has easy axis in the plane of the films and a low Curie temperature of $T_c \approx 225\,K$. Following, the Slater-Pauling rule the magnetization is expected to be $-1\mu_B$/f.u., whereas the measured moment by Kurt *et al.*[186] is $\approx 1.65\mu_B$/f.u.. On the other hand, the full Heusler composition Mn_2RuGa should have moment of $1\mu_B$/f.u., whereas the experimental value is $0.44\mu_B$/f.u.. The incompatibility is perhaps related to small tetragonal distortion (up to 3 %). It is worth noting, that the end compositions seem to obey the magnetization slope of $2\mu_B$/Ru. It is conceived and realized by Kurt *et al.*[186], that for the ideal Ru concentration $x \approx 0.5$, zero magnetic moment is achieved. In this case, the composition $Mn_2Ru_{0.5}Ga$ is half-way between the half-Heusler and the full Heusler family and it obeys yet another law for the magnetization: $m = N_v - 21$. The spin polarization of the compensated $Mn_2Ru_{0.5}Ga$ has been measured by PCAR and the extracted value is 54 %, whereas the spin polarization of the end member Mn_2Ga is de-

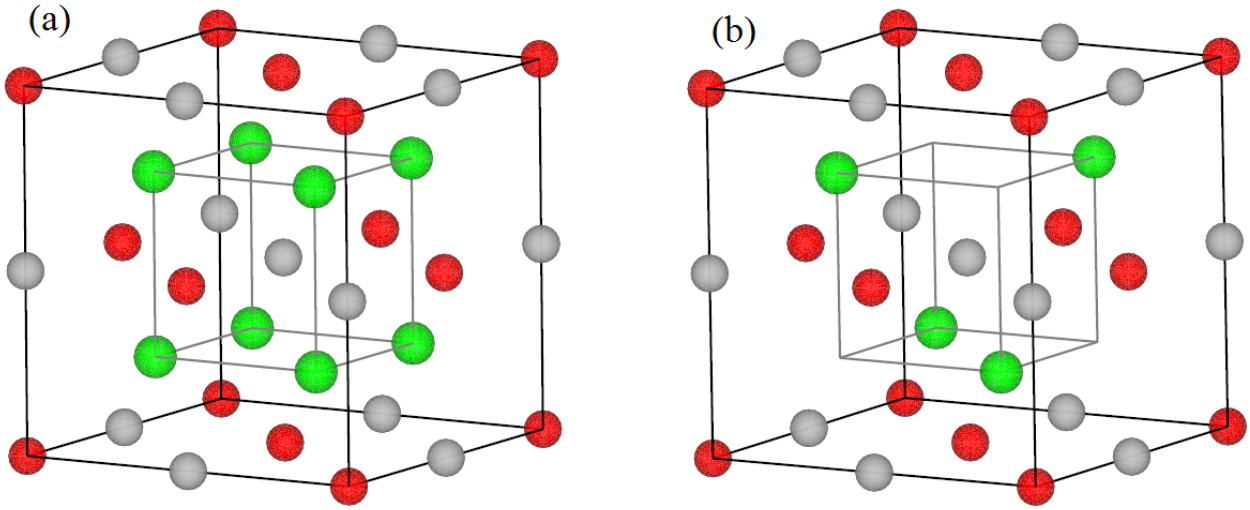

Figure 6.6: Panel (a)-$L2_1$ crystal structure of a full Heusler alloy X_2YZ (Mn_2RuGa) with X(green), Y(gray), and Z(red). Panel (b)-$C1_b$ half-Heusler XYZ (Mn_2Ga).

termined to be significantly lower 41 %. The Ru addition leads to higher Curie temperature. The Curie temperature is in the range from 500 K to 550 K for $0.7 > x > 0.3$. Furthermore, Ru doping leads to slight tetragonal distortion which drives the easy axis from the in-plane direction to perpendicular to plane direction. Finally, the role of Ru doping is to change the inter-lattice exchange interaction between the two Mn sublattices and in this way to vary the ferrimagnetic compensation temperature, T_{comp}.

Because of the low magnetization of the Mn_2Ru_xGa, magnetometry measurements are not very suitable for quick optimization. Anomalous Hall effect (AHE) in van der Pauw configuration is often used in order to extract swiftly key properties of an MRG blanket film. The AHE loops provide coercivity, sign, and may indicate the perpendicular magnetic anisotropy. The latter parameters are used during growth optimization. First, sputtering rates on the Mn_2Ga and Ru guns are determined in order to achieve the desired compositions. The PMA and its strength are mainly governed by the deposition temperature of the MRG and its post-deposition *in-situ* annealing. The existence of secondary phase might as well be spotted in the AHE loops. Tuning of the Ru concentration leads to different compensation temperature for the ferrimagnet (T_{comp}) and the dependence between the x and T_{comp} and between the bi-axial strain and T_{comp} have been investigated by Thiyagarajah *et al.*[340]. It is important to note that the maximum coercivity indicates the location of T_{comp} in MRG because following the classical Stoner-Wolfarth model the anisotropy field (and, hence, the coercivity) diverges when the magnetization tends to zero

$$\mu_0 H_{\text{an}} = \frac{2K_{\text{u}}^{\text{MRG}}}{M^{\text{MRG}}}, \tag{6.5}$$

where $K_{\text{u}}^{\text{MRG}}$ and M^{MRG} are the uniaxial anisotropy and the saturation magnetization of MRG,

respectively. Very important is the observation that the AHE signal has different sign above and below T_{comp} (see Fig. 6.7 (a)). When high-magnetic field is applied, the MRG magnetization direction must follow the orientation of the applied field which means that above and below T_{comp}, the MRG magnetization does not change sign which is shown on the $M(H)$ loops above and below compensation (see Fig. 6.8 (b)). So, why does the AHE changes sign? The AHE is sensitive not only to the bare magnetization but to the spin dependent scattering of the conduction electrons on the magnetic moment of the atoms. The reason for the sign reversal is that the spin polarization of the conduction electrons switches its sign with respect to the overall magnetization. Critism has ben expressed by Galanakis *et al.*[105] that our interpretation of the switching AHE signal is incorrect. However, the correlation between the diverging $\mu_0 H_{\mathrm{c}}^{\mathrm{MRG}}$ and the observed zero magnetic moment is strongly reinforced by the comparison between the AHE signal (Fig. (6.7)) and the $M(T)$ magnetometry(6.8 (a)). The AHE effect is measured at temperatures from 10 K to 350 K in field up to $\mu_0 H = 14\,\mathrm{T}$ (see Fig. (6.7) (a)). It is apparent from the AHE loops that $T_{\mathrm{comp}} \approx 250\,\mathrm{K}$, where the strange hysteresis loop is due to complicated domain dynamics. At the T_{comp}, the applied field is insufficient to saturate the composition and the ferrimagnetic domains rotation is incomplete. The AHE signal changes sign when the compensation is passed*. Furthermore, the $\mu_0 H_{\mathrm{c}}^{\mathrm{MRG}}$ decreases both below and above T_{comp} due to the increase in the MRG magnetization. Another quick and reliable approach to extract the compensation temperature of MRG is to measure the temperature dependence of the AHE signal in high constant magnetic field. When $R_{\mathrm{xy}}(T)$ is measured, the compensation temperature corresponds to the maximum signal change because the AHE signal switches sign. Unfortunately, the AHE measurement in van der Pauw configuration always contains some longitudinal resistance pick-up R_{xx}. The approach to uncover the compensation is then to take the derivative $\mathrm{d}R_{\mathrm{xy}}/\mathrm{d}T$ and determine the point of maximum derivative. The extracted T_{comp} by the derivative approach corresponds very well to the temperature determined by AHE loops and $M(T)$ scans.

Both the $M(T)$ magnetometry and $\mathrm{d}R_{\mathrm{xy}}/\mathrm{d}T$ peak derivative result in extracted $T_{\mathrm{comp}} \approx 253\,\mathrm{K}$. The SQUID $M(T)$ magnetometry is performed on the same sample by saturating it at 10 K in $\mu_0 H = 5\,\mathrm{T}$, and warming it up through compensation in small field of $\mu_0 H = 5\,\mathrm{mT} < \mu_0 H_{\mathrm{c}}^{\mathrm{MRG}\dagger}$. In this configuration, the MRG magnetization goes through zero and it is antiparallel with respect to the applied field above T_{comp}. On the other hand, the full hysteresis loops, $M(H)$, at 200 K (below T_{comp}) and at 300 K (above T_{comp}) demonstrate that the MRG moment always follows the direction of the applied magnetic field when saturated in high field. The latter observation comes as a confirmation that the AHE signal inversion is due to sign change of the Fermi level spin polarization. The spin polarization sign reversal implies strongly that the Fermi level spin polarization

*Note the shape of the AHE loops at 10 K and 350 K, for instance.

†The field must be low in order to eliminate the significant diamagnetic contribution from the MgO substrate and to be below the coercive field of MRG.

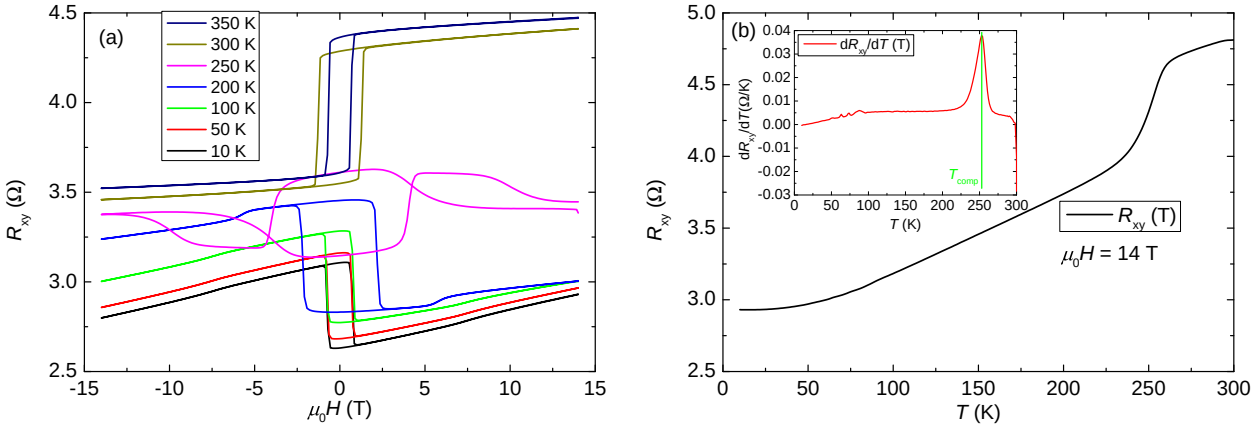

Figure 6.7: AHE data of an $Mn_2Ru_{0.9}Ga$ blanket film with approximate $T_{\text{comp}} = 250\,\text{K}$. Panel (a)-AHE loops at multiple temperatures from 10 K to 350 K and in applied field $\mu_0 H = \pm 14\,\text{T}$. The AHE signal changes its sign above 250 K. Panel (b)-AHE signal dependence on the temperature from 300 K to 10 K in constant magnetic field of $\mu_0 H = 14\,\text{T}$. The point of maximum slope corresponds to the compensation temperature. The inset demonstrates $dR_{\text{xy}}/dT(T)$, the maximum value of the derivative demonstrates T_{comp}.

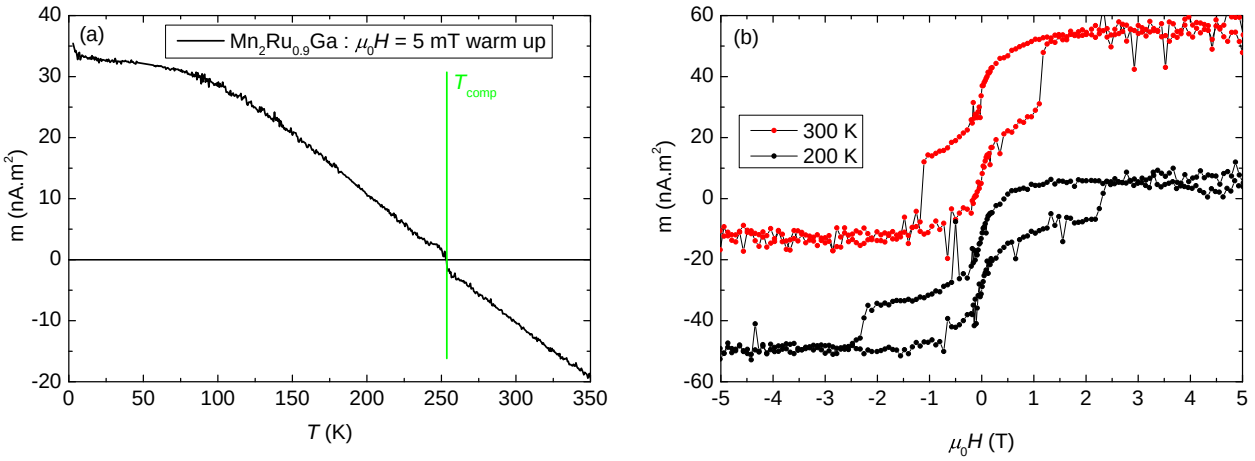

Figure 6.8: SQUID magnetometry measurements on an $Mn_2Ru_{0.9}Ga$ with compensation temperature of $T_{comp} \approx 250\,\text{K}$, the AHE data on the same sample is presented in Fig. (6.7). The applied magnetic field is perpendicular to the plane of the sample. Panel (a)-$M(T)$ data acquired on warm up in small applied field of $\mu_0 H = 5\,\text{mT}$. The sample was first saturated in 5 T at 10 K. Note that the magnetic moment switches from positive to negative at the compensation point. Panel (b)-$M(H)$ hysteresis curves on the same sample acquired at 300 K and 200 K, above and below compensation, respectively. Do note that the magnetization is always positive when the sample is saturated. The two curves are offset vertically for clarity. For this sample, the magnetic moment $\rightarrow$ magnetization is: $10\,\text{nA}\,\text{m}^2 \rightarrow 7.9\,\text{kA}\,\text{m}^{-1}$. Hence, the saturation magnetization at 300 K is $M_s \approx 26\,\text{kA}\,\text{m}^{-1}$.

is determined by one of the Mn sublattices rather than the overall magnetization. This is further demonstrated to be the case in magnetic tunnel junctions with a compensated MRG electrode in Sec. (6.6). The PMA of the sample is confirmed as well, however, the existence of a non-negligible secondary component is present which appears to be stronger that the one observed on the AHE loops*.

*Apart from possible misalignments, the secondary component might be due to partial oxidation of a not-well capped sample. The time difference between the AHE and SQUID measurements is approximately 1 year, and the sample might have oxidized due to moisture despite the fact that it is capped with 3 nm of AlO_x.

6.4 Tunneling magnetoresistance realized with Mn_2Ru_xGa

The MTJ stack structures are grown by sputtering in a fully automated Shamrock deposition system. The stack structure is as follows: MgO(001-substrate)/ MRG(40)/ Al(0.6)/ MgO(1.5)/ CoFeB(1.0)/ Ta(0.3)/ CoFeB(0.9)/ MgO(0.7)/ Ta(3.0)/ Ru(4.0), where the thickness of each layer is indicated in brackets in nanometers (see Fig. (6.9)). The MRG electrode is deposited by co-sputtering from Mn_2Ga and Ru target. The deposition current on the Ru gun is kept constant, while the current of Mn_2Ga gun is varied in order to change the x of the composition and tune T_{comp}. The MRG electrode is normally deposited at temperatures from 300 °C to 350 °C, while the rest of the stack is deposited at room temperature. It is demonstrated that such conditions provide good crystallinity and improved surface roughness. The latter is of critical importance for the growth of MTJs. The MRG electrode is grown relatively thick, 40 nm, because the disorder in ultrathin MRG films is significant and the crystallinity is poor. Extensive details on the growth of MRG thin films, as well as the dependence of the compensation temperature on the Ru concentration x and the tetragonal distortion can be found in [186, 340, 193]. A dusting layer of Al-0.6 nm is deposited immediately after the MRG electrode. The purpose of this layer is twofold: first, it improves the MRG roughness, so that the deposited insulating barrier on top is smoother, second, Al provides a diffusion barrier against Mn atoms.* Finally, the top ferromagnetic electrode CoFeB/Ta/CoFeB/MgO and a capping layer of Ta/Ru are deposited. The structure of the top ferromagnetic electode is often known as a "frame"[290]. Perpendicular magnetic anisotropy of CoFe is provided through surface anisotropy either with a heavy metal or with MgO. In the case of the "frame", the two ultrathin CoFeB layers are provided with surface anisotropy at both interfaces and furthermore the dipole-dipole interaction between them stabilizes the easy-axis of the composite electrode. The frame structure is used in the present stack because it provides better thermal stability against annealing and achieves higher uniaxial anisotropy[290].

The resistance contribution (if any) of the ultrathin MgO(0.7 nm) layer in the frame electrode has to be roughly two orders of magnitude smaller than the resistance of the main tunnel barrier†. The magnetic tunnel junctions are patterned by three step ultra-violet lithography, Ar-ion milling, and definition of the top contact by lift-off process of an electron beam deposited Cr(10)/Au(150) top layer. The junctions sizes are $6\,\mu m \times 6\,\mu m$ and $20\,\mu m \times 20\,\mu m$. Most of the presented data in this thesis is obtained on $20\,\mu m \times 20\,\mu m$ junctions due to the lower resistance of these junctions (16 kΩ to 24 kΩ). It should be noted that the small junctions have been cross-checked as well and they demonstrate consistently the same TMR values as the bigger ones. The resistance-area product is

*Other configurations with Ta and Hf insertion layers have been tested. However, they have not shown good TMR effect. It has been confirmed by time-of-flight secondary-ion-mass-spectroscopy that there is significant diffusion of Mn into the MgO barrier when these two materials are used as diffusion barrier.

†Derived by the trend in Yuasa *et al.*[403] and in Fig. (6.3) that the resistance of an MgO-based MTJ changes by an order of magnitude for every 0.4 nm.

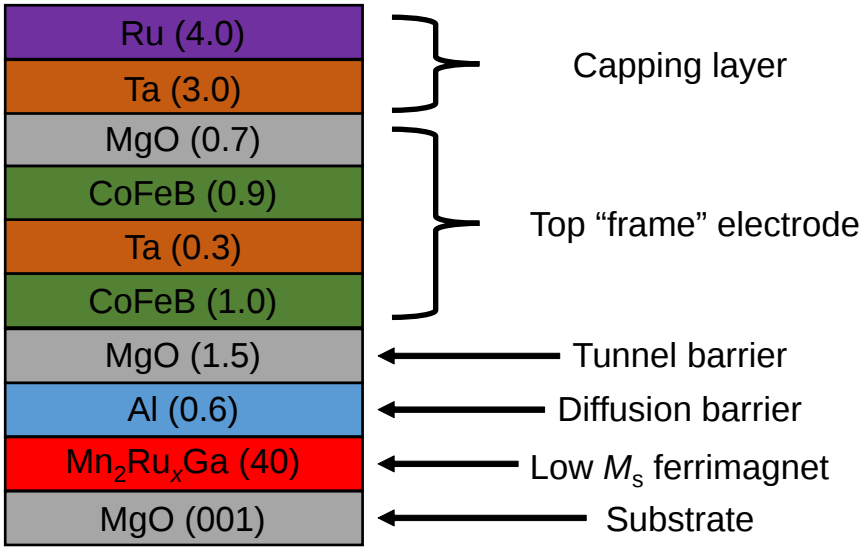

Figure 6.9: Schematic representation of the MTJs structure with MRG bottom electrode. The thickness of each layer is indicated in brackets in nm.

checked to be roughly constant for the two kinds, and the parallel state resistance of the $6\,\mu m \times 6\,\mu m$ is around $120\,k\Omega$.

The positive voltage contact is connected to the top of the stack, and the negative voltage contact to the bottom one (MRG). In this way, positive bias corresponds to electrons tunneling from the MRG into the CoFe, while negative bias corresponds to electrons tunneling from the CoFe into the MRG. All MTJs are wedge bonded on a wire bonder without any heating of the chips or of the electrical puck. All d.c. electrical measurements are performed with a Keithley 2400 source-meter in a two-point configuration. The contribution from the series resistance of the bottom MRG electrode has been measured separately and found to never exceed $500\,\Omega$. In this way, the contribution towards the overall resistance in the low bias regime is always below $3.3\,\%$* and no appreciable magnetoresistance is measured on the MRG bottom contact. The a.c. measurements are performed in two-point configuration with voltage sourced by a Keithley 2400 and modulated with the internal oscillator of a Perkin Elmer 7265 lock-in amplifier (LIA), the current modulated signal is preamplifier with a bandwidth filter (Stanford Research 570) and synchronously detected again by the LIA. All measurements are performed in a Physical Properties Measurement System in temperature range from $2\,K$ to $400\,K$ and magnetic field of up to $\mu_0 H = 14\,T$.

The tunneling magnetoresistance of a junction annealed at $T = 350\,^\circ C$ is presented in Fig.(6.10). Panel (a) shows the TMR effect observed at applied bias of $U = 10\,mV$. This is essentially a close to zero bias TMR effect in which case the tunneling happens between the Fermi levels of the MRG and the CoFe electrodes. The first noticeable feature is the high TMR of $40\,\%$ at $T = 10\,K$. It will

*In fact, if all resistances are corrected for the bottom electrode contribution, the TMR values are slightly higher. This correction is not done as it affects insignificantly the values.

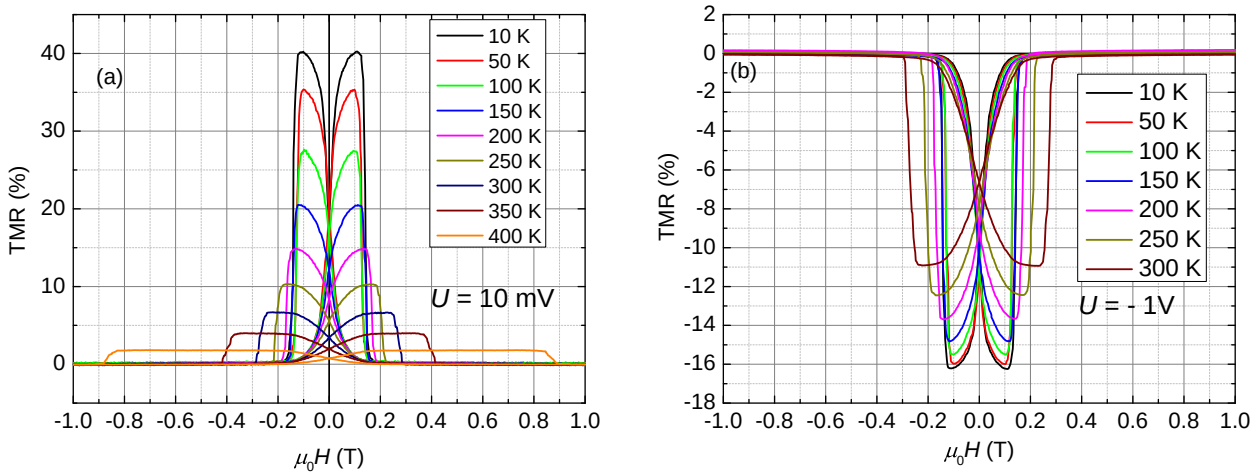

Figure 6.10: Tunneling magnetoresistance of an MTJ annealed at $T = 350\,^{\circ}\mathrm{C}$. Panel (a) shows the TMR effect at applied bias $U = 10\,\mathrm{mV}$ at different temperature. Panel (b) shows the TMR at the same MTJ but at applied bias of $U = -1\,\mathrm{V}$.

be latter shown that the transport in the present MTJs is incoherent, *i.e.* the Δ band MgO filtering is not efficient in our case. In light of this, a low temperature high TMR implies high Fermi level spin polarization of the MRG electrode. Another important observation is the the coercive field of MRG, it gradually increases from 150 mT to 900 mT between 10 K to 400 K. The increase in the coercive field of MRG is mainly governed by the diminishing magnetization as the compensation temperature is approached. The composition is $x \approx 1.0$ in this particular MRG, which implies rather high T_{comp} ($> 400\,\mathrm{K}$). Important observation is the strong temperature decrease of the low bias TMR. The TMR effect decreases from 40 % at $T = 10\,\mathrm{K}$ to 6.6 % at $T = 300\,\mathrm{K}$. This is a high, six-fold decrease of the TMR, the reasons for it are discussed latter. The PMA of the CoFe electode is not very well defined which is evidenced by the rotation of the CoFe magnetization at close to zero field. The latter is perhaps due to rough interfaces in the top ferromagnetic "frame" electrode.

On the right hand side of Fig. (6.10), the TMR effect at applied bias of $U = -1\,\mathrm{V}$ is presented. The TMR effect is negative. Applied bias of such magnitude and polarity means that electrons are tunneling from the Fermi level of the CoFe towards a level high above the Fermi level of MRG. It is well-established that the TMR effect in standard CoFe/MgO/CoFe and CoFe/AlO_x/CoFe does not change sign (see Fig. (6.3)). Hence, the change of the TMR sign might be broadly speaking due to three effects: significant energy dependence of the spin polarization of MRG, very complicated tunneling probabilities through the barrier and inelastic (magnon) scattering at the interfaces. The discussion is left for later. Another important observation on panel (b) is that the TMR($-1\,\mathrm{V}$) is actually far more temperature robust than the TMR(10 mV). The latter is a rather puzzling observation because a higher applied bias implies normally excitation of more inelastic processes (both phonon and magnon related scattering). Finally, it is crucial to note that the coercive fields of

MRG at $U = 10\,\mathrm{mV}$ and $U = -1\,\mathrm{mV}$ are essentially the same.

The TMR sign change implies that there is a zero TMR value at negative bias in between $10\,\mathrm{mV}$ and $-1\,\mathrm{V}$. Full TMR(U) dependences at temperatures of $T = 10\,\mathrm{K}$ and $T = 300\,\mathrm{K}$ are presented in Fig.(6.11) for a chip annealed at $350\,^{\circ}\mathrm{C}$. An MTJ is set in the antiparallel state and a current-voltage characteristic is measured, then it is set in the parallel state and the another current-voltage characteristic is measured, then the two curves are used to calculate the TMR(U). The discussion starts with the low temperature curve. The negative bias tunneling corresponds to electrons tunneling from the E_F of CoFe towards the conduction band of MRG. The negative bias branch demonstrates a sharp decrease in the TMR value and TMR $= 0$ at $U \approx -250\,\mathrm{mV}$. Then, the TMR turns negative and remains essentially constant for $U < -0.5\,\mathrm{V}$. This rather flat voltage dependence is strange, since the more energetic tunneling electrons will tend to experience more pronounced inelastic scattering processes. Positive applied bias corresponds to electrons tunneling from the E_F of MRG towards the bulk conduction band of CoFe. The TMR effect does not change sign along the positive bias dependence, however, the lineshape of TMR(U) is much different than the expected one. This tunneling configuration essentially probes the CoFe spin-split levels above the E_F, however, the TMR is expected to decrease to half of its zero-bias value at significantly higher bias (see Fig. 6.4). The latter implies that there is a spin-flip scattering process in the barrier (or at the interfaces) which causes the the sharp decrease of the TMR at $U > 0\,\mathrm{V}$. This is further evidenced by the unusual plateau in the TMR(U) dependence measured around $U \approx 0.5\,\mathrm{V}$.

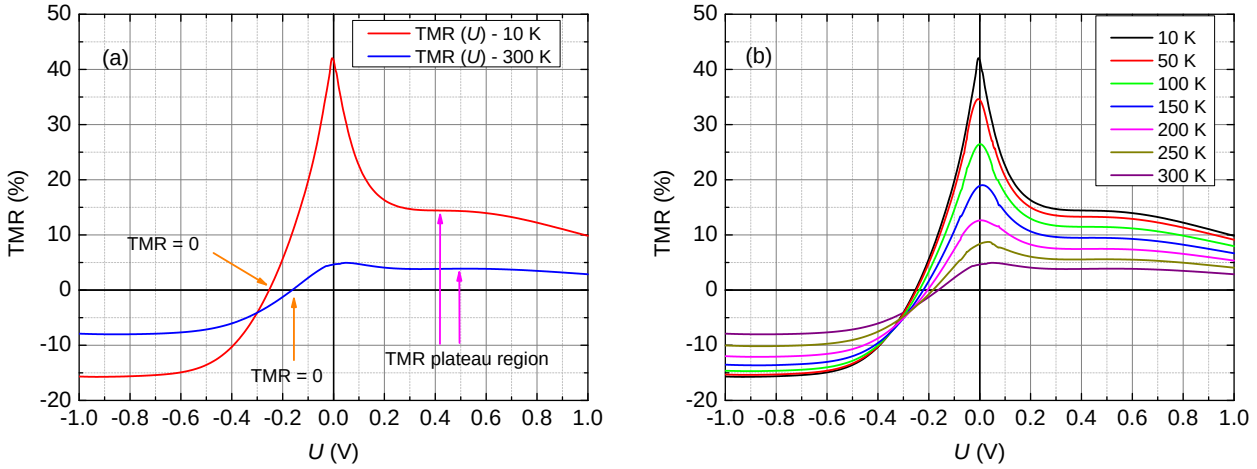

Figure 6.11: TMR(U)for an $Mn_2Ru_{1.0}Ga$ MTJ annealed at $350\,^{\circ}\mathrm{C}$. Panel (a) - The red curve shows the TMR(U) at $10\,\mathrm{K}$, and the blue curve represents the TMR(U) at $300\,\mathrm{K}$. The zero TMR points are indicated with orange arrows and the local TMR plateau at positive bias is indicated with magenta arrows. Panel (b) - TMR(U) at various different temperatures.

The TMR(U) at $T = 300\,\mathrm{K}$ shows some similarities to the low temperature curve: the TMR changes sign at negative bias, the TMR is relatively voltage independent at high negative bias and there is a local plateau at $U \approx 0.5\,\mathrm{V}$. There are, however, two distinct differences. First of all, it is apparent that the close-to-zero-bias TMR ratio shrinks disproportionately with respect to the rest of

the dependence. Second, the TMR $=$ 0 point shifts towards zero bias by roughly $\Delta U = 100\,\mathrm{mV}$ from $-250\,\mathrm{mV}$ (at $T = 10\,\mathrm{K}$) to $-150\,\mathrm{mV}$ (at $T = 300\,\mathrm{K}$). This again implies that the zero-bias TMR is more heavily suppressed than the rest of the dependence. The physical process cannot be attributed to inelastic scattering as this will be more pronounced at higher biases rather than at low, close to zero, bias. However, a possible explanation is the process of resonant scattering from impurities in the barrier. Impurities might form resonant scattering levels very close to the Fermi level of the insulation barrier[346]. The overall TMR(U) behaviour at various temperatures is plotted in Fig. 6.11 (b). The TMR plateau region around $U \approx 0.5\,\mathrm{V}$ increases in size. In fact, there is a small local dip formation around $U \approx 0.25\,\mathrm{V}$, this dip formation is an absolutely clear indication of a resonant scattering within the barrier with levels at $U \approx 250\,\mathrm{mV}$. It is very probable that there are more resonant scattering levels, however, there are indirect proofs for them. This dip is much more pronounced in other samples which will be discussed later (see Fig. (6.21) and Fig. (6.43)).

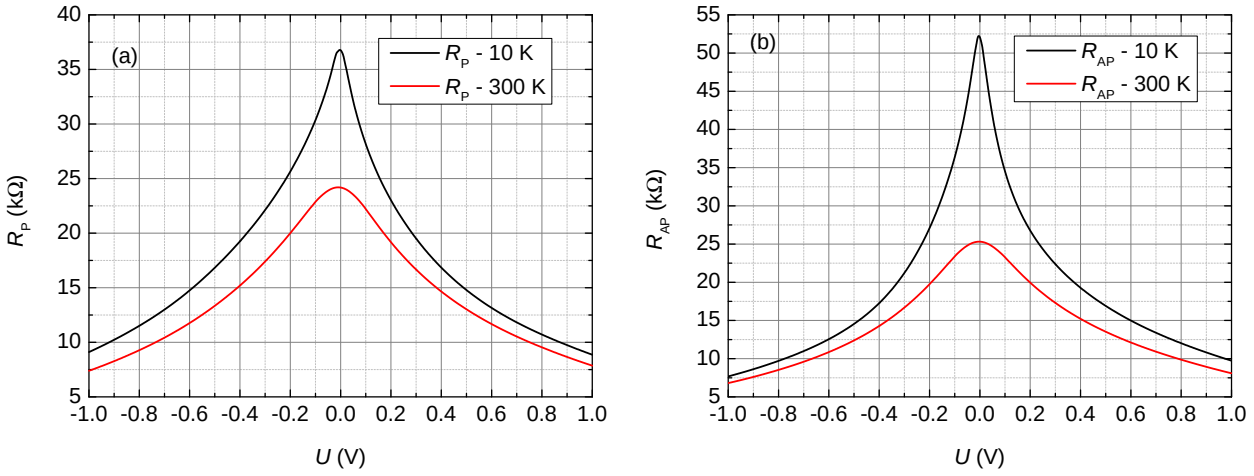

Figure 6.12: Parallel (R_P) and antiparallel (R_AP) resistance dependence on the applied bias U at $T = 10\,\mathrm{K}$ and $T = 300\,\mathrm{K}$. Panel (a) shows the $R_{\mathrm{P}(U)}$ at $T = 10\,\mathrm{K}$ and $T = 300\,\mathrm{K}$. Panel (b) shows the $R_{\mathrm{AP}(U)}$ at $T = 10\,\mathrm{K}$ and $T = 300\,\mathrm{K}$.

It is beneficial to have a discussion on the bias dependences of the parallel (R_P) and antiparallel (R_AP) resistance states which are shown in Fig. (6.12). Panel (a) represents the voltage dependence of the R_P, and panel (b)-the voltage dependence of the R_AP. The parallel resistance state is more sensitive to tunneling processes, which are not effected by magnetic processes (magnon excitation and spin-split density of states structure). First of all, R_P demonstrates good symmetry between the positive and negative bias branches. This indicates that there is no significant charging imbalance accumulated at the two interfaces of the MTJ*. Furthermore, it is obvious that there is a disproportionately large decrease of the close to zero bias resistance between 10 K and 300 K compared to

*If one of the interfaces has tendency to trap charges then the resistance behaviour for positive and negative bias would be significantly different.

the high bias resistance. The line-shape of the $R_P(U)$ demonstrates very concave structure, in fact standard very high TMR CoFe/MgO/CoFe tunnel junctions demonstrate normally $R_P(U)$ which resembles roughly the shape of an inversed parabola. The sharp zero bias decrease of R_P is a clear proof of incoherent tunneling process. Another possible contribution towards the effect is hopping conductance through impurity states in the insulating barrier. As the temperature is decreased, the energy gap between the hopping states (Δ_g) is comparable to the thermal excitation energy (k_BT) and consequently the probability ($\propto e^{-\Delta_g/k_BT}$) for hopping conductance through the barrier is lowered, and, therefore, the resistance is increased. Whereas at higher temperature the hopping process probability is increased due to the higher thermal activation energy, hence, hopping conductance might become dominant over tunneling, and this leads to significantly lower R_P at 300 K compared to 10 K. The $R_{AP}(U)$ is more striking. A pronounced asymmetry in the bias dependence is observed which is a clear indication that the overall TMR(U) behaviour is predominantly determined by the $R_{AP}(U)$ behaviour. The latter means that the asymmetry in the TMR(U) is governed by spin scattering related processes. As expected, the zero-bias resistance decrease between 10 K and 300 K in the R_{AP} is even higher than the decrease in the R_P.

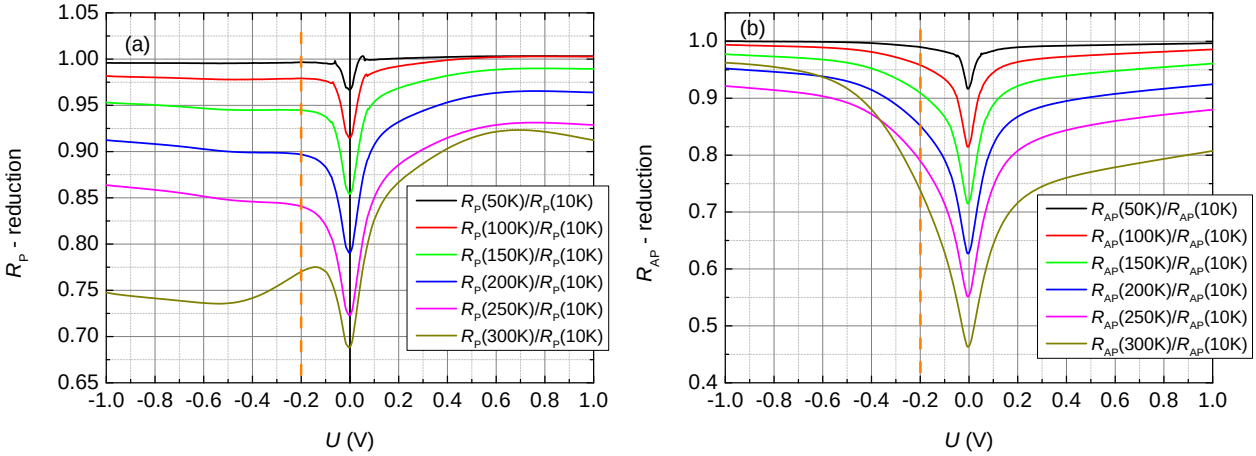

Figure 6.13: Parallel (R_P) and antiparallel (R_{AP}) resistance reduction as a function of the applied bias U. Panel (a) shows the $R_P(U)$ reduction for different temperature ratios 50 K/10 K, 100 K/10 K, 150 K/10 K, 200 K/10 K, 250 K/10 K, and 300 K/10 K. Panel (b) shows the $R_{AP}(U)$ reduction as a function of the applied bias U for the same temperature ratios. The orange, vertical dotted lines ($U \approx -0.2$ V) indicate roughly the position where TMR switches sign.

In order to investigate how the reduction evolves with the temperature, the different reductions are plotted $R(50\,\mathrm{K})/R(10\,\mathrm{K})$, $R(100\,\mathrm{K})/R(150\,\mathrm{K})$, $R(200\,\mathrm{K})/R(10\,\mathrm{K})$, $R(250\,\mathrm{K})/R(10\,\mathrm{K})$, $R(300\,\mathrm{K})/R(10\,\mathrm{K})$ for R_{AP} and R_P in Fig. (6.13). The dependence is rather unusual. First of all, the R_P has its strongest reduction at $U \approx 0$ V. This is atypical since inelastic scattering processes are more pronounced at higher biases. At positive bias the reduction in R_P decreases sharply which indicates that the tunneling process is less inelastic. On the other hand, R_{AP} is almost constant along the negative bias branch for $U < -0.2$ V. The antiparallel resistance R_{AP} shows behaviour which demonstrates that the spin-flip related processes are most pronounced at close to zero bias.

The spin-flip scattering, however, is suppressed at higher voltages, both positive and negative. This is a strong implication that there is resonant spin-flip scattering states in the MgO barrier which are very close to E_F. The latter are perhaps due to Mn atoms which have diffused from the MRG into the MgO barrier. It is crucial to note that there is essentially no reduction in the R_{AP} at $U = -1\,V$. Strictly speaking, the definition of R_{AP} and R_P has to be swapped once the TMR turns negative*. The behaviour of R_{AP} and R_P reduction is in sharp contrast with the typical behaviour of MTJs with both coherent (MgO-based)[291] and incoherent (AlO_x-based) barriers.

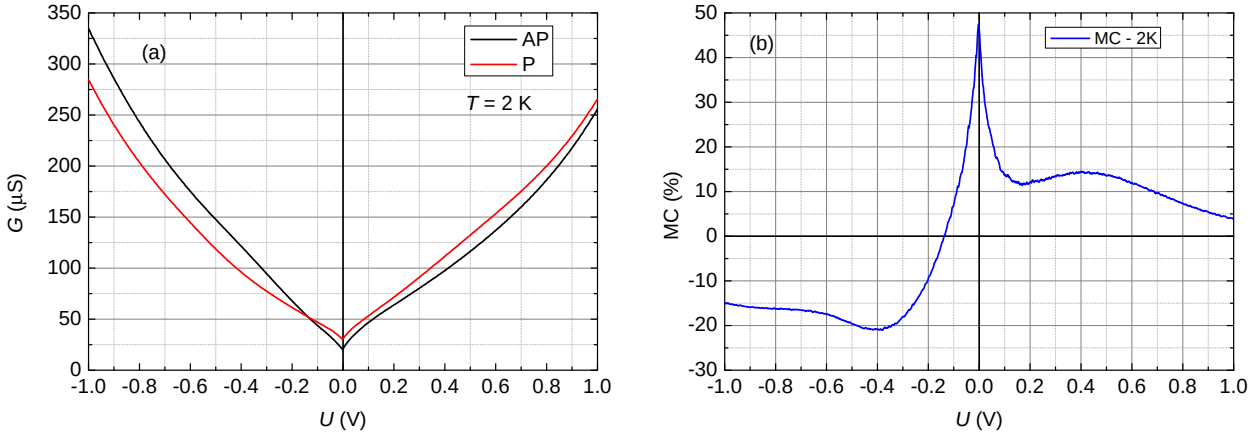

Figure 6.14: Differential conductance (G) of an MTJ at 2 K. Panel (a)-G in parallel (red curve) and antiparallel state (black curve). Panel(b)-magnetoconductance calculated from the two curves in Panel (a).

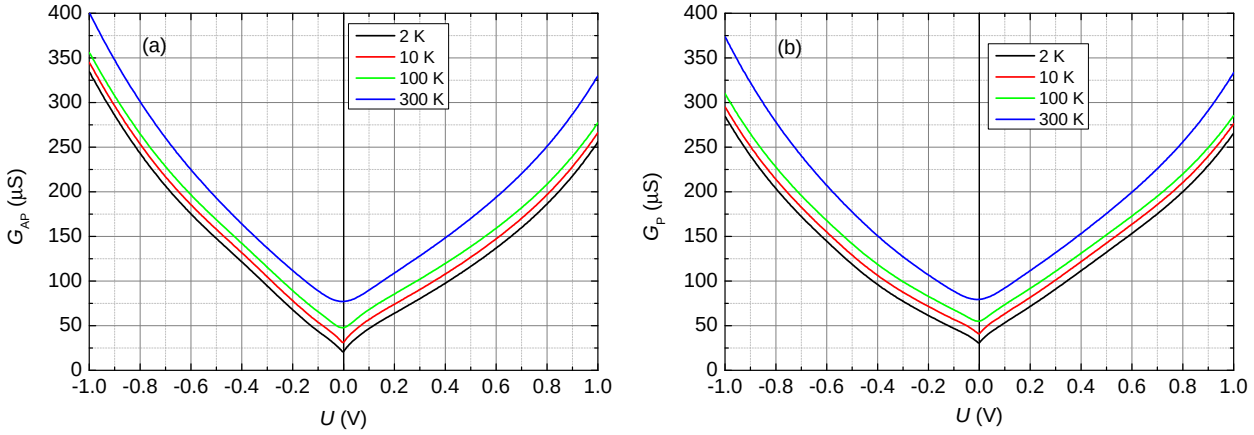

Figure 6.15: Differential conductance G_{AP} on panel (a) and G_P on panel (b) at $T = 2\,K$, 10 K, 100 K, and 300 K. The curves at 2 K are kept as they are, and each of the others is offset vertically by 10 mS with respect to the lower temperature.

Differential conductance spectroscopy with AC modulation is measured on the junctions in order to get higher quality data close to zero bias. The experimental setup is similar to the one for PCAR discussed before (see Sec. (2.2) and Sec. (2.3)), however, the d.c. staircase voltage

*R_{AP} and R_P are defined in terms of mutual magnetization orientation, not in terms of "effective" spin polarization orientation.

waveform, provided by a Keithley 2400, is modulated with 3 mV from the internal oscillator of a Perkin Elmer 7265 lock-in amplifier at a frequency of 1.23 kHz. The ac-dc modulation is achieved with differential amplifiers. The modulated waveform is fed into the junction and then the a.c. current signal is amplified by a current preamplified (Stanford Research 570) in the bandwidth from 0.3 kHz to 3 kHz with 6 db/octave. Differential conductance is measured both in AP and P configuration of an MTJ at temperatures 2 K, 10 K, 100 K, and 300 K. The AP and P curves and the magnetoconductance (MC) curve are presented in Fig. (6.14). It is obvious that a zero-bias anomaly exists at very low bias in the P resistance state, something which is not typical for MgO-based tunnel junctions[365], but usual in AlO_x-based tunnel junctions[409]. This implies that there are inelastic scattering processes in the barrier or at the interfaces at energies very close to the Fermi level. The magnetoconductance curve is the ac analog of the TMR(U) dependence* and, in fact, the original Julliere's model[154] is applied to ac conductances and not to the dc obtained signal. The peak of MC is equal to 48 % close to zero bias. Since, it has been proven that tunneling in our MTJs is incoherent, the Δ-band filtering is not efficient and, hence, it can be assumed that the spin polarization of the CoFe electrode is $\approx$ 45 %, this will imply that following the Julliere's formula the MRG spin polarization is 43 %. The magnetoconductance demonstrates as well a local minimum ($U \approx 0.15$ V) and then a local maximum ($U \approx 0.4$ V) at positive bias. Because the MC is more sensitive towards the DOS structure and the tunneling probability as a function of applied bias than the TMR, this would imply specific spin loss (most likely by resonant scattering) at ≈ 0.15 V. This process will be discussed later in cases where it is more pronounced.

The currents in the parallel and antiparallel resistance states are determined by the spin-split density of states overlap of the two ferromagnetic electrodes. The expression is furthermore multiplied with the different spin-dependent tunneling probabilities ($T_{\uparrow,\downarrow}, T_{\downarrow\uparrow}, T_{\uparrow\uparrow}, T_{\downarrow,\downarrow}$) and and the difference between the Fermi distributions ($f(E) - f(E - eV)$) in the two electrodes

$$I_{\mathrm{AP}}(U) \propto \int_{-\infty}^{+\infty} \left[D_1^{\uparrow}(E) T_{\uparrow\downarrow}(E - qU) D_2^{\downarrow}(E - qU) + D_1^{\downarrow}(E) T_{\downarrow\uparrow}(E - qU) D_2^{\uparrow}(E - qU) \right]$$
$$(f(E) - f(E - qU))\,\mathrm{d}E$$
$$I_{\mathrm{P}}(U) \propto \int_{-\infty}^{+\infty} \left[D_1^{\uparrow}(E) T_{\uparrow\uparrow}(E - qU) D_2^{\uparrow}(E - qU) + D_1^{\downarrow}(E) T_{\downarrow\downarrow}(E - qU) D_2^{\downarrow}(E - qU) \right]$$
$$(f(E) - f(E - qU))\,\mathrm{d}E,$$

where $D_1^{\uparrow}$, $D_1^{\downarrow}$, $D_2^{\uparrow}$, and $D_2^{\downarrow}$ are the spin-split density of states in the two ferromagnetic electrodes.

*MC = $(G_{\mathrm{P}} - G_{\mathrm{AP}})/G_{\mathrm{AP}}$

Then the differential conductances $G_{\mathrm{AP}} = \mathrm{d}I_{\mathrm{AP}}/\mathrm{d}U$, and $G_{\mathrm{P}} = \mathrm{d}I_{\mathrm{P}}/\mathrm{d}U$ are

$$G_{\mathrm{AP}}(U) \propto \int_{-\infty}^{+\infty} \left[D_1^{\uparrow}(E) T_{\uparrow\downarrow}(E-qU) D_2^{\downarrow}(E-qU) + D_1^{\downarrow}(E) T_{\downarrow\uparrow}(E-qU) D_2^{\uparrow}(E-qU) \right] \frac{\partial f(E-qU)}{\partial V} \mathrm{d}E$$

$$G_{\mathrm{P}}(U) \propto \int_{-\infty}^{+\infty} \left[D_1^{\uparrow}(E) T_{\uparrow\uparrow}(E-qU) D_2^{\uparrow}(E-qU) + D_1^{\downarrow}(E) T_{\downarrow\downarrow}(E-qU) D_2^{\downarrow}(E-qU) \right] \frac{\partial f(E-qU)}{\partial V} \mathrm{d}E,$$

The integration is from $-\infty$ to $+\infty$, however, the sensible numerical limits are set by the spread of the Fermi distributions difference. In principle, the differentiation $\mathrm{d}/\mathrm{d}U$ must act on $D_2^{\downarrow}(E-qU)$ and $D_2^{\uparrow}(E-qU)$, however, in small bias and for large exchange splitting approximation the spin-split density of states might be assumed to be constant. The transmission probabilities should also be differentiated but in amorphous barrier approximation it can be assumed that there is no particular spin dependent transmission and the transmission probability is not bias dependent at least at low bias. That means that essentially only the Fermi distributions difference is differentiated.

The Fermi level derivative can be approximated by a Gaussian distribution with full-width-half-maximum (FWHM) of $\approx 3.8 k_{\mathrm{B}}T$. At low temperatures, the derivative might be assumed to be a delta function $\delta(E-qU)$. Then at close to zero bias:

$$G_{\mathrm{AP}}(0) = D_1^{\uparrow}(E_{\mathrm{F}}) D_2^{\downarrow}(E_{\mathrm{F}}) + D_1^{\downarrow}(E_{\mathrm{F}}) D_2^{\uparrow}(E_{\mathrm{E}})$$
$$G_{\mathrm{P}}(0) = D_1^{\uparrow}(E_{\mathrm{F}}) D_2^{\uparrow}(E_{\mathrm{F}}) + D_1^{\downarrow}(E_{\mathrm{F}}) D_2^{\downarrow}(E_{\mathrm{F}}).$$

Then the magnetoconductance at zero bias is

$$MC(0) = \frac{G_{\mathrm{P}} - G_{\mathrm{AP}}}{G_{\mathrm{AP}}}. \tag{6.6}$$

Starting from the product of the two spin polarization values:

$$P_1 P_2 = \frac{D_1^{\uparrow} - D_1^{\downarrow}}{D_1^{\uparrow} + D_1^{\downarrow}} \frac{D_2^{\uparrow} - D_2^{\downarrow}}{D_2^{\uparrow} + D_2^{\downarrow}}. \tag{6.7}$$

It can be easily checked that

$$\frac{G_{\mathrm{P}}}{G_{\mathrm{AP}}} = \frac{1 + P_1 P_2}{1 - P_1 P_2}, \tag{6.8}$$

hence

$$MC(0) = \frac{G_{\mathrm{P}}}{G_{\mathrm{AP}}} - 1 = \frac{2 P_1 P_2}{1 - P_1 P_2}, \tag{6.9}$$

which is exactly the Julliere's formula for the TMR effect.

Furthermore, the separate G_{AP} and G_P scans are used in order to determine the barrier height. The preferred method in this case is the Brinkman's approach[42] and not the Simmons's one[306]. The reason is that the former can account for asymmetric barrier properties whereas the latter assumes symmetric barrier. It is observed from the differential conductance graphs that the barrier is slightly asymmetric. The simplified formula does not account for image charges and is accurate within 10 % for barrier width $d > 10$Å[42]:

$$\frac{G(U)}{G(0)} = 1 - \left(\frac{A_0 \Delta\phi^{3/2}}{16\bar{\phi}}\right) eU + \left(\frac{9A_0^2}{128\bar{\phi}}\right)(eU)^2, \tag{6.10}$$

where $\Delta\phi = \phi_2 - \phi_1$ is the barrier height asymmetry, $A_0 = 4\sqrt{2m}d/3\hbar^*$, and $G(0) = (3.16 \times 10^{10}\sqrt{\bar{\phi}}/d)exp(-1.025d\sqrt{\bar{\phi}})$. The barrier width d is in Å, and the potentials are in V. There is a known problem in applying Brinkman's fit to magnetic tunnel junctions. Since the model is essentially expansion in powers of U at low temperatures, it is inherently more sensitive when it is applied to the low bias region. However, the low bias dip anomaly features at low temperature cannot be fitted with a parabola because of that the analysis is focused here on the differential conductances measured at $T = 300$ K. Three approached are attempted here:

- The curves are fitted for $|U| > 0.4$ V,
- The curves are fitted for $|U| < 0.2$ V,
- The curves are fitted for $|U| < 0.1$ V

The barrier thickness $d = 15$Å is kept as constant.

The extracted values in the high bias region ($|U| > 0.4$ V) are not physical because the expected maximum height for thick MgO barrier is $\phi_{MgO} = 3.9$ eV[†](see Fig. (6.16)). The median barrier height for the antiparallel and parallel state is $\phi_{AP} = 4.879$ eV and $\phi_P = 4.940$ eV, respectively. These unrealistic values demonstrate that Brinkman's fit is not applicable for high bias. A further complication is the fact that for $U < -0.2$ V the role of antiparallel and parallel curves are switched because the TMR changes sign.

The next attempt for Brinkman's fit is on the same curves but in the voltage range $|U| < 0.2$ V in Fig. (6.17). In that case, the extracted barrier height is $\phi_{AP} = 0.755$ eV and $\phi_P = 0.881$ eV, respectively. These values are closer to the values reported in literature where $\phi \leqslant 1.0$ eV. It should be noticed that the obtained fits do not match well the experimental data.

*Where the standard dimensions kg and J s are used for the two constants.

†Assuming the the barrier height is half of the bulk-band gap of MgO-$\Delta_{MgO} = 7.8$ eV.

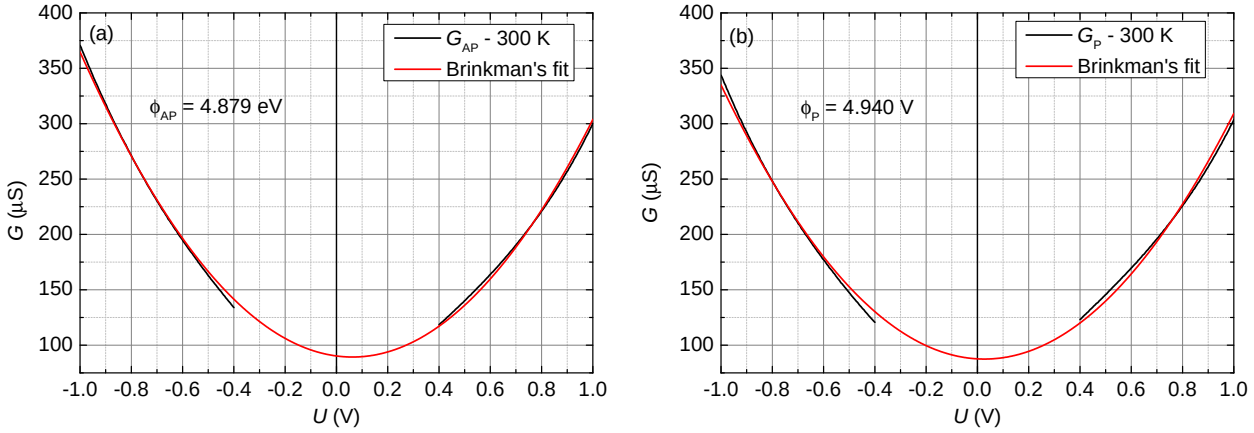

Figure 6.16: Differential conductance G_{AP} on panel (a) and G_{P} on panel (b) at $T = 2\,\mathrm{K}$ in voltage range $|U| > 0.4\,\mathrm{V}$ along with the Brinkman quadratic fit and the extracted average barrier height $\phi_{\mathrm{AP}} = 4.879\,\mathrm{eV}$ and $\phi_{\mathrm{P}} = 4.940\,\mathrm{eV}$ for the antiparallel and the parallel case, respectively.

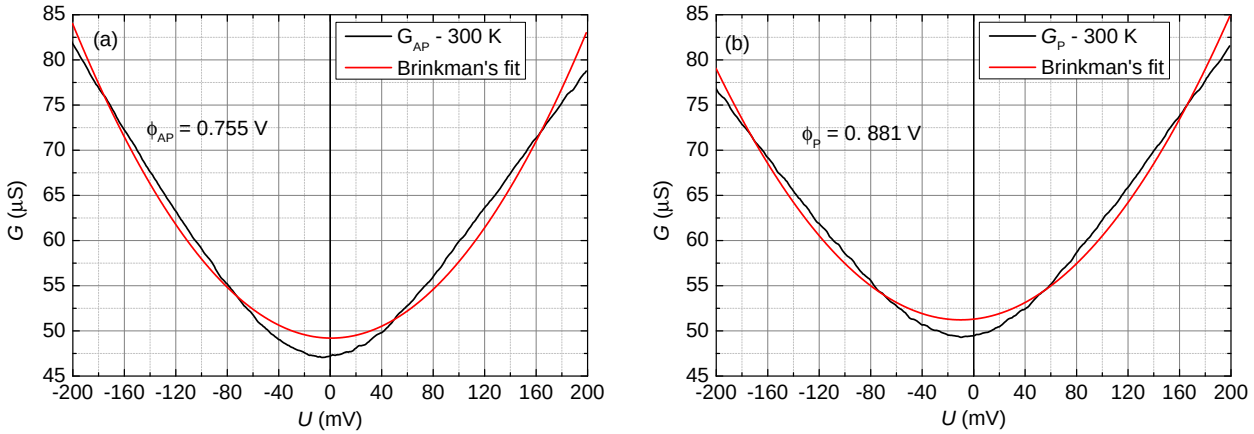

Figure 6.17: Differential conductance G_{AP} on panel (a) and G_{P} on panel (b) at $T = 2\,\mathrm{K}$ in voltage range $|U| < 0.2\,\mathrm{V}$ along with the Brinkman quadratic fit and the extracted average barrier height $\phi_{\mathrm{AP}} = 0.755\,\mathrm{eV}$ and $\phi_{\mathrm{P}} = 0.881\,\mathrm{eV}$ for the antiparallel and the parallel case, respectively.

Finally, the differential conductance is analyzed in the voltage rage $|U| < 0.1\,\mathrm{V}$ in Fig. (6.18). The extracted barrier height for the antiparallel and parallel state is $\phi_{\mathrm{AP}} = 0.497\,\mathrm{eV}$ and $\phi_{\mathrm{P}} = 0.587\,\mathrm{eV}$, respectively. These values are slightly lower that the values obtained on high TMR MTJs before [268, 291]. This might be related to hopping conductance through the MgO barrier in the presented MTJs. Also, it must be noticed that the barrier height in the antiparallel state is higher than the parallel state one $\phi_{\mathrm{AP}} < \phi_{\mathrm{P}}$ which is strange considering the fact that $R_{\mathrm{AP}} > R_{\mathrm{P}}$. However, it has been shown and analyzed before that such unphysical relation is due to defects in the barrier [291]. Because Brinkman's model depends on the normalization with the zero bias conductance, it is not possible to directly take the second derivative of the differential conductance in order to extract the barrier height as a function of the applied bias.

Furthermore, Brinkman's fits demonstrate barrier asymmetry only as a shift of the parabola from $U = 0\,\mathrm{mV}$. On the other hand, the experimental conductance shows minimum of the con-

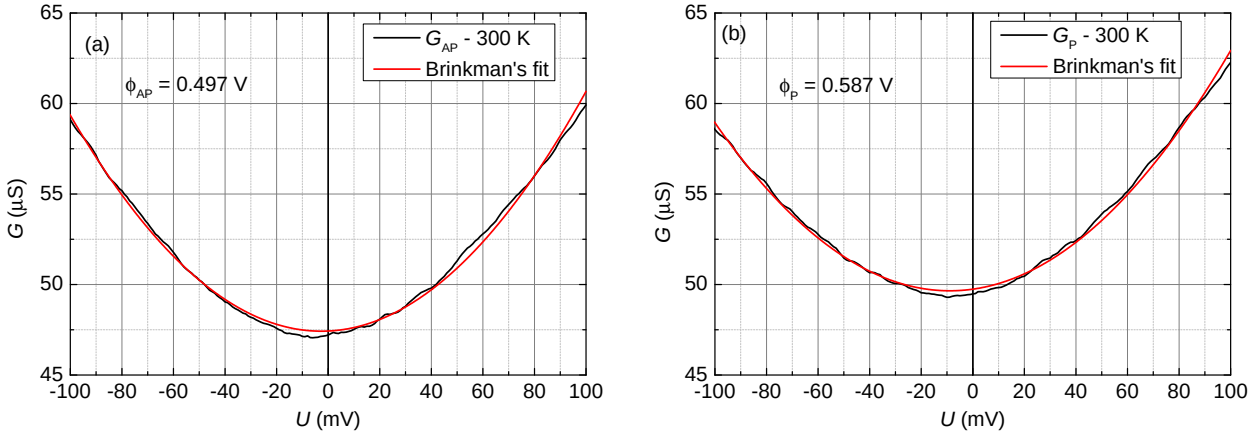

Figure 6.18: Differential conductance G_{AP} on panel (a) and G_{P} on panel (b) at $T = 2\,\mathrm{K}$ in voltage range $|U| < 0.1\,\mathrm{V}$ along with the Brinkman quadratic fit and the extracted average barrier height. $\phi_{\mathrm{AP}} = 0.497\,\mathrm{eV}$ and $\phi_{\mathrm{P}} = 0.587\,\mathrm{eV}$ for the antiparallel and the parallel case, respectively.

ductance close to zero-bias but asymmetric growth for positive and negative bias. The close to zero-bias minimum implies that there is no real barrier asymmetry (or interface charging), but the different growth rate means that the electron tunneling probabilities in the two directions are different. The latter is not accounted by the Brinkman's approach. It could be easily noticed in Fig. (6.15) that the AP and the P conductances have significant deviation from quadratic behaviour both at close to zero bias and at high positive and negative bias.

The dependence of the TMR ratio as a function of T_{anneal} is investigated as well. The patterned MTJ chips have been annealed in a high vacuum magnetic furnace with a base pressure better than $6 \times 10^{-6}\,\mathrm{mbar}$. Magnetic field $\mu_0 H = 800\,\mathrm{mT}$ is provided by a permanent magnet and the applied field direction is perpendicular to the surface of substrates. The annealing has four main effects:

- Barrier crystallization
- Crystallization of the CoFeB electrode
- Setting the anisotropy axis of the CoFe electrode
- Improved quality of the MRG electrode

First of all, it crystallizes the barrier. The amorphous (or poly-crystalline) barrier has inevitable defects which provide centers for hopping conduction transport. Each hopping step has finite probability to cause a spin-flip scattering and, hence, the tunneling probability in amorphous barriers is smaller. Second, the CoFeB are deposited amorphous. During the annealing, boron diffuses out and is absorbed by a getting layer (Ta in our case), and the CoFe electrode crystallizes. The crystallization of the CoFe electrode leads to higher spin polarization (see Fig. (6.2)). Finally, the crystallization of the CoFe interfaced on both side with a heavy metal (Ta) and MgO leads to induced perpendicular surface anisotropy. As the easy axis of the CoFe electrode is set perpendicular,

its magnetization stable orientation becomes colinear with the natural perpendicular easy-axis of MRG and, hence, the tunneling magnetoresistance is improved. The room temperature TMR ratios at applied biases of $U = 10\,\mathrm{mV}$ and $U = -1\,\mathrm{V}$ are plotted in Fig. (6.19) for non-annealed and annealed samples at T_{anneal} = 275 °C, 300 °C, 325 °C, and 350 °C*. The as-deposited MTJs exhibit the lowest TMR ratio of 1.7 % ($U = 10\,\mathrm{mV}$) and −4 % ($U = -1\,\mathrm{mV}$). The easy-axis is naturally in-plane and is gradually rotated out-of-plane as magnetic field is applied. There are two reasons why the TMR in the as-prepared sample is low: the magnetization of the CoFeB is never fully saturated in the antiparallel configuration of the MTJ and the CoFeB is amorphous. Because the MRG and CoFeB magnetization are then not aligned, the TMR is lower following the Slonchewski's rule (see Eq. (1.45) and Fig. (1.11)). Secondly, the amorphous CoFeB has lower spin polarization than the crystalline one and the crystallization of top ferromagnetic electrode increases the spin polarization. The annealing process does not cause any obvious change to the properties of the MRG, the coercivity stays constant. As the samples are annealed in the range $275\,^{\circ}\mathrm{C} \leq T_{\mathrm{anneal}} \leq 325\,^{\circ}\mathrm{C}$, some PMA in the CoFe electrode is induced and the TMR grows. The former is evidenced by the appearance of a plateau in the antiparallel resistance state. The rest of the values are summarized in Table 6.1 and Table 6.2. The annealing induces disproportionate increase of the TMR at different applied biases. For instance, the TMR($U = 10\,\mathrm{mV}$) for $T_{\mathrm{anneal}} = 275\,^{\circ}\mathrm{C}$ and 300 °C has essentially the same value, however, the TMR($U = -1\,\mathrm{V}$) is different. Particularly interesting is that the low bias region is more heavily affected because the low bias transport has to be more elastic than the high bias. The $R_{\mathrm{P}}(10\,\mathrm{mV})$, $R_{\mathrm{P}}(-1\,\mathrm{V})$, and $R_{\mathrm{AP}}(-1\,\mathrm{V})$ are plotted as a function of the annealing temperature as well in Fig. 6.19 (b). The observation that the low resistance state increases upon annealing contradicts with the usual decrease of the low resistance state in high-quality CoFe/MgO/CoFe MTJs (see Fig.(6.1)). There are a two possible reasons for that behaviour:

- Barrier crystallization without coherent tunneling
- Effective increase of the barrier width

The fact that the tunneling is incoherent in our structure will be proven conclusively in Fig. (6.20). Therefore, barrier crystallization with incoherent tunneling might be the reason. Furthermore, Al is known to be more electronegative than Mg, hence, upon annealing Al might extract some of the O atoms from the MgO and, hence, it may get partially oxidized. Since the $R_{\mathrm{P}}(10\,\mathrm{mV})$ for $T_{\mathrm{anneal}} = 350\,^{\circ}\mathrm{C}$ is roughly 1.5 times the $R_{\mathrm{P}}(10\,\mathrm{mV})$ for the as-prepared sample, the scenario of partial Al oxidation is very probably. Similar increase is observed for the resistance states (R_{AP}

*The chip annealed at $T_{\mathrm{anneal}} = 350\,^{\circ}\mathrm{C}$ is from another sample. Although it is prepared with the same deposition conditions, the MRG coercivity is slightly different. Because of that, the focus falls on the chips annealed up to 325 °C because they are from the same original piece.

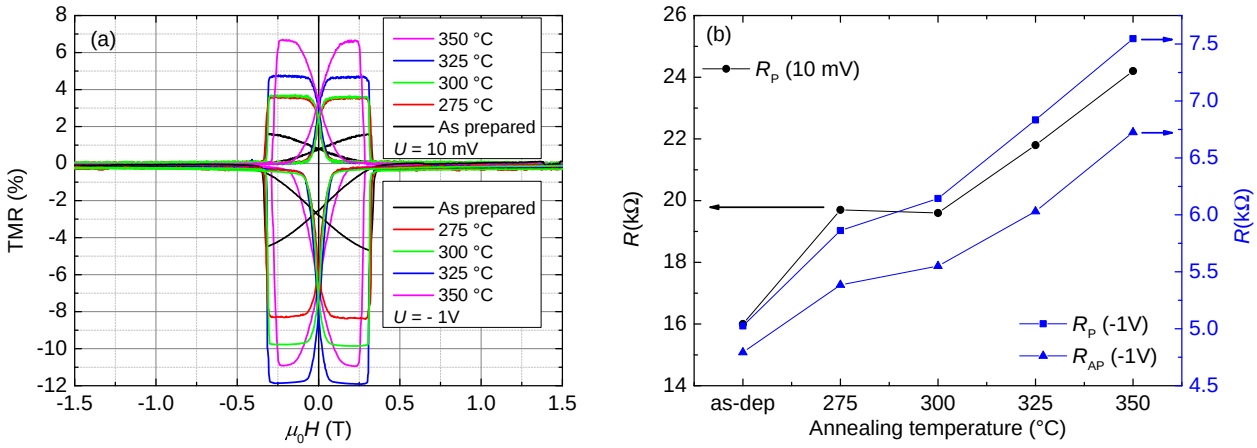

Figure 6.19: Panel(a)-TMR annealing dependence for applied biases of $U = 10\,\text{mV}$ and $U = -1\,\text{V}$ for as-deposited chips and chips annealed at $T_{\text{anneal}} = 275\,^{\circ}\text{C}, 300\,^{\circ}\text{C}, 325\,^{\circ}\text{C}$, and $350\,^{\circ}\text{C}$. Panel(b)-dependence of the parallel and antiparallel resistance states on the annealing temperature. The measurements are done on a junction with area of $400\,\mu\text{m}^2$ and $t_{\text{MgO}} = 1.5\,\text{nm}$.

and R_{P}) at applied bias of $U = -1\,\text{V}$ as well. Purposefully, both R_{AP} and R_{P} are presented for $U = -1\,\text{V}$ because R_{AP} becomes the low resistance state and R_{P}-the high resistance state for $U < -0.2\,\text{V}$. Another important observation is that the resistance-area product of our junctions is higher than the expected value for the nominal MgO thickness ($t_{\text{MgO}} = 1.5\,\text{nm}$). A possible explanation is that even the as-deposited junctions have slightly oxidized Al dusting layer due to its more electronegative nature.

TMR and R_{P} comparison for different annealing condition at applied bias $U = 10\,\text{mV}$						
Annealing	TMR(10 K)	TMR(300 K)	$\frac{TMR(300\,\text{K})}{TMR(10\,\text{K})}$	R_{P}(10 K)	R_{P}(300 K)	$\frac{R_{\text{P}}(300\,\text{K})}{R_{\text{P}}(10\,\text{K})}$
as prepared	10.6 %	1.6 %	0.15	27.7 kΩ	16.0 kΩ	0.58
275 °C	23.2 %	3.5 %	0.15	31.6 kΩ	19.7 kΩ	0.62
300 °C	27.8 %	3.6 %	0.13	31.6 kΩ	19.5 kΩ	0.62
325 °C	33.3 %	4.6 %	0.14	33.5 kΩ	21.8 kΩ	0.65
350 °C	40.3 %	6.6 %	0.16	36.1 kΩ	24.2 kΩ	0.67

Table 6.1: TMR and R_{P} comparison for different annealing condition at applied bias $U = 10\,\text{mV}$.

TMR and R_{AP} comparison for different annealing condition at applied bias $U = -1\,V$						
Annealing	TMR(10 K)	TMR(300 K)	$\frac{TMR(300\,K)}{TMR(10\,K)}$	R_{AP}(10 K)	R_{AP}(300 K)	$\frac{R_{AP}(300\,K)}{R_{AP}(10\,K)}$
as prepared	−6.7 %	−4.5 %	0.67	5.5 kΩ	4.8 kΩ	0.87
275 °C	−12.5 %	−8.3 %	0.66	6.2 kΩ	5.4 kΩ	0.87
300 °C	−14.5 %	−9.8 %	0.68	6.4 kΩ	5.6 kΩ	0.88
325 °C	−17.4 %	−11.9 %	0.68	6.8 kΩ	6.0 kΩ	0.88
350 °C	−16.2 %	−10.9 %	0.67	7.7 kΩ	6.7 kΩ	0.87

Table 6.2: TMR and R_{AP} comparison for different annealing condition at applied bias $U = -1\,V$.

In order to discuss further the physical processes of the TMR switching and the puzzling TMR decrease at different biases, the focus is placed on the samples which exhibit stable CoFe PMA ($T_{anneal} \leq 325\,°C$). The temperature dependence $R_P(T)$ has to be essentially constant for the case of coherent tunneling through MgO and decreases slightly for the case of tunneling through amorphous AlO_x (not more than 20 %). The $R_P(T)$ curves for MTJs annealed at different temperatures are plotted in Fig.(6.20 (a)). The first noticeable feature is that R_P decreases by roughly 35 % between 10 K and 300 K. This proves that the transport through our MTJs is incoherent. The incoherent transport is expected since the MRG does not have the required Δ-band symmetry in order to utilize the spin-filtering of MgO. Furthermore, the symmetry at the MRG/MgO interface is broken due to the insertion of the thin Al diffusion barrier. However, even incoherent tunneling in amorphous AlO_x does not exhibit such strong temperature decrease. Significant hopping conduction contribution is a possible reason for the stronger than expected R_P reduction. Another important observation is that the $R_P(T)$ is essentially independent of the T_{anneal}. It is not expected because the annealing should improve the barrier quality, and, hence, reduce the resistance decrease. The TMR(T) decrease demonstrates similar independence on the annealing temperature, see Fig. (6.20). This is unusual because the annealing treatment improves CoFe crystallinity (higher spin polarization), the MRG crystallinity (higher spin polarization) and the barrier quality. The overall TMR grows, however, the processes related to the temperature decrease are remarkably temperature independent. One hypothesis is that the TMR decrease is affected by a strong Fermi level spin polarization decrease of the MRG. The annealing improves significantly the CoFe electrode properties, however, its effect on the MRG is smaller. Another hypothesis is that the improved qualities are finely balanced by another type of degradation: Mn-diffusion related. Although the Al-diffusion layer reduces the Mn-diffusion, some migration has been measured in the MgO by time-of-flight secondary-ion-mass spectroscopy. The annealing-driven crystallization reduces the grain boundaries in the barrier which act as tunneling steps, but Mn diffused atoms will play the role of hopping conduction centers and thus contribute to the TMR(T) reduction. This possibility

will be discussed later (see Fig. (6.39), Fig. (6.42), and Fig. (6.43)). Perhaps the same reason is behind the $R_P(T)$ dependence. The temperature dependence at $U = -1\,V$ demonstrates similar independence on the annealing process. The $R_{AP}(T)$ at $U = -1\,V$ has much lower temperature dependence than the $R_P(T)$ at $U = 10\,mV$. $R_{AP}(-1\,V)$ decreases by approximately 12 % from 10 K to 300 K. *

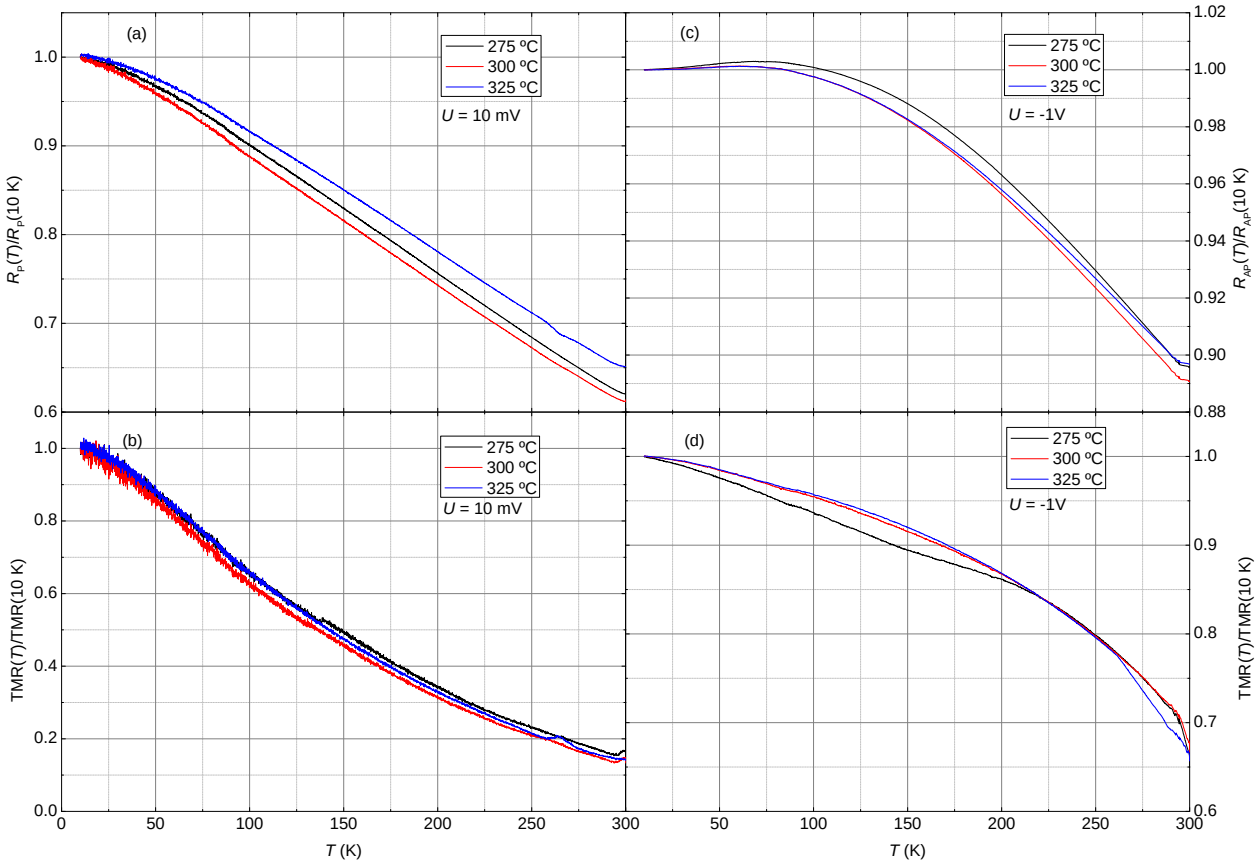

Figure 6.20: Temperature dependence of the TMR effect and the low resistance state in the MTJs for three different annealing temperatures 275 °C, 300 °C, and 325 °C. Panel (a) and (b)-$R_P(T)$ and TMR(T), respectively, for $U = 10\,mV$. Panel (c) and (d)-$R_{AP}(T)$ and TMR(T), respectively, for $U = -1\,V$.

The higher energy electron tunneling at applied bias of $U = -1\,V$ should lead to higher probability of inelastic processes: phonon- and magnon-related. Apparently, this is not the case in our MTJs, hence, the low bias transport is heavily affected by impurity related tunneling states in the barrier which are located close to E_F. The high negative bias transport is influenced less because most of the tunneling happens through the barrier levels above the resonant states. Furthermore, the TMR($U = -1\,V$) decrease demonstrate similarly very little dependence on the T_{anneal}. The electron

*The reader might notice that $R_{AP}(-1\,V)$ demonstrates a small excursion above normalized resistance values 1.0 on Fig. (6.20 (c))(small hill at $T \approx 75\,K$). In absolute terms, the maximum resistance deviation is 10 Ω. The reason for this behaviour is resistance contribution from the bottom MRG electrode. The sheet resistance of the MRG changes from 400 Ω(10 K) to 500 Ω(300 K). Hence, the resistance increase of the bottom electrode leads to the slight increase of the overall R_{AP}. The correction is negligible. The raw ratio for the R_{AP} is 5.1 kΩ/5.7 kΩ = 0.895, whereas the corrected ratio is 4.7 kΩ/5.2 kΩ = 0.904. The estimation is based on the chip with the smallest resistance - $T_{anneal} = 275\,°C$.

tunneling happens towards the MRG majority spin gap and in this case the spin polarization of the MRG is very high and with opposite sign (see Fig. (6.29))[186, 37]. The big "effective" MRG spin polarization explains the temperature robust TMR(-1 V). The curves for the non-annealed chips and the chips annealed at 350 °C are not plotted because the PMA is not well-defined in them and this leads to distorted temperature dependence. However, the bare ratios TMR(300 K)/TMR(10 K) and $R_P(300\,K)/R_P(10\,K)$ are calculated from the bare TMR(H) scans obtained on these samples. These ratios are summarized in Table (6.2) and Table (6.1).

A full range two dimensional TMR(U,T) dependence is presented in Fig. (6.21) for a sample with $T_{anneal} = 325\,°C$. Separate $I(V)$ curves have been measured each 5 K between 10 K and 300 K in AP and P resistance state in order to determine the TMR(U, T) dependence. The focus is on this sample because it exhibits the highest TMR ratios without compromising the PMA of CoFe due to high T_{anneal}. The very sharp TMR structure at zero-bias is observed. The gradual evolution of the zero TMR point is noticeable as well, so is the very temperature robust high negative bias TMR (at $U = -1\,V$). However, the extremely striking feature is the existence of a local dip at positive bias around $U = 0.3\,V$.* There is no possible spin-split density of states related argument which can explain a decrease followed by an increase in the TMR as the voltages is increased. Positive voltage corresponds to electrons tunneling from the Fermi level of MRG towards the bulk valence band of CoFe. The latter is very well-studied and known to exhibit no such sharp dependences due to the high exchange energy $E_{ex} \geqslant 1\,eV$ (see Fig. (6.4)). Since the effect cannot to be attributed to CoFe density of states features, it must be related to the tunneling probabilities through the barrier as a function of applied bias. This is a strong argument that resonant scattering states in the MgO barrier have detrimental effect on the overall TMR(U) dependence. Similar structure (both positive bias dip and negative bias TMR sign reversal) of the TMR(U, T) has been previously reported by Yang *et al.*[393] in CoFe/NiO/MgO/CoFe MTJs. Their initial interpretation is that the effects are due to resonant tunneling states. However, their subsequent analysis [395] has investigated that probably spin canting at the ferromagnetic/antiferromagnetic (CoFe/NiO) interface is the reason for the TMR sign reversal. It is possible that partial Mn oxidation at the MRG/MgO might result in antiferromagnetic MnO. However, since MnO has low Neel temperature ($\approx 120\,K$), this would imply that canting effect should disappear in the temperature range from 10 K to 300 K. No sharp decrease or abrupt behaviour change is observed in Fig. (6.21) and, therefore, spin canting is an unlikely explanation in our MTJs.

*It has to be stressed again that this sample is slightly different than the sample measured before with $T_{anneal} = 350\,°C$. Yet, the latter exhibited plateau at positive bias (see Fig. (6.11) which is a weaker manifestation of the same effect.

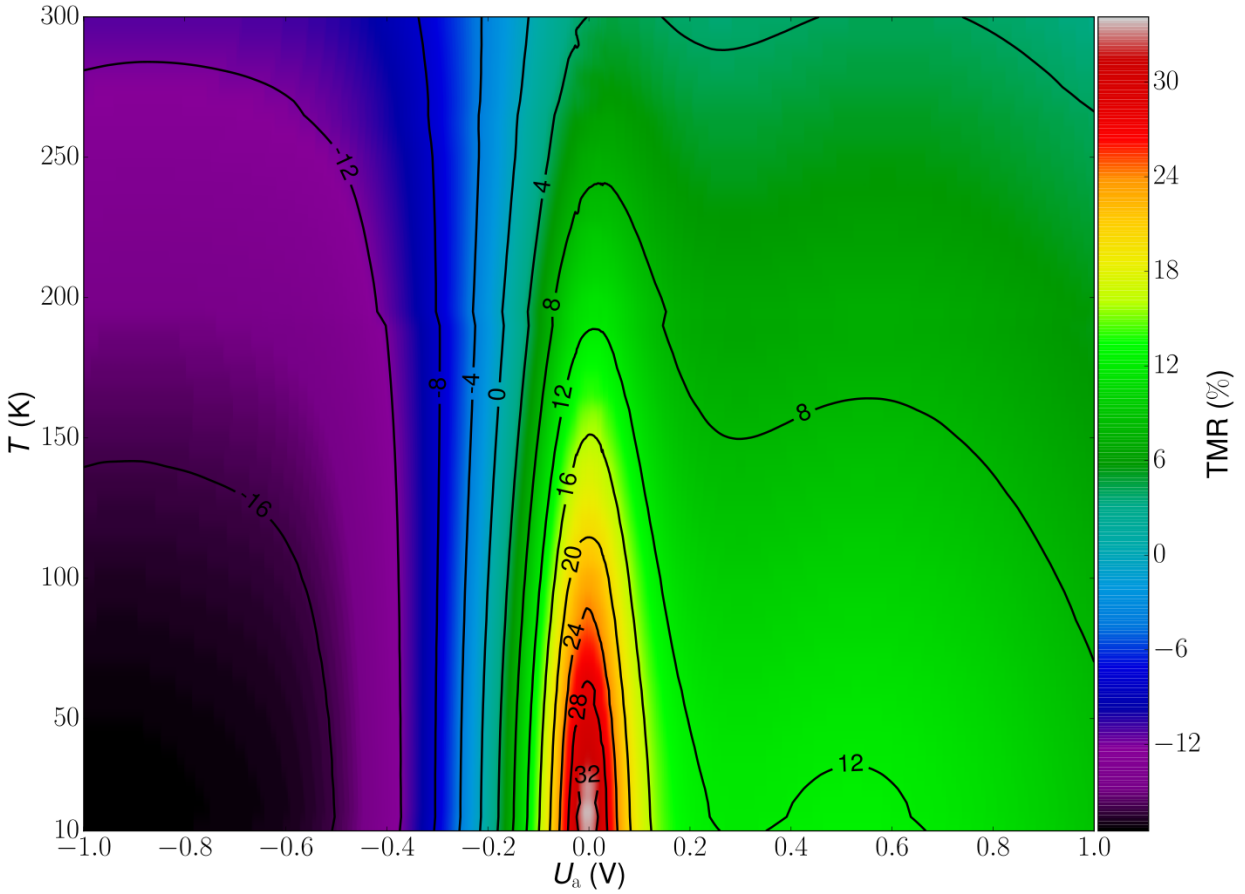

Figure 6.21: Three dimensional applied bias-temperature-TMR dependence of a sample annealed at $T_{\text{anneal}} = 325\,^{\circ}\text{C}$. Voltage step is $\Delta U = 1\,\text{mV}$, temperature step is $\Delta T = 5\,\text{K}$.

6.5 Reasons for a switch in the TMR sign a function of the applied bias

TMR-voltage dependence has been studied extensively in MTJs because the investigation of the TMR(U) provides insight into the quality of the MTJs. The higher the half-maximum bias is, the better the quality of the barrier is. Furthermore, the overall shape of the TMR(U) dependence carries information about the tunneling processes through the barrier. It has been demonstrated in some cases that the TMR might switch sign at different biases. Quantum well tunneling states, interface tunneling probability modification, resonant tunneling state, and interface disorder are some of the reasons which have been demonstrated to cause TMR(U) sign change[238, 70, 346, 344].

The first systematic investigation of TMR sign reversal has been done on Co/Au(t)/Al_2O_3/$Ni_{80}Fe_{20}$, where t_{Au} is varied from 0.1 nm to 1.2 nm. As the Au thickness increases, the TMR(U) curve changes substantially*. The TMR(U) curves for different t are shown in Fig. (6.22). The zero

*This is the first observation of negative TMR. In a separate article, direct spin polarization has been measured by

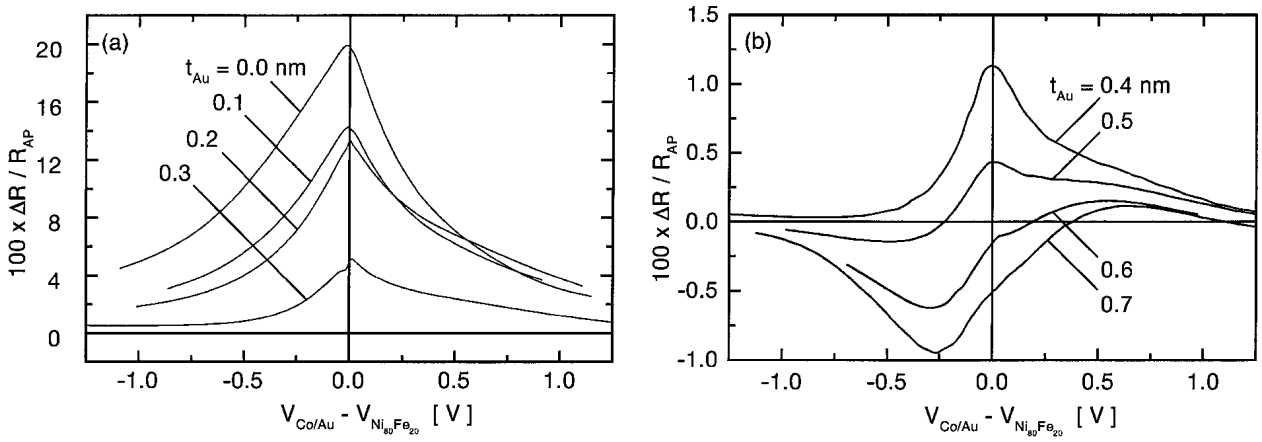

Figure 6.22: Quantum well states: TMR(U) curves on an Co/Au(t)/Al_2O_3/$Ni_{80}Fe_{20}$ MTJs. Panel (a)-$t \leq 0.3$ nm, panel (b)-$t \geq 0.4$ nm. The diagram is after Moodera *et al.*[238].

bias TMR decreases, furthermore, the TMR(U) shows stronger reduction for $U < 0$ V which corresponds to electrons tunneling towards the modified interface. The maximum value of the TMR is still at close to zero bias for $t_{\mathrm{Au}} < 0.5$ nm, however, for $0.6\,\mathrm{nm} > t_{\mathrm{Au}} > 0.4\,\mathrm{nm}$, the TMR switches sign at negative bias, however, for $t_{\mathrm{Au}} > 0.6$ nm, the zero bias TMR is negative and the sign change happens at positive bias. The maximum TMR is no longer at close to zero bias. The effect has been theoretical predicted and is known as quantum-well tunneling [359]. The insertion layer forms a quantum-well which modifies significantly the tunneling probabilities for the spin-up and spin-down electrons. Only 0.5 nm of Au insertion results in 40-times decrease of the zero bias TMR value! Similar QWS have been later demonstrated in NiFe/Ta_2O_5/Al_2O_3/NiFe[299], Co/Cu/Al_2O_3/Co[197], Co/Ru/Al_2O_3/Co [196], Co/Cu/Al_2O_3/NiFe[402], and Fe/Cr/MgO/Fe[123]. The work of Yuasa *et al.*[402] demonstrated that the TMR shows oscillatory behaviour as a function of the insertion layer thickness. This indicates that the QWS effect might be similar in nature to the RKKY coupling effect.

The chemical bonding between the ferromagnetic and the insulating barrier was demonstrated to affect the tunneling probabilities for spin-up and spin-down by Teresa *et al.*[70]. They have investigated MTJs with the structure Co/I/$La_{0.7}Sr_{0.3}MnO_3$(LSMO) where the insulating barrier, I, is picked among $SrTiO_3$(STO), $Ce_{0.69}La_{0.31}O_{1.845}$(CLO), and Al_2O_3(ALO). Different sign of the TMR effect was measured for different insulators. It is well-established that the Co/ALO results in positive spin polarization, but it is further confirmed that the LSMO/ALO tunneling spin polarization is positive as well in Fig. (6.23 (c))*. However, if ALO is replaced with STO, the TMR becomes negative (see Fig. (6.23 (a)). An additional barrier combination is cross-checked in order to find out whether the Co/STO interface or the LSMO/STO interface is responsible for the negative sign of the TMR effect. The composite Co/ALO/STO/LSMO MTJ structure exhibits pos-

superconducting tunneling spectrosopy Fe/Au/Al_2O_3/Al[236].

*The bare LSMO E_F spin polarization has been demonstrated to be positive as well [264].

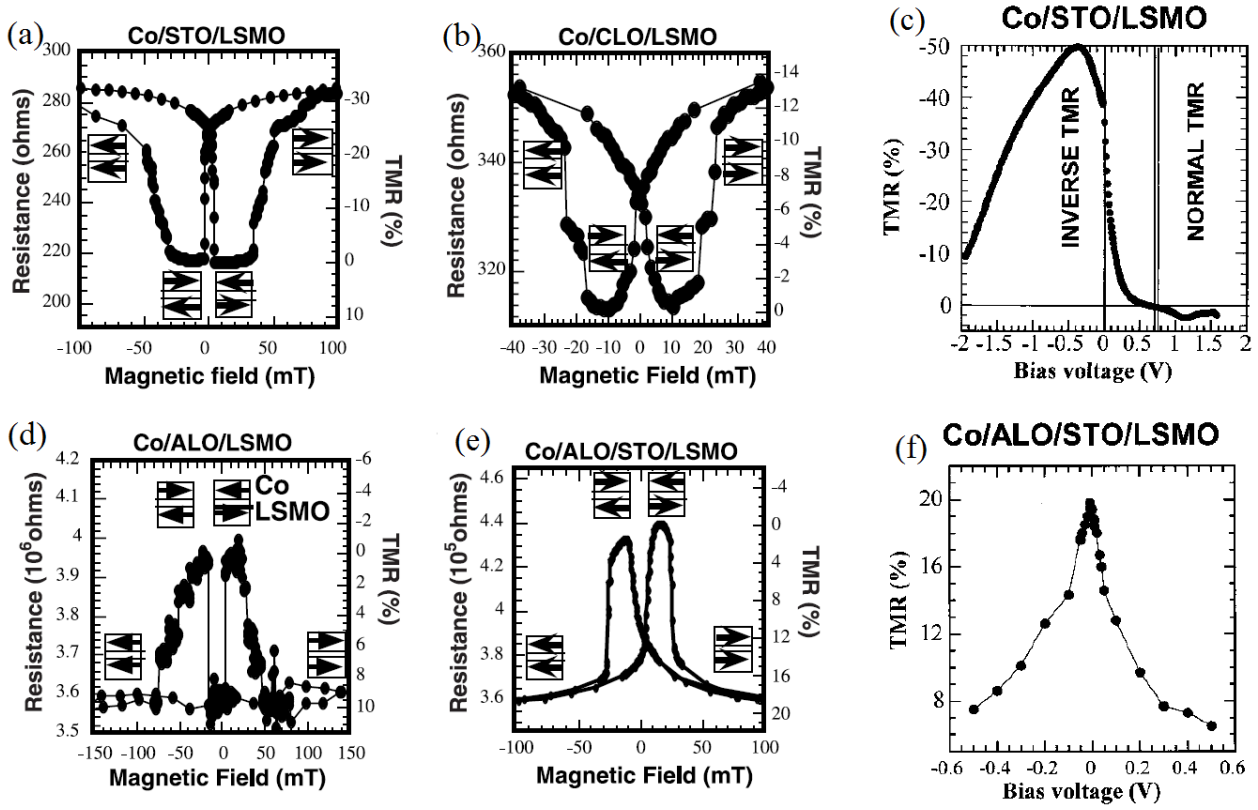

Figure 6.23: TMR effect between Co and LSMO with different insulation layers. Panel (a) TMR with $SrTiO_3$ barrier, panel (b) - TMR with CeLaO barrier, panel (c) - TMR(U) with $SrTiO_3$ barrier, panel (d) - TMR with Al_2O_3 barrier, panel (e) - TMR with $Al_2O_3/SrTiO_3$ barrier, and panel (e) - TMR(U) dependence with $Al_2O_3/SrTiO_3$ barrier. Please note that panel (a) demonstrates negative TMR, whereas panel (e) - positive one. The plots are after de Teresa *et al.*[70].

itive TMR effect (panel (d)) and, therefore, the Co/AlO and the LSMO/STO interfaces have both positive spin polarization. From the last observation, it follows that the Co/STO interface is responsible for the negative TMR effect in the Co/STO/LSMO MTJ structure (panel (a)). Therefore, the Co/STO interface spin polarization is negative. The latter means that the chemical bonding between the ferromagnet and the barrier has significant effect on the tunneling probabilities for the spin-up and the spin-down electrons. The negative tunneling polarization of the Co/STO interface can be explained as preferential tunneling of the d electrons and the latter have negative E_F spin polarization with respect to the overall magnetization. It is interesting to comment on the different TMR(U) behaviour for the STO and ALO/STO barriers (see Fig. (6.23) panel (c) and (f), respectively). The Fermi level of LSMO is situated above the Fermi level of Co for negative bias, and this is the other way around for positive bias. The TMR(U) reaches maximum negative TMR at $U \approx -0.4\,\mathrm{V}$ which corresponds well to the maximum in the spin-down DOS for Co. For higher negative bias, the difference between the spin-down DOS and spin-up DOS is lower and, hence, the "effective" negative spin polarization is decreased. The situation is different for $U > 0\,\mathrm{V}$, then the electrons tunnel from the Fermi level of the Co electrode towards the free states above the E_F

in LSMO. At high positive bias ($U = 0.7\,\mathrm{V}$), the contribution from the spin-up and the spin-down DOS of the Co d-bands is equal and the TMR crosses zero. The TMR grows positive for $U > 0.7\,\mathrm{V}$ because the spin-up DOS is higher than the spin-down DOS for deeper levels in the Co valence band. Furthermore, the TMR(U) of a Co/ALO/STO/LSMO demonstrates positive TMR for both positive and negative bias, as is usually the case. Both the Co/ALO and the LSMO/STOinterfaces have preferential transmission of s-electrons which have positive spin polarization.

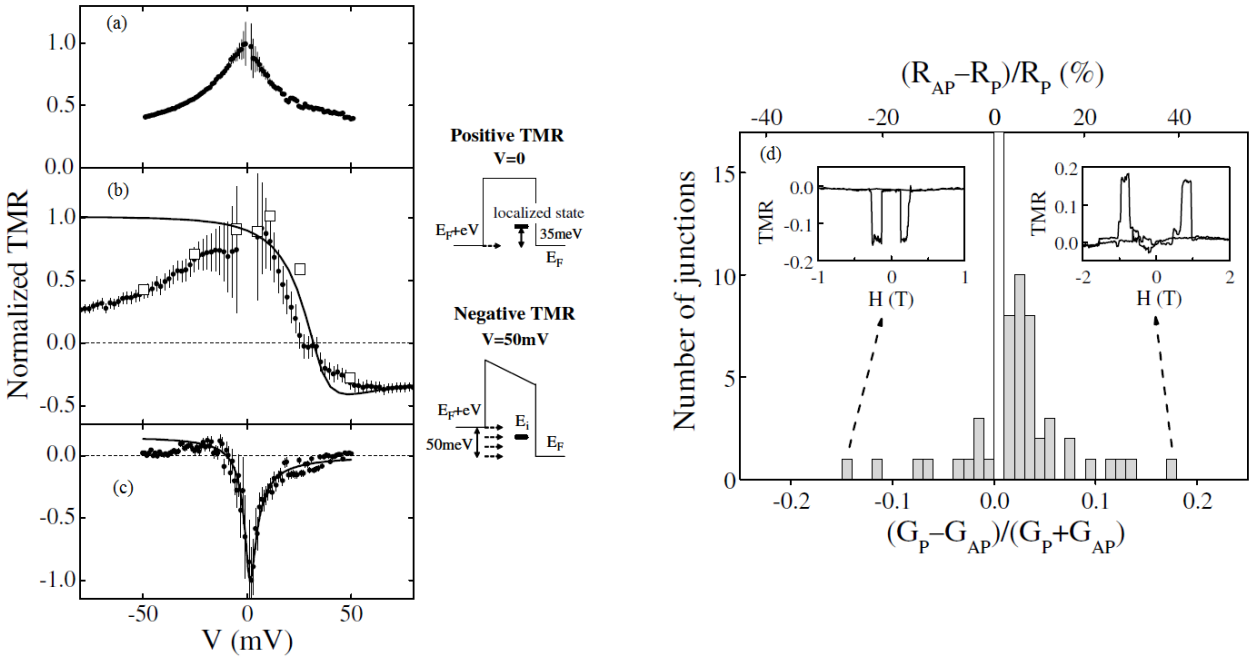

Figure 6.24: TMR of Ni/NiO/Co tunnel junctions. Panel (a)-demonstrates classical TMR(U) behaviour with gradual symmetric decrease as the bias is raised. Panel (b)-TMR(U) for a junction with a resonant level located approximately 35 meV above the Fermi level. The TMR is positive close to zero bias, however, it changes sign when the Fermi level of the left electrode is raised to the point of the resonant level. The schematic with the Fermi levels of the two electrodes and the position of the localized state is presented on the right-hand side of the panel. Panel (c)-TMR(U) of a junction with a narrow localized state at the Fermi level. Panel (d)-statistical distribution of the TMR effect. The distribution peaks at small positive TMR values. The samples are measured at 4 K. The plots are after Tsymbal *et al.*[346].

Another possibility for TMR sign reversal is the effect of resonant tunneling via localized states in the barrier. Tsymbal *et al.*[346] discuss the effect in the Ni/NiO/Co structure which has been electrodeposited in nanoporous polyester track-etched membranes. Large number of junctions have been investigated in order to understand the statistical spread in the zero-bias TMR value. TMR sign reversal is observed at various voltages because due to impurities (or incomplete oxidation of the NiO), there are different energy levels within the band gap of the insulating barrier. Tunneling through these levels might change the TMR sign at some energies. Furthermore, the distribution of these energy levels depends significantly on the deposition conditions and the related formation of paramagnetic defects into the barrier. The sign reversal of the TMR is explained by assisted tunneling through an impurity state in the insulator. The conductance in the case of localized states

is represented by

$$G(E) = \frac{4e^2}{h} \frac{\Gamma_1 \Gamma_2}{(E - E_\mathrm{i})^2 + (\Gamma_1 + \Gamma_2)^2}, \tag{6.11}$$

where E_i is the energy of the localized state, and $\Gamma_1/\hbar$ and $\Gamma_2/\hbar$ are the tunneling rates of an electron between the impurity level and the left and right ferromagnetic electrodes, respectively. The leak rates depend on the density of states of the two electrodes and the position of the impurity within the insulator: $\Gamma_1 \propto \rho_1 \exp(-2kx)$ and $\Gamma_2 \propto \rho_2 \exp(-2k(d-x))$, where k is the decay rate of the wave-function. It is assumed that the impurity state is located at x from the left electrode, and d is the barrier thickness. For magnetic electrodes, the respective rates are spin-dependent: $\Gamma_1^\uparrow \propto \rho_1^\uparrow \exp(-2kx)$, $\Gamma_1^\downarrow \propto \rho_1^\downarrow \exp(-2kx)$), etc.*. For tunneling far above, or far below the impurity states $|E - E_\mathrm{i}| >> (\Gamma_1 + \Gamma_2)$, then the conductance is $G^{j,l} \propto \rho_1^j \rho_2^l$, where j, and l are picked from $\uparrow$ and $\downarrow$. However, close to resonance $|E - E_\mathrm{i}| \approx 0$, and then the conductance is $G \propto \Gamma_1\Gamma_2/(\Gamma_1 + \Gamma_2)^2$. If the impurity state is located non-symmetrically in the barrier $|x| > |x-d|$, then $\Gamma_1 << \Gamma_2$, and, hence, $G \propto \Gamma_1/\Gamma_2 \propto \rho_1/\rho_2$. Respectively, for asymmetry towards the left electrode $|x| < |x-d|$: $G \propto \Gamma_2/\Gamma_1 \propto \rho_2/\rho_1$. It is assumed for definiteness that $\Gamma_1 << \Gamma_2$. Then the resonant spin dependent conductances and the parallel and antiparallel state conductances are calculated like:

$$G_\mathrm{AP}^\mathrm{res} \propto G^{\uparrow\downarrow} + G^{\downarrow\uparrow} \propto \frac{\rho_1^\uparrow}{\rho_2^\downarrow} + \frac{\rho_1^\downarrow}{\rho_2^\uparrow} \propto \frac{\rho_1^\uparrow \rho_2^\uparrow + \rho_1^\downarrow \rho_2^\downarrow}{\rho_1^\downarrow \rho_2^\uparrow}, \tag{6.12}$$

$$G_\mathrm{P}^\mathrm{res} \propto G^{\uparrow\uparrow} + G^{\downarrow\downarrow} \propto \frac{\rho_1^\uparrow}{\rho_2^\uparrow} + \frac{\rho_1^\downarrow}{\rho_2^\downarrow} \propto \frac{\rho_1^\uparrow \rho_2^\downarrow + \rho_1^\downarrow \rho_2^\uparrow}{\rho_1^\downarrow \rho_2^\uparrow}. \tag{6.13}$$

The numerators in the final expressions above have to be carefully noticed. The role of the antiparallel and parallel conductances are inverted under resonant conditions: $G_\mathrm{AP}^\mathrm{res} \propto G_\mathrm{P}$, and $G_\mathrm{P}^\mathrm{res} \propto G_\mathrm{AP}$. Therefore, the resonant $\mathrm{TMR}^\mathrm{res}$ is inverted with respect to the usual, off-resonant, TMR:

$$\mathrm{TMR}^\mathrm{res} = -\mathrm{TMR}. \tag{6.14}$$

When the resonant states are far away from the Fermi level, the TMR is high and positive as expected (see Fig. 6.24 (a)). It demonstrates the usual gradual symmetric decrease for positive and negative bias as well. If there are resonant scattering levels close above the Fermi level, the zero bias TMR is positive but switches to negative at small bias when the Fermi level of one of the electrodes is raised to the impurity level (Fig. (6.24) (b)). If the bias is increased further, tunneling through the resonant states decreases its contribution as more electrons tunnel through insulator bandgap region, which is free from defects. If the resonant level is positioned at the Fermi level and its width is small, then a sharp, narrow TMR negative switch is observed (Fig. (6.24) (c)). The authors have

*The situation becomes more complicated if the wave-function decay rates are spin-dependent as well.

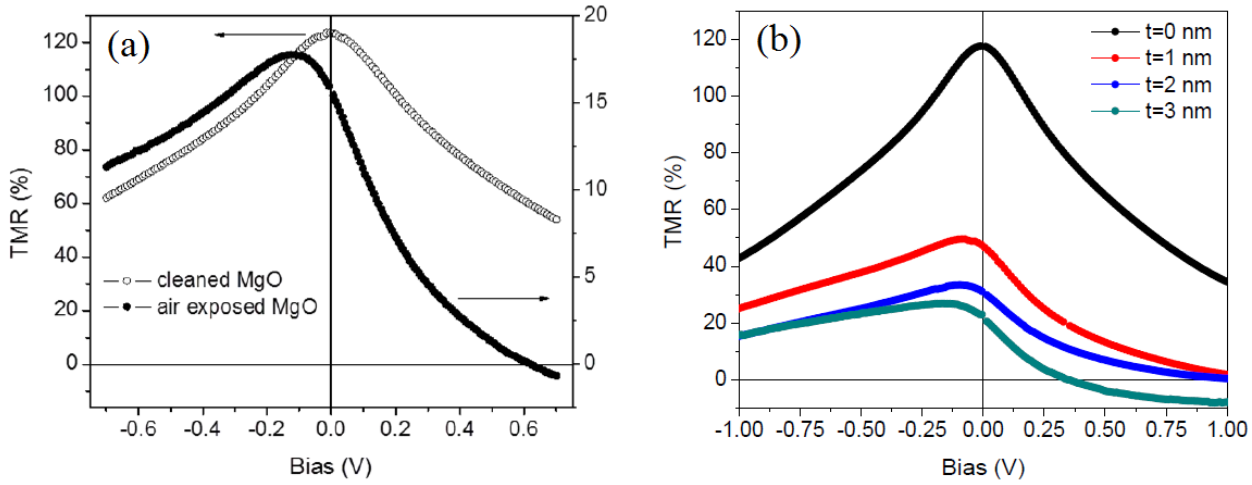

Figure 6.25: Panel (a)-TMR(U) dependence of a standard MgO-based MTJ. The stack has been exposed to atmosphere just after the MgO deposition (solid circles). The standard symmetric TMR(U) is recovered when the air-exposed MTJ is pre-etched with Ar-plasma before the deposition of the top ferromagnetic contact (empty circles). Similar result on intentionally C-contaminated MTJ interfaces has been reported before [343]. Panel (b)-TMR(U) dependence of an MTJ with a composite MgO/Alq3(t) tunnel barrier. Three different thicknesses of the organic barrier are presented. The graph is after H. Tokuc[344].

analyzed many devices and it has been concluded that the different zero bias TMR and TMR(U) is due to statistical distribution of disorder and the spread in the resonant levels distribution among the devices (Fig. (6.24) (d)). It has been demonstrated before that similar devices with larger pillar size show almost zero TMR due to the statistical averaging of the disorder[325].

Finally, Tokuc[344] has investigated the effect of composite barrier deposition or the exposure to atmosphere of MgO barrier on the TMR(U). Half MTJs with the structure Si/ SiO_2/ Ta(5)/- Ru(30)/ Ta(5)/ NiFe(5)/ IrMn(10)/ CoFeB(3)/ MgO(2) have been deposited by sputtering, then the vacuum is broken and the stack is transferred to another deposition chamber where a top electrode Alq3(t)/ Co(10)/ Cu(5) is deposited in a separate thermal evaporation system. TMR switches sign even for $t = 0$ when the MgO barrier is not pre-etched with low energy Ar plasma before the deposition of the top ferromagnet but this time at positive bias (see Fig. (6.25)). Positive bias corresponds to tunneling from the bottom towards the top ferromagnetic electrode in this case. The same effect has been observed as well in MTJs with purposefully carbon-contaminated interfaces[343]. The latter implies that the top MgO interface degradation due to atmosphere exposure is responsible for the TMR(U) behaviour. MgO is known to adsord readily water molecules. If the air-exposed MgO is Ar-etched *in situ*, the TMR(U) is symmetric and shows no indication of sign change up to 0.7 V. Furthermore, if organic Alq3 barrier is deposited on top of a pre-cleaned MgO and the top ferromagnetic layer is deposited afterwards, the TMR switch is observed again. The thicker the Alq3 barrier is, the stronger the TMR decrease is. The decrease in the zero-bias TMR correlates with the decrease of the zero-TMR point towards $U = 0$ V. Furthermore, it should be noted that the peak of the TMR effect moves towards higher negative voltage. Similar behaviour is demonstrated

in MTJs with MgO/Znq2 insulator. These observations show that composite barrier structures have detrimental effect on the overall TMR behaviour. This might be related as well to spin-filtering through the organic barrier because both positive and negative TMR values have been reported before.

6.6 Tunneling magnetoresistance in MTJs with a zero magnetization Mn_2Ru_xGa electrode

The TMR effect at small bias is determined by the spin polarization at the Fermi levels of the two ferromagnetic electrodes. Furthermore, it is generally accepted in the spin electronic community that the spin polarization P is linearly dependent on the magnetization M[224]. The latter is true for classical 3d ferromagnets which exhibit Stoner ferromagnetism. However, the Fermi level spin polarization is in effect a differential property of the density of states whereas the magnetization is in reality an integrated property of the spin-split density of states. Hence, such general statement ($P(T) \sim M(T)$) should not be always true. Ferrimagnetic compositions with conveniently tuned compensation temperatures provide excellent testing opportunity that this accepted correlation for many materials cannot be regarded as a strict dependence for all magnetically ordered compositions. It has been already discussed that the inversion in the AHE signal is a strong indication that the spin polarization of the MRG changes its sign from positive (below T_{comp}) to negative (above T_{comp}) at the compensation temperature (see Fig. (6.7) and Fig. (6.8))*. In this section, TMR data on MTJs with a compensated $Mn_2Ru_{0.8}Ga$ ($T_{comp} \approx 200\,K$) bottom electrode is presented.

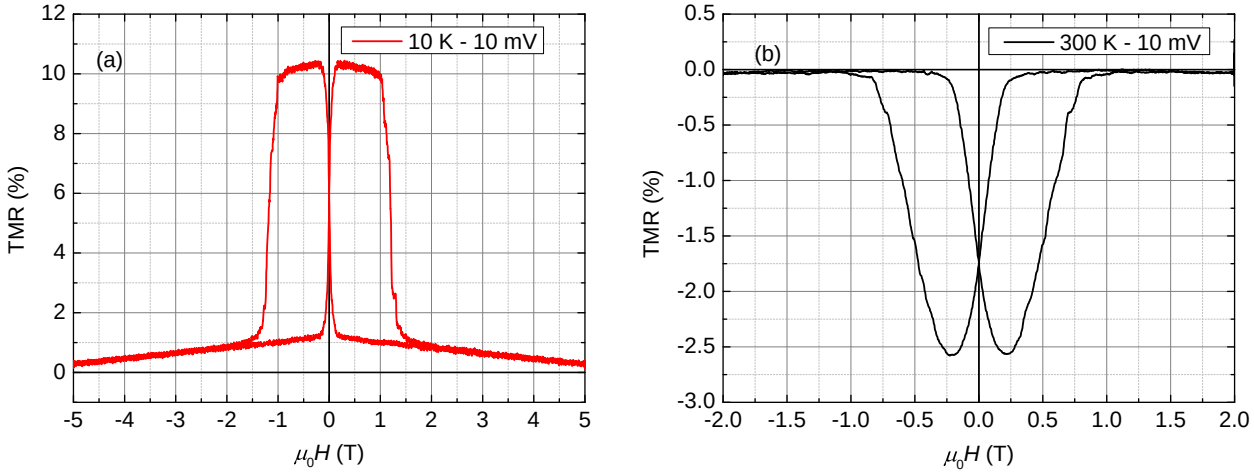

Figure 6.26: TMR of an MTJ with $Mn_2Ru_{0.8}Ga$ at applied bias U 10 mV . Panel(a) - TMR measured at 10 K. Panel(b) - TMR measured at 300 K. Note that TMR switches sign as a function of temperature at close to zero bias.

*The positive direction is the orientation of the MRG overall magnetization.

First of all, two magnetoresistance scans at 300 K and 10 K at low applied bias ($U = 10\,\mathrm{mV}$) are presented in Fig. (6.26). The MTJ chip is annealed at 325 °C and the size of the measured junctions is $6\,\mu\mathrm{m} \times 6\,\mu\mathrm{m}$. The TMR switches sign at low bias as a function of temperature unlike the previously extensively discussed sample. In order to confirm that the TMR switch is due to compensation of the MRG electrode, the divergence of the MRG coercive field must be observed. Additionally, figure (6.27) represents three TMR curves very close to the compensation temperature of the MRG ($T = 165\,\mathrm{K}$, 200 K, 235 K). The obtained TMR ratios are 4.5 %, 1.75 %, and −3.5 %, respectively. It has to be noticed that the maximum applied magnetic field is $\mu_0 H = 14\,\mathrm{T}$. The coercivity of MRG is above 10 T at $T = 200\,\mathrm{K}$, and, hence, this can be assumed to be very close to the compensation temperature. Furthermore, the fact that the MRG coercivity decreases both below and above 200 K is a clear indication that this is the T_{comp} for this particular MRG bottom electrode. The TMR has the same sign at $T = 165\,\mathrm{K}$ and $T = 200\,\mathrm{K}$ which means that strictly speaking T_{comp} is slightly above 200 K. Two more things have to be noted in the shape of these TMR scans. First, the MRG switch is not abrupt. It is evidenced by the fact that the AP to P state switch is not as rectangular as it has been in the previously investigated set of MTJs (Fig. (6.10)). The latter suggests that the MRG electrode does not have a well-defined PMA in these MTJs. Second, there is an appreciable high-field background after the MRG coercive field in the TMR loops. Since the anisotropy field of the CoFe cannot be above 2 T, the non-linear background is most likely related to an in-plane magnetization component of the MRG electrode. As the applied field is increased well above the coercivity of MRG, its small in-plane magnetization component is rotated gradually out-of-plane towards the vertical direction. The R_{P} of the MTJ decreases as the overall MRG magnetization gets more aligned with the CoFe magnetization. The latter effect is in agreement with the prediction of Slonchewski that the TMR effect depends on the cosine of the angle between the magnetization orientations of the two ferromagnetic electrodes (see Eq. (1.45) and Fig. (1.11)). At $T = 200\,\mathrm{K} \approx T_{\mathrm{comp}}$, the coercivity of the CoFe increases significantly as well. It is related to exchange coupling between the MRG electrode and the CoFe electrode through the MgO barrier*. Furthermore, there is an apparent decrease of the TMR when a full loop is recorded at $T = 200\,\mathrm{K} \approx T_{\mathrm{comp}}$. The MRG electrode is in a multi-domain state when full TMR scan is performed very close to the compensation temperature. This is attributed to small Ru concentration variation within a single MTJ and anisotropy angle spread due to the mosaicity of the MRG film. There is inevitable small, lateral Ru concentration difference within a single tunnel junction. This spread means that the different grains of the MRG electrode have tight distribution of their compensation temperatures. The spread is not very important for temperature very far from T_{comp} but it is critical close to T_{comp}. This would mean that very close to T_{comp} some of the grains would

*Exchange coupling has been achieved with MRG in MRG/Hf/CoFe stack but it is not discussed in this thesis. The exchange coupling sign has been determined to be independent of the compensation temperature and not due to direct dipole-dipole interaction.

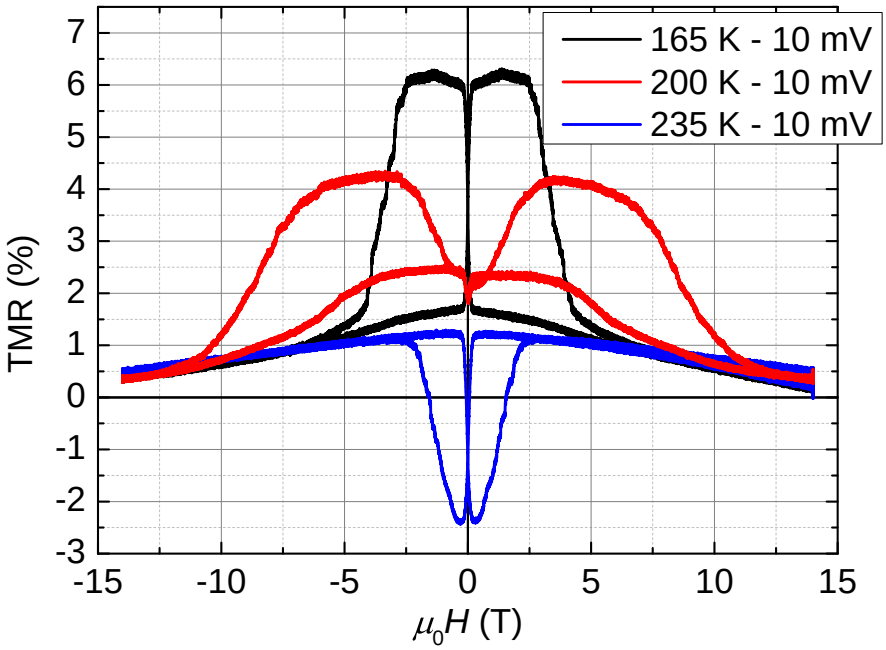

Figure 6.27: TMR of an MTJ with $Mn_2Ru_{0.8}Ga$ close to compensation at an applied bias $U = 10\,\mathrm{mV}$. The black curve is recorded just below compensation (165 K), the red curve-at compensation (200 K), and the blue curve just above compensation (235 K). Note that the maximum applied field is $\mu_0 H = 14\,\mathrm{T}$.

have already passed the compensation point. The grains which have undergone compensation and these which have not will then contribute spin polarization of opposite signs and, hence, the cumulative tunneling spin polarization will be decreased. This will lead to a reduced TMR value. The anisotropy variation within the MRG of a single MTJ has a similar detrimental effect. Since the MRG coercivity diverges, the magnetic field can no longer align the magnetization of the MRG and the CoFe electrode. This will mean that the angle (Θ_{comp}) between the M(MRG) and M(CoFe) will be significantly higher close to compensation that it is far away from compensation (Θ_{away}). Hence, $\cos(\Theta_{\mathrm{comp}}) < \cos(\Theta_{\mathrm{away}})$ and following the Slonchewski's rule this leads to lower TMR. The variation of the anisotropy due to mosaicity of the MRG exacerbates even further the situation because the anisotropy axes form a cone and the injection happens at different Θ's.

The discussion does not provide so far an unambiguous prove that there is a non-zero spin polarization at the very T_{comp}, it only points out that when full TMR loops are measured above and below the compensation temperature of MRG, the TMR sign switches. The TMR reversal is a strong indication that the Fermi level spin polarization is determined by one of the Mn sublattices rather than by the overall MRG moment because the latter stays aligned with the magnetic field in these high-field scans. When full loops are performed and the applied field is higher than the coercive field of MRG ($\mu_0 H_{\mathrm{app}} > \mu_0 H_{\mathrm{c}}^{\mathrm{MRG}}$), the MRG magnetization must follow the field orientation. This is because negative magnetic moment with respect to the magnetic field is unstable equilibrium position of the Zeeman magnetic energy. Therefore, the two Mn sublattices must inverse their magnetic moments in order to keep the overall magnetization positive, and because the Fermi level

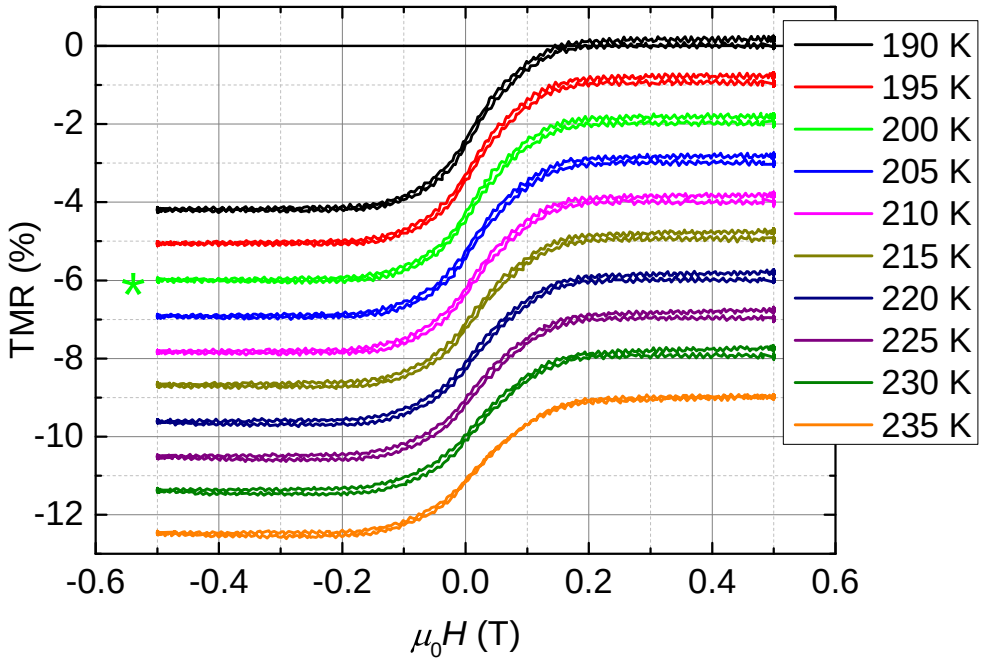

Figure 6.28: TMR minor loops measured from 235 K to 190 K at interval $\Delta T = 5$ K. The MTJ is saturated at 235 K in 14 T. The field sweep direction is positive→negative→positive, and, hence, the TMR effect is negative. The minor loop at 190 K is kept as it is, while each of the others is offset downwards by -1 % with respect to the previous loop. The compensation temperature is indicated with a green asterisk.

spin polarization is governed by one of the Mn sublattices, the TMR changes sign. Similar change in the TMR sign has been demonstrated in the ferrimagnetic composition Gd_xCo_{1-x} by Kaiser *et al.* [156]. They attribute that to higher contribution of the Co sublattice towards the Fermi level spin polarization. However, there is no clear demonstration of the TMR at T_{comp} in their work. In order to demonstrate non-zero spin polarization at the compensation temperature in our MTJs, minor loops in a field range much smaller than the MRG coercivity have to be measured. In this way, the CoFe electrode switches but the MRG magnetic state is left unperturbed. As it is discussed above, this means that the MRG magnetization goes through zero without having the added complexity of a multi-domain state. In order to do that, the temperature range from 235 K to 190 K has been chosen. The MTJ has been saturated in $\mu_0 H = 14$ T at $T = 235$ K, then minor loops have been acquired in the direction $0.5\,\text{T} \rightarrow -0.5\,\text{T} \rightarrow 0.5\,\text{T}$ at each 5 K (see Fig. (6.28)).

The TMR effect is negative, as expected, because the MRG is saturated above its compensation temperature. The ratio is -3.5 % at 235 K and -4.1 % at 190 K. The critical observation is that the TMR effect does not change sign in the temperature range when minor loops are performed. It has to be noticed that the TMR flips sign in the same temperature range when **major** loops are performed (see Fig. (6.27)). Furthermore, no sharp change in the TMR effect is observed as the MTJ is passed through the MRG compensation. The latter is a confirmation that the apparent decrease in the full TMR loop at T_{comp} is due to the multi-domain state supported by small sample imperfections. When the applied field $\mu_0 H_{app} < \mu_0 H_c^{MRG}$, the magnetization flips from positive to

negative because this is no longer a non-stable equilibrium configuration which has been evidenced before in the $M(T)$ scan (see Fig. (6.8)). However, because the spin polarities on the two Mn sublattices are not inversed, the Fermi level spin polarization does not change sign at all. This is exactly confirmed in the minor loop scans. In order to further clarify the different behaviour of the MTJ when full and minor loops are performed, a schematic diagram of the overall magnetization, Fermi level spin polarization, and Mn sublattice magnetic moments is presented in Fig. (6.29) as a function of temperature. It is assumed that the MRG is saturated at the lowest possible temperature on both panels. The Fermi level spin polarization is determined by the imbalance of Mn 4*c* and Mn 4*a* DOS.

The high coercivity, which is supported by the very low magnetization, of the MRG electrode should imply that the field immunity of our MTJs is rather high. TMR temperature dependence scans are performed through compensation in order to confirm that. First, the MTJ is saturated at $T = 10\,\mathrm{K}$ in $\mu_0 H = 14\,\mathrm{T}$, set in antiparallel configuration at $\mu_0 H = -0.5\,\mathrm{T}$, and the $R_{\mathrm{AP}}(T)$ is measured from 10 K to 300 K. Then the sample is cooled down again, saturated again at 10 K in $\mu_0 H = -14\,\mathrm{T}$ and set in parallel configuration at $\mu_0 H = -0.5\,\mathrm{T}$, and the $R_{\mathrm{P}}(T)$ dependence is measured from 10 K to 300 K. In this way, the TMR(T) dependence is calculated (Fig. (6.30) (a)-black curve). As expected the TMR has positive sign and no sharp change is observed at T_{comp}. The applied magnetic field is always below the coercive field of the MRG in this temperature range ($-0.5\,\mathrm{T} < \mu_0 H_{\mathrm{c}}^{\mathrm{MRG}}$). The TMR values range from 9 % (at $T = 10\,\mathrm{K}$) to 2 % (at $T = 300\,\mathrm{K}$). Furthermore, a similar measurement procedure has been applied but this time an MTJ has been saturated in antiparallel or parallel state at $T = 300\,\mathrm{K}$, above the compensation temperature. The same smooth TMR(T) behaviour is observed through T_{comp} but with negative TMR sign, which is expected (Fig. (6.30) (a)-red curve). It should be pointed out that these MRG-compensated MTJs are generally of lower quality: the resistance is rather low and the raw current-voltage characteristics indicates that there is a significant non-tunneling contribution. These MTJs have been probably partially shorted* and this leads to an appreciable reduction of the TMR. The TMR decreases approximately 4 times from 10 K to 300 K. The low resistance state (R_{P} for saturation below T_{comp}, and R_{AP} for saturation above T_{comp}) demonstrates again significant temperature decrease which indicates incoherent and defect-mediated tunneling (see Fig. (6.30) (b)). This along with the non-ideal PMA of the MRG are the main reasons why the measured TMR values are far below the expected results for a highly spin polarized composition. The sample imperfections cannot, however, undermine the fact that TMR effect has been demonstrated with a strictly zero moment ferrimagnet.

The demonstrated high-field stability of the MTJ state means that MRG has the potential to be used as an electrode in future MRAM-type devices, furthermore, there would be negligible cross-

*Or they had significant hopping conductance.

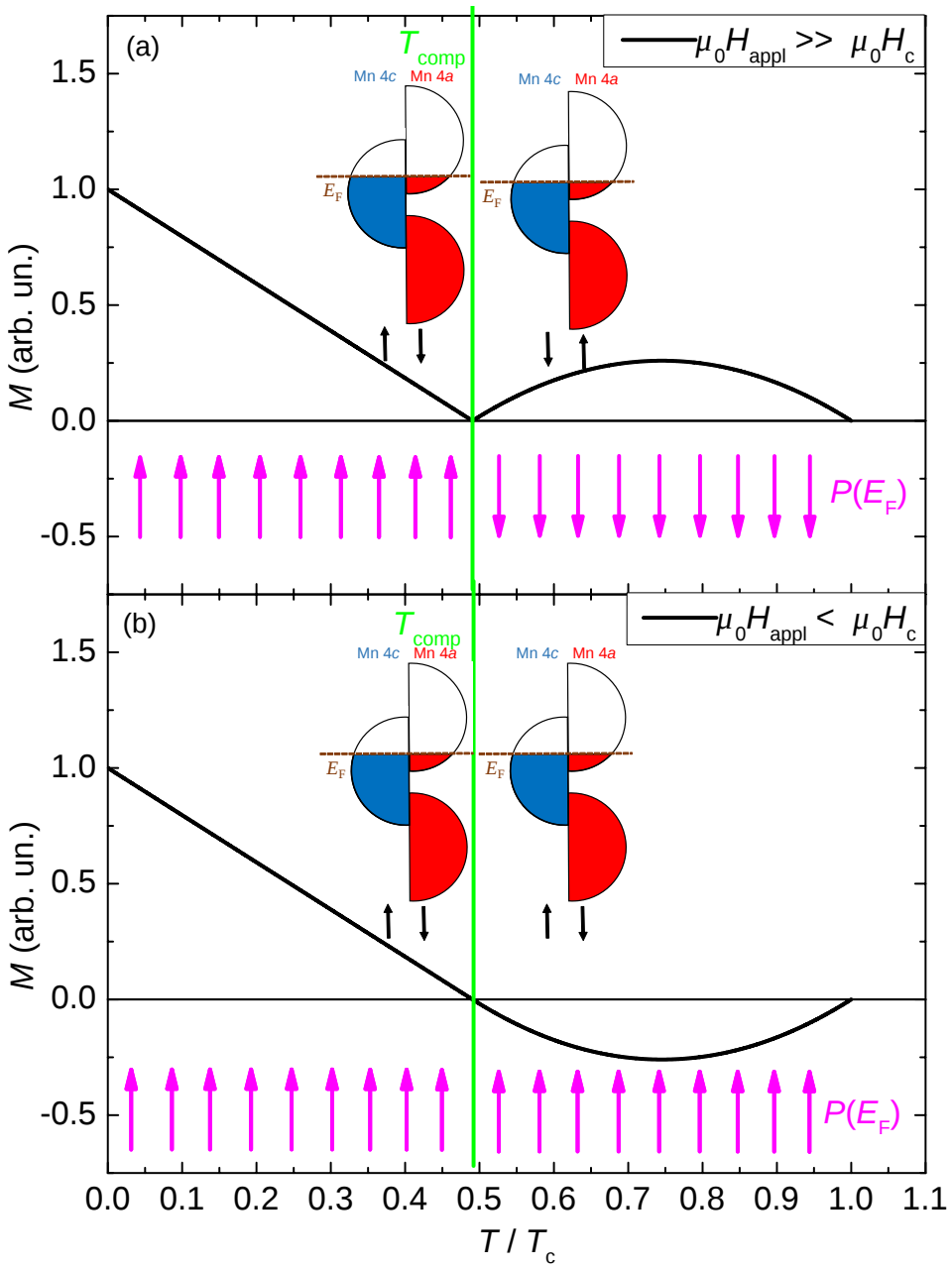

Figure 6.29: Schematic representation of the MRG DOS behaviour when it is passed through the compensation T_{comp}. Panel(a)-when the applied field is much higher than the MRG coercive field. Panel(b)-when the applied field is lower than the MRG coercive field. It is assumed that MRG is saturated at the lowest possible temperature in both cases. The black curves represent the MRG magnetization in arbitrary units. The magenta arrows indicate the Fermi level spin polarization orientation with respect to the applied field. The spin-split DOS represent the Mn sublattice magnetization behaviour. Do note that on panel (a) the spin orientations of the Mn 4*c* and Mn 4*a* flip their signs through T_{comp}. The Fermi level (E_F) is indicated with a brown horizontal dashed line. The compensation temperature is indicated with a green vertical line. The *x*-axis is normalized with respect to the Curie temperature T_C and it is assumed that $T_{comp} \approx 0.5T_C$.

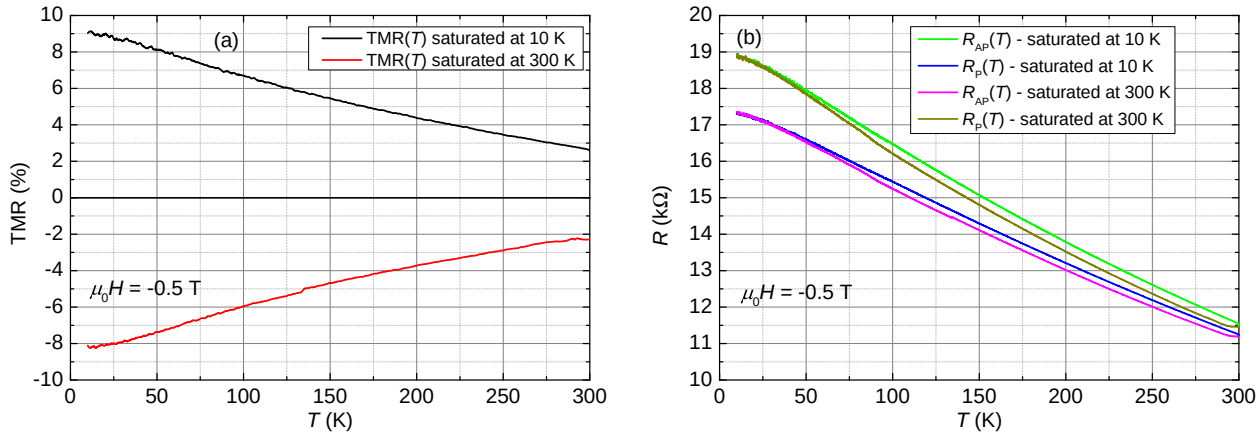

Figure 6.30: TMR and resistance scans as a function of temperature through compensation. Panel (a)-TMR(T) scan for saturation below T_{comp}(black curve) and above T_{comp}(red curve). Panel (b)-$R_{\mathrm{AP}}(T)$ and $R_{\mathrm{P}}(T)$ for saturation above and below compensation. That data is used for the curves on Panel (a). The applied magnetic field during each measurement is $\mu_0 H = -0.5\,\mathrm{T}$. The applied bias for all measurements is $U = 10\,\mathrm{mV}$.

talk between adjacent bits due to the low stray field from MRG.

6.7 Analysis of the barrier properties

The observation of high (40 %) TMR effect with MRG is very motivating. However, the MTJs exhibit characteristics which are not compatible with standard MTJs. There are two particularly interesting observations:

- The strong zero bias TMR decrease as a function of temperature
- TMR switching sign as a function of the applied bias

The strong zero-bias TMR reduction might be attributed to resonant scattering through impurities, multi-step tunneling, or magnon-excitation at the ferro-(ferri-)mangetic/MgO interfaces. The analysis will demonstrate that the most likely mechanism for the strong zero-bias TMR decrease is through resonant scattering. The TMR sign switching might be related to quantum-well formation in the Al dusting layer, modification of the electrode/barrier spins transmission probabilities, resonant scattering or density of states structure of the MRG electrode. The analysis will demonstrate that the sign change is probably related to the density of states structure of the MRG electrode. The analysis has been based mainly on the $R_{\mathrm{AP}}(T)$, $R_{\mathrm{P}}(T)$, TMR(T), and the differential spectroscopy of $\mathrm{d}I/\mathrm{d}V$, $\mathrm{d}^2I/\mathrm{d}V^2$.

First, the possibility of a multistep tunneling regime through the barrier is discussed. It has been proposed by Shang *et al.*[298] that the temperature decrease of the zero-bias TMR effect can be modelled successfully by the surface magnetization temperature dependence and the existence of multi-step tunneling process. A multi-step tunneling is based on a previous model of incoherent

tunneling through amorphous barrier by Glazman and Matveev [113]. The overall conductance of an MTJ depends on the elastic magneto-conductance and the spin-independent conductance G_{SI}:

$$G(\theta) = G_T(1 + P_1P_2\cos(\theta)) + G_{SI}, \tag{6.15}$$

where $\theta = 0°$ for parallel and $\theta = 180°$ for antiparallel state of an MTJ. The term G_T represents elastic direct tunneling and varies slightly with temperature due to the altered Fermi distribution broadening

$$G_T = G_0 CT/\sin(CT), \tag{6.16}$$

where G_0 is constant and $C = 1.387 \times 10^{-4} d/\sqrt{\phi}$: ϕ is the average barrier height in eV, and d is the barrier width in Å. For d (≈15 Å), and ϕ (≈ 1 eV), it can be shown that G_T is relatively temperature independent. From Eq. (6.15), it can be easily noticed that

$$G(0°) = G_T(1 + P_1P_2) + G_{SI} \tag{6.17}$$

$$G(180°) = G_T(1 - P_1P_2) + G_{SI} \tag{6.18}$$

$$G(0°) + G(180°) = 2G_{SI} + 2G_T \tag{6.19}$$

The spin-independent G_{SI} conductance is then equal to

$$G_{SI} = \langle G \rangle - G_T, \tag{6.20}$$

where $\langle G \rangle$ is the averaged conductance between the antiparallel and the parallel configurations. G_T is assumed to be a constant. $G_{SI} = 0.5(G(0°) + G(180°)) = 0.5(1/R_{AP} + 1/R_P)$ is assumed to be an average of the d.c. AP and P conductances*. The spin-independent conductance should follow a temperature power law

$$G_{SI} = aT^{\gamma} + b, \tag{6.21}$$

where γ determines the average number of tunneling steps: $\gamma(N) = N - [2/(N+1)]$. The G_{SI} is fitted for the sample annealed at 350 °C and it is extracted that the average number of tunneling steps at $U = 10$ mV is $N(10\,\text{mV}) = 2.2$, whereas the average number of tunneling steps at $U = -1$ V is $N(-1\,\text{V}) = 2.8$ (see Fig. (6.31)). It is obvious that the multistep tunneling is not the reason for our strong zero-bias TMR reduction because the higher number of tunneling steps at $U = -1$ V does not correlate with the significantly more temperature robust TMR(−1 V). Furthermore, this proves that the tunneling process in these MTJs can not be regarded as a pure incoherent tunneling.

*This assumption is made by Shang *et al.* [298]. Strictly speaking, G should be the differential conductance.

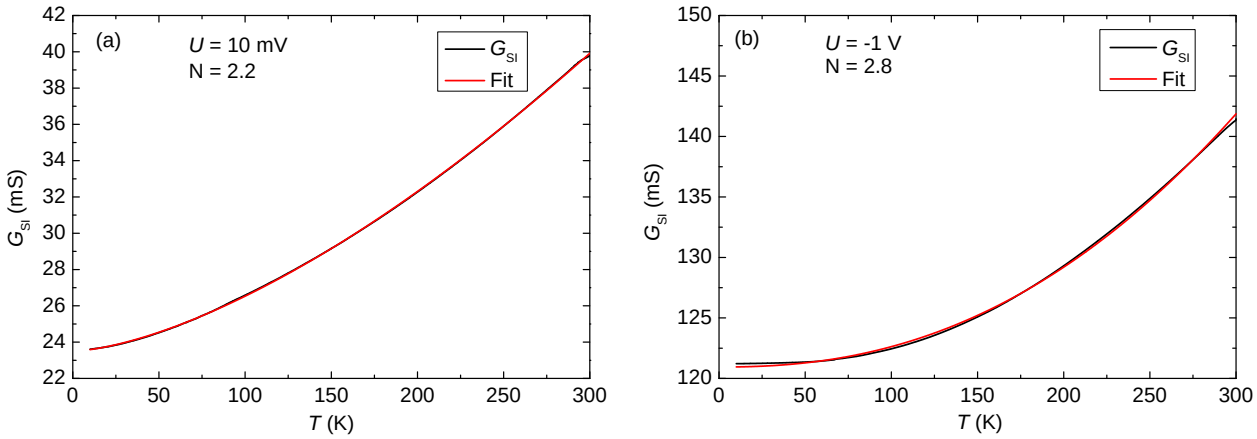

Figure 6.31: Spin independent conductance G_{SI} as a function of T for a chip annealed at 350 °C, the same as the one in Fig. (6.10) . Panel (a)-applied bias $U = 10\,\mathrm{mV}$ and extracted $\mathrm{N}(10\,\mathrm{mV}) = 2.2$, Panel (b)-applied bias $U = -1\,\mathrm{V}$ and extracted $\mathrm{N}(-1\,\mathrm{V}) = 2.8$.

There is, however, an interesting correlation which has been uncovered. If the data from Fig. (6.21) is fitted to the same model, then it is possible to extract the bias dependence of the average tunneling steps $N(U)$ (Fig. 6.32). The dependence demonstrates that the average tunneling steps at negative bias are more than the steps at positive bias. This is logical, since it is expected that the MRG-Al-MgO interface will be more disordered than the MgO-CoFe one. The focus moves to a more in-depth analysis of the 3D data plot from Fig. (6.21). First of all, the same analysis procedure for the spin-independent conductance, $G_{\mathrm{SI}}(T)$, is applied. This time, however, two separate definitions of the conductance are used: direct conductance ($G_{\mathrm{SI}}^{\mathrm{dc}}$) and differential conductance ($G_{\mathrm{SI}}^{\mathrm{ac}}$). Strictly speaking, Shang's model is an extension of an earlier model by Glazman and Matveev[113], where actually the differential conductance is analyzed. The two definitions should match close to zero-bias where the I-V characteristic are close to linear and, hence, the slope should be constant. However, Fig. (6.15) shows that these MTJs demonstrate pronounced cusp anomalies. $G_{\mathrm{SI}}^{\mathrm{ac}} \approx G_{\mathrm{SI}}^{\mathrm{dc}}$ for small applied biases, however, they differ significantly at higher bias as is apparent in Fig. (6.32), where the number of tunneling steps is practically equal for the two curves at zero bias. First of all, N_{ac} and N_{dc} are significantly higher at negative bias than they are at positive bias. That is somewhat expected because the MRG-Al-MgO interface is more disordered. Second, there are two broad peaks in the $N_{\mathrm{ac}}(U)$ dependence at $U \approx \pm 75\,\mathrm{mV}$. This is most probably related to low lying inelastic tunneling contribution (possibly due to resonant tunneling through diffused Mn atoms). It is important to point out that the TMR dip at $U = 0.3\,\mathrm{V}$ in Fig. (6.21) does not show up in the $N_{\mathrm{ac}}(U)$ dependence. $N_{\mathrm{ac}}(U)$ is derived from the spin-independent differential conductance, hence, the features should be more sensitive to non-magnetic excitation. This implies that the TMR(0.3 V) dip is attributable to spin scattering process. It is important to mention that the $N_{\mathrm{ac}}(U)$ dependence cannot be obtained by direct differentiation of the $N_{\mathrm{dc}}(U)$.

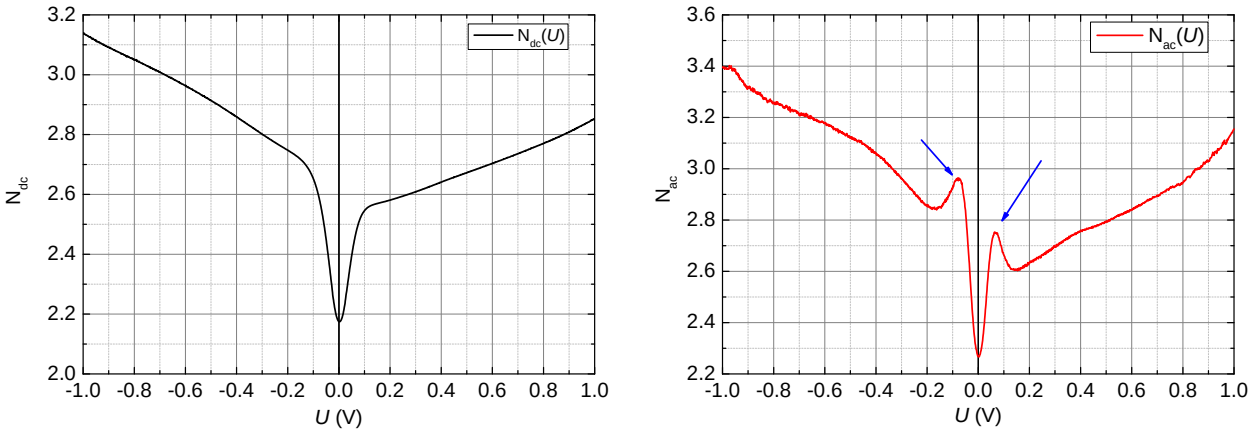

Figure 6.32: Number of tunneling steps determined for the chip annealed at 325 °C(see Fig. (6.21)). Panel (a)-determined from $G_{\mathrm{SI}}^{\mathrm{dc}}$, panel (b)-determined from $G_{\mathrm{SI}}^{\mathrm{ac}}$. Note the broad peaks at $\approx \pm 75$ mV indicated with blue arrows.

There is a famous critism expressed by Drewello *et al.* [79] about the applicability of this model for coherent tunneling. In this case, $R_{\mathrm{P}}(T)$ is constant and then the whole temperature evolution of the spin-independent conductance is determined by $R_{\mathrm{AP}}(T)$. The latter might lead to unrealistically high values of tunneling steps for coherent tunneling in high quality CoFe/MgO/CoFe MTJs. Therefore, this model is strictly not applicable to coherent tunneling. However, the $R_{\mathrm{P}}(T)$ of the MRG MTJs demonstrates that the transport in these devices is incoherent, hence, the presented model could be relevant in our case.

If it is started from the Eq. (6.15), the definitions of the tunneling magnetoresistance* and the parallel resistance are

$$\mathrm{TMR} = \frac{G_{\mathrm{P}} - G_{\mathrm{AP}}}{G_{\mathrm{P}}}, \tag{6.22}$$

$$= \frac{2P_1P_2}{1 + P_1P_2 + G_{\mathrm{SI}}/G_{\mathrm{T}}}, \tag{6.23}$$

$$\tag{6.24}$$

$$R_{\mathrm{P}} = \frac{1}{G_{\mathrm{T}}} \frac{1}{1 + P_1P_2 + G_{\mathrm{SI}}/G_{\mathrm{T}}}, \tag{6.25}$$

which demonstrates that in the presence of significant spin-independent conductance the TMR ratio may significantly deviate from the Julliere's prediction. Additionally, the difference $G(0°) - G(180°)$ is actually independent of the spin-indepedent conductance G_{SI}:

$$\Delta G = 2G_{\mathrm{T}}P_1P_2, \tag{6.26}$$

which means that it is more relevant to analyze the behaviour of $\Delta G(T)$ instead of the behaviour of $\mathrm{TMR}(T)$. The latter might be significantly affected by the spin-independent conductance. Fur-

*The pessimistic definition of the TMR is used here, as it is by Julliere, as well [154].

thermore, the spin polarization in standard ferromagnetic tunnel junctions is assumed to follow the surface magnetization temperature dependence (Bloch's law)

$$P(T) = P(0)(1 - \alpha T^{3/2}), \tag{6.27}$$

where the power $3/2$ is related to the dispersion of ferromagnetic spin-waves, and α is known as the surface exchange stiffness. The latter is significantly higher in thin films than it is in bulk samples. Of course, there is the problem that the same law cannot be applied to the MRG and, therefore, the following assumption is made:

$$P_{\mathrm{CoFe}}(T) = P_{\mathrm{CoFe}}(0)(1 - \alpha_{\mathrm{CoFe}} T^{3/2}), \tag{6.28}$$

$$P_{\mathrm{MG}}(T) = P_{\mathrm{MRG}}(0)(1 - \alpha_{\mathrm{MRG}} T^{\beta}), \tag{6.29}$$

where α_{CoFe}, α_{MRG} and β are kept as free fitting parameters. Attempt has been made to fit the temperature dependence of the TMR's with $\beta = 3/2$. The fitting procedure can not converge with such parameters.

$$\Delta G(T) = 2G_{\mathrm{T}}(T) P_{\mathrm{CoFe}}(T) P_{\mathrm{MRG}}(T) \tag{6.30}$$

$$\Delta G(10\,\mathrm{K}) = 2G_{\mathrm{T}}(10\,\mathrm{K}) P_{\mathrm{CoFe}}(10\,\mathrm{K}) P_{\mathrm{MRG}}(10\,\mathrm{K}) \tag{6.31}$$

The two equations above are normalized in order to get rid of the $P_{\mathrm{CoFe}}(0)$, $P_{\mathrm{MRG}}(0)$, and the G_{T} constants. Then

$$\frac{\Delta G(T)}{\Delta G(10\,\mathrm{K})} = \frac{1 - \alpha_{\mathrm{CoFe}} T^{3/2}}{1 - \alpha_{\mathrm{CoFe}} (10\,\mathrm{K})^{3/2}} \frac{1 - \alpha_{\mathrm{MRG}} T^{\beta}}{1 - \alpha_{\mathrm{MRG}} (10\,\mathrm{K})^{\beta}} \tag{6.32}$$

Using that expression, it is possible to fit the modified TMR dependence and extract the parameters for $U = 10\,\mathrm{mV}$ and $U = -1\,\mathrm{V}$ *.

The fitted parameters for the CoFe electrode do not match well with previously published data at low bias[298]. An unusual behaviour is that $\alpha_{\mathrm{CoFe}}(-1\,\mathrm{V}) < \alpha_{\mathrm{CoFe}}(10\,\mathrm{mV})$. This means that the CoFe spin polarization is more robust at high negative bias than it is at low bias, which is not true. There is no ground for comparison for the MRG parameters. The main point that must be mentioned is that β_{MRG} does not obey the behaviour of a ferromagnet. Also, if the extracted parameters from the fits are used, it can be calculated that actually the MRG spin polarization

*One might be tempted to leave the factor $3/2$ for the CoFe as a free fitting parameter as well. However, it can be shown that this is an ill-defined computational problem. The temperature dependences for the MRG and CoFe are functionally equivalent, then the fitting algorithm will converge to two nonphysical results, which depend on the initial conditions. If the initial guesses for the MRG and CoFe parameters are close, the fitting converges to an equal value for the two electrodes. This is obviously not possible. If the initial guesses for the parameters are significantly different, then the algorithm converges by "placing" the whole temperature dependence on one of the electrodes and leaving the other one essentially temperature independent. Obviously, this is not a realistic physical situation, too.

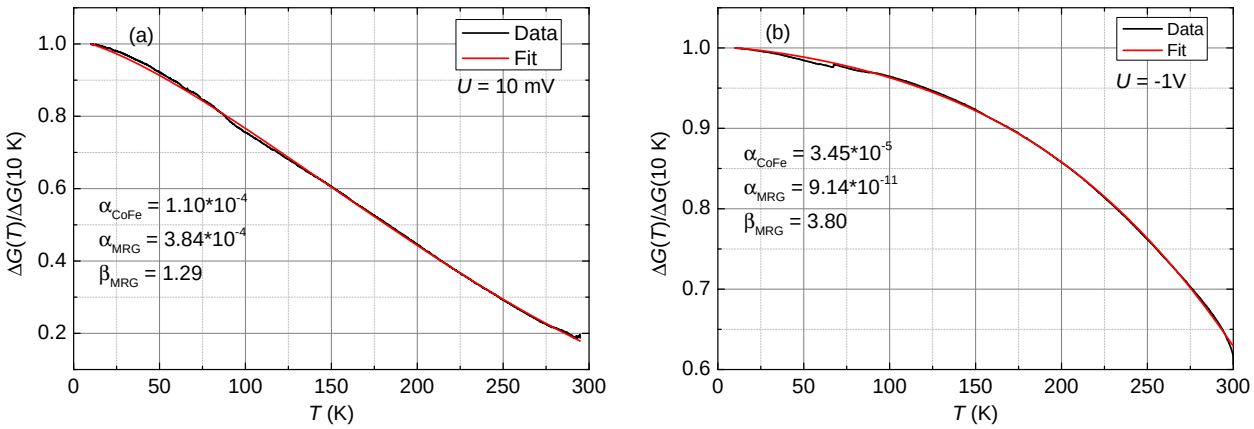

Figure 6.33: Fitting of the normalized TMR dependence following the SNJM model[298] along with the extracted parameters. Panel (a)-$U = 10\,\mathrm{mV}$, Panel (b)-$U = -1\,\mathrm{V}$.

decreases more with temperature. For instance, $P_{\mathrm{MRG}}(300\,\mathrm{K})/P_{\mathrm{MRG}}(10\,\mathrm{K}) \approx 0.76$ for $U = -1\,\mathrm{V}$ whereas the same ratio is ≈ 0.40 for $U = 10\,\mathrm{mV}$. However, this model can not distinguish between $P_{\mathrm{MRG}}(T)$ and barrier imperfections which might have similar detrimental effect. Another important criticism towards the model is that the extracted surface exchange stiffness parameters (α) cannot be determined by another independent technique. These values might only be compared to results by other authors. The question of the MRG spin polarization temperature dependence is an open one. Anomalous Hall Effect demonstrates constant spontaneous Hall angle in the range from 10 K to 400 K[340], however, this is not a direct proof. It has been shown by Betto *et al.*[27] that the moment on the Mn 4*c* has linear decrease with temperature, whereas the moment on the Mn 4*a* site stays relatively constant. Because the E_{F} is mainly determined by the Mn 4*c*, it is possible that the 4*c* sublattice magnetization decrease might affect the $P_{\mathrm{MRG}}(T)$. The latter dependence has not been investigated. In fact, the only technique which can investigate proper voltage and temperature dependence of spin polarization with good Fermi level resolution is SP-STM (see Chapter (1)).

Another possibility is that the low bias TMR decrease is due to magnon excitation at the ferromagnetic-insulator interface. The approach is developed by Zhang[409] and extended by Drewello[79]. The essence is fitting of the zero bias dip anomaly often observed in MTJs. The model assumes that there is magnon excitation cut-off energy E_{c}. The TMR(T, U) dependence at low temperature and low bias is

$$\mathrm{TMR}(0,U) = \mathrm{TMR}(0,0) - Q\frac{SeV}{E_{\mathrm{m}}}\frac{R_{\mathrm{AP}}(0,0)}{R_{\mathrm{P}}(0,0)}\left(\frac{1}{\zeta} - \zeta\right), \tag{6.33}$$

where TMR(0, 0), $R_{\mathrm{P}}(0,0)$, and $R_{\mathrm{AP}}(0,0)$ are TMR ratio, parallel and antiparallel resistance, respectively, at low temperature and low bias. The probability Q for a magnon to be involved in the tunneling process is left as a free fitting parameter. The spin parameter is S, and E_{m} is determined

by both the spin S and the Curie temperature T_C: $E_m = 3k_B T_C/(S+1)$. * It can be seen in Eq. (6.33) that the magnon excitation probability Q is scaled by S/E_m. Hence, these parameters do not affect the temperature dependence but only the value of Q. Furthermore, it is beneficial to use the whole configuration QS/E_m as a free fitting parameter. The parameter $\zeta = 2\rho_{AP}\rho_P/(\rho_{AP}^2+\rho_P^2)$ is the ratio of the products of density of states in the parallel and antiparallel state. It can assumed that this is equal to the ratio of the current densities or of the resistances $\zeta = \frac{j_{AP}(0,0)}{j_P(0,0)} = \frac{R_P(0,0)}{R_{AP}(0,0)}$, therefore, it is easy to notice that in a low bias approximation the TMR(0, U) is essentially a linear function of the applied bias:

$$\mathrm{TMR}(0,U) = \mathrm{TMR}(0,0) - Q\frac{SeU}{E_m}\frac{R_{AP}(0,0)}{R_P(0,0)}\left(\frac{R_{AP}(0,0)}{R_P(0,0)} - \frac{R_P(0,0)}{R_{AP}(0,0)}\right), \tag{6.34}$$

$$\mathrm{TMR}(0,U) = \mathrm{TMR}(0,0) - Q\frac{SeU}{E_m}\frac{R_{AP}(0,0)-R_P(0,0)}{R_P(0,0)}\frac{R_{AP}(0,0)+R_P(0,0)}{R_P(0,0)}, \tag{6.35}$$

$$\mathrm{TMR}(0,U) = \mathrm{TMR}(0,0)\left[1 - Q\frac{SeU}{E_m}\frac{R_{AP}(0,0)+R_P(0,0)}{R_P(0,0)}\right]. \tag{6.36}$$

The low bias temperature dependence of the two resistance states can then be presented in the form

$$R_P(T,0) = R_P(0,0)\left[1 + Q\zeta\frac{2S}{E_m}k_B T\ln\left(\frac{k_B T}{E_c}\right)\right]^{-1}, \tag{6.37}$$

$$R_{AP}(T,0) = R_{AP}(0,0)\left[1 + Q\frac{1}{\zeta}\frac{2S}{E_m}k_B T\ln\left(\frac{k_B T}{E_c}\right)\right]^{-1}. \tag{6.38}$$

The combination of parameters QS/E_m can be extracted from the TMR$(0,U)$ and used to fit the temperature scans $R_P(T,0)$ and $R_{AP}(T,0)$. Alternatively, it might be left as a fitting parameter

$$R_\alpha = R_\alpha(0,0)\left[1 + \beta_\alpha\ln\left(\frac{k_B T}{E_c}\right)\right]^{-1}, \tag{6.39}$$

where $\alpha = (P,AP)$ refers to parallel and antiparallel configuration. Furthermore, $\beta_P = 2SQ\zeta/E_m$ and $\beta_{AP} = 2SQ/(E_m\zeta)$. Then, each dependence R_α has two fitting parameters: β_α and E_c.

An analysis by Schleicher *et al.*[291] identifies particular kinds of oxygen defects in the MgO barrier by I-V characteristics and their temperature dependence. Oxygen defects and off-stoichiometry is expected in the MgO barrier of our devices because the electronegativity of the Al dusting layer is higher than the electronegativity of the Mg. The $I(V)$ characteristics are compared along the temperature axis. The essence of the analysis is to compare adjacent $I(V)$ curve at two close tem-

*The model is usually applied to MTJs with the same ferromagnetic electrodes. This is not our case. If MRG is assumed then $S = 5/2$ and $T_C = 550\,\mathrm{K}$.

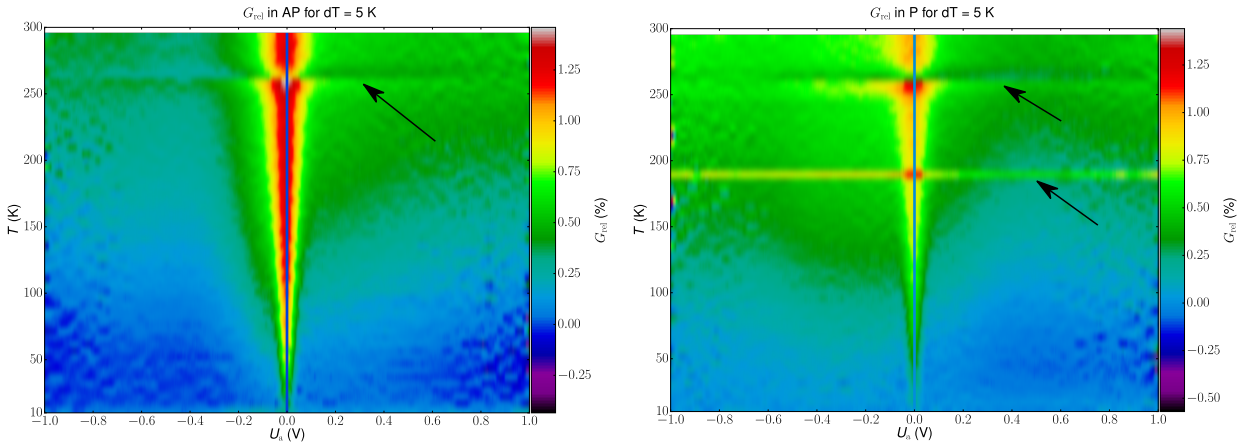

(a) G_{rel}^{AP} (b) G_{rel}^{P}

Figure 6.34: G_{rel} in the antiparallel (a) and parallel (b) configuration, respectively. Features, which are due to noise in the data are indicated with black arrows.

peratures in order to uncover thermally excited defects. Their plot presents I_{rel}:

$$I_{rel} = \frac{I(T+\Delta T)}{I(T)} - 1, \tag{6.40}$$

where $\Delta T = 5\,\mathrm{K}$ in our measurements, and $I(T)$ is an I-V for each particular temperature. In our analysis, both the direct current relation I_{rel} and the differential conductance relation G_{rel} have been calculated*. Only the data for the G_{rel} for the antiparallel state (panel (a)) and the parallel state (panel (b)) is presented in Fig. (6.34), because the two characteristics (G_{rel} and I_{rel}) exhibit essentially the same temperature behaviour.

No features similar to the ones reported by Schleicher *et al.*[291] are present. This does not necessarily mean that the barrier has no oxygen defects. It might imply that defects of other nature are more prevalent than oxygen defects.

Another approach proposed by Rottländer *et al.*[281] aims to extract the barrier height independently from the barrier thickness. In essence, the derivative of the logarithmic conductance is plotted as a function of the voltage:

$$g(V) = \frac{\mathrm{d}\ln[I(V)/V]}{\mathrm{d}V}. \tag{6.41}$$

There is approach which is similar but it traces the normalized difference between the $I(V)$ at a particular T and the $I(V)$ curve at the lowest possible possible T(10 K in our case)

$$\hat{I}(V) = \frac{I(V,T) - I(V,T_{\mathrm{lowest}})}{I(V,T_{\mathrm{lowest}})}, \tag{6.42}$$

*The differential conductance relative temperature decrease is defined in the same fashion $G_{rel} = \frac{G(T+\Delta T)}{G(T)} - 1$.

secondary broad cusps should be distinguished in the characteristic. It can be checked from this analysis on our junctions that no such features are observed up to $U = \pm 1\,\mathrm{V}$. The latter implies that the barrier height in the MTJs is higher.

Another approach proposed by Schleicher *et al.* [291] aims to determine the barrier height by observing the absolute and relative TMR decrease. Then, the plot for the absolute TMR thermal decrease using the formula:

$$\mathrm{TMR}_{\mathrm{abs}}(U,T) = \left(\frac{\mathrm{TMR}(U,T)}{\mathrm{TMR}(U,T_{\mathrm{ref}})} - 1 \right), \tag{6.43}$$

where the T_{ref} is the reference temperature which in our case is $T_{\mathrm{ref}} = 10\,\mathrm{K}$. Unfortunately, the full TMR decrease cannot be analyzed because of the TMR sign change. The latter leads to singularities when ratio with a TMR close to zero value is calculated. The data for $U > -0.1\,\mathrm{V}$ is, therefore, analyzed here. Significant drop in the $\mathrm{TMR}_{\mathrm{abs}}(U,T)$ is used as an indication for the barrier height. Furthermore, this potentially gives an opportunity to study its temperature dependence of the barrier height. The absolute TMR decrease graph is presented in Fig. 6.35 . No dip feature is observed in our voltage range ($U < 1\,\mathrm{V}$). The graph demonstrates that the most pronounced TMR decrease happens at close to zero bias in marked contrast with high quality MgO MTJs [291]. On the other

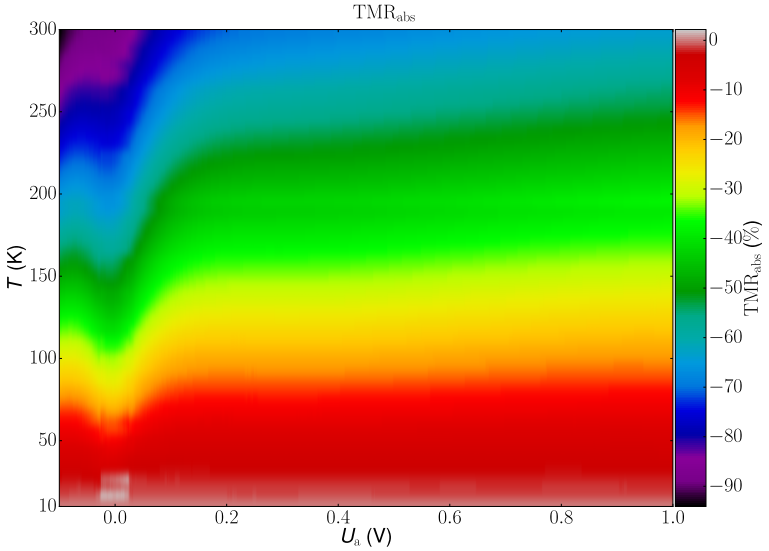

Figure 6.35: Absolute TMR decrease of the MTJ presented on Fig. (6.21). The bias range is $-0.1\,\mathrm{V} < U < 1\,\mathrm{V}$.

hand, the relative TMR decrease is:

$$\mathrm{TMR}_{\mathrm{rel}}(U,T) = \left(\frac{\mathrm{TMR}(U,T+\Delta T)}{\mathrm{TMR}(U,T)} - 1 \right). \tag{6.44}$$

Graphs are presented for $\mathrm{d}T = 5\,\mathrm{K}$ and $\mathrm{d}T = 10\,\mathrm{K}$ in Fig. (6.36). The higher $\mathrm{d}T$ usually results in more distinguishable features, however, this is not the case in these MTJs. Both plots have no

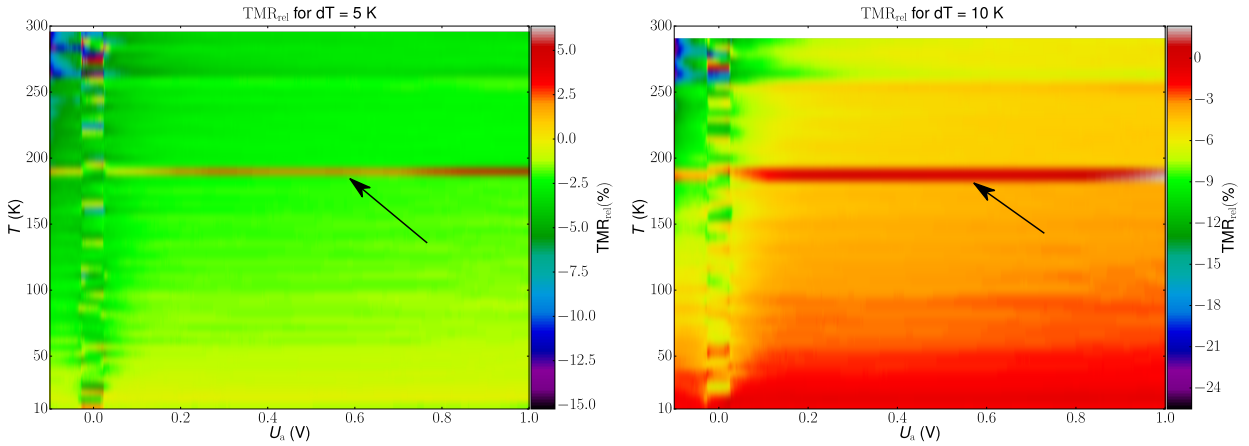

(a) Relative TMR decrease for dT = 5 K

(b) Relative TMR decrease for dT = 10 K

Figure 6.36: Relative TMR decrease for the MTJ presented on Fig. (6.21). Two features, which are caused by noise, are indicated with black arrows.

obvious dip features in contrast to the ones observed in [291]. The latter two analyses confirm that our MTJs does not exhibit magnetrotransport properties commensurate with other high quality MgO-based MTJs. Finally, the same data set is used to calculate the asymmetry in the resistance in Fig. 6.37. The antiparallel and the parallel resistance asymmetries are defined as follows: $\tilde{R}_{\mathrm{AP}}(V) = (R_{\mathrm{AP}}(V) - R_{\mathrm{AP}}(-V)) \times 100/R_{\mathrm{AP}}(V)$ and $\tilde{R}_{\mathrm{P}}(V) = (R_{\mathrm{P}}(V) - R_{\mathrm{P}}(-V)) \times 100/R_{\mathrm{P}}(V)$. Important observation in the $\tilde{R}_{\mathrm{AP}}$ is the asymmetry decrease around $U = 70\,\mathrm{mV}$ at low temperature which gets smeared with temperature and is practically absent above 200 K. This implies that the low lying localized resonant levels discussed before (Fig. (6.43)) in the barrier have different leak rates towards the two electrodes. The latter confirms the assumption which has been made earlier. The high bias ($U = 1\,\mathrm{V}$) $\tilde{R}_{\mathrm{AP}}$ has high value and of $\approx 20\,\%$ and it is almost temperature independent. The parallel resistance state has its highest asymmetry at intermediate voltages 400 mV. This peak asymmetry is temperature smeared. Even more peculiar is the temperature dependence of $\tilde{R}_{\mathrm{P}}$ at $U = 1\,\mathrm{V}$. The asymmetry is first negative at low temperatures ($T < 100\,\mathrm{K}$) and then positive at $T > 200\,\mathrm{K}$. This is possibly related to disordered very thin oxide at one of the interfaces which traps charges*. It is more probable to be at the MRG-Al-MgO interface. Inelastic electron tunneling spectroscopy (IETS) is often used in order to find evidence for defects or particular excitations. For instance, CoFe magnon and MgO phonon excitations could be uncovered by IETS. The technique has also been used in investigation of semiconducting structures, superconductors and tunnel junctions with organic molecules. The second derivative, $\mathrm{d}^2I/\mathrm{d}V^2$, has to be obtained. There are, apparently, three approaches: double differential of a raw $I(V)$ data (the worst approach), single differentiation of a $\mathrm{d}I/\mathrm{d}V$ data obtained by LIA(acceptable and the most widely used approach), and direct second derivative by detection of the second harmonic signal shifted

*The asymmetry effect is not very high, anyway.

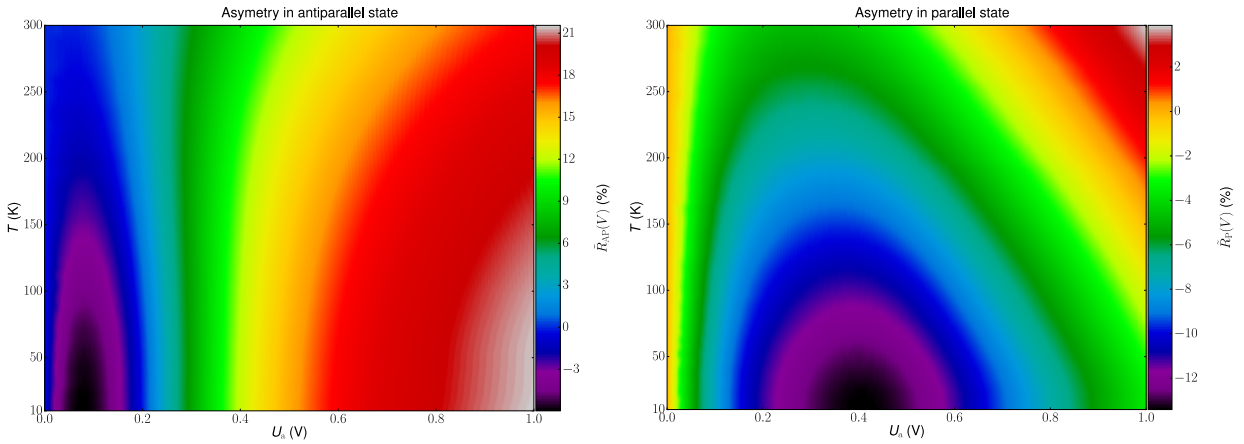

(a) $\tilde{R}_{AP}$ (b) $\tilde{R}_P$

Figure 6.37: Resistance asymmetry $\tilde{R}$ for the cases of antiparallel (panel (a)) and parallel state (panel (b)). The data is obtained on a chip annealed at 325 °C (see Fig. (6.21)).

by π phase with respect to the reference signal (the best, however, rarely used approach). Correlation between resonant features observed in tunneling spectroscopy and transmission electron microscopy of the investigated devices has been given by Teixeira *et al.*[337]. The numerical differentiation followed by smoothing of the data often produces spurious "oscillations" which might be wrongly attributed to resonant scattering. Here, the first derivative is taken from the LIA measurements in Fig. (6.15) and it is numerically differentiated to obtain the IETS at $T = 2\,\mathrm{K}$ (see Fig. (6.38)). First of all, there are pronounced low bias spikes both in the parallel and antiparal-

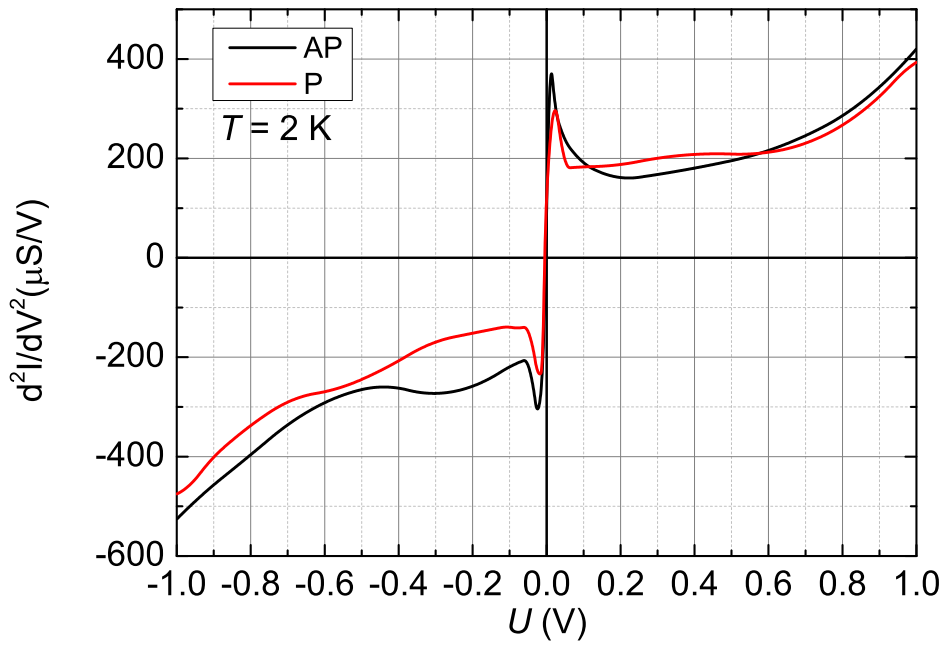

Figure 6.38: Inelastic electron tunneling spectroscopy measured in antiparallel (black) and parallel state (red). The data is measure at low temperature ($T = 2\,\mathrm{K}$) on a chip annealed at 350 °C.

lel curves and these are attributed usually to interface magnon excitations[409, 239] or magnetic impurities[368]. The positive bias demonstrates significant difference between the AP and P curves for $0.1\,\mathrm{V} < U <$
$0.6\,\mathrm{V}$, this correlates roughly with the plateau on the TMR(U) curves. This feature is attributed to spin-flip scattering by paramagnetic impurities in the barrier. Similar, but more pronounced, feature is observed at negative bias ($-0.5\,\mathrm{V} < U < -0.05\,\mathrm{V}$) and corresponds roughly to the high slope on the TMR(U) curve where the TMR switches sign. Very prominent is the lack of two important peaks which are usually observed in MTJs with MgO and CoFe: the MgO phonon peak and the CoFe magnon peak. The MgO phonon peak is usually observed at $U \approx 80\,\mathrm{mV}$[80, 339]. Its lack is an indication that the MgO barrier of our tunnel junctions is not well-crystallized or is poly-crystalline which isis probably due to Mn diffusion. The CoFe bulk magnon peak should be observed as secondary structure in the AP curve [18] but is not present as well. This implies that the MgO/CoFe interface is relatively rough and the CoFe electrode has not crystallized properly too.

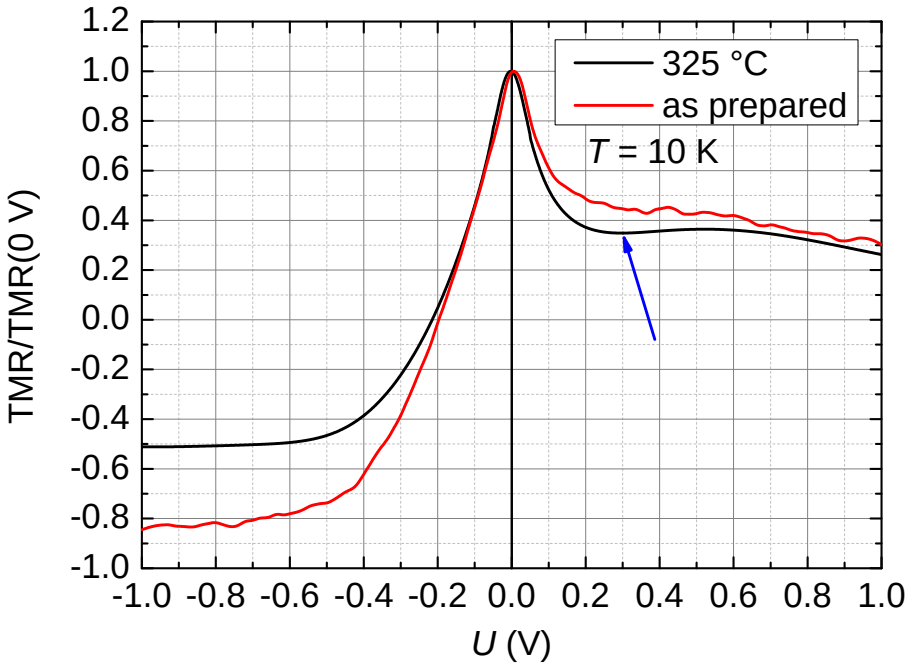

Figure 6.39: TMR(U) behaviour comparison between an as-prepared and an annealed at 325 °C MTJ. The measurements are performed at 10 K and each curve is normalized to the maximum TMR at low bias. Blue arrow indicates the voltage range where the contribution from resonant states is most pronounced. The MTJs are physically from the same chip but treated differently.

The MTJ chips annealed at different temperatures demonstrate essentially the same temperature decrease of key values like $R_\mathrm{P}(T)$ and TMR(T) (see Fig. (6.20)). The TMR(U) behaviour of the same sample in the non-annealed and the annealed at 325 °C state is presented now in Fig. (6.39). The measurements are performed at 10 K and the two curves are normalized to their respective

zero bias TMR values. The two curves have the same quantitative behaviour. However, the as prepared MTJ demonstrates smaller TMR decrease for positive bias and it has greater relative TMR at high negative bias than the annealed chip. Pronounced difference in the line-shape of the two curves is obvious in the bias range from 0.2 V to 0.4 V. The as prepared MTJ data shows gradual decrease with no local minimum. The annealed device exhibits sharper TMR drop, then local dip and finally a small plateau and almost a return towards the line shape of the the non-annealed device. This behaviour is ascribed to Mn diffusion during the annealing process. The diffused Mn atoms create resonant scattering states inside the MgO barrier. The resonant scattering states lead to stronger spin-flip scattering and thus the TMR(U) decreases and reaches a local minimum when the contribution of tunneling through these defects states is the highest. For higher bias, the MRG Fermi level is raised above the resonant states and the TMR increases slightly. This comparison between the TMR(U) in an annealed and a non-annealed sample gives a possible explanation why TMR(T) and $R_P(T)$ have relatively constant behaviour for different annealing conditions. The annealing improves the crystallinity of the barrier and the electrodes but leads to creation of more resonant scattering states located just above the Fermi level of the MgO. Therefore, the beneficial and the detrimental effects are finely balanced.

A sample without insertion layer has been investigated in order to understand whether the Al dusting layer forms quantum well states which can alter significantly the TMR(U) behaviour (see Fig. (6.22)). The investigated MTJ chips have bottom electrode with the approximate composition $Mn_2Ru_{0.6}Ga$ which has compensation temperature $T_{comp} = 100\,K$. The full TMR-applied field curves for $U = 10\,mV$ are presented in Fig. (6.40). As before, the diverging coercive field of the MRG at 100 K is the indication for the compensation. The TMR has positive sign below T_{comp} and negative sign above T_{comp}. The MRG electrode is significantly oxidized and this is apparent from the order of magnitude lower TMR values with respect to the values obtained with Mn_2Ru_1Ga/Al/MgO (see Fig. 6.10). The highest measured TMR is 4.5 % at 10 K. The high-field background demonstrates positive magnetoresistance in contrast with what is expected for not-perfectly aligned anisotropy axes of the MRG and the CoFe electrodes (see Fig. 6.27). The TMR(U) behaviour is the most important reason for investigating this sample. The TMR changes sign again for negative bias, i.e. electron tunneling towards the MRG. Quantum well states in the previous MTJs (Fig. (6.10)) can be ruled out as an explanation because the same qualitative TMR(U) behaviour is observed here without Al insertion here. Furthermore, different spin-dependent tunneling probabilities due to chemical bonding at the MRG-MgO interface is not a possible explanation for the TMR(U) dependence as well (see Fig. (6.23)). Additionally, the spin-split density of states inversion is clearly demonstrated here too. The sample has been saturated in $\mu_0 H = 14\,T$ at 200 K (above compensation), set in anti-parallel state and then cooled down through T_{comp} in small applied field. Then, the same procedure has been applied but this time the sample has been set in

parallel state at 200 K. The black curve on Fig. (6.40 (b)) has been calculated in this way. The curves obtained by saturation above and below compensation are essentially symmetric with respect to the zero TMR line. This is a strong indication that the TMR sign switch is due to the energy dependence of the MRG spin-split density of states.

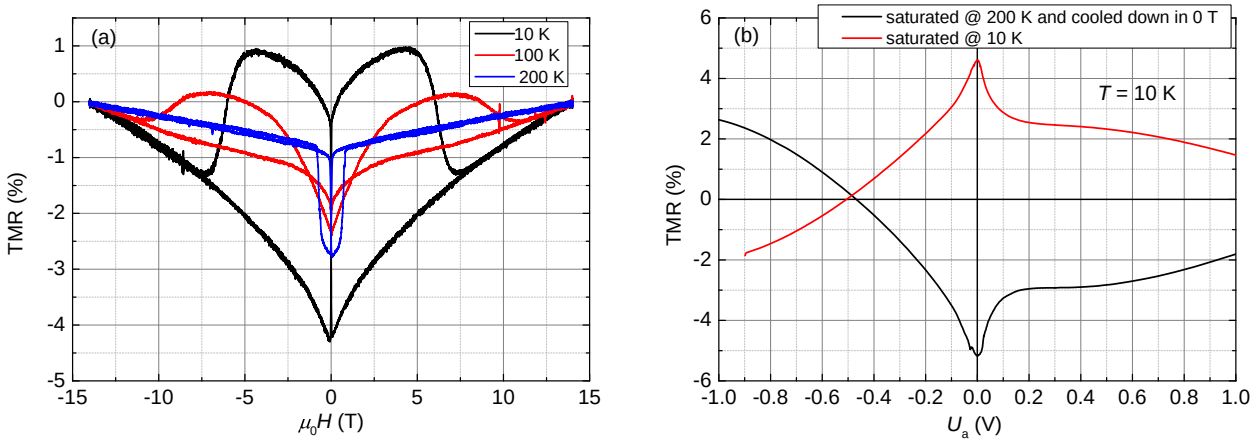

Figure 6.40: TMR measurements on MTJs with $Mn_2Ru_{0.6}Ga$ and no Al insertion layer. The compensation temperature is approximately 100 K. Panel (a)-TMR($\mu_0 H$) scans at temperatures: 10 K, 100 K, and 200 K and applied bias $U = 10$ mV. Panel(b)-TMR(U) dependences measured at 10 K for an MTJ set at 10 K-red curve and 200 K-black curve (above compensation).

It is instructive to comment on the unusual behaviour of the high-field background. When the magnetic field increases, this should lead to better alignment of the magnetization axes of the MRG and CoFe electrode and, therefore, the resistance must decrease. On the contrary, this sample with no Al insertion layer demonstrates the opposite behaviour and the resistance of the MTJ increases for higher applied magnetic field. The reason for this observation is tilted anisotropy axes of the MRG and CoFe electrodes away from the nominal z-axis of the MTJ (or (001) crystallographic orientation). The anisotropy axes are tilted off the nominal direction most probably due to interface roughness ("orange-peel" barrier). The MRG anisotropy depends critically on the tetragonal distortion while the ultrathin CoFe perpendicular magnetic anisotropy depends on the hybridization at the CoFe-MgO interface. Therefore, it is justified to assume that high surface roughness would lead to off vertical easy axes for the magnetization of the two electrodes. The schematic of the two anisotropy axes is presented in Fig. (6.41) for the case of $T = 10$ K. For zero magnetic field, the two electrodes anisotropy axes are aligned but tilted. As the magnetic field is increased, the magnetization of the CoFe will tend to align with the direction of the applied magnetic field. The latter leads to opening of an angle between the magnetization of the MRG and CoFe electrode and, therefore, the resistance gets higher following the Slonczewski's rule (see Eq. (1.43)). The MRG magnetization is less susceptible to rotation by the field due to its anisotropy field. The high-field background is less pronounced as the temperature is increased (see the three different temperatures in Fig. (6.40)). The interface MRG perpendicular magnetic anisotropy is perhaps strongly tem-

perature dependent in these MTJs and because of that the MRG magnetization gets more aligned with the applied field direction for higher temperature. In the latter case, the cone opening between the MRG and CoFe magnetizations is smaller and, hence, the high-field magnetoresistance is less pronounced.

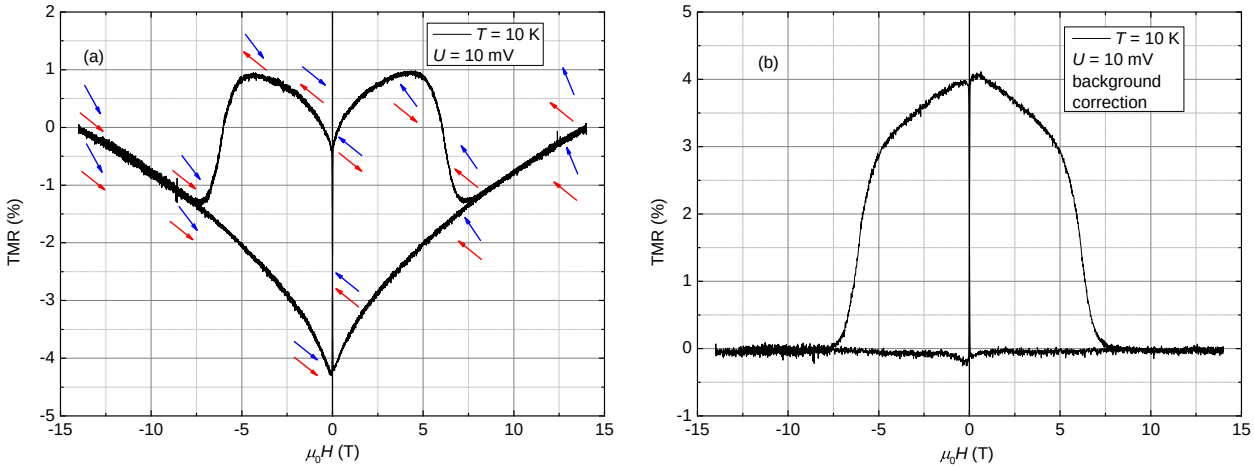

Figure 6.41: Panel (a) - TMR loop for an MTJ without Al insertion layer at $T = 10\,\mathrm{K}$. The mutual MRG and CoFe magnetization orientations are indicated with arrows: blue arrows for CoFe, red arrows for MRG. The TMR scan is performed in the following direction: $14\,\mathrm{T} \rightarrow 0\,\mathrm{T} \rightarrow -14\,\mathrm{T} \rightarrow 0\,\mathrm{T} \rightarrow 14\,\mathrm{T}$. When the magnetization arrows are above the graph, this corresponds to the initial field scan: $14\,\mathrm{T} \rightarrow -14\,\mathrm{T}$. When the magnetization arrows are below the graph, this corresponds to the field scan in the opposite direction: $-14\,\mathrm{T} \rightarrow 14\,\mathrm{T}$. Panel (b) - the same TMR loop from panel (a) after background correction.

A sample which has been prepared in conditions similar to the one on Sec. (6.4) will be discussed now in order to emphasize even further the effect of resonant tunneling contribution. The device structure is essentially the same as the one in Fig. (6.10). The only difference is that the Al insertion layer has been deposited by RF sputtering and then post-annealed *in-situ* whereas the same layer has bee deposited by DC sputtering in the previous stack. It has been investigated afterwards that the Al layer is flatter when it is deposited by RF sputtering, however, the uniformity is compromised due to the post-annealing. The lack of uniformity creates areas where the MRG electrode is in direct contact with the tunnel barrier and, hence, Mn migration is more pronounced. First of all, the TMR(H) scans are presented in Fig. (6.42) (a) for applied bias $U = -1\,\mathrm{V}$. It is apparent that the coercivity of the MRG increases slightly with increasing temperature which is a proof that the $T_{\mathrm{comp}} > 300\,\mathrm{K}$ which confirms that the bottom electrode is close to the Mn_2Ru_1Ga composition. The TMR is negative for this bias as before. More important is the unusual behaviour of the TMR(U) curves at 10 K and 300 K. The zero-bias TMR at 10 K in these junctions is significantly lower than the TMR observed before which indicates that the defect states in the barrier have higher concentration. The low temperature TMR(U) behaviour demonstrates dual crossing of the zero TMR line this time-both at positive and negative voltages. Such behaviour is not expected at positive bias because the spin-split density of states in CoFe are well-studied and no sign inversion

is expected, because the CoFe spin polarization has constant sign (see Fig. (6.4)). Therefore, the sign change should be attributed to the tunneling probabilities through the barrier. The reason for this behaviour is that the resonant spin-flip scattering contribution in these MTJs is far stronger than in the previous ones (see Fig. (6.11)). In this case, the spin-flip scattering rate is so high that it reverses the TMR sign. Furthermore, the TMR at the positive bias branch first decreases sharply and then increases. This implies that the resonant scattering levels in the MgO barrier are mainly located around 100 meV-300 meV above the Fermi level of the MgO barrier. For applied bias $U > 200$ mV, the negative TMR starts decreasing. In other words, the contribution from the spin-flip scattering is lowered as the Fermi level of the MRG electrode is raised significantly above the impurity levels. For high positive bias the TMR approaches its usual positive value, because there is higher and higher contribution from electrons which tunnel through part of the MgO bandgap which is less affected by impurity levels. The TMR(U) curve at 300 K demonstrates sharp collapse of the zero bias TMR and the TMR close to the Fermi level becomes negative at high temperature. The low bias TMR values have been confirmed by full TMR(H) scans. They could be understood if there are resonant states very close to the Fermi level of the MgO barrier. As the temperature is raised, the thermal excitation and Fermi level broadening are sufficient so that more electrons tunnel through the resonant states and their spin polarization is reversed. The distribution of the resonant states in the MgO bandgap is probably as follows: there are states just above the Fermi level but their contribution towards the spin-flip scattering is not the highest, the highest contribution comes from states which are located between 100 meV and 300 meV, and it looks like there is very little distribution of spin-flip states above 300 meV. Unfortunately, the distribution of resonant states below the MgO Fermi level cannot be investigated due to the fact the tunneling process happens above the E_F.

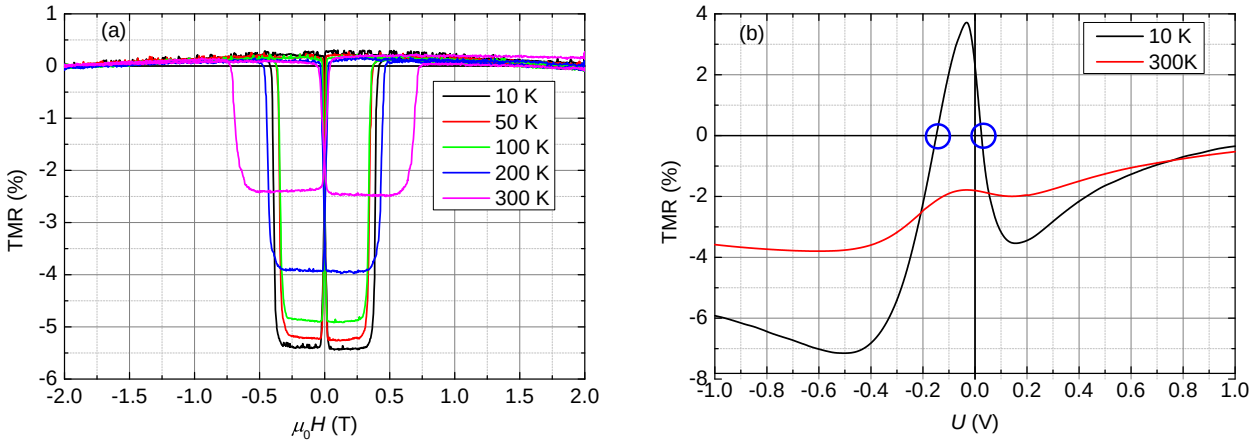

Figure 6.42: Example of the detrimental effects of resonant tunneling in MTJs with Mn_2Ru_1Ga bottom electrode. The MTJ is annealed in the magnetic annealing furnace at 325 °C. Panel (a)-TMR(H) curves measured at applied bias $U = -1$ V and at different different temperatures. Panel (b)-TMR(U) of the same junction obtained at 10 K and 300 K. Note that the TMR is negative for positive bias this time in contrast with Fig. (6.11). The points where the TMR(U) curve at 10 K switches sign are indicated with blue circles.

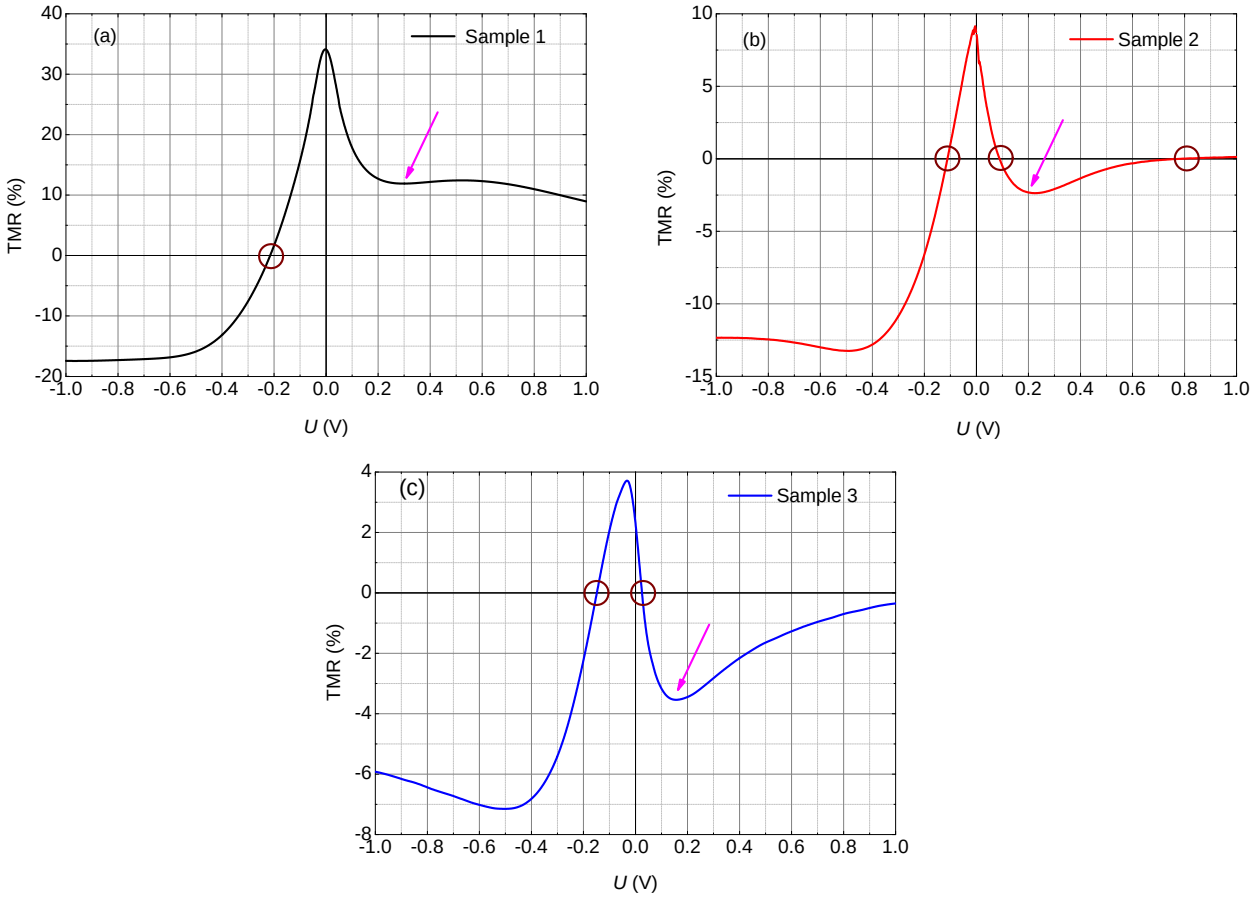

Figure 6.43: Comparison of the resonant tunneling contribution between three samples prepared under similar conditions. All three MTJ chips are annealed at 325 °C. The temperature is 10 K for each measurement. Panel (a)-the sample with the highest TMR and best control of the Mn diffusion, this is sample presented completely in Fig. (6.21). Panel (b)-sample with intermediate quality and more pronounced resonant scattering contribution. Note that the TMR crosses twice the zero line for positive bias. Panel (c)-sample with the most apparent resonant scattering contribution. The TMR crosses zero for positive bias and does not changes sign back up to $U = 1$ V. Magenta arrows indicate on each graph the most obvious feature from the resonant spin-flip scattering contribution. The points, where the TMR changes sign, are indicated with brown circles. The resonant scattering contribution gradually increases from panel (a) through panel (c).

Three TMR(U) curves measured at 10 K on three different MTJ samples are presented in Fig. (6.43). They demonstrate quantitatively the same behaviour, however, it is emphasized that the contribution from the resonant tunneling is different for the three samples. The higher contribution of defect states result in zero-bias TMR decrease and in change of the TMR sign at positive bias. The most obvious resonant states population is around 200 mV. As the spin-flip scattering increases around $U = 200$ mV, the TMR drops sharper around this bias. The best Mn migration control is achieved in Fig. (6.43 (a)), because the resonant states appear only as a slight dip. Medium quality MTJ is presented in Fig. (6.43 (b)), where stronger spin-flip scattering results in TMR double sign change at positive bias. First, the TMR crosses positive $\rightarrow$ negative at $U \approx 100$ mV, and then it crosses again this time negative $\rightarrow$ positive at $U \approx 700$ mV. Finally, the worst quality is presented in Fig. (6.43 (c)), it has the lowest low bias TMR and the TMR crosses from positive $\rightarrow$ negative

sign sharply at around 20 mV and the TMR stays negative up to $U = 1\,\mathrm{V}$, although there is a tendency to switch back to the expected positive values at $U > 1\,\mathrm{V}$. Figuratively speaking, one might imagine that the resonant scattering is a strong force which distorts the overall TMR(U) curve from its usual quasi-quadratic form (Fig. (6.4)) towards the profiles in Fig. (6.43). This distortion affects significantly the low bias transport as well. Therefore, the presently achieved TMR maximum values are not limited by the spin polarization of the MRG but by the quality of the MTJs (in particular the quality of the barrier).

After the comparison between the TMR(U) behaviour in the non-annealed and the annealed sample and the discussion of the three similar samples, a simple schematic picture of the resonant scattering levels in our MTJs can be envisioned. It is reasonable to assume that that in these MRG-based MTJs, the resonant tunneling does not happen through discrete energy levels in the MgO barrier but rather through small bands. Discrete level resonant scattering should lead to very sharp features in the differential spectroscopy at low temperature, however, this is not the case. Furthermore, the depth and the profile of the TMR dip observed at $U \approx 0.25\,\mathrm{V}$ in Fig. (6.21) does not change significantly from 10 K to 300 K. The latter means that the thermal excitation energy has little effect on the resonant scattering contribution. This can be the case if bands with energy width bigger than the thermal excitation energy are formed.

6.8 Conclusion and outlook

The observation of high TMR ratios of up to 40 % (at $T = 10\,\mathrm{K}$) with very low magnetization Mn_2Ru_1Ga is a strong indication that high spin polarization can be achieved irrespective of the magnetization value. Furthermore, the demonstration of appreciable TMR at the very compensation temperature of the MTJ with $Mn_2Ru_{0.8}Ga$ is even a stronger proof that the magnitude of the spin polarization does not necessarily depend on the magnitude and sign of the magnetic moment. The demonstrated broad temperature (10 K to 300 K) high-field (up to $\mu_0 H = 0.5\,\mathrm{T}$) stability of these MRG-based MTJs holds a promise that similar compensated half-metallic ferrimagnetic compositions have high chance to become a basic building block in next generation MRAM-based memory. At the moment, MRG is not a potential candidate for application in memory stack due to its relatively low uniaxial anisotropy $K_\mathrm{u} \approx 0.04\,\mathrm{MJ/m^3}$. The MRG research has already generated significant interest in the spin electronic community. Recently, the Heusler composition $(Mn_{0.5}Co_{0.5})_2VAl$* has been synthesized by arc-melting and demonstrated to have spin polarization of 60 % by PCAR. The Curie temperature is though very low for practical devices $T_\mathrm{C} \approx 105\,\mathrm{K}$[72]. High TMR of -35 % at room temperature has been measured in Mn_3Ge-based MTJs [151].

More in-depth analysis on the TMR dependence as a function of the insertion layer thickness is underway. New insertion compositions will be investigated in order to find out which one leads to the highest TMR effect. Ideally, a magical new combination of diffusion barrier/tunnel barrier has to be developed. The diffusion barrier should simultaneously block efficiently Mn ions while having low spin diffusion length, so that the injected spin polarization from the MRG is not heavily reduced before tunneling through the barrier. Furthermore, the diffusion barrier should possess good band matching both to the MRG and to the barrier. This may sound as a rather daunting task but similar achievement has been recently performed in current-perpendicular-to-plane GMR stacks of $Co_2FeGa_{0.5}Ge_{0.5}$/NiAl/Ag- Zn/NiAl/$Co_2FeGa_{0.5}Ge_{0.5}$[155] †. Another idea is to eliminate the need for diffusion barrier altogether, however, the attempts to produce MTJs with decent TMR without insertion layer have failed so far. It is a possibility that the TMR sign switch which is demonstrated for the sample without insertion layer is due to formation of MnO at the interface which essentially creates quantum well states (Fig. (6.22)). There are indication from other experiments that the MRG crystalline quality improves when it is annealed *ex-situ* in temperatures from 350 °C to 400 °C. Unfortunately, the CoFe/Ta frame electrode in the present MTJ stacks starts losing PMA when annealed at $T > 350\,^\circ\mathrm{C}$. A possible improvement to the configuration is to

*It should have $0\mu_\mathrm{B}$/f.u. following the Slater-Pauling rule.

†NiAl has been theoretically predicted to provide very good band matching with the ferromagnetic $Co_2FeGa_{0.5}Ge_{0.5}$. It is latter demonstrated that the spin diffusion length of NiAl is rather low and it has been deposited as ultrathin, dusting layers on the interfaces.

replace Ta with W. It has been demonstrated that a W-based composite electrode maintains PMA at $T \leq 450\,^{\circ}$C[5, 309].

The study of the spin polarization temperature dependence in MRG is of fundamental importance. The latter could be achieved by either spin-resolved photoemission spectroscopy or spin-polarized scanning tunneling spectroscopy *. The constant temperature behaviour of the spontaneous Hall angle is a strong point that the spin polarization does not change with temperature but this is an indirect proof.

The barrier analysis has demonstrated that the tunneling process in these devices is incoherent and heavily affected by defects. In-depth analysis of the MTJs by high-resolution transmission electron microscopy will shed more light on the correlation between the barrier structure/disorder and the observed changes in the TMR(U) behaviour.

Finally, MRG is the first member of a new family of magnetic materials-compensated half-metallic ferrimagnets. Such materials hold significant potential to be integrated in future memory elements due to their high coercivity, *i.e.* high magnetic field immunity, which is governed by the low magnetization. Furthermore, observation of TMR at the very T_{comp} provides an opportunity for a realization of exchange mode ferrimagnetic resonance in MTJ nano-pillars at the MRG compensation point, which should be essentially terahertz spin-transfer torque based oscillators[340].

*SP-STM provides better energy resolution close to E_{F}.

Chapter 7

Conclusion and outlook

"People wait all week for Friday, all year for summer, all life for happiness."

Unknown author

PCAR has demonstrated the ability to quantify the degree of in-plane spin ordering in topological insulators(TIs). The extracted very high in-plane spin polarization demonstrates that TIs hold great potential to be integrated in future spin electronic devices. Furthermore, point contact spectroscopy has provided direct insight into the band structure of these degenerate semiconducting compositions at magnetic fields higher than the quench field of the superconducting tip. Paramagnetic (chromium and vanadium) doping is demonstrated to reduce the spin polarization values. The latter is attributed to spin-flip scattering from the moment of the paramagnetic ions. Higher vanadium doping concentration induces ferromagnetic order with perpendicular magnetic anisotropy. For the composition investigated, which has a low Curie temperature of $T_C \approx 11.6\,K$, the spin polarization decreases to 50 % which is attributed to the competition between the in-plane spin order of the pristine TIs and the perpendicular magnetization of the magnetic TIs. Furthermore, the interfacing between topological insulators and superconductors will continue as the latter system is predicted to host in some cases Majorana fermions (or Andreev bound states), low energy excitations which are supposed to offer fault-tolerant quantum computing.

The spin polarization of the disordered $Fe_{60}Al_{40}$ compositions is investigated to increase from essentially zero to 46 % as a function of the irradiation dose, while the Curie temperature reaches 620 K at the same time. The spontaneous Hall angle reaches a value of 3 % which is among the highest recorded on magnetic compositions, although it is not investigated whether the mechanism is intrinsic or extrinsic.

The lack of the spin polarization sign resolution, one of the shortcomings of the PCAR method, has been addressed by high-field Andreev reflection experiments with type-II superconductors with relatively low average atomic number: MgB_2 and Nb-Ti. High-field Andreev reflection and spin

polarization extraction has been achieved with both compositions and the sign has been correctly extracted with the MgB_2 superconductor. The latter is confirmed in large area MgB_2/CoFe junctions in configuration in which the magnetic field is applied in plane of the MgB_2 superconducting electrode.

Finally, high tunneling magnetoresistance of up to 40 % has been realized in magnetic tunnel junctions with the compensated half-metallic ferrimagnet Mn_2Ru_xGa. More importantly, finite tunneling magnetoresistance has been achieved with a ferrimagnetic electrode with a strictly zero magnetization. Furthermore, broad temperature range (10 K-300 K) high magnetic field (at least 0.5 T) immunity is achieved with the same devices. The analysis of the transport properties demonstrates that the values are currently limited by the imperfect control of Mn diffusion.

The presented results in this thesis have answered many questions. As it is usually the case with research, potential new experimental directions open up as well. A short outlook is given below for each of the result chapters.

Topological insulators will continue to be a hot research topic in foreseeable future. First of all, magnetic topological insulators have achieved recently Curie temperature of up to 110 K and the long sought-after quantum anomalous Hall effect (QAHE) has been demonstrated as well. Our PCAR methodology can easily be transferred to mK temperature range in order to study the spin polarization in the QAHE regime. Furthermore, the achieved high-field PCAR with Nb-Ti implies that this superconducting wire can be directly used for investigation of the spin polarization field dependence on ferromagnetic TIs. As the coercive field of V-doped TIs reaches about 1.1 T, high-field PCAR might shed more light on the transport properties as the magnetization is switched. Direct gating of TI compositions should suppress the bulk conductance of topological insulators, and therefore increase the spin polarization. PCAR measurements of the TI spin polarization with gating is a possible straight-forward experimental extension.

The spin polarization of the irradiated $Fe_{60}Al_{40}$ composition has reached 46 %, a value comparable with the spin polarization of the exemplary $Co_{1-x}Fe_x$. It is an open question whether the spin polarization will increase with higher irradiation dose. Furthermore, the spontaneous Hall angle of up to 3 % requires further investigation. It is beneficial to study the temperature dependence of the latter in order to understand whether extrinsic or intrinsic mechanisms are responsible for this high values. It is interesting whether the spontaneous Hall angle will increase above this value for higher irradiation dose. It will be curious to investigate as well whether higher irradiation will lead to higher Curie temperature and what would be the maximum achieved value.

Mn_2Ru_xGa is the first member of a broad class of ferrimagnetic compositions: compensated half-metallic ferrimagnets. The material has already demonstrated high spin polarization and high TMR values (although quickly decreasing with temperature). The notorious tendency of Mn to diffuse will have to be controlled in future devices in order to reach the physical limits of the high

Mn_2Ru_xGa spin polarization. The most important research direction is device improvement and better control of Mn migration either through new dusting layers between Mn_2Ru_xGa and the MgO barrier or with some "magical" growth/annealing procedure which crystallizes better the ferrimagnetic electrode. Particularly interesting is the possibility to achieve ferrimagnetic resonance mode with Mn_2Ru_xGa as the expected frequency is approximately 0.7 THz. Spin-transfer torque-based nano-oscillators with Mn_2Ru_xGa has the opportunity to generate on chip THz-radiation. A functionality which will revolutionize the field of data transfer.

Appendix A

List of publications

Publications:

1. D. Betto, Y.-C. Lau, K. Borisov, K. Rode, P. Stamenov, J.M.D. Coey, K. Kummer, and N.B. Brookes. Structure, element-specific magnetism and mangeto- transport properties of epitaxial DO_{22} Mn_2Fe_xGa thin films (submitted in PRB).

2. K. Borisov, C.-Z. Chang, J. S. Moodera, and P. Stamenov. High Fermi level spin polarization in the $(Bi_{1-x}Sb_x)_2Te_3$ family of topological insulators: A point-contact Andreev reflection study. Physical Review B **94**, 094415 (2016).

3. K. Borisov, D. Betto, Y.-C. Lau, C. Fowley, A. Titova, N. Thiyagarajah, G. Atcheson, J. Lindner, A. M. Deac, J. M. D. Coey, P. Stamenov, and K. Rode. Tunneling magnetoresistance of the half-metallic compensated ferrimagnet Mn_2Ru_xGa, Applied Physics Letters **108**, 192407 (2016).

4. D. Betto, K. Rode, N. Thiyagarajah, Y.-C. Lau, K. Borisov, G. Atcheson, M. Žic, T. Archer, P. Stamenov, J.M.D. Coey. The zero-moment half metal: How could it change spin electronics? AIP Advances **6**, 056601 (2016).

5. N. Thiyagarajah, Y.-C. Lau, D. Betto, K. Borisov, J.M.D. Coey, and K. Rode. Giant spontaneous Hall effect in zero-moment Mn_2Ru_xGa, Applied Physics Letter **106**, 122402 (2015).

6. K. Borisov, J. Alaria, J.M.D. Coey, and P. Stamenov. High field magnetotransport and point contact Andreev reflection measurements on $CuCr_2Se_4$ and $CuCr_2Se_3Br$-Degenerate magnetic semiconductor single crystals. Journal of Applied Physics **115**, 17C717 (2014).

Appendix B

PPMS cool down from warm dewar

This short manual is based on a procedure by Dr. Plamen Stamenov which has been used multiple times. If the reader has never dealt with cryogenic liquids, the procedure has to be performed with an experienced member from the group. Although this procedure is specifically focused on the PPMS system, it can be applied to cool down of other cryostats with small modifications as well. This is a two day procedure: the system is flushed with helium gas and pre-cooled with liquid nitrogen during the first day and liquid helium is transfer during the second day.

- The insulation vacuum of the system has to be pumped down through the insulation vacuum valve (see Fig. (B.1) (b)). The pressure has to be $\leqslant 10^{-5}$ mbar.

- The pump on the PPMS system has to be checked. If it is an oil mist pump, make sure that it has enough oil and it does not need a service. If it is a scroll pump, make sure that the pump does not need a service. The best way to check the pump is to test its pumping capacity through the gas system of the PPMS controller. Open the gas monitor program GasMon32, open fully the proportional valve and disconnect the pumping line from the cooling annulus*. When the pump is pumping on atmosphere, the flow on the GasMon32 must show around 4.1-4.2 L min^{-1}. If it does not, there is something wrong with the pump.

- Make sure you have at least one full bottle of CP grade helium gas.

- Make sure that you have at least 150 L of liquid helium in the dewar. The cool down operation will consume around 120 L if everything goes smoothly.Make sure that your next helium dewar will arrive shortly afterwards: 3-4 days after the cool down.

- Order around 120 ltrs of liquid nitrogen.

*When the system is warm the proportional valve opens fully when you set low temperature 5 K at high rate 20 K min^{-1}. Alternatively, the system control can be aslept from the GasMon32: File-Advanced-password: "quandsn", and then the angle on the proportional valve can be controlled.

- Connect the helium gas line on one of the ports of the PPMS, the other port should be blank (see Fig. (B.2) (a)).

- From MultiVu: set the system to go 5 K with a rate of 20 K min^{-1}. The first value will deactivate completely the heaters, while the second will open fully the proportional valve. The reason for that is to flush helium gas through the impedance and cooling annulus with maximum flow.

- Open the helium gas bottle. Make sure you give enough pressure but not too much (0.1-0.2 bar). You can check whether the system is at positive pressure by placing a finger wet with IPA/ethanol at the back of the hissing valve.

- Leave the helium gas to flush through the system for 2-3 hours. This must dry out any residual moisture. Make sure in the meantime that the nitrogen dewars are full and collected.

- Open slightly more the pressure on the helium gas bottle.

- Start liquid nitrogen transfer in the nitrogen jacket. Since the system is warm, there will be violent evaporation. REMINDER: WINDOWS AND DOORS HAVE TO BE ALWAYS OPEN WHEN TRANSFERRING CRYOGENIC LIQUIDS! It will take approximately 30 L for the nitrogen jacket to be cooled down and then the pitch of the exhaust sound will change. Keep transferring until the nitrogen jacket is full. Close the nitrogen jacket with the two caps. There will be serious nitrogen boil-off (since most of the system is still warm) and most likely one of the pressure relief valves will freeze. This is all fine, defrost it every now and then with the hot air gun. There is a problem only if both pressure relief valves freeze. You might be tempted to open up the caps to release the pressure: DO NOT DO THAT*!

- It is advisable to connect the helium purge line to the dewar in order to save helium gas. Close the safety valve on the liquid helium dewar. Shake the helium dewar to create overpressure inside. Open slightly the pressurization valve on the helium dewar. Switch quickly the gas line from the bottle to the dewar. Open fully the pressurization valve on the helium dewar. The pressure from the helium dewar provides the gas for flushing the impedance valve and the cooling annulus.

- After you have switched for providing the gas from the dewar, check again with a wet (IPA/ethanol) finger at the hissing valve that there is positive pressure in the system.

- Shake the liquid helium dewar a few more times in order to create overpressure. Leave the PPMS overnight, the liquid nitrogen will go its job.

*The overpressure will create a jet of cold nitrogen gas and liquid droplets into the air.

- First thing in the morning: check that there is positive pressure in the PPMS. Again check the overpressure at the hissing valve with an IPA/ethanol finger.

- Top up the nitrogen jacket. The system has lost a lot of liquid nitrogen overnight. If the temperature of the system is around 150 K, it is convenient to start the real helium cool down. If not, wait for more. You may leave the PPMS one more night to get pre-cooled from the nitrogen.

- If the temperature is around 150 K, it is time for starting the liquid helium transfer. On the helium transfer line, make sure that you have the longest extension on the end which will go in the PPMS. The cold gas and then the liquid helium must flow at the very bottom of the system. On the supply dewar side of the line, the extension should be enough to reach the bottom of the dewar.

- Lower the transfer line in the liquid helium dewar. Lower it only half-way, it should be just touching the liquid. Lower the transfer line in the PPMS dewar all the way to the bottom of the PPMS dewar.

- Close the pressurization valve on the helium dewar. Swap quickly the other port on the PPMS dewar with a blank.

- Make sure that there is positive pressure in the PPMS dewar.

- Lower the transfer line gradually in the liquid helium dewar over the next 0.5-1.0 hour. Make sure that you always have positive pressure and good exhaust. When the transfer line has reached the bottom of the helium supply dewar, it has to be raised around 5 cm from the bottom. In this way, ice particles or other dirt which settle at the bottom will not be transferred during the cool down.

- When the transfer line has reached its final position in the helium dewar, the latter must be pressurized with the external helium bottle. Make sure that the line is purged well with helium gas before connecting it to the dewar. NITROGER, OXYGEN, AND WATER VAPOUR MUST NOT ENTER THE DEWAR!

- Start the pressurization on the helium supply dewar. The required pressure is around 0.2 bar.

- The GasMon32 program must be opened. Right-click on the helium monitor and measure the level. Refresh the helium level monitor in this way every 15-20 minutes. If everything has gone fine so far, you must be at around $-5\,\%$.

- Keep an eye on the pressure from the helium bottle. Make sure that it does not drop because the transfer must not be terminated.
- The helium condenses when the level reaches 0 %.
- Shortly after that the exhaust timing nature will change to a steady, high exhaust.
- The flow through the proportional valve should change around 0 % level and it should be around 2.5-2.9 L min^{-1}.
- It is advisable to start PPMS data logging at that stage (MultiVu: Utilities → Log Data → Mark all fields in the three Tabs → Start acquiring with an interval 10 s).
- When the level reaches 40 %, the impedance valve is fully immersed in liquid and, hence, protected from the atmosphere. You should close the impedance valve by setting new temperature (or putting the system in standby) and this will save helium.
- The pitch of the exhaust will decrease significantly when the level goes above 55 % because the magnet is fully immersed and most of the system is already cold.
- Stop the transfer when level has reached 80 %-85 %*. Let the system to settle for 2-3 hours and preferably overnight, the dynamics in the liquid helium is still high.
- Test the cooling of the system. Set the temperature to 2 K and the cooling rate to 20 K min^{-1} and cool down from initial temperature $T \geq 200$ K. The flow has to be above 2.5 L min^{-1} when the proportional valve is fully open† this means that there is a leak in the gas control system of the PPMS. The system should manage to reach 2 K. Make sure that the base temperature can be maintained for an hour.
- Congratulations! You should be having a cold and working PPMS system. Now measure your samples. If something has failed, as a wise person says: Find out what your are doing wrong and stop doing it!

*Some people might prefer to terminate the transfer earlier at around 70 % but since the transfer line is already cold, it might be better to reach higher level.

†Stable flows up to 2.7 L min^{-1} have been reached. If the flow is above 3.0 L min^{-1}

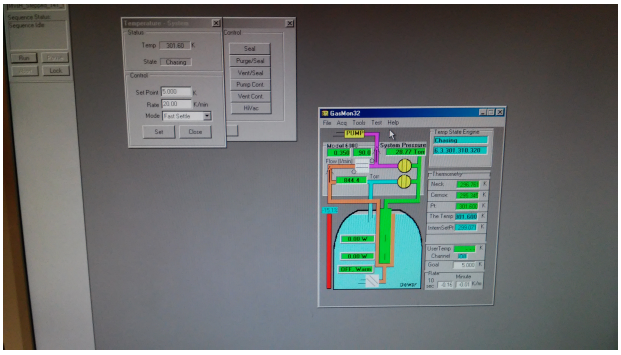

(a) Setting low temperature before starting the He gas flushing of the system.

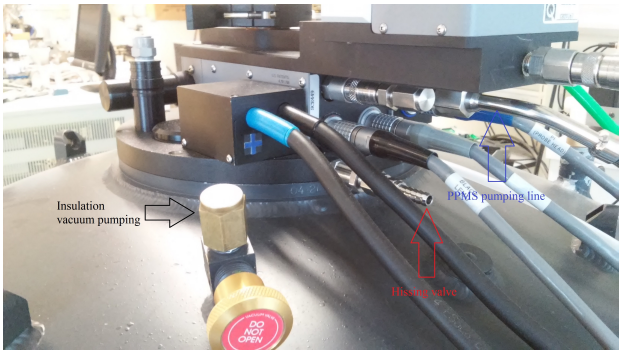

(b) Relative TMR decrease for dT = 10 K

Figure B.1: Setting low temperature and high cooling rate before flushing the system with He (panel (a)), the hissing valve and the pumping line are indicated (panel (b)).

(a) The helium gas is connected to one of the transfer ports, the other one is blanked.

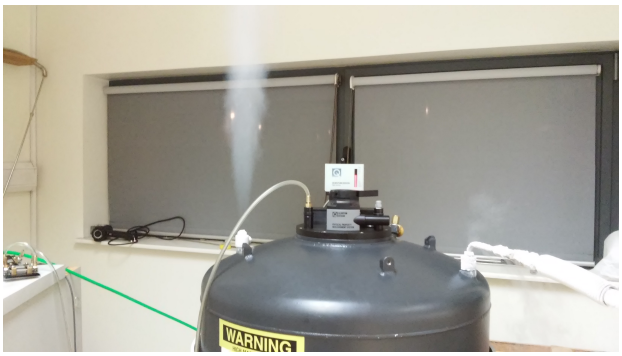

(b) Pre-cooling with nitrogen.

Figure B.2: The He gas line (panel (a)) and the nitrogen pre-cooling procedure (panel (b)).

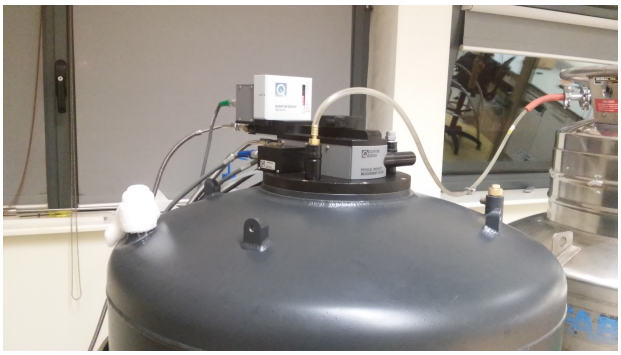

(a) The He gas line is swapped to the He supply dewar.

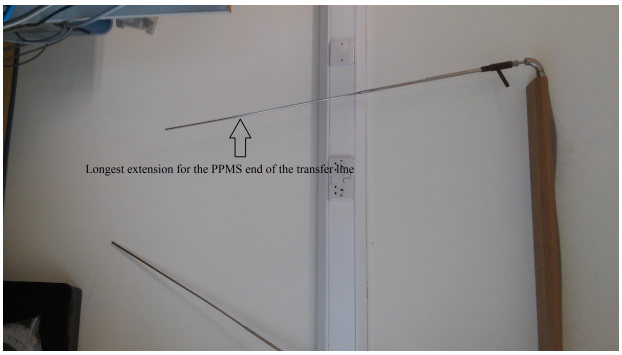

(b) The He transfer line must have the longest possible extension on the PPMS end in order to reach the bottom of the PPMS dewar.

Figure B.3: The He gas line (panel (a)) and the nitrogen pre-cooling procedure (panel (b)).

Appendix C

Wire bonding MTJs

This is a short procedure how to wedge bond MTJs. It is supposed that the operator has initial training on wedge-bonding, *i.e.* the wedge can be mounted, the wire can be threaded, and the main device settings are known. The procedure is given for bonding to PPMS pucks. The given settings are for the wedges used in our lab and for our bond pads. The bond pads on the samples are Cr(10 nm)/Au(150 nm). The PPMS puck bond pads are gold plated copper. The bonding settings settings have to be adjusted for different adhesion layers.

- Sonicate the MTJ chip in IPA in order to clean any organic residue on the surface.
- Clean well the bond pads on the PPMS puck.
- Glue the chip to a PPMS puck, so the contact bond pads are aligned with the bond pads of the chip.
- Make bonds between the bond pads on the PPMS puck which you plan to use for connecting the MTJs (these are V+ and V- usually).
- Ground yourself with the anti-static wrist strap.
- Connect one of the puck bond pads to ground.
- Wire bond one of the MTJ contacts.
- Wire bond the other MTJ contact.
- Disconnect the grounding cable. The bonded MTJ should be shorted through the PPMS bond pads.
- Ground yourself and have a look at the bonded MTJ under microscope.

- Disconnent the shorting string of wire between the PPMS bond pads with a small needle (for instance, W tip for probe station micromanipulators)
- Check the *I-V* curve of the bonded MTJ, *i.e.* make sure that it has not blown during the procedure.
- Congratulations! You should have a bonded MTJ. If it is a short, find another victim on the chip and repeat the procedure.

Below, I have outlined the settings which have worked for me with the wedges currently in use.

Wire bonding between PPMS resistivity puck bond pads			
Bonding	Power	Time	Force
First bond PPMS puck	2.0	1.4	1.0
Second bond PPMS puck	2.0	3.5	3.0

Table C.1: Wire bonding parameters which have worked for bonding between bond pads of a PPMS resistivity puck.

Wire bonding between an MTJ bond pad and a PPMS resistivity puck bond pad			
Bonding	Power	Time	Force
First bond MTJ chip	2.0	3.0	1.0
Second bond PPMS puck	2.0	3.5	3.0

Table C.2: Wire bonding parameters which have worked for bonding between an MTJ chip and a PPMS resistivity puck.

A few more remarks on the bonding parameters for semi-automatic bonding:

- Tail parameter: keep the highest possible (9). The tail determines how much wire is left under the wedge after a bonding has finished. If the tail is too short, the wedge will not be well covered with wire and wire bonding does not work. However, too long tail might in principle be a problem if the bond pads on the chip are too close. The longest tail setting has worked for the MTJs in this work (bond-pads 50 µm-100 µm with a distance between the bond pads of 100 µm). Shortening of the tail usually requires more frequent rethreading.
- Loop parameter: This determines how high the wedge retracts after the first bond. This parameter should be slightly higher than the height of both the first and the second bonds*. The loop must be set just before the first bond is made. The loop parameter should be slightly larger than the search height when the wedge is close to the first bonding position. For instance, if the search height is 7.0, the loop has to be between 7.5-8.0.
- Speed parameter: This parameter has been 3.6 for all bonding throughout my thesis.

*The chip bond pads and the chip carrier bond pads are usually at very similar heights.

Appendix D

SQUID oven measurements

SQUID magnetometry with its unrivaled sensitivity is a very important tool for investigation of new compositions. The SQUID oven has the possibility to determine the Curie temperature of thin films. The SQUID oven is a dewar itself with internal diameter of 4 mm and the whole inside sample space is heated up*. The SQUID oven sample rod finish approximately 13 cm above the the center of the pick-up coils. Therefore, the experimental physicist should come up with a good idea how to bring the sample within the pick-up coils. If the sample is bulk, perhaps, the best approach is to seal it inside a quartz cylinder. However, thin films represent a more complicated story. One has to find intelligent way to bring them down to the sample space. In this case, we wrap the samples in Al foil and hook the Al foil with the sample to the sample rod†. The heating temperature must be limited to nothing higher than 750 K because of the low melting point of Al. If a sample with in-plane magnetization has to be measured, the sample size should be $3\,\text{mm} \times 4\,\text{mm}$ and the long side of the sample has to be along the axis of the oven. If the sample has perpendicular magnetic anisotropy, then the size must be $2\,\text{mm} \times 2\,\text{mm}$ so that the diagonal is below 3 mm. A short procedure for in-plane measurement is outlined below:

- Stretch some good length of Al kitchen foil ($30\,\text{cm} \times 30\,\text{cm}$).
- You need a very sharp surgical blade.
- Mark out stripes with length $\approx 22\,\text{cm} - 24\,\text{cm}$ and width 1.2 cm.
- Cut out the stripes.
- Fold one stripe along its length axis in half-width, so that you get Al foil at angle of $\approx 90°$.

*Unlike the Quantum Design PPMS VSM oven which uses a ceramic platform with integrated heater and temperature sensor.

†The technique is after Dr. Plamen Stamenov.

- Put the sample so that its long edge lies along the formed angle. The sample must be approximately 12 cm – 14 cm from the Al end which will be attached to the sample rod. THIS IS VERY IMPORTANT FOR BEING ABLE TO CENTER THE SAMPLE WITHIN THE PICK-UP COILS.
- Gently fold the Al foil around. Squash it as much as possible but be carefully around the sample, as the sharp edges might tear the foil.
- Make a small hole with sharp tweezers at the end of the folded Al foil.
- Get a thin copper wire ($r \approx 0.1$ mm). If the wire is insulated, burn the insulation with a lighter under a fume hood. Use the copper wire in order to attach the sample to the sample rod. There should be a small hole at the bottom of the sample rod for the SQUID oven as well.
- Make sure (again) with a ruler that the sample is at least 12 cm below the end of the rod. You will be able to get a good centering even if the sample is around 11 cm, however, if the sample is at around 10 cm, the centering will fail due to the fact that the sample is at the end of the range. On the RSO, 12 cm corresponds roughly to 2 cm, and 10 cm from the bottom of the rod to 0 cm in the RSO.
- Unscrew the RSO head and remove it from the SQUID. Insert the SQUID oven following the procedure in the SQUID manual.
- The mounting of the suspended, folded sample is a two person operation. This is because the folded aluminium "holder" is easily bendable.
- One person holds the RSO driving motor, so that the bore is clear from both ends. The other person passes the sample rod with the suspended sample through the motor head.
- After the sample is passed through the RSO head, one person lifts the head while the other is holding the sample rod.
- The sample is inserted into the oven and lowered gently down. After that the RSO head is adjusted on top of the oven, screwed and the sample space is evacuated.
- Make sure that the vacuum is good. This is critical for the SQUID measurements with the oven.
- Center your sample. Make sure that the measurement frequency is low (0.5 Hz), and the amplitude is small as well (1 cm). Otherwise big acceleration might cut the copper wire or the Al foil.

The sample can be mounted as well in perpendicular direction. Greater care should be taken and the forming of the Al foil around the sample is trickier. However, it is doable. The Curie temperature of the tetragonal Heusler alloy Mn_2Fe_xGa has been determined in this way and it is presented in Fig. (2.13).

Appendix E

SQUID devices: a brief introduction

The presented material is a brief introduction to the physics of SQUID devices. The exposition has been submitted by the author of this thesis as a course work in the post-graduate course on Magnetic Sensor by J.M.D. Coey in Trinity College Dublin. A few sections are dropped from the original work: the mixed SQUID-GMR sensor[263], the gradiometers section and the SQUID application section.

E.1 Introduction

The physics behind a **S**uperconducting **QU**antum **I**nterference **D**evice (**SQUID**) is the Josephson effect. The Josephson effect is the existence of a non-zero current in an unbiased Superconductor-Insulator- Superconductor (SIS) structure. In the following subsections I will lay down the basic Josephson relations. They will be used extensively to explain the principle of operation of the SQUIDs, which are the most sensitive magnetic sensors up-to-date. The Josephson effect is a tunnelling of Cooper pairs from the first superconducting electrode (S1) to the second superconducting electrode (S2) through an insulating barrier. Although the original Josephson prediction was for tunnelling through a thin insulating layer, nowadays, the "barrier" is more generally referred to as a "weak-link". In Sec.(E.2), the flux quantization is derived and the general theory of a Josephson junction following Feynman's approach. The basic structure and electric properties of an a.c. SQUID are presented in Sec.(E.3). The same properties but for a d.c. SQUID are reviewed in Sec.(E.4). In Sec.E.5, the different kinds of weak-links are commented, the basic and flux-locked readout circuits for an a.c. and d.c. SQUID are presented. Some used gradiometers as pickup coils are reviewed as well. In Sec.(E.6), the sensitivity, noise and gain characteristics of the two SQUID configurations are briefly given.

E.2 Flux in a superconducting loop

E.2.1 Flux in a homogeneous superconducting ring

In the Ginzburg-Landau (GL) phenomenological treatment of the superconductivity, the Cooper pairs condensate wavefunction is represented as

$$\Psi(\mathbf{r}) = |\Psi(\mathbf{r})|e^{i\theta}. \tag{E.1}$$

where $|\Psi(\mathbf{r})|^2$ is the Cooper pairs density

$$\rho_s = |\Psi(\mathbf{r})|^2. \tag{E.2}$$

If the Ginzburg-Landau expression for the Gibbs free energy is varied with respect to the vector potential $\mathbf{A}$, the variational derivative must be zero, in this way the second GL equation is obtained

$$\nabla \times (\nabla \times \mathbf{A}) + \frac{i\hbar e^*}{2m^*}(\Psi^*\nabla\Psi - \Psi\nabla\Psi^*) + \frac{e^{*2}}{m^*}\mathbf{A}|\Psi|^2 = 0, \tag{E.3}$$

where m^* and e^* are the mass and the charge of a Cooper pair. Assuming the London-Landau gauge $\nabla.\mathbf{A} = 0$, we get $\nabla \times (\nabla \times \mathbf{A}) = -\nabla^2\mathbf{A}$. We use the definition for a vector potential $\mathbf{B} = \nabla \times \mathbf{A}$, and put into the Maxwell equation $\nabla \times \mathbf{B} = \mu_0\mathbf{J}$, we get the result for the current density:

$$\mu_0\mathbf{J} = -\frac{i\hbar e^*}{2m^*}(\Psi^*\nabla\Psi - \Psi\nabla\Psi^*) - \frac{e^{*2}}{m^*}\mathbf{A}|\Psi|^2. \tag{E.4}$$

Calculating the gradient of Ψ

$$\nabla\Psi = i\Psi\nabla\theta + e^{i\theta}\nabla|\Psi|, \tag{E.5}$$

and plugging it back into the expression for the current density, we get

$$\mu_0\mathbf{J} = \frac{\hbar e^*}{m^*}|\Psi|^2\nabla\theta - \frac{e^{*2}}{m^*}|\Psi|^2\mathbf{A}. \tag{E.6}$$

Let us now consider a superconducting loop placed in a magnetic field (Fig.(E.1)), and we integrate the above expression along a closed contour along the superconductor

$$\frac{m^*}{e^{*2}}\oint\frac{\mu_0\mathbf{J}}{|\Psi|^2}.\mathrm{d}\mathbf{l} = \frac{\hbar}{e^*}\oint\nabla\theta.\mathrm{d}\mathbf{l} - \oint\mathbf{A}.\mathrm{d}\mathbf{l} \tag{E.7}$$

The superparticle condensate wavefunction must be a single-valued function, then the contour integral over the phase must be a multiple of 2π:

$$\oint \nabla\theta.\mathrm{d}\mathbf{l} = 2\pi n, \tag{E.8}$$

then the expression could be rewritten as

$$\frac{m^*}{e^{*2}} \oint \frac{\mu_0 \mathbf{J}}{|\Psi|^2}.\mathrm{d}\mathbf{l} + \oint \mathbf{A}.\mathrm{d}\mathbf{l} = n\Phi_0 \tag{E.9}$$

where the quantum of flux Φ_0 is

$$\Phi_0 = \frac{h}{e^*} = \frac{h}{2e}. \tag{E.10}$$

Applying the Stokes' theorem for the circulation of the vector potential

$$\oint \mathbf{A}.\mathrm{d}\mathbf{l} = \int \mathbf{B}.\mathrm{d}\mathbf{S} = \Phi, \tag{E.11}$$

we get finally

$$\frac{m^*}{e^{*2}} \oint \frac{\mu_0 \mathbf{J}}{|\Psi|^2}.\mathrm{d}\mathbf{l} + \Phi = n\Phi_0 \tag{E.12}$$

Equation (E.12) expresses that the sum of enclosed flux Φ and the contour integral of the current density $\mathbf{J}$ is quantized. But the supercurrent flows in a thin layer on the outer sheath, thus the current density on the central contour is zero, and the expression reduces to $\Phi = n\Phi_0$.

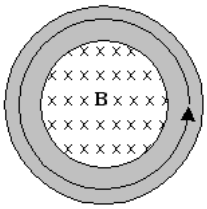

Figure E.1: Superconducting loop with applied magnetic field and indicated contour of integration.

E.2.2 General theory of Josephson effect

The following derivations follow the pedagogical approach of Feynman [96] and Poole Jr *et al.* [153].Let us consider the case of two superconductors, S1 and S2 on Fig. (E.2), separated with an insulating barrier. If the barrier is thick enough, the superconductors do not alter their properties via proximity effect. Then the time-dependent Schrödinger equations for the two superconducting

condensates are:

$$\mathrm{i}\hbar\frac{\mathrm{d}\Psi_1}{\mathrm{d}t} = H_1\Psi_1, \tag{E.13}$$

$$\mathrm{i}\hbar\frac{\mathrm{d}\Psi_2}{\mathrm{d}t} = H_2\Psi_2, \tag{E.14}$$

where Ψ_i and H_i are the wavefunctions and the Hamiltonians in the two superconductors respectively. It is assumed that a voltage V is applied between the superconductors. (The special case of zero bias Josephson effect could easily be seen once the general equations are present.) If the zero of the potential is assumed to occur in the middle of the insulating barrier, then, superconductor 1 is at $-\frac{1}{2}V$ potential, and superconductor 2 is at $\frac{1}{2}V$. Because each Cooper pair carries a charge $-2e$, the potential energy of the pairs in $+eV$ and $-eV$, respectively. The existence of the barrier could be accounted with the introduction of coupling between the wavefunctions:

$$\mathrm{i}\hbar\frac{\mathrm{d}\Psi_1}{\mathrm{d}t} = eV\Psi_1 + K\Psi_2, \tag{E.15}$$

$$\mathrm{i}\hbar\frac{\mathrm{d}\Psi_2}{\mathrm{d}t} = -eV\Psi_2 + K\Psi_1, \tag{E.16}$$

where K is the coupling constant. The square of a wavefunction is the probability that paired electrons are present at a particular region. Then, the two wavefunctions could be rewritten as

$$\Psi_1 = (\rho_{s_1})^{1/2}e^{i\theta_1}, \tag{E.17}$$

$$\Psi_2 = (\rho_{s_2})^{1/2}e^{i\theta_2}, \tag{E.18}$$

$$\phi = \theta_2 - \theta_1, \tag{E.19}$$

where ρ_{s_1} and ρ_{s_2} are the densities of super electrons in the left and right superconductors, and ϕ is the phase difference across the barrier. The derivatives of E.17,E.18 are straightforwardly calculated

$$\frac{\mathrm{d}\Psi_1}{\mathrm{d}t} = \left(\frac{1}{2}\frac{1}{(\rho_{s_1})^{1/2}}\frac{\mathrm{d}\rho_{s_1}}{\mathrm{d}t} + (\rho_{s_1})^{1/2}i\frac{\mathrm{d}\theta_1}{\mathrm{d}t}\right)e^{i\theta_1}, \tag{E.20}$$

$$\frac{\mathrm{d}\Psi_2}{\mathrm{d}t} = \left(\frac{1}{2}\frac{1}{(\rho_{s_2})^{1/2}}\frac{\mathrm{d}\rho_{s_2}}{\mathrm{d}t} + (\rho_{s_2})^{1/2}i\frac{\mathrm{d}\theta_2}{\mathrm{d}t}\right)e^{i\theta_2}. \tag{E.21}$$

If the above derivatives are plugged back into the coupled wave equations E.15 and E.16, we could obtain a system of complex equations for the time dependence of the pair densities and the

phase difference:

$$\hbar\rho_{s_1}\frac{\mathrm{d}d\theta_1}{\mathrm{d}t} = -eV\rho_{s_1} - K(\rho_{s_1}\rho_{s2})^{1/2}\cos(\phi), \tag{E.22}$$

$$\hbar\rho_{s_2}\frac{\mathrm{d}\theta_2}{\mathrm{d}t} = eV\rho_{s_1} - K(\rho_{s_1}\rho_{s2})^{1/2}\cos(\phi), \tag{E.23}$$

$$\frac{\hbar}{2}\frac{\mathrm{d}\rho_{s_1}}{\mathrm{d}t} = K(\rho_{s_1}\rho_{s_2})^{1/2}\sin(\phi), \tag{E.24}$$

$$\frac{\hbar}{2}\frac{d\rho_{s_2}}{\mathrm{d}t} = -K(\rho_{s_1}\rho_{s_2})^{1/2}\sin(\phi). \tag{E.25}$$

The first two equation above are determined by the matching of the real parts, and the last two are obtained by matching the imaginary parts. The current density could be obtained by subtracting equations E.24 and E.25 and multiplying the result with the electron charge e

$$J = e\frac{\mathrm{d}(\rho_{s_1} - \rho_{s_2})}{\mathrm{d}t}, \tag{E.26}$$

which is equal to

$$J = J_\mathrm{c}\sin(\phi), \tag{E.27}$$

where the critical current density is

$$\boxed{J_\mathrm{c} = \frac{4eK(\rho_{s_1}\rho_{s_2})^{1/2}}{\hbar}}, \tag{E.28}$$

where the coupling constant K is of unknown value. However, we can elicit more information from equations E.22 and E.23. Dividing them by ρ_{s_1} and ρ_{s_2}, respectively, and then taking the difference, we get

$$\frac{d(\theta_2 - \theta_1)}{dt} = \frac{2eV}{\hbar} - K\cos(\phi)\left(\left(\frac{\rho_{s_1}}{\rho_{s_2}}\right)^{1/2} - \left(\frac{\rho_{s_2}}{\rho_{s_1}}\right)^{1/2}\right). \tag{E.29}$$

The factor in the brackets multiplying the $K\cos(\phi)$ is zero but it is a bit unclear at first sight. The reason is that, in fact, $\rho_{s_1} = \rho_{s_2}$. The change of the super electrons densities is happening for a short duration. In real situation, superconductors 1 and 2 are either connected to a voltage supply or they form a superconducting loop with a weak link. In both cases, ρ_{s_1} and ρ_{s_2} are equilibrated. Hence, we can summarize the **Josephson relations** into

$$\boxed{\begin{aligned} J &= J_\mathrm{c}\sin(\phi) && \text{(E.30)}\\ \frac{\mathrm{d}\phi}{\mathrm{d}t} &= \frac{2e}{\hbar}V && \text{(E.31)} \end{aligned}}$$

Equation E.30 is often called the d.c. Josephson effect. It is essentially the observation of direct

current flowing through a Josephson junction in the absence of any applied voltage. Equation E.31 is called the a.c. Josephson junction. Under voltage bias, the phase difference changes with a rate determined by the second Josephson relation. As a consequence, an a.c. current flows through the junction.

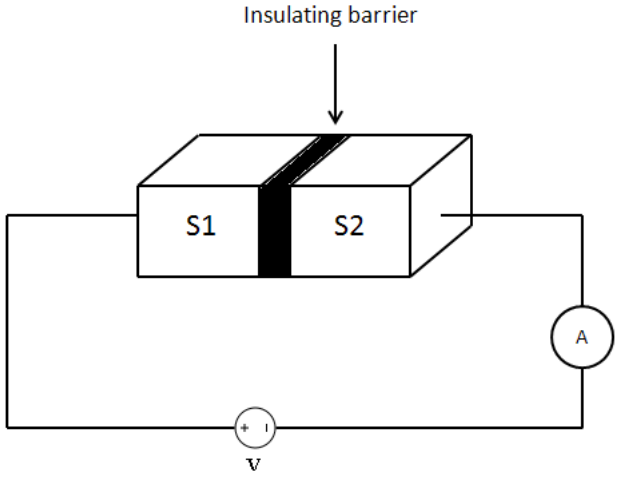

Figure E.2: Picture of a Josephson junction.

E.3 Principle of operation of an a.c. SQUID

An a.c. SQUID is essentially a superconducting loop with one weak link as pictured on Fig.(E.3 A).

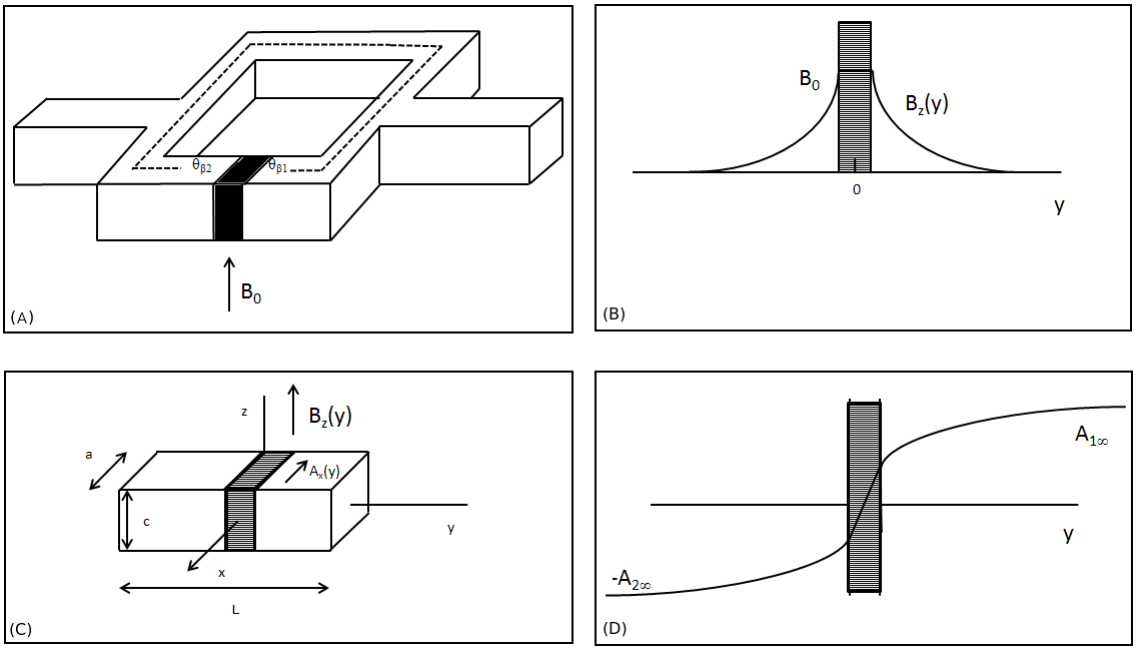

Figure E.3: Josephson junction. Field and vector potential behaviour.

E.3.1 Josephson junction diffraction equation

Let us consider Equation [E.7] along the contour ($A \to B \to C \to D$) on Fig.(E.4). The current flows perpendicularly to the barrier. Thus the current integrals on $B \to C$ and $D \to A$ are zero. On the $A \to B$ and $C \to D$, the current line integrals are non-zero but with opposite signs and thus cancel out. We get a simple relation between the phase difference and the vector potential:

$$\oint \Delta\theta.\mathrm{d}\mathbf{l} = \frac{2\pi}{\Phi_0} \oint \mathbf{A}.\mathrm{d}\mathbf{l}. \tag{E.32}$$

The magnetic field $B_0\hat{\mathbf{k}}$ is applied along the vertical z direction. The thickness of the insulating barrier is d and the cross-sectional dimensions are a and c as shown on the Fig.(E.3). The magnetic field has no component along the x and y axes, but its z-component does vary along the y-axis

$$\mathbf{B} = B_z(y)\hat{\mathbf{k}}. \tag{E.33}$$

The reason for the y-axis variation is that the field penetrates through the barrier and has a constant value there, but it dies out exponentially in the two superconductor S1 and S2 with characteristic length λ, the penetration depth. The applied field is described in terms of the vector potential $\mathbf{B} = \Delta \times \mathbf{A}$:

$$\mathbf{A} = A_x(y)\hat{\mathbf{i}}, \tag{E.34}$$

hence

$$\mathbf{A} = -yB_0\hat{\mathbf{i}} \qquad |y| \leq \frac{1}{2}d. \tag{E.35}$$

Deep into the superconductors, the field B_z goes to zero and the vector potential $\mathbf{A}$ to constant values. Let us assign asymptotic values for the vector potential of A_1 in S_1 and $-A_2$ in S_2 respectively. The phase difference $\theta_1(x) - \theta_{10}$ could be evaluated by integrating $\Delta\theta.d\mathbf{l}$ along the contour $A \to B \to C \to D$. The last operation is equivalent to integrating $A.d\mathbf{l}$ along the same path. But A is essentially a vector normal to the paths $A \to B$ and $C \to D$, hence its integral along them is zero. The only non-zero result comes from $B \to C$, so we get

$$\theta(x) = \theta_{10} + \frac{2\pi}{\phi_0}A_1(x - x_0), \tag{E.36}$$

in a similar fashion, we get the phase of the wavefunction in S_2. Then the phase difference is

$$\theta(x) = \theta_2 - \theta_1 = \theta_0 + \frac{2\pi}{\Phi_0}(A_1 + A_2)x, \tag{E.37}$$

the factor $(A_1 + A_2)$ could be evaluated by forming a large contour which encloses the whole barrier and goes in the two superconductors. Using Stokes' theorem, the resulting circulation gives the flux

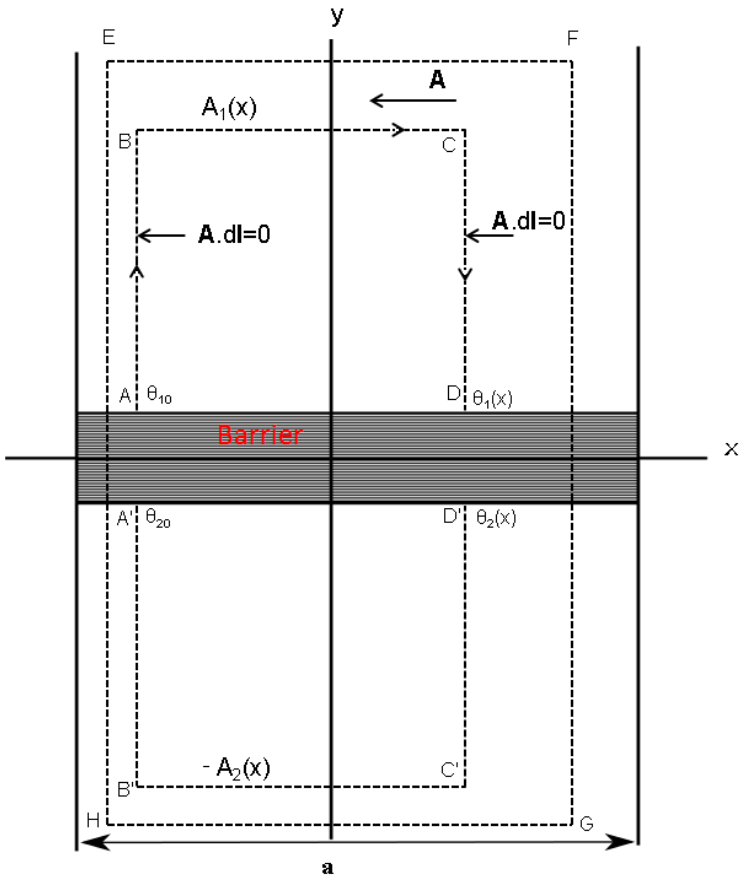

Figure E.4: Josephson junction.

threading the junction,

$$\Phi = \int \mathbf{B}.\mathrm{d}\mathbf{S} = \oint \mathbf{A}.\mathrm{d}\mathbf{l}. \tag{E.38}$$

The reasoning is the same as in the contours above, hence

$$\Phi = a\,(A_1 + A_2)\,, \tag{E.39}$$

then $(A_1 + A_2) = \Phi/a$, and putting back this expression into E.37, we obtain

$$\phi(x) = \phi_0 + \frac{2\pi\Phi}{\Phi_0}.\frac{x}{a}, \tag{E.40}$$

inserting back the final expression into the first **Josephson relation**, and integrating along the x, we arrive at an expression for the total current I flowing through the junction

$$I = J_c \int \sin(\phi(x))\mathrm{d}x\mathrm{d}z, \tag{E.41}$$

after straightforward integration, we obtain the famous *Josephson junction diffraction equation*

$$\boxed{I = I_c \frac{\sin(\pi\Phi/\Phi_0)}{\pi\Phi/\Phi_0},} \tag{E.42}$$

where we have assumed that $\sin(\phi_0) = 1$. The above expression has the same mathematical behaviour as the Fraunhoffer diffraction from a single slid. The Fraunhoffer diffraction is the light distribution which is obtained when a narrow single slid is illuminated with monochromatic light with wavelength λ. The variable of the x-axis is then $\pi d \sin(\theta)/\lambda$, where d is the width of the slid and θ is the angle of observation.

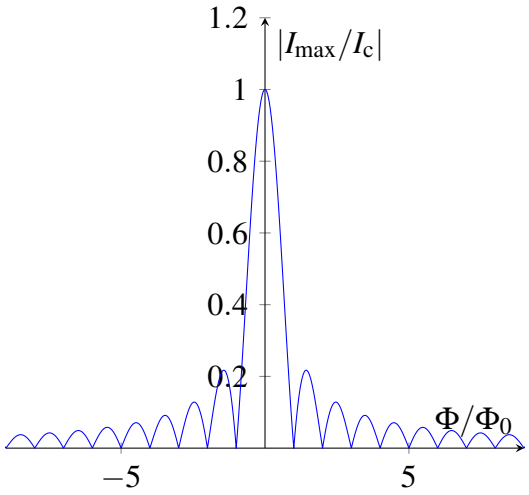

Figure E.5: Maximum zero-voltage current as a function of the magnetic flux.

E.3.2 McCumber parameter and hysteresis

Consider an experimental situation in which the applied magnetic field is zero, but the junction is biased by a current source (current-driven junction). We shall obtain the DC current-voltage characteristic. Josephson junctions always have a shunting resistance associated with the passage of normal state electron through the barrier (such normal state electrons always exist in superconductors). The shunting resistance R is connected in parallel to the junction. Furthermore, the barrier thickness is around $1-2$ nm, hence, the two superconducting electrodes will have non-negligible capacitance. This simplified model is known as RCSJ (resistance and capacitance shunted junction).The capacitance of the SIS structure is in parallel as well. The bias current is then a sum of three terms

$$I = I_c \sin(\phi) + \frac{V}{R} + C\frac{dV}{dt}. \tag{E.43}$$

Using the second **Josephson relation** $V = (\hbar/2e)\mathrm{d}\phi/\mathrm{d}t$, we arrive at a second order non-linear differential equation for ϕ:

$$I = I_\mathrm{c}\sin(\phi) + \frac{\hbar}{2eR}\frac{\mathrm{d}\phi}{\mathrm{d}t} + \frac{\hbar C}{2e}\frac{\mathrm{d}^2\phi}{\mathrm{d}t^2}. \tag{E.44}$$

The time-averaged value of the voltage, hence $\langle \mathrm{d}\phi/\mathrm{d}t \rangle$, must be taken to obtain the current-voltage characteristic. As a good first approximation, assume that $C = 0$ (which is reasonable for point-contacts and small-area tunnel junctions). Then the voltage of the resistively shunted Josephson junction can be derived:

$$V = \frac{\hbar}{2e}\left\langle \frac{d\phi}{dt} \right\rangle = \begin{cases} 0 & for \quad I < I_\mathrm{c} \\ I_\mathrm{c}R\sqrt{I^2/I_\mathrm{c}^2 - 1} & for \quad I \geq I_\mathrm{c}. \end{cases} \tag{E.45}$$

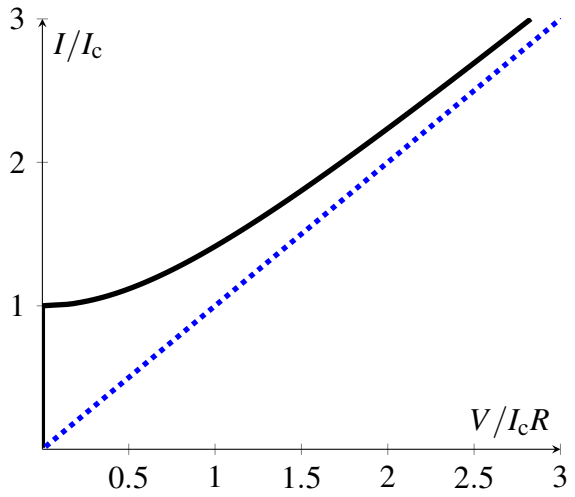

Figure E.6: The black curve is a nonhysteretic RSJ I-V characteristic ($\beta_\mathrm{c} \ll 1$). The blue dotted one is simply the bisector, which is the asymptote of the I-V Josephson junction curve, it is the I-V curve of a resistor R as well.

The resulting $I-V$ characteristic is a nonhysteretic for a junction in the zero-capacitance limit. It is presented on Fig.(E.6). In order to appreciate the complete physical picture the non-zero capacitance model must be considered

$$I = \frac{\hbar C}{2e}\frac{\mathrm{d}^2\phi}{\mathrm{d}t^2} + \frac{\hbar G}{2e}\frac{\mathrm{d}\phi}{\mathrm{d}t} + I_\mathrm{c}\sin(\phi), \tag{E.46}$$

where $G = 1/R$ is the conductance. The equation could be rewritten using the following variables:

characteristic frequency $\omega_\mathrm{c} = (2e/\hbar)(I_\mathrm{c}/G)$
McCumbert parameter $\beta_\mathrm{c} = \omega_\mathrm{c}C/G$
normalized time $\tau = \omega_\mathrm{c}t$
normalized current $i = I/I_\mathrm{c}$

$$\beta_c \frac{d^2\phi}{d\tau^2} + \frac{d\phi}{d\tau} + \sin(\phi) = i. \tag{E.47}$$

This set of parameters was first proposed by McCumbert. This is a nonlinear second- order differential equation and it must be solved numerically. The parameter β_c, known as the McCumbert's parameter, determines the hysteretic properties of the Josephson junction

$$\boxed{\beta_c = \frac{2\pi I_c R^2 C}{\Phi_0}.} \tag{E.48}$$

The bigger β_c is, the more hysteretic the junction is. On Fig.(E.7 (b) (c)), the path taken for sweeping up the current does not coincide with the path for sweeping down the current. The hysteresis could be reduced by shunting the junction with an additional resistor R_s in parallel to the junction. This approach had been used, however, in the 1980s, the thin-film Josephson junction technology developed by IBM for digital SQUID devices enabled creation of tunnel junctions of area as small as 1μm. This improvement reduced the capacitance, and McCumbert parameter $\beta_c \ll 1$ is easily obtainable.

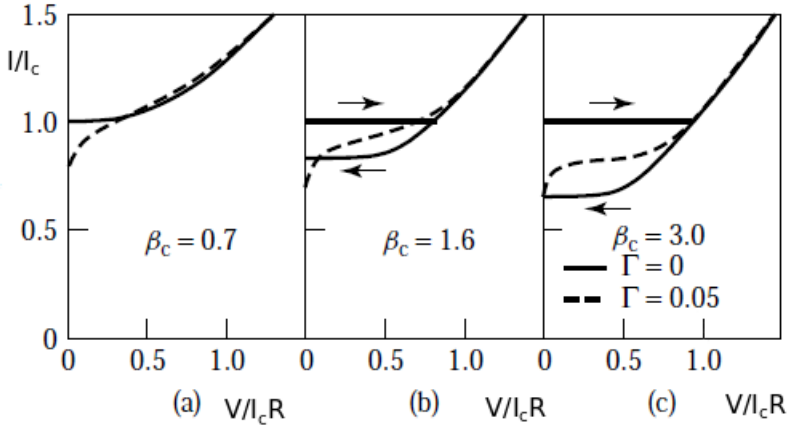

Figure E.7: Numerical simulations of hysteretic properties of Josephson junction. The solid curves are obtained at zero temperature. The parameter $\Gamma = 2\pi kT/I_c\Phi_0$ is known as the normalized thermal energy. The dotted curves are numerically obtained when the Nyquist noise current contribution is added in the RCSJ model. The picture is taken from [10].

E.3.3 Principle of operation

The a.c. SQUID consists of a superconducting loop with inductance L with one Josephson junction with critical current I_c and characterized by a nonhysteretic $I-V$ curve. The total flux Φ_t entering the loop has two terms - the externally applied flux Φ_e and the flux due to the circulating

current along the loop

$$\Phi_t = \Phi_e - LI = \Phi_e - LI_c \sin(2\pi\Phi_t/\Phi_0), \tag{E.49}$$

where the first **Josephson relation** $I = I_c \sin(\phi)$ has been used and, furthermore, the phase difference must comply with the flux quantization condition

$$\phi + 2\pi\Phi_t/\Phi_0 = 2\pi n. \tag{E.50}$$

Introducing an important parameter $\beta_L = 2LI_c/\Phi_0$. Thus the relation between the externally applied flux and the total flux is

$$\frac{\Phi_t}{\Phi_0} = \frac{\Phi_e}{\Phi_0} - \frac{\beta_L}{2}\sin(2\pi\Phi_t/\Phi_0). \tag{E.51}$$

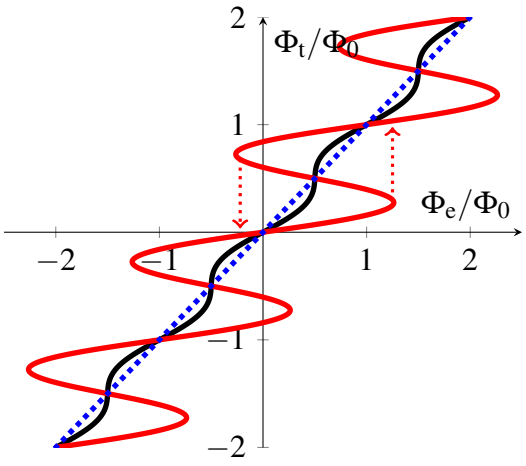

Figure E.8: The total flux Φ_t in an a.c. SQUID as a function of the externally applied flux Φ_e. The black curve corresponds to $\beta_L = 1$, the red one to $\beta_L = 2$, and the blue dotted line is $\Phi_t = \Phi_e$. A hysteresis behaviour is present for $\beta_L > 1$. It is discernible, that the red curve is in effect a succession of quasilinear regions with jumps between them. These jumps are associated with energy dissipation in the SQUID ring, and are crucial for the operation of the detector.

The red curve on Fig.(E.8) is actually a succession of quasilinear regions with jumps between them. Only the regions with positive slope are stable. The effect is that an increase (or decrease) of the external flux Φ_e leads to jumps in the total flux Φ_t. In this way, a hysteretic behaviour is present as the flux is ramped up and down. These jumps are associated with energy dissipation of the order $I_c\Phi_0$. The AC SQUID is inductively coupled (mutual inductance M) to a resonant tank L_TC_T circuit. An RF current source supplies a current to the tank circuit, in this way inducing a flux in the SQUID loop. The current is typically in the radio-frequency range (The AC SQUID is often called a RF SQUID). The voltage across the coil of the resonant circuit depends on the magnitude of the RF current and the value of the externally applied flux. I-V curves for an RF SQUID for flux values $n\Phi_0$ and $(n+1/2)\Phi_0$ are shown on Fig. (E.9). When the RF current is fixed at particular values, the voltage turns out to be a triangular-shaped dependence with amplitude $\omega L_T\Phi_0/2M$ and

period Φ_0. The optimum flux-to-voltage transfer is

$$\frac{\partial V}{\partial \Phi} = \frac{\omega L_T}{M}. \tag{E.52}$$

A more detailed treatment is presented in Sec.(E.6). From Fig.(E.9), it is visible that the suitable working points are at current bias I_2, and I_4. Whereas, I_1 and I_3 present basically no response of the voltage under flux change. In practice, an AC SQUID is always operated at the first voltage step (biased at current I_2 on Fig. (E.9)). In conclusion, RF SQUIDs are less sensitive than the DC SQUIDs although comparable sensitivity can be reached if the operating frequency is in the gigahertz range.

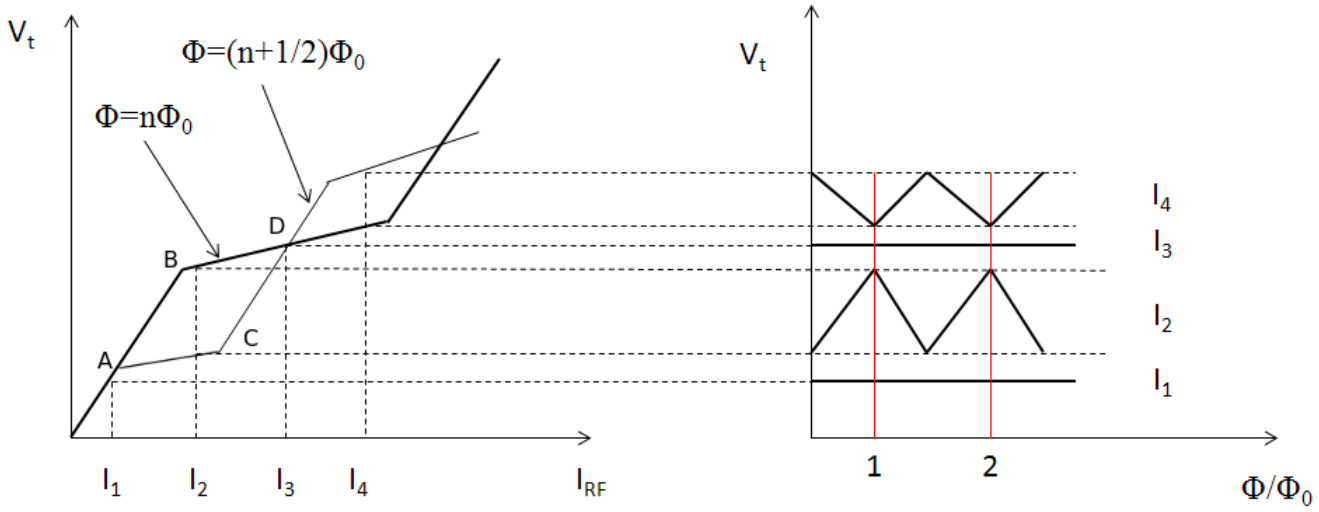

Figure E.9: I-V characteristic of an AC SQUID. The flux-voltage transfer function $V - \Phi$ as a dependence on the I_{RF} current is presented on the right-hand side.

E.4 Principle of operation of a DC SQUID

E.4.1 Structure and Interference equation

The d.c. SQUID is in principle a superconducting loop with two weak links. Integrating along the dashed line from Fig.(E.10) the expression for the phase difference in a two-junction loop is

$$(\theta_{\alpha 2} - \theta_{\alpha 1}) - (\theta_{\beta 2} - \theta_{\beta 1}) = \frac{2\pi\Phi}{\Phi_0}. \tag{E.53}$$

Then using the phase difference equation, we arrive at

$$\phi_\alpha = \phi_\beta + 2\pi\Phi/\Phi_0. \tag{E.54}$$

The total current flowing through this parallel arrangement of Josephson junctions is the sum of

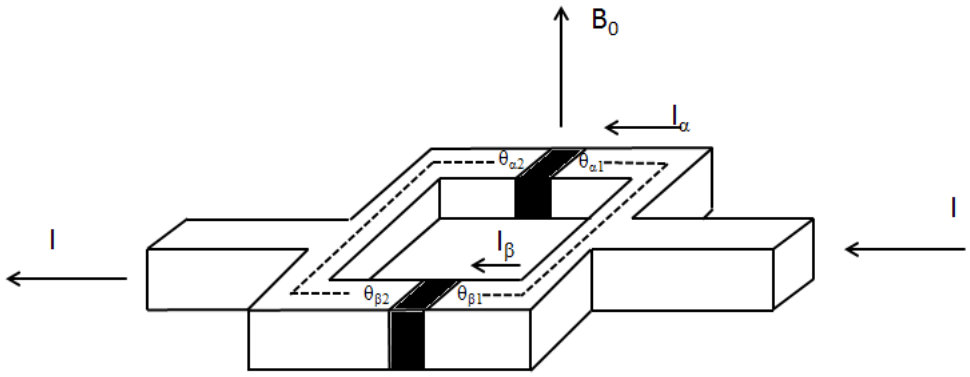

Figure E.10: Schematic structure of a d.c. SQUID loop.

the individual currents in the two sections,

$$I = I_\alpha + I_\beta, \tag{E.55}$$

where each current satisfies the first **Josephson relation** $I = I_{ci}\sin(\phi_i)$,

$$I = I_{c\alpha}\sin(\phi_\alpha) + I_{c\beta}\sin(\phi_\beta) \tag{E.56}$$

$$= I_{c\alpha}\sin(\phi_\alpha) + I_{c\beta}\sin\left[\phi_\alpha - 2\pi\frac{\Phi}{\Phi_0}\right], \tag{E.57}$$

assuming that the critical currents are the same in both arms $I_{c\alpha} = I_{c\beta} = I_c$, the total current is expressed as

$$I = I_c\left(\sin(\phi_\alpha) + \sin\left[\phi_\alpha - \frac{2\pi\Phi}{\Phi_0}\right]\right), \tag{E.58}$$

the value for the maximum current could be found by finding the zero of the first derivative $\mathrm{d}I/\mathrm{d}\phi_\alpha = 0$, the values for the phase differences are then

$$\phi_\alpha = \frac{1}{2}\pi + \frac{\pi\Phi}{\Phi_0}, \tag{E.59}$$

$$\phi_\beta = \frac{1}{2}\pi - \frac{\pi\Phi}{\Phi_0}. \tag{E.60}$$

It can be straightforwardly proven that the obtained extremum is a maximum. The maximum current in a balanced d.c. SQUID is

$$I = 2I_\mathrm{c}\left|\cos(\pi\Phi/\Phi_0)\right|. \tag{E.61}$$

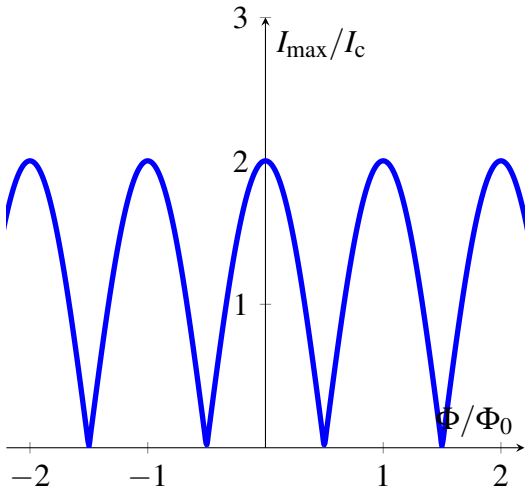

Figure E.11: Maximum current dependence $I_{\max}$ of a balanced two Josephson junctions loop ($I_{\mathrm{c}\alpha} = I_{\mathrm{c}\beta}$) on the normalized applied flux Φ/Φ_0.

The last equation is often referred to as *Josephson loop interference equation*. It has the same mathematical form as the one describing the interference pattern in the famous Young's double slits experiment. When the two current are not equal, it is more intricate to determine the expression for the maximum current. Starting with the system of equations for the total current and its derivative

$$I = I_{\mathrm{c}\alpha}\sin(\phi_\alpha) + I_{\mathrm{c}\beta}\sin\left[\phi_\alpha - 2\pi\frac{\Phi}{\Phi_0}\right], \tag{E.62}$$

$$\frac{\mathrm{d}I}{\mathrm{d}\phi_\alpha} = I_{\mathrm{c}\alpha}\cos(\phi_\alpha) + I_{\mathrm{c}\beta}\cos\left[\phi_\alpha - 2\pi\frac{\Phi}{\Phi_0}\right] = 0. \tag{E.63}$$

Squaring the two equations

$$I_{\max}^2 = I_{c\alpha}^2 \sin^2(\phi_\alpha) + I_{c\beta}^2 \sin^2\left[\phi_\alpha - 2\pi\frac{\Phi}{\Phi_0}\right] + 2I_{c\alpha}I_{c\beta}\sin(\phi_\alpha)\sin\left[\phi_\alpha - 2\pi\frac{\Phi}{\Phi_0}\right], \tag{E.64}$$

$$0 = I_{c\alpha}^2 \cos^2(\phi_\alpha) + I_{c\beta}^2 \cos^2\left[\phi_\alpha - 2\pi\frac{\Phi}{\Phi_0}\right] + 2I_{c\alpha}I_{c\beta}\cos(\phi_\alpha)\cos\left[\phi_\alpha - 2\pi\frac{\Phi}{\Phi_0}\right]. \tag{E.65}$$

Summing the two equation, we will eliminate the dependence on ϕ_α

$$I_{\max}^2 = I_{c\alpha}^2 + I_{c\beta}^2 + 2I_{c\alpha}I_{c\beta}\left[\cos(\phi_\alpha)\cos\left(\phi_\alpha - 2\pi\frac{\Phi}{\Phi_0}\right) + \sin(\phi_\alpha)\sin\left(\phi_\alpha - 2\pi\frac{\Phi}{\Phi_0}\right)\right], \tag{E.66}$$

$$= I_{c\alpha}^2 + I_{c\beta}^2 + 2I_{c\alpha}I_{c\beta}\cos\left(\frac{2\pi\Phi}{\Phi_0}\right), \tag{E.67}$$

$$= I_{c\alpha}^2 + I_{c\beta}^2 + 2I_{c\alpha}I_{c\beta}\cos\left(\frac{2\pi\Phi}{\Phi_0}\right) + 2I_{c\alpha}I_{c\beta} - 2I_{c\alpha}I_{c\beta}, \tag{E.68}$$

$$= (I_{c\alpha} - I_{c\beta})^2 + 2I_{c\alpha}I_{c\beta}\left[1 + \cos\left(\frac{2\pi\Phi}{\Phi_0}\right)\right], \tag{E.69}$$

$$= (I_{c\alpha} - I_{c\beta})^2 + 4I_{c\alpha}I_{c\beta}\cos^2\left(\frac{\pi\Phi}{\Phi_0}\right), \tag{E.70}$$

and we get the final result for the maximum current

$$\boxed{I_{\max} = \left[(I_{c\alpha} - I_{c\beta})^2 + 4I_{c\alpha}I_{c\beta}\cos^2\left(\frac{\pi\Phi}{\Phi_0}\right)\right]^{1/2}} \tag{E.71}$$

E.4.2 Working point and screening parameter

When a d.c. SQUID is unbiased and is under external flux, there is an effective current circulating around the loop

$$I_{\text{circ}} = \frac{1}{2}(I_\alpha - I_\beta), \tag{E.72}$$

which leads to the existence of self-induced flux LI_{circ}. Then the total flux Φ_{t} through the loop is

$$\Phi_{\text{t}} = \Phi_{\text{e}} + LI_{\text{circ}}, \tag{E.73}$$

$$= \Phi_{\text{e}} + \frac{1}{2}L(I_\alpha - I_\beta). \tag{E.74}$$

Furthermore, the phase differences must comply with the flux quantization condition of the loop

$$\phi_\alpha - \phi_\beta = 2\pi\Phi_{\text{t}}/\Phi_0. \tag{E.75}$$

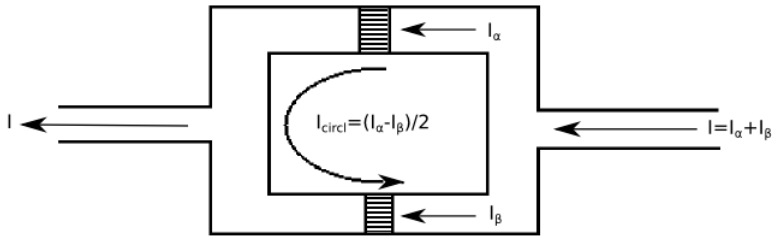

Figure E.12: Circulating supercurrent in a current biased DC SQUID.

Substituting E.75 into E.73 yields for the circulating current

$$I_{\mathrm{circ}} = \frac{(\phi_\alpha - \phi_\beta)\Phi_0 - 2\pi\Phi_{\mathrm{e}}}{2\pi L}. \tag{E.76}$$

The two junctions are described as in E.3.2 by the RCSJ model. The equations for the two junctions are

$$I_\alpha = \frac{1}{2}I + I_{\mathrm{circ}} = I_{\mathrm{c}\alpha}\sin(\phi_\alpha) + V_\alpha/R + C\frac{\mathrm{d}V_\alpha}{\mathrm{d}t}, \tag{E.77}$$

$$I_\beta = \frac{1}{2}I - I_{\mathrm{circ}} = I_{\mathrm{c}\beta}\sin(\phi_\beta) + V_\beta/R + C\frac{\mathrm{d}V_\beta}{\mathrm{d}t}, \tag{E.78}$$

where R_{s} and C are the shunting resistance and capacitance, respectively, and I is the biasing current. Here, we shall assume again that the critical currents for the two junctions are the same $I_{\mathrm{c}\alpha} = I_{\mathrm{c}\beta} = I_{\mathrm{c}}$, as well as equal resistance and capacitance.

$$I = I_\alpha + I_\beta \tag{E.79}$$

$$= \frac{\hbar C}{2e}\frac{\mathrm{d}^2(\phi_\alpha+\phi_\beta)}{\mathrm{d}t^2} + \frac{\hbar}{2eR}\frac{\mathrm{d}(\phi_\alpha+\phi_\beta)}{\mathrm{d}t} + I_{\mathrm{c}}\left(\sin(\phi_\alpha)+\sin(\phi_\beta)\right). \tag{E.80}$$

After introducing the auxiliary variables $\gamma = (\phi_\alpha+\phi_\beta)/2$ and $\zeta = (\phi_\alpha-\phi_\beta)/2$

$$I = \frac{\hbar C}{e}\frac{d^2\gamma}{dt^2} + \frac{\hbar}{eR}\frac{\mathrm{d}\gamma}{\mathrm{d}t} + 2I_{\mathrm{c}}\sin(\gamma)\cos(\zeta) \tag{E.81}$$

$$\frac{I}{2I_{\mathrm{c}}} \equiv i = \frac{\hbar C}{2eI_{\mathrm{c}}}\frac{\mathrm{d}^2\gamma}{\mathrm{d}t^2} + \frac{\hbar}{2eRI_{\mathrm{c}}}\frac{\mathrm{d}\gamma}{\mathrm{d}t} + \sin(\gamma)\cos(\zeta). \tag{E.82}$$

Using the McCumbert parameter $\beta_{\mathrm{c}} = (2\pi I_{\mathrm{c}}R^2C)/(\Phi_0)$ and another time variable $\tau = 2\pi RI_{\mathrm{c}}t/\Phi_0$, we get

$$i = \beta_{\mathrm{c}}\frac{\mathrm{d}^2\gamma}{\mathrm{d}\tau^2} + \frac{\mathrm{d}\gamma}{\mathrm{d}\tau} + \sin(\gamma)\cos(\zeta). \tag{E.83}$$

Continuing in a similar fashion, we take the difference $I_\alpha - I_\beta$ and we obtain another equation

$$\beta_c \frac{d^2\zeta}{d\tau^2} + \frac{d\zeta}{d\tau} + \cos(\gamma)\sin(\zeta) - \frac{2}{\pi\beta_L}\left(\zeta - \frac{\pi\Phi_e}{\Phi_0}\right) = 0, \tag{E.84}$$

where we used the definition for the screening parameter $\beta_L = 2LI_c/\Phi_0$, and the expression for the circulating current I_{circ} from Eq.(E.76). In this way, we arrived at a system of coupled differential equations for the variables γ and ζ

$$0 = \beta_c \frac{d^2\zeta}{d\tau^2} + \frac{d\zeta}{d\tau} + \cos(\gamma)\sin(\zeta) - \frac{2}{\pi\beta_L}\left(\zeta - \frac{\pi\Phi_e}{\Phi_0}\right), \tag{E.85}$$

$$i = \beta_c \frac{d^2\gamma}{d\tau^2} + \frac{d\gamma}{d\tau} + \sin(\gamma)\cos(\zeta). \tag{E.86}$$

We refer again to a simplified model where the circulating current is zero $I_{circ} = 0$, thus $\Phi_t = \Phi_e$ and $\zeta = (\phi_\alpha - \phi_\beta)/2 = \pi\Phi_e/\Phi_0$. Then from Eq.(E.86), we obtain an equation similar to the one for an a.c. SQUID in the RCSJ model

$$I = 2I_c\cos(\pi\Phi_e/\Phi_0)\sin(\gamma) + \frac{\Phi_0}{2\pi}\frac{2}{R}\frac{d\gamma}{d\tau} + \frac{\Phi_0}{2\pi}2C\frac{d^2\gamma}{d\tau^2}. \tag{E.87}$$

Hence, the d.c. SQUID behaves, in a crude approximation, as an a.c. SQUID with shunting resistance $R/2$ and capacitance $2C$. Then the current-voltage characteristics in the limit $\beta_c \ll 1$ for $I > I_c$ is

$$V = \frac{R}{2}\sqrt{I^2 - I_c^2}, \tag{E.88}$$

in this way we could obtain the voltage-to-flux transformation characteristic. Consider the derivative $\partial V/\partial\Phi_e$, and find the optimal working point

$$\frac{\partial V}{\partial \Phi_e} = -\frac{2\pi I_c R}{\Phi_0}\frac{I_c\sin(\pi\Phi_e/\Phi_0)\cos(\pi\Phi_e/\Phi_0)}{\sqrt{I^2 - I_c^2}}. \tag{E.89}$$

By taking the derivative $\partial/\partial\Phi_e(\partial V/\partial\Phi_e) = 0$, the point of maximum flux-to-voltage transfer could be found

$$\boxed{\frac{\Phi_e}{\Phi_0} = \left(\frac{n}{2} + \frac{1}{4}\right).} \tag{E.90}$$

Although the above calculation is overly simplified, it gives the correct result for the working points. If the system of coupled differential equations is solved numerically the full picture of the transfer function could be obtained(Fig. (E.14)). A d.c. SQUID is operated under current bias and under externally applied magnetic flux. The voltage change is measured and it determines the applied flux.

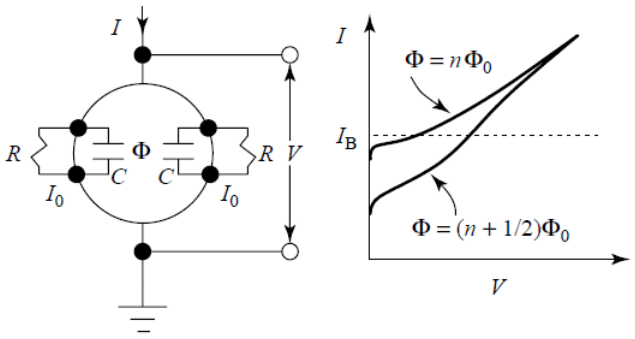

Figure E.13: (a) - The d.c. SQUID with the RCSJ circuit model; (b) - I-V characteristics of a d.c. SQUID in the cases of integer and half-integer applied flux.

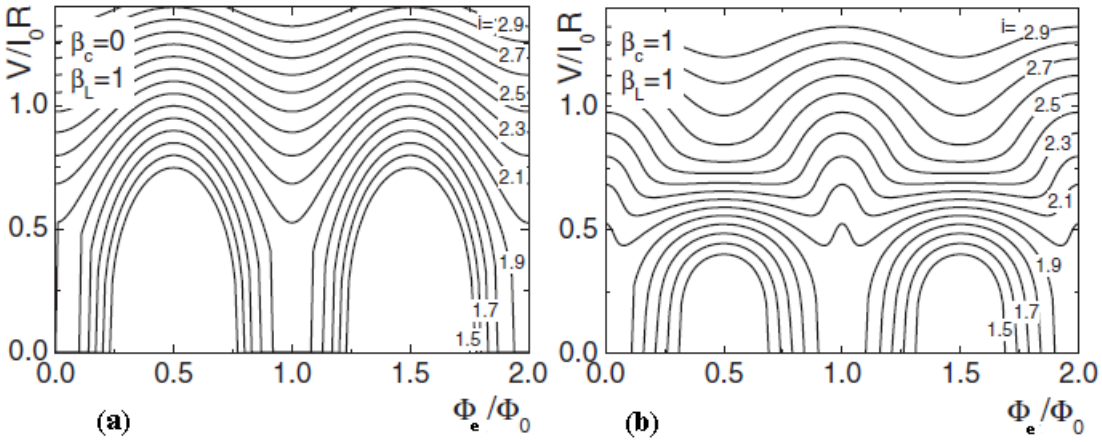

Figure E.14: Numerical simulation for the flux-voltage transfer function of a d.c. SQUID. For two set of parameter β_L and β_C, the dependence on the reduced current $i = I/2I_0$ is studied. (a) $\beta_L = 1$, $\beta_C = 0$; (b) - $\beta_L = 1$, $\beta_C = 1$. Obviously, the quality of the transfer degrades as the McCumbert parameter β_C is increased. The picture is taken from [62].

In the readout electronic circuits, described in Sec.(E.5), it is explained how the d.c. SQUID is operated at optimal working conditions.

E.5 Measuring principles, gradiometers, flux-locked loops

E.5.1 Different structure of weak links

Although the original Josephson prediction was for tunnelling through a thin insulating layer, nowadays, the "barrier" is more generally referred to as a "weak-link". When the critical current in the contact region is much lower than these in the superconductors, the contact is called a weak-link. The weak-link could be just a point-contact between two superconductor, where a sharpened superconducting wire is pressed lightly on another superconductor. This device structure is particularly useful because the resistance and capacitance of the junction are negligible, and this leads to a non- hysteretic I-V curve. The I-V curve of a Josephson junction was explained in Sec. (E.3.2). Another used device structure is the microbridge weak link, where the connection between the two superconductor is a narrowing of the conduction channel. A problem is that the shunting resistance is temperature dependant because of the temperature dependence of the coherence length in superconductors $\xi(T)$. Finally, there is the thin film tunnel junction technique which uses a thin insulating layer as a separator between the two superconductors. Nowadays, because of the advances in thin-film deposition, thin-film tunnel junctions are the only practical devices for low-T_c SQUID technology [62]. In high- temperature superconducting SQUIDS using $YBa_2Cu_3O_{7-\delta}$ (YBCO), naturally occurring weak links or microbridges patterns in thin films are the used type of junctions. The production of high-quality high- temperature superconductors is nontrivial. Usually regrinding, compressing, and sintering repeatedly are necessary. The resulting bulk material is a fine-grained ceramic, brittle, with high-density of defects and grain boundaries. A contemporary method, specially for high-T_c superconductors, utilizes their very short coherence length ξ. A very narrow interruption of superconducting properties could be achieved by depositing the material across a naturally occurring grain boundary in a substrate like $SrTiO_3$. The superconducting film forms defects along the length of the grain boundary. Thus the grain boundary forms a weak link between the two parts of the superconducting film. When it comes to grain boundary junctions, a major problem is the possible high reduction of critical current. Due to the $d_{x^2-y^2}$ character of the wavefunction in high-T_c ceramics, grains misorientation at the boundaries represent an obstacle for the current transport. The importance here is the reproducibility of critical current density properties for different grain boundary junctions.

E.5.2 Measurement principles

E.5.2.1 AC SQUID basic readout

In its simplest form, the readout scheme consists of an a.c. SQUID inductively coupled via a mutual inductance M to a RF current-driven tank L_TC_T-circuit. An oscillatory flux modulation

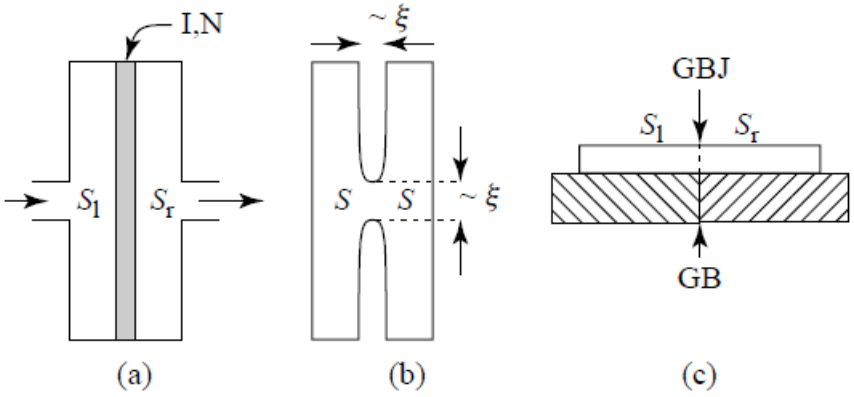

Figure E.15: Different type of weak links. (a) - insulating barrier between two superconductors; (b) - microbridge; (c) - grain boundary junction. Methods (b) and (c) are specially used in high-T_c superconductors. The picture is taken from [10].

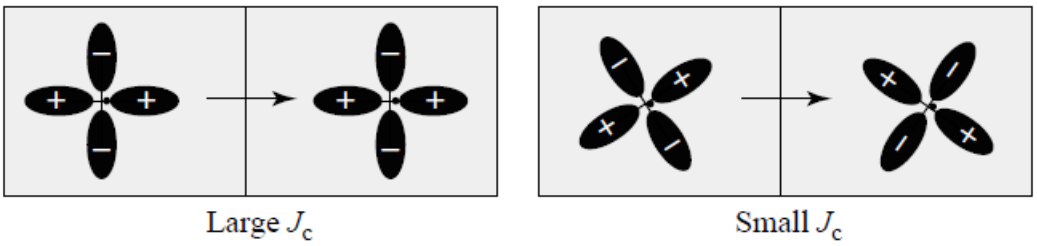

Figure E.16: Different type of weak links. (a) - insulating barrier between two superconductors; (b) - microbridge; (c) - grain boundary junction. Methods (b) and (c) are specially used in high-T_c superconductors. The picture is taken from [10].

is applied to the SQUID ring via the tank inductance L_T normally in the range 20-30 MHz [106]. Then the current circulating in the SQUID ring is $MQI_T \sin(\omega_0 t)$, where Q is the quality factor of the tank circuit, I_T is the current, and ω_0 is the set frequency. The DC flux Φ_e, which must be measured, is fed through another input coil coupled to the SQUID loop. **To measure a change in Φ_e, it is sufficient to amplify and detect any change in the RF voltage in the resonant circuit.** Let us assume that at the beginning $\Phi_e = n\Phi_0$, and the current I_t is set too low to produce internal flux transitions. When Φ_e is altered to $(n+1/2)\Phi_0$, the SQUID undergoes changes in its internal flux state. The jumping between two internal flux states is in effect a transition from one quasilinear region on the Φ_t/Φ_e characteristic to another quasilinear branch on Fig.(E.8). These changes lead to energy dissipation, and these energy changes are drawn from the energy in the tank circuit. As a result, there will be a drop in the mean voltage amplitude in the resonance circuit. After a low-noise amplification, a direct voltage which is periodic in Φ_e could be detected.

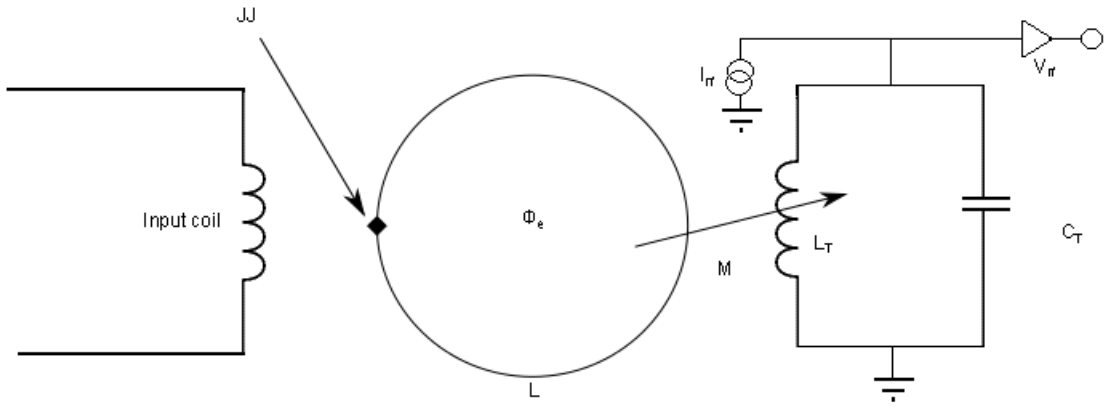

Figure E.17: Basic readout circuit of an a.c. SQUID.

E.5.2.2 DC SQUID basic readout

The DC SQUID basic readout circuit is much simpler than the one for an AC SQUID. The essential elements of the detection system of a DC SQUID are presented in Fig. (E.18). First of all, a means of direct current biasing the junctions, then, a low-noise amplifier detects the voltage change through the junctions, which is the result of the externally applied flux Φ_e. The DC SQUID is biased by a constant current into the finite voltage regime. The output voltage is a periodic function of the applied flux. The current bias point which gives the system its maximum gain, which is in effect the first derivative $\partial V/\partial\Phi$ Eq.(E.89), varies as the applied flux changes. Obviously, a variable gain is not a desired characteristic. In real d.c. SQUIDs a gain-linearising circuit, based on negative feedback is used.

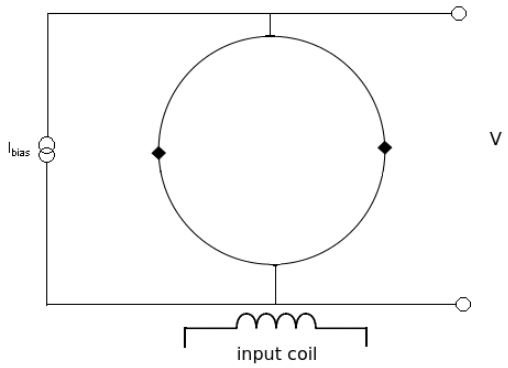

Figure E.18: Basic readout circuit of an d.c. SQUID.

E.5.3 Flux-locked loops

Flux-locked loops are the contemporary electronic circuits used for detection in SQUID-based sensors. In effect, they are just one additional feedback supplied in the above circuits. In a nutshell,

the flux through the SQUID is kept constant with modulation. The aim is to operate the SQUID at a maximum of the flux-voltage transfer function.

E.5.3.1 RF SQUID flux-locked circuit

The triangular response shown in Fig.(E.9) means that the RF SQUID is in effect a linear detector of magnetic flux when the changes are in the range $\pm\Phi_0$. In order to make this detector linear in a larger range, a negative feedback is used. A flux modulation of amplitude $\pm\Phi_0/2$ is applied via the tank circuit coil. The detected RF voltage is fed to a lock-in amplifier, referenced by the modulation signal. The output can be used to apply feedback flux, via a feedback resistor and the RF tank coil.

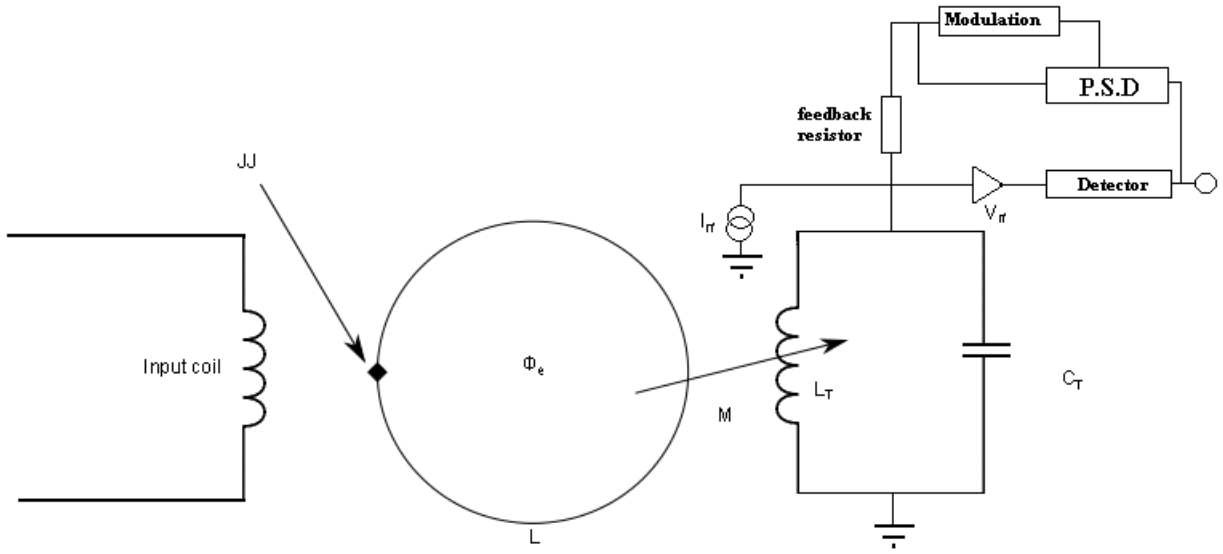

Figure E.19: Flux-locked circuit of an a.c. SQUID.

E.5.3.2 DC SQUID flux-locked circuit

If a DC SQUID is biased with only a direct current while a linear flux change is applied, the voltage across the ring varies periodically as a function of the flux. The variation is not strictly sinusoidal, and depends on the parameters of the SQUID Fig.(E.14). A gain-linearising circuit with negative feedback is used in real SQUIDs. In addition to the input coil, a second modulation coil is coupled to the superconducting ring. This coil is flux modulated with amplitude $\Phi_0/2$ and frequency ω_0. The voltage output of the SQUID ring is amplified, phase-sensitively detected (P.S.D), and fed back into the same coil. The feedback ensures that the sum of the applied flux and the fed-back flux is constant, and maintained at an optimal working point in accordance with Eq.(E.89). In this way, the gain of the device is linearised.

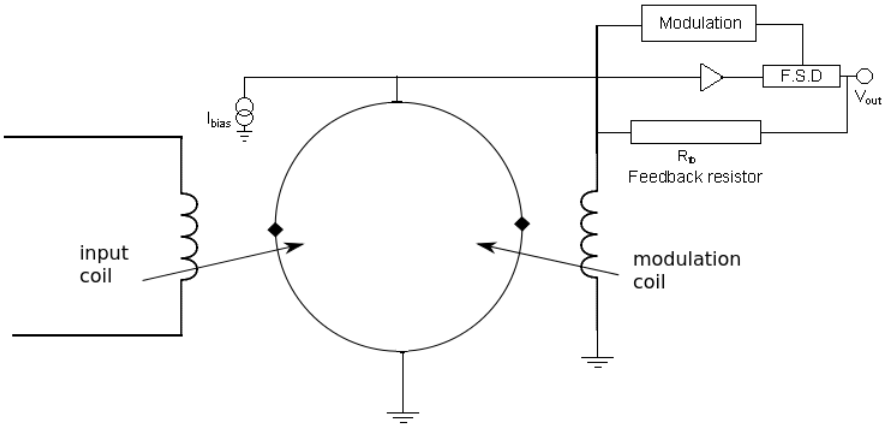

Figure E.20: Flux-locked circuit of a d.c. SQUID.

E.6 Sensitivity of SQUIDs

E.6.1 Sensitivity, noise and gain of an a.c. SQUID

The main noise contributors in an an a.c. SQUID-based detector are the parts from its readout circuit. Let us consider a linear approximation for the behaviour of $\Phi_e(\Phi_t)$:

$$\Phi_t = \Phi_e + LI_s \quad for \quad \Phi_e \approx n\Phi_0, \tag{E.91}$$

where I_s is the supercurrent circulating in the SQUID loop. If the mutual inductance between the ring and the input coil is M, and the current flowing in the pickup coil is I, then the externally applied field to the SQUID is $\Phi_e(t) = MI(t)$. But the flux between the input coil and superconducting loop must be null, hence

$$LI_s + MI = 0 \Rightarrow I_s = -MI/L. \tag{E.92}$$

While n is fixed because the current I is not sufficient to cause transitions, there will be just two contributions to the voltage V across the tank inductor are

$$V = i\omega L_T I + I\omega M I_s = i\omega L_T I(1-k^2), \tag{E.93}$$

where k is the coupling between the ring and the coil, expressed as $M^2 = k^2 L L_T$. The ring is normally weakly coupled to the tank coil $k^2 \ll 1$ (the condition $k^2 Q \approx 1$ should be satisfied for reasons that will be clarified). The increase of the RF current in the tank coil at the beginning is

$$I = Q\,[1 - exp(\omega_0 t/2Q)]\, I_0 \sin(\omega_0 t). \tag{E.94}$$

When the current exceeds the threshold $I_c L/M$, then $I_s > I_c$, the SQUID ring makes a transition to the neighbouring internal flux state (n+1), in a time of order L/R. This time is typically much shorter than the RF oscillation. Hence, the transition happens at constant flux through the resonant tank circuit. At any time, the total flux threading the tank coil is

$$\Phi_t = L_T I_T + M I_s - I_T M^2/L. \tag{E.95}$$

When the flux through the SQUID ring changes with $1\Phi_0$, the supercurrent change is $|\Delta I_s| = \Phi_0/L$. The resulting change in the inductor current is

$$|\Delta I_T| = \Phi_0 k^2/(M(1-k^2)). \tag{E.96}$$

Half a cycle later the ring undergoes another flux change in the opposite direction. The average voltage across the tank inductor is

$$\langle V \rangle = \omega_0 L_T (1-k^2) L I_c/M = \omega L Q I_0/\sqrt{2}. \tag{E.97}$$

So far, we assumed that the applied flux consists only of alternating term. When there is a time-independent term $\tilde{\Phi}_e$, the onset of internal flux state transitions will occur when the the sum of the alternating and constant term is LI_c. It could be shown that, this happens at

$$|V| = (\omega L_T/M)(1-k^2)(LI_c - \tilde{\Phi}_e). \tag{E.98}$$

The voltage modulation amplitude dV which is produced as Φ_e is changed could be expressed as

$$\mathrm{d}V = \omega_0 \Phi_0 L_T (1-k^2)/2M, \tag{E.99}$$

where $\Phi_0/2$ is the supposed flux change. It could be mistakenly considered that the modulation could be unlimitedly increased by decreasing the mutual inductance M. In fact, if the coupling k is made too small, then the tank circuit will be less sensitive to the dissipated energy. The above equation does not show that, actually, k and Q are interdependent. The slope of I-V curve between between constant voltage steps is

$$\frac{V}{I_c} = \omega_0 L_T Q \sqrt{2}, \tag{E.100}$$

and the length of each constant voltage step is

$$\Delta I_c = 2\Phi_0 k^2/M(1-k^2). \tag{E.101}$$

If we try to match the above two conditions, so that the point B, which is the start of the step for integer quanta, lies above the end of the step for half- integer quanta, then the optimum is $k^2Q \approx 1$. Further reduction of the coupling k will move point B to the right and then the full voltage separation between the steps will not be available. The condition $k^2Q \approx 1$ maximises the flux-voltage transfer ratio $\partial V/\partial\Phi$ for an AC SQUID. For a change in the flux $\mathrm{d}\Phi_\mathrm{e}$ at the input, the available energy change is $\mathrm{d}E = (\mathrm{d}\Phi^2)/2L$, and this change happens in a bandwidth $\mathrm{d}f$, then the available signal power is $\mathrm{d}E \times \mathrm{d}f$. The available output power from this change is

$$\mathrm{d}P = \mathrm{d}V^2/2R = (\mathrm{d}V/\mathrm{d}\Phi)^2(\mathrm{d}\Phi^2/2R), \tag{E.102}$$

using the relation for a quality factor $Q = \omega_0 L/R$ for a parallel circuit, we get the power gain

$$g = \omega_0 Q^2/\mathrm{d}f. \tag{E.103}$$

For an RF SQUID working at frequency 30 MHz with Q=50, and in a signal bandwidth 1kHz the power gain is 5×10^8[106]. This is a remarkable number, which explains why RF SQUIDs could be used as amplifiers. Taking into account the condition $k^2Q \approx 1$, and a typical value of $Q \approx 50-100$, it is clear that $k^2 \ll 1$, and we can assume that $(1-k^2) \approx 1$ in Eq.(E.99). The transfer function for an AC SQUID is then

$$V_\Phi = \partial V/\partial\Phi = \omega_0 L_\mathrm{T}/M. \tag{E.104}$$

The two main contributors to the noise characteristic are the superconducting loop noise itself and the amplifier voltage noise. Then the flux sensitivity is

$$S_\Phi = S_\mathrm{loop} + S_\mathrm{amp}/V_\Phi^2. \tag{E.105}$$

In the next subsection (E.6.2), it will be estimated that the flux sensitivity of the loop itself is a few $10^{-6}\Phi_0/\sqrt{Hz}$. Typical value for a commercially available preamplifier voltage noise is $1nV/\sqrt{Hz}$. The transfer coefficient is normally $V_\Phi \approx 100\mu V/\Phi_0$. As a result, the amplifier flux noise contribution is $10^{-5}\Phi_0/\sqrt{Hz}$. Typically, the sensitivity of an AC SQUID is limited by the properties of the readout circuits.

E.6.2 Sensitivity, noise and gain of a d.c. SQUID

For RF SQUIDs, the external circuit noise is almost always much more significant than the noise of the SQUID ring itself. For DC SQUIDs, the situation is usually the opposite. The reason is that the preamplifier noise could be suppressed by using a step-up transformer at cryogenic temperature. Extensive review of all the noise suppression means could be found in [62]. Then,

the two main physical effect are the Nyquist voltage noise and the current fluctuation related to the normal state resistance of the junctions. Two identical Josephson junctions with equal resistance R have thermal noise voltage spectrum

$$S(V) = 4kTR/2, \tag{E.106}$$

and furthermore, there will be current fluctuation in the ring with spectral density

$$S(I) = 8kT/R, \tag{E.107}$$

and in approximation, we could assume that these noise contributions are uncorrelated. Although, in practice, circulating noise current will generate new voltage contribution across the junctions, and vice versa. The flux spectral noise density $S(\Phi)$ is simply related to the minimum detectable energy in unit bandwidth dE and to $S(V)$ and $S(I)$:

$$dE = S(\Phi)/2L = \left(\frac{S(V)}{(\partial V/\partial \Phi)^2} + \frac{S(I)}{(\partial I/\partial \Phi)^2} \right) /2L. \tag{E.108}$$

In principle, the above analysis must be carried out by numerical simulation of the RCSJ, but this time with adding the voltage contributing terms. A simple solution which is correct within a small numerical factor could be given. It could be shown that the maximum change in critical current which can be produced by an applied flux is $\Phi_0/2L$, and this happens when the flux is changed by $\Phi_0/2$. Then, we assume that $\partial I/\partial \Phi \approx 1/L$. In a similar fashion, it could be estimated

$$\partial V/\partial \Phi \approx (\partial V/\partial I)(\partial I/\partial \Phi) = R/2L. \tag{E.109}$$

Plugging back these two expressions into Eq.(E.108), we obtain the minimum detectable energy dE determined by the thermal fluctuations in the SQUID loop

$$\mathrm{d}E \approx 8kTL/R. \tag{E.110}$$

Then the minimum detectable energy could be converted to minimum detectable flux by $\mathrm{d}E = d\Phi^2/2L$, hence

$$\boxed{d\Phi = 4L\sqrt{kT/R}.} \tag{E.111}$$

For a typical SQUID with inductance $L \sim 1nH$, and resistance $R \sim 1\Omega$, operating at $T = 4.2K$, a sensitivity $\mathrm{d}\Phi \sim 10^{-5}\Phi_0 Hz^{-1/2}$ is attainable. Experimental work at IBM during 1980s with impedance of the loops as low as few pH confirmed the validity of the above expression. An important point to be made is that the sensitivity is $\mathrm{d}\Phi \sim 1/\sqrt{R}$ whereas the McCumbert's parameter

$\beta_c \sim R^2$. Hence, the production of extremely low resistance junction is not desired because that would sacrifice sensitivity. The gain of a d.c. SQUID is more complicated because of the non-linear behaviour of the flux-to-voltage transfer function. Nevertheless, a simple treatment is given by J C Gallop [106]. Consider that a the d.c. SQUID is biased by a direct current $I > I_{c\alpha} + I_{c\beta}$ (which is bigger than the sum of the critical currents for the two junctions). A time- average voltage $\langle V \rangle$ exists across the junctions. The application of external flux leads to flow of circulating current whose frequency is determined by $\langle V \rangle$ in accordance with the **second Josephson relation**. If the junctions have resistance R, and the loop induction is L, above a frequency $f \sim R/\pi L$, the circulating supercurrent will be damped by the significant impedance. The total voltage change resulting from the flux change Φ_0 is

$$I_{\rm circ} R \sim \Delta V < \Phi_0 R/\pi L. \tag{E.112}$$

Hence, the maximum circulating current is $I_{\rm circ}^{\rm max} \lesssim \Phi_0/\pi L$. When an oscillating signal $\Phi_0 \sin(\omega t)$ is supplied, the input energy per one cycle is $E_{\rm in} = \Phi_0^2/2L$, and the input power is then $P_{\rm in} = \omega E_{\rm in} = \omega\Phi_0^2/2L$. But the output power is

$$I_{\rm circ}^{\rm max} \Delta V/2 \sim (I_{\rm circ}^{\rm max})^2 R \sim \frac{R\Phi_0^2}{2\pi^2 L^2}. \tag{E.113}$$

Then the limit on the power gain g is

$$g = \frac{P_{\rm out}}{P_{\rm in}} \lesssim \frac{R}{\pi^2 L\omega}. \tag{E.114}$$

Sometimes, the maximum frequency $\omega_p = R/L$ is referred to as the pump frequency of the d.c. SQUID.

Bibliography

[1] M Abid, H Lassri, R Krishnan, M Nývlt, and Šišnovský. Magnetic studies of Fe/Pt multilayers. *Journal of Magnetism and Magnetic Materials*, 214(1 - 2):99 – 104, 2000.

[2] A. A. Abrikosov. On the magnetic properties of superconductors of the second group. *JETP*, 5:1174–1182, 1957.

[3] Tatsushi Akazaki, Takehito Yokoyama, Yukio Tanaka, Hiro Munekata, and Hideaki Takayanagi. Evaluation of spin polarization in p-$In_{0.96}Mn_{0.04}As$ using Andreev reflection spectroscopy including inverse proximity effect. *Phys. Rev. B*, 83:155212, Apr 2011.

[4] G A Perez Alcazar and E Galvao da Silva. Mössbauer effect study of magnetic properties of $Fe_{1-q}Al_q$, $0 < q \leq 0.5$, alloys in the disordered phase. *Journal of Physics F: Metal Physics*, 17(11):2323, 1987.

[5] Gwang-Guk An, Ja-Bin Lee, Seung-Mo Yang, Jae-Hong Kim, Woo-Seong Chung, and Jin-Pyo Hong. Highly stable perpendicular magnetic anisotropies of CoFeB/MgO frames employing W buffer and capping layers. *Acta Materialia*, 87:259 – 265, 2015.

[6] P. W. Anderson and Y. B. Kim. Hard Superconductivity: Theory of the Motion of Abrikosov Flux Lines. *Rev. Mod. Phys.*, 36:39–43, Jan 1964.

[7] Tsuneya Ando, Yukio Matsumoto, and Yasutada Uemura. Theory of Hall Effect in a Two-Dimensional Electron System. *Journal of the Physical Society of Japan*, 39(2):279–288, 1975.

[8] Yuichiro Ando, Takahiro Hamasaki, Takayuki Kurokawa, Kouki Ichiba, Fan Yang, Mario Novak, Satoshi Sasaki, Kouji Segawa, Yoichi Ando, and Masashi Shiraishi. Electrical detection of the spin polarization due to charge flow in the surface state of the topological insulator $Bi_{1.5}Sb_{0.5}Te_{1.7}Se_{1.3}$. *Nano Letters*, 14(11):6226–6230, 2014. PMID: 25330016.

[9] AF Andreev. Thermal conductivity of the intermediate state of superconductors. *Zh. Eksperim. i Teor. Fiz.*, 46, 1964.

[10] Kristian Fossheim ans Asle Sudbo. *Superconductivity: Physics and Applications*. John Wiley and Sons Ltd., 2004.

[11] T. Arakane, T. Sato, S. Souma, K. Kosaka, K. Nakayama, M. Komatsu, T. Takahashi, Zhi Ren, Kouji Segawa, and Yoichi Ando. Tunable Dirac cone in the topological insulator $Bi_{2-x}Sb_xTe_{3-y}Se_y$. *Nat Commun*, 3:636, Jan 2012.

[12] Anthony Arrott and Hiroshi Sato. Transitions from ferromagnetism to antiferromagnetism in iron-aluminum alloys. experimental results. *Phys. Rev.*, 114:1420–1426, Jun 1959.

[13] M. Asen, K. Keck, and P. Bouillon. Overheating effects in metallic point contacts. *Solid State Communications*, 70(9):869 – 871, 1989.

[14] M. N. Baibich, J. M. Broto, A. Fert, F. Nguyen Van Dau, F. Petroff, P. Etienne, G. Creuzet, A. Friederich, and J. Chazelas. Giant magnetoresistance of (001)Fe/(001)Cr magnetic superlattices. *Phys. Rev. Lett.*, 61:2472–2475, Nov 1988.

[15] Lakhan Bainsla, A.I. Mallick, A.A. Coelho, A.K. Nigam, B.S.D.Ch.S. Varaprasad, Y.K. Takahashi, Aftab Alam, K.G. Suresh, and K. Hono. High spin polarization and spin splitting in equiatomic quaternary CoFeCrAl heusler alloy. *Journal of Magnetism and Magnetic Materials*, 394:82 – 86, 2015.

[16] Lakhan Bainsla, K. G. Suresh, A. K. Nigam, M. Manivel Raja, B. S. D. Ch. S. Varaprasad, Y. K. Takahashi, and K. Hono. High spin polarization in CoFeMnGe equiatomic quaternary Heusler alloy. *Journal of Applied Physics*, 116(20), 2014.

[17] Rantej Bali, Sebastian Wintz, Falk Meutzner, René Hübner, Richard Boucher, Ahmet A. Ünal, Sergio Valencia, Andreas Neudert, Kay Potzger, Jürgen Bauch, Florian Kronast, Stefan Facsko, Jürgen Lindner, and Jürgen Fassbender. Printing nearly-discrete magnetic patterns using chemical disorder induced ferromagnetism. *Nano Letters*, 14(2):435–441, 2014.

[18] Do Bang, T. Nozaki, D. D. Djayaprawira, M. Shiraishi, Y. Suzuki, A. Fukushima, H. Kubota, T. Nagahama, S. Yuasa, H. Maehara, K. Tsunekawa, Y. Nagamine, N. Watanabe, and H. Itoh. Inelastic tunneling spectra of MgO barrier magnetic tunneling junctions showing large magnon contribution. *Journal of Applied Physics*, 105(7), 2009.

[19] John Bardeen and M. J. Stephen. Theory of the motion of vortices in superconductors. *Phys. Rev.*, 140:A1197–A1207, Nov 1965.

[20] L. Berger. Side-Jump Mechanism for the Hall Effect of Ferromagnets. *Phys. Rev. B*, 2:4559–4566, Dec 1970.

[21] L. Berger. Emission of spin waves by a magnetic multilayer traversed by a current. *Phys. Rev. B*, 54:9353–9358, Oct 1996.

[22] Stephan Berko and Joel Zuckerman. Polarized positron annihilation in ferromagnets. *Phys. Rev. Lett.*, 13:339–341, Sep 1964.

[23] Stephan Berko and Joel Zuckerman. Polarized positron annihilation in ferromagnets. *Phys. Rev. Lett.*, 14:89–89, Jan 1965.

[24] R. Bernal-Correa, A. Rosales-Rivera, P. Pineda-Gómez, and N.A. Salazar. Structural and magnetic properties of $Fe_{60}Al_{40}$ alloys prepared by means of a magnetic mill. *Journal of Alloys and Compounds*, 495(2):491 – 494, 2010. 15th International Symposium on Metastable, Amorphous and Nanostructured Materials.

[25] B. Andrei Bernevig, Taylor L. Hughes, and Shou-Cheng Zhang. Quantum Spin Hall Effect and Topological Phase Transition in HgTe Quantum Wells. *Science*, 314(5806):1757–1761, 2006.

[26] B. Andrei Bernevig and Shou-Cheng Zhang. Quantum Spin Hall Effect. *Phys. Rev. Lett.*, 96:106802, Mar 2006.

[27] Davide Betto, Naganivetha Thiyagarajah, Yong-Chang Lau, Cinthia Piamonteze, Marie-Anne Arrio, Plamen Stamenov, J. M. D. Coey, and Karsten Rode. Site-specific magnetism of half-metallic Mn_2Ru_xGa thin films determined by x-ray absorption spectroscopy. *Phys. Rev. B*, 91:094410, Mar 2015.

[28] G. Binasch, P. Grünberg, F. Saurenbach, and W. Zinn. Enhanced magnetoresistance in layered magnetic structures with antiferromagnetic interlayer exchange. *Phys. Rev. B*, 39:4828–4830, Mar 1989.

[29] Randall C. Black and Frederick C. Wellstood. *Measurements of Magnetism and Magnetic Properties of Matter*, pages 391–440. Wiley-VCH Verlag GmbH and Co. KGaA, 2006.

[30] G. E. Blonder and M. Tinkham. Metallic to tunneling transition in Cu-Nb point contacts. *Phys. Rev. B*, 27:112–118, Jan 1983.

[31] G. E. Blonder, M. Tinkham, and T. M. Klapwijk. Transition from metallic to tunneling regimes in superconducting microconstrictions: Excess current, charge imbalance, and supercurrent conversion. *Phys. Rev. B*, 25:4515–4532, Apr 1982.

[32] M Bode. Spin-polarized scanning tunnelling microscopy. *Reports on Progress in Physics*, 66(4):523, 2003.

[33] M. Bode, M. Getzlaff, and R. Wiesendanger. Spin-Polarized Vacuum Tunneling into the exchange-split surface state of Gd(0001). *Phys. Rev. Lett.*, 81:4256–4259, Nov 1998.

[34] M. Bode, M. Getzlaff, and R. Wiesendanger. Quantitative aspects of spin-polarized scanning tunneling spectroscopy of Gd(0001). *Journal of Vacuum Science and Technology A*, 17(4):2228–2232, 1999.

[35] Stefano Bonetti, Pranaba Muduli, Fred Mancoff, and Johan Åkerman. Spin torque oscillator frequency versus magnetic field angle: The prospect of operation beyond 65 GHz. *Applied Physics Letters*, 94(10), 2009.

[36] K. Borisov, J. Alaria, J. M. D. Coey, and P. Stamenov. High field magnetotransport and point contact andreev reflection measurements on cucr2se4 and cucr2se3brâĂŤdegenerate magnetic semiconductor single crystals. *Journal of Applied Physics*, 115(17):17C717, 2014.

[37] K. Borisov, D. Betto, Y.-C. Lau, C. Fowley, A. Titova, N. Thiyagarajah, G. Atcheson, J. Lindner, A. M. Deac, J. M. D. Coey, P. Stamenov, and K. Rode. Tunnelling magnetoresistance of the half-metallic compensated ferrimagnet Mn_2Ru_xGa. *Applied Physics Letters*, 108(19), 2016.

[38] K. Borisov, C.-Z. Chang, J. S. Moodera, and P. Stamenov. High Fermi-level spin polarization in the $(Bi_{1-x}Sb_x)_2Te_3$ family of topological insulators: A point contact Andreev reflection study. *Phys. Rev. B*, 94:094415, Sep 2016.

[39] V. Braccini, A. Gurevich, J. E. Giencke, M. C. Jewell, C. B. Eom, D. C. Larbalestier, A. Pogrebnyakov, Y. Cui, B. T. Liu, Y. F. Hu, J. M. Redwing, Qi Li, X. X. Xi, R. K. Singh, R. Gandikota, J. Kim, B. Wilkens, N. Newman, J. Rowell, B. Moeckly, V. Ferrando, C. Tarantini, D. Marré, M. Putti, C. Ferdeghini, R. Vaglio, and E. Haanappel. High-field superconductivity in alloyed MgB_2 thin films. *Phys. Rev. B*, 71:012504, Jan 2005.

[40] Werner Brandt and Robert Paulin. Positron implantation-profile effects in solids. *Phys. Rev. B*, 15:2511–2518, Mar 1977.

[41] W.R. Branford, S.B. Roy, S.K. Clowes, Y. Miyoshi, Y.V. Bugoslavsky, S. Gardelis, J. Giapintzakis, and L.F. Cohen. Spin polarisation and anomalous Hall effect in NiMnSb films. *Journal of Magnetism and Magnetic Materials*, 272âĂŞ276, Supplement:E1399 – E1401, 2004. Proceedings of the International Conference on Magnetism (ICM 2003).

[42] W. F. Brinkman, R. C. Dynes, and J. M. Rowell. Tunneling conductance of asymmetrical barriers. *Journal of Applied Physics*, 41(5):1915–1921, 1970.

[43] Christoph Brune, Andreas Roth, Hartmut Buhmann, Ewelina M. Hankiewicz, Laurens W. Molenkamp, Joseph Maciejko, Xiao-Liang Qi, and Shou-Cheng Zhang. Spin polarization of the quantum spin Hall edge states. *Nat Phys*, 8(6):485–490, Jun 2012.

[44] Ronald C. Bruno and Brian B. Schwartz. Magnetic field splitting of the density of states of thin superconductors. *Phys. Rev. B*, 8:3161–3178, Oct 1973.

[45] Y. Bugoslavsky, Y. Miyoshi, S. K. Clowes, W. R. Branford, M. Lake, I. Brown, A. D. Caplin, and L. F. Cohen. Possibilities and limitations of point-contact spectroscopy for measurements of spin polarization. *Phys. Rev. B*, 71:104523, Mar 2005.

[46] W. H. Butler, X.-G. Zhang, T. C. Schulthess, and J. M. MacLaren. Spin-dependent tunneling conductance of Fe|MgO|Fe sandwiches. *Phys. Rev. B*, 63:054416, Jan 2001.

[47] A. I. Buzdin. Proximity effects in superconductor-ferromagnet heterostructures. *Rev. Mod. Phys.*, 77:935–976, Sep 2005.

[48] J. W. Cable, L. David, and R. Parra. Neutron study of local environment effects and magnetic clustering in $Fe_{0.7}Al_{0.3}$. *Phys. Rev. B*, 16:1132–1137, Aug 1977.

[49] Sandor Caplan and Gerald Chanin. Critical-field study of superconducting aluminum. *Phys. Rev.*, 138:A1428–A1433, May 1965.

[50] Christiane Caroli and Kazumi Maki. Fluctuations of the Order Parameter in Type-II Superconductors. I. Dirty Limit. *Phys. Rev.*, 159:306–315, Jul 1967.

[51] P. Chalsani, S. K. Upadhyay, O. Ozatay, and R. A. Buhrman. Andreev reflection measurements of spin polarization. *Phys. Rev. B*, 75:094417, Mar 2007.

[52] B. S. Chandrasekhar. A note on the maximum critical field of high - field superconductors. *Applied Physics Letters*, 1(1):7–8, 1962.

[53] Cui-Zu Chang, Jinsong Zhang, Xiao Feng, Jie Shen, Zuocheng Zhang, Minghua Guo, Kang Li, Yunbo Ou, Pang Wei, Li-Li Wang, Zhong-Qing Ji, Yang Feng, Shuaihua Ji, Xi Chen, Jinfeng Jia, Xi Dai, Zhong Fang, Shou-Cheng Zhang, Ke He, Yayu Wang, Li Lu, Xu-Cun Ma, and Qi-Kun Xue. Experimental Observation of the Quantum Anomalous Hall Effect in a Magnetic Topological Insulator. *Science*, 340(6129):167–170, 2013.

[54] Cui-Zu Chang, Jinsong Zhang, Minhao Liu, Zuocheng Zhang, Xiao Feng, Kang Li, Li-Li Wang, Xi Chen, Xi Dai, Zhong Fang, Xiao-Liang Qi, Shou-Cheng Zhang, Yayu Wang, Ke He, Xu-Cun Ma, and Qi-Kun Xue. Thin films of magnetically doped topological insulator

with carrier-independent long-range ferromagnetic order. *Advanced Materials*, 25(7):1065–1070, 2013.

[55] Cui-Zu Chang, Weiwei Zhao, Duk Y. Kim, Haijun Zhang, Badih A. Assaf, Don Heiman, Shou-Cheng Zhang, Chaoxing Liu, Moses H. W. Chan, and Jagadeesh S. Moodera. High-precision realization of robust quantum anomalous Hall state in a hard ferromagnetic topological insulator. *Nat Mater*, 14(5):473–477, May 2015. Letter.

[56] C. Chappert, H. Bernas, J. Ferré, V. Kottler, J.-P. Jamet, Y. Chen, E. Cambril, T. Devolder, F. Rousseaux, V. Mathet, and H. Launois. Planar patterned magnetic media obtained by ion irradiation. *Science*, 280(5371):1919–1922, 1998.

[57] Y. L. Chen, J.-H. Chu, J. G. Analytis, Z. K. Liu, K. Igarashi, H.-H. Kuo, X. L. Qi, S. K. Mo, R. G. Moore, D. H. Lu, M. Hashimoto, T. Sasagawa, S. C. Zhang, I. R. Fisher, Z. Hussain, and Z. X. Shen. Massive Dirac Fermion on the Surface of a Magnetically Doped Topological Insulator. *Science*, 329(5992):659–662, 2010.

[58] Yi-Jiunn Chien. *Transition Metal-Doped* Sb_2Te_3 *and* Bi_2Te_3 *Diluted Magnetic Semiconductors*. PhD thesis, The University of Michigan, Michigan, United States of America, 2007.

[59] Hyoung Joon Choi, David Roundy, Hong Sun, Marvin L. Cohen, and Steven G. Louie. The origin of the anomalous superconducting properties of MgB_2. *Nature*, 418(6899):758–760, Aug 2002.

[60] J E Christopher and H M Darley. Zero bias resistance peak in compensated germanium tunnel junctions. *Journal of Physics C: Solid State Physics*, 11(12):2589, 1978.

[61] In Chang Chu, Masaaki Doi, Masashi Sahashi, Ammanabrolu Rajanikanth, Yukiko Takahashi, and Kazuhiro Hono. Spin Polarization of Alternate Monatomic Epitaxial $[Fe/Co]_n$ Superlattice. *Japanese Journal of Applied Physics*, 51(9R):093006, 2012.

[62] John Clarke and Alex I. Braginski. *The SQUID Handbook: Fundamentals and Technology of SQUIDs and SQUID systems, Vol.1*. Wiley-VCH, 2004.

[63] A. M. Clogston. Upper limit for the critical field in hard superconductors. *Phys. Rev. Lett.*, 9:266–267, Sep 1962.

[64] J. W. Conley, C. B. Duke, G. D. Mahan, and J. J. Tiemann. Electron tunneling in metal-semiconductor barriers. *Phys. Rev.*, 150:466–469, Oct 1966.

[65] Leon N. Cooper. Bound Electron Pairs in a Degenerate Fermi Gas. *Phys. Rev.*, 104:1189–1190, Nov 1956.

[66] D Daghero, P Pecchio, G A Ummarino, F Nabeshima, Y Imai, A Maeda, I Tsukada, S Komiya, and R S Gonnelli. Point-contact Andreev-reflection spectroscopy in $Fe(Te,Se)$ films: multiband superconductivity and electron-boson coupling. *Superconductor Science and Technology*, 27(12):124014, 2014.

[67] D. Daghero, M. Tortello, G. A. Ummarino, J.-C. Griveau, E. Colineau, R. Eloirdi, A. B. Shick, J. Kolorenc, and R. Lichtenstein, A. I.and Caciuffo. Strong-coupling d-wave superconductivity in $PuCoGa_5$ probed by point-contact spectroscopy. *Nat Commun*, 3:786, Apr 2012. Article.

[68] André Dankert, Johannes Geurs, M. Venkata Kamalakar, Sophie Charpentier, and Saroj P. Dash. Room temperature electrical detection of spin polarized currents in topological insulators. *Nano Letters*, 15(12):7976–7981, 2015. PMID: 26560203.

[69] P. G. De Gennes and G. Sarma. Some relations between superconducting and magnetic properties. *Journal of Applied Physics*, 34(4):1380–1385, 1963.

[70] Jose Maria De Teresa, Agnès Barthélémy, Albert Fert, Jean Pierre Contour, François Montaigne, and Pierre Seneor. Role of metal-oxide interface in determining the spin polarization of magnetic tunnel junctions. *Science*, 286(5439):507–509, 1999.

[71] Y.S. Dedkov, M. Fonin, U. Rüdiger, and G. Güntherodt. Spin-resolved photoelectron spectroscopy of the MgO/Fe(110) system. *Applied Physics A*, 82(3):489–493, 2006.

[72] B. Deka, A. Srinivasan, R.K. Singh, B.S.D.Ch.S. Varaprasad, Y.K. Takahashi, and K. Hono. Effect of Co substitution for Mn on spin polarization and magnetic properties of ferrimagnetic Mn_2VAl. *Journal of Alloys and Compounds*, 662:510 – 515, 2016.

[73] Wen Deng, Yu Yang Huang, Yu Xia Li, Li Yuan Qin, and Qin Guan Tian. Studies of $3d$ Electrons and Hyperfine Interactions in Ordered and Disordered $Fe_{50}Al_{50}$ Alloys. In *New Materials, Applications and Processes*, volume 399 of *Advanced Materials Research*, pages 908–911. Trans Tech Publications, 2 2012.

[74] Quantum Design. *Physical Property Measurement System, Hardware Manual, Part Number 1070-150, B5, page 4-8*. San Diego, USA, February 2008.

[75] Rik Dey, Tanmoy Pramanik, Anupam Roy, Amritesh Rai, Samaresh Guchhait, Sushant Sonde, Hema C. P. Movva, Luigi Colombo, Leonard F. Register, and Sanjay K. Banerjee. Strong spin-orbit coupling and zeeman spin splitting in angle dependent magnetoresistance of bi2te3. *Applied Physics Letters*, 104(22):223111, 2014.

[76] M. Donath, B. Gubanka, and F. Passek. Temperature-Dependent Spin Polarization of Magnetic Surface State at Gd(0001). *Phys. Rev. Lett.*, 77:5138–5141, Dec 1996.

[77] Jan Willem Frederik Dorleijn. *Electrical conduction in ferromagnetic metals*. PhD thesis, TU Delft, Delft University of Technology, 1977.

[78] D. H. Douglass. Magnetic field dependence of the superconducting energy gap. *Phys. Rev. Lett.*, 6:346–348, Apr 1961.

[79] V. Drewello, J. Schmalhorst, A. Thomas, and G. Reiss. Evidence for strong magnon contribution to the TMR temperature dependence in MgO based tunnel junctions. *Phys. Rev. B*, 77:014440, Jan 2008.

[80] Volker Drewello, Markus Schäfers, Oliver Schebaum, Ayaz Arif Khan, Jana Münchenberger, Jan Schmalhorst, Günter Reiss, and Andy Thomas. Inelastic electron tunneling spectra of MgO-based magnetic tunnel junctions with different electrode designs. *Phys. Rev. B*, 79:174417, May 2009.

[81] Lingjie Du, Ivan Knez, Gerard Sullivan, and Rui-Rui Du. Observation of quantum spin Hall states in InAs/GaSb bilayers under broken time-reversal symmetry. *arXiv preprint arXiv:1306.1925*, 2013.

[82] Ye Du, T. Furubayashi, T. T. Sasaki, Y. Sakuraba, Y. K. Takahashi, and K. Hono. Large magnetoresistance in current-perpendicular-to-plane pseudo spin-valves using $Co_2Fe(Ga_{0.5}Ge_{0.5})$ heusler alloy and AgZn spacer. *Applied Physics Letters*, 107(11), 2015.

[83] A. I. D'yachenko, V. A. D'yachenko, V. Yu. Tarenkov, and V. N. Krivoruchko. Spin polarization of charge carriers and Andreev reflection in (LaCa)MnO/superconductor point contacts. *Physics of the Solid State*, 48(3):432–440, 2006.

[84] Jeffrey S. Dyck, Pavel Hájek, Petr Lošt'ák, and Ctirad Uher. Diluted magnetic semiconductors based on $Sb_{2-x}V_xTe_3$ $(0.01 < x < 0.03)$. *Phys. Rev. B*, 65:115212, Mar 2002.

[85] R. C. Dynes, V. Narayanamurti, and J. P. Garno. Direct measurement of quasiparticle-lifetime broadening in a strong-coupled superconductor. *Phys. Rev. Lett.*, 41:1509–1512, Nov 1978.

[86] Gert Eilenberger. Transformation of Gorkov′s equation for type II superconductors into transport-like equations. *Zeitschrift für Physik*, 214(2):195–213, 1968.

[87] Dieter Elefant and Rudolf Schäfer. Low-temperature resistivity, magnetoresistance, and domain-wall resistance of highly pure single- and polycrystalline iron. *Phys. Rev. B*, 91:064403, Feb 2015.

[88] Matthias Eltschka. *Scanning Tunneling Microscopy using Superconducting Tips to Probe Absolute Spin Polarization*. PhD thesis, Ecole Polytechnique Federale de Lausanne, Lausanne, Switzerland, 2015.

[89] Matthias Eltschka, Berthold Jäck, Maximilian Assig, Oleg V. Kondrashov, Mikhail A. Skvortsov, Markus Etzkorn, Christian R. Ast, and Klaus Kern. Probing absolute spin polarization at the nanoscale. *Nano Letters*, 14(12):7171–7174, 2014.

[90] Matthias Eltschka, Berthold Jäck, Maximilian Assig, Oleg V. Kondrashov, Mikhail A. Skvortsov, Markus Etzkorn, Christian R. Ast, and Klaus Kern. Superconducting scanning tunneling microscopy tips in a magnetic field: Geometry-controlled order of the phase transition. *Applied Physics Letters*, 107(12), 2015.

[91] B. N. Engel, J. Akerman, B. Butcher, R. W. Dave, M. DeHerrera, M. Durlam, G. Grynkewich, J. Janesky, S. V. Pietambaram, N. D. Rizzo, J. M. Slaughter, K. Smith, J. J. Sun, and S. Tehrani. A 4-Mb toggle MRAM based on a novel bit and switching method. *IEEE Transactions on Magnetics*, 41(1):132–136, Jan 2005.

[92] M. R. Eskildsen, M. Kugler, S. Tanaka, J. Jun, S. M. Kazakov, J. Karpinski, and Ø. Fischer. Vortex imaging in the π band of magnesium diboride. *Phys. Rev. Lett.*, 89:187003, Oct 2002.

[93] Yabin Fan, Pramey Upadhyaya, Xufeng Kou, Murong Lang, So Takei, Zhenxing Wang, Jianshi Tang, Liang He, Li-Te Chang, Mohammad Montazeri, et al. Magnetization switching through giant spin–orbit torque in a magnetically doped topological insulator heterostructure. *Nature materials*, 13(7):699–704, 2014.

[94] R.M. Feenstra, Joseph A. Stroscio, and A.P. Fein. Tunneling spectroscopy of the Si(111) 2×1 surface. *Surface Science*, 181(1):295 – 306, 1987.

[95] A. Fert and O. Jaoul. Left-Right Asymmetry in the Scattering of Electrons by Magnetic Impurities, and a Hall Effect. *Phys. Rev. Lett.*, 28:303–307, Jan 1972.

[96] R. P. Feynman. *Lectures on Physics, Vol. 3, Chap. 21*. Addison-Wesley, New York, 1965.

[97] K. H. Fischer. On the electrical resistivity of spin glasses. *Zeitschrift für Physik B Condensed Matter*, 34(1):45–53, 1979.

[98] P. P. Freitas, F. A. Cardoso, V. C. Martins, S. A. M. Martins, J. Loureiro, J. Amaral, R. C. Chaves, S. Cardoso, L. P. Fonseca, A. M. Sebastiao, M. Pannetier-Lecoeur, and C. Fermon. Spintronic platforms for biomedical applications. *Lab Chip*, 12:546–557, 2012.

[99] Bretislav Friedrich and Dudley Herschbach. Stern and Gerlach: How a bad cigar helped reorient atomic physics. *Physics Today*, 56(12):53–59, 2003.

[100] Liang Fu and C. L. Kane. Topological insulators with inversion symmetry. *Phys. Rev. B*, 76:045302, Jul 2007.

[101] Liang Fu and C. L. Kane. Superconducting Proximity Effect and Majorana Fermions at the Surface of a Topological Insulator. *Phys. Rev. Lett.*, 100:096407, Mar 2008.

[102] Liang Fu, C. L. Kane, and E. J. Mele. Topological insulators in three dimensions. *Phys. Rev. Lett.*, 98:106803, Mar 2007.

[103] Shunsuke Fukami, Chaoliang Zhang, Samik DuttaGupta, Aleksandr Kurenkov, and Hideo Ohno. Magnetization switching by spin-orbit torque in an antiferromagnet-ferromagnet bilayer system. *Nat Mater*, 15(5):535–541, May 2016.

[104] Peter Fulde and Richard A. Ferrell. Superconductivity in a strong spin-exchange field. *Phys. Rev.*, 135:A550–A563, Aug 1964.

[105] I. Galanakis, K. Özdoğan, E. ŞaşÄśoğlu, and S. Blügel. Effect of disorder on the magnetic properties of cubic Mn_2Ru_xGa compounds: A first-principles study. *Journal of Applied Physics*, 116(3), 2014.

[106] J. C. Gallop. *SQUIDs, the Josephson Effects and Superconducting Electronics*. Adam Hilger, 1991.

[107] Z. Gercsi, A. Rajanikanth, Y. K. Takahashi, K. Hono, M. Kikuchi, N. Tezuka, and K. Inomata. Spin polarization of Co_2FeSi full-Heusler alloy and tunneling magnetoresistance of its magnetic tunneling junctions. *Applied Physics Letters*, 89(8), 2006.

[108] S. Geschwind and L. R. Walker. Exchange resonances in gadolinium iron garnet near the magnetic compensation temperature. *Journal of Applied Physics*, 30(4):S163–S170, 1959.

[109] I. Giaever, H. R. Hart, and K. Megerle. Tunneling into superconductors at temperatures below 1 K. *Phys. Rev.*, 126:941–948, May 1962.

[110] Ivar Giaever. Energy gap in superconductors measured by electron tunneling. *Phys. Rev. Lett.*, 5:147–148, Aug 1960.

[111] J. A. Gifford, G. J. Zhao, B. C. Li, Brian D. Tracy, J. Zhang, D. R. Kim, David J. Smith, and T. Y. Chen. Continuous control of spin polarization using a magnetic field. *Applied Physics Letters*, 108(21), 2016.

[112] V. L. Ginzburg and L. D. Landau. On the theory of superconductivity. *Zh. Eksp. Teor. Fiz,*, 20:1064, 1950.

[113] LI Glazman and KA Matveev. Inelastic tunneling across thin amorphous films. *Zh. Eksp. Teor. Fiz*, 94:343, 1988.

[114] A. A. Golubov and U. Hartmann. Electronic structure of the Abrikosov vortex core in arbitrary magnetic fields. *Phys. Rev. Lett.*, 72:3602–3605, May 1994.

[115] A. A. Golubov and M. Yu. Kupriyanov. Theoretical investigation of Josephson tunnel junctions with spatially inhomogeneous superconducting electrodes. *Journal of Low Temperature Physics*, 70(1):83–130, 1988.

[116] R. S. Gonnelli, D. Daghero, G. A. Ummarino, V. A. Stepanov, J. Jun, S. M. Kazakov, and J. Karpinski. Direct Evidence for Two-Band Superconductivity in MgB_2 Single Crystals from Directional Point-Contact Spectroscopy in Magnetic Fields. *Phys. Rev. Lett.*, 89:247004, Nov 2002.

[117] L. P. Gor'kov. Microscopic Derivation of the Ginzburg-Landau Equations in the Theory of Superconductivity. *JETP*, 9:1364–1367, 1959.

[118] Hirotaka Gotoh, Yoichi Takeda, Hidefumi Asano, Jianping Zhong, Ammanabrolu Rajanikanth, and Kazuhiro Hono. Antiferromagnetism and spin polarization in double perovskite $SrLaVMoO_6$. *Applied Physics Express*, 2(1):013001, 2009.

[119] Tanja Graf, Claudia Felser, and Stuart S.P. Parkin. Simple rules for the understanding of Heusler compounds. *Progress in Solid State Chemistry*, 39(1):1 – 50, 2011.

[120] J. Gramich, P. Brenner, C. Sürgers, H. v. Löhneysen, and G. Goll. Experimental verification of contact-size estimates in point-contact spectroscopy on superconductor/ferromagnet heterocontacts. *Phys. Rev. B*, 86:155402, Oct 2012.

[121] M. Gregor, T. Plecenik, R. Sobota, J. Brndiarova, T. Roch, L. Satrapinskyy, P. Kus, and A. Plecenik. Influence of annealing atmosphere on structural and superconducting properties of MgB_2 thin films. *Applied Surface Science*, 312:97 – 101, 2014. 8th Solid State Surfaces and Interfaces.

[122] G. S. Grest. Monte Carlo study of the transition from a ferromagnet to a spin glass in Fe-Al alloys. *Phys. Rev. B*, 21:165–168, Jan 1980.

[123] F. Greullet, C. Tiusan, F. Montaigne, M. Hehn, D. Halley, O. Bengone, M. Bowen, and W. Weber. Evidence of a Symmetry-Dependent Metallic Barrier in Fully Epitaxial MgO Based Magnetic Tunnel Junctions. *Phys. Rev. Lett.*, 99:187202, Nov 2007.

[124] K. K. Gupta and V. S. Mathur. Magnetic field dependence of energy gap in superconductors. *Phys. Rev.*, 121:107–117, Jan 1961.

[125] LiC H., van't ErveO M. J., RobinsonJ T., LiuY., LiL., and JonkerB T. Electrical detection of charge-current-induced spin polarization due to spin-momentum locking in Bi_2Se_3. *Nat Nano*, 9(3):218–224, Mar 2014. Article.

[126] M. Hakimi, M. Venkatesan, K. Rode, K. Ackland, and J. M. D. Coey. The zero-magnetization Heusler ferrimagnet. *Journal of Applied Physics*, 113(17), 2013.

[127] S. S. Hanna and R. S. Preston. Positron polarization demonstrated by annihilation in magnetized iron. *Phys. Rev.*, 106:1363–1364, Jun 1957.

[128] S. S. Hanna and R. S. Preston. Polarization of positrons and annihilation in ferromagnetic materials. *Phys. Rev.*, 109:716–720, Feb 1958.

[129] K. E. H. M. Hanssen and P. E. Mijnarends. Positron-annihilation study of the half-metallic ferromagnet nimnsb: Theory. *Phys. Rev. B*, 34:5009–5016, Oct 1986.

[130] K. E. H. M. Hanssen, P. E. Mijnarends, L. P. L. M. Rabou, and K. H. J. Buschow. Positron-annihilation study of the half-metallic ferromagnet nimnsb: Experiment. *Phys. Rev. B*, 42:1533–1540, Jul 1990.

[131] X. Hao, J. S. Moodera, and R. Meservey. Spin-filter effect of ferromagnetic europium sulfide tunnel barriers. *Phys. Rev. B*, 42:8235–8243, Nov 1990.

[132] J. J. Hauser. Electrical and structural properties of amorphous metal—metal-oxide systems. *Phys. Rev. B*, 7:4099–4111, May 1973.

[133] W. Heitler and F. London. Wechselwirkung neutraler atome und homöopolare bindung nach der quantenmechanik. *Zeitschrift für Physik*, 44(6):455–472, 1927.

[134] Warren E. Henry. Spin Paramagnetism of Cr^{+++}, Fe^{+++}, and Gd^{+++} at Liquid Helium Temperatures and in Strong Magnetic Fields. *Phys. Rev.*, 88:559–562, Nov 1952.

[135] Conyers Herring. Critique of the Heitler-London Method of Calculating Spin Couplings at Large Distances. *Rev. Mod. Phys.*, 34:631–645, Oct 1962.

[136] H. F. Hess, R. B. Robinson, R. C. Dynes, J. M. Valles, and J. V. Waszczak. Scanning-Tunneling-Microscope Observation of the Abrikosov Flux Lattice and the Density of States near and inside a Fluxoid. *Phys. Rev. Lett.*, 62:214–216, Jan 1989.

[137] H. F. Hess, R. B. Robinson, and J. V. Waszczak. Vortex-core structure observed with a scanning tunneling microscope. *Phys. Rev. Lett.*, 64:2711–2714, May 1990.

[138] Shinobu Hikami, Anatoly I. Larkin, and Yosuke Nagaoka. Spin-orbit interaction and magnetoresistance in the two dimensional random system. *Progress of Theoretical Physics*, 63(2):707–710, 1980.

[139] J.I. Hong, S. Sankar, A.E. Berkowitz, and W.F. Egelhoff Jr. On the perpendicular anisotropy of Co/Pd multilayers. *Journal of Magnetism and Magnetic Materials*, 285(3):359 – 366, 2005.

[140] Y. S. Hor, P. Roushan, H. Beidenkopf, J. Seo, D. Qu, J. G. Checkelsky, L. A. Wray, D. Hsieh, Y. Xia, S.-Y. Xu, D. Qian, M. Z. Hasan, N. P. Ong, A. Yazdani, and R. J. Cava. Development of ferromagnetism in the doped topological insulator $Bi_{2-x}Mn_xTe_3$. *Phys. Rev. B*, 81:195203, May 2010.

[141] Y. S. Hor, A. J. Williams, J. G. Checkelsky, P. Roushan, J. Seo, Q. Xu, H. W. Zandbergen, A. Yazdani, N. P. Ong, and R. J. Cava. Superconductivity in $Cu_xBi_2Se_3$ and its Implications for Pairing in the Undoped Topological Insulator. *Phys. Rev. Lett.*, 104:057001, Feb 2010.

[142] A. Houshang, E. Iacocca, P. Dürrenfeld, S. R. Sani, J. Åkerman, and R. K. Dumas. Spin-wave-beam driven synchronization of nanocontact spin-torque oscillators. *Nat Nano*, 11(3):280–286, Mar 2016. Article.

[143] D. Hsieh, Y. Xia, D. Qian, L. Wray, J. H. Dil, F. Meier, J. Osterwalder, L. Patthey, J. G. Checkelsky, N. P. Ong, A. V. Fedorov, H. Lin, A. Bansil, D. Grauer, Y. S. Hor, R. J. Cava, and M. Z. Hasan. A tunable topological insulator in the spin helical Dirac transport regime. *Nature*, 460(7259):1101–1105, Aug 2009.

[144] D. Hsieh, Y. Xia, L. Wray, D. Qian, A. Pal, J. H. Dil, J. Osterwalder, F. Meier, G. Bihlmayer, C. L. Kane, Y. S. Hor, R. J. Cava, and M. Z. Hasan. Observation of unconventional quantum spin textures in topological insulators. *Science*, 323(5916):919–922, 2009.

[145] G. P. Huffman. *Amorphous magnetism. Proceedings of the International Symposium on Amorphous Magnetism, Aug. 17-18 1972, Detroit, Michigan, U.S.A.* edited by H. O. Hooper and A. M. de Graaf. *Journal of Applied Crystallography*, 6(5):424, Oct 1973.

[146] Igor Žutić and Oriol T. Valls. Tunneling spectroscopy for ferromagnet/superconductor junctions. *Phys. Rev. B*, 61:1555–1566, Jan 2000.

[147] D. Ihle. Wigner-Seitz approximation for the description of the mixed state of type II superconductors. *physica status solidi (b)*, 47(2):423–428, 1971.

[148] S. Ikeda, J. Hayakawa, Y. Ashizawa, Y. M. Lee, K. Miura, H. Hasegawa, M. Tsunoda, F. Matsukura, and H. Ohno. Tunnel magnetoresistance of 604 % at 300 K by suppression of Ta diffusion in CoFeBâĹŢMgOâĹŢCoFeB pseudo-spin-valves annealed at high temperature. *Applied Physics Letters*, 93(8), 2008.

[149] S Ikeda, K Miura, H Yamamoto, K Mizunuma, HD Gan, M Endo, Sl Kanai, J Hayakawa, F Matsukura, and H Ohno. A perpendicular-anisotropy CoFeB-MgO magnetic tunnel junction. *Nature materials*, 9(9):721–724, 2010.

[150] Werner Jellinghaus and Miguel Pedro de Andrés. Einfluß der Nachbarelemente des Eisens auf den Hall-Effekt eisenreicher Mischkristalle. *Annalen der Physik*, 462(3-4):189–200, 1961.

[151] Jaewoo Jeong, Yari Ferrante, Sergey V. Faleev, Mahesh G. Samant, Claudia Felser, and Stuart S. P. Parkin. Termination layer compensated tunnelling magnetoresistance in ferrimagnetic Heusler compounds with high perpendicular magnetic anisotropy. *Nat Commun*, 7, Jan 2016.

[152] Nian Ji, M. S. Osofsky, Valeria Lauter, Lawrence F. Allard, Xuan Li, Kevin L. Jensen, Hailemariam Ambaye, Edgar Lara-Curzio, and Jian-Ping Wang. Perpendicular magnetic anisotropy and high spin-polarization ratio in epitaxial $Fe-N$ thin films. *Phys. Rev. B*, 84:245310, Dec 2011.

[153] Ch. Poole Jr., H. Farach, R. Creswick, and Prozorov. *Lectures on Physics, Chap. 15, Second Edition*. Elsevier, 2007.

[154] M. Julliere. Tunneling between ferromagnetic films. *Physics Letters A*, 54(3):225 – 226, 1975.

[155] J. W. Jung, Y. Sakuraba, T. T. Sasaki, Y. Miura, and K. Hono. Enhancement of magnetoresistance by inserting thin NiAl layers at the interfaces in $Co_2FeGa_{0.5}Ge_{0.5}$/Ag/

$Co_2FeGa_{0.5}Ge_{0.5}$ current-perpendicular-to-plane pseudo spin valves. *Applied Physics Letters*, 108(10), 2016.

[156] Christian Kaiser, Alex F. Panchula, and Stuart S. P. Parkin. Finite tunneling spin polarization at the compensation point of rare-earth-metal–transition-metal alloys. *Phys. Rev. Lett.*, 95:047202, Jul 2005.

[157] C. L. Kane and E. J. Mele. Quantum Spin Hall Effect in Graphene. *Phys. Rev. Lett.*, 95:226801, Nov 2005.

[158] C. H. Kant, O. Kurnosikov, A. T. Filip, P. LeClair, H. J. M. Swagten, and W. J. M. de Jonge. Origin of spin-polarization decay in point-contact Andreev reflection. *Phys. Rev. B*, 66:212403, Dec 2002.

[159] Cornelius Hendrik Kant. *Probing spin polarization : Point contacts and tunnel junctions*. PhD thesis, Technische Universiteit Eindhoven, 1 2005.

[160] J. Kaplan and C. Kittel. Exchange frequency electron spin resonance in ferrites. *The Journal of Chemical Physics*, 21(4):760–761, 1953.

[161] VR Karasik and I Yu Shebalin. Superconducting properties of pure niobium. *Soviet Journal of Experimental and Theoretical Physics*, 30:1068, 1969.

[162] Robert Karplus and J. M. Luttinger. Hall effect in ferromagnetics. *Phys. Rev.*, 95:1154–1160, Sep 1954.

[163] S. V. Karthik, T. M. Nakatani, A. Rajanikanth, Y. K. Takahashi, and K. Hono. Spin polarization of CoâĂŞFe alloys estimated by point contact Andreev reflection and tunneling magnetoresistance. *Journal of Applied Physics*, 105(7), 2009.

[164] S. V. Karthik, A. Rajanikanth, T. M. Nakatani, Z. Gercsi, Y. K. Takahashi, T. Furubayashi, K. Inomata, and K. Hono. Effect of Cr substitution for Fe on the spin polarization of $Co_2Cr_xFe_{1x}Si$ Heusler alloys. *Journal of Applied Physics*, 102(4), 2007.

[165] Tadao Kasuya. A Theory of Metallic Ferro− and Antiferromagnetism on Zener′s Model. *Progress of Theoretical Physics*, 16(1):45–57, 1956.

[166] S. N. Kaul, W. Kettler, and M. Rosenberg. Evidence for a magnetic contribution to the electrical resistivity in amorphous $Fe_{80}B_{20-x}C_x$ alloys. *Phys. Rev. B*, 33:4987–4997, Apr 1986.

[167] S. Kawai, H. Ando, H. Sakakibara, Y. Kuroki, T. Hajiri, K. Ueda, and H. Asano. Magnetic and transport properties of antiperovskite nitride Co_3FeN films. In *2015 IEEE Magnetics Conference (INTERMAG)*, pages 1–1, May 2015.

[168] Atsuo Kawasuso, Masaki Maekawa, Yuki Fukaya, Atsushi Yabuuchi, and Izumi Mochizuki. Spin-polarized positron annihilation measurements of polycrystalline fe, co, ni, and gd based on doppler broadening of annihilation radiation. *Phys. Rev. B*, 83:100406, Mar 2011.

[169] P. Kharel, P. Thapa, P. Lukashev, R. F. Sabirianov, E. Y. Tsymbal, D. J. Sellmyer, and B. Nadgorny. Transport spin polarization of high Curie temperature MnBi films. *Phys. Rev. B*, 83:024415, Jan 2011.

[170] Tae Hee Kim and Jagadeesh S. Moodera. Demonstration of all in situ magnesium diboride superconductor thin-film tunnel junctions. *Applied Physics Letters*, 85(3):434–436, 2004.

[171] C. Kittel. Theory of antiferromagnetic resonance. *Phys. Rev.*, 82:565–565, May 1951.

[172] Naoki Kiyohara, Takahiro Tomita, and Satoru Nakatsuji. Giant Anomalous Hall Effect in the Chiral Antiferromagnet Mn_3Ge. *Phys. Rev. Applied*, 5:064009, Jun 2016.

[173] Reinhold Kleiner. Fundamentals. In Paul Seidel, editor, *Applied Superconductivity: Handbook on Devices and Applications, First Edition*, chapter 1, pages 1–104. Wiley-VCH Verlag GmbH I& KGaA, 2015.

[174] A. W. Kleinsasser, T. N. Jackson, D. McInturff, F. Rammo, G. D. Pettit, and J. M. Woodall. Crossover from tunneling to metallic behavior in superconductor âĂŘ semiconductor contacts. *Applied Physics Letters*, 57(17):1811–1813, 1990.

[175] K. v. Klitzing, G. Dorda, and M. Pepper. New Method for High-Accuracy Determination of the Fine-Structure Constant Based on Quantized Hall Resistance. *Phys. Rev. Lett.*, 45:494–497, Aug 1980.

[176] Satoshi Kokado and Masakiyo Tsunoda. Anisotropic Magnetoresistance Effect: General Expression of AMR Ratio and Intuitive Explanation for Sign of AMR Ratio. In *Advanced Engineering Materials III*, volume 750 of *Advanced Materials Research*, pages 978–982. Trans Tech Publications, 10 2013.

[177] Satoshi Kokado, Masakiyo Tsunoda, Kikuo Harigaya, and Akimasa Sakuma. Anisotropic magnetoresistance effects in Fe, Co, Ni, Fe_4N, and half-metallic ferromagnet: A systematic analysis. *Journal of the Physical Society of Japan*, 81(2):024705, 2012.

[178] Jun Kondo. Resistance minimum in dilute magnetic alloys. *Progress of Theoretical Physics*, 32(1):37–49, 1964.

[179] Markus König, Steffen Wiedmann, Christoph Brüne, Andreas Roth, Hartmut Buhmann, Laurens W. Molenkamp, Xiao-Liang Qi, and Shou-Cheng Zhang. Quantum Spin Hall Insulator State in HgTe Quantum Wells. *Science*, 318(5851):766–770, 2007.

[180] A. E. Koshelev and A. A. Golubov. Mixed state of a dirty two-band superconductor: Application to MgB_2. *Phys. Rev. Lett.*, 90:177002, Apr 2003.

[181] Xufeng Kou, Shih-Ting Guo, Yabin Fan, Lei Pan, Murong Lang, Ying Jiang, Qiming Shao, Tianxiao Nie, Koichi Murata, Jianshi Tang, Yong Wang, Liang He, Ting-Kuo Lee, Wei-Li Lee, and Kang L. Wang. Scale-Invariant Quantum Anomalous Hall Effect in Magnetic Topological Insulators beyond the Two-Dimensional Limit. *Phys. Rev. Lett.*, 113:137201, Sep 2014.

[182] A. Kubetzka, M. Bode, O. Pietzsch, and R. Wiesendanger. Spin-polarized scanning tunneling microscopy with antiferromagnetic probe tips. *Phys. Rev. Lett.*, 88:057201, Jan 2002.

[183] Takahide Kubota, Sumito Tsunegi, Mikihiko Oogane, Shigemi Mizukami, Terunobu Miyazaki, Hiroshi Naganuma, and Yasuo Ando. Half-metallicity and Gilbert damping constant in $Co_2Fe_xMn_{1x}Si$ Heusler alloys depending on the film composition. *Applied Physics Letters*, 94(12), 2009.

[184] IO Kulik, AN OmelâĂŹYanchuk, and RI Shekhter. Electrical conductivity of point microbridges and phonon and impurity spectroscopy in normal metals. *Sov. J. Low Temp. Phys*, 3(12):740–748, 1977.

[185] H. Kurt, N. Baadji, K. Rode, M. Venkatesan, P. Stamenov, S. Sanvito, and J. M. D. Coey. Magnetic and electronic properties of $D0_{22}$-Mn_3Ge (001) films. *Applied Physics Letters*, 101(13), 2012.

[186] H. Kurt, K. Rode, P. Stamenov, M. Venkatesan, Y.-C. Lau, E. Fonda, and J. M. D. Coey. Cubic Mn_2Ga thin films: Crossing the spin gap with ruthenium. *Phys. Rev. Lett.*, 112:027201, Jan 2014.

[187] H. Kurt, K. Rode, M. Venkatesan, P. Stamenov, and J. M. D. Coey. High spin polarization in epitaxial films of ferrimagnetic Mn_3Ga. *Phys. Rev. B*, 83:020405, Jan 2011.

[188] H. Kurt, K. Rode, M. Venkatesan, P. Stamenov, and J. M. D. Coey. $Mn_{3-x}Ga$ ($0 \leq x \leq 1$): Multifunctional thin film materials for spintronics and magnetic recording. *Physica Status Solidi (b)*, 248(10):2338–2344, 2011.

[189] R. Kurzawa, K.-P. Kämper, W. Schmitt, and G. Güntherodt. Spin-resolved photoemission study of in situ grown epitaxial Fe layers on W(110). *Solid State Communications*, 60(10):777 – 780, 1986.

[190] W. K. Kwok, U. Welp, G. W. Crabtree, K. G. Vandervoort, R. Hulscher, and J. Z. Liu. Direct observation of dissipative flux motion and pinning by twin boundaries in $YBa_2Cu_3O_{7-\delta}$ single crystals. *Phys. Rev. Lett.*, 64:966–969, Feb 1990.

[191] W. K. Kwok, U. Welp, V. M. Vinokur, S. Fleshler, J. Downey, and G. W. Crabtree. Direct observation of intrinsic pinning by layered structure in single-crystal $YBa_2Cu_3O_{7-\delta}$. *Phys. Rev. Lett.*, 67:390–393, Jul 1991.

[192] A. I. Larkin and Yu. N. Ovchinnikov. Inhomogenous state of superconductors. *JETP*, 20:762, 1965.

[193] Yong-Chang Lau. *Magnetic thin films for spin-transfer torque applications*. PhD thesis, Department of Physics, University of Dublin, College Green, Dublin, 2 2016.

[194] R. B. Laughlin. Quantized Hall conductivity in two dimensions. *Phys. Rev. B*, 23:5632–5633, May 1981.

[195] Jerome M. Lavine. Extraordinary Hall-Effect Measurements on Ni, Some Ni Alloys, and Ferrites. *Phys. Rev.*, 123:1273–1277, Aug 1961.

[196] P. LeClair, B. Hoex, H. Wieldraaijer, J. T. Kohlhepp, H. J. M. Swagten, and W. J. M. de Jonge. Sign reversal of spin polarization in $Co/Ru/Al_2O_3/Co$ magnetic tunnel junctions. *Phys. Rev. B*, 64:100406, Aug 2001.

[197] P. LeClair, H. J. M. Swagten, J. T. Kohlhepp, R. J. M. van de Veerdonk, and W. J. M. de Jonge. Apparent spin polarization decay in Cu-dusted $Co/Al_2O_3/Co$ tunnel junctions. *Phys. Rev. Lett.*, 84:2933–2936, Mar 2000.

[198] James L. Levine. Density of states of a short-mean-free-path superconductor in a magnetic field by electron tunneling. *Phys. Rev.*, 155:373–378, Mar 1967.

[199] Niv Levy, Tong Zhang, Jeonghoon Ha, Fred Sharifi, A. Alec Talin, Young Kuk, and Joseph A. Stroscio. Experimental evidence for *s*-wave pairing symmetry in superconducting $Cu_xBi_2S_3$ single crystals using a scanning tunneling microscope. *Phys. Rev. Lett.*, 110:117001, Mar 2013.

[200] CH Li, OMJ vant Erve, YY Li, L Li, and BT Jonker. Electrical detection of the helical spin texture in a *p*-type topological insulator Sb_2Te_3. *Scientific Reports*, 6, 2016.

[201] S. Li, Y. K. Takahashi, T. Furubayashi, and K. Hono. Enhancement of giant magnetoresistance by $L2_1$ ordering in $Co_2Fe(Ge_{0.5}Ga_{0.5})$ Heusler alloy current-perpendicular-to-plane pseudo spin valves. *Applied Physics Letters*, 103(4), 2013.

[202] Yufan Li, Dazhi Hou, Li Ye, Yuan Tian, Jianli Xu, Gang Su, and Xiaofeng Jin. Evidence of the side jump mechanism in the anomalous Hall effect in paramagnets. *EPL (Europhysics Letters)*, 110(2):27002, 2015.

[203] Jacob Linder, Yukio Tanaka, Takehito Yokoyama, Asle Sudbø, and Naoto Nagaosa. Unconventional superconductivity on a topological insulator. *Phys. Rev. Lett.*, 104:067001, Feb 2010.

[204] Hong-xi Liu, Yusuke Honda, Tomoyuki Taira, Ken-ichi Matsuda, Masashi Arita, Tetsuya Uemura, and Masafumi Yamamoto. Giant tunneling magnetoresistance in epitaxial $Co_2MnSi/MgO/Co_2MnSi$ magnetic tunnel junctions by half-metallicity of Co_2MnSi and coherent tunneling. *Applied Physics Letters*, 101(13), 2012.

[205] J. Logan and M. Yung. The low-temperature electrical resistivity of amorphous iron-phosphorus alloys. *Journal of Non-Crystalline Solids*, 21(1):151 – 154, 1976.

[206] J. C. Loudon, S. Yazdi, T. Kasama, N. D. Zhigadlo, and J. Karpinski. Measurement of the penetration depth and coherence length of MgB_2 in all directions using transmission electron microscopy. *Phys. Rev. B*, 91:054505, Feb 2015.

[207] Joseph Maciejko, Chaoxing Liu, Yuval Oreg, Xiao-Liang Qi, Congjun Wu, and Shou-Cheng Zhang. Kondo effect in the helical edge liquid of the quantum spin Hall state. *Phys. Rev. Lett.*, 102:256803, Jun 2009.

[208] S. Maekawa and U. Gafvert. Electron tunneling between ferromagnetic films. *IEEE Transactions on Magnetics*, 18(2):707–708, Mar 1982.

[209] R. Magno and J. G. Adler. Data calibration in electron tunneling spectroscopy. *Review of Scientific Instruments*, 52(2):217–223, 1981.

[210] Kazumi Maki and Peter Fulde. Equivalence of different pair-breaking mechanisms in superconductors. *Phys. Rev.*, 140:A1586–A1592, Nov 1965.

[211] S. Mangin, D. Ravelosona, J. A. Katine, M. J. Carey, B. D. Terris, and Eric E. Fullerton. Current-induced magnetization reversal in nanopillars with perpendicular anisotropy. *Nat Mater*, 5(3):210–215, Mar 2006.

[212] M. Mao, M. Miller, P. Johnson, H.-C. Tong, C. Qian, L. Miloslavsky, C.-Y. Hung, J. Wang, and H. Hegde. Ion beam sputtered spin-valve films with improved giant magnetoresistance response. *Journal of Applied Physics*, 85(8):4454–4456, 1999.

[213] J. Mathon and A. Umerski. Theory of tunneling magnetoresistance of an epitaxial Fe/MgO/Fe(001) junction. *Phys. Rev. B*, 63:220403, May 2001.

[214] Ph. Mavropoulos, N. Papanikolaou, and P. H. Dederichs. Complex band structure and tunneling through ferromagnet /insulator /ferromagnet junctions. *Phys. Rev. Lett.*, 85:1088–1091, Jul 2000.

[215] I. I. Mazin, A. A. Golubov, and B. Nadgorny. Probing spin polarization with andreev reflection: A theoretical basis. *Journal of Applied Physics*, 89(11):7576–7578, 2001.

[216] W. L. McMillan and J. M. Rowell. Lead phonon spectrum calculated from superconducting density of states. *Phys. Rev. Lett.*, 14:108–112, Jan 1965.

[217] Markus Meinert and Manuel P. Geisler. Phase stability of chromium based compensated ferrimagnets with inverse Heusler structure. *Journal of Magnetism and Magnetic Materials*, 341:72 – 74, 2013.

[218] C. Meingast and D. C. Larbalestier. Quantitative description of a very high critical current density NbTi superconductor during its final optimization strain. II. Flux pinning mechanisms. *Journal of Applied Physics*, 66(12):5971–5983, 1989.

[219] C. Meingast, P. J. Lee, and D. C. Larbalestier. Quantitative description of a high J_c NbTi superconductor during its final optimization strain. I. Microstructure, t_c,âĂL'h_{c2}, and resistivity. *Journal of Applied Physics*, 66(12):5962–5970, 1989.

[220] R. Mélin. Spin-resolved Andreev reflection in ferromagnet-superconductor junctions with Zeeman splitting. *EPL (Europhysics Letters)*, 51(2):202, 2000.

[221] A. R. Mellnik, J. S. Lee, A. Richardella, J. L. Grab, P. J. Mintun, M. H. Fischer, A. Vaezi, A. Manchon, E.-A. Kim, N. Samarth, and D. C. Ralph. Spin-transfer torque generated by a topological insulator. *Nature*, 511(7510):449–451, Jul 2014. Letter.

[222] E Menéndez, J Sort, M O Liedke, J Fassbender, S Surinach, M D Bar, and J Nogués. Twofold origin of the deformation-induced ferromagnetism in bulk $Fe_{60}Al_{40}$ (at. *New Journal of Physics*, 10(10):103030, 2008.

[223] R. Meservey and D. H. Douglass. Energy gap measurements by tunneling between superconducting films. II. magnetic field dependence. *Phys. Rev.*, 135:A24–A33, Jul 1964.

[224] R. Meservey, D. Paraskevopoulos, and P.M. Tedrow. Measurements of the spin polarization of electrons tunneling from ferromagnetic alloys of the 3*d* metals. *Physica B+C*, 91:91 – 95, 1977.

[225] R. Meservey, P. M. Tedrow, and Ronald C. Bruno. Tunneling measurements on spin-paired superconductors with spin-orbit scattering. *Phys. Rev. B*, 11:4224–4235, Jun 1975.

[226] R. Meservey and P.M. Tedrow. Spin-polarized electron tunneling. *Physics Reports*, 238(4):173 – 243, 1994.

[227] J. Millstein and M. Tinkham. Tunneling into superconducting films in a magnetic field. *Phys. Rev.*, 158:325–332, Jun 1967.

[228] Ioan Mihai Miron, Kevin Garello, Gilles Gaudin, Pierre-Jean Zermatten, Marius V. Costache, Stephane Auffret, Sebastien Bandiera, Bernard Rodmacq, Alain Schuhl, and Pietro Gambardella. Perpendicular switching of a single ferromagnetic layer induced by in-plane current injection. *Nature*, 476(7359):189–193, Aug 2011.

[229] T. Miyazaki and N. Tezuka. Giant magnetic tunneling effect in $Fe/Al_2O_3/Fe$ junction. *Journal of Magnetism and Magnetic Materials*, 139(3):L231 – L23, 1995.

[230] Y. Miyoshi, Y. Bugoslavsky, and L. F. Cohen. Andreev reflection spectroscopy of niobium point contacts in a magnetic field. *Phys. Rev. B*, 72:012502, Jul 2005.

[231] Y. Miyoshi, Y. Bugoslavsky, M. H. Syed, T. Robinson, L. F. Cohen, L. J. Singh, Z. H. Barber, C. E. A. Grigorescu, S. Gardelis, J. Giapintzakis, and W. Van Roy. Comparison of free surface polarization of NiMnSb and Co_2MnSi. *Applied Physics Letters*, 88(14), 2006.

[232] S. Mizukami, A. Sugihara, S. Iihama, Y. Sasaki, K. Z. Suzuki, and T. Miyazaki. Laser-induced THz magnetization precession for a tetragonal Heusler-like nearly compensated ferrimagnet. *Applied Physics Letters*, 108(1), 2016.

[233] S. Mizukami, F. Wu, A. Sakuma, J. Walowski, D. Watanabe, T. Kubota, X. Zhang, H. Naganuma, M. Oogane, Y. Ando, and T. Miyazaki. Long-lived ultrafast spin precession in manganese alloys films with a large perpendicular magnetic anisotropy. *Phys. Rev. Lett.*, 106:117201, Mar 2011.

[234] D. J. Monsma and S. S. P. Parkin. Spin polarization of tunneling current from ferromagnet/Al_2O_3 interfaces using copper-doped aluminum superconducting films. *Applied Physics Letters*, 77(5):720–722, 2000.

[235] J. S. Moodera, Lisa R. Kinder, Terrilyn M. Wong, and R. Meservey. Large magnetoresistance at room temperature in ferromagnetic thin film tunnel junctions. *Phys. Rev. Lett.*, 74:3273–3276, Apr 1995.

[236] J. S. Moodera, M. E. Taylor, and R. Meservey. Exchange-induced spin polarization of conduction electrons in paramagnetic metals. *Phys. Rev. B*, 40:11980–11982, Dec 1989.

[237] Jagadeesh S. Moodera, , Joaquim Nassar, and George Mathon. Spin-tunneling in ferromagnetic junctions. *Annual Review of Materials Science*, 29(1):381–432, 1999.

[238] Jagadeesh S. Moodera, Janusz Nowak, Lisa R. Kinder, Paul M. Tedrow, René J. M. van de Veerdonk, Bart A. Smits, Maarten van Kampen, Henk J. M. Swagten, and Wim J. M. de Jonge. Quantum well states in spin-dependent tunnel structures. *Phys. Rev. Lett.*, 83:3029–3032, Oct 1999.

[239] Jagadeesh S. Moodera, Janusz Nowak, and Rene J. M. van de Veerdonk. Interface magnetism and spin wave scattering in ferromagnet-insulator-ferromagnet tunnel junctions. *Phys. Rev. Lett.*, 80:2941–2944, Mar 1998.

[240] J. H. Mooij. Electrical conduction in concentrated disordered transition metal alloys. *Physica Status Solidi (a)*, 17(2):521–530, 1973.

[241] J. E. Moore and L. Balents. Topological invariants of time-reversal-invariant band structures. *Phys. Rev. B*, 75:121306, Mar 2007.

[242] V.L. Moruzzi and D.T. Teaney. Specific heat of EuS. *Solid State Communications*, 1(6):127 – 131, 1963.

[243] Sourin Mukhopadhyay, Sudesh Kumar Dhar, and Pratap Raychaudhuri. Study of spin fluctuations in using point contact Andreev reflection spectroscopy. *Applied Physics Letters*, 93(10), 2008.

[244] Sourin Mukhopadhyay, Pratap Raychaudhuri, Devang A. Joshi, and C. V. Tomy. Temperature dependence of transport spin polarization in $NdNi_5$ from point-contact Andreev reflection. *Phys. Rev. B*, 75:014504, Jan 2007.

[245] S. Murphy, J. Osing, and I.V. Shvets. Irreversible nanoscale morphology transformation of an Fe film on Mo(1 1 0) induced by a magnetic STM tip. *Surface Science*, 547(1âĂŞ2):139 – 148, 2003.

[246] B. Nadgorny, I. I. Mazin, M. Osofsky, R. J. Soulen, P. Broussard, R. M. Stroud, D. J. Singh, V. G. Harris, A. Arsenov, and Ya. Mukovskii. Origin of high transport spin polarization in

$La_{0.7}Sr_{0.3}MnO_3$: Direct evidence for minority spin states. *Phys. Rev. B*, 63:184433, Apr 2001.

[247] B. Nadgorny, R. J. Soulen, M. S. Osofsky, I. I. Mazin, G. Laprade, R. J. M. van de Veerdonk, A. A. Smits, S. F. Cheng, E. F. Skelton, and S. B. Qadri. Transport spin polarization of Ni_xFe_{1-x} : Electronic kinematics and band structure. *Phys. Rev. B*, 61:R3788–R3791, Feb 2000.

[248] Jun Nagamatsu, Norimasa Nakagawa, Takahiro Muranaka, Yuji Zenitani, and Jun Akimitsu. Superconductivity at 39 K in magnesium diboride. *Nature*, 410(6824):63–64, Mar 2001.

[249] S. R. Nagel. Temperature dependence of the resistivity in metallic glasses. *Phys. Rev. B*, 16:1694–1698, Aug 1977.

[250] T. M. Nakatani, A. Rajanikanth, Z. Gercsi, Y. K. Takahashi, K. Inomata, and K. Hono. Structure, magnetic property, and spin polarization of $Co_2FeAl_xSi_{1x}$ Heusler alloys. *Journal of Applied Physics*, 102(3), 2007.

[251] A. Narahara, K. Ito, T. Suemasu, Y. K. Takahashi, A. Ranajikanth, and K. Hono. Spin polarization of Fe_4N thin films determined by point-contact Andreev reflection. *Applied Physics Letters*, 94(20), 2009.

[252] Ajaya K. Nayak, Julia Erika Fischer, Yan Sun, Binghai Yan, Julie Karel, Alexander C. Komarek, Chandra Shekhar, Nitesh Kumar, Walter Schnelle, Jürgen Kübler, Claudia Felser, and Stuart S. P. Parkin. Large anomalous Hall effect driven by a nonvanishing Berry curvature in the noncolinear antiferromagnet Mn_3Ge. *Science Advances*, 2(4), 2016.

[253] A. D. Naylor, G. Burnell, and B. J. Hickey. Transport spin polarization of the rare-earth transition-metal alloy $Co_{1-x}Gd_x$. *Phys. Rev. B*, 85:064410, Feb 2012.

[254] Y. Köseoǵlu nd B. Aktaş, F. Yildiz, D.K. Kim, M. Toprak, and M. Muhammed. ESR studies on high-t_c superconductor MgB_2. *Physica C: Superconductivity*, 390(3):197 – 203, 2003.

[255] Branislav Nikolić and Philip B. Allen. Electron transport through a circular constriction. *Phys. Rev. B*, 60:3963–3969, Aug 1999.

[256] M. S. Osofsky, L. Cheng, W. E. Bailey, K. Bussmann, and D. Parker. Measurement of the transport spin polarization of FeV using point-contact Andreev reflection. *Applied Physics Letters*, 102(21), 2013.

[257] R. P. Panguluri, K. C. Ku, T. Wojtowicz, X. Liu, J. K. Furdyna, Y. B. Lyanda-Geller, N. Samarth, and B. Nadgorny. Andreev reflection and pair-breaking effects at the superconductor/magnetic semiconductor interface. *Phys. Rev. B*, 72:054510, Aug 2005.

[258] R. P. Panguluri, B. Nadgorny, T. Wojtowicz, W. L. Lim, X. Liu, and J. K. Furdyna. Measurement of spin polarization by Andreev reflection in ferromagnetic $In_{1x}Mn_xSb$ epilayers. *Applied Physics Letters*, 84(24):4947–4949, 2004.

[259] R. P. Panguluri, G. Tsoi, B. Nadgorny, S. H. Chun, N. Samarth, and I. I. Mazin. Point contact spin spectroscopy of ferromagnetic MnAs epitaxial films. *Phys. Rev. B*, 68:201307, Nov 2003.

[260] R. P. Panguluri, Changgan Zeng, H. H. Weitering, J. M. Sullivan, S. C. Erwin, and B. Nadgorny. Spin polarization and electronic structure of ferromagnetic Mn_5Ge_3 epilayers. *Physica Status Solidi (b)*, 242(8):R67–R69, 2005.

[261] Raghava P. Panguluri, P. Kharel, C. Sudakar, R. Naik, R. Suryanarayanan, V. M. Naik, A. G. Petukhov, B. Nadgorny, and G. Lawes. Ferromagnetism and spin-polarized charge carriers in In_2O_3 thin films. *Phys. Rev. B*, 79:165208, Apr 2009.

[262] Raghava P. Panguluri, B. Nadgorny, T. Wojtowicz, X. Liu, and J. K. Furdyna. Inelastic scattering and spin polarization in dilute magnetic semiconductor $(Ga,Mn)Sb$. *Applied Physics Letters*, 91(25), 2007.

[263] Myriam Pannetier, Claude Fermon, Gerald Le Goff, Juha Simola, and Emma Kerr. Femtotesla magnetic field measurement with magnetoresistive sensors. *Science*, 304(5677):1648–1650, 2004.

[264] J.-H. Park, E. Vescovo, H.-J. Kim, C. Kwon, R. Ramesh, and T. Venkatesan. Direct evidence for a half-metallic ferromagnet. *Nature*, 392(6678):794–796, Apr 1998.

[265] Jeong-Heon Park, Chando Park, Taehee Jeong, Matthew T. Moneck, Noel T. Nufer, and Jian-Gang Zhu. CoPt multilayer based magnetic tunnel junctions using perpendicular magnetic anisotropy. *Journal of Applied Physics*, 103(7), 2008.

[266] S. S. P. Parkin. Systematic variation of the strength and oscillation period of indirect magnetic exchange coupling through the 3 *d*, 4 *d*, and 5 *d* transition metals. *Phys. Rev. Lett.*, 67:3598–3601, Dec 1991.

[267] S. S. P. Parkin, N. More, and K. P. Roche. Oscillations in exchange coupling and magnetoresistance in metallic superlattice structures: Co/Ru, Co/Cr, and Fe/Cr. *Phys. Rev. Lett.*, 64:2304–2307, May 1990.

[268] Stuart S. P. Parkin, Christian Kaiser, Alex Panchula, Philip M. Rice, Brian Hughes, Mahesh Samant, and See-Hun Yang. Giant tunnelling magnetoresistance at room temperature with MgO (100) tunnel barriers. *Nat Mater*, 3(12):862–867, Dec 2004.

[269] S. J. Pickart and R. Nathans. Unpaired spin density in ordered Fe_3Al. *Phys. Rev.*, 123:1163–1171, Aug 1961.

[270] D. T. Pierce, R. J. Celotta, G. âĂŘC. Wang, W. N. Unertl, A. Galejs, C. E. Kuyatt, and S. R. Mielczarek. The gaas spin polarized electron source. *Review of Scientific Instruments*, 51(4):478–499, 1980.

[271] A. Plecenník, M. Grajcar, Š. Beňačka, P. Seidel, and A. Pfuch. Finite-quasiparticle-lifetime effects in the differential conductance of $Bi_2Sr_2CaCu_2O_y$ / Au junctions. *Phys. Rev. B*, 49:10016–10019, Apr 1994.

[272] W. P. Pratt, S.-F. Lee, J. M. Slaughter, R. Loloee, P. A. Schroeder, and J. Bass. Perpendicular giant magnetoresistances of Ag/Co multilayers. *Phys. Rev. Lett.*, 66:3060–3063, Jun 1991.

[273] E. M. Pugh and T. W. Lippert. Hall e.m.f. and intensity of magnetization. *Phys. Rev.*, 42:709–713, Dec 1932.

[274] D.C. Ralph and M.D. Stiles. Spin transfer torques. *Journal of Magnetism and Magnetic Materials*, 320(7):1190 – 1216, 2008.

[275] P. Raychaudhuri, A. P. Mackenzie, J. W. Reiner, and M. R. Beasley. Transport spin polarization in $SrRuO_3$ measured through point-contact Andreev reflection. *Phys. Rev. B*, 67:020411, Jan 2003.

[276] Cong Ren, J. Trbovic, R. L. Kallaher, J. G. Braden, J. S. Parker, S. von Molnár, and P. Xiong. Measurement of the spin polarization of the magnetic semiconductor EuS with zero-field and Zeeman-split Andreev reflection spectroscopy. *Phys. Rev. B*, 75:205208, May 2007.

[277] W. H. Rippard, M. R. Pufall, S. Kaka, S. E. Russek, and T. J. Silva. Direct-current induced dynamics in $Co_{90}Fe_{10}/Ni_{80}Fe_{20}$ point contacts. *Phys. Rev. Lett.*, 92:027201, Jan 2004.

[278] Karsten Rode, Nadjib Baadji, Davide Betto, Yong-Chang Lau, Hüseyin Kurt, M. Venkatesan, Plamen Stamenov, Stefano Sanvito, J. M. D. Coey, Emiliano Fonda, Edwige Otero, Fadi Choueikani, Philippe Ohresser, Florence Porcher, and Gilles André. Site-specific order and magnetism in tetragonal Mn_3Ga thin films. *Phys. Rev. B*, 87:184429, May 2013.

[279] Falk Röder, Gregor Hlawacek, Sebastian Wintz, René Hübner, Lothar Bischoff, Hannes Lichte, Kay Potzger, Jürgen Lindner, Jürgen Fassbender, and Rantej Bali. Direct depth- and

lateral- imaging of nanoscale magnets generated by ion impact. *Scientific Reports*, 5:16786 EP, Nov 2015.

[280] Andreas Roth, Christoph Brüne, Hartmut Buhmann, Laurens W. Molenkamp, Joseph Maciejko, Xiao-Liang Qi, and Shou-Cheng Zhang. Nonlocal transport in the quantum spin Hall state. *Science*, 325(5938):294–297, 2009.

[281] P. Rottländer, M. Hehn, and A. Schuhl. Determining the interfacial barrier height and its relation to tunnel magnetoresistance. *Phys. Rev. B*, 65:054422, Jan 2002.

[282] Rahul Roy. Topological phases and the quantum spin Hall effect in three dimensions. *Phys. Rev. B*, 79:195322, May 2009.

[283] M. A. Ruderman and C. Kittel. Indirect exchange coupling of nuclear magnetic moments by conduction electrons. *Phys. Rev.*, 96:99–102, Oct 1954.

[284] Benjamin Sacépé, Jeroen B. Oostinga, Jian Li, Alberto Ubaldini, Nuno J. G. Couto, Enrico Giannini, and Alberto F. Morpurgo. Gate-tuned normal and superconducting transport at the surface of a topological insulator. *Nat Commun*, 2:575, Dec 2011.

[285] Y. Sakuraba, S. Kokado, Y. Hirayama, T. Furubayashi, H. Sukegawa, S. Li, Y. K. Takahashi, and K. Hono. Quantitative analysis of anisotropic magnetoresistance in co2mnz and co2fez epitaxial thin films: A facile way to investigate spin-polarization in half-metallic heusler compounds. *Applied Physics Letters*, 104(17), 2014.

[286] Y. Sakuraba, M. Ueda, Y. Miura, K. Sato, S. Bosu, K. Saito, M. Shirai, T. J. Konno, and K. Takanashi. Extensive study of giant magnetoresistance properties in half-metallic $Co_2(Fe,Mn)Si$-based devices. *Applied Physics Letters*, 101(25), 2012.

[287] P Samuely, P Szabó, Z Pribulová, M E Tillman, S L Bud′ko, and P C Canfield. Possible two-gap superconductivity in $NdFeAsO_{0.9}F_{0.1}$ probed by point-contact Andreev-reflection spectroscopy. *Superconductor Science and Technology*, 22(1):014003, 2009.

[288] J. Sanchez-Barriga, A. Varykhalov, G. Springholz, H. Steiner, R. Kirchschlager, G. Bauer, O. Caha, E. Schierle, E. Weschke, A. A. Unal, S. Valencia, M. Dunst, J. Braun, H. Ebert, J. Minar, E. Golias, L. V. Yashina, A. Ney, V. Holy, and O. Rader. Nonmagnetic band gap at the Dirac point of the magnetic topological insulator $(Bi_{1-x}Mn_x)_2Se_3$. *Nat Commun*, 7, Feb 2016.

[289] Satoshi Sasaki, M. Kriener, Kouji Segawa, Keiji Yada, Yukio Tanaka, Masatoshi Sato, and Yoichi Ando. Topological Superconductivity in $Cu_xBi_2Se_3$. *Phys. Rev. Lett.*, 107:217001, Nov 2011.

[290] H. Sato, M. Yamanouchi, S. Ikeda, S. Fukami, F. Matsukura, and H. Ohno. Perpendicular-anisotropy CoFeB-MgO magnetic tunnel junctions with a MgO/CoFeB/Ta/CoFeB/MgO recording structure. *Applied Physics Letters*, 10(2), 2012.

[291] F. Schleicher, U. Halisdemir, D. Lacour, M. Gallart, S. Boukari, G. Schmerber, V. Davesne, P. Panissod, D. Halley, H. Majjad, Y. Henry, B. Leconte, A. Boulard, D. Spor, N. Beyer, C. Kieber, E. Sternitzky, O. Cregut, M. Ziegler, F. Montaigne, E. Beaurepaire, P. Gilliot, M. Hehn, and M. Bowen. Localized states in advanced dielectrics from the vantage of spin- and symmetry-polarized tunnelling across MgO. *Nat Commun*, 5, Aug 2014. Supplementary information available for this article at http://www.nature.com/ncomms/2014/140804/ncomms5547/suppinfo/ncomms5547_S1.html.

[292] Andreas Schmehl, Venu Vaithyanathan, Alexander Herrnberger, Stefan Thiel, Christoph Richter, Marco Liberati, Tassilo Heeg, Martin Rockerath, Lena Fitting Kourkoutis, Sebastian Muhlbauer, Peter Boni, David A. Muller, Yuri Barash, Jurgen Schubert, Yves Idzerda, Jochen Mannhart, and Darrell G. Schlom. Epitaxial integration of the highly spin-polarized ferromagnetic semiconductor euo with silicon and gan. *Nat Mater*, 6(11):882–887, Nov 2007.

[293] Thomas L. Schmidt, Stephan Rachel, Felix von Oppen, and Leonid I. Glazman. Inelastic electron backscattering in a generic helical edge channel. *Phys. Rev. Lett.*, 108:156402, Apr 2012.

[294] D.S. Schmool, E. Araújo, M.M. Amado, M. Alegria Feio, D. Martín Rodríguez, J.S. Garitaonandia, and F. Plazaola. Magnetic properties of the Fe-rich Fe_xAl_{1x} alloy system. *Journal of Magnetism and Magnetic Materials*, 272 âĂŞ 276, Part 2:1342 – 1344, 2004.

[295] Klaus M. Seemann, Vincent Baltz, Maureen MacKenzie, John N. Chapman, Bryan J. Hickey, and Christopher H. Marrows. Diffusive and ballistic current spin polarization in magnetron-sputtered $L1_0$-ordered epitaxial FePt. *Phys. Rev. B*, 76:174435, Nov 2007.

[296] Christoph Seibel, Jürgen Braun, Henriette Maaß, Hendrik Bentmann, Jan Minár, Tatyana V. Kuznetsova, Konstantin A. Kokh, Oleg E. Tereshchenko, Taichi Okuda, Hubert Ebert, and Friedrich Reinert. Photoelectron spin polarization in the $bi_2te_3(0001)$ topological insulator: Initial- and final-state effects in the photoemission process. *Phys. Rev. B*, 93:245150, Jun 2016.

[297] L. Shan, Y. Huang, C. Ren, and H. H. Wen. Vortex overlapping in a BCS type-II superconductor revealed by Andreev reflection spectroscopy. *Phys. Rev. B*, 73:134508, Apr 2006.

[298] Chang He Shang, Janusz Nowak, Ronnie Jansen, and Jagadeesh S. Moodera. Temperature dependence of magnetoresistance and surface magnetization in ferromagnetic tunnel junctions. *Phys. Rev. B*, 58:R2917–R2920, Aug 1998.

[299] Manish Sharma, Shan X. Wang, and Janice H. Nickel. Inversion of spin polarization and tunneling magnetoresistance in spin-dependent tunneling junctions. *Phys. Rev. Lett.*, 82:616–619, Jan 1999.

[300] Yu V Sharvin. On the possible method for studying Fermi surfaces. *Zh. Eksperim. i Teor. Fiz.*, 48, 1965.

[301] Masayuki Shiga and Yoji Nakamura. Mössbauer study of bcc Fe-Al alloys near the critical concentration. *Journal of the Physical Society of Japan*, 40(5):1295–1299, 1976.

[302] Iduru Shigeta, Osamu Murayama, Toru Hisamatsu, Alexander Brinkman, Alexander A. Golubov, Yukio Tanaka, Masakazu Ito, Hans Hilgenkamp, and Masahiko Hiroi. Spin polarization of Fe-rich ferromagnetic compounds in $Ru_{2x}Fe_xCrSi$ Heusler alloys. *Journal of Physics and Chemistry of Solids*, 72(5):604 – 607, 2011. Spectroscopies in Novel Superconductors 2010SNS 2010.

[303] Joel D. Shore, Ming Huang, Alan T. Dorsey, and James P. Sethna. Density of states in a vortex core and the zero-bias tunneling peak. *Phys. Rev. Lett.*, 62:3089–3092, Jun 1989.

[304] Prabodh Shukla and Michael Wortis. Spin-glass behavior in iron-aluminum alloys: A microscopic model. *Phys. Rev. B*, 21:159–164, Jan 1980.

[305] R.D. Shull, H. Okamoto, and P.A. Beck. Transition from ferromagnetism to mictomagnetism in FeâĂŤAl alloys. *Solid State Communications*, 20(9):863 – 868, 1976.

[306] John G. Simmons. Generalized thermal J âĂŘ V characteristic for the electric tunnel effect. *Journal of Applied Physics*, 35(9):2655–2658, 1964.

[307] Surjeet Singh, Goutam Sheet, Pratap Raychaudhuri, and Sudesh Kumar Dhar. $CeMnNi_4$: A soft ferromagnet with a high degree of transport spin polarization. *Applied Physics Letters*, 88(2), 2006.

[308] S. Skalski, O. Betbeder-Matibet, and P. R. Weiss. Properties of superconducting alloys containing paramagnetic impurities. *Phys. Rev.*, 136:A1500–A1518, Dec 1964.

[309] Witold Skowroński, Takayuki Nozaki, Duong D. Lam, Yoichi Shiota, Kay Yakushiji, Hitoshi Kubota, Akio Fukushima, Shinji Yuasa, and Yoshishige Suzuki. Underlayer mate-

rial influence on electric-field controlled perpendicular magnetic anisotropy in CoFeB/MgO magnetic tunnel junctions. *Phys. Rev. B*, 91:184410, May 2015.

[310] J. C. Slonczewski. Conductance and exchange coupling of two ferromagnets separated by a tunneling barrier. *Phys. Rev. B*, 39:6995–7002, Apr 1989.

[311] J.C. Slonczewski. Current-driven excitation of magnetic multilayers. *Journal of Magnetism and Magnetic Materials*, 159(1):L1 – L7, 1996.

[312] J. Smit. The spontaneous Hall effect in ferromagnetics II. *Physica*, 24(1):39 – 51, 1958.

[313] Gabor A. Somorjai. *Chemistry in Two Dimensions: Surfaces*. Cornell University Press, The address, 1 edition, 1981.

[314] R. J. Soulen, J. M. Byers, M. S. Osofsky, B. Nadgorny, T. Ambrose, S. F. Cheng, P. R. Broussard, C. T. Tanaka, J. Nowak, J. S. Moodera, A. Barry, and J. M. D. Coey. Measuring the spin polarization of a metal with a superconducting point contact. *Science*, 282(5386):85–88, 1998.

[315] A. Srinivasan, A. Rajanikanth, Y.K. Takahashi, and K. Hono. Magnetic properties and spin polarization of $Co_2Mn(Si_xSn_{1x})$ alloys containing two $L2_1$ phases. *Journal of Alloys and Compounds*, 514:195 – 198, 2012.

[316] P. Stamenov. Point contact andreev reflection from erbium: The role of external magnetic field and the sign of the spin polarization. *Journal of Applied Physics*, 111(7), 2012.

[317] P. Stamenov and J. M. D. Coey. Fermi level spin polarization of polycrystalline thulium by point contact andreev reflection spectroscopy. *Journal of Applied Physics*, 109(7), 2011.

[318] Plamen Stamenov. *Metals, Semimetals and Semiconductors for Spinelectronics*. PhD thesis, Department of Physics, University of Dublin, Department of Physics, University of Dublin, 10 2007.

[319] Mary Beth Stearns. Simple explanation of tunneling spin-polarization of Fe, Co, Ni and its alloys. *Journal of Magnetism and Magnetic Materials*, 5(2):167 – 171, 1977.

[320] M. D. Stiles and A. Zangwill. Anatomy of spin-transfer torque. *Phys. Rev. B*, 66:014407, Jun 2002.

[321] G. J. Strijkers, Y. Ji, F. Y. Yang, C. L. Chien, and J. M. Byers. Andreev reflections at metal/superconductor point contacts: Measurement and analysis. *Phys. Rev. B*, 63:104510, Feb 2001.

[322] Anders Ström, Henrik Johannesson, and G. I. Japaridze. Edge dynamics in a quantum spin hall state: Effects from rashba spin-orbit interaction. *Phys. Rev. Lett.*, 104:256804, Jun 2010.

[323] Gang Su, Yufan Li, Dazhi Hou, Xiaofeng Jin, Houfang Liu, and Shouguo Wang. Anomalous hall effect in amorphous $Co_{40}Fe_{40}B_{20}$. *Phys. Rev. B*, 90:214410, Dec 2014.

[324] H Suderow, I Guillamón, J G Rodrigo, and S Vieira. Imaging superconducting vortex cores and lattices with a scanning tunneling microscope. *Superconductor Science and Technology*, 27(6):063001, 2014.

[325] Yoshitaka Suezawa, Fumiaki Takahashi, and Yasuo Gondō. Spin-polarized electron tunneling in $Ni/Al_2O_3/Co$ junction and large magnetoresistance of Ni/Co double layers. *Japanese Journal of Applied Physics*, 31(10A):L1415, 1992.

[326] J. Z. Sun. Spin-current interaction with a monodomain magnetic body: A model study. *Phys. Rev. B*, 62:570–578, Jul 2000.

[327] Kyoichi Suzuki, Yuichi Harada, Koji Onomitsu, and Koji Muraki. Edge channel transport in the InAs/GaSb topological insulating phase. *Phys. Rev. B*, 87:235311, Jun 2013.

[328] L. Taillefer, J. Flouquet, and G.G. Lonzarich. Normal and superconducting phases of heavy fermions. *Physica B: Condensed Matter*, 169(1):257 – 270, 1991.

[329] S. Takahashi. Local environment effects in cold-worked Fe-Al alloys. *Journal of Magnetism and Magnetic Materials*, 54:1065 – 1066, 1986.

[330] Y. K. Takahashi, N. Hase, M. Kodzuka, A. Itoh, T. Koganezawa, T. Furubayashi, S. Li, B. S. D. Ch. S. Varaprasad, T. Ohkubo, and K. Hono. Structure and magnetoresistance of current-perpendicular-to-plane pseudo spin valves using $Co_2Mn(Ga_{0.25}Ge_{0.75})$ Heusler alloy. *Journal of Applied Physics*, 113(22), 2013.

[331] Yukiko K. Takahashi and Kazuhiro Hono. Spin polarization in heusler alloy films. In Claudia Felser and Atsufumi Hirohata, editors, *Heusler Alloys: Properties, Growth, Applications*, pages 295–318. Springer International Publishing, Cham, 2016.

[332] Jianshi Tang, Li-Te Chang, Xufeng Kou, Koichi Murata, Eun Sang Choi, Murong Lang, Yabin Fan, Ying Jiang, Mohammad Montazeri, Wanjun Jiang, Yong Wang, Liang He, and Kang L. Wang. Electrical detection of spin-polarized surface states conduction in $(Bi_{0.53}Sb_{0.47})_2Te_3$ topological insulator. *Nano Letters*, 14(9):5423–5429, 2014. PMID: 25158276.

[333] A. Taylor and R.M. Jones. Constitution and magnetic properties of iron-rich iron-aluminum alloys. *Journal of Physics and Chemistry of Solids*, 6(1):16 – 37, 1958.

[334] P. M. Tedrow and R. Meservey. Spin Polarization of Electrons Tunneling from Films of Fe, Co, Ni, and Gd. *Phys. Rev. B*, 7:318–326, Jan 1973.

[335] P. M. Tedrow, J. E. Tkaczyk, and A. Kumar. Spin-polarized electron tunneling study of an artificially layered superconductor with internal magnetic field: EuO-Al. *Phys. Rev. Lett.*, 56:1746–1749, Apr 1986.

[336] P.M. Tedrow and R. Meservey. Spin-dependent electron tunneling in superconducting vanadium and vanadium-titanium thin films. *Physics Letters A*, 69(4):285 – 286, 1978.

[337] J. M. Teixeira, J. Ventura, J. P. Araujo, J. B. Sousa, P. Wisniowski, S. Cardoso, and P. P. Freitas. Resonant tunneling through electronic trapping states in thin MgO magnetic junctions. *Phys. Rev. Lett.*, 106:196601, May 2011.

[338] P. Thapa, G. Lawes, B. Nadgorny, R. Naik, C. Sudakar, W.J. Schaff, and A. Dixit. Ferromagnetism and spin polarization in indium nitride, indium oxynitride, and Cr substituted indium oxynitride films. *Applied Surface Science*, 295:189 – 193, 2014.

[339] P. A. Thiry, M. Liehr, J. J. Pireaux, and R. Caudano. Infrared optical constants of insulators determined by high-resolution electron-energy-loss spectroscopy. *Phys. Rev. B*, 29:4824–4826, Apr 1984.

[340] Naganivetha Thiyagarajah, Yong-Chang Lau, Davide Betto, Kiril Borisov, J. M. D. Coey, Plamen Stamenov, and Karsten Rode. Giant spontaneous Hall effect in zero-moment Mn_2Ru_xGa. *Applied Physics Letters*, 106(12), 2015.

[341] Yuan Tian, Li Ye, and Xiaofeng Jin. Proper Scaling of the Anomalous Hall Effect. *Phys. Rev. Lett.*, 103:087206, Aug 2009.

[342] Michael Tinkham. *Introduction to superconductivity*. Dover Publications, Inc., The address, 2 edition, 2004.

[343] C Tiusan, F Greullet, M Hehn, F Montaigne, S Andrieu, and A Schuhl. Spin tunnelling phenomena in single-crystal magnetic tunnel junction systems. *Journal of Physics: Condensed Matter*, 19(16):165201, 2007.

[344] Huseyin Tokuc. *Investigation of Organic/Ferromagnetic Interface and Magnetoresistive Characteristics of Small Molecule Organic Semiconductors*. PhD thesis, Department of Physics, University of Dublin, 8 2013.

[345] M. Tortello, D. Daghero, G. A. Ummarino, R. S. Gonnelli, V. A. Stepanov, and J. S. Kim. Point-Contact Andreev-Reflection Spectroscopy in the Fe-based Superconductor $LaFeAsO_{1x}F_x$. *Journal of Superconductivity and Novel Magnetism*, 22(6):553–557, 2009.

[346] E. Y. Tsymbal, A. Sokolov, I. F. Sabirianov, and B. Doudin. Resonant inversion of tunneling magnetoresistance. *Phys. Rev. Lett.*, 90:186602, May 2003.

[347] Evgeny Y Tsymbal, Oleg N Mryasov, and Patrick R LeClair. Spin-dependent tunnelling in magnetic tunnel junctions. *Journal of Physics: Condensed Matter*, 15(4):R109, 2003.

[348] C. S. Turel, I. J. Guilaran, P. Xiong, and J. Y. T. Wei. Andreev nanoprobe of half-metallic CrO_2 films using superconducting cuprate tips. *Applied Physics Letters*, 99(19), 2011.

[349] J. Unguris, A. Seiler, R. J. Celotta, D. T. Pierce, P. D. Johnson, and N. V. Smith. Spin-polarized inverse photoelectron spectroscopy of solid surfaces: Ni(110). *Phys. Rev. Lett.*, 49:1047–1050, Oct 1982.

[350] I. T. M. Usman, K. A. Yates, J. D. Moore, K. Morrison, V. K. Pecharsky, K. A. Gschneidner, T. Verhagen, J. Aarts, V. I. Zverev, J. W. A. Robinson, J. D. S. Witt, M. G. Blamire, and L. F. Cohen. Evidence for spin mixing in holmium thin film and crystal samples. *Phys. Rev. B*, 83:144518, Apr 2011.

[351] J. M. Valentine and C. L. Chien. Determination of spin polarization of Gd and Dy by point-contact Andreev reflection. *Journal of Applied Physics*, 99(8), 2006.

[352] T. Valet and A. Fert. Theory of the perpendicular magnetoresistance in magnetic multilayers. *Phys. Rev. B*, 48:7099–7113, Sep 1993.

[353] T. Valla, Z.-H. Pan, D. Gardner, Y. S. Lee, and S. Chu. Photoemission Spectroscopy of Magnetic and Nonmagnetic Impurities on the Surface of the Bi_2Se_3 Topological Insulator. *Phys. Rev. Lett.*, 108:117601, Mar 2012.

[354] H. van Leuken and R. A. de Groot. Half-metallic antiferromagnets. *Phys. Rev. Lett.*, 74:1171–1173, Feb 1995.

[355] P. C. van Son, H. van Kempen, and P. Wyder. Andreev reflection and geometrical resonance effects for a gradual variation of the pair potential near the normal-metal – superconductor interface. *Phys. Rev. B*, 37:5015–5023, Apr 1988.

[356] B.S.D.Ch.S. Varaprasad, A. Rajanikanth, Y.K. Takahashi, and K. Hono. Highly spin-polarized $Co_2MnGa_{0.5}Sn_{0.5}$ Heusler compound. *Acta Materialia*, 57(9):2702 – 2709, 2009.

[357] B.S.D.Ch.S. Varaprasad, A. Rajanikanth, Y.K. Takahashi, and K. Hono. Spin polarization measurements of $Co_2Mn(Ga_{0.5}Sn_{0.5})$ thin films. *Journal of Magnetism and Magnetic Materials*, 323(23):3092 – 3097, 2011.

[358] B.S.D.Ch.S. Varaprasad, A. Srinivasan, Y.K. Takahashi, M. Hayashi, A. Rajanikanth, and K. Hono. Spin polarization and Gilbert damping of $Co_2Fe(Ga_xGe_{1x})$ Heusler alloys. *Acta Materialia*, 60(18):6257 – 6265, 2012.

[359] A. Vedyayev, N. Ryzhanova, C. Lacroix, L. Giacomoni, and B. Dieny. Resonance in tunneling through magnetic valve tunnel junctions. *EPL (Europhysics Letters)*, 39(2):219, 1997.

[360] M. Veldhorst, M. Snelder, M. Hoek, T. Gang, V. K. Guduru, X. L. Wang, U. Zeitler, W. G. van der Wiel, A. A. Golubov, H. Hilgenkamp, and A. Brinkman. Josephson supercurrent through a topological insulator surface state. *Nat Mater*, 11(5):417–421, May 2012.

[361] I. Vincze. Average magnetization of FeAl alloys. *Physica Status Solidi (a)*, 7(1):K43–K47, 1971.

[362] A. Wachowiak, J. Wiebe, M. Bode, O. Pietzsch, M. Morgenstern, and R. Wiesendanger. Direct observation of internal spin structure of magnetic vortex cores. *Science*, 298(5593):577–580, 2002.

[363] Dexin Wang, C. Nordman, J. M. Daughton, Zhenghong Qian, and J. Fink. 70 % TMR at room temperature for SDT sandwich junctions with CoFeB as free and reference layers. *IEEE Transactions on Magnetics*, 40(4):2269–2271, July 2004.

[364] L. Wang, T. Y. Chen, and C. Leighton. Spin-dependent band structure effects and measurement of the spin polarization in the candidate half-metal CoS_2. *Phys. Rev. B*, 69:094412, Mar 2004.

[365] S. G. Wang, R. C. C. Ward, G. X. Du, X. F. Han, C. Wang, and A. Kohn. Temperature dependence of giant tunnel magnetoresistance in epitaxial $Fe/MgO/Fe$ magnetic tunnel junctions. *Phys. Rev. B*, 78:180411, Nov 2008.

[366] Roald K. Wangsness. Sublattice effects in magnetic resonance. *Phys. Rev.*, 91:1085–1091, Sep 1953.

[367] Richard Watts-Tobin, Lorenz Kramer, and Werner Pesch. Density of states, entropy, and specific heat for dirty type II superconductors at arbitrary temperature. *Journal of Low Temperature Physics*, 17(1):71–86, 1974.

[368] H.-X. Wei, Q.-H. Qin, Q.-L. Ma, X.-G. Zhang, and X.-F. Han. Inelastic electron tunneling spectrum from surface magnon and magnetic impurity scatterings in magnetic tunnel junctions. *Phys. Rev. B*, 82:134436, Oct 2010.

[369] G. K. Wertheim, V. Jaccarino, J. H. Wernick, and D. N. E. Buchanan. Range of the exchange interaction in iron alloys. *Phys. Rev. Lett.*, 12:24–27, Jan 1964.

[370] P. S. Westbrook and A. Javan. Finite-bias resistance peaks in nanoscale superconductor–normal-metal Ta-W point contacts. *Phys. Rev. B*, 59:14606–14611, Jun 1999.

[371] G Wexler. The size effect and the non-local Boltzmann transport equation in orifice and disk geometry. *Proceedings of the Physical Society*, 89(4):927, 1966.

[372] R. Wiesendanger, H.-J. Güntherodt, G. Güntherodt, R. J. Gambino, and R. Ruf. Observation of vacuum tunneling of spin-polarized electrons with the scanning tunneling microscope. *Phys. Rev. Lett.*, 65:247–250, Jul 1990.

[373] Roland Wiesendanger. Spin mapping at the nanoscale and atomic scale. *Rev. Mod. Phys.*, 81:1495–1550, Nov 2009.

[374] J. R. Williams, A. J. Bestwick, P. Gallagher, Seung Sae Hong, Y. Cui, Andrew S. Bleich, J. G. Analytis, I. R. Fisher, and D. Goldhaber-Gordon. Unconventional Josephson Effect in Hybrid Superconductor-Topological Insulator Devices. *Phys. Rev. Lett.*, 109:056803, Jul 2012.

[375] E.P. Wohlfarth. A simple band theory interpretation of the spin polarized photoelectron data for nickel and cobalt. *Physics Letters A*, 36(2):131 – 132, 1971.

[376] E. L. Wolf and D. L. Losee. Spectroscopy of Kondo and Spin-Flip Scattering: High-Field Tunneling Studies of Schottky-Barrier Junctions. *Phys. Rev. B*, 2:3660–3687, Nov 1970.

[377] E. L. Wolf, D. L. Losee, D. E. Cullen, and W. Dale Compton. Anomalous metal-semiconductor tunneling near the Mott transition. *Phys. Rev. Lett.*, 26:438–442, Feb 1971.

[378] E. L. Wolf, R. H. Wallis, and C. J. Adkins. Compensation independence of anomalous metal-semiconductor tunneling near the Mott transition. *Phys. Rev. B*, 12:1603–1607, Aug 1975.

[379] G. T. Woods, R. J. Soulen, I. Mazin, B. Nadgorny, M. S. Osofsky, J. Sanders, H. Srikanth, W. F. Egelhoff, and R. Datla. Analysis of point-contact andreev reflection spectra in spin polarization measurements. *Phys. Rev. B*, 70:054416, Aug 2004.

[380] Michael A. Woolf and F. Reif. Effect of magnetic impurities on the density of states of superconductors. *Phys. Rev.*, 137:A557–A564, Jan 1965.

[381] D. C. Worledge and T. H. Geballe. Maki analysis of spin-polarized tunneling in an oxide ferromagnet. *Phys. Rev. B*, 62:447–451, Jul 2000.

[382] L. Andrew Wray, Su-Yang Xu, Yuqi Xia, David Hsieh, Alexei V. Fedorov, Yew San Hor, Robert J. Cava, Arun Bansil, Hsin Lin, and M. Zahid Hasan. A topological insulator surface under strong Coulomb, magnetic and disorder perturbations. *Nat Phys*, 7(1):32–37, Jan 2011.

[383] Lin Wu, Kai Zhu, Di Yue, Yuan Tian, and Xiaofeng Jin. Anomalous Hall effect in localization regime. *Phys. Rev. B*, 93:214418, Jun 2016.

[384] W. Wulfhekel, H.F. Ding, and J. Kirschner. Tunneling magnetoresistance through a vacuum gap. *Journal of Magnetism and Magnetic Materials*, 242 - 245, Part 1:47 – 52, 2002. Proceedings of the Joint European Magnetic Symposia (JEMS'01).

[385] Wulf Wulfhekel and Jürgen Kirschner. Spin-polarized scanning tunneling microscopy on ferromagnets. *Applied Physics Letters*, 75(13):1944–1946, 1999.

[386] Bin Xia, Yu Wu, Hui Wen Ho, Chang Ke, Wen Dong Song, Cheng Hon Alfred Huan, Jer Lai Kuo, Wei Guang Zhu, and Lan Wang. A possible origin of room temperature ferromagnetism in Indium - Tin oxide thin film: Surface spin polarization and ferromagnetism. *Physica B: Condensed Matter*, 406(17):3166 – 3169, 2011.

[387] K. Xia, P. J. Kelly, G. E. W. Bauer, and I. Turek. Spin-dependent transparency of ferromagnet/superconductor interfaces. *Phys. Rev. Lett.*, 89:166603, Sep 2002.

[388] Y. Xia, D. Qian, D. Hsieh, L. Wray, A. Pal, H. Lin, A. Bansil, D. Grauer, Y. S. Hor, R. J. Cava, and M. Z. Hasan. Observation of a large-gap topological-insulator class with a single Dirac cone on the surface. *Nat Phys*, 5(6):398–402, Jun 2009.

[389] Jiang Xiao, A. Zangwill, and M. D. Stiles. Boltzmann test of Slonczewski's theory of spin-transfer torque. *Phys. Rev. B*, 70:172405, Nov 2004.

[390] Su-Yang Xu, Madhab Neupane, Chang Liu, Duming Zhang, Anthony Richardella, L. Andrew Wray, Nasser Alidoust, Mats Leandersson, Thiagarajan Balasubramanian, Jaime Sanchez-Barriga, Oliver Rader, Gabriel Landolt, Bartosz Slomski, Jan Hugo Dil, Jurg Osterwalder, Tay-Rong Chang, Horng-Tay Jeng, Hsin Lin, Arun Bansil, Nitin Samarth, and M. Zahid Hasan. Hedgehog spin texture and Berry's phase tuning in a magnetic topological insulator. *Nat Phys*, 8(8):616–622, Aug 2012.

[391] Su-Yang Xu, Y. Xia, L. A. Wray, S. Jia, F. Meier, J. H. Dil, J. Osterwalder, B. Slomski, A. Bansil, H. Lin, R. J. Cava, and M. Z. Hasan. Topological phase transition and texture inversion in a tunable topological insulator. *Science*, 332(6029):560–564, 2011.

[392] F. J. Yang, Y. Sakuraba, S. Kokado, Y. Kota, A. Sakuma, and K. Takanashi. Anisotropic magnetoresistance in $Co_2(Fe,Mn)Si$ Heusler epitaxial films: A fingerprint of half-metallicity. *Phys. Rev. B*, 86:020409, Jul 2012.

[393] H. Yang, S. Yang, C. Kaiser, and S. Parkin. Resonant inversion of tunneling magnetoresistance using MgO/NiO barriers. In *Magnetics Conference, 2006. INTERMAG 2006. IEEE International*, pages 865–865, May 2006.

[394] Hyunsoo Yang, See-Hun Yang, Christian Kaiser, and Stuart Parkin. Tunneling spin polarization measurements from ferromagnet/MgO tunnel junctions using NbN superconductor. *Applied Physics Letters*, 88(18), 2006.

[395] Hyunsoo Yang, See-Hun Yang, Dong-Chen Qi, Andrivo Rusydi, Hiroyo Kawai, Mark Saeys, Titus Leo, David J. Smith, and Stuart S. P. Parkin. Negative tunneling magnetoresistance by canted magnetization in MgO/NiO tunnel barriers. *Phys. Rev. Lett.*, 106:167201, Apr 2011.

[396] I. K. Yanson and Yu. G. Naidyuk. Advances in point-contact spectroscopy: two-band superconductor mgb2 (review). *Low Temperature Physics*, 30(4):261–274, 2004.

[397] IK Yanson. Nonlinear effects in the electric conductivity of point junctions and electron-phonon interaction in normal metals. *Soviet Journal of Experimental and Theoretical Physics*, 39:506, 1974.

[398] Oleg V. Yazyev, Joel E. Moore, and Steven G. Louie. Spin polarization and transport of surface states in the topological insulators bi_2se_3 and bi_2te_3 from first principles. *Phys. Rev. Lett.*, 105:266806, Dec 2010.

[399] E.P. Yelsukov, E.V. Voronina, and V.A. Barinov. Mössbauer study of magnetic properties formation in disordered Fe-Al alloys. *Journal of Magnetism and Magnetic Materials*, 115(2):271 – 280, 1992.

[400] Kei Yosida. Magnetic properties of Cu-Mn alloys. *Phys. Rev.*, 106:893–898, Jun 1957.

[401] C. Y. You, T. Ohkubo, Y. K. Takahashi, and K. Hono. Boron segregation in crystallized MgO/amorphous-$Co_{40}Fe_{40}B_{20}$ thin films. *Journal of Applied Physics*, 104(3), 2008.

[402] S. Yuasa, T. Nagahama, and Y. Suzuki. Spin-polarized resonant tunneling in magnetic tunnel junctions. *Science*, 297(5579):234–237, 2002.

[403] Shinji Yuasa, Taro Nagahama, Akio Fukushima, Yoshishige Suzuki, and Koji Ando. Giant room-temperature magnetoresistance in single-crystal Fe/MgO/Fe magnetic tunnel junctions. *Nat Mater*, 3(12):868–871, Dec 2004.

[404] Changgan Zeng, Yugui Yao, Qian Niu, and Hanno H. Weitering. Linear Magnetization Dependence of the Intrinsic Anomalous Hall Effect. *Phys. Rev. Lett.*, 96:037204, Jan 2006.

[405] Zhongming Zeng, Pedram Khalili Amiri, Ilya N. Krivorotov, Hui Zhao, Giovanni Finocchio, Jian-Ping Wang, Jordan A. Katine, Yiming Huai, Juergen Langer, Kosmas Galatsis, Kang L. Wang, and HongWen Jiang. High-power coherent microwave emission from magnetic tunnel junction nano-oscillators with perpendicular anisotropy. *ACS Nano*, 6(7):6115–6121, 2012. PMID: 22663148.

[406] Duming Zhang, Jian Wang, Ashley M. DaSilva, Joon Sue Lee, Humberto R. Gutierrez, Moses H. W. Chan, Jainendra Jain, and Nitin Samarth. Superconducting proximity effect and possible evidence for Pearl vortices in a candidate topological insulator. *Phys. Rev. B*, 84:165120, Oct 2011.

[407] H. J. Zhang, S. Yamamoto, Y. Fukaya, M. Maekawa, H. Li, A. Kawasuso, T. Seki, E. Saitoh, and K. Takanashi. Current-induced spin polarization on metal surfaces probed by spin-polarized positron beam. *Scientific Reports*, 4:4844 EP, Apr 2014. Article.

[408] J. Zhang, C.-Z. Chang, Z. Zhang, J. Wen, X. Feng, K. Li, M. Liu, K. He, L. Wang, X. Chen, Q.-K. Xue, X. Ma, and Y. Wang. Band structure engineering in $(Bi_{1-x}Sb_x)_2Te_3$ ternary topological insulators. *Nature Communications*, 2(1), 2011.

[409] S. Zhang, P. M. Levy, A. C. Marley, and S. S. P. Parkin. Quenching of magnetoresistance by hot electrons in magnetic tunnel junctions. *Phys. Rev. Lett.*, 79:3744–3747, Nov 1997.

[410] Shufeng Zhang and Peter M. Levy. Conductivity perpendicular to the plane of multilayered structures. *Journal of Applied Physics*, 69(8):4786–4788, 1991.